FRIEDRICH-SCHILLER-
UNIVERSITÄT
JENA

Novel Ru-photosensitizer as versatile building blocks for (molecular) architectures

Dissertation

(kumulativ)

zur Erlangung des akademischen Grades

doctor rerum naturalium (Dr. rer. nat.)

vorgelegt dem Rat der Chemisch-Geowissenschaftlichen Fakultät

der Friedrich-Schiller-Universität Jena

von Dipl.-Chem. Tina Mede, geb. Schlotthauer

geboren am 20.04.1989 in Schmalkalden

Gutachter:

1. Prof. Dr. Ulrich. S. Schubert − FSU Jena…….
2. Prof. Dr. Benjamin Dietzek − FSU Jena

   ……..…….

Tag der öffentlichen Verteidigung: 18.Mai.2018

Table of content

Documentation of authorship

This section contains a list of individual authors' contributions to the publications reprinted in this thesis.

P1) " Asymmetric cyclometalated Ru^{II} polypyridyl-type complexes with π-extended carbanionic donor sets" T. Schlotthauer,[1] G. A. Parada,[2] H. Görls,[3] S. Ott,[4] M. Jäger,[5] U. S. Schubert,[6] *Inorg. Chem.* **2017**, *56*, 7720-7730.						
Author	1	2	3	4	5	6
Conceptual contribution	×				×	
Synthesis and characterization of the complexes	×					
Spectroscopic characterization		×		×		
Chrystallographic characterization			×			
Computational results					×	
Preparation of the manuscript	×				×	
Correction of the manuscript	×	×		×	×	×
Supervision of T. Mede					×	×
Proposal for crediting publication equivalents	1.0					

P2) "Exploring the coordination mechanism towards multi-functionalized Ru^{II} polypyridyl-type sensitizer: An experimental and computational study" T. Mede,[1] M. Jäger,[2] U. S. Schubert,[3] submitted.			
Author	1	2	3
Conceptual contribution	×	×	
Synthesis	×		
Computational results		×	
Preparation of the manuscript	×		
Correction of the manuscript	×	×	×
Supervision of T. Mede		×	×
Proposal for crediting publication equivalents	1.0		

P3) **“**“Chemistry-on-the-complex”: Functional Ru^{II} polypyridyl-type sensitizer as divergent building blocks**”** T. Mede,[1] M. Jäger,[2] U. S. Schubert,[3] submitted.			
Author	1	2	3
Conceptual contribution	×	×	
Preparation of the manuscript	×		
Correction of the manuscript	×	×	×
Supervision of T. Mede		×	×
Proposal for crediting publication equivalents	0.5		

P4) “Mild electropolymerization and monitoring of continuous film formation for photoredox-active Ru metallopolymers” T. Schlotthauer,[1] C. Friebe,[2] A. Schwenke,[3] M. Jäger,[4] U. S. Schubert,[5] *J. Mater. Chem. C* **2017**, *5*, 2636-2648.					
Author	1	2	3	4	5
Conception of the manuscript	×	×		×	
Synthesis of complexes	×				
Electropolymerization and characterization	×	×			
Preparation of the manuscript	×	×			
SEM imaging			×		
Correction of the manuscript	×	×	×	×	×
Supervision of T. Mede				×	×
Proposal for crediting publication equivalents	1.0				

P5) "Modular assembly of poly(naphthalene diimide) and Ru(II) dyes for an efficient light-induced charge separation in hierarchically controlled polymer architectures" R. Schroot,[1] T. Schlotthauer,[2] U. S. Schubert,[3] M. Jäger,[4] *Macromolecules* **2016**, *49*, 2112-2123.				
Author	1	2	3	4
Conception of the manuscript	×	×		×
Synthesis of monomers, polymers, complexes and dyads	×	×		
Preparation of the manuscript	×	×		
Spectroscopic characterization	×	×		
Correction of the manuscript	×	×	×	×
Supervision of T. Mede			×	×
Proposal for crediting publication equivalents	1.0	1.0		

P6) "Hydrophilic poly(naphthalene diimide)-based acceptor-photosensitizer dyads: Towards water-processible modular photoredox-active architectures" R. Schroot,[1] T. Schlotthauer,[2] M. Jäger,[3] U. S. Schubert,[4] *Macromol. Chem. Phys.* **2017**, *218*, 1600534.				
Author	1	2	3	4
Conception of the manuscript	×		×	
Synthesis and characterization of monomers, polymers, and dyad	×			
Complex synthesis and characterization		×		
Preparation of the manuscript	×	×		
Correction of the manuscript	×	×	×	×
Supervision of T. Mede			×	×
Proposal for crediting publication equivalents	1.0	0.5		

P7) "A *multi*donor-photosensitizer-*multi*acceptor triad for long-lived directional charge separation" T. Schlotthauer,[1] R. Schroot,[2] S. Glover,[3] L. Hammarström,[4] M. Jäger,[5] U. S. Schubert,[6] *PCCP* **2017**, *19*, 28572-28578.						
Author	1	2	3	4	5	6
Conceptual contribution	×	×			x	
Synthesis of monomers and polymers		×				
Complex synthesis	×					
Synthesis and characterization of dyad and triad	×					
Spectroscopic studies			×			
Preparation of the manuscript	×	×			×	
Correction of the manuscript	×	×	×	×	×	×
Supervision of T. Mede					×	×
Proposal for crediting publication equivalents	1.0	0.5				

P8) "Extending long-lived charge separation between donor and acceptor blocks in novel copolymer architectures featuring a sensitizer core." R. Schroot,[1] T. Schlotthauer,[2] B. Dietzek,[3] M. Jäger,[4] U. S. Schubert,[5] *Chem. Eur. J.* **2017**, *23*, 16484-16490.					
Author	1	2	3	4	5
Conception of the manuscript	×			×	
Synthesis and characterization of monomers, polymers, dyad and triad	×				
Complex synthesis and characterization		×			
Transient absorption spectroscopy				×	
Preparation of the manuscript	×	×			
Correction of the manuscript	×	×	×	×	×
Supervision of T. Mede				×	×
Proposal for crediting publication equivalents	1.0	0.5			

Erklärung zu den Eigenanteilen des Promovenden/der Promovendin sowie der weiteren Doktoranden/Doktorandinnen als Koautoren an den Publikationen und Zweitpublikationsrechten bei einer kumulativen Dissertation

Für alle in dieser kumulativen Dissertation verwendeten Manuskripte liegen die notwendigen Genehmigungen der Verlage („Reprint permissions") für die Zweitpublikation vor.

Die Co-Autoren der in dieser kumulativen Dissertation verwendeten Manuskripte sind sowohl über die Nutzung, als auch über die oben angegebenen Eigenanteile der weiteren Doktoranden/Doktorandinnen als Co-Autoren an den Publikationen und Zweitpublikationsrechten bei einer kumulativen Dissertation informiert und stimmen dem zu (es wird empfohlen, diese grundsätzliche Zustimmung bereits mit Einreichung der Veröffentlichung einzuholen bzw. die Gewichtung der Anteile parallel zur Einreichung zu klären).

Die Anteile des Promovenden sowie der weiteren Doktoranden/Doktorandinnen als Co-Autoren an den Publikationen und Zweitpublikationsrechten bei einer kumulativen Dissertation sind in der Anlage aufgeführt

Name Promovend	Datum	Ort	Unterschrift
Tina Mede	09.03.2018	Jena	

Ich bin mit der Abfassung der Dissertation als publikationsbasiert, d.h. kumulativ, einverstanden und bestätige die vorstehenden Angaben. Eine entsprechend begründete Befürwortung mit Angabe des wissenschaftlichen Anteils des Doktoranden/der Doktorandin an den verwendeten Publikationen werde ich parallel an den Rat der Fakultät der Chemisch-Geowissenschaftlichen Fakultät richten.

Name Erstbetreuer(in)	Datum	Ort	Unterschrift
Prof. Dr. Ulrich S. Schubert	09.03.2018	Jena	

1. Introduction

The utilization of environmentally friendly energy represents an important topic in today's society. Furthermore, the CO_2 emission is on a high level and can be decreased by the application of renewable energy sources. The political goal of Germany which was described in December 2014 is an emission reduction to 40% until 2020 for the climatic protection of the earth. In order to achieve this goal the coal and nuclear power stations have to be turned off, resulting in an energy gap which has to be compensated. Consequently, the importance of chemical research seems to be higher than ever before to overcome these problems. In this regard, energy in the form of chemical bond energy can be a useful tool. Furthermore solar energy converting systems are of high interest.[1-3] The research on suitable materials for this approach contains a range of metals and complexes, clusters and oxides out of them. The properties of the compounds strongly influence the overall performance of materials, *i.e.* efficiencies over long lifetimes to the range of absorpted light. At the moment, no ideal system is existing, so that the continuing investigations are of high social, economically and academically importance.

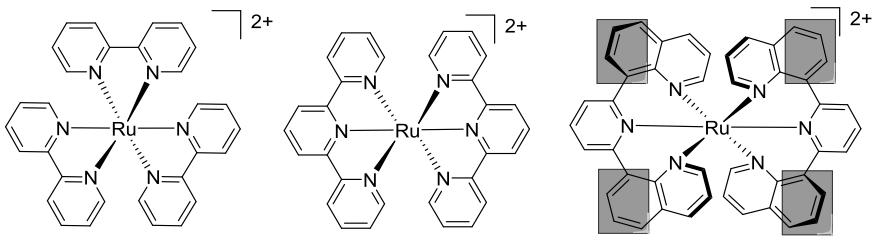

Scheme 1.1: Schematic representation of Ru^{II} complexes with expanded bite angle $[Ru(dqp)_2]^{2+}$(right) in contrast to the parental complexes $[Ru(bpy)_3]^{2+}$(left) and $[Ru(tpy)_2]^{2+}$(middle); extension of bite angles in gray boxes.

The usage of ruthenium polypyridine complexes as light harvesters was introduced in the 1970s and is still ongoing. The variety of ligands is still growing, due to the tunable ligand scaffold, which leads to plenty of photophysical and electrochemical properties. The most intensively investigated ligands are 2,2'-bipyridine (bpy)[4-5] and 2,2',6',2-terpyridine (tpy),[6] which exhibits differences in geometry and photophysics. While $[Ru(bpy)_3]^{2+}$ shows nearly ideal photophysical behavior for solar cell application, the geometry of terpyridines seems to be ideal for directional charge transport.[7] Unfortunately, the geometry of the $[Ru(bpy)_3]^{2+}$ complexes leads to the formation of isomers, which demand a further difficult separation step, while this is not the case for $[Ru(tpy)_2]^{2+}$ complexes. The generation of an ideal charge transfer from the

photosensitizer to the transport units requires significantly a long excited life time state. This ability for a charge transport can be proven by emission spectroscopy. In the ideal case the metal-to-ligand-charge-transfer (MLCT) transitions are centered between 400 and 500 nm and can be excited. An electron from the highest occupied molecular orbital (HOMO), which is located at the ruthenium center, is transferred to the LUMO from the ligand scaffold leading to the ^{1}MLCT. This ^{1}MLCT state can be transfered *via* inter system crossing to the emissive ^{3}MLCT state (see Figure 1.1a) or the nonradiative ^{3}MC state. In the case of $[Ru(bpy)_3]^{2+}$ the ^{3}MLCT state is lowered in comparison to the nonradiative ^{3}MC state (Figure 1.1b) and shows emission, while for $[Ru(tpy)_2]^{2+}$ the ^{3}MC state is preferred (Figure 1.1c), leading to a quenching of the ^{3}MLCT state resulting in thermal deactivation.[5, 8] This results in lifetimes around 0.25 ns, which is much shorter in comparison to the one of $[Ru(bpy)_3]^{2+}$ (850 ns).[4] To omit this effect the ^{3}MLCT has to be lowered or the ^{3}MC state has to be increased. The geometry of the ligand system strongly influences the lowering of the ^{3}MLCT state. A nearly perfect octahedral geometry with bite angles around 180 ° stabilizes this ^{3}MLCT state. However, the problem of the $[Ru(tpy)_2]^{2+}$ is a too small bite angle of the pyridine units. As a consequence, the geometry seems to be perfect for a directional charge transport but not for an ideal behavior of the long lived excited state, which is necessary for an efficient charge transfer.

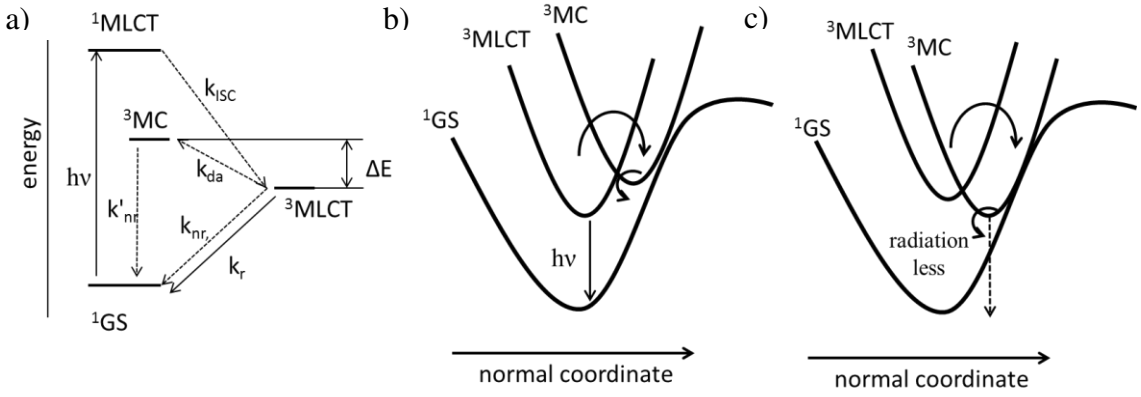

Figure 1.1: Simplified Jablonski scheme of Ru^{II} polypyridyl complexes. (a) Potential well diagram for ^{3}MC higher than ^{3}MLCT (b) and potential well diagram for ^{3}MLCT higher than ^{3}MC. Adapted from Balzani *et al*. (reprinted from ref. [9]).

On the basis of this information, a wide range of ligands where formed to overcome the limitations of these compounds to accomplish nearly perfect properties. The functionalization with electron withdrawing or donating groups on the ligand scaffold or the broadening of the bite angle by introducing spacing units between the pyridines

improves the lifetime. The list starts with smaller groups like alkynes,[11-12] vinylidenes[13] or pyrimidyls,[14] but the more extended delocalization leads to the stabilization of the LUMO resulting in a deactivation. Better choices (in this case) are bridging units with groups like keto,[15] amines[16] or phenyl[17-19] spacing units. Higher ligand field splitting, which benefits the lifetimes, can be reached with strong σ-donating ligands like *N*-heterocyclic or mesoionic carbenes.[20-23] The introduction of metalating units into the ligand field can improve the light harvesting nature, due to their σ-donating effect, resulting in a raise of the ^{3}MC state. The coordinated carbonic unit contributes to the excited state by a ligand orbital part in the HOMO. The excited state changes exactly to a MLLCT state leading to the absorption of visible light in a widened area.[33] Further donor substituents on these complexes improve the light harvesting behavior.[34]

The option of changing the pyridine units against quinolines leads also to the desired effect, because of the extended heterocycle. These complexes based on the 2,6-diquinolinepyridine (dqp) ligand show an excellent photophysical and electrochemical behavior with excited states life time around 3 µs, due to their nearly perfect octahedral geometry with a bite angle of 178 °.[24] This new complex type is utilized as photosensitizer in D−P−A triads due to the highly efficient charge separation,[25] in bichromic complexes coupled to an anthracene unit,[26] and will be exploited for the labeling of polycaprolactones,[27] in metallopolymers *via* polymerization[28] or in electropolymerizations.[29-30] The functionalization is possible in the *para* position of the centered pyridine unit as well as on the peripheral quinoline units. A hexaarylated complex was reported by Schlotthauer *et al*. which bears bromphenyl and tolyl or anisol groups on the peripheral units.[31] Furthermore mixed complexes containing one tpy and one dqp ligand can be utilized in medicine as $^1O_2$-generator.[32]

The usage of these ruthenium complexes as modular building units could increase the efficacy of materials for light driven energy conversion. Their ideal photophysical and electrochemical performance make them favorable for all energy systems. One type of solar cells, where complexes are used, is the bulk heterojunction solar cell. This device contains the light harvesting unit directly in combination with the photosensitizer and the energy storage unit, like a triad system of donor-photosensitizer-acceptor (D−P−A).[35] Consequently, these molecules that are based on special units, guarantee the efficient charge generating, separation and electron transfer. The functional building

blocks are the light harvesting unit, which often is united with the photosensitizer in one to collect the sun light and to achieve the conversion into energy, secondly the electron acceptor unit with an efficient transfer as well as storage of the free electron and thirdly the donor unit which rebuilt the ground state of the photosensitizer.

In particular an efficient synthetic strategy is required for the incorporation in a wide application field. The $[Ru(dqp)_2]^{2+}$ complexes show some problems during their synthesis due to low yields as well as an elaborate purification process. To omit this, a novel strategy for the formation of high yielded ruthenium complexes is needed, which can subsequently functionalized on the ligand scaffold following a chemistry-on-the-complex strategy. Therefore powerful coupling techniques are required and the photophysical behavior has to be preserved upon functionalization. The example of Kumar *et al.* (Scheme 1.2), where a ruthenium triad which bears an acceptor unit as well as a donor unit on the ligand scaffold is synthesized, reveals the significant synthetic effort for the construction of such a triad, when the functionalities are introduced into the ligand before the coordination step. In total ten steps are necessary for the formation of this triad. For this application the chemistry-on-the-complex methodology is beneficial due to an efficient synthesis, where the individual units are prepared separately and combined in a final step. These donor and acceptor units can be small molecules like in the example above, which proofed an efficient charge separation of 95%. Nevertheless, small molecules also lead to a fast recombination. This problem can be avoided by the application of polymer units, which can increase the spatial separation, because of their linear character, as well as the electron transport through the polymer chain. In particular, a simple change results in the repetition of every single step. To avoid this, a ruthenium core bearing two functionalities, which can be easily coupled, is more advantageous and would be the golden thread for this thesis. Furthermore the syntheses and characterization of a series of asymmetric metalating ruthenium complexes based on the $[Ru(dqp)_2]^{2+}$ are investigated, because of their

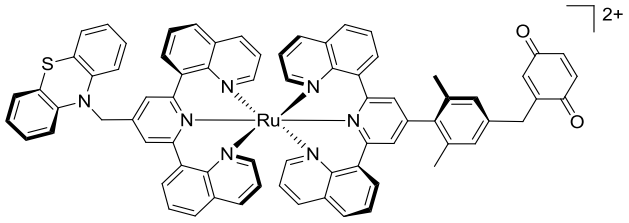

Scheme 1.2: Schematic representation of a triad including, benzoquinone as acceptor, phenothiazine as donor and $[Ru(dqp)_2]^{2+}$ as photosensitizer.[36]

improved absorption behavior. Chapter 2 deals with the formation of the asymmetric metalating ruthenium complexes and the improvement of the synthesis and purification of the ruthenium complex units. Next, a selection of ruthenium complexes will be introduced to show their modular incorporation in several architectures *via* the chemistry-on-the-complex strategy. This will be presented in Chapter 3, including a range of coupling techniques, which are published in the literature. Cross-coupling reactions and a range of established reaction types can be realized on the complex scaffold utilizing standard conditions. The binding to active materials like redox active compounds or DNA, cells, polymers, sugars or amino acids can be achieved. In particular, the incorporation in dyad and triad systems as well as the coupling to biomaterials via amidation reaction for labeling is high of interest. This will assist to find the optimal coupling strategy for the application in electropolymerized films along with polymeric dyad and triad systems.

Afterwards the usage of complexes as monomer units for metal containing polymers is investigated, which enables the film formation directly on a conducting surface. Thus, Chapter 4 deals with the electropolymerization of a $[Ru(dqp)_2]^{2+}$ complex. The beneficial electrochemical properties of these complexes can support the oxidation process of the electropolymerizable units. A wide variety of functional groups are able to electropolymerize; the most common ones are vinyls,[37-48] thiophenes[29, 49-57] or triarylamines.[58-61] With this in mind, it is possible to construct photoactive switchable films on ITO coated glass slides, which can be used for photo catalysis by adding a catalyst to the surface. The light would be absorbed by the polymer and the charges will be transported through the film to the active units, where the catalysis can be realized. For this purpose, the ligand scaffold is functionalized with two bithiophene groups, which lowers the oxidation potentials and achieves a controllable electropolymerization process. Moreover, investigations of finding optimal polymerization conditions are performed and solvents, time, charging type and the utilization of additives are tested.

The stepwise synthetic strategy is finally implemented in the synthesis of the first polymeric D-P-A triad, which reveals an efficient charge transfer and will be presented in Chapter 5. The system consists of the polymers polytriarylamines (pTARA) and polynaphthalendiimide (pNDI). These polymers have been proven to be standard polymers for the application in redox-active systems. In particular, the pTARA was investigated in previous work in our group. Both polymers were received *via* the NMP-

polymerization after successful monomer synthesis. This controlled polymerization technique enables a low dispersity and a uniform chain end, which is necessary for further functionalization. In this work different coupling mechanisms will be described and a first triad system was isolated.

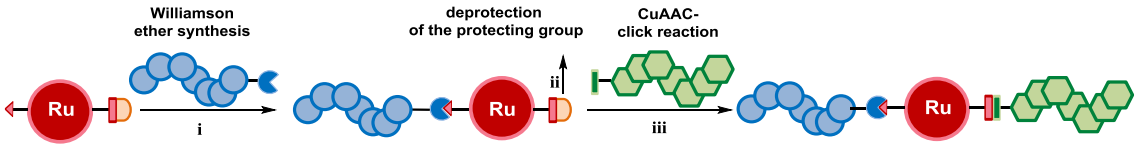

Scheme 1.3: Schematic representation of the step-wise synthetic approach for the construction of polymeric D-P-A triads.

The stepwise construction of this polymeric triad out of the individual building blocks is visualized in Scheme 1.3 and was proven *via* SEC and NMR spectroscopy. After the first promising results of the photo physical characterization, further triads were synthesized. Among others a new polymer was introduced. The pTARA was replaced by a conjugated polycarbazol (pCarb), which was prepared by cross-coupling reaction or Grignard type reaction.[62] The construction of these modular architectures shows the synthetic potential of the synthetic approach which is enabled *via* chemistry-on-the-complex methodology.

2. Coordination conditions

Parts of this chapter have been published in P1: T. Schlotthauer, G. A. Parada, H. Görls, S. Ott, M. Jäger, U. S. Schubert. *Inorg. Chem.* **2017**, *56,* 7720-7730 and P2: T. Mede, M. Jäger, U. S. Schubert, submitted.

2.1 Asymmetric cyclometalated ruthenium complexes

Metalating complexes as presented in Chapter 1 show excellent photophysical properties and an absorption range over the entire visible area. The utilization of these compounds as modular building blocks should increase the efficacy of the light harvesting unit, but the coordination of the metalating ligands to form the complexes is quite challenging. In comparison to the dqp ligands, they exhibit the same hindrance of

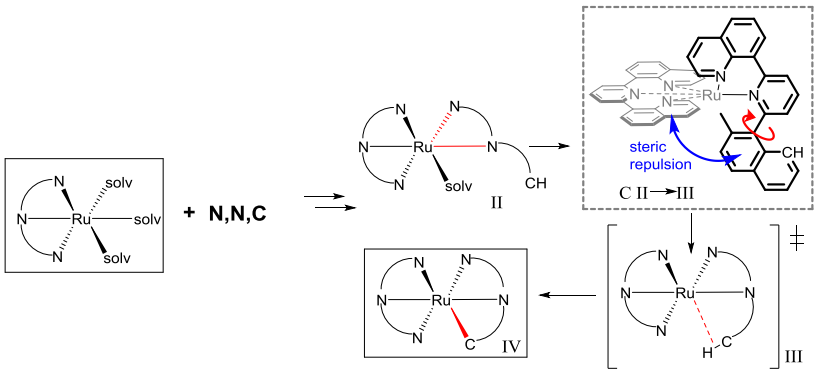

Scheme 2.1: Coordination pathway of metalating ligands: N,N,C-pathway; boxes indicate starting and final structures. Brackets indicate energy-rich intermediates and/or transition states, red color indicates newly formed bonds.

sterical effects (Scheme 2.1), while additionally higher temperatures are required for the formation of C-Ru bonding *via* a proton abstraction. The ligand synthesis of the metalating complexes was proceeded by a stepwise Suzuki coupling (Scheme 2.2). During the synthesis of the dqp ligand an intermediate of single coupled quinoline was observed and further applied as starting material. This compound is preferentially

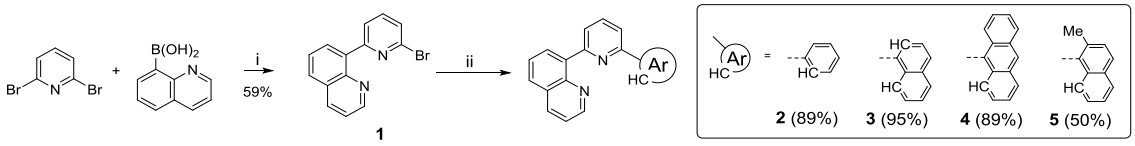

Scheme 2.2: Schematic representation of the synthesis of the metalation ligands *via* double Suzuki coupling. (i) $Pd(dba)_2$, dppp, K_2CO_3, $MeCN/H_2O$, 1 h, 140 °C. (ii) aryl boronic acid, $Pd(dba)_2$ SPHOS, K_2CO_3, $MeCN/H_2O$, 1 h, 140 °C.

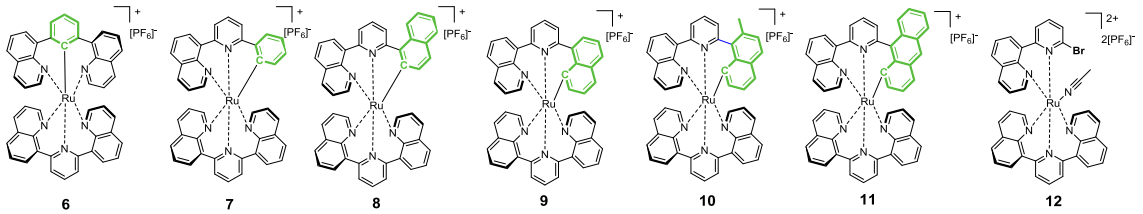

Figure 2.1: Representations of complexes prepared in this study featuring central cyclometalation (**6**), peripheral cyclometalation with five-membered chelates (**7** and **8**) or six-membered chelates (**9**–**11**), and a related bidentate complex (**12**, see text).

Table 2.1: Optimized reaction conditions for complexes **6**–**12**.

	ligand	*solvent*	*T [°C]*	*Time [h]*	*base*	*Product*	*Isolated yield [%]*
1	dqPhH	EG	200[e]	1.5	-	**6**	73[a]
2	**3**	EG	200[e]	1.5	-	**9**[h]	10[a,h]
3	**3**	DMF	160[e]	1.5	-	**8**	12[a]
4	**5**	DMF	160[e]	1.5	-	**10**	16[a]
5	**4**	DMF	160[e]	4	-	**11**[h]	<5
6	**2**	DMF	160[f,i]	4	-	**7**	78[b]
7	**1**	EG	120	16		**12**	49
8	**2**	EG	160[f]	16	lutidine	**7**	74[a]
9	**3**	EG	160[f]	16	lutidine	**8** + **9**[h]	-[h] (3:7)[b]
10	**3**	EG	160[g]	16	lutidine	**8** + **9**[h]	34[b] (2:1)[b,c]
11	**5**	EG	160[f]	3	lutidine	**10**	37[d]
12	**4**	EG	160[f]	16	lutidine	**11**	<5
13	**3**	EG	160[f]	0.7	$NaHCO_3$	**8**	55[d]
14	**4**	EG	160[f]	2.5	$NaHCO_3$	**11**[h]	75[d,h]
15	**5**	EG	160[f]	3	$NaHCO_3$	**10**	68[d,h]

a) Purification by two consecutive silica columns: CH_2Cl_2/MeOH and MeCN/H_2O/aq. KNO_3 adapted from ref.[25]. b) Ratio from NMR analysis, yield calculated *via* an internal standard. c) Further purification by fractionalized crystallization. d) Purification by single column on amino-decorated silica. e) Microwave heating. f) Oil bath heated before synthesis (thermally equilibrated). g) Oil bath heated during synthesis. h) not isolated. i) Stepwise: 70 °C for 16 h, 120 °C for 4 h, 160 °C for 4 h; onset of product formation at 160 °C. See text for further explanation. EG is ethylene glycol.

formed by the application of dppp instead of SPHOS and was isolated in a yield of 59%. The ligand formation was achieved by the application of the commercially available boronic acids of benzene, naphthalene and anthracene. The coordination of these new ligands **2-5** was investigated during the search for the best reaction conditions. Table 2.1 provides an overview about the parameters and the respective results. While the complexation in pure solvents just leads to the complex formation of the phenyl ligand **2** (see Table 2.1 for tested reaction conditions), the usage of a base seems to be necessary, since proton abstraction is the major part of the complexation. Therefore, 2,6-lutidine should be an ideal candidate due to its organic character, which improves

the solubility. Nevertheless, the complexation of the ligands with the anthracenyl **4** and methylnaphthyl moiety **5** is still hindered. The inorganic base $NaHCO_3$, with a similar pKs value of 6.35 (lutidine pKs 6.6), allows the formation of the complexes **7**, **8**, **10**, and **11** in higher yields and shorter reaction times.

The purification was achieved by column chromatography on a flash master system using cartridges with amino functionalized silica. This method enables a rapid purification of the partly unstable complexes without the assignment of an aqueous or ionic eluent.

The Figure 2.1 displays the structures of all synthesized complexes. While the structure of the phenyl functionalized complex **7** shows the 5-membered structure of the metalating unit, the naphthyl ligand leads to the two different structures **8** and **9**. Besides the fact that the five membered complexation is preferred due to the sterically effect, both complexes could be synthesized. In most approaches a mixture of the isomers was formed, where the content of the 6-membered coordination (**9**) is about 5%. Surprisingly, the first technique with ethylene glycol at 200 °C forces the formation of the 6-membered coordination type. Unfortunately, this isomer degrades after short time and was challenging to isolate. In all further investigations only the 5-membered coordination compound **8** was received. The methyl group (**10**) was introduced to block

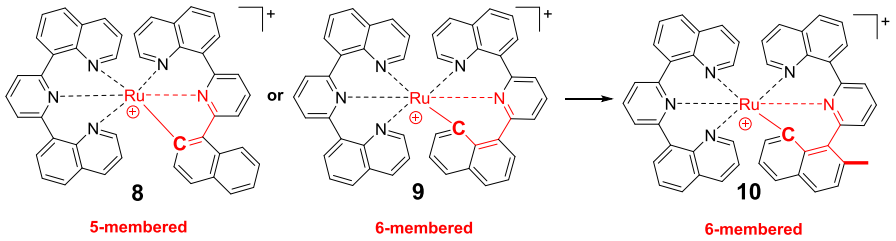

Scheme 2.3: Schematic representation of the metalating coordination modes of the naphthyl coordinating complexes **8**-**10**; 5 membered and 6 membered ring displayed in red.

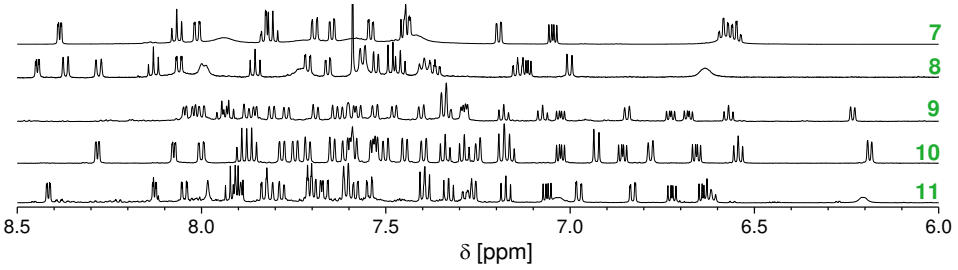

Figure 2.2: ^{1}H NMR spectra of complexes **7**−**11** (CD_3CN, 600 MHz, aromatic region) showing signal broadening of the five-membered chelates (**7** and **8**) and a characteristic high-field shift of the six-membered chelates around 6.2 ppm (**9**−**11**) (Reprinted with permission from Ref.[63] Copyright 2017 American Chemical Society).

the 5-membered coordination position to overcome this problem and to generate a 6-membered metalating complex (difference of all three coordination modes are summarized in Scheme 2.3). These 5- and 6-membered complexes reveal a different behavior in the proton NMR spectra (Figure 2.2). For the 5-membered complexes **7** and **8** a broadening of a part of the signals is observed and can be explained by the small conformational barrier. In contrast the 6-membered complexes **9** and **10** show well resolved NMR spectra in a similar manner to the $[Ru(dqp)_2]^{2+}$ based complexes, while this torsion is hindered at the 6-membered complexes.

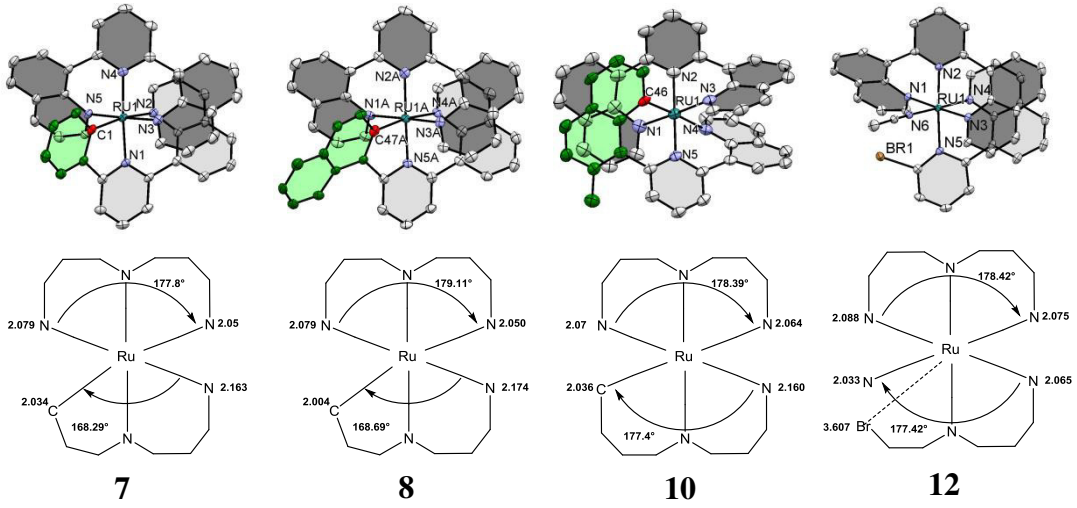

Figure 2.3: Molecular structures of the complexes **7, 8, 10**, and **12**. The carbanionic donor (red) and the cyclometalating subunit (green) are highlighted. Note the absence of π stacking of the cyclometalating fragment (green) in the case of five-membered chelation (**7** and **8**) but its occurrence for six-membered chelation (**10**). Thermal ellipsoids are drawn at a probability level of 50%, and cocrystallized solvent molecules, disoriented counterions, and hydrogen atoms are omitted for clarity. See bottom and Table 2.2 for selected structural details (Reprinted with permission from Ref.[63] Copyright 2017 American Chemical Society).

The solid state structures of the X-ray crystallography measurements revealed further information of the observed structures. The crystallization of the complexes **7**, **8**, **10** and the non-metalating complex **12** was successful by diffusion controlled crystallization from diethyl ether into the complex-acetonitrile solution. The complexes **9** and **11** are not stable enough to generate suitable crystals. Figure 2.3 depicts the solid state structures of these metalating complexes in comparison with the monoquinolinepyridine coordinated complex. Selected bond length and angles can be found in Table 2.2. For all structures the ruthenium core shows a octahedral conformation, while the internal bond angles are in the same range like for the $[Ru(dqp)_2]^{2+}$ (180 °) or the $[Ru(tpy)_2]^{2+}$ (169 °) complexes. In general, the typical behavior of the $[Ru(dqp)_2]^{2+}$ complex is preserved, so that the Ru-N/C bonding of the central unit is shorter than the Ru-N/C distances of the

peripheral units. Furthermore all neighbored quinoline units show π-π-stacking with a distance of around 3.5 Å. The same observations can be found for the peripheral naphthyl unit of complex **10**. More commonly all Ru-C bonds are shorter as the corresponding Ru-N bond. This influences the *trans* standing Ru-N bonding, which is slightly longer, due to the *trans* effect. For example, the complex **7** reveals a bond length of Ru-N_{qu} of 2.163 Å *trans* coordinated to the Ru-C bond (2.034 Å). This consequence is not visible at the symmetric dqp-ligand with a bond length of 2.07 Å and 2.064 Å bond lengths.

Table 2.2: Selected crystallographic data of cyclometalated complexes (**6**, **7**, **8**, **10**) and **12**.

complex	*Ru–N^{qu}* [Å]	*Ru–N/C^{central}* [Å]	*Ru–C/N^{periphera}* [Å]	*N/C^{central}–Ru–C/N^{peripheral}* [°]	*N^{qu}–Ru–C/N^{peripheral}*[°]	*Dihedral distorsion*[b] [°]	*stacking*[c] [Å]
6[d]	2.076 ±0.008	2.013 ±0.002	2.061 ±0.003	89.2 ±0.1	179.1 ±0.6	35.1 ±0.9	3.492 ±0.044
7	2.163	2.022	2.034	80.3	168.3	1.5	-
8	2.180 ±0.006	2.009 ±0.004	2.009 ±0.005	80.4 ±0.0	168.9 ±0.5	9.4 ±0.6	-
10	2.160	2.044	2.036	89.6	177.5	41.0	3.455
12	2.065	2.133	2.033[e]	95.0[e]	175.3[e]	-	-

Furthermore, the π-π-stacking of the quinoline units leads to a dihedral bite angle of 41 ° for complex **10**, while the complexes **7** and **8** show no effect with dihedral bite angles of 1.5 ° (**7**) and 9.4 ° (**8**), respectively. The non-metalating complex **12** reveals similar Ru-N_{ligand} bond lengths as the parental complex $[Ru(dqp)_2]^{2+}$, while the bond length to the nitrogen of the free acetonitrile is shortened (2.033 Å) in comparison to the ligand, because of missing sterical hindrance. The bromine in **12** has no effect of the

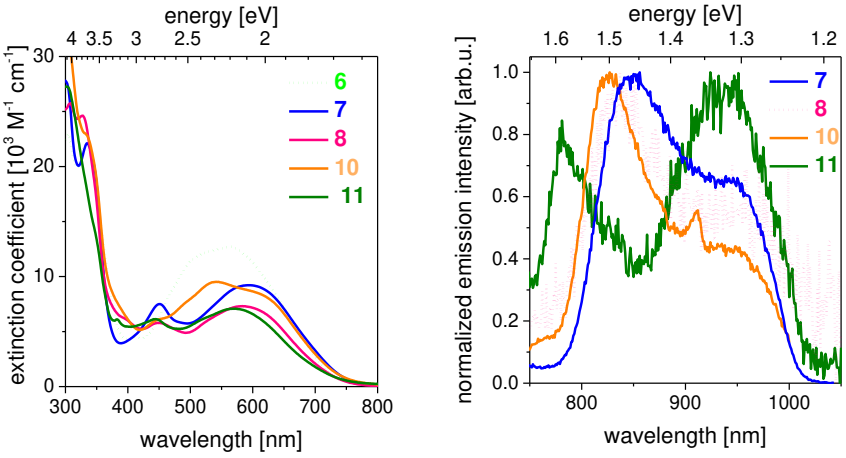

Figure 2.4: Photophysical data of cyclometalated complexes: (a) absorption spectra taken in MeCN solution at room temperature; (b) emission spectra taken at 77 K in EtOH/MeOH glass (4/1 v/v, λ_{exc} 500 nm (**7**, **8**, and **10**) or 700 nm (**11**)) (Reprinted with permission from Ref.[63] Copyright 2017 American Chemical Society).

coordination area with a distance higher than 3 Å to the metal center, which allows the usage in coupling reactions. UV-Vis and emission spectroscopy measurements were performed in acetonitrile and the results are summarized in Figure 2.4 and Table 2.3. The absorption spectra show intense absorption in the UV area according to the ligand transition and a broad absorption between 400 and 750 nm. Moreover, the complexes generate only weak emissions, which were observed at 77 K. The slightly bathochromic shift in comparison to the centered metalating complex **6** reaches values of 847 nm (**7**), 837 nm (**8**), while similar results were found for **10** (826 nm). This reflects the vibronic progression as reported for **6** and show that the excited state is located at the dqp fragment. The corresponding excitation spectra identify this state as a MLCT. In contrast, **11** creates two emission peaks, one at 730 nm and one at 925 nm, while the first one seems to be assigned to an impurity, the second one is similar to the other complexes. This may be explained by the photo instability of the complex.

The excited state lifetimes of the complexes **7**, **8** and **10** were measured at room temperature for a better comparison with the literature. Monoexponential emission decay is determined with lifetimes of 14 ns (**7**) and 20 ns (**8** and **10**). This does not follow the $[Ru(bpy)_3]^{2+}$ based energy gap law, which characterizes the relationship between the emission energy and the nonradiative decay to the ground state and should predict the observed emission lifetime and the very low quantum efficiencies. The calculation $\partial \ln(k_{nr})/\partial E_{em}$ of the complexes reveal a lifetime around 2 ns. The real value, which is one order higher, can be explained by the enhanced octahedral structure, which is similar to the $[Ru(dqp)_2]^{2+}$ complexes.

These results can be verified by TD-DFT calculations, whereby the analysis of the electronic properties in terms of the molecule orbitals was made. Therefore, the dispersion correction function ωB95xD reproduces the X-ray structures. The highest occupied molecule orbital (HOMO) is localized on the d orbital of the ruthenium with a part of the cyclometalated fragment, while the lowest unoccupied molecular orbital (LUMO) is localized at the dqp ligand. These are appropriated for the 5-membered cyclometalated complexes **6-8**. In contrast, the 6-membered complex **10** contributed a part to the LUMO. In conclusion, the calculated values are in the same range than the experimental data. The energies as well as the associated oscillator strength of the electronic transitions match with the measurements. These can be visualized with the EDDMs that depict the electron density by the regions of accumulation. The long

wavelength absorption possesses a ^{1}MLLCT state, while the ^{1}MLCT was found as intermediate and the IL (intraligand) transition is assigned as the shoulder at lower wavelengths. All these results were shown for complex **10**. The IL in complex **11** is bathochromic shifted, which explains the photo instability. The triplet state was optimized from the ground state by spin density difference plots and Mulliken atomic spin analyses according to the characteristic molecular fragments. Therefore, the complexes **7**, **8** and **10** generate typical spin values for the Ruthenium and the quinoline for the lowest energy of the ^{3}MLCT, while **11** reveals significant reduced values. Consequently, the ^{3}MLCT state Ru-C bond is comparable to the $[Ru(dqp)_2]^{2+}$. In summary, the calculations confirm similar results as the measurements.

Table 2.3: Photophysical and electrochemical properties of the cyclometalated complexes.

complex	*absorption [nm] (ε [10^3 $M^{-1}cm^{-1}$])*	*emission [nm] (eV) at 77 K*	*lifetime [ns][d] at 293 K*	$E^{ox}_{1/2}(Ru^{3+/2+})$ *[V] (ΔEp [mV])*	$E^{red}_{1/2}(L^{0/-1})$ *[V] (ΔEp [mV])*
6	500(11.4), 565 (12.7)	824 (1.50)[a]	16[a]	–0.08[a]	–2.00[a]
7	451(7.5), 594 (9.2)	847 (1.46)	13	–0.07 (68)	–1.92 (70)
8	448 (5.8), 585 (7.3)	837 (1.48)	20[e]	–0.17 (57)	–1.99 (60)
10	446s (6.1), 542 (9.5), 610s (8.5)	826 (1.50)	17	–0.15 (63)	–1.98 (85)
11	448 (5.8), 571 (7.1)	611 (2.02), 935 (1.33)[c]	2.7 (78%), 9.2 (22%)[b]	–0.13 (67)	–1.99 (81)

a) From Ref [64]. b) bi-exponential emission decay fit, relative amplitudes given in parentheses. c) short-wavelength emission assigned to anthracene-subunit, longest-wavelength emission assigned to ^{3}MLCT (see text and SI for more details). d) From time-correlated single photon counting data. e) From flash photolysis emission and transient absorption data (see Supporting Information for details).

The electrochemical properties of the complexes were examined *via* cyclic voltammetry and the redox potentials are given in the Table 2.3. The potentials are cathodically shifted in comparison to the enhanced π-system and are quasi reversible for the complexes **7**, **8** and **10**, except for the complex **11** which shows a second irreversible oxidation.

In summary a series of new asymmetric cyclometalated ruthenium complexes based on $[Ru(dqp)_2]^{2+}$ were synthesized. The functionalized phenyl, naphthyl and antracenyl units lead to an enhanced absorptivity over the whole visible area. The shortened lifetimes are still long enough for an efficient charge transfer.

2.2 Systematic coordination improvement of dqp based ligands

An effective synthesis is required for the coordination of the ligands, bearing functionalized groups for incorporation and usage as building block for larger systems.

The coordination of the dqp ligand can be directly achieved with $RuCl_3$ species to form a homoleptic complex with ethylmorpholine in an EtOH-water mixture. The parental complex $[Ru(dqp)_2](PF_6)_2$ can also be synthesized in ethylene glycol at 200 °C. These harsh conditions lead to the complex with the appearance of isomers, while substitutions were not tolerated.[24, 65-66] In case of functionalized heteroleptic complexes, a stepwise methodology is the option of choice. For this approach, a complex precursor has to be synthesized, which bears three coordinated solvent molecules beside one ligand, (foremost acetonitrile). The synthetic steps are: 1.) The coordination of the ligand to the $RuCl_3$ starting material, 2.) the transformation into the acetonitrile precursor and 3.) the complexation of the second ligand. This stepwise synthetic route offers a better control over the side products. Transformation of the chloride against acetonitrile at 80 °C facilitates the chance of specific complexation *via* stable intermediates. Further enhancement of the first coordination step could be achieved by the usage of a thioether ruthenium species.[31, 67] $RuCl_3$ as ruthenium compound is a byproduct of the industry and contains further ruthenium compounds and oxidation states aside from the main species. The thioether-ruthenium compound is homogeneous, which could be analyzed and proven by NMR spectroscopy and thin layer chromatography (TLC). The final complexation of the non-functionalized dqp ligand or mono-functionalized ones are satisfying *via* standard coordination conditions using alcohol, like ethylene glycol or 1-butanol as solvents, but with increase of the ligand scaffold the coordination of the functionalized dqps becomes more challenging. Multiarylated systems disclose low complexation conversions with a maximum of 20%.

In this chapter, a detailed study about the influence of solvent, time and temperature is presented to generate the coordination of highly functionalized ruthenium polypyridyl complexes. For the investigations, the $[Ru(dqp)(MeCN)_3]^{2+}$ complex was used as starting material and reacted with tpy or dqp as ligands. In contrast to $[Ru(tpy)_2]^{2+}$, $[Ru(dqp)_2]^{2+}$ requires considerably higher reaction temperatures for the coordination, due to the more hindered ligand geometry. The challenge is to find reaction conditions as mild as possible for the labile ligands in the best achievable yield.

Furthermore, the coordination of larger systems like a polycaprolactone-macroligand in ethylene glycol is hampered and leads to an undefined splitting of the polymer chain. The reason is the insolubility of these larger ligand systems in the common solvents like ethylene glycol. The coordination of such a macroligand shows the best results in a

solvent like DMF,[27] but the solubility remains a critical parameter for more complex systems. This information estimates DMF as a promising solvent for complexation and offers a better solubility of the ligand systems and, consequently, higher conversions with less side products. Coordination tests with the parental ligand dqp were carried out with the $[Ru(dqp)(DMF)_3]^{2+}$-complex and with the more stable acetonitrile complex in DMF to see if there is a difference during coordination and in the obtained yields. A

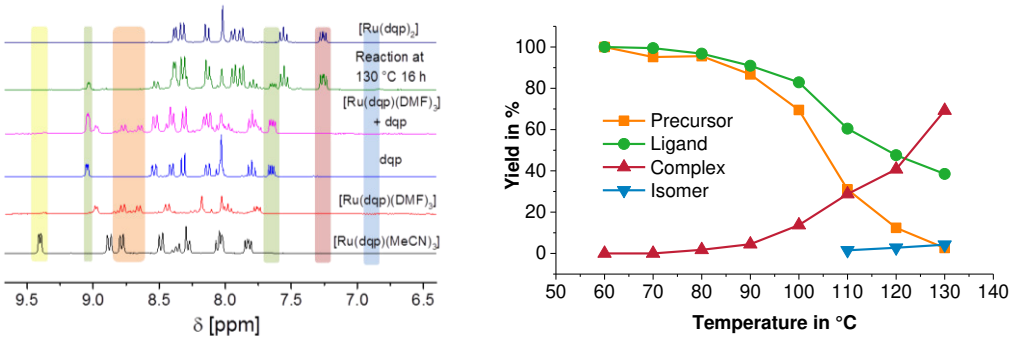

Figure 2.5: Left: Comparison of the several states of coordination from bottom to top: $[Ru(dqp)(MeCN)_3]^{2+}$ complex, $[Ru(dqp)(DMF)_3]^{2+}$ complex after heating at 120 °C for 2 hours, pure Ligand in DMF, $[Ru(dqp)(DMF)_3]^{2+}$ complex plus dqp ligand before heating, reaction progress after stepwise heating measured after 16 hours at 130 °C, pure complex $[Ru(dqp)_2]^{2+}$ **13**. The changes of main signals are marked: Yellow: $[Ru(dqp)(MeCN)_3]^{2+}$ complex, green: ligand, orange: $[Ru(dqp)(DMF)_3]^{2+}$ complex. Right: Progress of marked NMR signals to follow the conversion of the educts *via* intermediate to the products.

stepwise heating of the reaction mixture was used to find out which pathway leads to the best results. In addition the starting temperature and the conversion of the reaction can be detailed. The $[Ru(dqp)(DMF)_3]^{2+}$ complex was synthesized by heating $[Ru(dqp)(MeCN)_3]^{2+}$ to 120 °C for almost 2 hours in DMF, subsequently the reaction mixture was cooled to room temperature and dqp as ligand was added (Figure 2.5). The heating occurs in 10 °C steps for 16 h each step starting at 60 °C. A first indication of the complex is received at 80 °C by analysis of the proton NMR spectrum in particular by examining the signal at 7.2 ppm. Further heating increases the conversion and ceases at 130 °C with a conversion of 70%. Surprisingly, the coordination test **14** starting with $[Ru(dqp)(MeCN)_3]^{2+}$ leads to slightly higher yields of 79% than the $[Ru(dqp)(DMF)_3]^{2+}$ complex **13**. The formation to the $[Ru(dqp)(DMF)_3]^{2+}$ form occurs during the heating process, whereby no precursor formation is necessary. The NMR signals of the formed $[Ru(dqp)(DMF)_3]^{2+}$ precursor do not totally disappear, which can be assumed by the formation of more than one $[Ru(dqp)(DMF)_3]^{2+}$ complex. The investigations on the parental $[Ru(dqp)_2]^{2+}$ complex gave first hints for improvement, but works also well for all standard reaction conditions like ethanol or ethylene glycol. Highly functionalized

ligand systems are more challenging because of sterically effects, changed solubility and reactive groups. Therefore, the success of the complex formation of dqp (**13** and **14**), dqp(PhBr)$_2$ (**15**), dqpPhCCTIPS (**16**) or dqpBr (**17**) is improved in comparison to published results.

The synthesis of homo- and heteroleptic hexa-functionalized ruthenium complexes (Scheme 2.4) is challenging due to the high potential of side reactions as well as the low solubility of the functionalized ligands. In previous reports was it possible to synthesize the complex **22** with a yield of 14% for the heteroleptic complex and 21 to 32% for the homoleptic complex along a two-step coordination mechanism in ethylene glycol. Through application of the $[Ru(dqp)(DMF)_3]^{2+}$ variation and the analysis *via* proton NMR spectroscopy, a high conversion can be recognized after 4.5 hours, reaching 90% after 28 hours. In the same manner two new complexes **23** and **24** could be synthesized with yields of 58% and 77%, respectively.

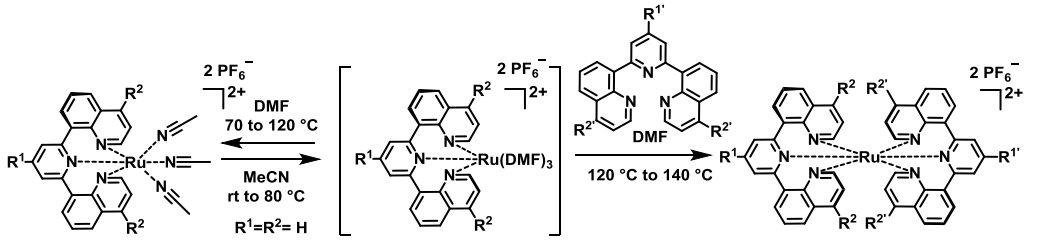

13&14) $R^1=R^{1'}=R^2=R^{2'}$= H
15) $R^1=R^{1'}=R^2$=H, $R^{2'}$= PhBr
16) R^1=OH, $R^{1'}$= PhCCTIPS, $R^2=R^{2'}$= H
17) R^1= H, $R^{1'}$= Br, $R^2=R^{2'}$= H
18) R^1=H, $R^{1'}$= PhBr, $R^2=R^{2'}$= H
19) $R^1=R^{1'}=R^2$=H, $R^{2'}$= Ph(th)$_2$
20) R^1= PhBr, $R^{1'}=R^2$= H, $R^{2'}$= Ph(th)$_2$
21) $R^1=R^{1'}=R^2$= H, $R^{2'}$= PhEDOT
22) $R^1=R^{1'}$= PhBr, $R^2=R^{2'}$= PhMe
23) R^1= PhBr, $R^{1'}$= OH, $R^2=R^{2'}$= PhMe
24) R^1=H, $R^{1'}$= PhBr, R^2= H, $R^{2'}$= PhOMe

Scheme 2.4: Schematic representation of the stepwise synthesis of the homo- and heteroleptic $[Ru(dqp)_2]^{2+}$- complexes including the solvent ligand change to the $[Ru(dqp)(DMF)_3]^{2+}$ precursor and back on the left side.

Table 2.4: Overview of the synthesis of $[Ru(dqp)_2]^{2+}$ complexes with the obtained yields using DMF as solvent and variation in temperature and reaction time.

	Precursor	*ligand*	*T [°C]*	*Time [h]*	*Yield [%]*
13	dqp[c]	dqp	60 to 130	grad	69[a]
14	dqp	dqp	60 to 130	grad	79 [a]
15	dqp	dqp(PhBr)$_2$	140	48	52
16	dqpOH	dqpPh-CCTIPS	140	48	51
17	dqp	dqpBr	140	48	73
18	dqp	dqpPhBr	140	16	74
19	dqpPhBr(PhMe)$_2$	dqpPhBr(PhMe)$_2$	140	28	90 [a]
20	dqpPhBr(PhMe)$_2$	dqpOH(PhMe)$_2$	140	16	58
21	dqp	dqpPhBr(PhOMe)$_2$	140	40	77
22	dqp	dqp(Ph(th)$_2$)$_2$	120	16	61
23	dqpPhBr	dqp(Ph(th)$_2$)$_2$	120	48	32
24	dqp	dqp(PhEDOT)$_2$	120	16	38

Finally nonpolar ligands were tested, which were bearing bithiophene (**19**) or EDOT (**21**) units for potential application in electropolymerizations, with a low solubility in most organic solvents. These complex systems were synthesized so far by chemistry-on-the-complex mechanisms, offering low yields in the most cases. Nevertheless, the electropolymerizable moiety can be damaging at high temperatures. The coordination of the bithiophene-functionalized ligand leads to the complex **19** with an isolated yield of 61% by using DMF at 120 °C for 16 hours of classical thermal heating. The alternative synthesis occurs *via* Suzuki cross-coupling reactions using $Pd(dba)_2$ and SPHOS as catalytic system and reaches a yield of around 30%.[68] The same reaction conditions were used to form the EDOT functionalized ruthenium complex **21**. The yield of 7% (unpublished) *via* a cross-coupling reaction results from the bad solubility and a challenging purification procedure, which represents a key fact in the most complex syntheses. With the coordination of the dqp-$(PhEDOT)_2$ ligand in DMF a yield of 38% is achieved (five-fold increased yield). In the same range a three times functionalized complex could be synthesized bearing a PhBr-group on the pyridine unit of the precursor and two bithiophene moieties on the phenyl of the peripheral quinoline units **20**. This enables the complex synthesis of electropolymerizable monomers in an acceptable yield.
This detailed experimental study of the coordination of heteroleptic $[Ru(dqp)_2]$-type complexes was examined *via* computational methods.

All experimental results are summarized in Scheme 2.4 and Table 2.4. In particular, the complex syntheses of **15** to **24** show the improvement of the reaction conditions and enable the application of these complexes as modular building units for the incorporation in larger systems. The highly functionalized complexes **16** and **22** were taken as examples for their utilization in the chemistry-on-the-complex methodology and will be discussed in the next chapters.

3. "Chemistry-on-the-complex" − A versatile tool for the incorporation of ruthenium complexes as modular units

Parts of this chapter have been published in P3) Tina Mede, Michael Jäger, Ulrich S. Schubert, submitted.

This chapter focusses on the chemistry-on-the-complex methodology. As described in Chapter 2.2, the coordination especially of larger ligand systems is challenging. However, the new conditions (vide supra) improve the yield and reduce the formation of side products but a loss of product is still given. In contrast, the chemistry-on-the-complex methodology offers the possibility of incorporation in larger systems *via* an architecture set. The utilization of the complex as a building unit is timesaving, because the individual units can be exchanged or modified without changing of the whole structure of the final architecture as the coupling reaction is the last step. Otherwise, the construction requires a functionalized macroligand and a coordination step at the end. This represents a significant effort when just small changes are necessary in the subunits. This chapter deals with a range of suitable reactions directly on the ligand scaffold, including the introduction of functional groups as well as of cross-coupling reactions, amidation reactions, nucleophilic substitutions and many more (Scheme 3.1). Furthermore it will provide an overview of tailored purification protocols of highly functionalized complexes or architectures thereof. In particular, the application of different column materials in combination with eluents will be presented.

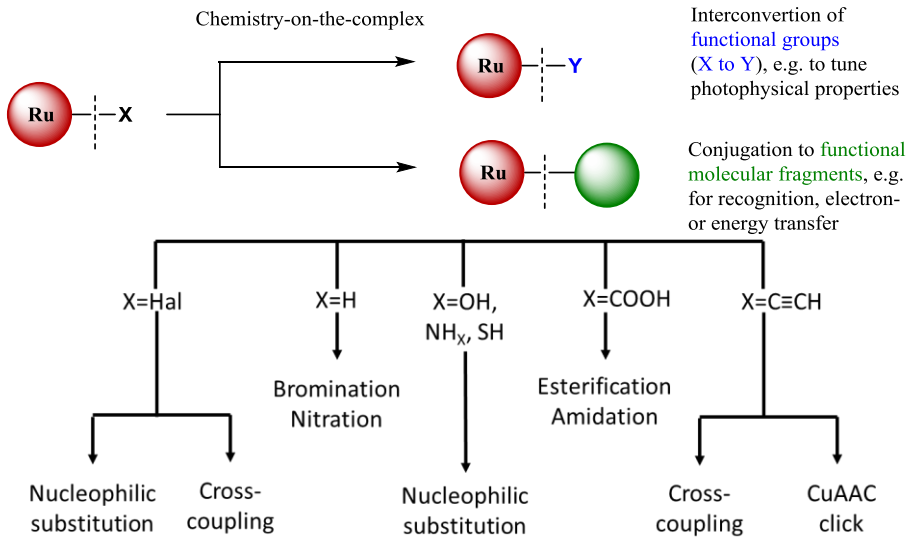

Scheme 3.1: Schematic representation of the chemistry-on-the-complex strategy outgoing from the different functionalization.

3.1 Reactions

The utilization of ruthenium complexes in a wide field of applications is well-known, while the task of chemistry-on-the-complex is not. The synthesis of $[Ru(tpy)_2]^{2+}$ and $[Ru(bpy)_3]^{2+}$ based complexes are widely introduced and collected in several books. In particular, for the construction of macrocycles and star-shaped molecules the chemistry-on-the-complex strategy is inevitable (Scheme 3.2).[69-71]

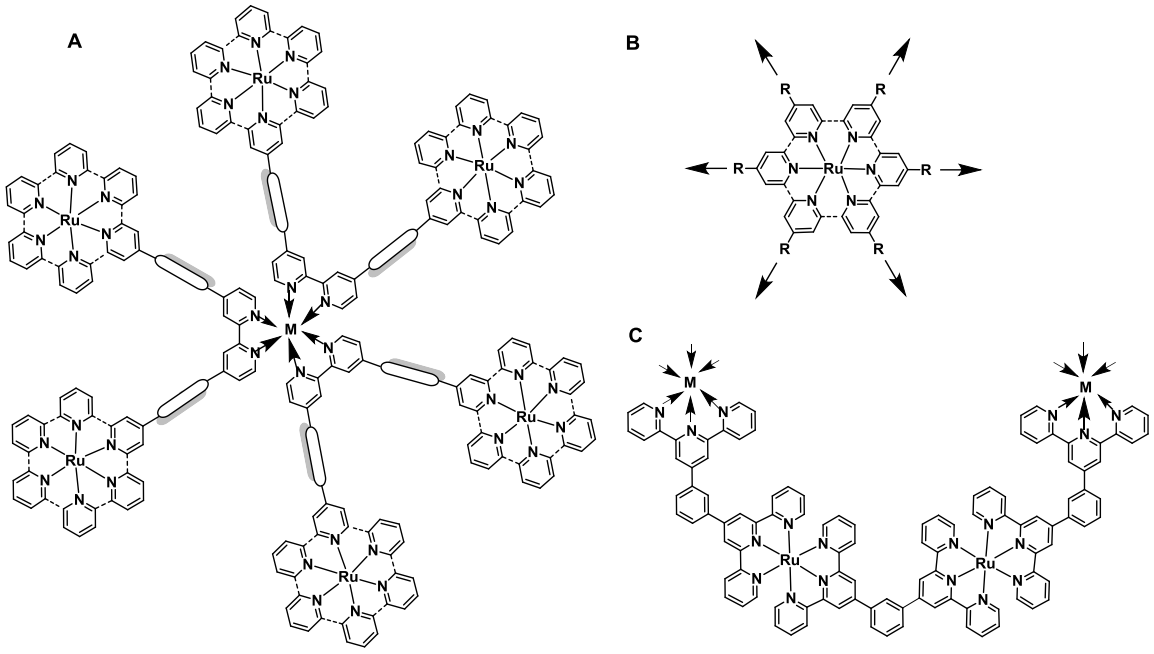

Scheme 3.2: Schematic representation for the formation of star-shaped ruthenium complexes and macrocycles.[69-71]

The functionalization of the ligands before coordination is the common and challenging way, but it is also achievable on the complex. Scheme 3.3 depicts an overview of conditions for the functionalization of the ligand scaffold with small reactive groups. In particular, the deviation of metalating ligands is very effective. The proton in the para position of the carbanionic unit can be easily exchanged, because of the electron withdrawing effect of the metalation. As a result it is possible to introduce halogen atoms like Cl,[72] Br[73-78] and I[73] as well as a nitro moiety.[79-82] The reduction of the latter ones to amines is achievable by Raney nickel or palladium. The introduced chloride can be converted into CN *via* $ZnCN_2$ in a catalytic reaction with $Pd_2(dba)_3$, dppf, and zinc dust.[83-84] Halogens are furthermore suitable substitution units

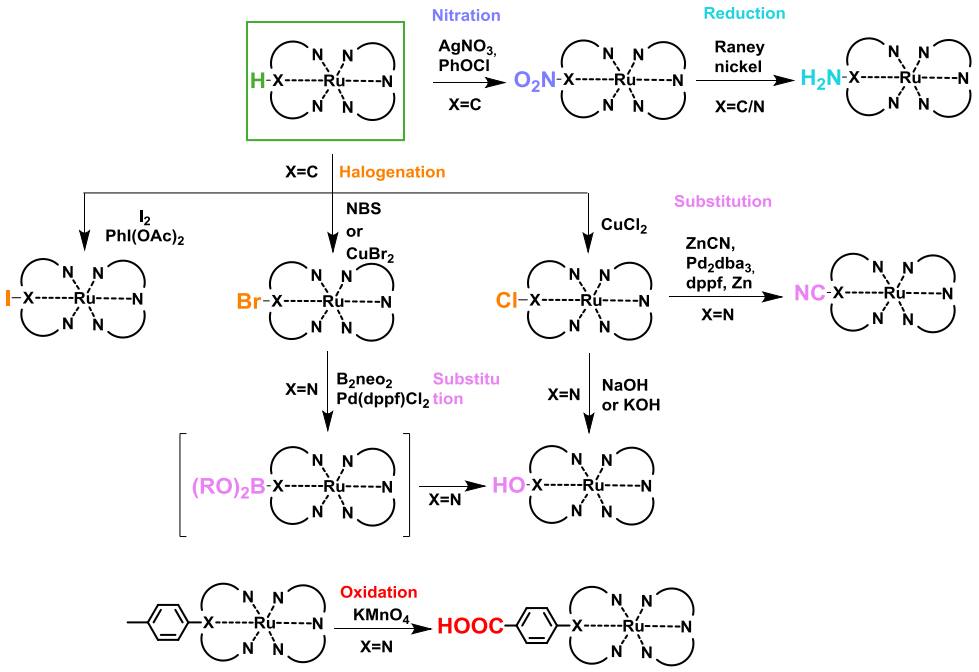

Scheme 3.3: Schematic representation of the functionalization methods on the ligand scaffold on a polypyridiyl complex.

for the incorporation of a hydroxide, which offers the ability for nucleophilic substitutions.[85-87] With a methyl group it is also possible to introduce acid groups with the view to esterification and amidation reactions.[88] Consequently, a wide range of substituents can be incorporated into the backbone of the ligand. In particular, with halogens a lot of suitable reactions strategies are available for further functionalization. One often used and well-known methodology is the cross-coupling reaction. Surprisingly, for the Sonogashira cross-coupling reaction, no special catalyst for the reactions with complexes is required and the standard conditions are satisfying. Ruthenium complexes are very redox stable and do not influence the catalytic process. The catalytic systems concentrate on $Pd(PPh_3)_4$, $Pd(PPh_3)_2Cl_2$, $Pd(dppf)Cl_2$, $Pd_2(dba)_3$ in combination with $AsPh_3$ and CuI. Moreover, bases and solvents are common, because of the good solubility of the complexes in polar solvents. DMF, THF, MeCN or benzene as solvent are used with bases like piperidine, diisopropylamine, trimethylamine or Hünigs base. The same is mentioned for the synthesis with Suzuki cross-coupling reactions. The groups of Vrabel[89-90] and Yang[91] investigated the differences between the two synthetic ways (Scheme 3.4). Both points out that with a Suzuki cross-coupling higher yields could be achieved. Furthermore, the Suzuki cross-coupling leads to a direct C-C between two aromatic units without an bridging unit in contrast to the Sonogashira reaction where an acetylene unit is present for the C-C

coupling. Less appropriated than the cross linking of Suzuki and Sonogashira are the catalytic cross-coupling reactions Stille and Negishi. Just a few examples are reported where these techniques are used. Due to the toxicity of the Stille reagents and the task that larger stannan compounds are not distillable anymore, the use of this reactions

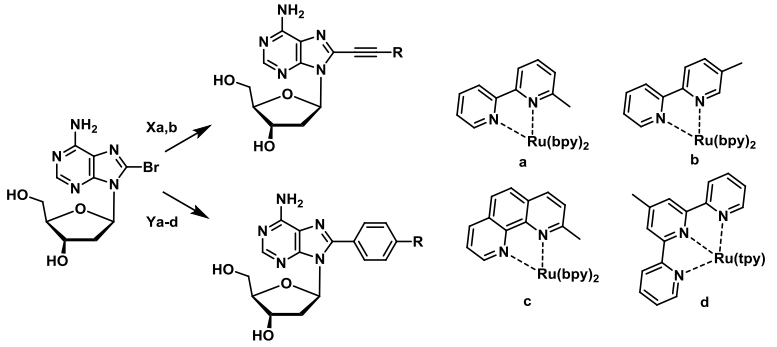

Reagent	*Product*	*Yield (%)*
Xa	12a	16
Xb	12b	0
Ya	13a	55
Yb	13b	86
Yc	13c	80
Yd	13d	52

Scheme 3.4: Schematic representation of the differences in yield using Suzuki or Sonogashira cross-coupling of a sugar to different ruthenium complexes.[88-89]

types is limited. The group of Trouillet *et al.* aimed to build up a copolymer of ruthenium complexes with bridging terthiophene units in the middle.[92] The reaction of the bpy ligand with a following complexation step failed. This is the reason why the authors investigated the polymerization on the ligands scaffold of the complex and achieved a polymer with a weight of around M_n 70,000 g/mol and a conversion of 50% (Scheme 3.5).

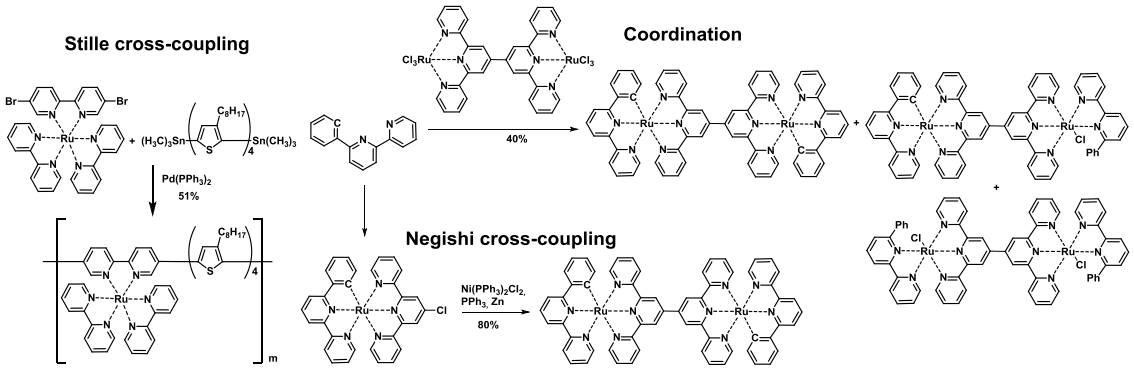

Scheme 3.5: Schematic representation of the Stille reaction to form a metal containing polymer and Negishi reaction for the synthesis of bimolecular complexes. [92-93]

A similar behavior was observed for the Negishi reaction (Scheme 3.5). The coordination of a double cored ruthenium dyad leads to a lot of isomers. This can be avoided by the Negishi cross-coupling of two complexes to the desired complex as shown by Constable *et al.*.[93]

Another excellent example for the chemistry-on-the-complex strategy is the amidation reaction. The C-N coupling of acids and amines enables an easy functionalization especially for the application in the field of biomaterials. It is a useful tool for the labeling of DNA, amino acids in general, sugars or cells. The reaction is harmless for biomaterials and the labeling with ruthenium complexes enables an imaging of cells or their circulations in the body. The good chemical stability of the ruthenium compound allows the utilization as a signaling molecule. The labeling *via* the amidation reaction is frequently used and, hence, the most investigated of the chemistry-on-the-complex strategy. Moreover, it is also suitable for other applications *e.g.* the functionalization of carbon nanotubes[94] or in catalytic systems to a cobalt complex for protein inhibition.[95] Furthermore two ruthenium bipyridine complexes were coupled *via* a bridging

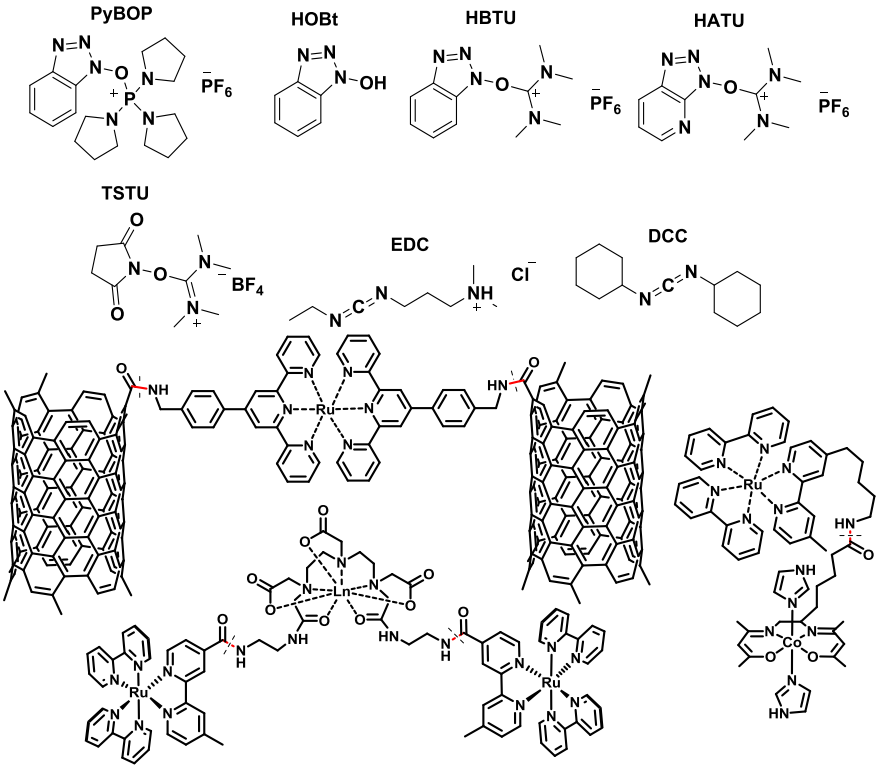

Scheme 3.6: Schematic representation of amidation agents and examples. [94-96]

lanthanide complex.[96] The amidation gets assistance from a number of helping agents like benzotriazol and carbodiimid derivatives or simple bases like triethylamine, diisopropylethylamine or pyridine, while the yields reaches from low to excellent in any combination (Scheme 3.6).

Additionally, the click reactions as well as examples for the nucleophilic substitutions are reported. Click reactions of ruthenium complexes are described at the side chain

functionality of acrylic polymers,[97] by bioconjugates and can also be approached for the synthesis of hexaarylated star-shaped molecules.[98] The standard conditions using a combination of copper(II) sulfate with sodium ascorbate are still applied, while another utilizing pentamethyldiethylenetriamine (PMDETA) as ligand with copper(I) bromide is a promising alternative.[99] The single loaded copper species serves as catalytic unit, which is stabilized by PMDETA. This pathway is very beneficial for harsher reaction conditions and can be used in polar solvents like DMF, without the addition of water, while with ascorbic acid a solvent transfer agent is required, because of the worse miscibility of the solvents. Mostly mixtures of chloroform and water are used, where an addition of ethanol as transfer agent is necessary.

A nucleophilic substitution can be carried out between a halogenated compound, from fluorine to iodine with a molecule including nitrogen, sulfur or oxygen in the presence of a base. The latter is called Williamson ether synthesis. In the case of chlorine also KI can be added, which transfers the chlorine *via* a Finkelstein reaction to the more active iodine for an easier substitution. For all three types, examples *via* chemistry-on-the-complex are displayed in Scheme 3.7. The Williamson ether synthesis represents a favorable technique for the formation of trimers, pentamers or heptamers, as shown by Constable *et al.*.[70, 86, 100-101] The coupling occurs between the hydroxyl group of the centered metal complex with an osmium or ruthenium core and the brominated or chlorinated ruthenium complex.[101] Alkylic amines as well as aromatic ones like pyridines can be used for the nucleophilic substitution. The latter forms a third positive charge after the reaction, which has to be taken into account during the characterization. An example of a hexafunctionalized complex bearing six pyridines on the ligand scaffold is displayed in Scheme 3.7,[102] whereby *via* nucleophilic substitution six anchoring groups were added.

An example for the nucleophilic substitution with thioethers was published by Wild *et al.*.[103] The synthesis of a metal containing polymer was realized by a complex functionalization with two tpy ligands. For this purpose the pentafluorophenyl functionalized complex was reacted with a thioether bridge. The polymerization then occurs by the complexation of further metal centers.

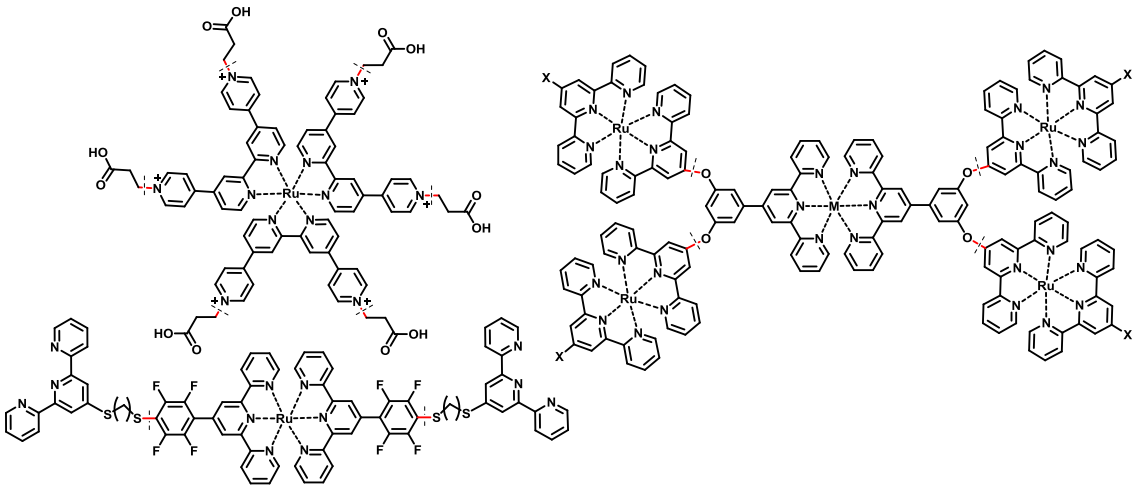

Scheme 3.7: Schematic representation of examples of nucleophilic substitution. [100-103]

In general, metal containing polymers can be formed by standard polymerization reactions. The complex can be embedded in the backbone like mentioned before as well as in the side chain or as end chain functionalization. Furthermore it can be divided by the reaction mechanism. The ruthenium complex could serve as monomer unit or the polymerization occurs *via* coordination of the ligand to the metal core. Well-known are the following polymerization techniques: Free radical polymerization of the monomers methacrylate,[104-105] vinyls[106-108] or styrene,[109] or RAFT,[110-112] ROMP[113-114] and electropolymerization directly on a surface.

3.2 Purification

Generally, the purification of ruthenium complexes represents a challenging hindrance during the synthesis as well as their functionalization. This is caused by the solubility behavior and the difficult separation of isomers and loaded species. The easiest purification methods therefore are washing or precipitation. The isomer separation as well as purification from charged side products requires an enormous effort. Easy purification methods like crystallization can solve this problem, but they are accompanied with a loss of product, which is inacceptable for expensive molecules with a demanding synthetic effort. The best results of purification are achieved *via* column chromatography. Among the usage of silica gel and aluminum oxide, a wide range of functionalized silica and size exclusion materials are available which allow a limitation not only by polarity but also by size and chirality (Scheme 3.8).

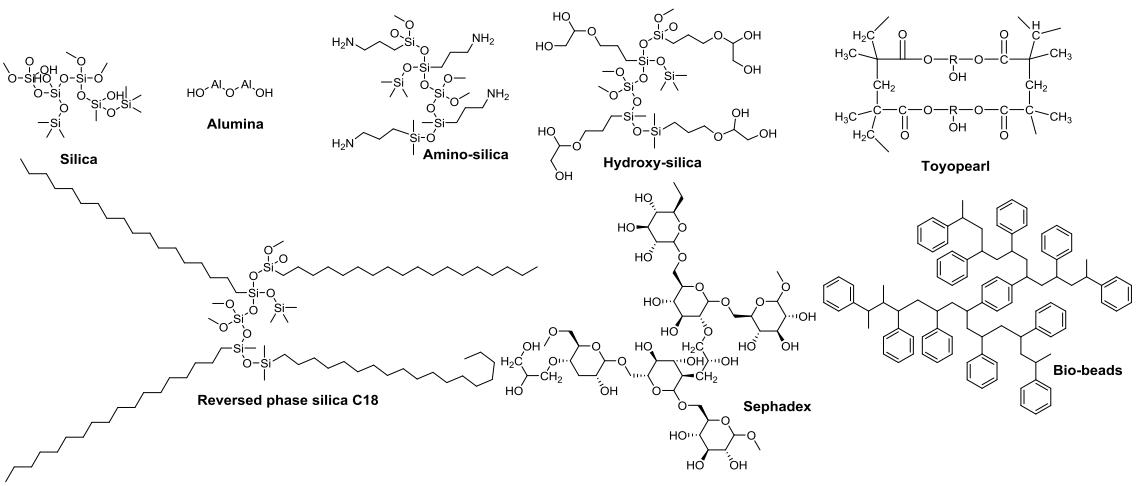

Scheme 3.8: Schematic representation of stationary phases for column chromatography and size exclusion chromatography.

Depending on the separation problem different stationary phases can be applied. Silica gel as the standard purification material is the most utilized one and can be combined with eluent systems from polar mixtures like CH_2Cl_2/MeCN over protic organic mixtures like CH_2Cl_2/MeOH up to aqueous eluent mixtures including salts to increase the ionic strength. The mixtures of acetonitrile, water and aq. KNO_3 are famous, but also KPF_6 is assigned. Nearly the same can be found for aluminum oxide, with regard to the different pH values of the material. The loaded complexes can flow through the column but little separation of similar loaded species is reached. With a small polarity difference the functionalized silica gels represent a good candidate for separation. They are available with a wide range of functionalizations, like amino, diol, cyanide groups or reversed phase with different number length of the alkyl chains. A further advantage is the lack of salts in the eluent and, therefore, an additional anion exchange is avoided. Sephadex is a functionalized dextran, where the index describes the functionalization (CM (Carboxymethyl) or SP (Sulfopropyl), or unfunctionalized Sephadex C-25 and the number describes the grade of porosity. These Sephadex materials are utilized for the separation of isomers. For the isolation of different sized molecules, Sephadex LH (hydroxypropylate) or Sephadex G (without functionalization) and similar products like Superdex as well as Biobeads and Toyopearl are commercially available.

The size exclusion materials differ in the composition and an overview is displayed in Table 3.1. Biobeads consists of polystyrene with divinylbenzene as cross-linker. Sephadex is formed of branched sugars and Toyopearls are cross-linked polymethacrylates. This large number of column chromatography material can solve a

wide range of the different separation difficulties depending on size, charge and chirality.

Table 3.1: Overview of size exclusion material with the size exclusion limit.

Size-exclusion material	*Compound*	*Variations*	*Exclusion limit*[a]
Bio beads	Polystyrene	SX1	600 to 14000
		SX3	< 2000
		SX 8	< 1000
		SX 12	< 400
Toyopearl	Polymetharylate	HW 40	< 3000
		HW-50	< 18000
		HW-55	< 150000
		HW-65	< 1000000
		HW-75	< 50000000
Sephadex	Dextran	LH 20	4000 to 5000
		G 10	700
		15	1500
		25	1000 to 5000
		50	1000 to 30000
		75	3000 to 70000
		100	<100000

[a] tested with dextran and poly(ethylene glycol) respectively poly(ethylene oxide).

In summary, the chemistry-of-the-complex strategy enables a range of applications in the synthesis of metal complex containing architectures. The practicable approach offers the possibility to use the complexes as building unit for an easy incorporation into larger systems, devices and biomaterial application, while the great variety of solid column chromatography materials is available for an efficient separation.

4. Electropolymerization

Parts of this chapter have been published in P4 T. Schlotthauer, C. Friebe, A. M. Schwenke, M. Jäger, U. S. Schubert, *J. Mater. Chem. C* **2017**, *5*, 2636-2648.

As mentioned in the Chapter 3, the chemistry-on-the-complex strategy is applied in the synthesis of metallopolymers especially *via* electropolymerization. This polymerization technique achieves a polymeric film formation by an electrochemical oxidation at the potential of the polymerizable group. The excellent electrochemical behavior of the complexes can be used to support the electropolymerization process. The oxidation potential of the ruthenium complex can be tuned by the introduction of functional groups and shows favorable values around 0.7 V *vs.* $Fc^{I/0}$ for $Ru^{III/II}$,[65] which is lower than the potential of the electropolymerizable thiophene group(0.9 V *vs.* $Fc^{I/0}$), but can be utilized because of a charge transfer to the polymerizable group. The usage of the electropolymerization for the formation of metallopolymer films is well-known, but so far the focus was set on the characteristics of the final film. The conditions of the electropolymerization procedure may have a significant influence on the properties of the film, *i.e.*, homogeneity, peak splits and subsequently their redox ability but are far less studied. For a consistent film growth a wide range of parameters were optimized and analyzed, pH-value, solvents and additives were changed.

4.1 Synthesis and electropolymerization study

Previously, a $[Ru(dqp)_2]^{2+}$ complex bearing two thiophene moieties suitable for electropolymerization was synthesized.[115-116] Thin films with a surface coverage of about 10^{-9} mol·cm^{-2} were obtained, which offered electrochromism and redox-switchable conductivity, but were limited with regard to the formation of thicker structures due to the abortion of the polymerization process after a short time. Thicker films were obtained *via* co-polymerization with thiophene, but they show undefined and unstable electrochemistry.[116] Thus, a replacement of the thienyl unit with a bithienyl possesses lower potentials that are required for electropolymerization. This is expected to lead to minimized side reactions and defects, because the polymerization needs to last longer and should produce films that exhibit less electron traps. Beneficially, on the one hand, the formed defined and π-conjugated quarterthiophene bridging units have an

easy accessible energy level and, therefore, an improved charge-transfer behavior.[117] On the other hand, an energy reservoir effect[118] potentially leads to enhanced effective excited-state lifetimes.

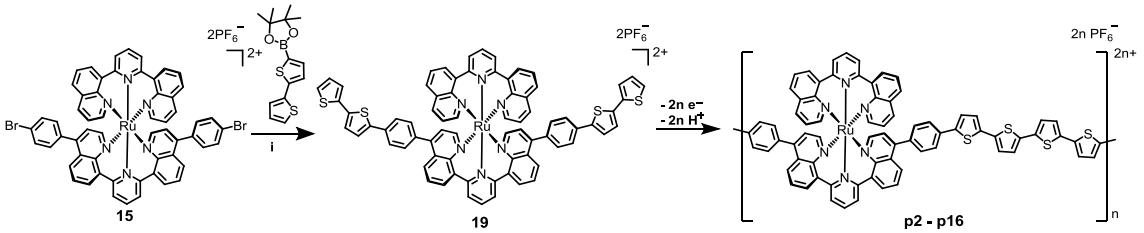

Scheme 4.1: Schematic representation of the synthesis of the bithiophene functionalized complex *via* C cross-coupling ((i) $Pd(dba)_2$, SPHOS, K_2CO_3, MeCN/H_2O (2:1), 100 °C) and subsequent electrochemical polymerization.

The chemistry-on-the-complex approach provides the basis of the monomer synthesis and the electropolymerization itself. The synthesis of the complex $[Ru(dqp)(dqp(Phth_2)_2)]^{2+}$ **19** *via* Suzuki cross-coupling was adapted from previously published results using the bromo-functionalized complex $[Ru(dqp)(dqp(PhBr)_2)]^{2+}$ **15** and the bithiophene boronic acid pinacol ester (Scheme 4.1).[115] The reaction mixture was heated in a MeCN/H_2O mixture to 100 °C for 16 h. The purification of the complex was carried out *via* column chromatography using amino-functionalized silica with a mixture of dichloromethane and methanol (98:2), and final diffusion-controlled crystallization. As mentioned in the first chapter, the synthesis of the bifunctionalized complex can also be achieved by ligand coordination with a higher yield of 61%.

A closer look on the electropolymerization of the thiophene-functionalized complex **p1** shows a constant growth of the polymer film until the 50th cycle and starts to level off until cycle 100 (Figure 4.1). Further electropolymerization leads to a deformation of the potential curve, which shows a degradation of the film and the properties. An oxidation agent is necessary to electropolymerize the thiophene-based complex. The boron trifluoride etherate ($BF_3 \cdot Et_2O$) has a short lifetime in aerated solutions. By an adoption of these conditions for the electropolymerization of the bithiophene-functionalized complex **p2** the film growth degrades very fast (entry 2 in Table 4.1). $BF_3 \cdot Et_2O$ leads also to the formation of side products, which can be seen by the storage of the solution. Even at −18 °C the solution turns brown, while a further electropolymerization is impossible. The oxidation potential of bihiophene has a much lower value and is

easier to oxidize, whereby no oxidation agent is required. A test series on ITO-coated glass slides were started where solvents, salts, additives like $BF_3{\cdot}Et_2O$, pH value, the potential modes, range and reaction times are investigated to identify the best electropolymerization conditions. Without $BF_3{\cdot}Et_2O$ the electropolymerization of **p3** grows smoothly and no side product is obtained (Figure 4.1 and entry 3 in Table 4.1). Furthermore, a higher final cathodic charge of $5.7{\times}10^{-3}$ C·cm^{-2} is reached. During the electropolymerization a proton is abstracted, which turns the solution acidic. The addition of 2,6-lutidine as base for **p4** or water for **p5a/b** was tested to neutralize this proton (entry 4 and 5 Table 4.1). Surprisingly, both lead to a decrease of the polymerization and the formation of side products, while the addition of HPF_6 generates a slower electropolymerization of **p6** without side effects (entry 6 in Table 4.1).

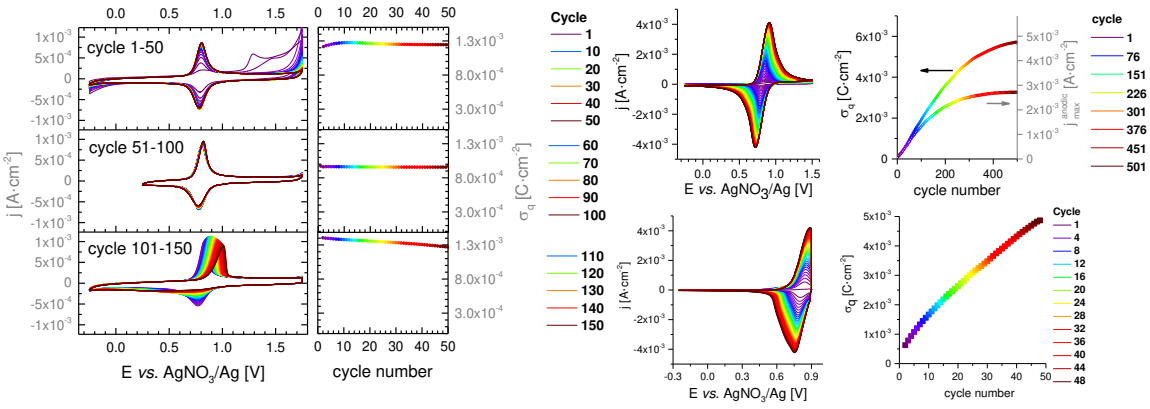

Figure 4.1: Development of the CV of **p1** during potentiodynamic electropolymerization (potentials *vs.* $AgNO_3$/Ag, 200 mV·s^{-1}, 0.1 M Bu_4NPF_6 in MeCN, 5 vol% $BF_3{\cdot}Et_2O$) of thienyl-equipped complex, (top left) initial growth (cycles 1 to 50, applying −0.25 to +1.75 V), (middle left) stagnation of growth (cycles 51 to 100, applying +0.25 to +1.75 V), and (bottom left) over-oxidation of the film (cycles 101 to 150, applying −0.25 to +1.75 V with 5 s rest time at +1.75 V). Arrows indicate evolution of peak currents during cycling. Right panel displays cathodic charges per half-cycle. Note the offset in (middle left) due to the shorter reduction time caused by the changed vertex potential (from −0.25 to +0.25 V), and decreasing cathodic charges in (bottom left) assigned to over-oxidation. (top right) $BF_3{\cdot}Et_2O$-free conditions: Development of the cyclic voltammogram of **19** (left) during potentiodynamic electropolymerization (in MeCN with 0.1 M Bu_4NPF_6, 200 mV·s^{-1}). (Right) Cathodic charge (left axis) and peak current (right axis) over the course of the polymerization. (bottom right) Continuous potentiostatic electropolymerization of **p15** (+0.9 V *vs.* $AgNO_3$/Ag, 240 min; 0.1 M Bu_4NPF_6 in MeCN; CV measured after every 5 min). Development of the CV (a) and of the corresponding cathodic charges (b). Note the larger cathodic CV wave due to the hold time. (Reprinted with permission from Ref.[119] by permission of The Royal Society of Chemistry).

In another approach after 500 cycles of the electropolymerization the monomer solution was used for a second and a third run (**p7a-c** entry 7 in Table 4.1). It was noticed that with every run of the same solution the performance decreased. While the first run reaches a cathodic potential of $6.1{\times}10^{-3}$ C·cm^{-2}, the second run only shows a charge of $3.7{\times}10^{-3}$ C·cm^{-2} and after the third one $1.7{\times}10^{-3}$ C·cm^{-2} was received. The reason seems to be the protonation of the solution. Analysis of the solution shows that a side product was formed. The ESI-ToF-MS identifies the species as an O_2-adduct of the complex,

which can also be recognized in the change of the NMR spectra. For the purification of the solution the mixture was dried and washed with MeOH to remove the salt and excess of protonated solvent. Afterwards the mixture was measured again and compared with the crude and a fresh solution (**p8a-c** entry 8 in Table 4.1). The partly recovered solution shows better results than the crude one, but cannot reach the values of the fresh solution. Nevertheless, this proofs that a recovery is possible. The change of the electrolyte salt to Bu_4NClO_4, which increases the polymerization in the case of PEDOT,[120] results in a lower solubility of the monomer and, therefore, a slower film growth **p9a/b** (entry 9 in Table 4.1). The change of the solvent to dichloromethane results in similar values for **p10** (entry 10 in Table 4.1), but shows in the beginning a different behavior of the potential due to the lower mobility.

Table 4.1: Summary of electropolymerized films.

entry	*film*	E_{polym} [b] *[V]*	*Cycle Number or time*	*Additive/ conditions*	σ_g *[$\times 10^{-3}$ C·cm^{-2}]*	Γ *[$\times 10^{-8}$ mol·cm^{-2}]*
1	**p1**	–0.25 to 1.75		$BF_3{\cdot}Et_2O$	1.3	1,4
2	**p2**	–0.25 to 1.75		$BF_3{\cdot}Et_2O$	4.3	4.5
3	**p3**	–0.25 to 1.50		-	5.7	5.8
4	**p4**	–0.25 to 1.50	500	lutidine	-[c]	-[c]
5	**p5a**	–0.25 to 1.50	500	H_2O (1 mol%)	2.6	2.7
	p5b	–0.25 to 1.50	500	H_2O (1 mol%)	1.8	1.9
6	**p6**	–0.25 to 1.50	500	HPF_6 (0.3 mM)	3.1	3.2
7	**p7a**	–0.25 to 1.50	500		5.9	6.1
	p7b				3.7	3.9
	p7c				1.6	1.7
8	**p8a**	–0.25 to 1.20	500	pristine	3.9	4.0
	p8b			crude	1.6	1.7
	p8c			re-purified	2.7	2.8
9	**p9a**	–0.25 to 1.50	500	Bu_4NClO_4[d]	2.2	2.3
	p9b				1.1	1.1
10	**p10**	–0.25 to 1.50	500	CH_2Cl_2[e]	4.4	4.6
11	**p11**	1.1	60 min	-	4.2[f]	4.4[f]
12	**p12**	1.0	60 min	-	5.3[f]	5.5[f]
13	**p13**	0.9	60 min	-	2.0[f]	2.1[f]
14	**p14a**	1.0	60 min	-	1.6[f]	1.7[f]
	p14b		+60 min	[g]	3.2[f]	3.3[f]
	p14c		+60 min	[g]	4.5[f]	4.7[f]
15	**p15**	0.9	240 min	-	4.9[f]	5.0[f]
16	**p16**	0.9	60 min	CH_2Cl_2[e]	3.2[f]	3.3[f]

a) Performed in 0.1 M Bu_4NPF_6 in MeCN solutions containing the complex in 1 mg·mL^{-1}, if not stated otherwise. b) Stated *vs.* $AgNO_3$/Ag. c) Non-defined CV assigned to decomposition. d) Bu_4NClO_4 instead of Bu_4NPF_6. e) CH_2Cl_2 instead of MeCN. f) Note that potentiostatic data is affected by different charging and potentials compared to potentiodynamically prepared films. g) Fresh monomer solution after 60 min.

Another potential mode is the potentiostatic electropolymerization. A continuous potential of a higher value than the oxidation potentialis used and is hold for a several time. Every five minutes a potentiodynamic cyclization was done to follow the polymerization degree. A 60 minutes electropolymerization should provide the same

range like the potentiodynamic version. Three different potentials were investigated 1.1 V (**p11**), 1.0 V (**p12**) and 0.9 V (**p13**) to overcome the over-oxidation which results in side reactions (entry 11 to 13 in Table 4.1). All three lead to the formation of the ruthenium complex film by a constant film growth, but the cathodic charges and peak forms/splits are different. Whereas the potentials of **p11** and **p12** reach higher values in the same range as the dynamic electropolymerization, **p13** leads to a tightened peak form and, therefore, a peak split. The time of the electropolymerization has a significant influence on the film growth. By refreshing the solution every 60 minutes at 1.0 V for **p14a-c** a continuous growth was the result until 180 minutes (entry 14 in Table 4.1). Surprisingly, the electropolymerization at 0.9 V over 240 minutes without refreshing leads to **p15** with a high cathodic charge of 4.9×10^{-3} C·cm^{-2} and an even sharpened peak curve in the CV (entry 15 in Table 4.1). Finally, the potentiostatic electropolymerization in dichloromethane was investigated at 0.9 V with duration of 60 minutes (**p16**) and leads to similar values (Figure 4.1 and entry 16 in Table 4.1). In conclusion, both techniques show analogous results and enable a mild electropolymerization in acetonitrile and dichloromethane without the addition of bases, acids and oxidation agents. This detailed mechanistic study was never reported before, but can be serve as basis for following work in the area of electropolymerization.

4.2 Structure and morphology

The structure and morphology of the ruthenium complex metallopolymers on the ITO coated glass slides were investigated *via* optical profilometry and scanning electron microscopy (SEM). The electropolymerized films exhibited no homogenous and smooth morphology, rather they showed a surface with one height that was covered with spherical agglomerates, which can be seen on the SEM images (Figure 4.2 a-c). Measurements with secondary electron detection provide a significant better contrast in the height profile. It can be seen that the structure of the electropolymerized films looks like the combination of various agglomerates. By a closer look on the edge (Figure 4.2 d and e) the agglomeric structure in the middle of the film can be recognized. The detection of the film thickness with SEM is problematic because of the agglomeration and the fact that a broken edge is required. Consequently, the optical profilometry was applied to calculate a film thickness (Figure 4.2 g-i).

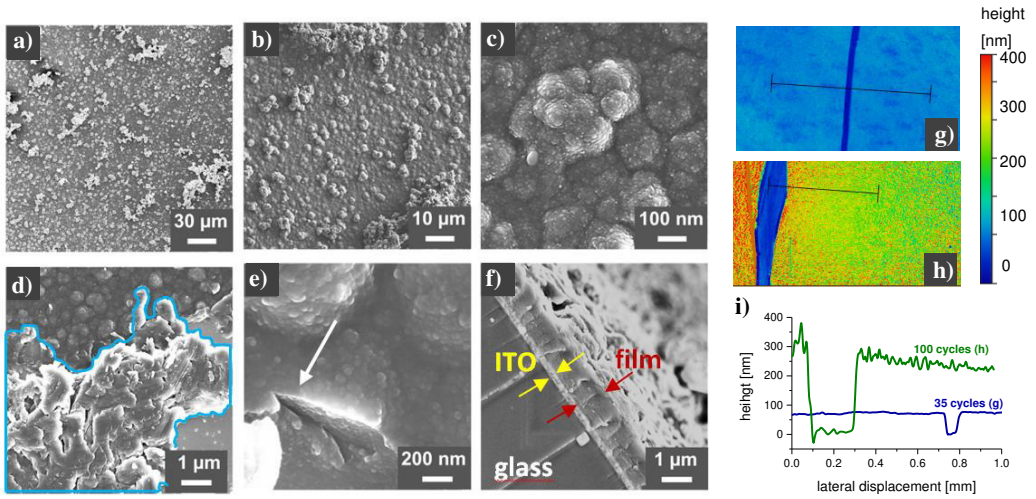

Figure 4.2: Representative SEM images of electropolymerized films on ITO-coated glass slides (0.1 M Bu_4NPF_6 in MeCN). (a–c) Surface of intact films at different magnification values (a, c) and secondary electron detection (b) for more realistic depth perception. (d) Scratched surface showing intact region (upper part), displaced debris from scratching (blue-framed area) and slide surface (bottom right). (e) Scratched surface showing internal spherical substructure. (i) Cross-section of manually broken slide showing glass support, ITO layer (yellow), and film (red) as marked by arrows of intact thick film. (g,h) Optical profilometry images of electropolymerized films on ITO-coated glass slides after 35 cycles (**p17**, top) or 100 cycles (**p18**, bottom). (i) Cross-sectional profiles in the edge region of the films. Bottom of scratch assigned to the slide surface (Reprinted with permission from Ref.[119] by permission of The Royal Society of Chemistry).

Therefore a scratch was made on the surface. The ITO layer is much harder than the polymerization film, so the difference of the height to the ITO layer were measured. The scratches on the electropolymerized film with cyclization numbers of 35 and 100 were compared and show with 70 nm and 230 nm a constant increase of the film thicknesses in the beginning of the electropolymerization of a factor of around three. This is in good agreement with the cycling number. Additionally, a cycle depended measurement revealed the correlation of the cycling number with the film thickness (unpublished results) (Figure 4.3).

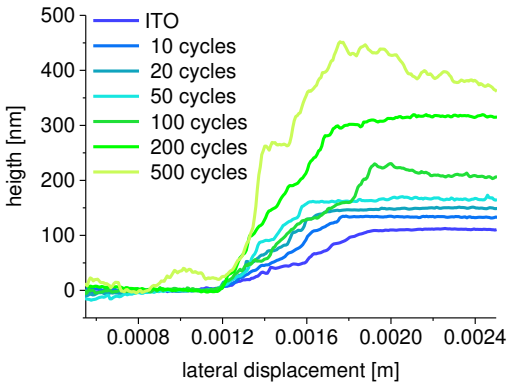

Figure 4.3: Profilometry measurements of different thicknesses in comparison ITO depending on the cycling number. Electropolymerization was performed on ITO glass slide potentiodynamic potentials applying −0.25 to +1.2 V *vs.* $AgNO_3/Ag$, 200 $mV \cdot s^{-1}$, 0.1 M Bu_4NPF_6 in MeCN.

4.3 Optical and electrochemical properties

Cyclic voltammetry, electrochemical impedance spectroscopy, spectro-electrochemistry as well as steady state UV-Vis and emission spectroscopy were utilized. The CVs of the films were measured in fresh electrolyte solution and reproduced the end state of the electropolymerization in shape, potential, current density and cathodic charge. The potential of 0.73 V combines the Ru^{III}/Ru^{II} oxidation with the oxidation of the quarterthiophene units. In contrast, the peak split revealed larger differences between the several films. The milder the electropolymerization conditions the smaller is the peak split with the best results for the electrostatically variation with a peak split of 2.5 mV by a scan rate of 2 mV/s.

Electronic impedance measurements were performed in the range from 1 Hz to 1 MHz. The projected Nyquist plots display a semicircle for the potentials in the oxidized area, with a maximum of 0.8 V to get a film conductivity of 1 to 5×10^{-6} $S\cdot cm^{-1}$ depending on the surface porosity.

The steady state UV-Vis spectra of the obtained films mirror the absorption properties of the monomers. The MLCT is slightly bathochromic shifted due to the influence of the quarterthiophene units, which results also in a shifted emission to 780 nm.

In summary, the bithiophene decorated ruthenium complexes were synthesized *via* the chemistry-on-the-complex strategy using the Suzuki cross-coupling reaction. The electropolymerization conditions were improved to identify a mild technique for generating an almost homogeny and linear grown film. The best techniques are potentiodynamic in acetonitrile without the addition of an oxidation agent. The variation of H_2O, acids, solvents and salt resulted in differences in the film growth but the electropolymerization still takes place. The mildest reaction conditions were found for the potentiostatic polymerization at 0.9 V.

5. Modularly assembled photoredox-active dyads and triads

Parts of this chapter have been published in P) R. Schroot, T. Schlotthauer, U. S. Schubert, M. Jäger, *Macromolecules* **2016**, *49*, 2112-2123. P) R. Schroot, T. Schlotthauer, M. Jäger, U. S. Schubert, *Macromol. Chem. Phys.* **2017**, *218*, 1600534. P) T. Schlotthauer, R. Schroot, S. Glover, L. Hammarström, M. Jäger, U. S. Schubert, *Phys. Chem. Chem. Phys*. **2017**, *19*, 28572-28578. P) R. Schroot, T. Schlotthauer, B. Dietzek, M. Jäger, U. S. Schubert, *Chem. Eur. J.* **2017**, *23*, 16484-16490.

Another possible application of $[Ru(dqp)_2]^{2+}$ complexes in combination with the chemistry-on-the-complex strategy is their application as photosensitizer in photoredox-active dyad or triad systems. This chapter deals with the stepwise modular and orthogonal assembly as well as with the spectroscopic characterization of the synthesized dyads and triads. The modular architectures of these structures can be achieved *via* a stepwise formation of well-defined starting materials, which guarantee a complete and defect free synthesis.

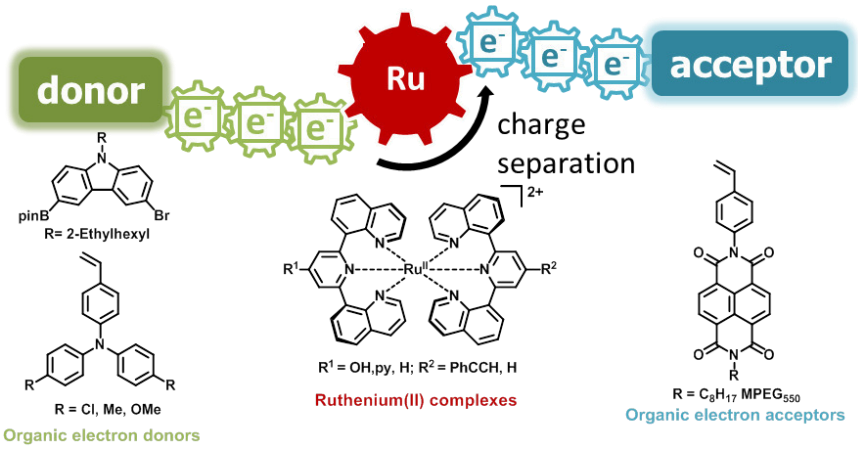

Figure 5.1: Schematic representation of the D-P-A triad with applied units.

5.1 Complex synthesis as modular unit

The incorporated polymers, which form the active acceptor and donor units, were prepared in the Schubert group by a controlled NMP polymerization using a functionalizable initiator to reach low dispersity with a specific end group. In this way, a functionalized polynaphthalene diimide as acceptor polymer and a polytriarylamine as donor polymer were obtained. Both contain alkyl chains for a higher solubility in

common solvents, *i.e.* the NDI polymer is functionalized with an ethylhexyl chain, while TARA bears butyl chains in the para position of the phenyls.[121] A polycarbazol (pCarb) was investigated to generate a conjugated donor polymer. The compound was prepared *via* Suzuki coupling polymerization to introduce a defined chain end.

The exchange of the achieved Cl-functionality against an azide moiety followed a standard reaction protocol with NaN_3. Whereas the Cl-moiety was used for nucleophilic substitution, the newly introduced azide was accessible for the CuAAC reaction. The complex synthesis was realized as described in the second chapter (Scheme 5.1). The ligands, acetonitrile precursor and the complexes bearing the alcohol and the bromophenyl substitution **C2** were adopted from published results. [28, 122-123]

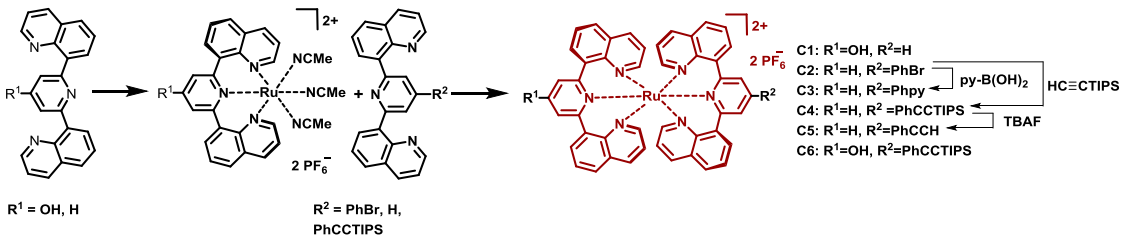

Scheme 5.1: Schematic representation of the coordination of the $[Ru(dqp)_2]^{2+}$ complexes with functionalization on the complex.

A Suzuki cross-coupling reaction was realized using potassium carbonate, $Pd(dba)_2$ and SPHOS as catalyst and the boronic acid of the pyridine as reagent in acetonitrile to introduce the pyridine unit on the complex **C3**. After overnight heating at 100 °C the complex was purified *via* column chromatography using diol functionalized silica gel as stationary phase and a mixture of dichloromethane and methanol as eluent. The complex **C3** was isolated in a yield of 67%. The alkyne functionalized complex **C4** was synthesized *via* Sonogashira cross-coupling and the standard catalyst $Pd(PPh_3)_4$ and CuI in DMF were utilized. The dry triethylamine as well as the triisopropylsilylacetylene were added at 60 °C and the reaction mixture was heated overnight and subsequently purified *via* column chromatography with silica gel using an eluent mixture of acetonitrile, water and aqueous potassium nitrate with a yield of 91%. The deprotection was realized using TBAF in THF/MeOH at 0 °C to achieve a quantitative conversion to **C5**.

For the synthesis of the bifunctionalized complex, which is necessary for the triads, the complexes were coordinated from the hydroxyl functionalized $[Ru(dqp)_2]^{2+}$ acetonitrile precursor. The second ligand already bears the C≡CH-function protected with TIPS to form **C6**. The coordination takes place as mentioned in Chapter 2.2 using DMF as solvent at 140 °C. The purification was performed like previously described for **16** with an additional diffusion controlled crystallization step to gain a yield of 51%. The protection group remained intact during the entire synthetic procedure.

5.2 Dyad formation and characterization

A first series of pNDI containing dyads should provide an overview of suitable linkage strategies (Scheme 5.2). Therefore the CuAAC click reactions as well as two nucleophilic substitutions were tested regarding their conditions, yields and photophysical effects. A reference complex was synthesized to each dyad, following the same reaction conditions. The complexes were coupled with the specific functionalized benzene (**C7** to **C9**) to reach a similar structure and overcome effects of the new substituent. These complexes were used for the spectroscopic measurements as reference compounds.

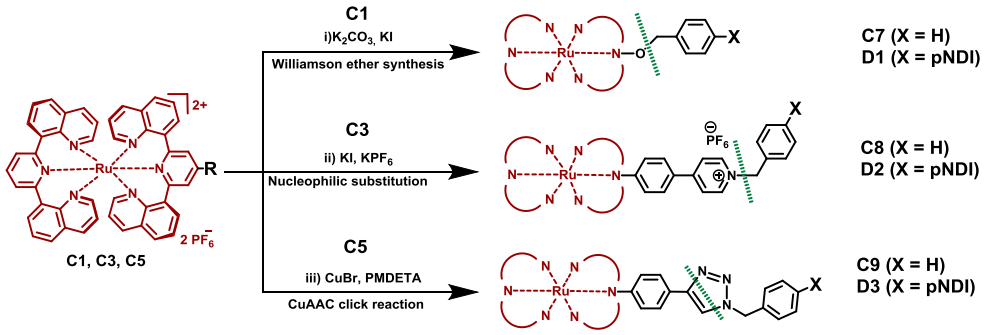

Scheme 5.2: Synthesis of the reference complexes **C7**–**C9** and the respective dyads **D1**–**D3**.

The Williamson ether synthesis for the chain end functionalization was reported for the formation of a pTARA-Ru-dyad[121] as well as for the pNDI.[124] The usage of K_2CO_3 alone achieves only low yields. In this work KI was added which guarantees a more efficient coupling to **D1** with a yield of 55%. This *in situ* Finkelstein reaction exchanges the chloride from the polymer end group to the more reactive iodide, which results in an increased yield. The reaction was monitored *via* thin layer

chromatography as well as 3D size exclusion chromatography (SEC) measurements and the mixture was purified by column chromatography using diol and amino functionalized silica gel as stationary phase. Older protocols using aluminum oxide and a mixture of dichloromethane and methanol as eluent could not achieve a full separation. The analysis *via* ^{1}H NMR spectroscopy and MALDI-ToF-MS revealed the successful purification yielding the pure product. In the same manner a polymeric dyad **D4** of the PEG-functionalized pNDI was realized. In contrast, the purification was rather difficult because of the solubility of the dyad in water. Therefore a size exclusion chromatography using Toyopearl as stationary material was performed. After two runs a pure fraction was achieved with a yield of 70%. Another coupling mechanism is the quaternization of the pyridine unit, which resulted in a further charge of the corresponding dyad. For an efficient conversion KI and KPF_6 were added to obtain a more reactive coupling and to provide a similar non-binding anion. After purification, the dyad **D2** could be obtained with a yield of 40%, due to the small reaction scale with sampling and purification on a column chromatography using aluminum oxide. The last dyad **D3** was prepared *via* CuAAC click reaction between the alkyne containing complex $[Ru(dqp)(dqpPhCCH)](PF_6)_2$ and the azide decorated pNDI. The standard reaction conditions of the click reaction using copper(II) sulfate in combination with sodium ascorbate as catalytic system are impracticable because of the solubility. An alternative route was reported by Sun *et al.* who applied Cu(I)Br and PMDETA as catalytic system.[99] The amino ligand ensures the stabilization of the copper compound and, therefore, the oxidation state. The reaction was performed at room temperature and 3D SEC showed full conversion after 16 hours. The purification was performed on amino functionalized silica gel packed column chromatography and reaches a yield of 71%.

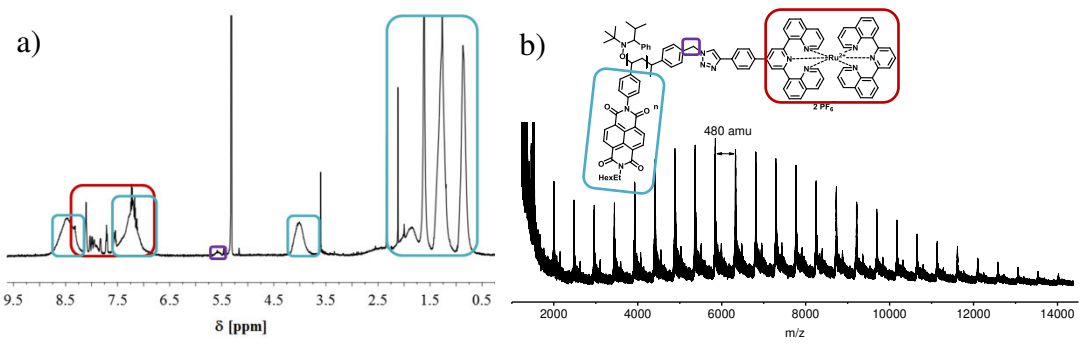

Figure 5.2: (a) NMR (CD_2Cl_2) and (b) MALDI-ToF-MS of the dyad **D3** *via* click reaction, show units and bridging methylene group.

All dyads were characterized *via* NMR spectroscopy and MALDI-ToF-MS (Figure 5.2). The NMR spectra displayed the clear signals of the ruthenium complexes framed by the widened NDI polymer signals, while the successful coupling can be seen by the shift of the bridging methylene proton next to the coupling group from 4.3 to 5.6 ppm. Furthermore MALDI-ToF-MS confirmed this result. All dyads show a nearly same contribution with isotop patterns of the ruthenium compound, whereas the dyads **D1** and **D3** revealed a cleavage of the initiator group (TIPNO). In contrast the pyridinium bridging unit on dyad **D2** led to a cleavage of the complex by forming a cyclopentadienyl moiety. In conclusion all three coupling procedures were successful.

5.3 Spectroscopic characterization of the dyads

Spectroscopic measurements were done to confirm that the coupling group has a low impact on the photophysical behavior of the ruthenium dye. The dyads should be able

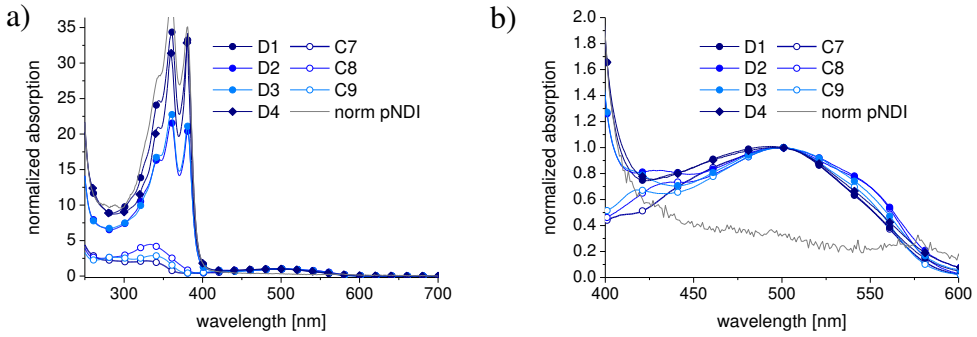

Figure 5.3: Absorption data of the reference complexes (**C7**−**C9**) and the corresponding dyads (**D1**−**D4**) in dichloromethane. (a) UV−Vis spectral region illustrating the dominant UV absorption of the pNDI chains. (b) Inset of the MLCT region illustrating preserved optical properties of the Ru photosensitizer (gray area depicts the low-energy tail of the pNDI absorption).

to generate an efficient charge transfer from the ruthenium photosensitizer to the acceptor polymer. The absorption spectra of the dyads **D1** to **D4** and their reference complexes **C7** to **C9** in comparison with the non-functionalized pNDI are displayed in Figure 5.3. The polymer signals are centered in the UV region and showed maxima of the $\pi \rightarrow \pi^*$ transitions at 360 and 380 nm. The ligand based transitions can be found in the same area, but disappeared because of the large polymer signals. More importantly, the MLCT peak of the $[Ru(dqp)_2]^{2+}$ complexes can be found in the visible region between 400 and 600 nm with a maximum of 500 nm without any overlay with the NDI- units.

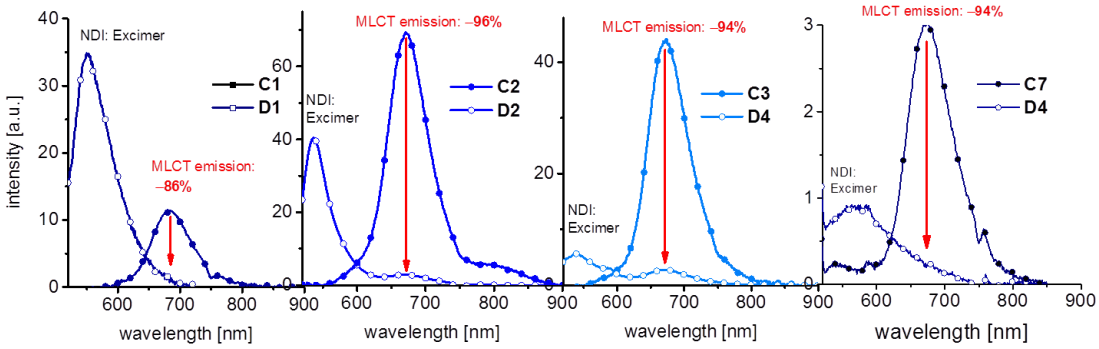

Figure 5.4: Emission data of the reference complexes and the corresponding dyads (aerated dichloromethane, room temperature, iso-absorbing solutions at 500 nm excitation). Arrows indicate quenching of the ^{3}MLCT emission (in %) of the dyad *vs.* the reference complex, respectively. Note the lower emission intensity of **C7** compared to **C8** and **C9** caused by a lower intrinsic quantum yield (not reported). (a) Ether-linked complex **C7** (b, c) Pyridinium- and triazole-linked congeners.

Furthermore, the coupling units show no impact to the location of the MLCT. This might be necessary to guarantee the single excitation of the complex. Moreover, the absorption behavior of the complex and the polymer are combined in the absorption spectra of the dyads. No interactions of the unit in the ground state occur and the units can be seen as separated building blocks. The steady state emission spectroscopy can help to gain a first hint of energy transfer. The MLCT emission which occurs for all Ru-dqp complexes should disappear by quenching of the acceptor units of the dyads. Therefore, the dyads in comparison with the specific reference complexes were measured in aerated dichloromethane (Figure 5.4). The excitation of the MLCT with a wavelength of 500 nm led to an emission between 600 and 800 nm with a maximum of 690 nm. The large difference between **C7** and the other complexes is caused by the OH group which is directly coupled on the ligand scaffold without a phenyl spacer and leads to a bathochromic shift of the emission wavelength. In all cases the emission of the dyads is reduced in contrast to the complexes with efficiencies between 86% and 96%. These are calculated in the difference of the spectra at the maximum wavelength. Following, an efficient charge transfer occurs independently from the bridging unit. These investigations allow a modular approach by using these different coupling mechanisms to form a first polymeric triad system.

5.4 Modular assembly to generate the first polymeric triad

Based on the coupling test series it is now possible to form polymeric triad systems. The Williamson ether synthesis in combination with the click reaction seems to be the most favorable combination for the modular strategy. The synthesis sequence starts

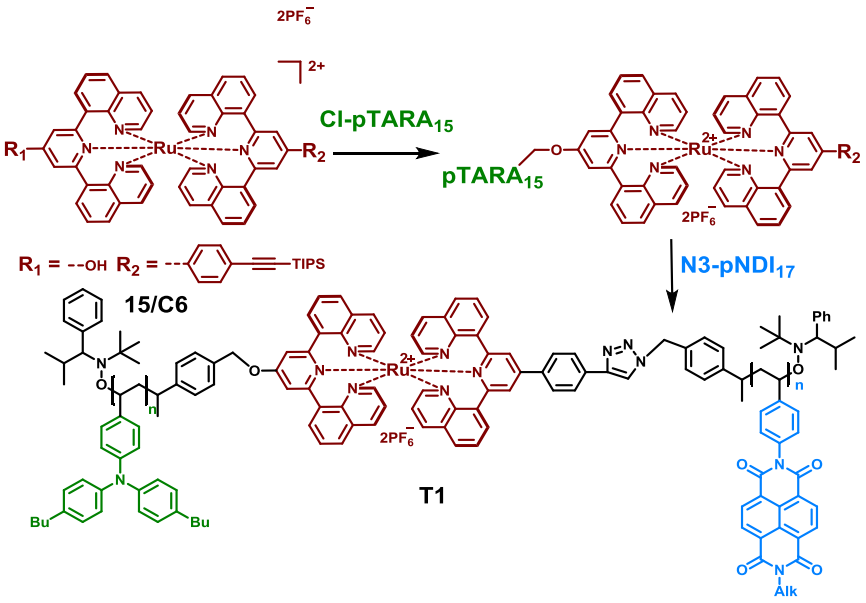

Scheme 5.3: Schematic representation of the stepwise synthesis of the polymeric triad.

with the nucleophilic substitution, followed by deprotection of the TIPS group and finally the click reaction, according to their activity and yield (Scheme 5.3). The Williamson ether synthesis between the pTARA polymer and the bifunctionalized ruthenium complex **C6** was achieved with K_2CO_3 and KI as mentioned above to form the dyad **D6**. The isolation of the formed dyad was achieved by preparative size-exclusion chromatography using a Toyopearl HW-55F resin on a flash master system. The purification according to the hydrodynamic volume avoids typical challenges related to the ordinary column chromatography of metal complexes, *i.e.* adsorption of the analyte on the solid phase or minor polarity differences. The successful functionalization is readily verified by proton NMR spectroscopy (Figure 5.5) due to the appearance of the typical broad TARA resonance (6.5 to 7.0 ppm) and smaller signals corresponding to the Ru(II) complex (signals from 6.5 to 8.2 ppm). Moreover, the signal of the methylene protons of the polymer end group shifts from 4.6 ppm to approximately 5.2 ppm upon functionalization. A further proof is given by the 3D data of the diode- SEC, which showed the overlapping absorption spectra of polymer and ruthenium complexes in one molecule.

Next, the TIPS protecting group of the dyad was cleaved, whereby the acetylene group became accessible for the second coupling step. Therefore the compound was stirred with $(n\text{-Bu})_4NF$ in THF. The excess of $(n\text{-Bu})_4NF$ was finally removed by washing with MeCN. The quantitative deprotection was verified by the disappearance of the TIPS signal at 1.18 ppm in the proton NMR spectrum.

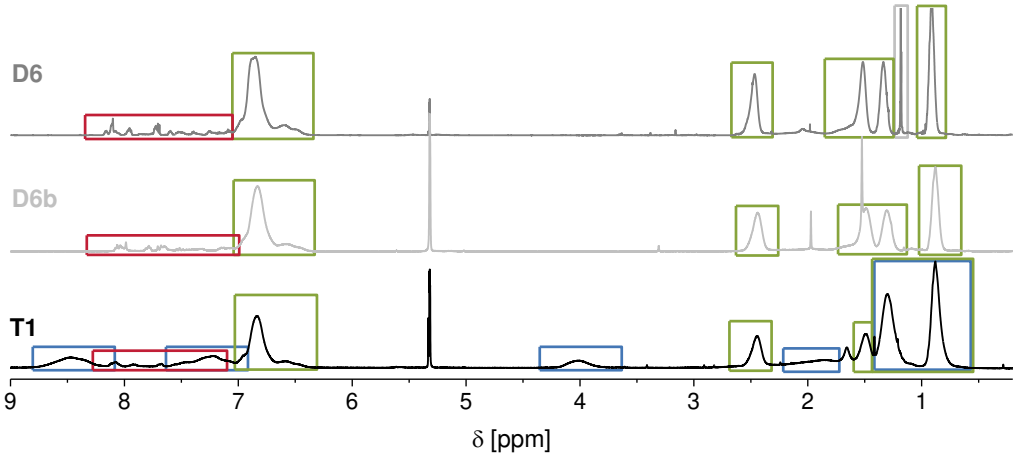

Figure 5.5: Comparison of the proton NMR spectra of dyad, deportection and triad showing distributions of the Ru(II) complex (red), the polytriarylamine (green) and the polynaphthalene diimide (blue). The successful deprotection of **D6** is verified by the disappearance of the TIPS signal (grey).

The deprotected dyad is termed **D6b**. For the final coupling step, *i.e.* the linking of **D6b** with the polymer **pNDI**, the CuAAC reaction was applied. The temperature was increased to 80 °C because a test reaction did not show any conversion at room temperature. The required higher temperature is assigned to the kinetic effects, *i.e.* low diffusion coefficients of the macromolecules, a higher viscosity of the reaction mixture at room temperature and the sterically hindrance resulting from the reaction of two polymers. The reaction progress was monitored by UV-Vis SEC until no further conversion was detected. The separation of the triad **T1**, excess of polymer and residual **D6b** was achieved by preparative SEC using Toyopearl HW55 as stationary phase. As the triad and the dyad do not elute completely baseline separated, two runs were necessary to isolate **T1** in good yields. The compound was characterized by NMR spectroscopy and UV-Vis SEC. The proton NMR spectrum showed the typical broad resonances of the NDI monomer unit from 8.3 to 9.0 ppm and 7.0 to 7.5 ppm as well as the resonances of the TARA unit (6.3 to 7.0 ppm). Additionally, small signals corresponding to the ruthenium complex (7.5 to 8.3 ppm) and two broad resonances from the linking methylene bridges (5.6 and 5.2 ppm) were clearly distinguished. Due

to the known challenges attributed to the recording of MALDI-TOF spectra of block copolymers, no analyzable spectrum could be recorded.

5.5 Spectroscopic characterization of the triad

The triad was analyzed *via* steady state emission spectroscopy and time resolved transient absorption spectroscopy to guarantee the preserved photophysical behavior of the ruthenium complex and their photosensitizer properties for generating a charge separated state with following transfer to the polymers. The first step thereby is the absorption of light by the MLCT transition of the ruthenium complex. After excitation the long lived ^{3}MLCT state occurs after intersystem crossing and energy separation with transfer to the acceptor units. The coupled donor unit can reduce the complex back to the ground state. The basic analysis of this process can be reached by steady state spectroscopy followed by the more complex time resolved transient emission spectroscopy. The synthesized triad **T1** was analyzed in the same way as the dyads. An absorption spectrum includes the triad as well as the dyad, a reference complex and the free polymers (see Figure 5.6). In the case of **T1** the absorption spectrum shows the

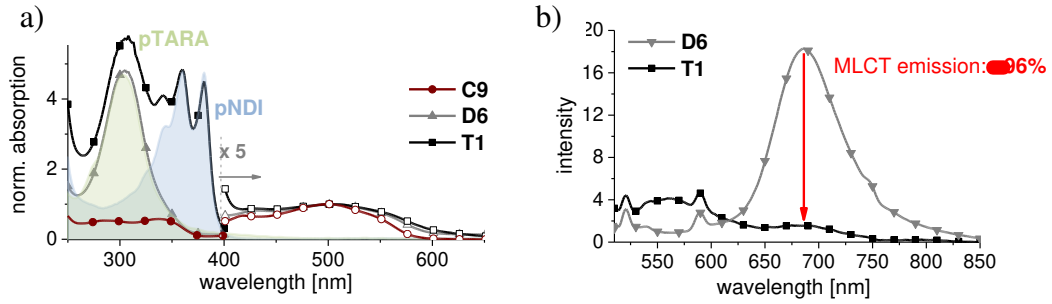

Figure 5.6: a) Absorption spectra of the polymeric building blocks pTARA (green-shaded area) and pNDI (blue-shaded area), reference complex **C9** (red curve) and the triad (black curve). Note the amplified signal (×5, dashed line) to illustrate the weak absorption band of the single Ru photosensitizer unit (400 to 600 nm). b) Steady-state emission spectra of the precursor dyad (grey line, triangles) and the triad (black line, rectangles). Note polymer-based emission (<650 nm) and the ^{3}MLCT emission (around 700 nm), the latter revealing strong quenching (−96%) between dyad (D–P) and triad after subtracting residual polymer-based emission.

perfect addition of the single units. All maxima for the NDI (360 and 380 nm), TARA (300 nm) and $[Ru(dqp)_2]^{2+}$ complex (500 nm) can be identified. As described above, the charge transfer can be visualized by the measurement of the emission spectrum of the MLCT band. Therefore, the dyad **D6** was used as exact prestage that bears the

C≡C−TIPS group. The excitation wavelength was 500 nm, which resulted in the ruthenium based ^{3}MLCT emission around 685 nm. The pTARA unit of the dyad is not able for a reductive quenching due to the unfavorable energetic potential of 0.2 eV. After coupling to the NDI polymer the compound was measured again and the intense ^{3}MLCT emission disappears because of the oxidative quenching and, therefore, the charge transfer to the acceptor units. The effective quenching with a yield of 96% showed the desired electron transfer of these architectures.

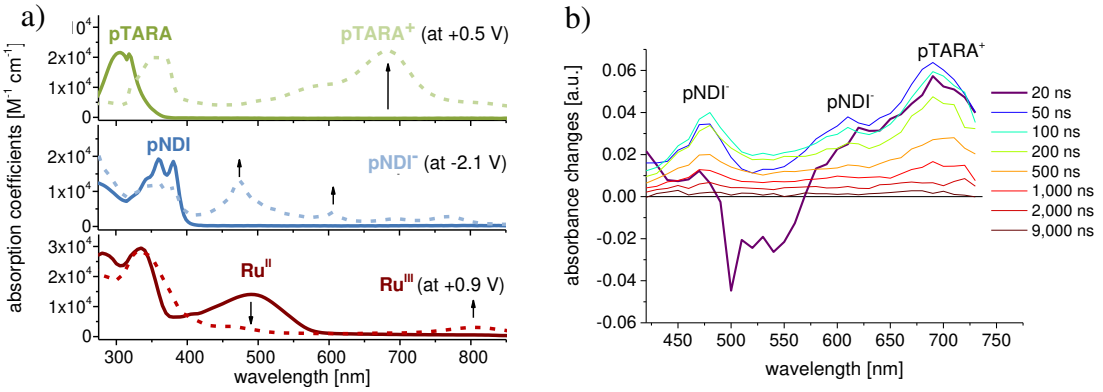

Figure 5.7: (a) Spectro-electrochemical data (in 0.1 M nBu_4NPF_6 in CH_2Cl_2, potentials *vs.* $Fc^{+/0}$) of the **pTARA** block (top), the **pNDI** block (middle), and the Ru reference complex (bottom). Spectro-electrochemical data taken from refs[124-125]. (b) TA data showing the rapid formation of a charge-separated state and slow subsequent recombination. Note the fast ^{1}MLCT recovery, as well as the positive TA signatures of $pNDI^-$ (475 and 610 nm) and $pTARA^+$ (690 nm) (Reprinted with permission from Ref.[126] by permission of The Royal Society of Chemistry).

A more detailed analysis of this energy transfer can be achieved *via* time resolved emission and transient absorption measurements. For this purpose, the solutions were irradiated by a laser pulse with a defined wavelength and the recombination decay process is followed *via* absorption spectroscopy. Thereby, the oxidized and reduced species can be visualized to follow the transfer process. Figure 5.7 shows the spectra of the oxidized and reduced specimens of the individual units which were previously recorded and are used to identify appearing signals in the TA data. In the case of **pTARA** the intense band at 300 nm decrease while new peaks at 350 and 690 nm are formed. In the reduced form the **pNDI** unit showed two new peaks at 475 and 610 nm while the MLCT absorption of Ru-dqp decreased with a new peak formation above 750 nm. The transient absorption spectrum of the triad **T1** revealed the peak appearance of the desired oxidized and reduced species in dependence of the time. The bleach around 680 nm is assigned to the emission of the ruthenium. After irradiation the peak bleach of the $[Ru(dqp)_2]^{2+}$ complex MLCT identifies the oxidation which immediately gets transferred to the reduced $pNDI^-$ and the oxidized $pTARA^+$ by

recovery of the MLCT to form D^+-P-A^-. The recombination decay of the TA signals is now importantly longer than in the dyad, which underlines a multiple process with biexponential kinetics of the recombination decay of 430 ns (71%) and 2400 ns (29%). The multiexponential recombination decay contributes to the charge separated state after further charge transfer steps inside of the polymer. Due to the potentials of the single units an oxidative quenching of the Ruthenium excitation is identified. The small voltage difference of the oxidation potential of the ruthenium complex (0.7 V) and the pTARA (0.5 V) cannot undergo reductive quenching.

These results confirmed the postulated preservation of the photophysical behavior of the ruthenium complex. The coupling to two polymer units with different coupling strategies had no influence, but with the modular character the formation of the triad seems to be facile with less synthetic effort in comparison to classic procedures. An additional triad which bears a conjugated donor polymeric could be realized to show the flexible usage of this ruthenium unit

5.6 A second triad with conjugated donor unit

In analogy the second triad **T2** was formed including the **pCarb** as donor unit, which was polymerized *via* a Suzuki cross-coupling reaction. In contrast to the triad **T1** the bridging units of the donor and acceptor units were switched. Consequently, the **pNDI** was first coupled *via* Williamson ether synthesis, followed by deprotection and click reaction of the **pCarb** (Scheme 5.4). That showed one more time the flexible usage of the linking strategy. A reference dyad **D5** was also achieved in the same manner for

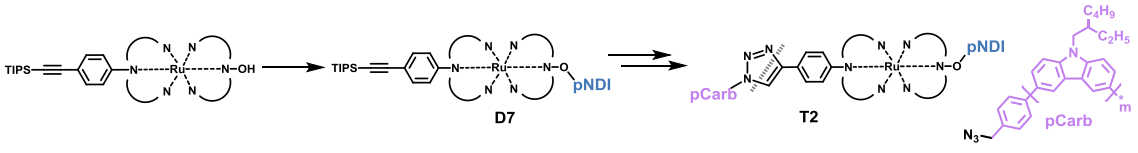

Scheme 5.4: Schematic representation of the modular assembly of the photosystem D_n–P–A_m **T2**.

the comparison of the spectroscopic investigations. By a look at the absorption spectra of **T2** a different behavior is displayed in contrast to **T1** (Figure 5.8). Here the polycarbazole signals in the UV range disappeared below the signals of NDI. The synthesized dyad **D7** could not be used to compare the dyad with the triad **T2**, because

it should already show the quenched emission, due to the fact that the NDI unit was coupled first. Therefore the carbazol-Ru-dyad **D5** was synthesized and served as reference for the measurement. A similar behavior was found for the triad **T2** with an emission quenching of furthermore 96%. In contrast to **pTARA** the oxidation potential of **pCarb** is 0.22 V that is able to a partial reductive quenching, which can be seen in the dyad but not in the triad **T2**.

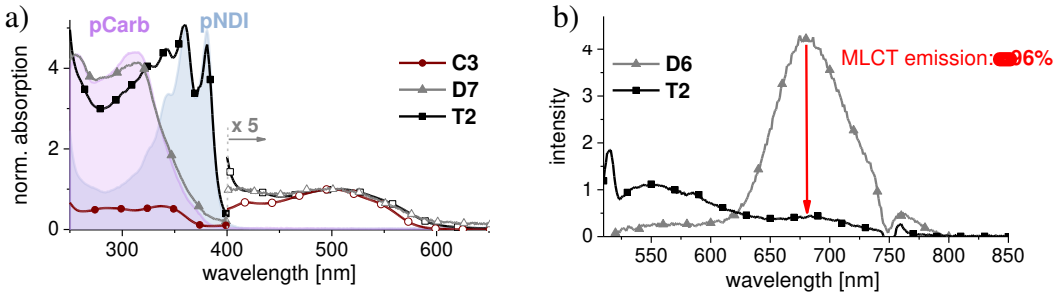

Figure 5.8: (a) Absorption spectra of the polymeric building blocks pCarb (purple-shaded area) and pNDI (blue-shaded area), reference complex (red curve) and the triad (black curve). Note the amplified signal (×5, dashed line) to illustrate the weak absorption band of the single Ru photosensitizer unit (400 to 600 nm). (b) Steady-state emission spectra of the reference dyad (grey line, triangles) and the triad (black line, rectangles). Note polymer-based emission (<650 nm) and the ^{3}MLCT emission (around 700 nm), the latter revealing strong quenching (−96%) between dyad (Dn–P) and triad after subtracting residual polymer-based emission.

Similar to **T1** an oxidative quenching seems to be the mechanism with a three times longer recombination decay. This means the associated lifetimes of the biexponential kinetic are 700 ns (83%) and more important 7200 ns (17%) for the charge separated state after charge transfer in the polymer. An explanation is provided in the conjugated system, which is able to stabilize the charges in the polymer unit (Figure 5.9).

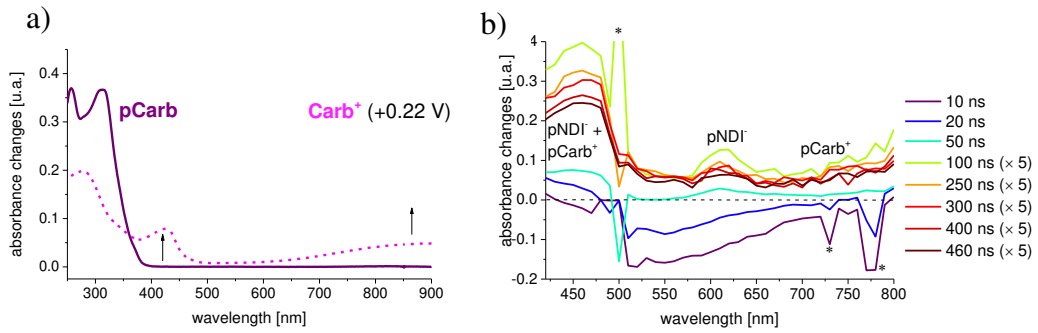

Figure 5.9: (a) Redox titration of polymer **pCarb** with $SbCl_5$ solution (in aerated CH_2Cl_2, RT) show the evolution of new absorption bands at 430 nm and above 600 nm; find **pNDI** Ru reference in Figure 5.7. (b): Transient absorption data of D_n–P–A_m from 10 to 460 ns showing the formation of absorption features characteristic for the reduced **pNDI** (470 and 605 nm) and the oxidized pCarb$^+$ (430 and above 600 nm) (purged solution, CH_2Cl_2, excitation at 500 nm). Note, that all spectra from 100 to 460 ns were scaled by the factor five to enhance the visibility of the spectral change. (Reprinted with permission from Ref.[127] Copyright Wiley-VCH Verlag GmbH & Co. KGaA, Weinheim).

These results revealed an efficient fully charge separated state for both triads **T1** and **T2** with a difference in the lifetime of this state. Whereas the coupling strategy has no influence on the charge separation behavior, the conjugation showed a three times longer lifetimes. Unpublished results exhibit furthermore an enhancement of the lifetime by using a **pTARA** block-copolymer (unpublished results). This polymer bears functional groups of methyl and methoxy. These units have different oxidation potentials which result in a gradient in the donor polymer. That leads to a reductive quenching of the ruthenium with an easier access to the charge separated state. Furthermore, a charge transfer from one block to the other occured with an increased lifetime of the second step. The Table 5.1 provides an overview of the synthesized dyads and triads and their emission quenching.

The variety of compounds with the different flexible linkers demonstrates the significance of the chemistry-on-the-complex strategy independent from the polymer units.

Table 5.1: Overview of the prepared dyads and triads as well as the respective polymeric building blocks and utilized Ru(II) complexes with linking strategy and emission quenching efficiency.

	Starting material	*Donor polymer*	*Acceptor polymer*	*Linking reaction*	*Emission quenching*
D1	Ru(dqp)(dqpOH) **C1**		Cl-pNDI$_{17}$	WES	86%
D2	Ru(dqp)(dqpPhpy) **C3**		Cl-pNDI$_{17}$	PQ	96%
D3	Ru(dqp)(dqpPhCCH) **C5**		N_3-pNDI$_{17}$	CuAAC	94%
D4	Ru(dqp)(dqpOH) **C1**		Cl-pNDI$_{10}$-PEG$_{10}$	WES	94%
D5	Ru(dqp)(dqpPhCCH) **C5**	N_3-pCarb$_{15}$		CuAAC	
D6	Ru(dqpOH)(dqpPhCCTIPS) **C6**	Cl-pTARA$_{15}$		WES	
D7	Ru(dqpOH)(dqpPhCCTIPS) **C6**		Cl-pNDI$_{19}$	WES	
T1	**D6b**	Cl-pTARA$_{15}$	N_3-pNDI$_{17}$	CuAAC	96%
T2	**D7**	N_3-pCarb$_{15}$	Cl-pNDI$_{19}$	WES	96%

6. Summary

Ruthenium polypyridyl complexes are interesting for a wide range of applications. The incorporation of ruthenium complexes as modular units in larger hierarchical architectures represents a promising approach for improvements of well-known materials as shown by the formation of metallopolymeric films for catalysis and the synthesis of redox active polymeric donor-photosensitizer-acceptor triads for the conversion of light into chemical bond energy.

The construction of such large well-defined architectures by convential synthetic pathways results in a large synthetic effort so that a new efficient strategy had to be developed. The stepwise assembly, where the redox active units can be used like a construction kit provides a facile access to a modular use in which single parts can be exchanged without the repetition of the complete synthesis. Hence, capable synthetic pathways for the single units as well as the coupling step are required. The chemistry-on-the-complex methodology offers an alternative pathway to classical procedures and, thus, guarantees a modular assembly.

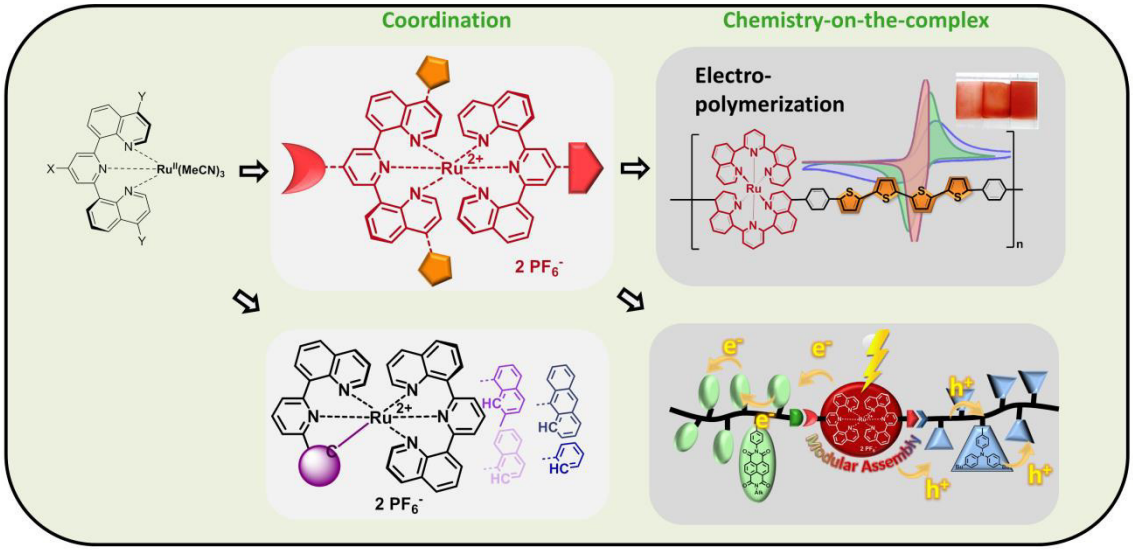

Figure 6.1: Schematic representation of synthesis of ruthenium-dqp-complexes as building units for the incorporation in electropolymerized films as well as in dyads and triads for an efficient charge transfer

In this thesis, an efficient synthetic strategy for the assembly of polymeric D-P-A systems was presented. Therefore, the usage of the $[Ru(dqp)_2]^{2+}$ photosensitizer was incorporated into a D-P-A triad.

In this regard the application of the complex in the architectures required the preservation of the photophysical and electrochemical behavior of the complex, which can be influenced by the functionalization. Spectroscopic measurements were investigated to confirm this preservation.

$[Ru(dqp)_2]^{2+}$ complexes show nearly ideal photophysical and electrochemical properties for the usage in energy transfer applications *i.e.* enhanced absorption in the visible wavelength, long lifetime of the excited state and redox stability, for the incorporation in redox active devices, but the synthesis becomes more and more challenging with the increase of the ligand scaffold. An efficient synthetic strategy was found by a test series, *i.e.* by variation of temperature, solvents and ruthenium starting materials. The coordination to form heteroleptic ruthenium complexes takes place in a stepwise manner with an acetonitrile intermediate. The complex formation at 130 to 140 °C in DMF resulted in the best yields. During the reaction the acetonitrile units were exchanged by the solvent molecules, which simplify the coordination of the ligand due to the weaker bond strength to the metal core. With this knowledge a series of functionalized ruthenium complexes could be prepared. In particular, the complexes **16** (functionalized with hydroxide and acetylene protected TIPS group) and **22** (bearing bithiophene units) were utilized for further incorporation and reached yields around 60%, while other solvents did not led to a complex formation and the functionalization with bithiophene boronic acid *via* Suzuki cross-coupling achieved a yield of only 30%.

The formation of polymer films including ruthenium complexes is a common method for the layer formation on surfaces, but the mechanistic details are not well understood. The film thickness as well as the homogeneity of the materials is poorly investigated and is strongly influenced by the utilized solvent, salt, additive, pH-value, time as well as voltage mode and makes significant differences on the resulted films. The new bithiophene complexe **22** are favorable for the detailed investigation of the electropolymerization, because the oxidation potential of the ruthenium core correlates with the oxidation potential of the bithiophene unit resulting in an increased electropolymerization behavior. Noteworthy, this combination enables the mildest reaction conditions, while a thiophene moiety requires $BF_3{\cdot}Et_2O$ for an electropolymerization. $BF_3{\cdot}Et_2O$ oxidizes the thiophene unit, but leads, therefore, to an uncontrolled polymerization and to a degradation of the complex. In contrast, bithiophene bearing complexes achieves a controlled electropolymerization with

correlating film thicknesses without $BF_3 \cdot Et_2O$. In comparison, additives, bases, water and other salts than $TBAPF_6$ revealed a negative influence on the reaction. The potentiodynamic mode, which is characterized by a cyclic behavior from 0 to 1 V enabled the controlled formation of the films only in acetonitrile. However, after around 500 cycles a leveling off can be observed. The potentiostatic mode at a constant potential of 0.9 V can be performed in acetonitrile or dichloromethane and reaches similar film thicknesses as the dynamic created films. The film thicknesses were determined *via* profilometry and SEM measurements. Nevertheless, it can be recognized that the surfaces of the films are rough and formed by colloidal structures instead of a homogeneous smooth interface. Furthermore, the film was analyzed after the electropolymerization regarding their photophysical properties. Thereby, it can be seen that the absorption behavior as well as the emission of the pristine complex is preserved, which makes this topic to a positive example of the modular usage of ruthenium complexes in larger systems.

The bifunctional complex **16**, bearing one hydroxyl and one protected acetylene moiety, was incorporated in polymeric triad systems. Therefore, effective coupling strategies were required. In this purpose, the nucleophilic substitution with a pyridine unit, the Williamson ether synthesis of the hydroxyl function and the click reaction were established. The reactions were investigated by the chain end functionalization of the acceptor polymer pNDI. All three linking protocols resulted in the corresponding dyads in adequate yields, which showed energy transfer to the p-NDI unit as analyzed by fluorescence spectroscopy and a quenching of the emission from 86 to 96% was observed.

The stepwise synthetic strategy was applied for the preparation of the first polymeric D-P-A triad consisting of a pTARA donor polymer, a pNDI acceptor polymer and the bifunctionalized ruthenium complex **16**. The synthetic pathway starts with the Williamson ether synthesis between the pTARA and the ruthenium complex. The second step was the deprotection of the acetylene group and finally the coupling of the pNDI polymer *via* click reaction. All intermediates and the product were purified following a new purification protocol which includes the automated size exclusion chromatography with Toyopearl as solid state material. The dyads from the complex as well as the triad from the dyads were isolated by the combined separation ability of size

exclusion and polarity. The compounds were identified and characterized with NMR spectroscopy and 3D SEC.

Afterwards, the UV-Vis measurements additionally confirmed the linkage *via* the absorption spectra that showed the perfect superposition of the single compounds. Whereas the steady state fluorescence spectroscopy verified the efficient energy transfer, the MLCT emission of the ruthenium complexes in the dyad was quenched in contrast to the triad with a conversion of 96%. Time resolved transient spectroscopic measurements confirmed these results and enabled a more detailed analysis. The fast oxidative quenching was realized by the pNDI polymer of the ruthenium excitation under 50 ns, which was transferred to the ground state *via* the reduction of the pTARA polymer. The recombination decay was bifunctional with a time scales of 430 ns and 2400 ns.

In summary, the incorporation of the ruthenium complex in a polymeric architecture was successful *via* the chemistry-on-the-complex approach, whereas the linkage protocols showed no effect on the photophysical and electrochemical nature. This could be confirmed by the construction of a second triad, using a conjugated pCarb as donor unit. Furthermore, the inverted linkage strategy was tested and similar results in the spectroscopic measurements were reached.

These results proofed that the application of the chemistry-on-the-complex methodology represents a powerful tool and enables the incorporation of ruthenium complexes in larger systems no matter which polymer is desired while the photophysical behavior of the complexes is preserved.

Moreover, the energy transfer from the ruthenium MLCT to the acceptor unit is so fast that even the metalating complexes, which were synthesized in the first chapter, have lifetimes long enough to generate an efficient transfer. The favorable absorption abilities can subsequently be used in the triad system, while the functionalization of the metalating complexes is simple, which is described in Chapter 3.

These examples verified the successful usage of the $[Ru(dqp)_2]^{2+}$ complexes in combination with the chemistry-on-the-complex strategy and offer them numerous applications in the fields of electronic devices as well as biomaterial imaging and catalytic systems.

7. Zusammenfassung

Rutheniumpolypyridylkomplexe sind für vielzählige Anwendungsgebiete interessant. Der Einbau von Rutheniumkomplexen in größere Architekturen, die diese als modulare Einheit verwenden, wird eine effiziente Verbesserung bewirken. Zusammen mit der Bildung von Metall-haltigen Polymerfilmen für die Katalyse und der Bildung von redoxaktiven polymeren Donor-Photosensibilisator-Akzeptor-Triaden für die Umwandlung von Licht in chemische Bindungsenergie sind zwei Beispiele für die Anwendbarkeit dieser Verbindungsklasse zu finden.

Die Bildung solch großer Architekturen bedeutet einen enormen synthetischen Aufwand, weshalb eine effiziente Synthesestrategien benötigt werden. Der stufenweise Aufbau der redoxaktiven Einheiten könnte wie ein Baukasten genutzt werden, und würde dem modularen Einsatz einen leichten Zugang bieten, wobei einzelne Teile ohne großen synthetischen Aufwand ausgetauscht werden können. Daher sind effiziente Synthesewege für die einzelnen Einheiten sowie der Kopplungsschritte erforderlich. Die Chemie-am-Komplex Methode bietet einen alternativen Weg und garantiert einen modularen Aufbau.

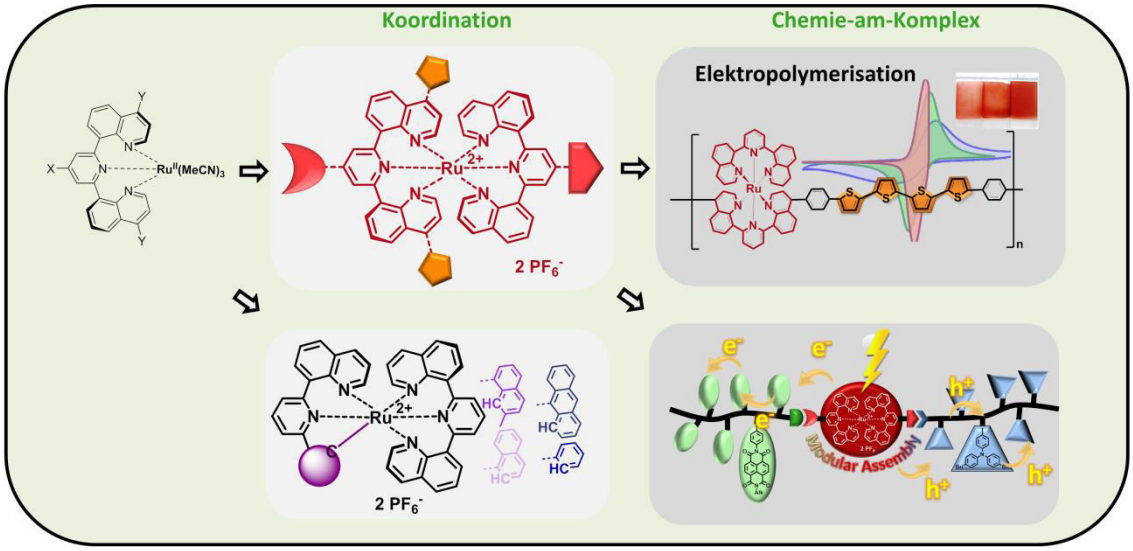

Abbildung 7.1: Schematische Darstellung der Synthese von $[Ru(dqp)_2]^{2+}$-Komplexen als Bausteine für den Einbau in elektropolymerisierte Filme sowie in Dyaden und Triaden für einen effizienten Ladungstransfer

In dieser Arbeit wurde ein effizienter Syntheseweg für den Aufbau polymerer D-P-A Systeme entwickelt. Dabei wurde die Bildung des $[Ru(dqp)_2]^{2+}$-Photosensibilisators als

modulare Einheit verbessert, eine effektive Kopplungsstrategie gefunden und erfolgreich in eine D-P-A-Triade eingebaut.

Eine wichtiger Fakt in dieser Hinsicht ist die Erhaltung des photophysikalischen und elektrochemischen Verhaltens des Komplexes, die durch die Funktionalisierung beeinflusst werden kann. Um diese Erhaltung zu bestätigen, wurden spektroskopische Messungen durchgeführt.

Ruthenium-dqp-Komplexe zeigen nahezu ideale photophysikalische und elektrochemische Eigenschaften für den Einbau in redoxaktive Bauelemente. Die Synthese wird jedoch mit zunehmendem Ligandenfeld immer anspruchsvoller. Eine effiziente Synthesestrategie konnte in einer Testreihe gefunden werden, in der Temperatur, Lösungsmittel und Ruthenium-Ausgangsmaterial untersucht wurden. Die Koordination zu heteroleptischen Rutheniumkomplexen erfolgt schrittweise über ein Acetonitril-Intermediat. Die Komplexbildung bei 130-140 °C in DMF ergibt hierbei die besten Ausbeuten. Während der Reaktion werden die Acetonitril-Einheiten durch die Lösungsmittelmoleküle des DMF ausgetauscht, was die Koordination des Liganden aufgrund der schwächeren Bindung an den Metallkern vereinfacht. Mit diesem Wissen konnte eine Reihe von funktionalisierten Rutheniumkomplexen hergestellt werden. Insbesondere wurden die Komplexe **16** (funktionalisiert mit Hydroxyl und Acetylen, geschützt durch eine TIPS-Schutzgruppe) und **22** (Bithiopheneinheiten tragend) für weitere Anwendungen verwendet und erreichten eine Ausbeute von etwa 60%, während andere Lösungsmittel nicht zu einer Komplexbildung führten. Mit der Funktionalisierung mittels Bithiophenboronsäure über eine Suzuki Kreuzkupplung wurde im Gegensatz dazu nur eine Ausbeute von 30% erreicht.

Diese Komplexe wurden erfolgreich in Elektropolymerisationsreaktionen zur Bildung eines Metallpolymerfilms auf einer Glasoberfläche und für den Einbau in polymeren D-P-A-Systemen verwendet.

Die Bildung von Polymerfilmen aus Rutheniumkomplexen ist ein weit verbreitetes Verfahren, zeigte jedoch einige Komplikationen. Die Filmdicke sowie die Homogenität des Materials sind bislang nur schlecht untersucht. Der Einfluss von Lösungsmittel, Salz, Additiv, pH-Wert, Zeit- und Spannungsmodus ist signifikant und macht große Unterschiede im resultierenden Film aus. Die neuen Bithiophenkomplexe sind für diese Untersuchungen besonders geeignet, da das Oxidationspotential des Rutheniumkerns

mit dem Oxidationspotential der Bithiopheneinheit korreliert, was zu einer verbesserten Elektropolymerisationsrate führt. Bemerkenswert bei dieser Kombination sind die milderen Reaktionsbedingungen, da Thiophengruppen $BF_3 \cdot Et_2O$ für eine Elektropolymerisation benötigen. $BF_3 \cdot Et_2O$ oxidiert die Thiopheneinheit, führt jedoch zu einer unkontrollierten Polymerisation und zu einer Zersetzung des Komplexes. Im Gegensatz dazu erreicht Bithiophen eine kontrollierte Elektropolymerisation mit korrelierenden Filmdicken. Im Vergleich dazu wirkt sich der Zusatz von Additiven, Basen, Wasser und anderen Salzen als $TBAPF_6$ negativ auf die Reaktion aus. Der potentiodynamische Modus, der durch ein zyklisches Verhalten von etwa 0 bis 1 V gekennzeichnet ist, ermöglicht die kontrollierbare Bildung der Filme vorzugsweise in Acetonitril, während nach etwa 500 Zyklen eine Abflachung zu sehen ist. Der potentiostatische Modus bei einem konstanten Potential von 0,9 V kann in Acetonitril oder Dichlormethan durchgeführt werden und erreicht ähnliche Filmdicken wie die mit dynamischer Weise erzeugten Filme. Die Schichtdicken wurden über Profilometrie und SEM-Messungen bestimmt. Nichtsdestotrotz ist ersichtlich, dass die Oberfläche der Filme rau ist und kolloidale Strukturen anstelle einer homogenen glatten Grenzfläche gebildet werden. Der Film wurde außerdem nach der Elektropolymerisation hinsichtlich seiner photophysikalischen Eigenschaften analysiert. Dabei zeigt sich, dass sowohl das Absorptionsverhalten als auch die Emission erhalten bleiben, was dieses Thema zu einem positiven Beispiel für den modularen Einsatz von Rutheniumkomplexen in größeren Systemen macht.

Weiterhin wurde der bifunktionelle Komplex **16**, der eine Hydroxyl- und eine geschützte Acetyleneinheit trägt, in polymere Systeme eingebaut. Dafür wurden effektive Kopplungsstrategien entwickelt und nach Untersuchungen die Nukleophile Substitution mit einer Pyridin-Einheit, die Williamson Ethersynthese mit der Hydroxyl-Funktion und die Click-Reaktion eingesetzt. Die Reaktionen wurden durch die Endkettenfunktionalisierung des Akzeptorpolymers pNDI ermöglicht. Alle drei Verknüpfungsprotokolle führen zu entsprechenden Dyaden, die einen Energietransfer zu der pNDI-Einheit zeigen, der mit Emissionspektroskopie analysiert wurde, und die Emission mit einer Effizienz von 86 bis 96% löschte.

Die schrittweise Synthesestrategie wurde untersucht, um die erste polymere D-P-A-Triade aufzubauen, die aus einem pTARA-Donor-Polymer, einem pNDI-Akzeptorpolymer und dem bifunktionalisierten Rutheniumkomplex **16** besteht. Der

Syntheseweg begann mit der Williamson-Ethersynthese zwischen dem pTARA-Polymer und dem Rutheniumkomplex. Der zweite Schritt war die Entschützung der Acetylengruppe mit anschließender CuAAC-Kupplung des pNDI-Polymers. Alle Verbindungen wurden nach einem neuen Reinigungsprotokoll gereinigt, das die automatisierte Größenausschlusschromatographie mit Toyopearl als Festkörpermaterial einschließt. Aufgrund der Trennungsfähigkeit nach Größe und Polarität wurden die Dyaden von dem Komplex sowie die Triade von den Dyaden getrennt isoliert. Der schrittweise Syntheseweg wurde mit NMR-Spektroskopie und 3D-SEC verfolgt.

Danach belegen die UV-Vis-Spektren die Verknüpfung auch über die Absorptionsspektren, die die Summe der einzelnen Verbindungen zeigen. Während die stationäre Fluoreszenzspektroskopie den effizienten Energietransfer bestätigte, wird die MLCT-Emission der Rutheniumkomplexe in der Triade im Gegensatz zur Dyade mit einem Umsatz von 96% ausgelöscht. Zeitaufgelöste spektroskopische Messungen bestätigen diese Ergebnisse und zeigen eine schnelle oxidative Löschung der Rutheniumanregung durch das pNDI-Polymer, die über die Reduktion des pTARA-Polymers in den Grundzustand überführt wurde. Die Lebensdauer des angeregten Zustandes ist monoexponentiell mit 430 ns von den Rutheniumkomplexen. Im Gegensatz dazu zeigen die polymeren Einheiten im Inneren des Polymers einen bifunktionellen Zerfall, der länger andauert.

Zusammenfassend war der Einbau des Rutheniumkomplexes in eine polymere Architektur über den Chemie-am-Komplex-Ansatz erfolgreich, wobei die Verknüpfungsprotokolle keine photophysikalischen und elektrochemischen Effekte zeigten. Dies konnte in Kooperation mit der Schubert-Gruppe durch den Aufbau einer zweiten Triade unter Verwendung eines konjugierten pCarbs als Donoreinheit bestätigt werden. Außerdem wurde die Verknüpfungsstrategie geändert, aber ähnliche Ergebnisse in den spektroskopischen Messungen wurden erreicht.

Dies beweist, dass die Anwendung der Chemie-am-Komplex Methodologie ein mächtiges Werkzeug ist und die Einführung von Komplexen in ein größeres System ermöglicht. Das photophysikalische Verhalten der Komplexe bleibt dabei erhalten.

Darüber hinaus ist der Energietransfer vom Ruthenium-MLCT zur Akzeptoreinheit so schnell, dass die im ersten Kapitel synthetisierten Metallierungskomplexe langlebig genug sind, um einen effizienten Transfer zu erzeugen. Die günstigen

Absorptionsfähigkeiten können dann im Triadensystem verwendet werden, während die Funktionalisierung der Metallierungskomplexe einfach ist, was in Kapitel 3 beschrieben wurde.

Diese Beispiele bestätigten die erfolgreiche Verwendung der Ruthenium-dqp-Komplexe in Kombination mit der Chemie-am-Komplex-Strategie und ermöglichen die Anwendungen in zahlreichen Gebieten der molekularen Elektronik sowie zur Einfärbung von Biomaterialien und in katalytischen Systemen.

8. References

[1] S. Kundu, A. Patra, *Chem. Rev.* **2017**, *117*, 712-757.

[2] L. A. Weinstein, J. Loomis, B. Bhatia, D. M. Bierman, E. N. Wang, G. Chen, *Chem. Rev.* **2015**, *115*, 12797-12838.

[3] V. Balzani, G. Bergamini, P. Ceroni, *Angew. Chem. Int. Ed.* **2015**, *54*, 11320-11337.

[4] A. Juris, V. Balzani, F. Barigelletti, S. Campagna, P. Belser, A. Von Zelewsky, *Coord. Chem. Rev.* **1988**, *84*, 85-277.

[5] D. W. Thompson, A. Ito, T. J. Meyer, *Pure Appl. Chem.* **2013**, *85*, 1257-1305.

[6] J.-P. Sauvage, J.-P. Collin, J.-C. Chambron, S. Guillerez, C. Coudret, V. Balzani, F. Barigelletti, L. De Cola, L. Flamigni, *Chem. Rev.* **1994**, *94*, 993-1019.

[7] E. Baranoff, J.-P. Collin, L. Flamigni, J.-P. Sauvage, *Chem. Soc. Rev.* **2004**, *33*, 147-155.

[8] J. R. Winkler, T. L. Netzel, C. Creutz, N. Sutin, *J. Am. Chem. Soc.* **1987**, *109*, 2381-2392.

[9] A. Juris, V. Balzani, F. Barigelletti, S. Campagna, P. Belser, A. von Zelewsky, *Coord. Chem. Rev.* **1988**, *84*, 85-277.

[10] E. A. Medlycott, G. S. Hanan, *Chem. Soc. Rev.* **2005**, *34*, 133-142.

[11] U. Siemeling, J. V. der Bruggen, U. Vorfeld, B. Neumann, A. Stammler, H. G. Stammler, A. Brockhinke, R. Plessow, P. Zanello, F. Laschi, F. F. de Biani, M. Fontani, S. Steenken, M. Stapper, G. Gurzadyan, *Chem. Eur. J.* **2003**, *9*, 2819-2833.

[12] A. Harriman, A. Mayeux, A. De Nicola, R. Ziessel, *PCCP* **2002**, *4*, 2229-2235.

[13] J. Gu, Y. Yan, B. J. Helbig, Z. Huang, T. Lian, R. H. Schmehl, *Coord. Chem. Rev.* **2015**, *282-283*, 100-109.

[14] Y. Q. Fang, N. J. Taylor, G. S. Hanan, F. Loiseau, R. Passalacqua, S. Campagna, H. Nierengarten, A. Van Dorsselaer, *J. Am. Chem. Soc.* **2002**, *124*, 7912-7913.

[15] F. Schramm, V. Meded, H. Fliegl, K. Fink, O. Fuhr, Z. Qu, W. Klopper, S. Finn, T. E. Keyes, M. Ruben, *Inorg. Chem.* **2009**, *48*, 5677-5684.

[16] A. Breivogel, M. Meister, C. Förster, F. Laquai, K. Heinze, *Chem. Eur. J.* **2013**, *19*, 13745-13760.

[17] M. Beley, J. P. Collin, J. P. Sauvage, H. Sugihara, F. Heisel, A. Miehe, *Dalton Trans.* **1991**, 3157-3159.

[18] C. R. Hecker, A. K. I. Gushurst, D. R. McMillin, *Inorg. Chem.* **1991**, *30*, 538-541.

[19] J. T. Hewitt, P. J. Vallett, N. H. Damrauer, *J. Phys. Chem. A* **2012**, *116*, 11536-11547.

[20] D. G. Brown, N. Sanguantrakun, B. Schulze, U. S. Schubert, C. P. Berlinguette, *J. Am. Chem. Soc.* **2012**, *134*, 12354-12357.

[21] J. Dinda, S. Liatard, J. Chauvin, D. Jouvenot, F. Loiseau, *Dalton Trans.* **2011**, *40*, 3683-3688.

[22] V. Friese, S. Nag, J. Wang, M.-P. Santoni, A. Rodrigue-Witchel, G. S. Hanan, F. Schaper, *Eur. J. Inorg. Chem.* **2011**, *2011*, 39-44.

[23] S. Sinn, B. Schulze, C. Friebe, D. G. Brown, M. Jäger, J. Kübel, B. Dietzek, C. P. Berlinguette, U. S. Schubert, *Inorg. Chem.* **2014**, *53*, 1637-1645.

[24] M. Abrahamsson, M. Jäger, T. Österman, L. Eriksson, P. Persson, H.-C. Becker, O. Johansson, L. Hammarström, *J. Am. Chem. Soc.* **2006**, *128*, 12616-12617.

[25] R. J. Kumar, S. Karlsson, D. Streich, A. R. Jensen, M. Jäger, H.-C. Becker, J. Bergquist, O. Johansson, L. Hammarström, *Chem. Eur. J.* **2010**, *16*, 2830-2842.
[26] G. Ragazzon, P. Verwilst, S. A. Denisov, A. Credi, G. Jonusauskas, N. D. McClenaghan, *Chem. Commun.* **2013**, *49*, 9110-9112.
[27] M. Schulze, M. Jäger, U. S. Schubert, *Macromol. Rapid Commun.* **2012**, *33*, 579-584.
[28] R. Schroot, C. Friebe, E. Altuntas, S. Crotty, M. Jäger, U. S. Schubert, *Macromolecules* **2013**, *46*, 2039-2048.
[29] C. Friebe, M. Jaeger, U. S. Schubert, *RSC Adv.* **2013**, *3*, 11686-11690.
[30] C. Friebe, H. Görls, M. Jäger, U. S. Schubert, *Eur. J. Inorg. Chem.* **2013**, *2013*, 4191-4202.
[31] T. Schlotthauer, B. Suchland, H. Görls, G. A. Parada, L. Hammarström, U. S. Schubert, M. Jäger, *Inorg. Chem.* **2016**, *55*, 5405-5416.
[32] A. Frei, R. Rubbiani, S. Tubafard, O. Blacque, P. Anstaett, A. Felgenträger, T. Maisch, L. Spiccia, G. Gasser, *J. Med. Chem.* **2014**, *57*, 7280-7292.
[33] C. Kreitner, E. Erdmann, W. W. Seidel, K. Heinze, *Inorg. Chem.* **2015**, *54*, 11088-11104.
[34] S. Aghazada, Y. Ren, P. Wang, M. K. Nazeeruddin, *Inorg. Chem.* **2017**, *21*, 13437-13445.
[35] L. Hammarström, *Acc. Chem. Res.* **2015**, *48*, 840-850.
[36] R. J. Kumar, S. Karlsson, D. Streich, A. Rolandini Jensen, M. Jäger, H.-C. Becker, J. Bergquist, O. Johansson, L. Hammarström, *Chem. Eur. J.* **2010**, *16*, 2830-2842.
[37] Z.-L. Gong, B.-B. Cui, W.-W. Yang, J. Yao, Y.-W. Zhong, *Electrochim. Acta* **2014**, *130*, 748-753.
[38] B.-B. Cui, C.-J. Yao, J. Yao, Y.-W. Zhong, *Chem. Sci.* **2014**, *5*, 932-941.
[39] B.-B. Cui, H.-J. Nie, C.-J. Yao, J.-Y. Shao, S.-H. Wu, Y.-W. Zhong, *Dalton Trans.* **2013**, *42*, 14125-14133.
[40] Z. Fang, S. Keinan, L. Alibabaei, H. Luo, A. Ito, T. J. Meyer, *Angew. Chem. Int. Ed.* **2014**, *53*, 4872-4876.
[41] R. M. Leasure, T. Kajita, T. J. Meyer, *Inorg. Chem.* **1996**, *35*, 5962-5963.
[42] J. A. Moss, R. Argazzi, C. A. Bignozzi, T. J. Meyer, *Inorg. Chem.* **1997**, *36*, 762-763.
[43] J. A. Moss, J. C. Yang, J. M. Stipkala, X. Wen, C. A. Bignozzi, G. J. Meyer, T. J. Meyer, *Inorg. Chem.* **2004**, *43*, 1784-1792.
[44] H.-J. Nie, J. Yao, Y.-W. Zhong, *J. Org. Chem.* **2011**, *76*, 4771-4775.
[45] J.-Y. Shao, C.-J. Yao, B.-B. Cui, Z.-L. Gong, Y.-W. Zhong, *Chin. Chem. Lett.* **2016**, *27*, 1105-1114.
[46] J.-H. Tang, Y.-Q. He, J.-Y. Shao, Z.-L. Gong, Y.-W. Zhong, J.-H. Tang, Y.-W. Zhong, *Sci. Rep.* **2016**, *6*, 35253.
[47] J. Yang, M. Sykora, T. J. Meyer, *Inorg. Chem.* **2005**, *44*, 3396-3404.
[48] C.-J. Yao, Y.-W. Zhong, H.-J. Nie, H. D. Abruna, J. Yao, *J. Am. Chem. Soc.* **2011**, *133*, 20720-20723.
[49] C. Friebe, H. Goerls, M. Jaeger, U. S. Schubert, *Eur. J. Inorg. Chem.* **2013**, *2013*, 4191-4202.
[50] K. Araki, H. Endo, G. Masuda, T. Ogawa, *Chem. Eur. J.* **2004**, *10*, 3331-3340.
[51] V. Aranyos, A. Hagfeldt, H. Grennberg, E. Figgemeier, *Polyhedron* **2004**, *23*, 589-598.
[52] C. Friebe, B. Schulze, H. Goerls, M. Jaeger, U. S. Schubert, *Chem. Eur. J.* **2014**, *20*, 2357-2366.

[53] F. Haddache, A. Le Goff, N. Spinelli, P. Gairola, K. Gorgy, C. Gondran, E. Defrancq, S. Cosnier, *Electrochim. Acta* **2016**, *219*, 82-87.
[54] W. Huang, L. Wang, H. Tanaka, T. Ogawa, *Eur. J. Inorg. Chem.* **2009**, 1321-1330.
[55] S. Sherry Zhu, R. P. Kingsborough, T. M. Swager, *J. Mater. Chem.* **1999**, *9*, 2123-2131.
[56] Q. Shu, C. Adam, N. Sojic, M. Schmittel, *Analyst* **2013**, *138*, 4500-4504.
[57] X. J. Zhu, B. J. Holliday, *Macromol. Rapid Commun.* **2010**, *31*, 904-909.
[58] C. Fan, C. Ye, X. Wang, Z. Chen, Y. Zhou, Z. Liang, X. Tao, *Macromolecules* **2015**, *48*, 6465-6473.
[59] M. Masuda, N. Nakamura, H. Ohno, *J. Electrochem. Soc.* **2013**, *160*, G3135-G3138.
[60] C.-J. Yao, Y.-W. Zhong, J. Yao, *Inorg. Chem.* **2013**, *52*, 10000-10008.
[61] H. B. Yildiz, B. B. Carbas, S. Sonmezoglu, M. Karaman, L. Toppare, *Int. J. Hydrogen Energy* **2016**, *41*, 14615-14629.
[62] R. Schroot, U. S. Schubert, M. Jäger, *Macromolecules* **2016**, *49*, 8801-8811.
[63] T. Schlotthauer, G. A. Parada, H. Görls, S. Ott, M. Jäger, U. S. Schubert, *Inorg. Chem.* **2018**, *56*, 7720-7730.
[64] M. Jäger, A. Smeigh, F. Lombeck, H. Görls, J.-P. Collin, J.-P. Sauvage, L. Hammarström, O. Johansson, *Inorg. Chem.* **2010**, *49*, 374-376.
[65] M. Abrahamsson, M. Jäger, R. J. Kumar, T. Österman, P. Persson, H.-C. Becker, O. Johansson, L. Hammarström, *J. Am. Chem. Soc.* **2008**, *130*, 15533-15542.
[66] M. Jaeger, R. J. Kumar, H. Goerls, J. Bergquist, O. Johansson, *Inorg. Chem.* **2009**, *48*, 3228-3238.
[67] M.-P. Santoni, A. K. Pal, G. S. Hanan, A. Proust, B. Hasenknopf, *Inorg. Chem. Commun.* **2011**, *14*, 399-402.
[68] T. Schlotthauer, C. Friebe, A. M. Schwenke, M. Jäger, U. S. Schubert, *J. Mater. Chem. C* **2017**.
[69] E. C. Constable, P. Harverson, *Polyhedron* **1999**, *18*, 1891-1901.
[70] E. C. Constable, C. E. Housecroft, M. Neuburger, I. Poleschak, M. Zehnder, *Polyhedron* **2003**, *22*, 93-108.
[71] I. Eryazici, G. R. Newkome, *New J. Chem.* **2009**, *33*, 345-357.
[72] S. H. Wadman, R. W. A. Havenith, M. Lutz, A. L. Spek, G. P. M. van Klink, G. van Koten, *J. Am. Chem. Soc.* **2010**, *132*, 1914-1924.
[73] C. Coudret, S. Fraysse, *Chem. Commun.* **1998**, 663-664.
[74] Z. Ji, M. He, Z. Huang, U. Ozkan, Y. Wu, *J. Am. Chem. Soc.* **2013**, *135*, 11696-11699.
[75] Z. Ji, G. Natu, Y. Wu, *ACS Appl. Mater. Interfaces* **2013**, *5*, 8641-8648.
[76] Z. Ji, Y. Wu, *J. Phys. Chem. C* **2013**, *117*, 18315-18324.
[77] B. Matt, C. Coudret, C. Viala, D. Jouvenot, F. Loiseau, G. Izzet, A. Proust, *Inorg. Chem.* **2011**, *50*, 7761-7768.
[78] V. L. Whittle, J. A. G. Williams, *Dalton Trans.* **2009**, 3929-3940.
[79] A. M. Clark, C. E. F. Rickard, W. R. Roper, L. J. Wright, *Organometallics* **1999**, *18*, 2813-2820.
[80] S. Despax, F. Jia, M. Pfeffer, P. Hebraud, *PCCP* **2014**, *16*, 10491-10502.
[81] L. Fetzer, B. Boff, M. Ali, M. Xiangjun, J.-P. Collin, C. Sirlin, C. Gaiddon, M. Pfeffer, *Dalton Trans.* **2011**, *40*, 8869-8878.
[82] C. Friebe, B. Schulze, H. Görls, M. Jäger, U. S. Schubert, *Chem. Eur. J.* **2014**, *20*, 2357-2366.
[83] C. E. McCusker, J. K. McCusker, *Inorg. Chem.* **2011**, *50*, 1656-1669.

[84] J. Wang, Y.-Q. Fang, G. S. Hanan, F. Loiseau, S. Campagna, *Inorg. Chem.* **2005**, *44*, 5-7.
[85] C. J. Aspley, J. A. Gareth Williams, *New J. Chem.* **2001**, *25*, 1136-1147.
[86] E. C. Constable, P. Harverson, C. E. Housecroft, E. Nordlander, J. Olsson, *Polyhedron* **2006**, *25*, 437-458.
[87] C. J. Wood, K. C. D. Robson, P. I. P. Elliott, C. P. Berlinguette, E. A. Gibson, *RSC Adv.* **2014**, *4*, 5782-5791.
[88] P. G. Potvin, P. U. Luyen, J. Bräckow, *J. Am. Chem. Soc.* **2003**, *125*, 4894-4906.
[89] M. Vrabel, R. Pohl, B. Klepetarova, I. Votruba, M. Hocek, *Org. Biomol. Chem.* **2007**, *5*, 2849-2857.
[90] M. Vrabel, R. Pohl, I. Votruba, M. Sajadi, S. A. Kovalenko, N. P. Ernsting, M. Hocek, *Org. Biomol. Chem.* **2008**, *6*, 2852-2860.
[91] J. Yang, J. K. Clegg, Q. Jiang, X. Lui, H. Yan, W. Zhong, J. E. Beves, *Dalton Trans.* **2013**, *42*, 15625-15636.
[92] L. Trouillet, A. De Nicola, S. Guillerez, *Chem. Mater.* **2000**, *12*, 1611-1621.
[93] E. C. Constable, A. M. W. Cargill Thompson, S. Greulich, *J. Chem. Soc., Chem. Commun.* **1993**, 1444-1446.
[94] H. Li, J. Wu, Y. Jeilani, C. Ingram, I. Harruna, *J. Nanopart. Res.* **2012**, *14*, 1-14.
[95] R. J. Holbrook, D. J. Weinberg, M. D. Peterson, E. A. Weiss, T. J. Meade, *J. Am. Chem. Soc.* **2015**, *137*, 3379-3385.
[96] S. J. A. Pope, B. J. Coe, S. Faulkner, R. H. Laye, *Dalton Trans.* **2005**, 1482-1490.
[97] Z. Fang, A. Ito, H. Luo, D. L. Ashford, J. J. Concepcion, L. Alibabaei, T. J. Meyer, *Dalton Trans.* **2015**, *44*, 8640-8648.
[98] N. Zabarska, A. Stumper, S. Rau, *Dalton Trans.* **2016**, *45*, 2338-2351.
[99] Y. Sun, Z. Chen, E. Puodziukynaite, D. M. Jenkins, J. R. Reynolds, K. S. Schanze, *Macromolecules* **2012**, *45*, 2632-2642.
[100] B. Bozic-Weber, E. C. Constable, E. Figgemeier, C. E. Housecroft, W. Kylberg, *Energy Environ. Sci.* **2009**, *2*, 299-305.
[101] E. C. Constable, R. W. Handel, C. E. Housecroft, A. F. Morales, B. Ventura, L. Flamigni, F. Barigelletti, *Chem. Eur. J.* **2005**, *11*, 4024-4034.
[102] N. Baumann, P. S. Gamage, T. N. Samarakoon, J. Hodgson, J. Janek, S. H. Bossmann, *J. Phys. Chem. C* **2010**, *114*, 22763-22772.
[103] A. Wild, A. Winter, M. D. Hager, H. Görls, U. S. Schubert, *Macromol. Rapid Commun.* **2012**, *33*, 517-521.
[104] A. M. Breul, J. Schaefer, C. Friebe, F. Schluetter, R. M. Paulus, G. Festag, M. D. Hager, A. Winter, B. Dietzek, J. Popp, U. S. Schubert, *Macromol. Chem. Phys.* **2012**, *213*, 808-819.
[105] E. Holder, M. A. R. Meier, V. Marin, U. S. Schubert, *J. Polym. Sci., Part A: Polym. Chem.* **2003**, *41*, 3954-3964.
[106] H. Shimakoshi, M. Nishi, A. Tanaka, K. Chikama, Y. Hisaeda, *Chem. Commun.* **2011**, *47*, 6548-6550.
[107] P. Giannopoulos, A. K. Andreopoulou, C. Anastasopoulos, D. Raptis, G. Sfyri, J. K. Kallitsis, P. Lianos, *RSC Adv.* **2016**, *6*, 8256-8266.
[108] Y. Lu, *Photochem. Photobiol. Sci.* **2010**, *9*, 392-397.
[109] M. Heller, U. S. Schubert, *Macromol. Rapid Commun.* **2002**, *23*, 411-415.
[110] B. Happ, C. Friebe, A. Winter, M. D. Hager, U. S. Schubert, *Eur. Polym. J.* **2009**, *45*, 3433-3441.
[111] B. Happ, J. Kubel, M. G. Pfeffer, A. Winter, M. D. Hager, B. Dietzek, S. Rau, U. S. Schubert, *Macromol. Rapid Commun.* **2015**, *36*, 671-677.
[112] T. Ueki, M. Shibayama, R. Yoshida, *Chem. Commun.* **2013**, *49*, 6947-6949.

[113] M. L. Disabb-Miller, Y. Zha, A. J. DeCarlo, M. Pawar, G. N. Tew, M. A. Hickner, *Macromolecules* **2013**, *46*, 9279-9287.
[114] Y. Zha, M. L. Disabb-Miller, Z. D. Johnson, M. A. Hickner, G. N. Tew, *J. Am. Chem. Soc.* **2012**, *134*, 4493-4496.
[115] C. Friebe, H. Görls, M. Jäger, U. S. Schubert, *Eur. J. Inorg. Chem.* **2013**, 4191-4202.
[116] C. Friebe, M. Jäger, U. S. Schubert, *RSC Adv.* **2013**, *3*, 11686-11690.
[117] B. J. Holliday, T. M. Swager, *Chem. Commun.* **2005**, 23-36.
[118] P. Manca, M. I. Pilo, G. Sanna, A. Zucca, G. Bergamini, P. Ceroni, *Chem. Commun.* **2011**, *47*, 3413-3415.
[119] T. Schlotthauer, C. Friebe, A. M. Schwenke, M. Jager, U. S. Schubert, *J. Mater. Chem. C* **2017**, *5*, 2636-2648.
[120] J. Heinze, B. A. Frontana-Uribe, S. Ludwigs, *Chem. Rev.* **2010**, *110*, 4724-4771.
[121] R. Schroot, C. Friebe, E. Altuntas, S. Crotty, M. Jaeger, U. S. Schubert, *Macromolecules* **2013**, *46*, 2039-2048.
[122] M. Jäger, L. Eriksson, J. Bergquist, O. Johansson, *J. Org. Chem.* **2007**, *72*, 10227-10230.
[123] M. Jäger, R. J. Kumar, H. Görls, J. Bergquist, O. Johansson, *Inorg. Chem.* **2009**, *48*, 3228-3238.
[124] J. Kübel, R. Schroot, M. Wächtler, U. S. Schubert, B. Dietzek, M. Jäger, *The J. Phys. Chem. C* **2015**, *119*, 4742-4751.
[125] R. Schroot, U. S. Schubert, M. Jäger, *Macromolecules* **2015**, *48*, 1963-1971.
[126] T. Schlotthauer, R. Schroot, S. Glover, L. Hammarstrom, M. Jager, U. S. Schubert, *PCCP.* **2017**, *19*, 28572-28578.
[127] R. Schroot, T. Schlotthauer, B. Dietzek, M. Jager, U. S. Schubert, *Chem. Eur. J.* **2017**, *23*, 16484-16490.

List of abbreviations

°C	Degree Celcius
3D	Three-dimensional
A	Acceptor
b	Block
bn	Benzyl
bpy	2,2'-bipyridine
Carb	Carbazole
CuAAC	Copper(I)-catalyzed Azide-Alkyne Cycloaddition
CV	Cyclic voltammetry
D	Donor
DCC	Dicyclohexylcarbodiimide
DIPEA	Diisopropylethylamine
DMF	*N*,*N*-Dimethylformamide
Dppf	1,1'-Bis(diphenylphosphino)ferrocene
dppp	1,3-Bis(diphenylphosphino)propane
dqp	2,6-Di(quinolin-8-yl)pyridine
EDDM	Electron-density difference maps
EDC	1-Ethyl-3-(3-dimethylaminopropyl)carbodiimide
EDOT	Poly(3,4-ethylenedioxythiophene)
ESI	Electron spray ionisation
g	Gram
h	Hour
HATU	1-[Bis(dimethylamino)methylene]-1H-1,2,3-triazolo[4,5-b]pyridinium 3-oxide hexafluorophosphate
HOMO	Highest occupied molecular orbital
HOBt	Hydroxybenzotriazole hydrate
hν	Light energy
IL	Intraligand
IR	Infrared
ITO	Indium tin oxide
LC	Ligand centered
LUMO	Lowest unoccupied molecular orbital
MALDI	Matrix-assisted laser desorption ionization
MC	Metal centered
min	Minute
mL	Milliliter
MLCT	Metal-to-ligand charge-transfer
MLLCT	Metal-and-to-ligand charge-transfer
mM	Millimol
M_n	Number average molar mass
MPEG 550	Poly(ethylene glycol) methyl ether, M_n 550 g/mol

MS	Mass spectrometry
NDI	Naphthalenediimide
nm	Nanometer
NMP	Nitroxide mediated polymerization
NMR	Nuclear magnetic resonance
ns	Nanosecond
OLED	Organic light-emitting diode
P	Photosensitizer
p	Poly
PDI	Dispersity
PEG	Poly(ethylene glycol)
ph	Phenyl
pin	Pinacolato
PMDETA	*N*,*N*,*N*′,*N*″,*N*″-Pentamethyldiethylenetriamine
ppm	Parts per million
py	Pyridyl
pyBOP	Benzotriazoloxytripyrrolidinophosphonium hexafluorophosphate
RAFT	Reversible addition−fragmentation chain-transfer
ROMP	Ring-opening metathesis polymerization
RT	Room temperature
SEC	Size-exclusion chromatography
SPhos	2-Dicyclohexylphosphino-2′,6′-dimethoxybiphenyl
t	Time
TA	Transient absorption
TARA	Triarylamine
TBAF	Tetrabutylammonium fluoride
TEA	Triethylamine
TD-DFT	Time-dependent density functional theory
THF	Tetrahydrofuran
TLC	Thin-layer chromatography
ToF	Time of Flight
Tpy	2,2’,6’,2-terpyridinetpy
TSTU	Tetramethyl-*O*-(*N*-succinimidyl)uronium tetrafluoroborate
UV	Ultraviolet
Vis	Visible
µs	Microsecond

List of structures

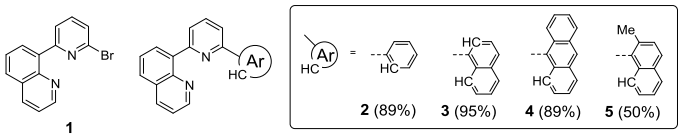

1

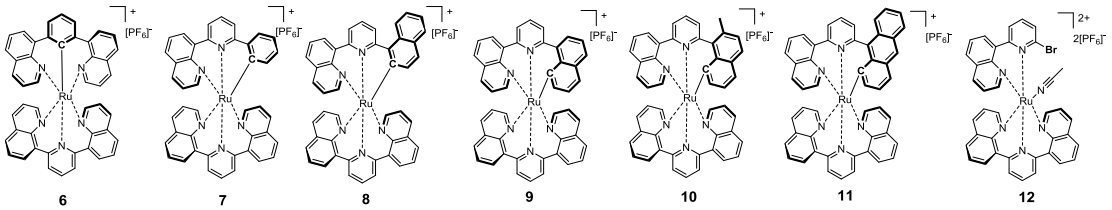

6 7 8 9 10 11 12

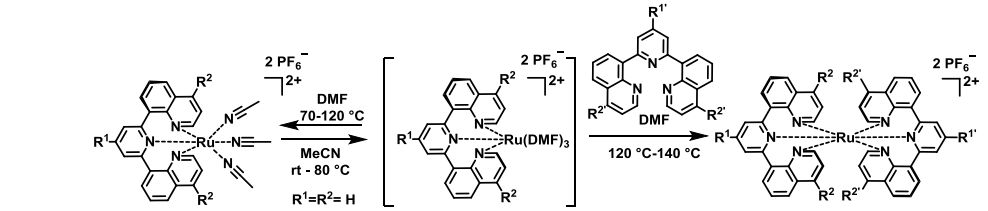

13&14) $R^1=R^{1'}=R^2=R^{2'}=$ H
15) $R^1=R^{1'}=R^2=$H, $R^{2'}=$ PhBr
16) $R^1=$OH, $R^{1'}=$ PhCCTIPS, $R^2=R^{2'}=$ H
17) $R^1=$ H, $R^{1'}=$ Br, $R^2=R^{2'}=$ H
18) $R^1=$H, $R^{1'}=$ PhBr, $R^2=R^{2'}=$ H
19) $R^1=R^{1'}=R^2=$H, $R^{2'}=$ Ph(th)$_2$
20) $R^1=$ PhBr, $R^{1'}=R^2=$ H, $R^{2'}=$ Ph(th)$_2$
21) $R^1=R^{1'}=R^2=$ H, $R^{2'}=$ PhEDOT
22) $R^1=R^{1'}=$ PhBr, $R^2=R^{2'}=$ PhMe
23) $R^1=$ PhBr, $R^{1'}=$ OH, $R^2=R^{2'}=$ PhMe
24) $R^1=$H, $R^{1'}=$ PhBr, $R^2=$ H, $R^{2'}=$ PhOMe

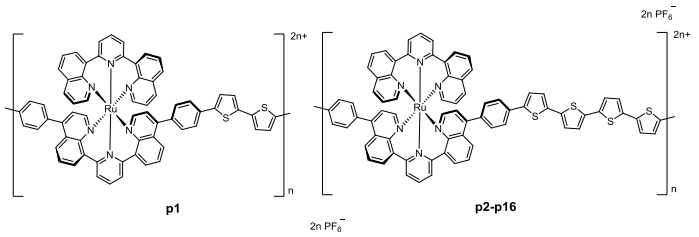

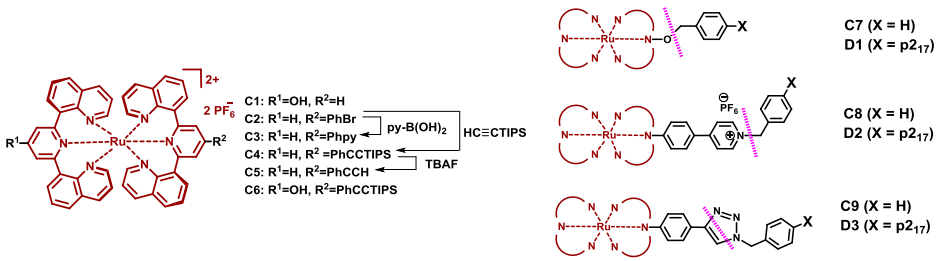

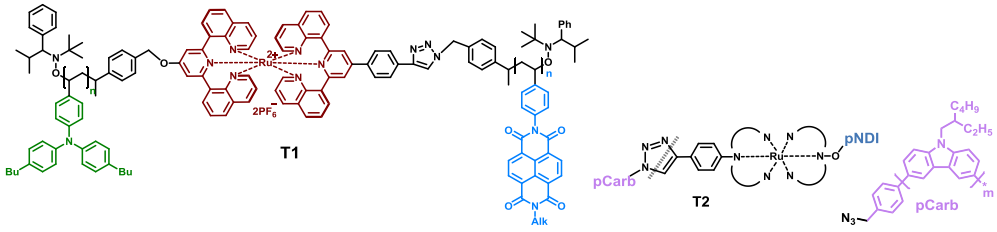

Curriculum vitae

Personal Data

Date of birth:	April, 20th 1989
Place of birth:	Schmalkalden, Germany

University Education

12/2013–present:	PhD student in the group of Prof. Dr. U. S. Schubert at the *Institute of Organic Chemistry and Macromolecular Chemistry* of the *Friedrich Schiller University Jena*, Germany
10/2013:	Diploma (equivalent to M.Sc.)
11/2012–9/2013:	Diploma thesis in the group of Prof. Dr. U. S. Schubert at the *Institute of Organic Chemistry and Macromolecular Chemistry* of the *Friedrich Schiller University Jena*, Germany, thesis title: "Synthesis and characterization of new multi-substituted and metalating photoredox-active ruthenium complexes"
10/2008–9/2013:	Studies of Chemistry at the *Friedrich Schiller University Jena*, Germany

Schooling

06/2008:	Abitur (university entrance certification) at the *BBZ Schmalkalden*, Schmalkalden, Germany

Jena, 09.03.2018

Tina Mede

Publication list

Peer-reviewed publications

[1] T. Kloubert, C. Müller, S. Krieck, T. Schlotthauer, H. Görls, M. Westerhausen, *Eur. J. Inorg. Chem.* **2012**, *2012*, 5991-6001.

[2] T. Schlotthauer, B. Suchland, H. Görls, G. A. Parada, L. Hammarström, U. S. Schubert, M. Jäger, *Inorg. Chem.* **2016**, *55*, 5405-5416.

[3] R. Schroot, T. Schlotthauer, U. S. Schubert, M. Jäger, *Macromolecules* **2016**, *49*, 2112-2123.

[4] R. Schroot, T. Schlotthauer, M. Jäger, U. S. Schubert, *Macromol. Chem. Phys.* **2017**, *218*, 1600534.

[5] T. Schlotthauer, C. Friebe, A. M. Schwenke, M. Jäger, U. S. Schubert, *J. Mat. Chem. C* **2017**, *5*, 2636-2648.

[6] T. Schlotthauer, G. A. Parada, H. Görls, S. Ott, M. Jäger, U. S. Schubert, *Inorg. Chem.* **2017**, *56*, 7720-7730.

[7] T. Schlotthauer, R. Schroot, S. Glover, L. Hammarström, M. Jäger, U. S. Schubert, *PCCP*, **2017**, *19*, 28572-28578.

[8] R. Schroot, T. Schlotthauer, B. Dietzek, M. Jäger, U. S. Schubert, C*hem. Eur. J.* **2017**, *23*, 16484-16490.

[9] T. Mede, M. Jäger, U.S. Schubert, submitted.

[10] T. Mede, M. Jäger, U.S. Schubert, submitted.

Poster presentations

[1] T. Schlotthauer, E. Altuntas, A. Baumgärtel, H. Görls, U. S. Schubert, M. Jäger, *Synthesis of Functionalized Tridentate Ligands With Large Bite Angles Designed For Photo-redoxactive Ruthenium Complexes*, ORCHEM Weimar, Germany, **2012**.

[2] T. Schlotthauer, Helmar Görls M. Jäger, U. S. Schubert, *New hexaarylated photoredox-active ruthenium(II)-complexes,* COST Meeting, Jena, Germany, **2014**.

[3] T. Schlotthauer, Helmar Görls M. Jäger, U. S. Schubert, *New hexaarylated photoredox-active ruthenium(II)-complexes,* JCF Frühjahrssymposium, Jena, Germany, **2014**.

[4] T. Schlotthauer, R. Schroot, H. Görls, M. Jäger, U. S. Schubert, *Modular assembly of hierarchical redox-active polymers with Ru(II) dyes for light-induced charge separation*, Polymers and Energy, GDCh Fachgruppentagung Makromolekulare Chemie, Jena, Germany, **2014**.

[5] T. Schlotthauer, R. Schroot, Ulrich S. Schubert, Michael Jäger, *Modular assembly of a redox-active Dn-P-Am system*, European Polymer Congress, Dresden, Germany, **2015**.

[6] R. Schroot, T. Schlotthauer, Ulrich S. Schubert, Michael Jäger, *Redox-active and Conjugated Polymers as Modular Building Blocks for Light-induced Directional Charge Transfer Cascades*, 25. Lecture Conference on Photochemistry, Jena, Germany, **2016**.

[7] T. Schlotthauer, R. Schroot, Ulrich S. Schubert, Michael Jäger, *Modular assembly of a redox-active Dn-P-Am system*, 25. Lecture Conference on Photochemistry, Jena, Germany, **2016**.

Acknowledgements

This thesis would not have been possible without the continuous help and support of many people.

First of all, I would like to thank Prof. Ulrich S. Schubert for giving me the opportunity to work on this highly interesting topic and to prepare my PhD thesis in his group.

Furthermore, I want to thank Dr. Michael Jäger for supervision and for always having an open ear for me. Your continuous support and detailed knowledge was crucial for the success of the thesis.

I am very grateful to spend my PhD time not just with colleagues. Moreover, I spend it with my best friends Robert Schroot und Ronny Tepper. It was a pleasure to share the office and/or the lab with you. I thank you for all the fun, your support, the helpful discussions and cooperation. Without you, I am sure: It was not possible to finish this.

I am very happy, to share the coffee breaks with Ronny Tepper, Robert Schroot, Anne-Kristin Trützschler, Dr. Kevin Barthelmes, Dr. Daniel Schmidt, Dr. Julia Kötteritzsch, Dr. Christian Friebe, Meike Leiske and Gabriele Sentis. I love it to support you with cakes and cookies and will always miss these moments.

In addition, many people helped me with measurements, organization and discussion of their results or executed other important tasks, *e.g.,* ordered chemicals and lab ware or maintained instruments. In this regard, I thank Dr. Helmar Görls, Dr. Sarah Crotty, Nicole Fritz, Annet Urbanek, Dr. Grit Festag, Sandra Köhn, Beate Lentvogt, Dr. Uwe Köhn, Sylvia Braunsdorf, Simone Burchardt and Franka Frister. Furthermore, I want to thank the NMR platform IAAC/IOMC, in particular Dr. Wolfgang Günther, Dr. Peter Bellstedt and most of all Gabriele Sentis, for many NMR measurements. Your effort enabled the fast characterization.

I want to thank the Schubert-group for the great time, the help and nice working atmosphere.

I would like to thank my Coauthors Robert Schroot, Dr. Christian Friebe, Dr. Almut Schwenke, Dr. Helmar Görls, Dr. Giovanny Parada, Prof. Sascha Ott, Dr. Starla Glover,

Prof. Dr. Leif Hammarström and Prof. Dr. Benjamin Dietzek for their cooperation and for being a part of my publications.

Furthermore, I want to thank my friends and family, especially my mother for her continuous support and understanding.

Finally, I want to thank my husband Ralf Mede. I cannot find the right words, how important you are for me. It is a pleasure to be a part of your life. I thank you for your understanding in hard times, for your support and your words that brings me back on the right way when it was necessary. Without you, it would not possible to finish this thesis.

Declaration of authorship / Selbstständigkeitserklärung

Ich erkläre, dass ich die vorliegende Arbeit selbständig und unter Verwendung der angegebenen Hilfsmittel, persönlichen Mitteilungen und Quellen angefertigt habe.

I certify that the work presented here is, to the best of my knowledge and belief, original and the result of my own investigations, except as acknowledged, and has not been submitted, either in part or whole, for a degree at this or any other university.

Jena, 09.03.2018

_____

Tina Mede

Publications P1 to P8

P1) T. Schlotthauer, G. A. Parada, H. Görls, S. Ott, M. Jäger, U. S. Schubert, "Asymmetric cyclometalated Ru^{II} polypyridyl-type complexes with π-extended carbanionic donor sets", *Inorg. Chem.* **2017**, *56*, 7720-7730.

P2) T. Mede, M. Jäger, U. S. Schubert, "Exploring the coordination mechanism towards multi-functionalized Ru^{II} polypyridyl-type sensitizer: An experimental and computational study", submitted.

P3) T. Mede, M. Jäger, U. S. Schubert, "'Chemistry-on-the-complex': Functional Ru^{II} polypyridyl-type sensitizer as divergent building blocks", submitted.

P4) T. Schlotthauer, C. Friebe, A. M. Schwenke; M. Jäger; U. S. Schubert, "Mild electropolymerization and monitoring of continuous film formation for photoredox-active Ru metallopolymers", *J. Mat. Chem. C* **2017**, *5*, 2636-2648.

P5) R. Schroot, T. Schlotthauer, U. S. Schubert, M. Jäger, "Modular assembly of poly(naphthalene diimide) and Ru(II) dyes for an efficient light-induced charge separation in hierarchically controlled polymer architectures", *Macromolecules* **2016**, *49*, 2112-2123.

P6) R. Schroot, T. Schlotthauer, M. Jäger, U. S. Schubert, "Hydrophilic poly(naphthalene diimide)-based acceptor–photosensitizer dyads: toward water-processible modular photoredox-active architectures", *Macromol. Chem. Phys.* **2017**, *218*, 1600534.

P7) T. Schlotthauer, R. Schroot, S. Glover, L. Hammarström, M. Jäger, U. S. Schubert, "A *multi*donor-photosensitizer-*multi*acceptor triad for long-lived directional charge separation", *PCCP*, **2017**, *19*, 28572-28578.

P8) R. Schroot, T. Schlotthauer, B. Dietzek, M. Jäger, U. S. Schubert, "*Block* copolymer-type architecture with a central Ru^{II} sensitizer core: Conjugated poly(carbazole) for enhanced charge separation", C*hem. Eur. J,* **2017**, *23*, 16484-16490.

Publication P1

Asymmetric cyclometalated Ru^{II} polypyridyl-type complexes with π-extended carbanionic donor sets

T. Schlotthauer, G. A. Parada, H. Görls, S. Ott, M. Jäger, U. S. Schubert, *Inorg. Chem.* **2017**, *56*, 7720-7730.

The paper as well as the supporting information (free of charge) is available online under: doi.org/10.1021/acs.inorgchem.7b00392

Inorganic Chemistry

Article

pubs.acs.org/IC

Asymmetric Cyclometalated Ru^{II} Polypyridyl-Type Complexes with π-Extended Carbanionic Donor Sets

Tina Schlotthauer,[†,‡] Giovanny A. Parada,[§,⊥] Helmar Görls,[∥] Sascha Ott,[§] Michael Jäger,*[,†,‡] and Ulrich S. Schubert*[,†,‡]

[†]Laboratory of Organic and Macromolecular Chemistry (IOMC), Friedrich Schiller University Jena, Humboldtstraße 10, 07743 Jena, Germany

[‡]Center for Energy and Environmental Chemistry Jena (CEEC Jena), Friedrich Schiller University Jena, Philosophenweg 7a, 07743 Jena, Germany

[§]Department of Chemistry, Ångström Laboratory, Uppsala University, Box 523, SE-75120 Uppsala, Sweden

[∥]Laboratory of Inorganic and Analytical Chemistry, Friedrich Schiller University Jena, Lessingstraße 8, 07743 Jena, Germany

Supporting Information

ABSTRACT: A series of novel cyclometalated Ru^{II} complexes were investigated featuring the tridentate dqp ligand platform (dqp is 2,6-di(quinolin-8-yl)pyridine), in order to utilize the octahedral coordination mode around the Ru center to modulate the electrochemical and photophysical properties. The heteroleptic complexes feature C_1 symmetry due to symmetry breaking by the peripheral five- or six-membered carbanionic chelate (phenyl, naphthyl, or anthracenyl units). The chelation mode is controlled by the steric effects and C−H activation selectivity of the ligand, which prompted the development of a general synthesis protocol. The optimized conditions to achieve high overall yields (55−75%) involve $NaHCO_3$ as the base and an simplified purification protocol: i.e., facile chromatographic separation using commercially available amino-functionalized silica applying nonaqueous salt-free conditions to omit the necessity of counterion exchange. The structural, photophysical, and electrochemical properties were studied in depth, and the results were corroborated by density functional theory (DFT) calculations. Steady state and time-resolved spectroscopy revealed red-shifted absorption (up to 750 nm) and weak IR emission (800−1000 nm) combined with prolonged emission lifetimes (up to 20 ns) in comparison to classical tpy-based (tpy is 2,2′:6′,2″-terpyridine) complexes. An enhanced stability was observed by blocking the reactive positions of the carbanionic ligand framework, while the reactive positions may be exploited for further functionalization.

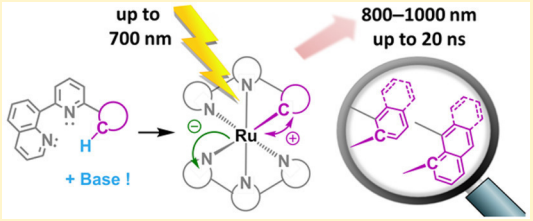

INTRODUCTION

Ru^{II} polypyridyl-type complexes exhibit an extraordinary combination of photophysical and redox properties,[1−3] which have led to their successful applications as photosensitizers in photovoltaic or photosynthetic devices,[4] functional building blocks in molecular machines, phototherapeutics, and sensing applications. The ground and excited state properties of the complexes are controlled by the ligand sphere, which usually consists of six donor atoms embedded in aromatic subunits that can be further connected to form chelating ligands. The resulting enormous number of conceivable ligand sets has fueled the exploration of polypyridyl-type Ru^{II} complexes by rational ligand design, aiming to modulate the inherent geometric and electronic features. In parallel, theoretical methodologies based on density functional theory (DFT) have evolved to become a valuable tool for chemists to assist in such rational ligand design:[5] e.g., to design complexes with tailored absorption to closely match the solar spectrum or to modulate and corroborate the experimentally determined excited state properties. In general, the frontier molecular orbitals of the typical polypyridyl-type complexes are composed of Ru d orbitals to constitute the highest molecular orbitals (HOMOs) and ligand-based MOs to form the lowest unoccupied molecular orbitals (LUMOs). Due to the large HOMO−LUMO gap of the archetypical $[Ru(bpy)_3]^{2+}$ or $[Ru(tpy)_2]^{2+}$ complexes, the resulting absorption profile omits an integral portion of the solar spectrum in the red region. One powerful strategy is to raise the HOMO energy by virtue of anionic donors: e.g., carbanionic or N-containing aromatic units.[6−12] This strategy has enabled the success of such Ru complexes in dye-sensitized solar cells since the seminal report by Grätzel,[13] aiming at high energy conversion efficacy and improved chemical stability as reported by the groups of van Koten, Berlinguette, and others.[8−12]

In the case of cyclometalated complexes, the triplet excited state is dominated by metal-to-ligand charge transfer (^{3}MLCT) character with some admixing of the cyclometalating donor,[2] as exemplified by plots of the HOMO (Ru-cyclometalating fragment) and the LUMO (polypyridyl-type ligands).[14]

Received: February 14, 2017
Published: July 5, 2017

DOI: 10.1021/acs.inorgchem.7b00392
Inorg. Chem. 2017, 56, 7720−7730

Although the excited state is best described by a metal ligand to ligand CT state (^{3}MLLCT), the term ^{3}MLCT will be used synonymously for simplicity. Notably, different donating/accepting organic subunits contribute to the HOMO/LUMO, which leads to the charge separation character of the excited state. In addition to the spectral properties, the lifetime of the excited state is an important parameter for efficient subsequent photochemical reactions (e.g., electron transfer) and is controlled by nonradiative and radiative deactivation pathways.[14,15] In the case of thermally activated pathways, the deactivation via accessible triplet metal-centered (^{3}MC) states has been identified. In order to diminish such a pathway, strong σ donors or an improved octahedral geometry has been utilized to increase the ligand field splitting to raise the barrier.[8,16−19] In the case of direct coupling with the ground state, the extent of spin−orbit coupling becomes important and structural features also become important.[20] The photoredox properties of the complexes are further tuned by systematically adjusting the frontier MO energies via functionalization of the ligand scaffold, e.g. of the carbanionic fragment by bromination via *N*-bromosuccinimide[21] or $CuBr_2$,[22,23] as well as nitration with $Cu(NO_3)_2$[22] or with $AgNO_3$ in the presence of PhCOCl.[24] Such "chemistry-on-the-complex" modifications do not only diversify the set of photophysical and electrochemical properties but also offer the possibility to incorporate the moiety into molecular systems aiming, for example, at energy conversion.

In this contribution, the synthesis of a series of novel cyclometalated Ru^{II} complexes was explored and the electrochemical and photophysical properties were investigated, including structural analysis by X-ray crystallography and a theoretical assessment based on density functional theory (DFT) (Figure 1). The cyclometalating ligands are derived

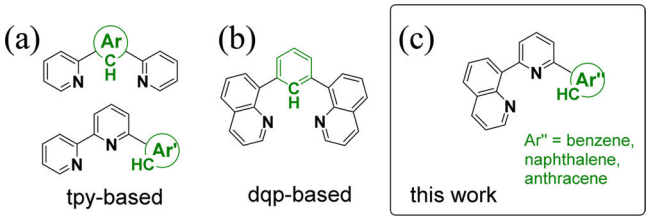

Figure 1. Representation of reported cyclometalating ligands based on the tpy framework by replacing one N by CH (a) in a symmetrical (top) and symmetry-broken arrangement (bottom), as well as the related cyclometalating dqp-based ligands featuring enhanced bite angles in a symmetrical form (b) and symmetry-broken arrangement (c, this work). Typical anionic fragments for ArX$^-$ and Ar′X$^-$ comprise C-based and N-based (hetero)cycles: e.g., benzene, triazoles, and pyrazole moieties. Ar″X$^-$ denotes carbanionic donors based on benzene, naphthalene, and anthracene (this work); dqp is 2,6-di(quinolin-8-yl)pyridine, and tpy is 2,2′:6′,2″-terpyridine.

from 2,6-di(quinolin-8-yl)pyridine (dqp), which has been shown to provide a larger bite angle that leads to prolonged excited state lifetimes of Ru^{II} polypyridyl-type complexes and also to one related cyclometalated complex.[25−28] In this work, one peripheral quinoline group of dqp is replaced by a phenyl, naphthyl, or anthracenyl moiety. Hence, such peripheral cyclometalation leads to a range of ligands that feature differently sized π systems and five- and six-membered chelates, as well as different mutual orientation and stacking of the aromatic subunits.

RESULTS AND DISCUSSION

Synthesis. The novel ligands were prepared by a modified Suzuki−Miyaura cross-coupling protocol reported for the synthesis of the symmetric cyclometalating dqPhH ligand (dqPhH is 2,6-di(quinolin-8-yl)benzene).[25] However, using an excess of 2,6-dibromopyridine with respect to 8-quinolineboronic acid (4/1) leads to low yields (∼20%) of the desired monofunctionalized intermediate **1**.[29] Presumably, the catalyst fragment is chelated by the formed product and undergoes the second coupling step, as corroborated by the formation of significant amount of dqp during our initial efforts to optimize this route.[30] Hence, the original monophosphine SPHOS (SPHOS is 2-dicyclohexylphosphino-2′,6′-dimethoxybiphenyl) was replaced by the bidentate phosphine ligand dppp (dppp is 1,3-di(diphenylphosphino)propane), which led to significantly increased yields of **1** (59%) even in a 1/1 ratio of the educts. The subsequent second Suzuki−Miyaura cross-coupling step employing the commercially available arylboronic acids of benzene, naphthalene, and anthracene yielded the asymmetric cyclometalating ligands **2**−**4** (Scheme 1). The ligands **2** and **4**

Scheme 1. Schematic Representation of the Ligand Synthesis (1−5) via Suzuki−Miyaura Cross Coupling[a]

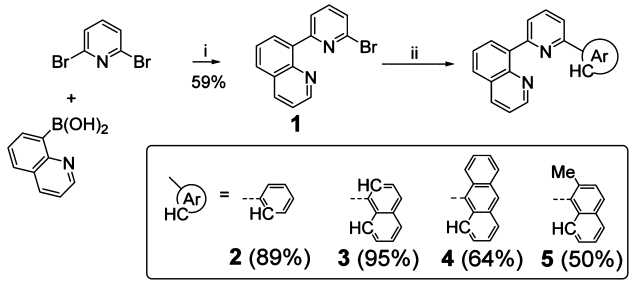

[a]Experimental conditions: (i) Pd(dba)$_2$, dppp, K_2CO_3, CH_3CN/H_2O, 2 h, 130 °C; (ii) arylboronic acid, Pd(dba)$_2$ SPHOS, K_2CO_3, CH_3CN/H_2O, 1−2 h, 130−140 °C. Metalation sites are indicated by CH.

lead specifically to five- and six-membered chelates, respectively, whereas ligand **3** featuring the naphthalene unit can adopt two coordination modes (vide infra). Since more forcing reaction conditions are generally required to promote six-membered vs five-membered chelates,[28] the coordinating position for the latter was blocked by a methyl group (ligand **5**). Excellent isolated yields were achieved except for **5**, which is attributed to the difficulties in removing detrimental impurities from the crude 2-methylnaphthyl-1-ylboronic acid following the same route as for 8-quinolineboronic acid. Such residual impurities may cause side reactions during the second coupling step and suggest further optimization; however, sufficient amounts of **5** were obtained for the subsequent complexation reactions.

With the cyclometalating ligands in hand, we investigated the synthesis of the corresponding complexes (Figure 2). Note that the order of the presented complexes reflects the main results from our optimization developments (Table 1), whereas a detailed discussion is provided in section 2 and Table S1 in the Supporting Information. The cyclometalation reaction typically requires higher temperatures in comparison to the coordination of related nitrogen donors. The symmetric complex **6** was readily prepared in 73% yield from [Ru(dqp)$(CH_3CN)_3$]-$(PF_6)_2$ and dqPhH in ethylene glycol using microwave heating (200 °C for 90 min) (Table 1, entry 1). In contrast, applying

DOI: 10.1021/acs.inorgchem.7b00392
Inorg. Chem. 2017, 56, 7720−7730

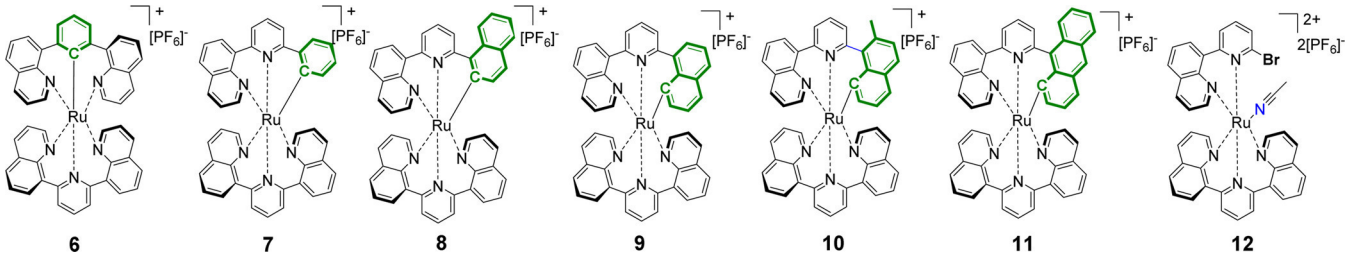

Figure 2. Representations of complexes prepared in this study featuring central cyclometalation (**6**), peripheral cyclometalation with five-membered chelates (**7** and **8**) or six-membered chelates (**9**–**11**), and a related bidentate complex (**12**, see text).

Table 1. Optimized Reaction Conditions for Complexes 6–12[a]

entry	ligand	solvent	T (°C)	time (h)	base	product	isolated yield (%)
1	dqPhH	EG	200[b]	1.5		**6**	73[c]
2	**3**	EG	200[b]	1.5		**9**[h]	10[c]
3	**1**	EG	120	16		**12**	49
4	**2**	EG	160[d]	16	lutidine	**7**	74[c]
5	**3**	EG	160[d]	0.7	$NaHCO_3$	**8**	55[e]
6	**4**	EG	160[d]	2.5	$NaHCO_3$	**11**	75[e]
7	**5**	EG	160[d]	3	$NaHCO_3$	**10**	68[e]

[a]For full details see Table S1 in the Supporting Information. EG is ethylene glycol. [b]Microwave heating. [c]Purification by two consecutive silica columns: CH_2Cl_2/CH_3OH and CH_3CN/H_2O/aqueous KNO_3 adapted from ref 25. [d]Oil bath heated before synthesis (thermally equilibrated). [e]Purification by single column on amino-decorated silica. See text for further explanation.

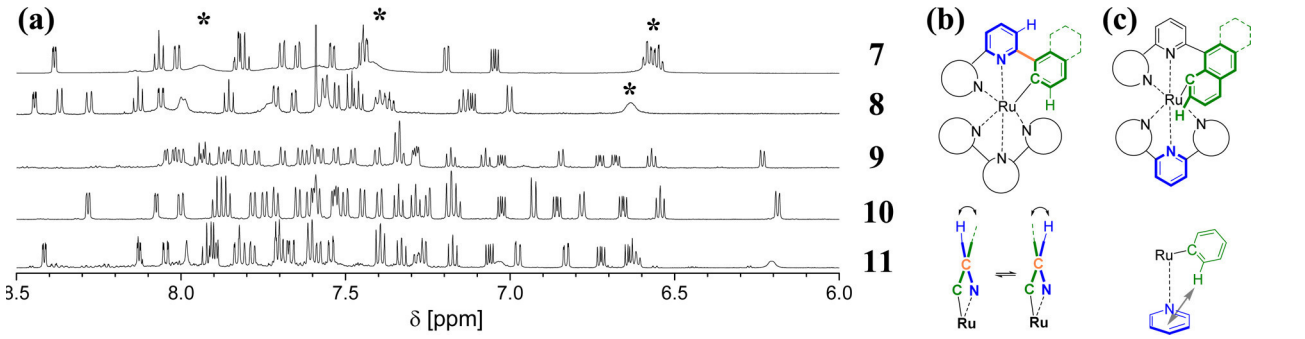

Figure 3. (a) ^{1}H NMR spectra of complexes **7**–**11** (CD_3CN, 600 MHz, aromatic region) showing signal broadening (marked by asterisk) of the five-membered chelates (**7** and **8**) and a characteristic high-field shift of the six-membered chelates around 6.2 ppm (**9**–**11**). (b) Schematic representation of structural motifs (pyridine in blue, carbanionic fragment in green, interannular C–C bond in orange) leading to Signal broadening in five-membered chelates assigned to conformational exchange (bottom, see text). (c) High-field shift of the *o*-H in the cyclometalating ring due to shielding by the nearby pyridine π system of dqp (bottom). See the X-ray structures for more details.

similar conditions for the chelation of the new chelating ligands gave significantly lower yields (<10%), leading to prohibitively elaborate purification efforts, while no product formation was noticed upon lowering the reaction temperature. For example, the geometrically related complex **9**, which differs from **6** only in the position of cyclometalation, was isolated at best in 10% yield (Table 1, entry 2). The reason is assigned to the required C–H activation, since the coordination of the related bidentate ligand precursor (**1**) devoid of the cyclometalating unit was found to occur already at 120 °C to yield complex **12** (49%; Table 1, entry 3). Efficient cyclometalation was finally achieved in the presence of base. Notably, the cyclometalation promoted by 2,6-lutidine was found to proceed significantly more easily for the least congested phenyl-decorated ligand **2** (74%, Table 1, entry 4) in comparison to ligands **3** (34%), **4** (<5%), and **5** (37%) (Table S1). In addition, the exceptionally low yield of the sterically most demanding ligand **4** suggests that steric factors control the C–H activation and Ru–C bond formation. These findings parallel a recent report on Cu(I)-catalyzed oxidative cyanation of related 2-pyridyl aromatics, which occurs readily except for the anthracene moiety, ascribed to steric limitations during the C–H activation.[31] This hypothesis is further corroborated by the improved yields using the smaller base $NaHCO_3$ (Table 1, entries 5–7), which afforded the remaining complexes **8** (55%), **10** (68%), and particularly **11** (75%). The high yields are also attributed to the developed simplified purification protocol—i.e., performing only a single chromatographic run using amino-functionalized silica and a CH_2Cl_2/CH_3OH eluent—without the need of subsequent counterion exchange.

Structural Analysis. The ^{1}H NMR spectra of the cyclometalated complexes **7**–**11** are depicted in Figure 3. Although the proton resonances are generally well resolved, some proton signals show an unusual signal broadening. This feature is observed for the five-membered chelates (**7** and **8**), while the six-membered congeners **9** and **10** exhibit the typical well-resolved spectra as for $[Ru(dqp)_2]^{2+}$ complexes (see also 2D NMR data in the Supporting Information).[32,33] This

DOI: 10.1021/acs.inorgchem.7b00392
Inorg. Chem. 2017, 56, 7720–7730

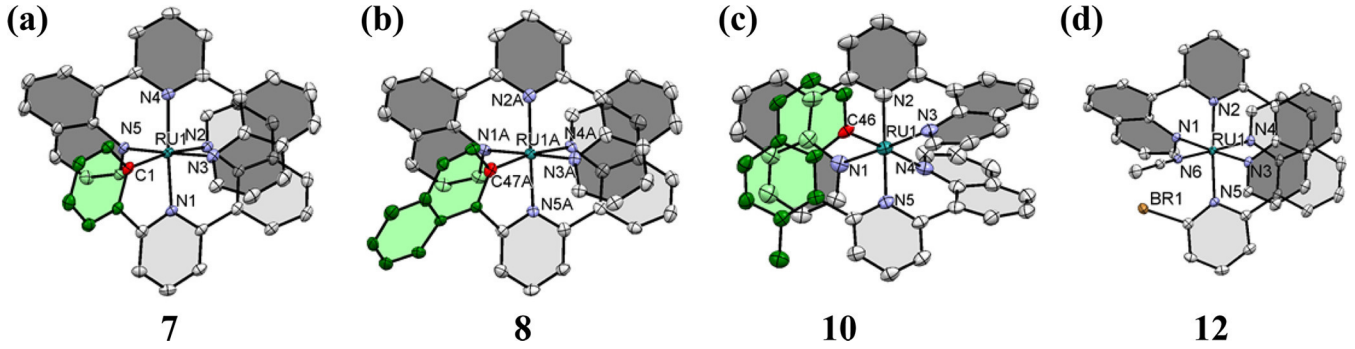

Figure 4. Molecular structures of the complexes **7** (a), **8** (b), **10** (c), and **12** (d). The carbanionic donor (red) and the cyclometalating subunit (green) are highlighted. Note the absence of π stacking of the cyclometalating fragment (green) in the case of five-membered chelation (**7** and **8**) but its occurrence for six-membered chelation (**10**). Thermal ellipsoids are drawn at a probability level of 50%, and cocrystallized solvent molecules, disoriented counterions, and hydrogen atoms are omitted for clarity. See Table 2 for selected structural details.

Table 2. Selected Crystallographic Data of Cyclometalated Complexes (6, 7, 8, 10) and 12[a]

complex	Ru−N^{qu} (Å)	Ru−N/C^{central} (Å)	Ru−C/N^{peripheral} (Å)	N/C^{central}−Ru−C/N^{peripheral} (deg)	N^{qu}−Ru−C/N^{peripheral} (deg)	dihedral distortion[b] (deg)	stacking[c] (deg)
6[d]	2.076 ± 0.008	2.013 ± 0.002	2.061 ± 0.003	89.2 ± 0.1	179.1 ± 0.6	35.1 ± 0.9	3.492 ± 0.044
7	2.163	2.022	2.034	80.3	168.3	1.5	
8	2.180 ± 0.006	2.009 ± 0.004	2.009 ± 0.005	80.4 ± 0.0	168.9 ± 0.5	9.4 ± 0.6	
10	2.160	2.044	2.036	89.6	177.5	41.0	3.455
12	2.065	2.133	2.033[e]	95.0[e]	175.3[e]		

[a]Averaged values and difference from the maximum/minimum observed values (see ref 32 for discussion). N^{qu} denotes the quinoline subunit, N/C^{central} denotes the central unit (phenyl for **6**, otherwise pyridine), C/N^{peripheral} denotes the peripheral (cyclometalating) unit (**7**, **8**, **10**) or quinoline (**6**) or acetonitrile (**12**). [b]Between pyridine and quinoline unit along the interannular C−C bond. [c]Distance between quinoline-C10 bridgehead atom and the center of gravity of the stacked benzene subunit. [d]Data from ref 25. [e]Data of acetonitrile ligand.

behavior can be explained by a small barrier of conformational exchange of the cyclometalating unit for **7** and **8** (Figure 3b), which is prevented in the case of six-membered congeners due to stacking.

In order to confirm this hypothesis and to validate subsequent theoretical calculations, the solid state structures were analyzed by X-ray crystallography and discussed with respect to related available data. The crystal structures were assessed as described previously: i.e., average values are reported in the case of an asymmetric environment.[32] Figure 4 depicts the solid state structures of representative complexes: i.e., the five-membered complexes **7** and **8**, the six-membered complex **10**, and the complex **12** (crystallographic data are given in Table 2). All complexes revealed a meridional coordination of the chelating ligands in an octahedral fashion: i.e., the internal bond angles defined by the Ru center and opposite/adjacent donor atoms are close to the typical values of dqp (180/90°) or tpy (169/80°), respectively.[25,32] The Ru−N(C) bond lengths also obey the general trends: (a) central Ru−N(C) bonds are shorter than the peripheral Ru−N(C) bonds, (b) Ru−C bonds are shorter than the corresponding Ru−N bonds, and (c) cyclometalation induces the lengthening of the opposite Ru−N bond (trans effect). For example, the central cyclometalation in the case of complex **6** leads to Ru−C and Ru−N^{py} bond lengths of 2.013 ± 0.002 and 2.093 ± 0.008 Å, respectively, while the peripheral cyclometalation displays slightly longer Ru−C bonds of 2.034 Å (**7**) and 2.036 Å (**10**), respectively. Complex **8** revealed, however, a shorter Ru−C bond (2.009 ± 0.005 Å) and a longer opposite Ru−N bond. The remaining Ru−N^{py} and Ru−N^{qu} bonds (2.03 and 2.07 Å, respectively) are in good agreement with those of the related complexes.[32] The observed π−π stacking distances of the quinoline subunits also parallel the typical values around 3.4−3.5 Å.[32] In line with the interpretation of the ^{1}H NMR data, a very small dihedral angle between the cyclometalating unit and the adjacent pyridine ring along the interannular C−C bond was observed in the case of five-membered **7** (1.5°) and **8** (9.4 ± 0.6°), in combination with an out-of-plane deformation of the carbanionic ring system. The latter can be rationalized by the distorted coordination polyhedron, which induces a nonplanar arrangement of the pyridine and carbanionic fragment along the connecting C−C axis, as sketched in Figure 3b. The crystal structure shows no major constraints for interconversion of both conceivable conformations and, thus, is expected to account for the observed signal broadening of the associated protons in the NMR data (vide supra). The five-membered chelation further prevents the π stacking to the nearby quinoline unit. In the case of six-membered chelation (**10**), the enforced stacking leads to similar internal dihedral angles (41.0°) and quinoline−naphthalene stacking (3.5 Å), as found for related noncyclometalated complexes.[32] The complex **12** shares similar structural features of the Ru(dqp) fragment, while the steric demand by the acetonitrile ligands and bromine substituent leads to an additional distortion of the coordination octahedron, as shown by the less ideal internal angles (±5.0°).

Density functional theory (DFT) calculations were performed to analyze the electronic properties in terms of molecular orbitals (MOs). Notably, the obtained nuclear geometries of the cyclometalated complexes employing the dispersion-corrected functional ωB95xD reproduced the X-ray data satisfyingly (Table S2 in the Supporting Information), in excellent agreement with our previous detailed analysis.[5,32] The electronic structure was analyzed in terms of the frontier molecular orbitals (Supporting Information), whereby the

DOI: 10.1021/acs.inorgchem.7b00392
Inorg. Chem. 2017, 56, 7720−7730

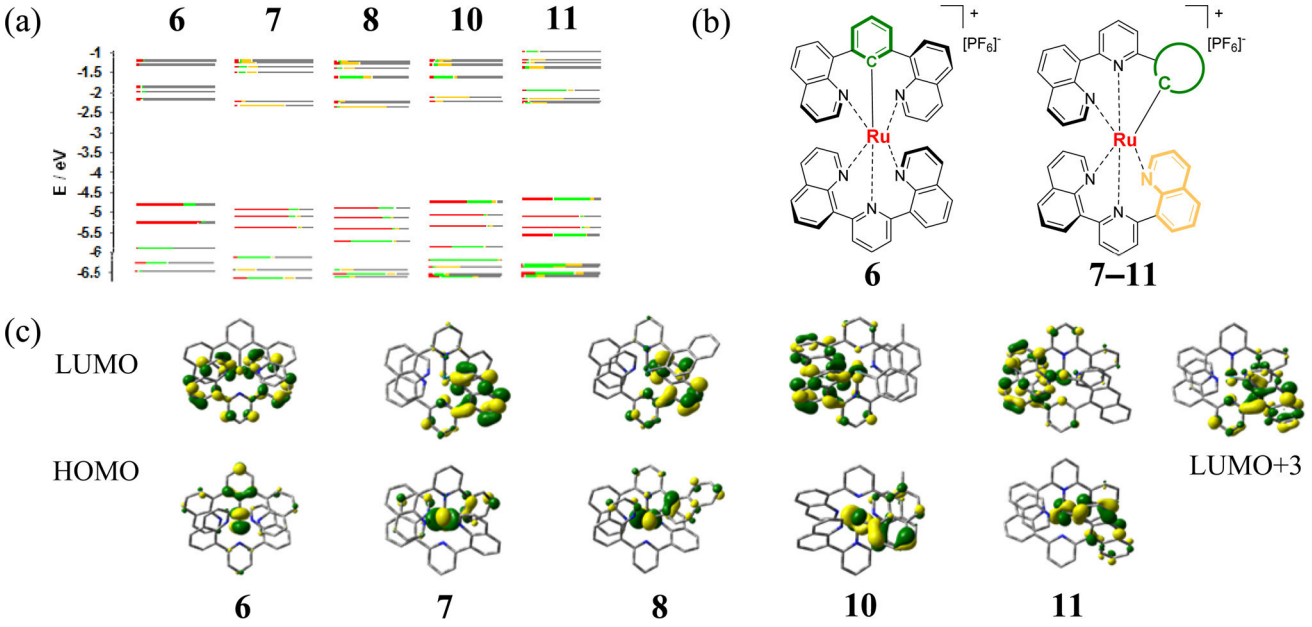

Figure 5. (a) Energy levels of MOs of complexes featuring central cyclometalation for **6** and peripheral cyclometalation with five-membered chelates (**7** and **8**) or six-membered chelates (**10** and **11**) with color code. (b) Molecular fragments partitioned by Mulliken population analysis: ruthenium (red), cyclometalating fragment (green) and its corresponding stacked-quinoline unit (orange), and remaining atoms (gray). (c) Frontier orbitals (HOMO and LUMO, isovalue 0.04) and LUMO+3 (**11**) (see text). See the Supporting Information for complete and enlarged MO plots.

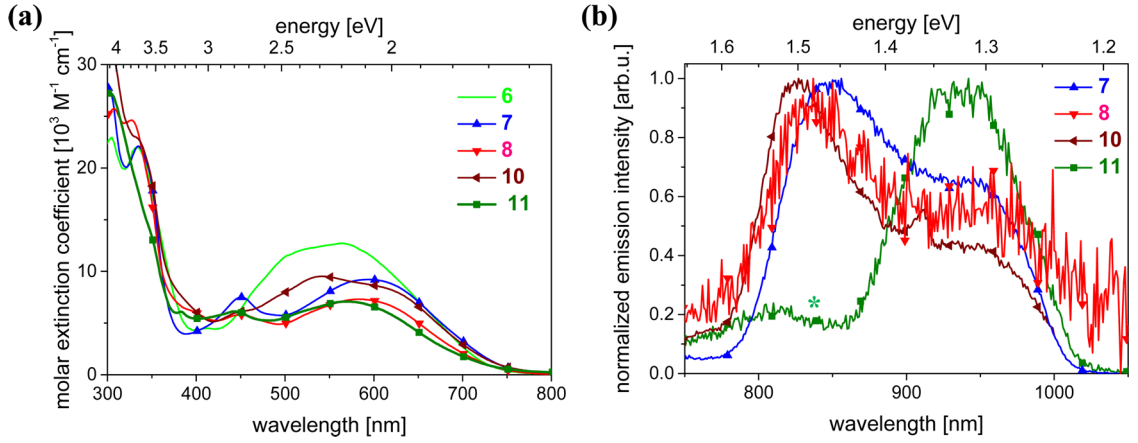

Figure 6. Photophysical data of cyclometalated complexes: (a) absorption spectra taken in CH_3CN solution at room temperature; (b) emission spectra taken at 77 K in C_2H_5OH/CH_3OH glass (4/1 v/v, λ_{exc} 500 nm (**7**, **8**, and **10**) or 700 nm (**11**)). The asterisk denotes a second emissive species. See the Supporting Information for excitation spectra.

Table 3. Photophysical and Electrochemical Properties of the Cyclometalated Complexes

complex	absorption (nm)[a] (ε 910^3 M^{-1} cm^{-1}))	emission (nm)[b] (eV) at 77 K	lifetime (ns)[a] at 293 K	$E^{ox}_{1/2}(Ru^{3+/2+})$[c] (V) (ΔE_p (mV))	$E^{red}_{1/2}(L^{0/-})$[c] (V) (ΔE_p (mV))
6[d]	500(11.4), 565 (12.7)[d]	824 (1.50)[d]	16[d]	−0.08[d]	−2.00[d]
7	451(7.5), 594 (9.2)	847 (1.46)	14	−0.07 (68)	−1.92 (70)
8	448 (5.8), 585 (7.3)	837 (1.48)	20[e]	−0.17 (57)	−1.99 (60)
10	446s (6.1), 542 (9.5), 610s (8.5)	826 (1.50)	20	−0.15 (63)	−1.98 (85)
11	448 (5.8), 571 (7.1)	935 (1.33)[e]	nd[f]	−0.13 (67)	−1.99 (81)

[a]In CH_3CN. [b]In EtOH/MeOH glass (4/1 v/v). [c]From CV in CH_3CN containing 0.1 M Bu_4NPF_6; potentials vs $Fc^{+/0}$, scan rate 100 mV s^{-1}. [d]Data from ref 25. [e]From flash photolysis emission and transient absorption data (see the Supporting Information for details). [f]No data given due to unknown photostability (see text and the Supporting Information for more details).

relative contribution of a specific molecular fragment is visualized by applying a color code (Figure 5).[32] The highest occupied molecular orbitals (HOMOs) are dominated by the Ru d orbitals (red) with the typical admixing of the cyclometalating fragment (green), while the lowest unoccupied molecular orbitals (LUMOs) are localized on the dqp moiety (gray). In the case of five-membered chelates (**7** and **8**), the nonstacked quinoline fragment dominates the LUMO (orange), whereas for the six-membered congeners (**10** and **11**) it dominates the LUMO+1 (Figure 5), which suggests a

DOI: 10.1021/acs.inorgchem.7b00392
Inorg. Chem. 2017, 56, 7720−7730

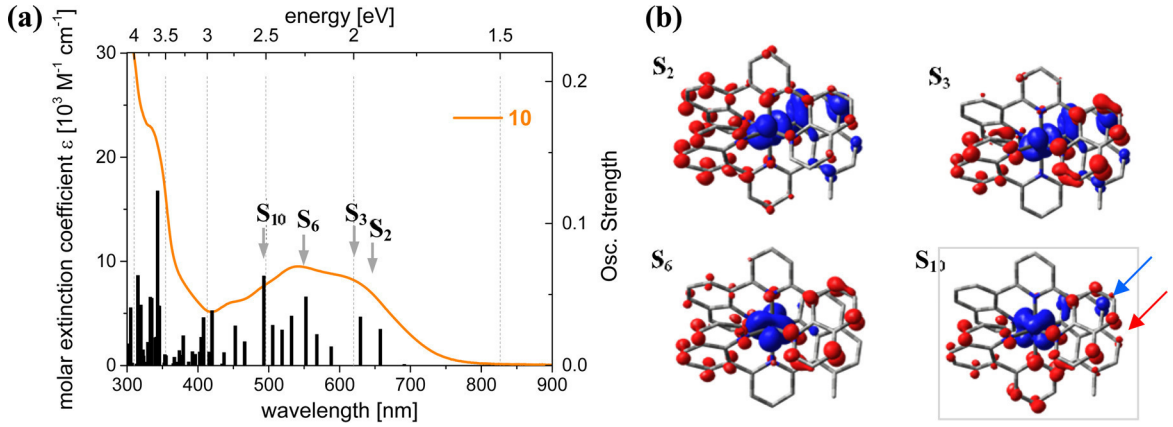

Figure 7. (a) TD-DFT data (ωB97xD/B3LYP, see Supporting Information for details) of **10** with vertical transitions (black bars) and experimental absorption spectra (orange). (b) Electron density difference maps (EDDM) of selected vertical transitions (red/blue indicate increase/decrease of electron density, isovalue drawn at 0.002). Note the ^{1}MLLCT character of S_2 and S_3, the ^{1}MLCT character of S_6, and the IL contribution of the cyclometalating fragment (S_{10}) guided by arrows.

different spatial localization of the excited state between both coordination modes. The extent of admixing of the cyclometalating fragment to the HOMOs increases with the energetic alignment with respect to the Ru d orbitals. In addition, the anthracene-based complex **11** displays a sizable contribution of the cyclometalating fragment also to the LUMO+3 (Figure 5c), which is only 0.3 eV above the LUMO and suggests the possibility of intraligand contributions (vide infra). In line with the C_1 symmetry of the complex, the orbital degeneracy of the HOMOs is slightly reduced, as shown by a comparison of the symmetric complex **6** vs the series **7**−**11** (Figure 5). Nevertheless, the HOMO and LUMO energies and the corresponding gaps remain fairly comparable throughout the series, which indicate similar optical and electrochemical properties. A more detailed theoretical assessment will be provided in conjunction with the experimental data.

Photophysical and Electrochemical Properties. UV−vis absorption and emission measurements were performed (Figure 6), and the data are summarized in Table 3. Generally, the absorption profiles of the complexes are composed of intense absorptions in the UV region assigned to ligand-centered transitions and a broad absorption band in the visible region stretching up to the NIR region (400−750 nm). In line with the typically low emission quantum yields of cyclometalated Ru^{II} complexes, the emission for the new complexes is also very weak and, thus, the corresponding spectra were taken at 77 K in alcoholic glass (Figure 6b). In comparison to the emission maximum of the reference complex **6** (824 nm),[25] a slight bathochromic shift was found for the five-membered cyclometalates **7** (847 nm) and **8** (837 nm), while no shift was noticed for the six-membered congener **10** (826 nm). Notably, the corresponding excitation spectra reproduce the absorption profiles, in line with the assignment of a ^{3}MLCT-based emission (Figure S49 in the Supporting Information). However, the anthracene-containing complex **11** showed a peculiar emission behavior. Despite the very weak emission intensity, two emission bands were detected around 730 and 925 nm, whereby the former is assigned to an impurity and the latter to the typical ^{3}MLCT emission (Figure S50 in the Supporting Information). These assignments are based on the excitation data: i.e., detection at 925 nm reproduced the bulk absorption profile in agreement with the previous complexes, while detection at 740 nm showed a distinct hypsochromically shifted profile (Figures S50 and S51 in the Supporting Information). Since photoinstability cannot be ruled out, we limit the following discussion to the five-membered cyclometalates **7** and **8**, as well as the six-membered cyclometalate **10**.

The emission profiles of the complexes show a vibronic progression similar to that reported for **6**,[25] which supports the assignment of an excited state localized on the common dqp fragment. The time-resolved emission spectra were taken at room temperature due to the higher sensitivity of the applied techniques and, thus, the given lifetimes refer to room temperature for better comparison with literature data (Figure S52 in the Supporting Information). The emissions decay monoexponentially with relatively long lifetimes for **7** (14 ns), **8** (20 ns), and **10** (20 ns). These values agree well with that of the structurally related congener **6** (16 ns). To the best of our knowledge, comprehensive time-resolved emission data of cyclometalated Ru complexes are limited to a few substituted tris(bipyridine)-based cyclometalated congeners, which are reported to be governed by the energy gap law.[34,35] The energy gap law describes the relationship between the emission energy (E_{em}) and the nonradiative decay (k_{nr}) directly to the ground state,[1] which practically dictates the observed emission lifetime as a consequence of the very low emission quantum yields.[14,15] From the available reported data for related complexes,[35] the slope $\partial(\ln k_{nr})/\partial E_{em}$ was calculated (−9.4 eV^{-1}; Figure S53 in the Supporting Information), which is on the same order as reported for noncyclometalated Ru^{II} complexes (−5.8 to −7.5 eV^{-1}).[36,37] On the basis of the nonsubstituted complex $[Ru(bpy)_2(ppy)]^{2+}$ (ppy is phenyl-2-pyridyl) emitting around 743 nm (1.67 eV, 77 K) with a lifetime of 13 ns (room temperature),[35] the extrapolation predicts for the bathochromically shifted emission of the complexes **7**, **8**, and **10** (ca. 0.2 eV) an emission lifetime of only 2 ns. This estimate agrees very well with that of a tpy-based complex $[Ru(dqp)(dpyx)]^+$ (dpyx is 4,6-dipyridyl-*m*-xylene), which showed an emission at 824 nm with a lifetime of 1.8 ns.[25] In contrast, the dqp-based complexes reveal longer lifetimes by 1 order of magnitude (ca. 20 ns) and, thus, oppose the energy gap law. This marked difference is assigned to the differences arising from the improved octahedral coordination geometry between tpy-based and dqp-based coordination, which parallels the results detailed for noncyclometalated complexes.[26] The fit

DOI: 10.1021/acs.inorgchem.7b00392
Inorg. Chem. 2017, 56, 7720−7730

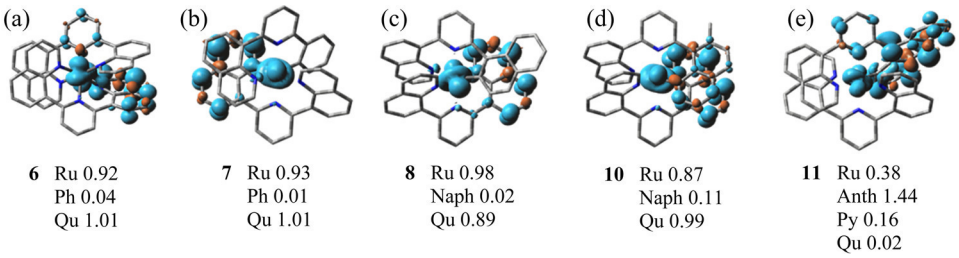

Figure 8. Spin density difference plot of the lowest-energy triplet states: five-membered chelates **6** (a), **7** (b), and **8** (c), as well as the six-membered chelates **10** (d) and **11** (e). Cyan/orange colors indicate excess of α/β spin density (isovalue drawn at 0.004). Spin densities of the Ru centers and cyclometalating fragment were determined by Mulliken analysis. Note the admixing of ^{3}LC contributions for **10** and ^{3}LC character of **11**. Ph is phenyl, Qu is quinoline, Naph is naphthalene, is anthracene, and Py is pyridine adjacent to Anth.

of the time-resolved emission data of complex **11** required two components with lifetimes of 2.7 ns (78%) and 9.2 ns (22%), respectively. Although a definite assignment is precluded due to the unknown photostability and very weak emission of the complex, the data qualitatively agree with the predicted shorter lifetime on the basis of the energy gap law. In summary, the new cyclometalated complexes parallel the reported behavior of the related N_6-coordinated congeners, which assigns a prolonged excited state lifetime to the improved octahedral geometry around the Ru^{II} center.[26]

The optical properties were assessed by time-dependent DFT (TD-DFT) calculations (see the Supporting Information for details). On the basis of the nuclear geometries using dispersion correction, the common B3LYP functional was used to avoid the energetic offset that is observed for range-separated functionals and to account for comparability with literature reports.[5,32] The energies and associated oscillator strengths of the electronic transitions match the experimental absorption profile well (Figure 7a and the Supporting Information). The transitions are visualized by electron-density difference maps (EDDMs), which depict the redistribution of electron density by regions of accumulation (red) and depletion of electron density (Figure 7b and the Supporting Information). The general features that were found throughout the series will be exemplified for the six-membered cyclometalated complex **10** (Figure 7b). The long-wavelength absorptions possess ^{1}MLLCT character, as shown by the donating contribution of the cyclometalating unit (blue). The typical ^{1}MLCT absorptions are found at intermediate wavelengths (S_6), while IL contributions can be assigned as the low-wavelength shoulder of the MLCT band (S_{10}) on the basis of the concomitant contribution of donation (blue) and depletion (red) within the cyclometalating unit.[38] The other complexes show a similar behavior (Supporting Information) except for the anthracene-based complex **11**, which possesses an intense and bathochromically shifted IL contribution (S_4 at 575 nm, Figure S59 in the Supporting Information), which could explain the observed (photo)instability.

The triplet excited states were optimized from the ground state geometries and analyzed by means of spin density difference plots and Mulliken atomic spin analyses (Figure 8), according to the characteristic molecular fragments as defined previously (Figure 5). In agreement with the frontier orbitals in the singlet ground state, the series of complexes (**6**–**8** and **10**) generally display lowest-energy ^{3}MLCT states with typical spin values of the Ru center (0.87–0.98) and of one quinoline subunit (0.89–1.01). In contrast, the lowest-energy triplet state of **11** revealed a significantly reduced Ru contribution (0.38) and the dominant localization on the anthracene fragment (1.44) and, thus, is best described as a ^{3}IL state that parallels the unusual photophysical properties of **11**. The admixing of the cyclometalating fragment is negligible for the symmetric complex **6** and the five-membered chelates **7** and **8** (<0.04), while the six-membered chelate **10** showed a sizable contribution (0.11) at the cost of the Ru center. The ^{3}MLCT state of **11** was obtained by starting from a suitable geometry guess. The corresponding spins of Ru (0.83), anthracene (0.15), and quinoline (0.98) resemble the values of the six-membered congener **10**. Finally, the ^{3}MC states were optimized from suitable nuclear geometries (Supporting Information), revealing the typical spin values of the Ru center (1.78–1.82) and the cyclometalating unit (<0.04). The characteristic structural features of the complexes in their various triplet states (Table S14 in the Supporting Information) with respect to the ground state data can be summarized as follows: in the ^{3}MLCT states, the Ru–C bond lengths remain comparable, while the dqp ligand shows both bond lengthening and shortening of the two Ru–quinoline bonds (±0.05 Å), as expected from the spin localization onto one quinoline subunit. In the ^{3}MC states, both Ru–quinoline bonds are significantly elongated (>+0.30 Å) to stabilize the involved d orbitals. Finally, the ^{3}IL state of **11** shows the anticipated marginal changes of the Ru–N bonds and a slight Ru–C bond shortening due to localization of the spin on the cyclometalating unit. In summary, the triplet state analysis is in qualitative agreement with the detailed reports on non-cyclometalated $[Ru(dqp)_2]^{2+}$.[39,40]

The electrochemical properties were determined by cyclic voltammetry (see the Supporting Information), and the redox potentials are compiled in Table 3. Figure 9 exemplifies the CV

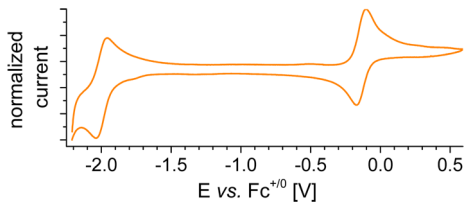

Figure 9. CV curve of **10** (CH_3CN, 0.1 M Bu_4NPF_6, scan rate 100 mV s^{-1}).

curve of complex **10**, which features reversible oxidation assigned to the Ru-cyclometalated fragment (−0.15 V vs $Fc^{+/0}$) and dqp-based ligand reduction (−1.98 V). The redox potentials shift according to the increased π system of the cyclometalating unit: i.e., the complexes **8**, **10**, and **11** display cathodic shifts (60–100 mV) with respect to **7**. In the case of

DOI: 10.1021/acs.inorgchem.7b00392
Inorg. Chem. 2017, 56, 7720–7730

11, irreversible oxidation processes were observed at anodic potentials beyond the reversible Ru-cyclometalated fragment. Notably, the smaller electrochemical gap of **11** parallels the assignment of the bathochromically shifted emission from the ^{3}MLCT emission state. In summary, the redox properties of the complexes match the previous assignments of a dqp-based ^{3}MLCT excited state.

CONCLUSION

A series of novel cyclometalated complexes was synthesized, which adopt five- and six-membered coordination of the peripheral π-extended carbanionic fragments based on benzene, naphthalene, or anthracene. The synthesis was optimized and identified the C−H activation as the limiting step, which is facilitated best by $NaHCO_3$ as the auxiliary base. The purification protocol was simplified to a single chromatographic run using commercially available amino-decorated silica gel, which ultimately leads to good to excellent isolated yields of up to 85%. The structural analysis by NMR spectroscopy and X-ray crystallography revealed the meridional coordination, whereby the latter confirmed the necessity to include dispersion-corrected functionals to reproduce the nuclear geometry by DFT calculations. The electrochemical analysis shows a cathodic shift of the redox potentials upon π-extended carbanionic donor sets, while the photophysical characterization revealed long excited state lifetimes (up to 20 ns). Notably, these lifetimes are 1 order of magnitude longer than those predicted by the energy gap law in comparison to related Ru^{II} cyclometalates. The properties were rationalized in terms of DFT calculations, which revealed the admixing of the cyclometalating unit to the HOMO. The EDDM analysis assisted the assignment of low-energy ^{1}MLLCT transitions, intermediate-energy ^{1}MLCT transitions similar to those of noncyclometalated complexes based on $[Ru(dqp)_2]$, and IL contribution at higher energies. The exceptional behavior of the anthracene complex is tentatively assigned to the intense IL contribution and high spin density residing on the anthracene moiety in the excited state. The complexes presented in this study suggest the possibility to further modulate the frontier orbitals in cyclometalating complexes in the periphery, while maintaining broad absorption and long excited state lifetimes, which are particularly attractive properties in view of efficient light-induced charge separation applications.

EXPERIMENTAL SECTION

All chemicals and solvents were purchased from Sigma-Aldrich, Fluka, ABCR, Acros Organics, Alfa Aesar, VWR, Apollo, or Carl Roth and were used without further purification unless otherwise specified. $[Ru(dqp)(CH_3CN)_3](PF_6)_2$[28] and dqPhH[25] were prepared according to literature procedures. Instrumentation details are provided in the Supporting Information.

8-(6-Bromopyridine-2-yl)quinoline (1). 2,6-Dibromopyridine (1.0 g, 4.22 mmol), quinoline-8-boronic acid (0.88 g, 5.06 mmol), bis(dibenzylideneacetone)palladium(0) (0.064 g, 0.12 mmol), 1,3-di(diphenylphosphino)propane (0.092 g, 0.22 mmol), and potassium carbonate (2.48 g, 17.94 mmol) were dissolved in a mixture of 5 mL of water and 10 mL of acetonitrile in a microwave tube. The vial was degassed by bubbling N_2 through the solution for 10 min and afterward heated to 130 °C for 2 h in the microwave. The reaction mixture was quenched in H_2O, extracted with dichloromethane (3 × 30 mL), and dried over Na_2SO_4. The crude product was adsorbed on silica and purified by flash column chromatography (hexane/ethyl acetate gradient from 100/0 to 70/30) to give 0.70 g (59%) of a white product. ^{1}H NMR (250 MHz, $CDCl_3$): δ 8.95 (dd, J = 4.0, 1.7 Hz, 1H), 8.22 (dd, J = 9.7, 3.3 Hz, 3H), 7.90 (d, J = 8.1 Hz, 1H), 7.67 (t, J = 7.7 Hz, 2H), 7.49 (d, J = 8.4 Hz, 1H), 7.46−7.40 (m, 1H). ^{13}C NMR (63 MHz, $CDCl_3$): δ 157.88, 150.33, 145.63, 141.55, 137.78, 136.92, 136.51, 131.64, 129.37, 128.59, 126.51, 126.36, 125.98, 121.13. MS HR-ESI ($[C_{14}H_9BrN_2]H^+$): m/z calcd 285.0022, found 285.0032; error 3.2 ppm. Anal. Calcd: C, 58.97; H, 3.18; N, 9.82. Found: C, 59.37; H, 3.20; N, 9.80. Mp = 116 °C.

8-(6-Phenylpyridin-2-yl)quinoline (2). Compound **1** (0.43 g, 1.58 mmol), phenylboronic acid (0.20 g, 1.60 mmol), 2-dicyclohexylphosphino-2′,6′-dimethoxybiphenyl (0.024 g, 0.06 mmol), bis(dibenzylideneacetone)palladium(0) (0.017 g, 0.03 mmol), and potassium carbonate (0.75 g, 5.43 mmol) were dissolved in a mixture of 5 mL of water and 10 mL of acetonitrile in a microwave tube. The vial was degassed by bubbling N_2 through the solution for 10 min and afterward heated to 135 °C for 2 h in the microwave. The reaction mixture was quenched in H_2O, extracted with dichloromethane (3 × 30 mL), and dried over Na_2SO_4. The crude product was adsorbed on silica and purified by flash column chromatography (dichloromethane/methanol gradient from 100/0 to 99/1) to yield 0.4 g (89%) of the product. ^{1}H NMR (400 MHz, $CDCl_3$): δ 8.99 (dd, J = 4.1, 1.8 Hz, 1H), 8.36 (dd, J = 7.2, 1.5 Hz, 1H), 8.23 (dd, J = 8.3, 1.8 Hz, 1H), 8.19−8.11 (m, 3H), 7.89 (t, J = 7.9 Hz, 2H), 7.76 (dd, J = 7.8, 0.7 Hz, 1H), 7.71 (dd, J = 8.2, 7.4 Hz, 1H), 7.52−7.48 (m, 2H), 7.47−7.39 (m, 2H). ^{13}C NMR (101 MHz, $CDCl_3$): δ 157.18, 156.57, 150.24, 146.00, 139.90, 139.08, 136.48, 136.16, 131.59, 128.78, 128.74, 128.68, 127.10, 126.59, 125.57, 120.99, 118.96. HR-ESI ($[C_{20}H_{14}N_2]H^+$) : m/z calcd 283.1230, found 283.1228; error 0.6 ppm. Mp = 94 °C.

8-(6-(Naphthalen-1-yl)pyridin-2-yl)quinoline (3). Naphthalen-1-ylboronic acid (0.072 g, 0.42 mmol), **1** (0.100 g, 0.35 mmol), $Pd(dba)_2$ (0.006 g, 0,01 mmol), S-PHOS (0.0086 g, 0.02 mmol), and potassium carbonate (0.145 g, 1.04 mmol) were dissolved in a mixture of H_2O (2.5 mL) and CH_3CN (5 mL) in a microwave tube. The vial was degassed by bubbling N_2 through the solution for 10 min and afterward heated to 130 °C for 2 h in the microwave. The reaction mixture was quenched in H_2O, extracted with dichloromethane (3 × 30 mL), and dried over Na_2SO_4. The crude product was adsorbed on silica and purified by flash column chromatography (hexane/ethyl acetate gradient) to yield 0.100 g (95%) of **3**. ^{1}H NMR (400 MHz, $CDCl_3$): δ 9.04 (dd, J = 4.2, 1.8 Hz, 1H, H^1), 8.39−8.34 (m, 1H, H^3), 8.29 (dd, J = 7.2, 1.5 Hz, 1H, H^6), 8.23 (dd, J = 8.3, 1.8 Hz, 1H, H^{16}), 8.19 (dd, J = 7.9, 1.0 Hz, 1H, H^{10}), 7.97 (t, J = 7.8 Hz, 1H, H^{11}), 7.94−7.90 (m, 2H, $H^{7,8}$), 7.88 (dd, J = 8.2, 1.5 Hz, 1H, H^{13}), 7.72 (dd, J = 7.1, 1.2 Hz, 1H, H^4), 7.66 (dd, J = 8.1, 7.3 Hz, 1H, H^5), 7.61 (dd, J = 7.7, 1.0 Hz, 1H, H^{12}), 7.57 (dd, J = 8.2, 7.1 Hz, 1H, H^9), 7.54−7.48 (m, 2H, $H^{14,15}$), 7.46 (dd, J = 8.3, 4.2 Hz, 1H, H^2). ^{13}C NMR (101 MHz, $CDCl_3$): δ 159.1, 156.8, 150.4, 146.1, 139.1, 136.6, 136.0, 134.1, 131.6, 131.5, 128.8, 128.3, 127.7, 126.7, 126.4, 126.2, 125.9, 125.4, 125.3, 123.6, 121.1. MS HR-ESI ($[C_{24}H_{16}N_2]H^+$): m/z calcd 333.1386, found 333.1394; error 2.4 ppm. Mp = 155 °C.

8-(6-(Anthracen-9-yl)pyridin-2-yl)quinoline (4). Anthracen-9-ylboronic acid (0.255 g, 0.5 mmol), **1** (0.120 g, 0.42 mmol), $Pd(dba)_2$ (0.007 g, 0.01 mmol), S-PHOS (0.010 g, 0.02 mmol), and potassium carbonate (0.174 g, 1.25 mmol) were dissolved in a mixture of H_2O (2.5 mL) and CH_3CN (5 mL) in a microwave tube. The vial was degassed by bubbling N_2 through the solution for 10 min and afterward heated to 130 °C for 2 h in the microwave. The reaction mixture was quenched in H_2O, extracted with dichloromethane (3 × 30 mL), and dried over Na_2SO_4. The crude product was adsorbed on silica and purified by flash column chromatography (dichloromethane/ethyl acetate gradient) to yield 0.220 g (64%) of **4**. ^{1}H NMR (400 MHz, $CDCl_3$): δ 9.08 (dd, 1H, J = 4.2, 1.8 Hz, 1H, H^{qu2}), 8.54 (s, 1H, H^{an9}), 8.37 (dd, J = 7.9, 0.9 Hz, 1H, H^{py3}), 8.27 (dd, J = 7.2, 1.5 Hz, 1H, H^{qu7}), 8.24 (dd, J = 8.3, 1.8 Hz, 1H, H^{qu4}), 8.06 (t, J = 7.7 Hz, 1H, H^{py4}), 8.05 (dm, J = 8.5 Hz, 2H, H^{an1}), 7.86 (dd, J = 8.2, 1.8 Hz, 1H, H^{qu5}), 7.85 (dm, J = 8.8 Hz, 2H, H^{an4}), 7.61 (dd, J = 8.2, 7.5 Hz, 1H, H^{qu6}), 7.54 (dd, J = 7.6, 1.0 Hz, 1H, H^{py5}), 7.48 (dd, J = 8.2, 4.2 Hz, 1H, H^{qu3}),), 7.46 (ddd, J = 8.4, 6.5, 1.2 Hz, 2H, H^{an2}), 7.40 (ddd, J = 8.4, 6.5, 1.2 Hz, 2H, H^{an3}). ^{13}C NMR (101 MHz, $CDCl_3$): δ 158.0 (C^{py5}), 157.3 (C^{py3}), 150.5 (C^{qu2}), 146.2 (C^{qu}), 138.8 (C^{qu}), 136.7 (C^{qu4}), 135.9 (C^{py4}), 135.8 (C^{an}), 132.0 (C^{qu7}), 131.7 (C^{an}), 130.4

DOI: 10.1021/acs.inorgchem.7b00392
Inorg. Chem. 2017, 56, 7720−7730

(C^{an}), 129.0 (C^{qu5}), 128.9 (C^{qu}), 128.5 (C^{qu7}), 127.6 (C^{an9}), 126.8 (C^{qu6}), 126.7 (C^{an4}), 125.8 (C^{an3}), 125.7 (C^{py3}), 125.4 (C^{py5}), 125.2 (C^{an2}), 121.2 (C^{qu3}). MS HR-ESI ($[C_{28}H_{18}N_2]H^+$): m/z calcd 383.1543, found 383.1530; error 3.2 ppm. Mp = 114 °C.

8-(6-(2-Methylnaphthalen-1-yl)pyridin-2-yl)quinoline (5). *Step A.* 1-Bromo-2-methylnaphthalene (1.010 g, 4.57 mmol) was dissolved in dry THF (30 mL) under inert conditions. At −78 °C *n*-BuLi (1.88 mL of 2.5 M stock solution) was added over 1 h and the mixture stirred for a further 30 min. After the slow addition of trimethyl borate (1.5 mL, 13.40 mmol) the reaction mixture was stirred for an additional 30 min and then warmed to room temperature. The solution was hydrolyzed with 3 M hydrochloric acid (25 mL), extracted with diethyl ether (3 × 30 mL), neutralized with sodium hydrogen carbonate, dried over Na_2SO_4, and filtered. The solvent was reduced by evaporation. The product was dried to yield crude (2-methylnaphthalen-1-yl)boronic acid (0.500 g, 59%).

Step B. Crude (2-methylnaphthalen-1-yl)boronic acid (0.300 g, 1.61 mmol), **1** (0.383 g, 1.34 mmol), $Pd(dba)_2$ (0.023 g, 0,04 mmol), S-PHOS (0.023 g, 0.08 mmol), and potassium carbonate (0.557 g, 4.03 mmol) were dissolved in a mixture of H_2O (2.5 mL) and CH_3CN (5 mL) in a microwave tube. The vial was degassed by bubbling N_2 through the solution for 10 min and afterward heated to 140 °C for 1 h in the microwave. The reaction mixture was quenched in H_2O, extracted with dichloromethane (3 × 30 mL), and dried over Na_2SO_4. The crude product was adsorbed on silica and purified by flash column chromatography (hexane/ethyl acetate gradient) to give 0.230 g (50%) of an off-white product, which was recrystallized in heptane. ^{1}H NMR (300 MHz, $CDCl_3$): δ 9.05 (d, J = 2.5 Hz, 1H, H^1), 8.44−8.11 (m, 3H, $H^{3,6,16}$), 7.98 (t, J = 7.7 Hz, 1H, H^{11}), 7.87−7.82 (m, 3H, $H^{7,8,11}$), 7.68−7.55 (m, 2H, $H^{4,5}$), 7.43 (m, 5H, $H^{12,9,14,15,2}$), 2.42 (s, 3H, H^{10}). ^{13}C NMR (76 MHz, $CDCl_3$): δ 158.6, 156.9, 150.2, 145.9, 138.7, 137.2, 136.5, 135.8, 133.6, 132.7, 132.1, 131.7, 128.8, 128.0, 127.8, 126.6, 126.0, 125.8, 125.1, 124.7, 124.0, 121.0, 77.5, 77.0, 76.6, 20.6. MS HR-ESI ($[C_{25}H_{18}\ N_2]H^+$): m/z calcd 347.1530, found 347.1543; error 3.6 ppm. Anal. Calcd: C, 86.68; H, 5.24; N, 8.09. Found: C, 86.60; H, 5.05; N, 7.94. Mp = 133 °C.

[Ru(dqp)(dqPh)](PF$_6$) (6). $[Ru(dqp)(CH_3CN)_3](PF_6)_2$ (0.102 g, 0.12 mmol) and dqPhH (0.040 g, 0.12 mmol) were dissolved in ethylene glycol (6 mL) in a microwave vial, which was then sealed and purged with N_2 for 10 min. The reaction mixture was heated for 90 min at 200 °C in the microwave. After it was cooled to room temperature, the crude product was precipitated upon addition to aqueous NH_4PF_6 solution. After filtration, the crude product was purified by flash column chromatography on silica (eluent CH_3CN/H_2O/KNO_3(aq) 40/4/1) to give the title compound (73%) as a purple product. Analytical data matched previous analyses.[25]

[Ru(dqp)(2)](PF$_6$) (7). $[Ru(dqp)(CH_3CN)_3](PF_6)_2$ (0.028 g, 0.03 mmol) and **2** (0.011 g, 0.03 mmol) were dissolved in DMF (1 mL) in a microwave vial, which was then purged with N_2 for 10 min and heated at 160 °C for 16 h. After the reaction mixture was cooled to room temperature, the crude mixture was precipitated in aqueous NH_4PF_6 solution. After filtration and washing with water, the crude product was purified by column chromatography with dichloromethane/CH_3OH (99/1) as eluent on amino-functionalized silica to yield 95% of **7**. ^{1}H NMR (600 MHz, CD_3CN): δ 8.39 (dd, J = 4.8, 1.4 Hz, 1H), 8.07 (t, J = 8.0 Hz, 1H), 8.02 (dd, J = 8.1, 1.4 Hz, 1H), 7.99−7.88 (m, 2H), 7.85−7.78 (m, 2H), 7.73 (s, 1H), 7.69 (t, J = 8.8 Hz, 2H), 7.66 (dd, J = 7.6, 6.7 Hz, 2H), 7.58 (s, 2H), 7.57−7.52 (m, 2H), 7.50−7.30 (m, 5H), 7.20 (dd, J = 7.4, 0.9 Hz, 1H), 6.59−6.54 (m, 4H) (not all protons unambiguously assignable due to peak broadening and overlapping signals; see the Supporting Information). ^{13}C NMR (151 MHz, CD_3CN): δ 194.20, 168.56, 158.08, 156.99, 156.64, 155.96, 147.75, 145.78, 145.14, 140.71, 138.58, 136.71, 136.02, 135.28, 134.44, 133.81, 131.51, 130.86, 128.57, 128.23, 127.59, 127.47, 127.16, 124.50, 123.89, 122.33, 121.77, 121.65, 117.73. MS HR-ESI ($[C_{43}H_{28}N_5Ru]^+$): m/z calcd 716.1383, found 716.1404; error 1.4 ppm.

[Ru(dqp)(3)](PF$_6$) (8 and 9). $[Ru(dqp)(CH_3CN)_3](PF_6)_2$ (0.028 g, 0.03 mmol), **3** (0.011 g, 0.03 mmol), and $NaHCO_3$ (0.003 g, 0,03 mmol) were dissolved in ethylene glycol (1 mL) in a microwave vial, which was then purged with N_2 for 10 min and heated at 160 °C for 40 min. After the reaction mixture was cooled to room temperature, the crude mixture was precipitated in aqueous NH_4PF_6 solution. After filtration and washing with water, the crude product was purified by column chromatography with CH_2Cl_2/CH_3OH (99/1) as eluent on amino-functionalized silica. Further purification was carried out via diffusion-controlled crystallization to separate the five-membered from the six-membered isomer. Data for the five-membered isomer (**8**) are as follows. ^{1}H NMR (600 MHz, CD_2Cl_2): δ 8.40 (dd, J = 4.7, 1.6 Hz, 1H), 8.32 (d, J = 8.0 Hz, 1H), 8.26 (d, J = 8.6 Hz, 1H), 8.11 (t, J = 8.0 Hz, 1H), 8.02 (dd, J = 8.2, 1.5 Hz, 2H), 8.04−7.97 (m, 2H), 7.93 (d, J = 7.7 Hz, 2H), 7.84−7.80 (m, 1H), 7.68 (dd, J = 8.1, 1.3 Hz, 1H), 7.64 (s, 1H), 7.62 (dd, J = 7.4, 1.3 Hz, 2H), 7.58−7.55 (m, 1H), 7.51 (d, J = 8.1 Hz, 2H), 7.50−7.47 (m, 2H), 7.45 (dd, J = 7.5, 1.0 Hz, 2H), 7.41 (t, J = 7.8 Hz, 2H), 7.37 (ddd, J = 8.4, 6.8, 1.4 Hz, 1H), 7.17−7.14 (m, 1H), 7.13 (dd, J = 7.3, 3.9 Hz, 1H), 7.02 (d, J = 8.1 Hz, 1H), 6.60 (s, 2H). ^{13}C NMR (151 MHz, CD_2Cl_2): δ 205.30, 168.83, 157.60, 156.65, 156.51, 154.70, 147.40, 144.73, 138.23, 138.04, 137.47, 135.84, 135.61, 134.92, 134.69, 134.45, 133.34, 131.87, 131.76, 130.84, 130.52, 129.67, 127.94, 127.62, 127.45, 127.44, 127.38, 126.94, 126.24, 125.92, 122.51, 121.91, 121.84, 121.31, 121.27, 121.16. MS HR-ESI ($[C_{47}H_{30}N_5Ru]^+$): m/z calcd 766.1539, found 766.1558; error 0.8 ppm. Data for the six-membered isomer (**9**) are as follows. ^{1}H NMR (600 MHz, CD_3CN): δ 8.08 (d, J = 5.0 Hz, 1H), 8.05 (d, J = 5.0 Hz, 1H), 8.03 (d, J = 8.1 Hz, 1H), 7.97 (t, J = 7.4 Hz, 1H), 7.96 (t, J = 8.2 Hz, 1H), 7.91 (d, J = 7.9 Hz, 1H), 7.89 (d, J = 5.0 Hz, 1H), 7.84 (d, J = 7.9 Hz, 1H), 7.80 (d, J = 8.2 Hz, 1H), 7.72 (d, J = 7.9 Hz, 1H), 7.67 (d, J = 8.2 Hz, 1H), 7.65−7.60 (m, 3H), 7.56 (d, J = 8.0 Hz, 1H),7.51 (d, J = 7.1 Hz, 1H), 7.44 (d, J = 8.2 Hz, 1H), 7.38−7.35 (m, 3H), 7.33−7.31 (m, 2H), 7.21 (t, J = 7.8 Hz, 1H), 7.11 (t, J = 7.8 Hz, 1H), 7.06 (dd, J = 8.0, 4.6 Hz, 1H), 6.88 (d, J = 7.6 Hz, 1H), 6.76 (dd, J = 8.0, 5.2 Hz, 1H), 6.71 (dd, J = 8.0, 5.2 Hz, 1H), 6.60 (t, J = 7.3 Hz, 1H), 6.27 (d, J = 6.7 Hz, 1H).

[Ru(dqp)(5)](PF$_6$) (10). $[Ru(dqp)(CH_3CN)_3](PF_6)_2$ (0.028 g, 0.03 mmol), **5** (0.012 g, 0.03 mmol), $NaHCO_3$ (1 equiv, 0.003 g, 0.03 mmol), and ethylene glycol (1 mL) were placed in a microwave vial, which was then sealed and purged with N_2 for 10 min. After the reaction mixture was heated at 160 °C for 3 h, it was cooled to room temperature and precipitated in aqueous NH_4PF_6 solution. After filtration and washing with water, the crude product was purified by column chromatography with dichloromethane/MeOH (99/1) as eluent on amino-functionalized silica. Final purification was done by diffusion- controlled crystallization from a acetonitrile solution and diethyl ether to obtain 70% of the pure complex. ^{1}H NMR (600 MHz, CD_3CN): δ 8.27 (d, J = 5.1 Hz, 1H), 8.07 (dd, J = 4.7, 0.9 Hz, 1H), 8.00 (dd, J = 8.0, 1.2 Hz,1H), 7.89 (t, J = 7.8 Hz, 1H), 7.86 (t, J = 8.1 Hz, 1H), 7.77 (d, J = 8.0 Hz, 1H), 7.74 (d, J = 8.0 Hz, 1H), 7.70 (d, J = 7.8 Hz, 1H), 7.64 (d, J = 7.9 Hz, 1H), 7.62−7.55 (m, 3H), 7.52 (dd, J = 7.2, 3.9 Hz, 2H), 7.49 (d, J = 8.1 Hz, 1H), 7.44 (d, J = 7.8 Hz, 1H), 7.39 (d, J = 8.1 Hz, 1H), 7.33 (t, J = 7.8 Hz, 1H), 7.28 (t, J = 7.8 Hz, 1H), 7.24 (d, J = 7.2 Hz, 1H), 7.19 (d, J = 8.0 Hz, 1H), 7.16 (t, J = 7.7 Hz, 1H), 7.02 (dd, J = 8.1, 4.8 Hz, 1H), 6.92 (d, J = 8.4 Hz, 1H), 6.85 (dd, J = 8.0, 5.1 Hz, 1H), 6.77 (d, J = 7.7 Hz, 1H), 6.65 (dd, J = 8.0, 5.2 Hz, 1H), 6.54 (t, J = 7.2 Hz, 1H), 6.18 (d, J = 6.7 Hz, 1H), 2.24 (s, 3H). ^{13}C NMR (151 MHz, CD_3CN): δ 187.86, 160.62, 159.54, 158.52, 158.49, 157.08, 156.93, 155.44, 148.27, 147.12, 139.59, 138.71, 137.43, 137.07, 135.87, 135.80, 135.67, 134.90, 134.74, 134.25, 133.70, 133.51, 132.90, 132.04, 130.65, 130.38, 130.23, 130.12, 129.55, 129.43, 128.47, 128.12, 127.95, 127.29, 127.11, 127.05, 127.03, 126.92, 126.82, 126.79, 124.31, 122.48, 122.01, 121.03, 119.91, 24.29. MS HR-ESI ($[C_{48}H_{32}N_5Ru]^+$): m/z calcd 780.1696, found 780.1725; error 2.1 ppm.

[Ru(dqp)(4)](PF$_6$) (11). $[Ru(dqp)(CH_3CN)_3](PF_6)_2$ (0.028 g, 0.03 mmol) and **4** (0.013 g, 0.03 mmol) were dissolved in 1 mL of ethylene glycol, and 1 equiv $NaHCO_3$ was added in a microwave vial, which was then sealed and purged with N_2 for 10 min. After it was heated for 2 h at 160 °C, the reaction mixture was cooled to room temperature and precipitated in aqueous NH_4PF_6 solution. After filtration and washing with water, the crude product was purified by column chromatography with amino-functionalized silica and dichloromethane/MeOH (99/1) as eluent to yield 85% of the complex. ^{1}H NMR (600 MHz, CD_3CN): δ 8.39 (dd, J = 5.1, 1.3 Hz, 1H), 8.10 (dd,

DOI: 10.1021/acs.inorgchem.7b00392
Inorg. Chem. 2017, 56, 7720−7730

J = 4.7, 1.5 Hz, 1H), 8.02 (dd, J = 8.1, 1.5 Hz, 1H), 7.95 (s, 1H), 7.89 (t, J = 7.9 Hz, 1H), 7.89−7.86 (m, 2H), 7.80 (dd, J = 7.6, 1.2 Hz, 1H), 7.79 (d, J = 8.2 Hz, 1H), 7.75 (d, J = 7.9 Hz, 1H), 7.69−7.67 (m, 2H), 7.66 (d, J = 8.4 Hz, 1H), 7.64 (dd, J = 8.2, 1.2 Hz, 1H), 7.58 (d, J = 7.4 Hz, 2H), 7.55 (dd, J = 7.3, 1.2 Hz, 1H), 7.52 (dd, J = 8.3, 1.2 Hz, 1H), 7.38−7.35 (m, 2H), 7.30 (dd, J = 8.1, 7.5 Hz, 1H), 7.27−7.22 (m, 2H), 7.14 (dd, J = 8.2, 7.4 Hz, 1H), 7.03 (dd, J = 8.1, 4.7 Hz, 1H), 7.00 (dm, J = 6.2 Hz, 1H), 6.95 (dd, J = 8.2, 1.1 Hz, 1H), 6.80 (dd, J = 8.0, 1.3 Hz, 1H), 6.69 (dd, J = 8.0, 5.2 Hz, 1H), 6.61 (dd, J = 8.0, 5.1 Hz, 1H), 6.59 (t, J = 7.3 Hz, 1H), 6.18 (d, J = 4.4 Hz, 1H). ^{13}C NMR (151 MHz, CD_3CN): δ 160.19, 159.42, 158.93, 158.74, 157.41, 156.91, 155.49, 154.20, 151.37, 148.17, 147.82, 146.99, 137.19, 136.80, 135.91, 135.43, 135.28, 134.94, 134.80, 134.39, 133.63, 133.52, 132.10, 131.96, 131.76, 130.68, 130.24, 130.12, 129.75, 129.26, 128.66, 128.49, 127.97, 127.17, 127.09, 127.06, 127.04, 126.91, 126.85, 126.84, 126.82, 125.04, 124.40, 122.46, 122.09, 121.73. MS HR-ESI ($[C_{51}H_{32}N_5Ru]^+$): m/z calcd 816.1696, found 816.1707; error 0.3 ppm.

[Ru(dqp)(1)](PF$_6$) (12). $[Ru(dqp)(CH_3CN)_3](PF_6)_2$ (0.100 g, 0.12 mmol) and **1** (0.033 g, 0.12 mmol) were dissolved in ethylene glycol (5 mL) in a microwave vial, which was then purged with N_2 for 10 min and heated at 120 °C for 16 h. After the reaction mixture was cooled to room temperature, the crude mixture was precipitated in aqueous NH_4PF_6 solution. After filtration and washing with water, the crude product was purified by column chromatography on silica using a mixture of CH_3CN/H_2O/saturated aqueous KNO_3 40/4/1 as eluent. Final purification was done via diffusion-controlled crystallization from acetonitrile and diethyl ether to obtain 61 mg of the product (49%). ^{1}H NMR (600 MHz, CD_3CN): δ 8.61 (d, J = 7.7 Hz, 2H), 8.37 (d, J = 4.8 Hz, 1H), 8.31 (d, J = 8.2 Hz, 1H), 8.25 (d, J = 5.1 Hz, 1H), 8.21 (d, J = 4.9 Hz, 1H), 8.11−8.03 (m, 3H), 7.98 (dd, J = 18.8, 8.0 Hz, 2H), 7.80 (d, J = 4.3 Hz, 2H), 7.64−7.58 (m, 3H), 7.56 (d, J = 7.7 Hz, 2H), 7.42 (d, J = 7.3 Hz, 1H), 7.35 (t, J = 7.7 Hz, 1H), 7.34−7.30 (m, 1H), 7.28 (t, J = 7.8 Hz, 1H), 7.22−7.17 (m, 1H), 7.06−7.00 (m, 1H), 1.93 (s, 3H). ^{13}C NMR (151 MHz, CD_3CN): δ 161.00, 160.83, 160.55, 159.65, 158.68, 158.04, 150.59, 148.44, 147.64, 146.32, 140.55, 139.64, 139.30, 138.70, 138.47, 135.98, 133.86, 133.64, 133.41, 132.84, 132.58, 132.21, 132.17, 132.13, 131.70, 129.85, 129.64, 129.28, 129.05, 129.00, 127.84, 127.81, 127.66, 127.39, 124.16, 123.01, 122.91. HR-ESI ($[[C_{39}H_{27}BrN_6Ru]^{2+}$ − CH_3CN): m/z calcd 359.5124, found 359.5139; error 3.6 ppm.

■ ASSOCIATED CONTENT

Supporting Information

The Supporting Information is available free of charge on the ACS Publications website at DOI: 10.1021/acs.inorgchem.7b00392.

Additional experimental details, NMR and mass spectra, crystallographic data, photophysical data, and computational details (PDF)

Accession Codes

CCDC 1526255−1526258 contain the supplementary crystallographic data for this paper. These data can be obtained free of charge via www.ccdc.cam.ac.uk/data_request/cif, or by emailing data_request@ccdc.cam.ac.uk, or by contacting The Cambridge Crystallographic Data Centre, 12 Union Road, Cambridge CB2 1EZ, UK; fax: +44 1223 336033.

■ AUTHOR INFORMATION

Corresponding Authors

*E-mail for M.J.: michael.jager.iomc@uni-jena.de.
*E-mail for U.S.S.: ulrich.schubert@uni-jena.de.

ORCID

Sascha Ott: 0000-0002-1691-729X
Michael Jäger: 0000-0003-0400-1812
Ulrich S. Schubert: 0000-0003-4978-4670

Present Address

⊥G.A.P.: Department of Chemistry, Yale University, P.O. Box 208107, 225 Prospect Street, New Haven, Connecticut 06520-8107, United States.

Notes

The authors declare no competing financial interest.

■ ACKNOWLEDGMENTS

We kindly thank Prof. Leif Hammarström for generous support to provide access to the time-resolved spectroscopy and low-temperature emission measurements. M.J. acknowledges financial support by the Carl-Zeiss-Foundation and the Friedrich Schiller University Jena ("Nachwuchsförderung"). U.S.S. acknowledges the support of the Deutsche Forschungsgemeinschaft (DFG). G.A.P. and L.H. acknowledge support from the Knut and Alice Wallenberg Foundation and the Swedish Energy Agency. We thank Benedikt Suchland for assistance during synthesis.

■ REFERENCES

(1) Thompson, D. W.; Ito, A.; Meyer, T. J. Ru(bpy)(3) (2+)* and other remarkable metal-to-ligand charge transfer (MLCT) excited states. *Pure Appl. Chem.* **2013**, *85*, 1257−1305.

(2) Campagna, S.; Puntoriero, F.; Nastasi, F.; Bergamini, G.; Balzani, V. In *Photochemistry and Photophysics of Coordination Compounds I*; Balzani, V., Campagna, S., Eds.; Springer-Verlag: Berlin, 2007; Vol. *280*, pp 117−214.

(3) Juris, A.; Balzani, V.; Barigelletti, F.; Campagna, S.; Belser, P. Vonzelewsky, A. RU(II) POLYPYRIDINE COMPLEXES - PHOTOPHYSICS, PHOTOCHEMISTRY, ELECTROCHEMISTRY, AND CHEMI-LUMINESCENCE. *Coord. Chem. Rev.* **1988**, *84*, 85−277.

(4) Gratzel, M. Photoelectrochemical cells. *Nature* **2001**, *414*, 338−344.

(5) Jaeger, M.; Freitag, L.; Gonzalez, L. Using computational chemistry to design Ru photosensitizers with directional charge transfer. *Coord. Chem. Rev.* **2015**, *304-305*, 146−165.

(6) Beley, M.; Collin, J. P.; Sauvage, J. P. HIGHLY COUPLED MIXED-VALENCE DINUCLEAR RUTHENIUM AND OSMIUM COMPLEXES WITH A BIS-CYCLOMETALATING TERPYRIDINE ANALOG AS BRIDGING LIGAND. *Inorg. Chem.* **1993**, *32*, 4539−4543.

(7) Wadman, S. H.; Lutz, M.; Tooke, D. M.; Spek, A. L.; Hartl, F.; Havenith, R. W. A.; van Klink, G. P. M.; van Koten, G. Consequences of N,C,N′- and C,N,N′-Coordination Modes on Electronic and Photophysical Properties of Cyclometalated Aryl Ruthenium(II) Complexes. *Inorg. Chem.* **2009**, *48*, 1887−1900.

(8) Bomben, P. G.; Robson, K. C. D.; Sedach, P. A.; Berlinguette, C. P. On the Viability of Cyclometalated Ru(II) Complexes for Light-Harvesting Applications. *Inorg. Chem.* **2009**, *48*, 9631−9643.

(9) Bomben, P. G.; Robson, K. C. D.; Koivisto, B. D.; Berlinguette, C. P. Cyclometalated ruthenium chromophores for the dye-sensitized solar cell. *Coord. Chem. Rev.* **2012**, *256*, 1438−1450.

(10) Wadman, S. H.; Kroon, J. M.; Bakker, K.; Lutz, M.; Spek, A. L.; van Klink, G. P. M.; van Koten, G. Cyclometalated ruthenium complexes for sensitizing nanocrystalline TiO2 solar cells. *Chem. Commun.* **2007**, 1907−1909.

(11) Wadman, S. H.; Kroon, J. M.; Bakker, K.; Havenith, R. W. A.; van Klink, G. P. M.; van Koten, G. Cyclometalated Organoruthenium Complexes for Application in Dye-Sensitized Solar Cells. *Organometallics* **2010**, *29*, 1569−1579.

(12) Kreitner, C.; Mengel, A. K. C.; Lee, T. K.; Cho, W.; Char, K.; Kang, Y. S.; Heinze, K. Strongly Coupled Cyclometalated Ruthenium Triarylamine Chromophores as Sensitizers for DSSCs. *Chem. - Eur. J.* **2016**, *22*, 8915−8928.

(13) O'Regan, B.; Gratzel, M. A LOW-COST, HIGH-EFFICIENCY SOLAR-CELL BASED ON DYE-SENSITIZED COLLOIDAL TIO2 FILMS. *Nature* **1991**, *353*, 737−740.

DOI: 10.1021/acs.inorgchem.7b00392
Inorg. Chem. 2017, 56, 7720−7730

(14) Kreitner, C.; Erdmann, E.; Seidel, W. W.; Heinze, K. Understanding the Excited State Behavior of Cyclometalated Bis-(tridentate)ruthenium(II) Complexes: A Combined Experimental and Theoretical Study. *Inorg. Chem.* **2015**, *54*, 11088−11104.
(15) Kreitner, C.; Heinze, K. Excited state decay of cyclometalated polypyridine ruthenium complexes: insight from theory and experiment. *Dalton Trans.* **2016**, *45*, 13631−13647.
(16) Brown, D. G.; Sanguantrakun, N.; Schulze, B.; Schubert, U. S.; Berlinguette, C. P. Bis(tridentate) Ruthenium−Terpyridine Complexes Featuring Microsecond Excited-State Lifetimes. *J. Am. Chem. Soc.* **2012**, *134*, 12354−12357.
(17) Robson, K. C. D.; Koivisto, B. D.; Berlinguette, C. P. Derivatization of Bichromic Cyclometalated Ru(II) Complexes with Hydrophobic Substituents. *Inorg. Chem.* **2012**, *51*, 1501−1507.
(18) Robson, K. C. D.; Koivisto, B. D.; Yella, A.; Sporinova, B.; Nazeeruddin, M. K.; Baumgartner, T.; Grätzel, M.; Berlinguette, C. P. Design and Development of Functionalized Cyclometalated Ruthenium Chromophores for Light-Harvesting Applications. *Inorg. Chem.* **2011**, *50*, 5494−5508.
(19) Wadman, S. H.; Havenith, R. W. A.; Hartl, F. e.; Lutz, M.; Spek, A. L.; van Klink, G. P. M.; van Koten, G. Redox Chemistry and Electronic Properties of 2,3,5,6-Tetrakis(2-pyridyl)pyrazine-Bridged Diruthenium Complexes Controlled by N,C,N′-BisCyclometalated Ligands. *Inorg. Chem.* **2009**, *48*, 5685−5696.
(20) Thompson, D. W.; Ito, A.; Meyer, T. J. Ru(bpy)(3) (2+)* and other remarkable metal-to-ligand charge transfer (MLCT) excited states. *Pure Appl. Chem.* **2013**, *85*, 1257−1305.
(21) Coudret, C.; Fraysse, S. Electrophilic functionalization of a cyclometallated ruthenium complex, an easy entry to new organometallic synthons. *Chem. Commun.* **1998**, 663−664.
(22) Friebe, C.; Schulze, B.; Görls, H.; Jäger, M.; Schubert, U. S. Designing Cyclometalated Ruthenium(II) Complexes for Anodic Electropolymerization. *Chem. - Eur. J.* **2014**, *20*, 2357−2366.
(23) Vilà, N.; Zhong, Y.-W.; Henderson, J. C.; Abruña, H. D. Anthracene-Bridged Binuclear Ruthenium Complexes: Electrochemical and Spectroscopic Evidence of Electronic Communication Through the π System. *Inorg. Chem.* **2010**, *49*, 796−804.
(24) Fetzer, L.; Boff, B.; Ali, M.; Xiangjun, M.; Collin, J.-P.; Sirlin, C.; Gaiddon, C.; Pfeffer, M. Library of second-generation cycloruthenated compounds and evaluation of their biological properties as potential anticancer drugs: Passing the nanomolar barrier. *Dalton Trans.* **2011**, *40*, 8869−8878.
(25) Jäger, M.; Smeigh, A.; Lombeck, F.; Görls, H.; Collin, J.-P.; Sauvage, J.-P.; Hammarström, L.; Johansson, O. Cyclometalated RuII Complexes with Improved Octahedral Geometry: Synthesis and Photophysical Properties. *Inorg. Chem.* **2010**, *49*, 374−376.
(26) Hammarström, L.; Johansson, O. Expanded bite angles in tridentate ligands. Improving the photophysical properties in bistridentate RuII polypyridine complexes. *Coord. Chem. Rev.* **2010**, *254*, 2546−2559.
(27) Abrahamsson, M.; Jäger, M.; Österman, T.; Eriksson, L.; Persson, P.; Becker, H.-C.; Johansson, O.; Hammarström, L. A 3.0 μs Room Temperature Excited State Lifetime of a Bistridentate RuII−Polypyridine Complex for Rod-like Molecular Arrays. *J. Am. Chem. Soc.* **2006**, *128*, 12616−12617.
(28) Jäger, M.; Kumar, R. J.; Görls, H.; Bergquist, J.; Johansson, O. Facile Synthesis of Bistridentate RuII Complexes Based on 2,6-Di(quinolin-8-yl)pyridyl Ligands: Sensitizers with Microsecond 3MLCT Excited State Lifetimes. *Inorg. Chem.* **2009**, *48*, 3228−3238.
(29) Laramee-Milette, B.; Hanan, G. S. Ruthenium bistridentate complexes with non-symmetrical hexahydro-pyrimidopyrimidine ligands: a structural and theoretical investigation of their optical and electrochemical properties. *Dalton Trans.* **2016**, *45*, 12507−12517.
(30) Unpublished results.
(31) Jin, J.; Wen, Q.; Lu, P.; Wang, Y. Copper-catalyzed cyanation of arenes using benzyl nitrile as a cyanide anion surrogate. *Chem. Commun.* **2012**, *48*, 9933−9935.
(32) Schlotthauer, T.; Suchland, B.; Goerls, H.; Parada, G. A.; Hammarstrom, L.; Schubert, U. S.; Jaeger, M. Aryl-Decorated Ru-II Polypyridyl-type Photosensitizer Approaching NIR Emission with Microsecond Excited State Lifetimes. *Inorg. Chem.* **2016**, *55*, 5405−5416.
(33) Jäger, M.; Eriksson, L.; Bergquist, J.; Johansson, O. Synthesis and Characterization of 2,6-Di(quinolin-8-yl)pyridines. New Ligands for Bistridentate RuII Complexes with Microsecond Luminescent Lifetimes. *J. Org. Chem.* **2007**, *72*, 10227−10230.
(34) Bomben, P. G.; Theriault, K. D.; Berlinguette, C. P. Strategies for Optimizing the Performance of Cyclometalated Ruthenium Sensitizers for Dye-Sensitized Solar Cells. *Eur. J. Inorg. Chem.* **2011**, *2011*, 1806−1814.
(35) Muro-Small, M. L.; Yarnell, J. E.; McCusker, C. E.; Castellano, F. N. Spectroscopy and Photophysics in Cyclometalated RuII-Bis(bipyridyl) Complexes. *Eur. J. Inorg. Chem.* **2012**, *2012*, 4004−4011.
(36) Ashford, D. L.; Glasson, C. R. K.; Norris, M. R.; Concepcion, J. J.; Keinan, S.; Brennaman, M. K.; Templeton, J. L.; Meyer, T. J. Controlling Ground and Excited State Properties through Ligand Changes in Ruthenium Polypyridyl Complexes. *Inorg. Chem.* **2014**, *53*, 5637−5646.
(37) Allen, G. H.; White, R. P.; Rillema, D. P.; Meyer, T. J. SYNTHETIC CONTROL OF EXCITED-STATE PROPERTIES - TRIS-CHELATE COMPLEXES CONTAINING THE LIGANDS 2,2′-BIPYRAZINE, 2,2′-BIPYRIDINE, AND 2,2′-BIPYRIMIDINE. *J. Am. Chem. Soc.* **1984**, *106*, 2613−2620.
(38) It should be noted that the selected isovalue may over- or underestimate the real contribution and should be regarded as a helpful tool for visualization.
(39) Österman, T.; Abrahamsson, M.; Becker, H. C.; Hammarström, L.; Persson, P. Influence of Triplet State Multidimensionality on Excited State Lifetimes of Bis-tridentate Ru-II Complexes: A Computational Study. *J. Phys. Chem. A* **2012**, *116*, 1041−1050.
(40) Österman, T.; Persson, P. Excited state potential energy surfaces of bistridentate Ru-II complexes - A TD-DFT study. *Chem. Phys.* **2012**, *407*, 76−82.

DOI: 10.1021/acs.inorgchem.7b00392
Inorg. Chem. 2017, 56, 7720−7730

Publication P2

Exploring the coordination mechanism towards multi-functionalized Ru^{II} polypyridyl-type sensitizer: An experimental and computational study

T. Mede, M. Jäger, U. S. Schubert, submitted.

Dalton Transactions

ARTICLE

Exploring the coordination mechanism towards multi-functionalized Ru^{II} polypyridyl-type sensitizer: An experimental and computational study

Received 00th January 20xx,
Accepted 00th January 20xx

DOI: 10.1039/x0xx00000x

www.rsc.org/

T. Mede,[a] M. Jäger,[a,b,*] and Ulrich S. Schubert[a,b,*]

Ru^{II} complexes based on functionalized 2,6-(diquinolin-yl)pyridine (dqp) ligand display excellent photophysical properties for similar applications as the ubiquitous 2,2'-bipyridine (bpy) or 2,2':6',2''-terpyridine (tpy) congeners. However, the synthesis of multi-functionalized $[Ru(dqp)_2]^{2+}$-based complexes is low-yielding to date, which hamperes their practical value to date. In this study, a universal high-yielding route is explored, including a unpreceded mechanistic investigation based on ^1H NMR. MS, and density-functional thorey. Solvent exchange of the percursor $[Ru(N^N^N)(MeCN)_3]$ by DMF lowered the required rection temperature for coordination of *N^N^N* considerbaly (by 30 °C), while the steric demand of the *N^N^N* ligand affects the rate-limiting step. Nevertheless, the onset of coordination of a tpy-derivative (60 °C) and (90 °C) are significantly milder than previous routes. The protocol was applied to the high-yielding synthesis of a series of multzi-functionalized Ru^{II} complexes of up to 90%, whereby hydroxy groups and losses during purification in case of minor side reactions lead to lower isolate yields.

Introduction

Ruthenium polypyridyl-type complexes combine beneficial electrochemical and photophysical properties, which constitutes their broad application in photocatalysis,[1-7] molecular photosynthesis,[8-11] as DNA labeling[12-14] and in dye-sensitized solar cells (DSSCs).[15-18] The majority of Ru^{II} photosensitizer are derived from 2,2'-bipyridine (bpy) or 2,2':6',2''-terpyridine (tpy) ligands.[19, 20] The former class features triplet metal-to-ligand-charge-transfer (^{3}MLCT) excited states with long life times on the microsecond timescale, whereas the latter class exhibits attractive geometrical features for rod-like assemblies, *e.g.*, to construct linear metallopolymers or donor-photosensitizer-acceptor (D–P–A) assemblies. In the last decade, a new Ru subclass evolved based on the tridentate 2,6-(diquinolin-8-yl)pyridine (dqp) framework.[21] As a consequence of the expanded bite angle,[22] the corresponding $[Ru(dqp)_2]^{2+}$-based complexes display an advantageous combination of both photophysical and geometrical properties, *e.g.*, prolonged excited state lifetimes up to several microseconds, absorption up to 600 nm leading to enhanced coverage of the terrestrial solar spectrum, near-infrared (NIR) emission around 700 nm, and enhanced photostability *vs.* the ubiquitous $[Ru(bpy)_3]^{2+}$ sensitizer.[21-24] The photophysical and electrochemical properties of the prototypical $[Ru(dqp)_2]^{2+}$ core have been further modulated through systematic ligand design, *e.g.*, by means of carbanionic donors,[25, 26] alternative heterocyclic subunits,[27] or peripheral functional groups. In this regard, the 4-position of the pyridine subunit was used to enhance the red-edge shoulder of the ^{1}MLCT absorption band, while the substituents on the quinoline unit can be used to tune the ^{3}MLCT emission energies,[28] in excellent agreement with the predictions by density functional theory (DFT).[28-30] Hence, aryl-substituents are attractive to increase the molar absorptivity and emission energy towards the NIR-region, without reducing the long excited state lifetimes.[28] Consequently, $[Ru(dqp)_2]^{2+}$ complexes represent promising candidates for medical applications,[31] photo-responsive electropolymerized coatings,[26, 32, 33] sensors,[34] and particularly for light-induced charge separation in photoredox-active dyads and triads.[34-39] However, the reported synthetic routes towards functionalized $[Ru(dqp)_2]^{2+}$ complexes are often low yielding with respect to the bpy- and tpy-based congeners. Hence, this study focuses on a mechanistic analysis of the coordination chemistry to develop a milder general protocol for this versatile sensitizer class, with particular emphasis on challenging multi-arylated and sensitive functional groups. Such compounds offer opportunities to complement or replace conventional $[Ru(bpy)_3]^{2+}$-based complexes or to act as building blocks for the aforementioned applications. A particularly attractive feature of the latter is the

[a] *Laboratory of Organic and Macromolecular Chemistry (IOMC)*
Friedrich Schiller University Jena
Humboldtstraße 10, 07743 Jena, Germany
[b] *Center for Energy and Environmental Chemistry Jena (CEEC Jena)*
Friedrich Schiller University Jena
Philosophenweg 7a, 07743 Jena, Germany
e-Mail: michael.jager.iomc@uni-jena.de, ulrich.schubert@uni-jena.de
Electronic Supplementary Information (ESI) available: [details of any supplementary information available should be included here]. See DOI: 10.1039/x0xx00000x

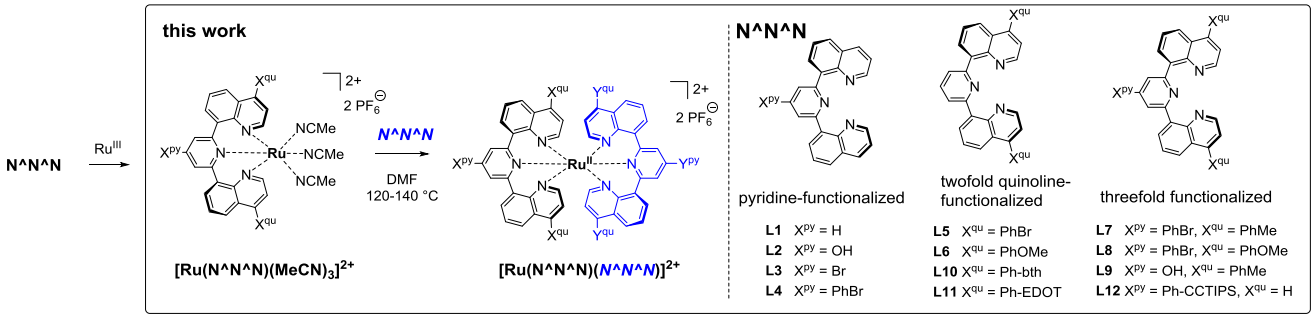

Scheme 1. Schematic representation of the generalized synthetic pathway towards (multi-)functionalized $[Ru(dqp)_2]^{2+}$-based complexes. See Table 1 for details of the corresponding functionalized Ru complexes.

modular character, which permits divergent "chemistry-on-the-complex" strategies to reduce the number of synthetic steps or to introduce sensitive moieties after coordination.

Results and discussion

$[Ru(dqp)_2]^{2+}$-based complexes decorated with simple EWG- and ERG-functionalities can be synthesized in good yields (typically between 40 and 77%) in alcoholic solvents at 140 °C,[40] but these conditions lead in case of the corresponding multi-arylated $[Ru(dqp)_2]^{2+}$ (*e.g.*, anisyl-, tolyl-, and bromoaryl-substituents) to substantially lower yields (14 to 32%).[28] Alternatively, DMF as a suitable solvent is employed in such demanding cases, *e.g.*, for related $[Ru(tpy)_2]$-based complexes,[41-46] or for cyclometalation reactions.[47] The manuscript is organized to briefly introduce the new ligand syntheses intermediates, followed by the exploration of the $[Ru(N^N^N)(MeCN)_3]^{2+}$ intermediate towards *bis*-tridentate $[Ru(N^N^N)(N^N^N)]^{2+}$ complexes (Scheme 1): (a) Solvent exchange with less coordinating DMF and DMSO ligands, (b) detailed reactivity studies towards dqp and a tpy-based congener, (c) a detailed computational mechanistic analysis and (d) the application of the optimized protocol. Hence, this study contains a range of dqp-based ligands (**L1–L12**), as well as a tpy derivative (**L13**), in order to elucidate the origin of the unusual required high reaction temperature. The applicability of the developed protocol will afterwards assessed for a series of *bis*-tridentate Ru^{II} complexes as summarized in Scheme 1.

Ligand and precursor synthesis. In addition to the parental dqp ligand (**L1**), a series of pyridine-functionalized ligands will be investigated bearing hydroxyl- (**L2**), bromo- (**L3**) and bromophenyl-substituents at the unit (**L4**). In view of the desired goal to simplify the synthesis protocols, the reported multistep synthesis of **L3,** starting from the nitro group via reduction, diazotation and Sandmeyer-type conversion to the halide,[48] can be replaced by the efficient transformation of **L2** into **L3** in a single steps using PBr_3 (68%) or $POBr_3$ (51%). In addition to the pyridine-functionalized ligands (**L2–L4**), twofold quinoline-decorated dqp ligands will be investigated, *i.e.*, bearing bromophenyl- (**L5**) or anisyl-groups (**L6**).[32] Notably, the ligands **L7** and **L8** combine the arylation-pattern at both the pyridine and the two quinoline subunits, which previously lead to particular low yields upon complexation.[28] Similarly, the new ligand **L9** was prepared in 68% yield and combines the arylation pattern of the quinoline units as well as the hydroxyl-substituent at the pyridine. The last group of ligands contains potential reactive groups, which were introduced after formation of the ligand framework. First, the *bis*-quinoline-decorated **L5** was converted by a Suzuki-Miyaura with commercial thiophene derivatives to yield the corresponding *bis*-bithienylphenyl (**L10**) and *bis*-3,4-ethylenedioxythienylphenyl (**L11**) in reasonable yields (42 to 44%). Secondly, the synthesis of triisopropylsilylethynyl-decorated **L12** was previously reported using Sonogashira coupling reaction of **L4**.[39] Next, the syntheses of the corresponding $[Ru(N^N^N)(MeCN)_3]^{2+}$ intermediates was achieved in analogy to our previously optimized protocols for dqp,[28, 32, 40] which also recently proved beneficial for related tpy's in demanding cases.[49-51]

Solvent exchange and stability. The absence of competing monodentate ligands (*e.g.*, chloride, MeCN) was reported crucial for successful coordination of *N^N^N*, so that our initial goal was to explore the scope of solvent exchange for $[Ru(dqp)(MeCN)_3]^{2+}$ by less coordinating solvents (Scheme 2, left). The reaction was followed by ^1H NMR spectroscopy (Scheme 2, right), which revealed systematic chemical shift differences of characteristic protons. The most diagnostic proton is the one at the 2-position of the quinoline subunit, which is positioned above the axial solvent ligand and, thus, experiences the deshielding effect of the solvent's π-bond. Re-visiting the available x-ray crystal structure of $[Ru(\mathbf{L1})(MeCN)_3]^{2+}$ and $[Ru(\mathbf{L7})(MeCN)_3]^{2+}$ confirmed this assignment,[28] so that the solvent exchange at various temperatures was conveniently followed by ^1H NMR analysis in the corresponding deuterated solvent. The exchange of the axially bound MeCN ligand by d_7-DMF in **A** occured around 70 °C to form intermediate **B**, as judged form the preserved symmetry of the signals and the marked downfield-shift (–0.4 ppm) of the H^2-quinoline protons (Scheme 2b) due the removal of the deshielding π-bond of MeCN. Likewise, the resonance of the corresponding CH_3CN resonances disappear (Figures S3), while the two trans-bound CH_3CN resonances remained almost unchanged. Continuing the heating to approximately 120 °C led to full exchange to the tentatively

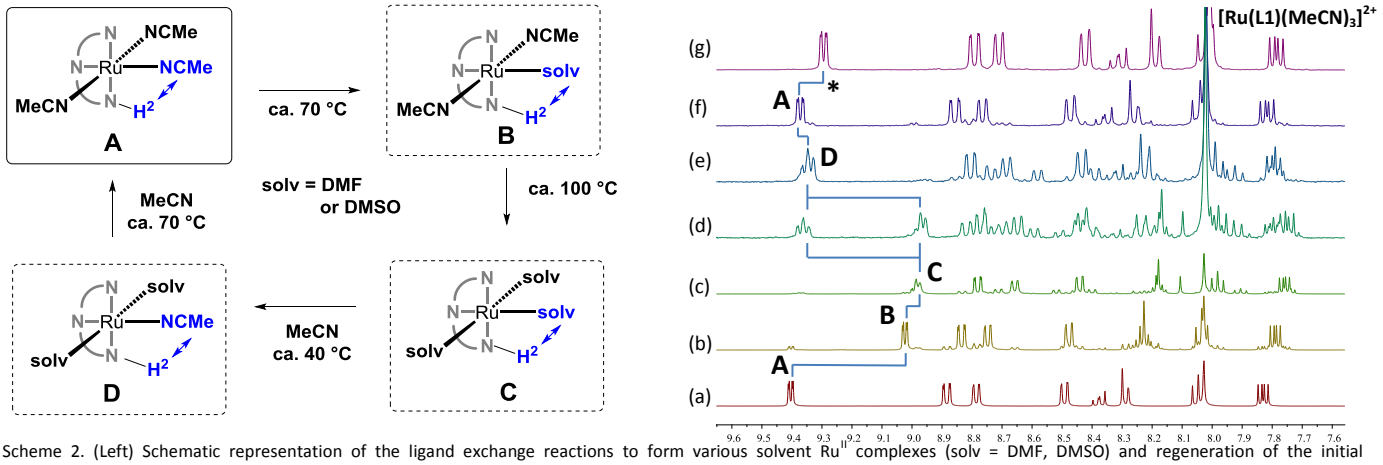

Scheme 2. (Left) Schematic representation of the ligand exchange reactions to form various solvent Ru^{II} complexes (solv = DMF, DMSO) and regeneration of the initial $[Ru(L1)(MeCN)3]^{2+}$ precursor. Note the preferential exchange at the axial position (shown in blue) vs. the displacement at the two trans-position (black) with respect to the pyridine ring. See text for more details and analysis. (Right) ^{1}H NMR spectra (300 MHz, aromatic region) taken during solvent exchange from $[Ru(\mathbf{L1})(MeCN)_3]^{2+}$ by d_7-DMF (a–c) to form tentatively assigned $[Ru(dqp)(DMF)_3]^{2+}$, and reversal solvent exchange with added CD_3CN (d–g) at given temperatures and times. Note the diagnostic chemical shifts of the H^2 proton, which is positioned above the axial solvent ligand (left), the systematic shifts due to different solvent compositions (d_7-DMF/CD_3CN, see also SI), and the complete regeneration of the $[Ru(dqp)(MeCN)_3]^{2+}$ (a *vs.* g).

assigned complex **C**. Notably, residual amounts of **B** and trace amounts of an unidentified specimen were noticeable, so that the reversal solvent exchange was monitored to test the degradation of the [Ru(N^N^N)]-fragment. Already at 40 °C, the replacement at the axial position of **C** was noticed to form **D**, as indicated by the characteristic high-field shift (+0.4 ppm). However, the spectra reveal multiple signal sets, which is tentatively assigned to various *mono*- and *bis*-substitution products as well as the lower symmetry induced by coordinated d_7-DMF *vs.* CD_3CN. More importantly, the spectrum became more simple around 70 °C, indicating replacement of the remaining d_7-DMF ligands of **D** to regenerate the initial specimen **A**, which was found complete at 80 °C. Notably, no sizable amounts of decomposition products were detected. The same solvent exchange behavior was found in d_6-DMSO, except that somewhat higher reaction temperatures were required for the regeneration process (Figure S5).

The NMR analysis was further corroborated by the COSY spectra of the intermediates **C** formed in d_6-DMSO (Figure S6) and d_7-DMF (Figure S7), which confirmed the expected spin systems. In addition, the ESI-ToF-MS analysis of an isolated batch of **C** (*vide infra*) identified $[Ru(dqp)(DMF)]^{2+}$ by means of its isotope pattern. Furthermore, thermal analysis of $[Ru(dqp)(MeCN)_3]^{2+}$ by gravimetry and calorimetry, coupled to MS and IR detection, revealed the endothermal cleavage of one MeCN ligand around 130 °C, according to the characteristic mass loss of 4% and the corresponding EI-MS peak and the IR spectrum of MeCN (Figure S9). These initial results show that the Ru(dqp)-fragment stays intact and the corresponding DMF-intermediate (**B**) can undergoes ligand displacement already around 40 °C, which may permit a milder protocol for the coordination of N^N^N.

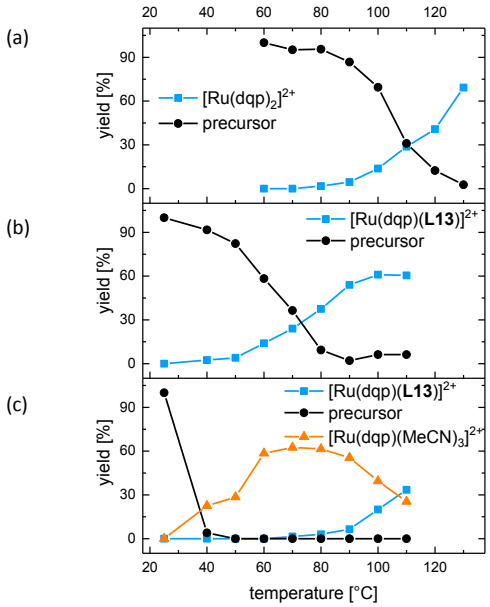

Figure 1. Kinetic analysis of the ^{1}H NMR data (300 MHz) for the complexation of $[Ru(dqp)(DMF)_3]^{2+}$ by (a) dqp (**L1**) in d_7-DMF, (b) tpy-based **L13** in d_7-DMF, and (c) tpy-based **L13** in d_7-DMF/CD_3CN mixture. Note the faster conversion of tpy *vs.* dqp (a *vs.* b), as well as the transient formation of the $[\{Ru(dqp)(MeCN)_3]^{2+}$ leading to retarded complexation (b *vs.* c). Lines are drawn to visualize the corresponding data points (symbols).

Reactivity screening for N^N^N coordination. The coordination of tridentate ligands to the preformed DMF-intermediate **C** was investigated in various solvents (see SI for details). In general, $[Ru(dqp)(MeCN)_3]^{2+}$ was heated in d_7-DMF at 120 °C until full conversion, and excess of solvent (80%) was removed from the heated sample by a N_2 stream. Note that the isolation of the DMF-precursor by complete removal of

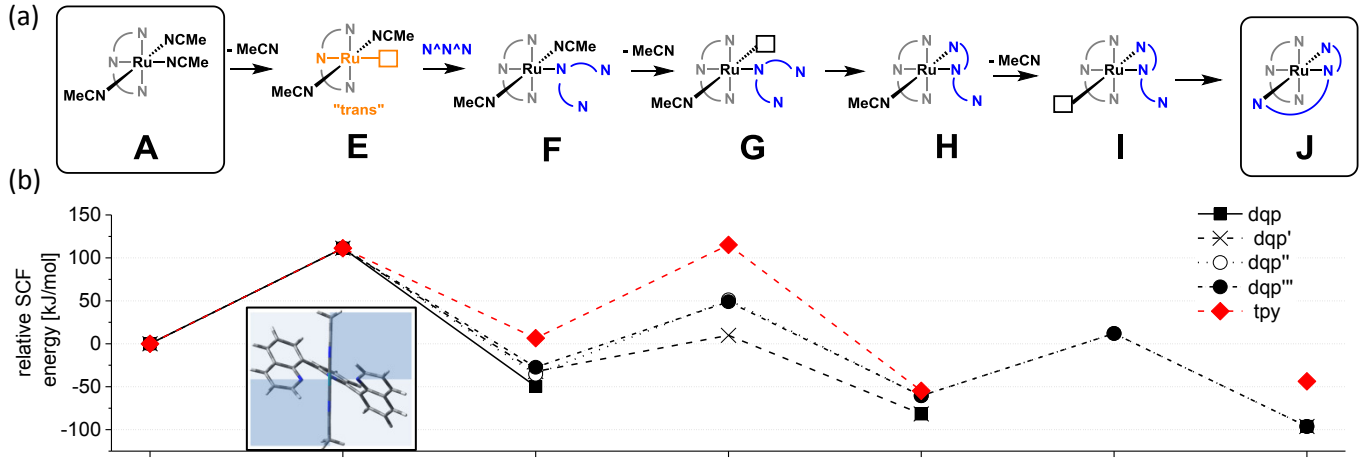

Scheme 3. (a) Schematic representation of a generalized sequence for the coordination of the N^N^N ligand (blue) via the de-coordination of MeCN from a [(Ru(N^N^N)(MeCN)$_3$] precursor (N^N^N are dqp or tpy, respectively). Note that the displayed structures represent proposed intermediates. (b) Energy profile of proposed intermediates for the reaction of [Ru(dqp)(MeCN)$_3$]$^{2+}$ with dqp (black) or tpy (red), as well as related [Ru(tpy)(MeCN)$_3$] with tpy (blue). See supporting information for potential energy profiles, transition state estimates and mechanistic details. Lines are drawn to visualize the pathways only. Note that structures A, F, H, and J represent N6-chelates, while structures E, G, and I contain open coordination sites to estimate the complex' inherent contribution to the activation barrier, which formally requires additional distortion or dihedral strain to accommodate the approaching ligand fragment (see supporting information for details). Inset shows the highest-energy intermediate **E** along the N^{py}–Ru–□ bond (orange in panel a), illustrating the helical symmetry of the bound dqp fragment and the resulting quadrants for the incoming ligand (light: empty space; dark: occupied space by the bound quinoline).

DMF led to irreproducible results, which indicates aggregation or precipitation of the degraded side product. More importantly, no free ligand was detected according to the ^{1}H NMR spectra, which would lead to undesired ligand scrambling in case of heteroleptic Ru^{II} complexes. After addition of equimolar amounts of the tridentate ligand and the respective solvent(s), the mixture was heated overnight in 10 °C intervals and analysed by ^{1}H NMR spectroscopy.

The kinetics of the educt conversion and the product formation are provided in Figure 1, for more detailed information see the supporting information (section 2.3.2) and Figures S10 to S12 for the corresponding ^{1}H NMR spectra. First, the onset of coordination was judged from 10% product formation. In the case of dqp (**L1**), the coordination begins around 90 °C, but requires >120 °C to reach high conversions (Figure 1a). In view of the related solvent exchange reaction occurring at around 40 °C (*vide supra*), this finding suggests that the N^N^N ligand affects the required reaction temperatures for coordination. In order to test this hypothesis, we investigated the previously reported tolyl-decorated terpyridine **L13**.[23] Indeed, the coordination began already below 60 °C to form the corresponding [Ru(dqp)(**L13**)]$^{2+}$ complex, and reached high conversions at around 90 °C (Figure 1b). Finally, the reactivity difference of the intermediate solvent complexes was assessed by admixing CD_3CN to monitor the competition between MeCN and **L13**. In agreement with the solvent exchange study, the DMF-precursor was converted quantitatively already at 40 °C, but no product formation was observed until 60 °C (Figure 1c). This result agrees with the previous observation that the stepwise exchange of the bonded d_7-DMF ligands occurs to form the corresponding [Ru(dqp)(CD_3CN)$_3$] around 60 to 80 °C. Around the same temperature, its conversion to the product begins. Notably, the formation of [Ru(dqp)(**L13**)]$^{2+}$ proceeded significantly slower and required higher temperatures than in the absence of the competing CD_3CN. The carefully inspection of the ^{1}H NMR spectra taken during the complexation reactions at various temperatures showed no accumulation of further intermediates (Figures S10–S12), which is tentatively assigned to the same coordination pathway as for dqp. In essence, the consumption of the solvent complexes parallels the product formation without noticeable degradation, irrespective of the temperature. These results suggest that the rate-limiting step for N^N^N coordination occurs in the early stage of the reaction and, thus, is favoured by less coordinating solvents (Figure 1b and c). However, the reactivity difference between dqp (**L1**) and a tpy-derivative (**L13**) further suggests, that the activation barrier of the rate-limiting step also depends on the ligand structure, as indicated by the higher reaction temperatures required for **L1** (Figure 1a and b). In summary, the preparation of the DMF-intermediate can be performed prior to the coordination of the N^N^N ligand, which facilitates the reaction in the case of tpy-based **L13** at significantly lower reaction temperatures (by 30 °C). In the case of dqp, the reaction temperatures required for the MeCN displacement by DMF and the one to coordinate dqp are similar, suggesting to use [Ru(dqp)(MeCN)$_3$]$^{2+}$ directly in DMF.

Mechanistic interpretation by DFT calculations. Although the syntheses of *bis*-tridentate Ru polypyridyl-type complexes are known since decades, no detailed mechanistic study concerning their coordination chemistry is published to the best of our knowledge. In order to corroborate our previous assignments based on experimental data, a computational analysis of a plausible reaction pathway was performed using density functional theory (DFT). This methodology is wellsuited

to complement missing or unavailable experimental data, in order to derive a comprehensive picture, as demonstrated for mapping the photochemical reactivity of the ^{3}MLCT state(s).[29, 30, 52-54]

The following discussion details the mechanistic pathway(s) based on plausible intermediates (Scheme 3 and supporting information). The exploration of the coordination pathways descend from the $[Ru(dqp)(MeCN)_3]^{2+}$ precursor (**A**). Note that for brevity, the position opposite to the coordinated pyridine of the $[Ru(N^{qu}\text{^}N^{py}\text{^}N^{qu})]$ fragment will be denoted as "*trans*", whereas the two other ones are denoted "*cis*". In agreement with the available x-ray crystallographic data,[28] the *trans*-bonded MeCN displays a considerably longer computed Ru–N bond (2.066 Å) than the *cis*-bonded MeCNs (2.040 Å). A potential energy scan (PES) of the elongation of the Ru–N bond confirmed the more facile breakage of the *trans*-bonded MeCN (Figure S30). The same trend was found for the corresponding $[Ru(dqp)(DMF)_3]^{2+}$ complex, which features a markedly longer initial Ru–O bond as well as less energy required to elongated the Ru–O bond (Figure S35). This finding parallels the observed higher reactivity for solvent displacement (*vide supra*). However, the following mechanistic analysis will be based for clarity on the (linear) MeCN ligand, which reduces the number of conceivable conformers in comparison to (non-linear) DMF ligand.

The first event towards bis-tridentate Ru^{II} complexes involves the dissociation of a MeCN ligand from **A**, since an alternative associative pathway is unlikely due to the steric congestion around the Ru atom. Notably, the energy required to form the de-coordinated intermediate (**E**) is significantly lower for the *trans*-MeCN (+111 kJ/mol) *vs.* the *cis*-MeCN (+139 kJ/mol). On the basis of simple Boltzmann statistics ($k \sim \exp(-E/kT)$), a ratio of k_{trans}/k_{cis} of 250/1 is calculated using ΔE = 28 kJ/mol, 298 K, and assuming identical pre-exponential factors. This result parallels the previous argumentation based on the Ru-N bond lengths, as well as the experimental ^{1}H NMR and TGA data (*vide supra*). Hence, the coordination pathway is likely to proceeds through **E** featuring an open coordination site in the *trans*-position, unless no higher barrier will be encountered later on. Next, the coordination of the N^N^N ligand occurs *via* the central pyridine N^{py} donor to form the corresponding complex **F**. Note that each quinoline subunit can adapt two different orientation with respect to the [Ru(dqp)] fragment (see structure of E in Scheme 3b). In essence, the sterically demanding *N*-heterocyclic part of unbound quinoline preferentially accommodates the vacant space pointing away the bound quinoline (Figure S37). As a result, four intermediates can form that differ in the degree of π–interactions and steric repulsion and, thus, lead to intermediates with considerably higher energy with respect to **F** (**F'**: +17 kJ/mol, **F''**: +14 kJ/mol, **F'''** +22 kJ/mol). Because of the restricted rotation along the interannular N^{py}-N^{qu} bond, the different intermediates cannot interconvert and descend in specific pathway denoted by the apostrophes. Notably, the replacement of the MeCN ligand by the N^{py}-coordinated dqp leads to a remarkable stabilization (–50 kJ/mol) for the lowest-energy intermediate **F**. Next, the loss of a *cis*-bonded MeCN from the **F** series occurs to form the corresponding **G** series (Figure S38). In case of the lowest-energy conformer **F**; the corresponding **G** intermediate converged directly to the N^{qu}-coordinated intermediate, since the quinoline unit is beneficial aligned with respect to the generated vacant coordination site. In contrast, the higher-energy conformers (**F'** to **F'''**) converged to their corresponding intermediates (**G'**: +42 kJ/mol, **G''**: +87 kJ/mol, **G'''** +77 kJ/mol). As expected, the loss of the *cis*-MeCN is endothermic but in all cases significantly less demanding in comparison to the first loss of the *trans*-MeCN (+111 kJ/mol). As expected, the inspection of the nuclear geometries revealed the release of internal distortion within the complex fragment, which further permits an enhanced stabilization by π-interactions of the aromatic subunits (Figure S38). Next, the coordination of the N^{qu} donor to the vacant coordination site occurs (Figure S40), which requires the rotation along the interannular C^{qu}–C^{py} bond and can be conveniently monitored by a potential energy scan (Figure 2). This process induces an additional internal strain to the high-energy intermediates. In case of the least favourable initial orientation of N^{qu} (**G'''**), a high rotational barrier (ca. +135 kJ/mol) due to the eclipse with nearby hydrogen atoms must be passed to convert to **G''**. In agreement with the direct convergence of the **G** starting guess to **H**, the related structure **G''** featuring a similar orientation of N^{qu} also displayed no barrier along the PES to yield **H''**. Based on this rational, the intermediate **G'** is expected to pass through a similar high rotational barrier as **G'''**. Consequently, the two pathways via **G'** and **G'''** are effectively blocked due to the high energy barrier, which consists of the endothermic loss of the MeCN and the rotational barrier. In contrast, the intermediate **G** and **G''** require only negligible rotation and, thus, qualitatively serves as estimates of the real transition state.[55]

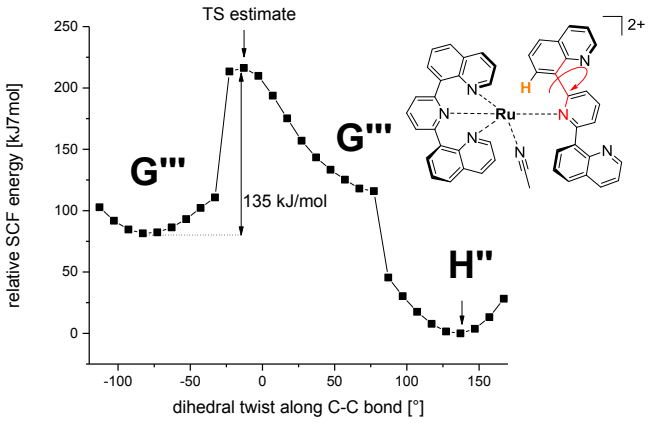

Figure 2. Potential energy scan (PES, SCF energies relative to H'') of the internal rotation along the interannular C^{py}–C^{qu} bond (red), Note the release of the accumulated dihedral strain around -30 ° and 60 °. See Figure S39 for details.

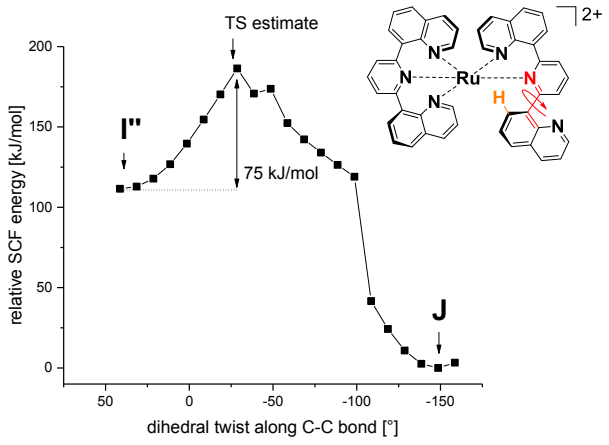

Figure 3. Potential energy scan (PES) of **I''** of the internal rotation along the interannular C^{py}–C^{qu} bond (red). Note the release of accumulated dihedral strain around -100 °to yield final **J**. See Figure S42 for details.

The next step involves the removal of the remaining *cis*-MeCN to generate the intermediates **I** and **I''**, In agreement with the preceding discussion of the replacement of MeCN by a quinoline unit, the starting guess for the beneficial orientation of the free quinoline unit with respect to the vacant coordination site (**I**) converged directly to the final product (Figure S41). Likewise, the unfavourable quinoline orientation (**I'',** +72 kJ/mol) requires the passage of a rotational barrier. Although this barrier is lower than before (+75 *vs.* +135 kJ/mol), the total energy required to form **I''** and to undergo the desired rotation amounts to +147 kJ/mol, which suggests that this pathway is effectively blocked. In summary, the exploration of the coordination sequence identified one preferential pathway, while the remaining three alternative pathways encounter larger barriers that exceed the initial loss of the *trans*-MeCN ligand.

Finally, the coordination pathway of tpy was qualitatively explored starting from **E** to deduce any difference (see supporting information); however, the results are less clear. In comparison to dqp, the tpy ligand features two outer pyridine units, which lead upon coordination to a more acute N^N^N bite angle of tpy (ca. 156 °) *vs.* dqp (180 °). Consequently, the tpy ligand also adopts a planar arrangement devoid of the dihedral ligand distortion and, thus, no stabilizing π-interactions with the [Ru(dqp)] fragment can occur. More importantly, the rotation along the interannular N^{py}–N^{py} bond is energetically less demanding. For example, the interconversion of the tpy-analogous intermediates $\mathbf{J_{tpy}}$ and $\mathbf{I_{tpy}''}$ gave a significantly lower barrier (Figure S44). Following our previous argumentation, the corresponding pathways may be connected, which qualitatively explains the faster reaction – since the rate-limiting step of initial MeCN loss is identical. A further analysis is beyond the scope of this work, *e.g.*, to assess the exact role of the functional to account for dispersion and to assign intrinsic reaction paths:

In summary, the energy profiles for the coordination of dqp and tpy reveal that the highest energy is required to replace the first

Table 1. Syntheses of functionalized of *bis*-tridentate $[Ru(dqp)_2]^{2+}$-based complexes.[a]

Entry	[Ru(N^N^N)(MeCN)$_3$]$^{2+}$		*N^N^N*		Temp. (time)	Yield[b]
	X^{py}	X^{qu}	Y^{py}	Y^{qu}	[°C (hr)]	[%]
1	H	H	H	H	130 (16)	79[c]
2	PhBr	PhMe	H	H	140 (48)	90[c]
3	H	H	Br	H	140 (48)	73
4	H	H	PhBr	H	140 (16)	74
5	H	H	H	PhBr	140 (48)	52
6	H	H	H	Ph-bth	120 (16)	61
7	H	H	H	Ph-EDOT	120 (16)	38[d]
8	H	H	PhBr	PhOMe	140 (40)	77
9	OH	H	PhBr	H	140 (24)	53
10	OH	H	PhCCTIPS	H	140 (48)	51[e]
11	PhBr	H	H	Ph-bth	120 (48)	32[d]
12	PhBr	PhMe	OH	PhMe	140 (16)	58
13	PhBr	PhMe	PhBr	PhMe	140 (28)	90[c]

[a] Ph is *para*-phenylen, th is 2-thienyl, bth is 2-bithienyl, EDOT is 3,4-ethylenedioxythienyl. [b] Isolated yields if not stated otherwise. [c] Yield determined from ^{1}H NMR analysis by internal standard. [d] Lower yields assigned to losses upon crystallization. [e] Taken from reference 39.

MeCN ligand, which is in excellent agreement with the experimental observation of the screening studies, *i.e.*, no sizable accumulation of other intermediates was observed. In conjunction with the milder reported reaction condition of tpy's[56, 57] *vs.* dqp ligands,[40] the rate-limiting step is likely to involve two factors: First, the higher steric repulsion in case of quinoline *vs.* pyridine, which destabilizes the transition state more effectively prior to the compensation by the Ru–N binding energy. Second, the analysis of undesired quinoline conformers followed a pathway with higher energy and only one of the four suggested pathway yields the final product. Noteworthy, the DFT calculations further confirm the stabilizing effect due to π-π interactions stacking of quinolines, which are present in $[Ru(dqp)_2]$ but not in $Ru(dqp)(tpy)]^{2+}$. This additional favorable contribution is in agreement with the reported extraordinary thermal and photochemical stability of $[Ru(dqp)_2]^{2+}$ complexes.[23]

General syntheses of *bis*-tridentate $[Ru(dqp)_2]^{2+}$-based complexes. The previous screening studies showed, that $[Ru(dqp)(MeCN)_3]$ can be directly converted in DMF, leading to $[Ru(dqp)_2]^{2+}$ in 79% yield according to quantification by ^{1}H NMR analysis (Table 1, entry 1). In order to test the general scope with respect to the precursor, threefold-functionalized [Ru(**L7**)(MeCN)$_3$] was reacted with dqp at 140 °C. Already after 4 hours, ^{1}H NMR analysis revealed a yield of 74%, which levelled around 90% after 48 hours (entry 2, Figure S16). Hence, the following reactions were performed at 120 to 140 °C for 16 to 48 hours, depending on the precise ligand structure. In the case pyridine-functionalized ligands, comparably high isolated yields were obtained for **L3** (73%, entry 3) and **L4** (74%, entry 4). In comparison, the related twofold quinoline-functionalized **L5** gave lower yields (52%, entry 5), even upon prolonged reaction times. Next, the coordination reactions of the *bis*-bithienylphenyl- (**L10**) and *bis*-EDOTphenyl-equipped (**L11**) ligands were tested, which

represent versatile building blocks for electropolymerized photoactive coatings.[26] Notably, the original synthesis via "chemistry-on-the-complex" resulted in low yields (<21%),[26] attributed to side reactions of the bithienyl- and EDOT-moieties which caused substantial losses upon purification *via* crystallization. Hence the reaction temperature for the coordination was lowered to 120 °C, in order to minimize potential thermal decomposition reactions. Indeed, the desired complex derived from **L10** was isolated in 61% yield already after 16 hours (entry 6). In the case of the related *bis*-EDOTphenyl ligand **L11** (38%, entry 7), lower isolated yields were obtained assigned to the loss upon incomplete crystallization. Nevertheless, the coordination route resulted in significantly higher yields than the twofold coupling on the pre-formed complex. In order to test the scope of the so far investigated $[Ru(dqp)(MeCN)_3]^{2+}$ precursor, the threefold arylated ligand **L8** (entry 8) was tested at 140 °C. Satisfyingly, high yields as before were obtained (77%, entry 8), indicating that the substitution pattern of the ligand is not limiting the overall yield. Next, the influence of the substitution pattern of the Ru precursor $[Ru(\mathbf{L})(MeCN)_3]^{2+}$ (**L** = **L2**, **L4**, **L7**) was investigated.

The reaction of the hydroxyl-decorated $[Ru(\mathbf{L2})(MeCN)_3]^{2+}$ with **L4** gave a yields of 53% (entry 9), which is consistent with the reported yield (51%), entry 10) of the related the triisopropylsilylethynyl-decorated derivative **L12**. The lower yield is tentatively assigned to the hydroxyl group, which was absent in the previous cases. Next, the bromophenyl-decorated precursor $[Ru(\mathbf{L4})(MeCN)_3]^{2+}$ was tested with the more challenging ligand **L10**, which led to high conversions at 120 °C but low isolated yield (32%, entry 11), ascribed to the known losses due to the required purification by crystallization. Finally, the threefold functionalized precursor $[Ru(\mathbf{L7})(MeCN)_3]^{2+}$ was reacted with the threefold functionalized ligands **L9** and **L7**. In the case of **L9**, similar isolated yields were obtained (58%, entry 12) as for the other hydroxyl-containing complexes (entries 9 and 10), suggesting that lower yields originate from side reactions of decorated complexes, since the order of coordination is reversed. The confirm the reliability and the scope of the developed protocol, the formation of the six-fold functionalized complex based on **L7** was ultimately investigated by ^{1}H NMR to exclude the influence of substance losses during purification. In line with the related NMR studies (entries 1 and 2), an excellent yield of 90% was observed (entry 13), which represent a significant improvement over the previous methods in alcoholic solvents reaching only 24 to 32%.

Experimental

See supporting information for details on instrumentation, syntheses, analytical characterization, computational results, and mechanistic details.

Conclusions

In this study, the scope of a mild formation of multi-functionalized $[Ru(dqp)_2]^{2+}$-based complexes *via* coordination was investigated, which can be low yielding even at elevated temperatures. Mechanistic details were obtained from solvent exchange reactions of the precursor $[Ru(dqp)(MeCN)_3]^{2+}$, revealing that the corresponding DMF-precursor undergoes ligand exchange reactions at milder conditions with MeCN (40 °C), a tpy derivative (60 °C), and dqp (90 °C). The different onset temperatures were assigned to the steric congestion during the rate-limiting step, which involves the de-coordination of the first solvent ligand as supported by the experimentally and computationally data. The mechanistic analysis may also serve to design and synthesize complexes with related monodentate or bidentate ligands, *e.g.*, for theranostic or energy conversion applications. In addition to the ground state reactivity, the mechanistic approach provides a platform for the related photochemical (excited state) and electrochemical pathways – synthetic tools that receive currently great interest – and will be reported in due course. The developed protocol ultimately proved superior to previous methodologies (alcoholic solvent, 140 °C) to prepare a series of functionalized *bis*-tridentate Ru^{II} complexes, including bromo-, hydroxyl-, bromophenyl-, anisyl-, electropolymerizable bithienyl or EDOT moieties, as well as protected alkynes for CuAAC reactions. Generally, high yields (51 to 90%) or likewise lower reaction temperatures (>90 °C) were obtained. The divergent set of functional groups further expands the so far underexplored application potential of this sensitizer class to photoactive molecular assemblies for light-induced charge separation, sensing, as well as photo-responsive coatings. To the best of our knowledge, this unpreceded mechanistic study provides detailed insights that are believed to also apply to related ligands or metal ions to stimulate an *a priori* design of novel complexes.

Acknowledgements

We thank the Deutsche Forschungsgesellschaft (DFG) and the Thüringer Ministerium für Wirtschaft, Wissenschaft und Digitale Gesellschaft (TMWWDG) for financial support.

Notes and references

The authors declare no competing financial interest. See supporting information for details on instrumentation, syntheses, analytical characterization, computational results, and mechanistic details.

1. E. Bae, W. Choi, J. Park, H. S. Shin, S. B. Kim and J. S. Lee, *J. Phys. Chem. B*, 2004, **108**, 14093-14101.
2. L. Duan, A. Fischer, Y. Xu and L. Sun, *J. Am. Chem. Soc.*, 2009, **131**, 10397-10399.
3. M. Elvington, J. Brown, S. M. Arachchige and K. J. Brewer, *J. Am. Chem. Soc.*, 2007, **129**, 10644-10645.
4. B. Gholamkhass, H. Mametsuka, K. Koike, T. Tanabe, M. Furue and O. Ishitani, *Inorg. Chem.*, 2005, **44**, 2326-2336.
5. H. Ozawa, M. Haga and K. Sakai, *J. Am. Chem. Soc.*, 2006, **128**, 4926-4927.

6. M. Sykora, M. A. Petruska, J. Alstrum-Acevedo, I. Bezel, T. J. Meyer and V. I. Klimov, *J. Am. Chem. Soc.*, 2006, **128**, 9984-9985.
7. T. P. Yoon, M. A. Ischay and J. Du, *Nat. Chem.*, 2010, **2**, 527-532.
8. J. H. Alstrum-Acevedo, M. K. Brennaman and T. J. Meyer, *Inorg. Chem.*, 2005, **44**, 6802-6827.
9. S. Berardi, S. Drouet, L. Francas, C. Gimbert-Surinach, M. Guttentag, C. Richmond, T. Stoll and A. Llobet, *Chem. Soc. Rev.*, 2014, **43**, 7501-7519.
10. M. Sykora, K. A. Maxwell, J. M. DeSimone and T. J. Meyer, *Proc. Natl. Acad. Sci. USA*, 2000, **97**, 7687-7691.
11. S. Tschierlei, M. Karnahl, M. Presselt, B. Dietzek, J. Guthmuller, L. González, M. Schmitt, S. Rau and J. Popp, *Angew. Chem. Int. Ed.*, 2010, **49**, 3981-3984.
12. A. Kienzler, R. Flehr, R. A. Kramer, S. Gehne, M. U. Kumke and W. Bannwarth, *Bioconjugate Chem.*, 2011, **22**, 1852-1863.
13. D. Ossipov, S. Gohil and J. Chattopadhyaya, *J. Am. Chem. Soc.*, 2002, **124**, 13416-13433.
14. D. Ossipov, P. I. Pradeepkumar, M. Holmer and J. Chattopadhyaya, *J. Am. Chem. Soc.*, 2001, **123**, 3551-3562.
15. A. Breivogel, S. Wooh, J. Dietrich, T. Y. Kim, Y. S. Kang, K. Char and K. Heinze, *Eur. J. Inorg. Chem.*, 2014, **2014**, 2720-2734.
16. C.-C. Chou, F.-C. Hu, K.-L. Wu, T. Duan, Y. Chi, S.-H. Liu, G.-H. Lee and P.-T. Chou, *Inorg. Chem.*, 2014, **53**, 8593-8599.
17. C.-C. Chou, F.-C. Hu, H.-H. Yeh, H.-P. Wu, Y. Chi, J. N. Clifford, E. Palomares, S.-H. Liu, P.-T. Chou and G.-H. Lee, *Angew. Chem. Int. Ed.*, 2014, **53**, 178-183.
18. H. Kisserwan, A. Kamar, T. Shoker and T. H. Ghaddar, *Dalton Trans.*, 2012, **41**, 10643-10651.
19. A. Juris, V. Balzani, F. Barigelletti, S. Campagna, P. Belser and A. Vonzelewsky, *Coord. Chem. Rev.*, 1988, **84**, 85-277.
20. S. Campagna, F. Puntoriero, F. Nastasi, G. Bergamini and V. Balzani, in *Photochemistry and Photophysics of Coordination Compounds I*, eds. V. Balzani and S. Campagna, Springer-Verlag Berlin, Berlin, 2007, vol. 280, pp. 117-214.
21. M. Abrahamsson, M. Jäger, T. Österman, L. Eriksson, P. Persson, H.-C. Becker, O. Johansson and L. Hammarström, *J. Am. Chem. Soc.*, 2006, **128**, 12616-12617.
22. L. Hammarström and O. Johansson, *Coord. Chem. Rev.*, 2010, **254**, 2546-2559.
23. M. Abrahamsson, M. Jäger, R. J. Kumar, T. Österman, P. Persson, H.-C. Becker, O. Johansson and L. Hammarström, *J. Am. Chem. Soc.*, 2008, **130**, 15533-15542.
24. M. Abrahamsson, H. C. Becker and L. Hammarstrom, *Dalton Trans*, 2017, **46**, 13314-13321.
25. M. Jäger, A. Smeigh, F. Lombeck, H. Görls, J.-P. Collin, J.-P. Sauvage, L. Hammarström and O. Johansson, *Inorg. Chem.*, 2010, **49**, 374-376.
26. T. Schlotthauer, C. Friebe, A. M. Schwenke, M. Jäger and U. S. Schubert, *J. Mater. Chem. C*, 2017, **5**, 2636-2648.
27. G. A. Parada, L. A. Fredin, M.-P. Santoni, M. Jäger, R. Lomoth, L. Hammarström, O. Johansson, P. Persson and S. Ott, *Inorg. Chem.*, 2013, **52**, 5128-5137.
28. T. Schlotthauer, B. Suchland, H. Görls, G. A. Parada, L. Hammarström, U. S. Schubert and M. Jäger, *Inorg. Chem.*, 2016, **55**, 5405-5416.
29. T. Oesterman and P. Persson, *Chem. Phys.*, 2012, **407**, 76-82.
30. T. Oesterman, M. Abrahamsson, H.-C. Becker, L. Hammarstroem and P. Persson, *J. Phys. Chem. A*, 2012, **116**, 1041-1050.
31. A. Frei, R. Rubbiani, S. Tubafard, O. Blacque, P. Anstaett, A. Felgenträger, T. Maisch, L. Spiccia and G. Gasser, *J. Med. Chem.*, 2014, **57**, 7280-7292.
32. C. Friebe, H. Görls, M. Jäger and U. S. Schubert, *Eur. J. Inorg. Chem.*, 2013, **2013**, 4191-4202.
33. C. Friebe, M. Jaeger and U. S. Schubert, *RSC Adv.*, 2013, **3**, 11686-11690.
34. G. Ragazzon, P. Verwilst, S. A. Denisov, A. Credi, G. Jonusauskas and N. D. McClenaghan, *Chem. Commun.*, 2013, **49**, 9110-9112.
35. R. J. Kumar, S. Karlsson, D. Streich, A. Rolandini Jensen, M. Jäger, H.-C. Becker, J. Bergquist, O. Johansson and L. Hammarström, *Chem. Eur. J.*, 2010, **16**, 2830-2842.
36. J. Kübel, R. Schroot, M. Wächtler, U. S. Schubert, B. Dietzek and M. Jäger, *J. Phys. Chem. C*, 2015, **119**, 4742-4751.
37. R. Schroot, T. Schlotthauer, U. S. Schubert and M. Jager, *Macromolecules*, 2016, **49**, 2112-2123.
38. R. Schroot, T. Schlotthauer, B. Dietzek, M. Jager and U. S. Schubert, *Chem. Eur. J.*, 2017, **23**, 16484-16490.
39. T. Schlotthauer, R. Schroot, S. Glover, L. Hammarstrom, M. Jaeger and U. S. Schubert, *Phys. Chem. Chem. Phys.*, 2017, **19**, 28572-28578.
40. M. Jaeger, R. J. Kumar, H. Goerls, J. Bergquist and O. Johansson, *Inorg. Chem.*, 2009, **48**, 3228-3238.
41. J. Wang, E. A. Medlycott, G. S. Hanan, F. Loiseau and S. Campagna, *Inorg. Chim. Acta*, 2007, **360**, 876-884.
42. M. Waechtler, J. Kuebel, K. Barthelmes, A. Winter, A. Schmiedel, T. Pascher, C. Lambert, U. S. Schubert and B. Dietzek, *Phys. Chem. Chem. Phys.*, 2016, **18**, 2350-2360.
43. M.-P. Santoni, E. A. Medlycott, G. S. Hanan, B. Hasenknopf, A. Proust, F. Nastasi, S. Campagna, C. Chiorboli, R. Argazzi and F. Scandola, *Dalton Trans.*, 2009, DOI: 10.1039/b820444f, 3964-3970.
44. C. Mikel and P. G. Potvin, *Inorg. Chim. Acta*, 2001, **325**, 1-8.
45. C. Goze, C. Sabatini, A. Barbieri, F. Barigelletti and R. Ziessel, *Inorg. Chem.*, 2007, **46**, 7341-7350.
46. M. Cavazzini, S. Quici, C. Scalera, F. Puntoriero, G. La Ganga and S. Campagna, *Inorg. Chem.*, 2009, **48**, 8578-8592.
47. T. Schlotthauer, G. A. Parada, H. Görls, S. Ott, M. Jäger and U. S. Schubert, *Inorg. Chem.*, 2017, **56**, 7720-7730.
48. M. Jäger, L. Eriksson, J. Bergquist and O. Johansson, *J. Org. Chem.*, 2007, **72**, 10227-10230.
49. U. S. Schubert, K. Barthelmes and A. Winter, *Eur. J. Inorg. Chem.*, 2016, **2016**, 5132-5142.
50. H. El-Batal, K. Guo, X. Li, C. Wesdemiotis, C. N. Moorefield and G. R. Newkome, *Eur. J. Org. Chem.*, 2013, **2013**, 3640-3644.
51. K. Barthelmes, J. Kuebel, A. Winter, M. Waechtler, C. Friebe, B. Dietzek and U. S. Schubert, *Inorg. Chem.*, 2015, **54**, 3159-3171.
52. L. A. Fredin and P. Persson, *J. Chem. Phys.*, 2016, **145**, 104310/104311-104310/104318.
53. C. Kreitner, E. Erdmann, W. W. Seidel and K. Heinze, *Inorg. Chem.*, 2015, **54**, 12046-12046.

54. C. Kreitner and K. Heinze, *Dalton Trans.*, 2016, **45**, 13631-13647.
55. Note that the search of the true transition state led to convergence problems.
56. A. Wild, A. Winter, F. Schlutter and U. S. Schubert, *Chem. Soc. Rev.*, 2011, **40**, 1459-1511.
57. U. S. Schubert, A. Winter and G. R. Newkome, *Terpyridine-based Materials: For Catalytic, Optoelectronic and Life Science Applications*, Wiley, 2012.

Supporting Information

Exploring the coordination mechanism towards multi-functionalized Ru^{II} polypyridyl-type sensitizer: An experimental and computational study

Tina Mede, Michael Jäger,* and Ulrich S. Schubert*

Table of content

1. Instrumentation

Thin-layer chromatography was performed on precoated aluminum sheets (silica gel 60 F254, Merck). Flash column chromatography was carried out on a Biotage Isolera One system using Biotage SNAP Cartridges (KP-Sil). The Biotage Initiator Sixty Microwave synthesizer was used for microwave reactions.

^{1}H and ^{13}C NMR spectra were recorded on a Bruker AC 250 (250 MHz), Bruker AC 300 (300 MHz) or a Bruker AC 600 (600 MHz) spectrometer at 298 K. Chemical shifts are reported in parts per million (ppm, δ scale) relative to the residual signal of the deuterated solvent.[1]

ESI-TOF-MS measurements were performed on a microTOF (Bruker Daltonics GmbH) mass spectrometer, which was equipped with an automatic syringe pump for sample injection. The pump was supplied from KD Scientific. It was operated in the positive ion mode. The standard electrospray ion (ESI) source was used to generate ions. Dichloromethane or acetonitrile were used as solvents. The ESI-Q-TOF-MS instrument was calibrated in the m/z range 50 to 3,000 amu using an internal calibration standard (Tunemix solution) which was supplied from Agilent.

2. Syntheses

All chemicals and solvents were purchased from Sigma-Aldrich, Fluka, ABCR, Acros Organics, Alfa Aesar, VWR, Apollo as well as Carl Roth and were used without further purification unless otherwise specified. Reported ligands and ruthenium complexes were prepared as described in the literature:

Ligands: 2,6-Di(quinolin-2-yl)pyridine (**L1**),[2] 2,6-di(quinolin-8-yl)pyridin-4-ol (**L2**),[2] 8,8'-(4-(4-bromophenyl)pyridine-2,6-diyl)diquinoline (**L4**),[2] 2,6-bis(4-(4-bromophenyl)quinolin-8-yl)pyridine (**L5**),[3] 2,6-bis(4-(4-methoxyphenyl)quinolin-8-yl)pyridine (**L6**),[4] 8,8'-(4-(4-bromophenyl)pyridine-2,6-diyl)bis(4-(p-tolyl)quinoline) (**L7**),[4] 8,8'-(4-(4-bromophenyl)pyridine-2,6-diyl)bis(4-(4-methoxyphenyl)quinoline) (**L8**),[4] 8,8'-(4-(4-((triisopropylsilyl)-ethynyl)phenyl)pyridine-2,6-diyl)diquinoline (**L12**),[5] 4'-(p-tolyl)-2,2':6',2''-terpyridine (**L13**).[6]

Ru precursor: $(iPrSPh)_2(MeOH)RuCl_3$,[7] [Ru(**L1**)$(MeCN)_3$]$(PF_6)_2$,[8] [Ru(**L2**)$(MeCN)_3$]$(PF_6)_2$,[8] [Ru(**L4**)$(MeCN)_3$]$(PF_6)_2$,[3] [Ru(**L7**)$(MeCN)_3$]$(PF_6)_2$[4] were prepared according to their literature procedures.

2.1. Overview of ligands

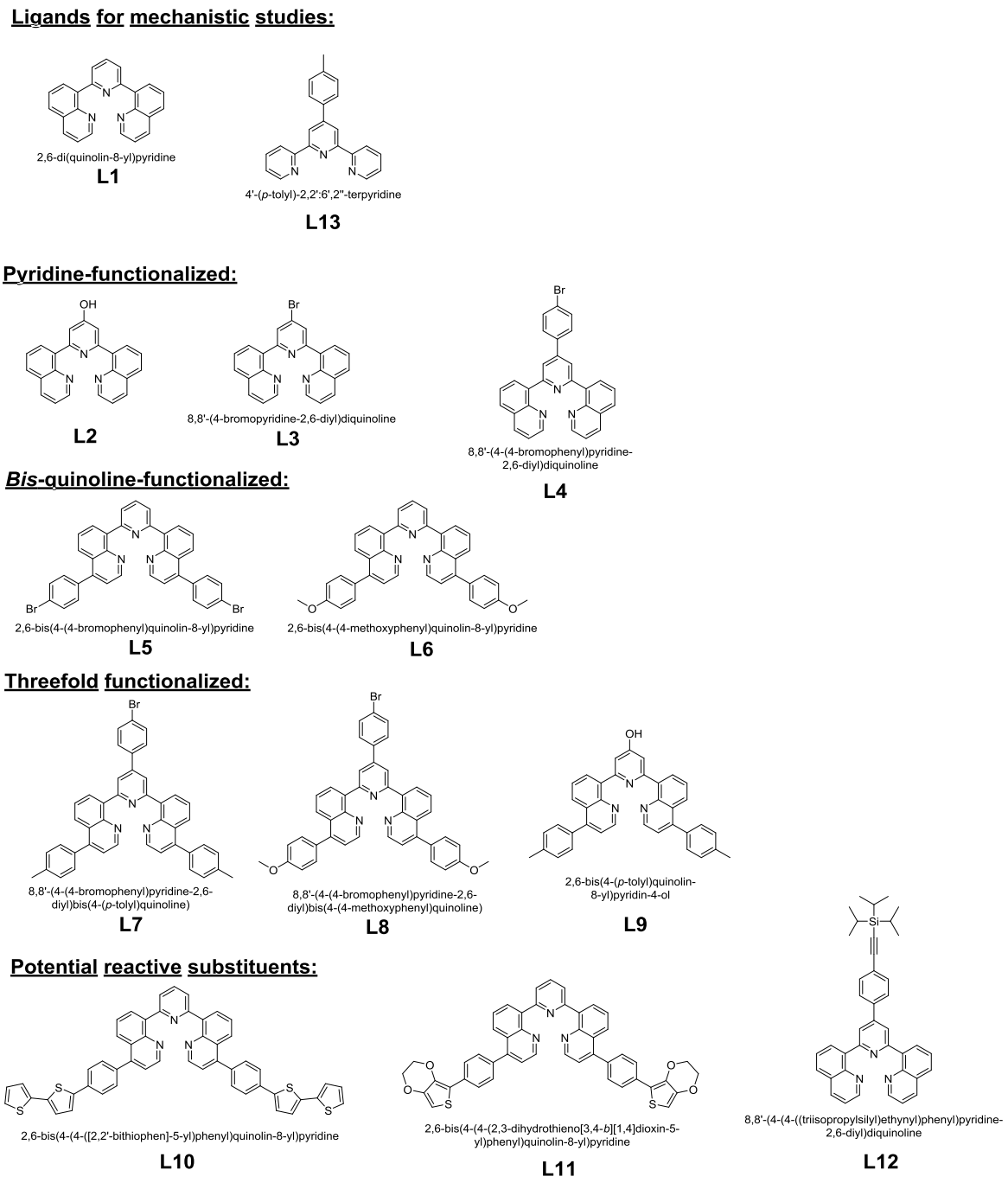

Figure S1. Schematic representation of the overview of ligand structures.

2.2. Coordination studies

General procedure: The experiments were carried out at the stated conditions (temperature, solvent, reagents, time) in a NMR tube using oil bath heating. After cooling to room temperature, ^{1}H NMR spectra were recorded on a 300 MHz spectrometer (16 scans), and the residual solvent signals served as the internal standard for quantification due its high boiling point. In case of temperature series, the samples were subjected to the next temperature step (going from low to high temperatures and/or extended reaction times).

2.2.1. Solvent exchange of $[Ru(dqp)(MeCN)_3]^{2+}$

According to the general procedure, using $[Ru(dqp)(MeCN)_3](PF_6)_2$ (20 mg, 0.024 mmol) and d_7-DMF (0.5 mL). ^{1}H NMR spectra were taken after heating to 70 °C for 16 hours, followed by heating to 120 °C for 4 hours (full conversion of educt observed, Figure S3).

After cooling to rt, MeCN (0.050 mL) was added and the solution was kept at room temperature for 24 hours. As no reaction was observed, additional MeCN (0.050 mL) was added and the temperature was raised stepwise as follows: (a) Heating to 40 °C for 24 hours, (b) addition of more MeCN (0.050 mL) and heating to 70 °C for 24 hours, and (c) heating to 80 °C for 16 hours (full regeneration of educt observed, Figure S4).

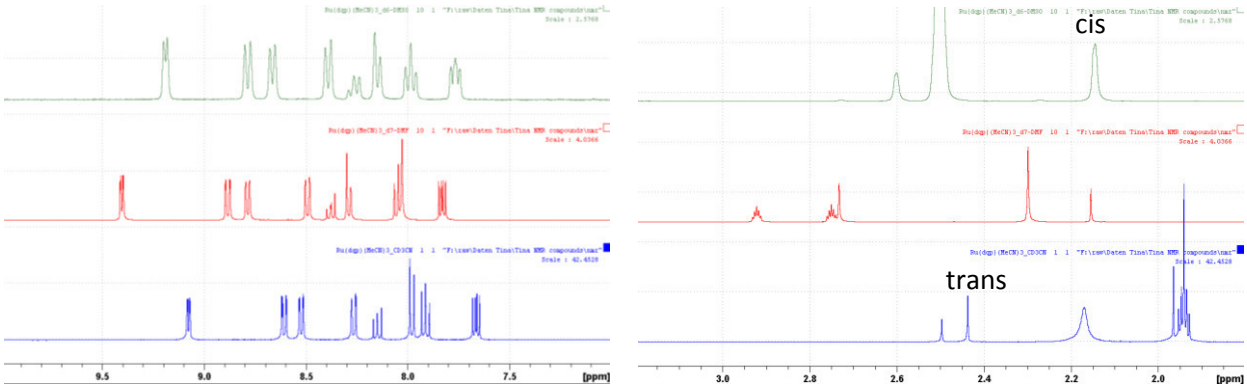

Figure S2. ^{1}H NMR spectra (300 MHz) of the $[Ru(dqp)(MeCN)_3]$ in d_7-DMF (top), d6-DMSO (middle) and CD_3CN (bottom) of the aromatic region (left) and the aliphatic region (right). Note the systematic high-field shifts due to the deshielding effect on all resonances caused by the solvent (d_7-DMF < d6-DMSO < CD_3CN)

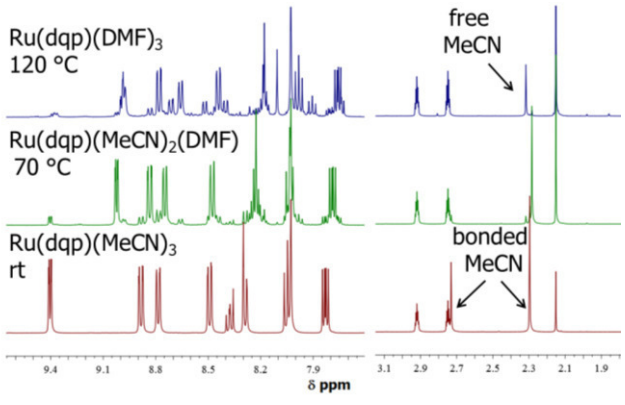

Figure S3. ^{1}H NMR spectra (300 MHz, d_7-DMF) taken during solvent exchange from $[Ru(dqp)(MeCN)_3]$ by d_7-DMF at given temperatures and times. Note the complete stepwise exchange of the *trans*-MeCN around 70 °C and the two remaining *cis*-MeCN ligands around 120 °C to yield the tentatively entitled $[Ru(dqp)(d_7\text{-DMF})_3]^{2+}$.

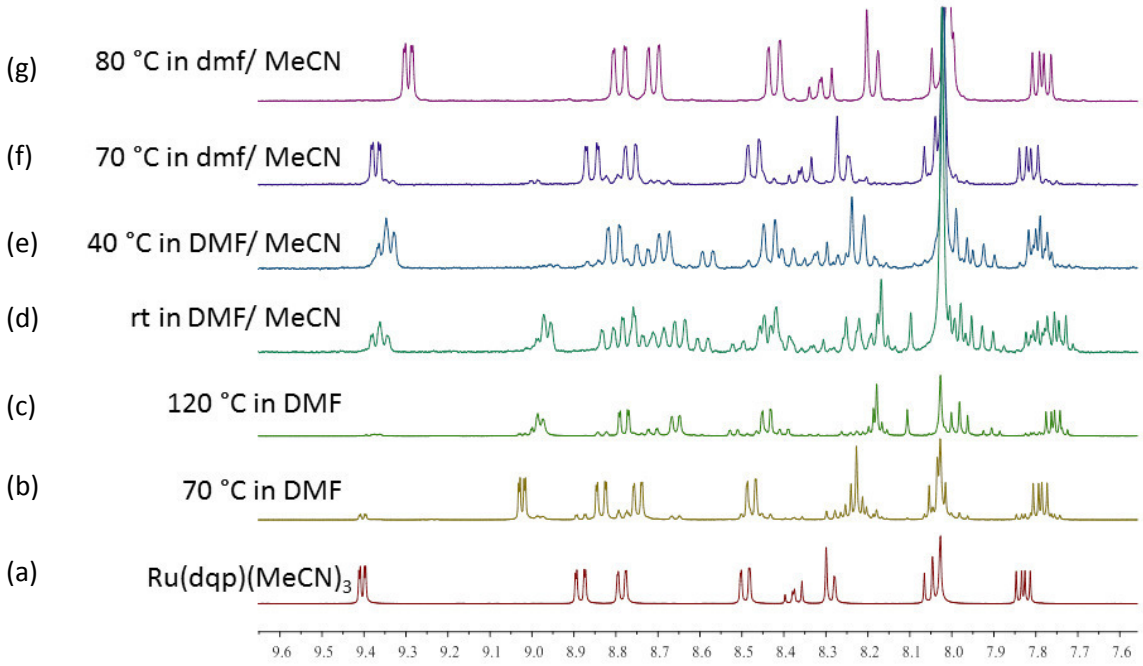

Figure S4. ^{1}H NMR spectra (300 MHz, aromatic region) taken during solvent exchange from $[Ru(dqp)(MeCN)_3]^{2+}$ by d_7-DMF (a–c) to form tentatively assigned $[Ru(dqp)(DMF)_3]^{2+}$, and reversal solvent exchange with added CD_3CN (d–g) at given temperatures and times. Note the apparent shifts of the signal sets due to different solvent compositions (d_7-DMF/MeCN), but the complete regeneration of the $[Ru(dqp)(MeCN)_3]^{2+}$ (a *vs.* g). The high-field shift arises from admixed CD_3CN, causing the shift as demonstrated for an authentic sample of $[Ru(dqp)(MeCN)_3]^{2+}$ (Figure S2).

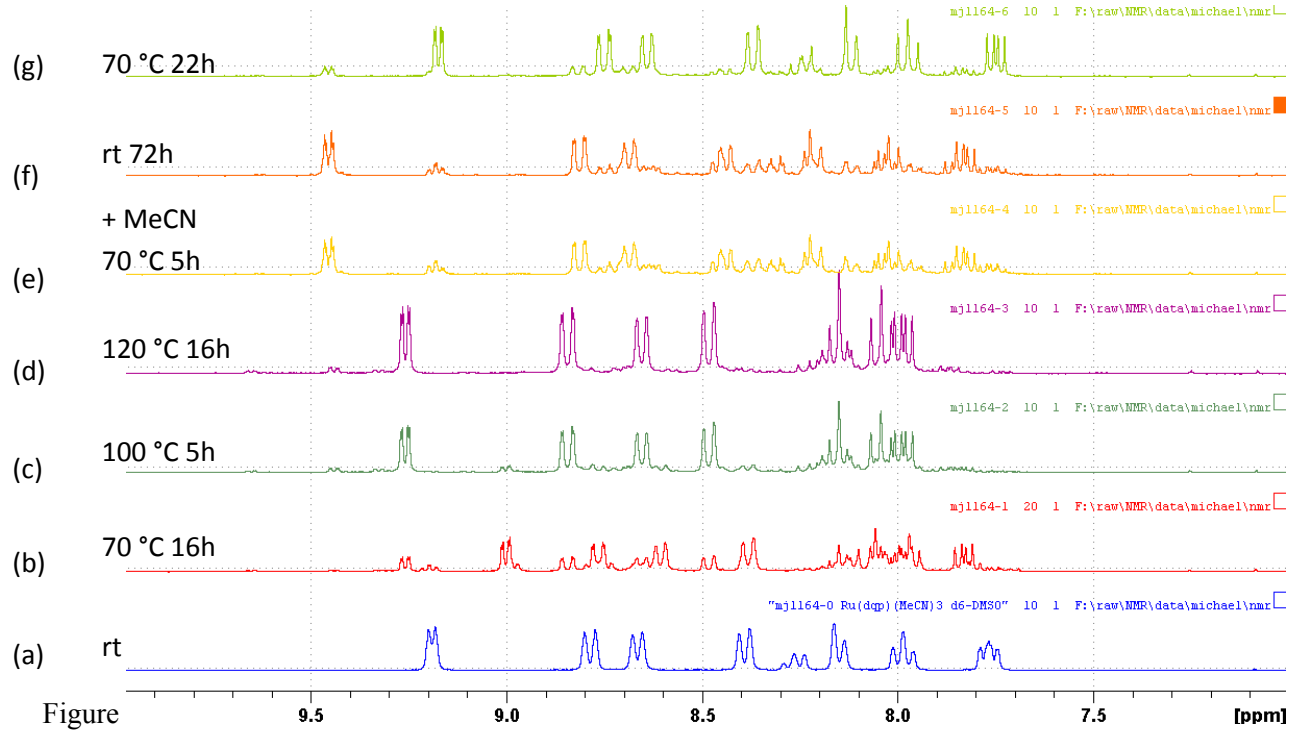

Figure S5. ^{1}H NMR spectra (300 MHz, d_6-DMSO, aromatic region) taken during solvent exchange from $[Ru(dqp)(MeCN)_3]^{2+}$ by d_6-DMSO (a–d) to form tentatively assigned $[Ru(dqp)(d_6\text{-DMSO})_3]^{2+}$, and reversal solvent exchange with added CD_3CN (e–g) at given temperatures and times. Note the apparent shifts of the signal sets due to different solvent compositions (d_7-DMF/MeCN), but the regeneration of the $[Ru(dqp)(MeCN)_3]^{2+}$ (a *vs.* g).

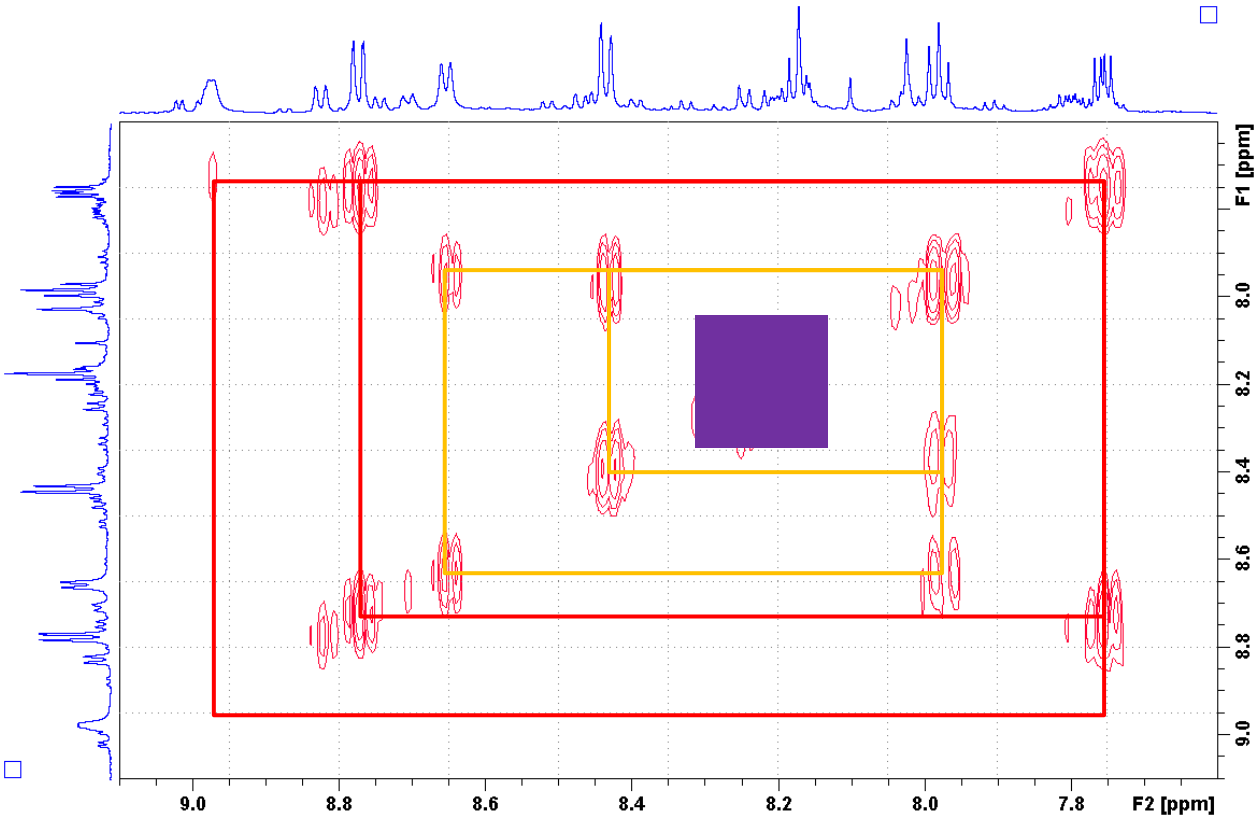

Figure S6. COSY spectrum (300 MHz, d_7-DMF, aromatic region) of entitled [Ru(dqp)(d_7-DMF)$_3$] illustrating the main spin systems marked in red, yellow and purple. See Figure S8a for proton assignment.

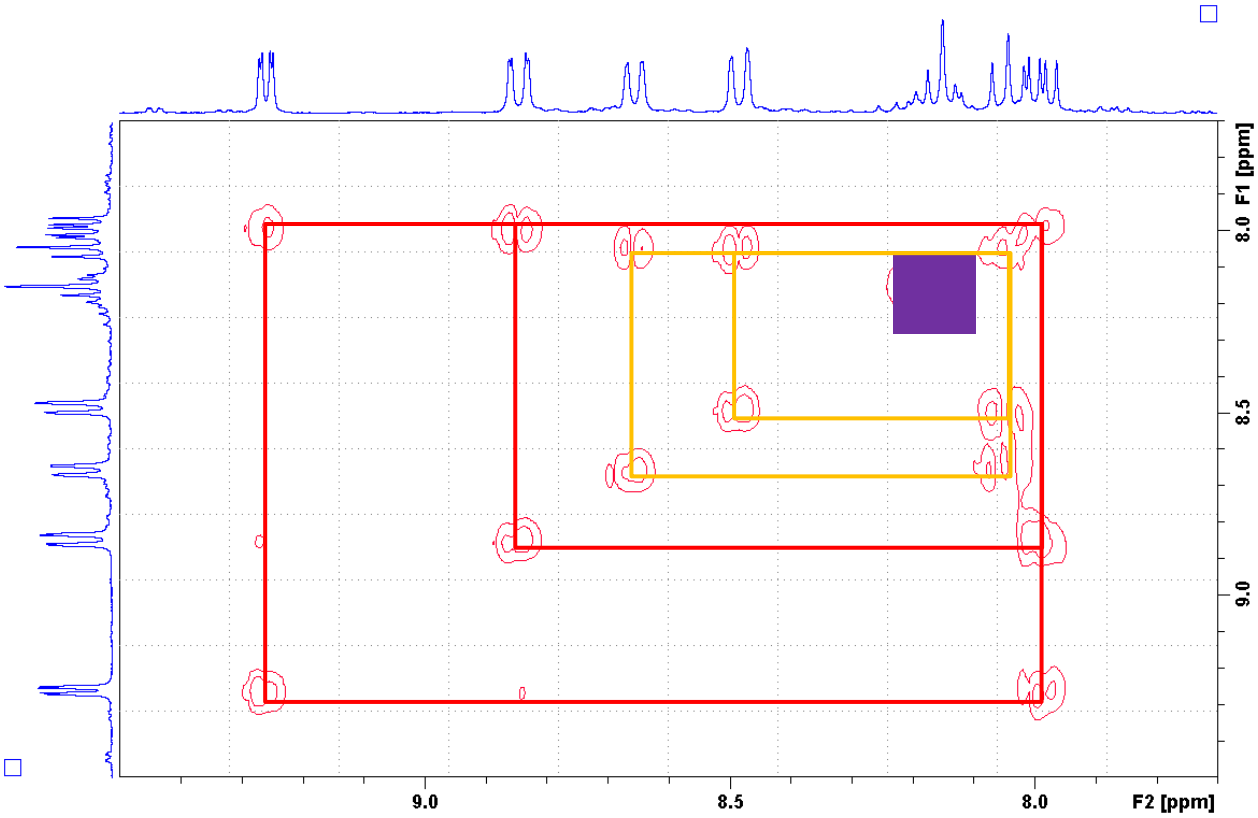

Figure S7. COSY spectrum (300 MHz, d_6-DMSO, aromatic region) of entitled [Ru(dqp)(d_6-DMSO)$_3$] illustrating the main spin systems marked in red, yellow and purple. See Figure S8a for proton assignment.

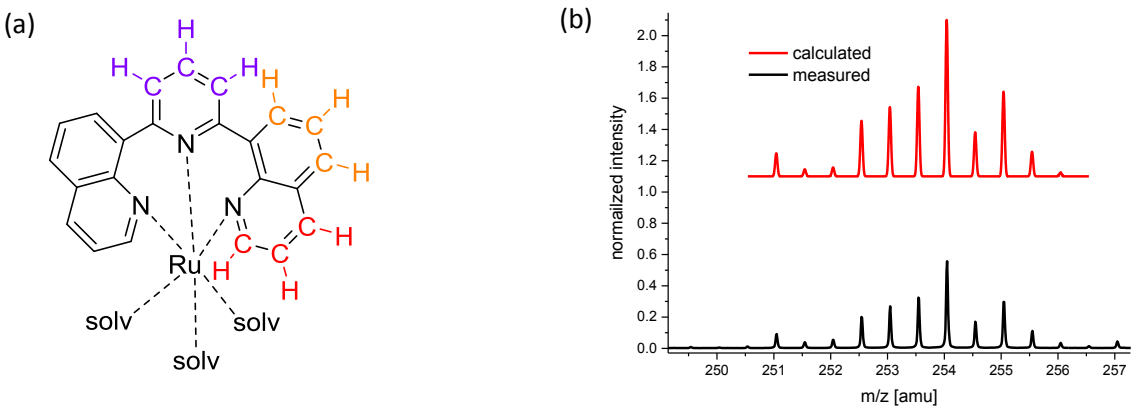

Figure S8. (a) Chemical structure of $[Ru(dqp)(solv)_3]^{2+}$ with characteristic spin systems of the pyridine subunit (purple) and the two sets in quinoline (yellow, and red). (b) ESI-ToF-MS spectrum and calculated isotope pattern of $[Ru(dqp)(DMF)_1]^{2+}$. Note that various undefined Ru specimen were also observed (not shown).

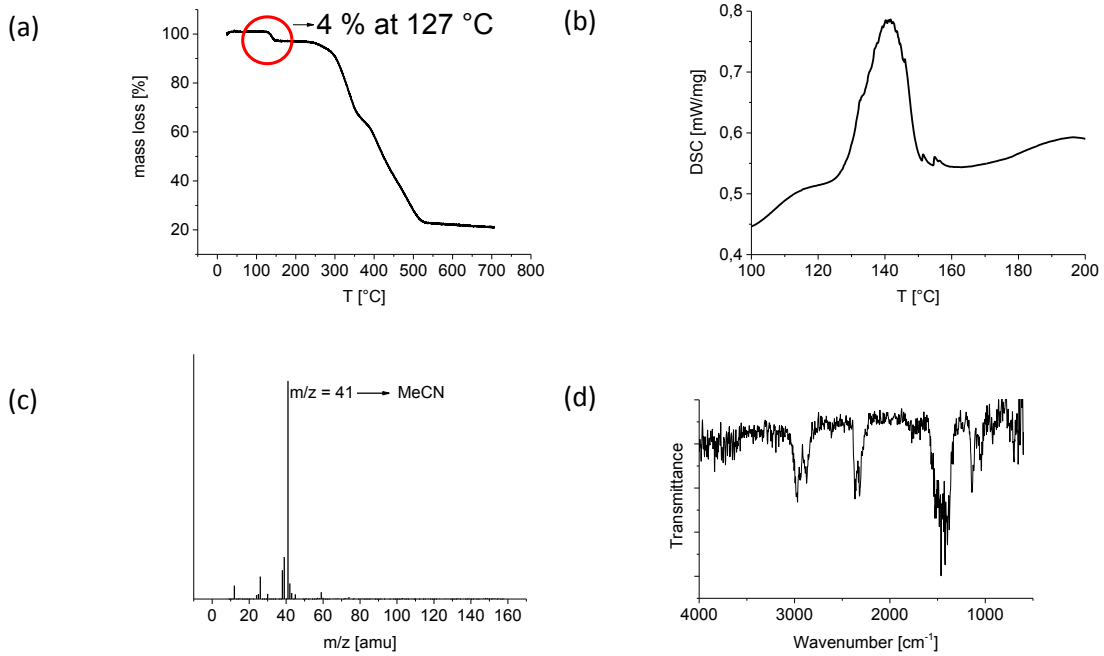

Figure S9. (a) TGA measurement of $[Ru(dqp)(MeCN)_3](PF_6)_2$, b) DSC measurement of $[Ru(dqp)(MeCN)_3](PF_6)_2$, c) MS spectrum of the weight loss at 127 °C; d) IR spectrum of the weight loss at 127 °C.

2.2.2. Coordination *via* $[Ru(dqp)(DMF)_3]^{2+}$ intermediate

$[Ru(dqp)(MeCN)_3](PF_6)_2$ (20 mg, 0.024 mmol) was dissolved in d_7-DMF (0.5 mL) in a NMR tube and heated to 120 °C for 16 h. After cooling to room temperature and confirmation of quantitative conversion by ^{1}H NMR spectroscopy, one equivalent of dqp (7.9 mg, 0.024 mmol) was added. The reaction progress was monitored as described in Section 2.2, *i.e.*, starting at 60 °C for 16 hours and later in 10 °C steps (^{1}H NMR spectra in Figure S14a). Note the onset of the product formation around 90 °C and the complete conversion at 130 °C (Figure S14b).

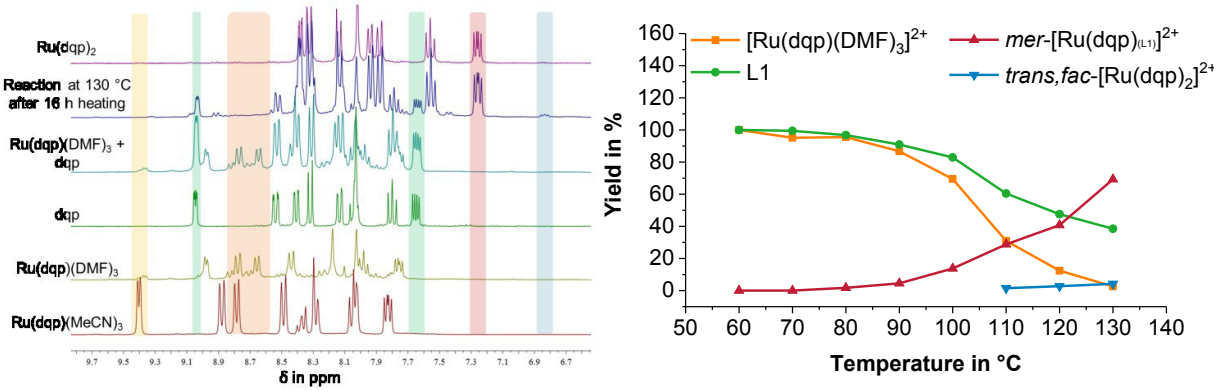

Figure S10. Left: Progress of the reaction with L1 in DMF at different temperatures staring from $[Ru(dqp)(DMF)_3]^{2+}$. Right: Kinetic analysis of characteristic species ($[Ru(dqp)(DMF)_3]^{2+}$ (orange), L1 (green) and $[Ru(dqp)_2]^{2+}$ as the meridonal isomer (red) and trans-facial isomer (blue)). Note the onset of product formation above 90 °C.

The $[Ru(dqp)(DMF)_3]^{2+}$ intermediate was prepared individually in a NMR tube as described above, and residual DMF was removed at 120 °C by a N_2 flow (reduced volume to ca. 0.1 mL). Next, one equivalent of terpyridine-based **L13** (7.63 mg, 0.024 mmol) and the solvent mixture (see Table S1) were added at room temperature, and a ^{1}H NMR was measured for subsequent analysis. The reaction progress was monitored as described in Section 2.2, *i.e.*, starting at 40 °C for 16 hours and later in 10 °C steps (Figure S11). Note that after 100 °C no further conversion was observed.

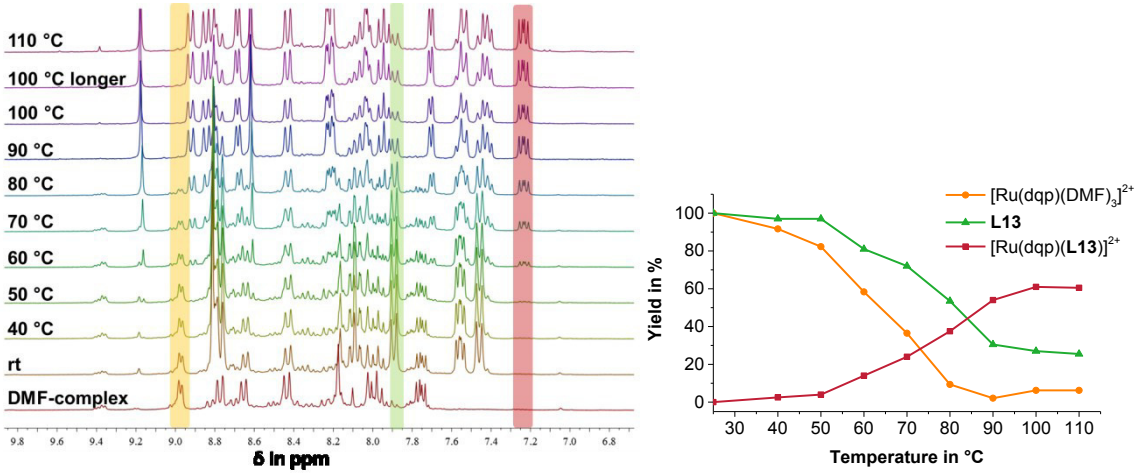

Figure S11. Left: Progress of the reaction with terpyridine-based L13 in DMF at different temperatures staring from $[Ru(dqp)(DMF)_3]^{2+}$. Right: Kinetic analysis of characteristic ($[Ru(dqp)(DMF)_3]^{2+}$ (orange), terpyridine-based L13 (green) and $[Ru(dqp)(L13)]^{2+}$ (red)). Note the onset of product formation around 60 °C.

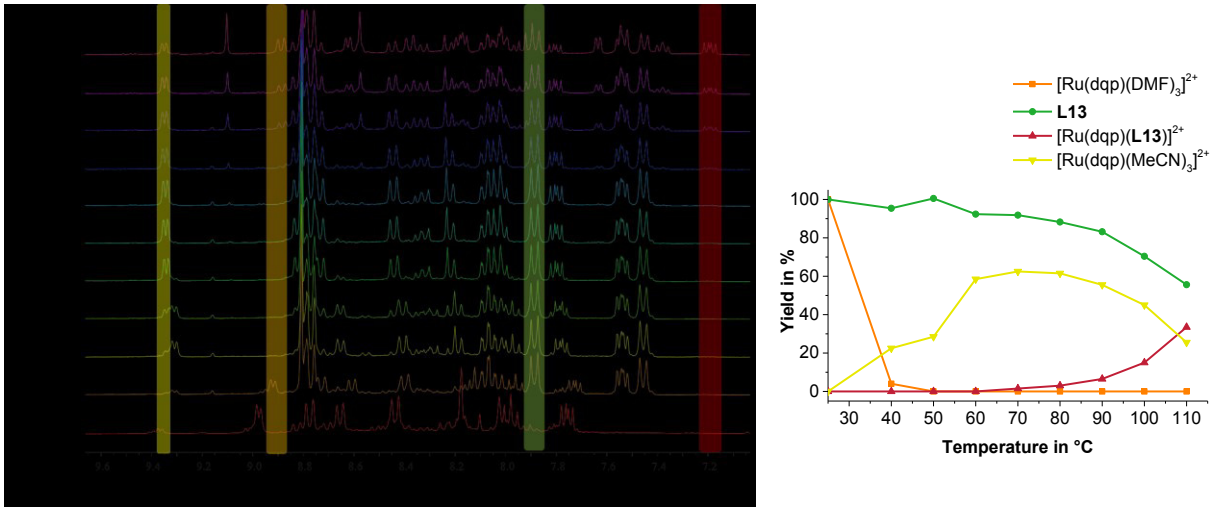

Figure S12. Left: Progress of the reaction with terpyridine-based L13 in DMF/acetonitrile mixture at different temperatures starting from $[Ru(dqp)(DMF)_3]^{2+}$. Right: Kinetic analysis of characteristic species ($[Ru(dqp)(DMF)_3]^{2+}$ (orange), terpyridine-based L13 (green), $[Ru(dqp)(L13)]^{2+}$ (red), and $[Ru(dqp)(MeCN)_3]^{2+}$ (yellow)).

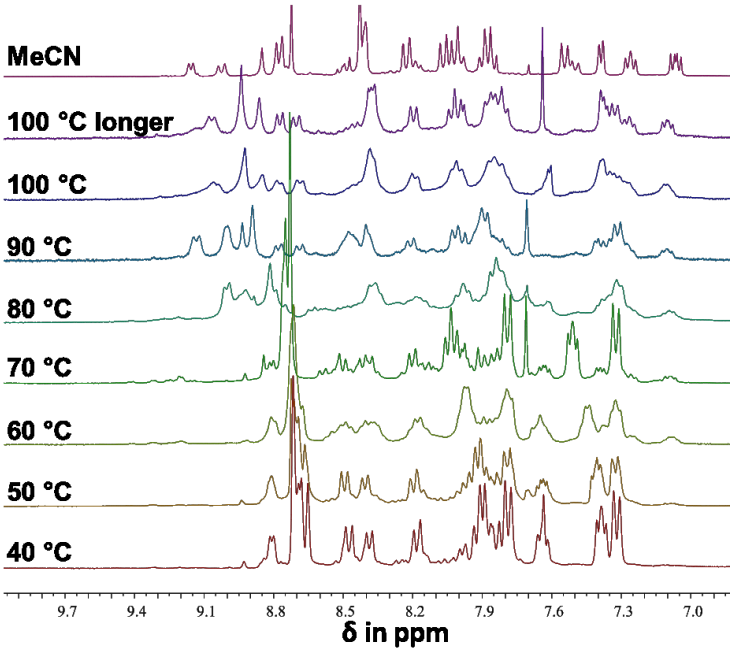

Figure S13. Progress of the reaction of terpyridine-based L13 in DMF/chloroform mixture at different temperatures starting from $[Ru(dqp)(MeCN)_3]^{2+}$. Note the broad overlapping signals that are tentatively assigned to insolubility and the chemical shift differences due to changing solvent composition due to evaporating $CHCl_3$, which preclude a definite assignment. Nevertheless, the onset of product formation occurs at 60 °C as judged from the signal around 7.1 ppm.

Table S1. Overview of reaction with $[Ru(dqp)(solvent)_3]$ complexes with terpyridine-based L13 in different solvent mixtures.

entry	precursor	Solvent Ratio 1/4	Onset of coordination [°C][a]	Yield at 100 °C [%][b]
1	$[Ru(dqp)(DMF)_3]^{2+}$	DMF	60	61
2	$[Ru(dqp)(DMF)_3]^{2+}$	DMF/MeCN[c]	90	39

3	$[Ru(dqp)(DMF)_3]^{2+}$	DMF/$CHCl_3$[c]	60	63
4	$[Ru(dqp)(DMF)_3]^{2+}$	DMF/MeOH[c]	-[c]	-[c]
5	$[Ru(dqp)(DMF)_3]^{2+}$	DMF/THF[c]	-[c]	-[c]
6	$[Ru(dqp)(DMF)_3]^{2+}$	DMF/CH_2Cl_2[c]	-[c]	-[c]
7	$[Ru(dqp)(MeCN)_3]^{2+}$	DMF	60	87

a) Onset estimated by ca. 10% product formation. b) Determined by ^{1}H NMR analysis using an internal standard. c) No product formation observed. C) DMF/solvent vol.-ratio ¼.

2.2.3. Direct coordination from $[Ru(dqp)(MeCN)_3]^{2+}$

General procedure: $[Ru(dqp)(MeCN)_3](PF_6)_2$ (20 mg, 0.024 mmol), 1 eq. of ligand (0.024 mmol), and d_7-DMF (0.5 mL) were placed in a NMR tube at room temperature and a ^{1}H NMR spectrum was recorded for analysis. The reaction progress was monitored as described in Section 2.2, *i.e.,* starting at 60 °C for 16 hours and later in 10 °C steps.

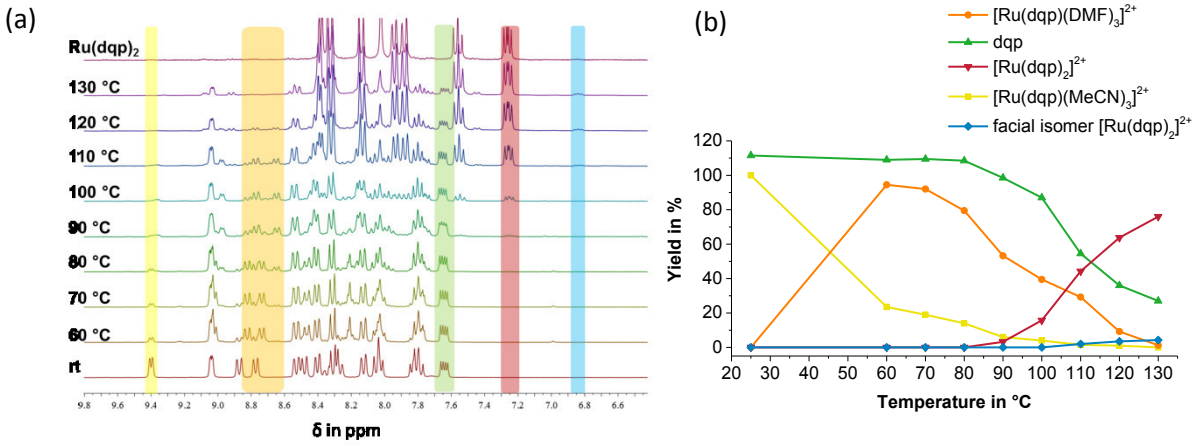

Figure S14. (a) Progress of the reaction with dqp in DMF at different temperatures starting from $[Ru(dqp)(MeCN)_3]^{2+}$. (b) Kinetic analysis of characteristic species: $[Ru(dqp)(DMF)_3]^{2+}$ (orange), free dqp (green), $[Ru(dqp)_2]^{2+}$ (red), $[Ru(dqp)(MeCN)_3]^{2+}$ (yellow), and facial isomer of $[Ru(dqp)_2]^{2+}$ (blue).

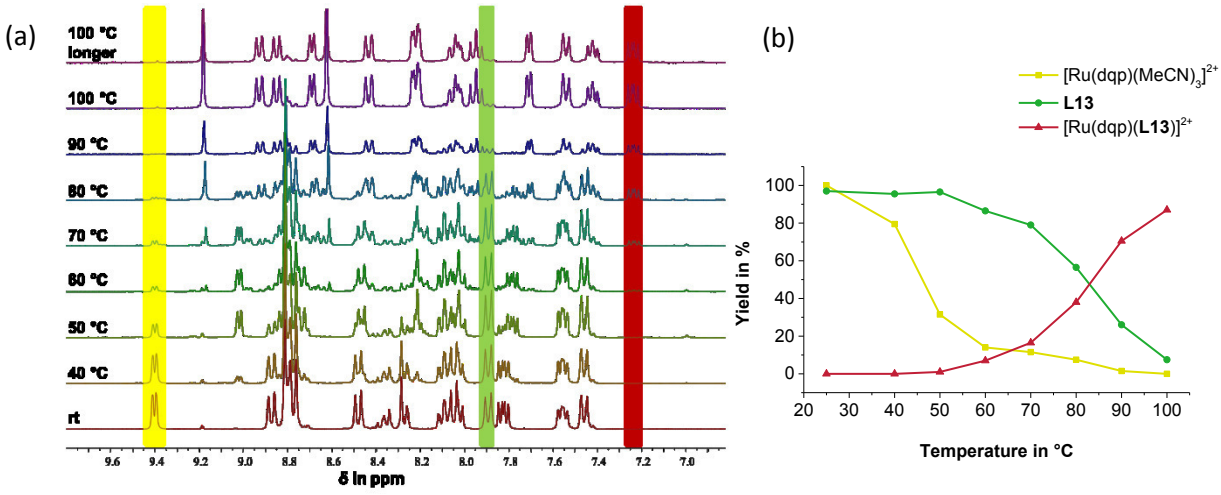

Figure S15. (a) Progress of the reaction with terpyridine-based L13 in DMF at different temperatures starting from $[Ru(dqp)(MeCN)]^{2+}$. (b) Kinetic analysis of characteristic species: $[Ru(dqp)(MeCN)_3]^{2+}$ (yellow), terpyridine-based L13 (green), and $[Ru(dqp)(L13)]^{2+}$ (red).

2.2.4. Screening for functionalized $[Ru(L7)(L1)]^{2+}$

Exemplarily kinetic analysis: $[Ru(\mathbf{L7})(MeCN)_3](PF_6)_2$ (24 mg, 0.02 mmol), dqp (13.6 mg, 0.02 mmol) and d_7-DMF (0.5 mL) were added to a NMR tube and heated to 140 °C. Individual ^{1}H NMR spectra were recorded after the given times (allowing the sample to cool to room temperature prior to measurement and afterwards continuing the reaction at 140 °C, Figure S16). Note the high conversion already after 4 hours.

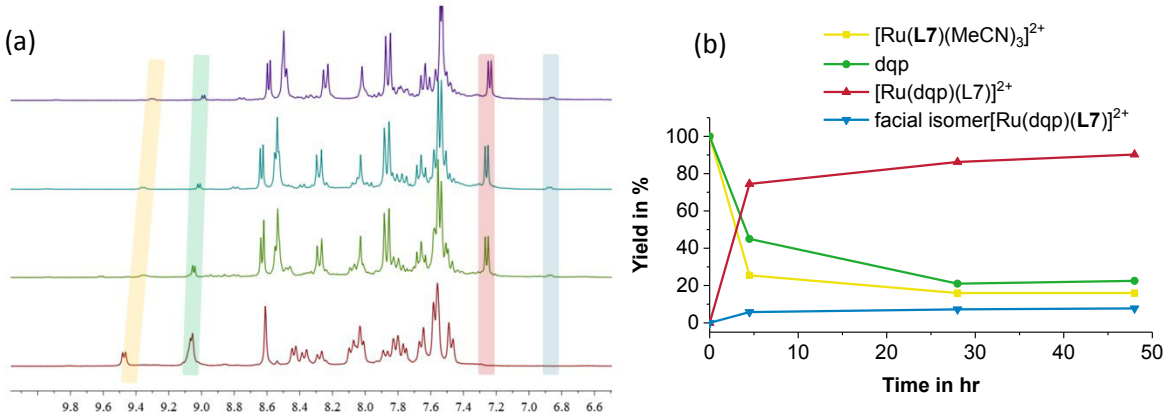

Figure S16. (a) Progress of the reaction of multi-arylated precursor $[Ru(L7)(MeCN)_3]^{2+}$ with dqp in d_7-DMF at different temperatures. (b) Kinetic analysis of characteristic species: $[Ru(L7)(MeCN)_3]^{2+}$ (yellow), dqp (green), $[Ru(dqp)(L7)]^{2+}$ (red) and the facial isomer (blue).

2.3. Ligand syntheses

8,8'-(4-Bromopyridine-2,6-diyl)diquinoline (L3):

New route from **L2** using PBr_3: **L2** (100 mg, 0.28 mmol) was dissolved in PBr_3 (2.8 mL, 30 mmol) and heated at 140 °C overnight. The solid mixture were quenched with water and neutralized with aqueous NaOH. Afterwards the product was extracted with dichloromethane, the solvent was evaporated under reduced pressure and the crude product was purified via flash column chromatography on silica using a gradient of dichloromethane/methanol to obtain 80 mg (68%) of the brominated ligand.

New route from L2 using $POBr_3$: **L2** (100 mg, 0.28 mmol) and $POBr_3$ (2.1 g, 7.3 mmol) were stored in a microwave tube and heated under inert conditions to 140 °C overnight. The solid mixture were quenched with water and neutralized with aqueous NaOH. Afterwards the product was extracted with dichloromethane, the solvent was evaporated under reduced pressure and the crude product was purified via flash column chromatography on silica using dichloromethane: methanol gradient as eluent was applied to obtain 60 mg (51%) of the brominated ligand.

The analytical data matched reported data.[2]

2,6-Bis(4-p-tolylquinolin-8-yl)pyridin-4-ol (L9): 2,6-Di(2'-aminophenyl)pyridin-4-ol (3.1 mmol) and the substituted 3-chloro-1-propan-1-one (6.8 mmol) were dissolved in THF (80 mL), NEt_3 (2.4 mL) were added and heated to reflux. After ^{1}H NMR showed full conversion, the reaction mixture was allowed to cool to room temperature; THF was evaporated under reduced pressure and diluted with dichloromethane (50 mL). The solution was neutralized with aqueous Na_2CO_3 until the

precipitate was dissolved. The organic layer was washed with H_2O and dried over Na_2SO_4, before it was adsorbed on silica and purified by flash column chromatography (dichloromethane/ethyl acetate 100/0 to 70/30 gradient) to isolate the *N*-alkylated intermediate (93%). The intermediate (3.1 mmol), triphenylchloromethane (7.75 mmol) and P_2O_5 (13.2 mmol) were dissolved in H_3PO_4 (85%, 12 mL) and heated to 90 °C until thin layer chromatography showed no further conversion. The brown solution was cooled to room temperature, diluted with H_2O (30 mL) and dichloromethane (50 mL) and neutralized with aqueous NaOH (3 M). After extraction and drying over Na_2SO_4, the crude product was adsorbed on silica and purified by flash column chromatography (dichloromethane/ ethyl acetate gradient) to isolate the product, which was dissolved in hot THF and crystallized in the fridge (73%). ^{1}H NMR (250 MHz, CD_2Cl_2): δ 15.42 (s, 1H, OH), 8.79 (d, J = 4.4 Hz, 2H, H1), 8.31 (d, J = 7.3 Hz, 2H, H8), 8.13 (d, J = 8.4 Hz, 2H, H6), 7.67 (t, J = 8.0 Hz, 2H, H7), 7.49 – 7.35 (m, 10H, H2, Ph), 7.05 (s, 2H, H9), 2.48 (s, 6H, CH3). ^{13}C NMR (63 MHz, CD_2Cl_2): δ 150.4, 149.7, 148.7, 146.6, 139.5, 135.3, 130.8, 130.0, 130.0, 129.9, 129.2, 128.2, 127.0, 122.3, 116.6, 21.6. MS: (MALDI-Tof-MS)[$C_{37}H_{27}N_3O]^{H+}$ m/z: 530.349 EA: calc: C: 83.91% H: 5.14% N: 7.93%; found: C: 83.66% H: 5.06% N: 8.10%. mp = 330 °C decomposition.

2,6-Bis(4-(4-([2,2'-bithiophen]-5-yl)phenyl)quinolin-8-yl)pyridine (**L10**): A microwave tube was charged with 2,6-bis[4-(4-bromophenyl)quinoline-8-yl]pyridine (1.172 g, 1.82 mmol), (5-bithienyl) boronic acid pinacol ester (1.281 g, 4,39 mmol), $Pd(PPh_3)_4$ (0.092 g, 0.08 mmol), Na_2CO_3 (0.506 g, 4.88 mmol), and a 1,2-dimethoxyethane/water mixture (10 mL, vol.-ratio 7/1). After sealing the tube, the mixture was purged with nitrogen for 10 minutes via a cannula. The reaction mixture was heated for 12 h at 85 °C using microwave irradiation. Afterwards the crude reaction mixture was partitioned in chloroform (200 mL) and aqueous ammonium chloride solution (200 mL, 5%). The organic layer was removed, washed with water, dried over Na_2SO_4, filtered and the solvent was removed under reduced pressure. The product was purified by flash column chromatography using the gradient mode and starting with an eluent mixture of toluene/ methanol 95/5 to 85/15 and finally dichloromethane/methanol 85/15. The product was recrystallized in THF to receive the desired ligand (0.64 g, 44%). ^{1}H NMR (600 MHz, d_6-DMSO): δ 9.03 (d, J = 4.3 Hz, 2H), 8.25 (dd, J = 7.2, 1.4 Hz, 2H), 8.14 – 8.09 (m, 2H), 8.02 (ddd, J = 8.2, 4.2, 2.8 Hz, 3H), 7.94 – 7.88 (m, 4H), 7.75 (dd, J = 8.4, 7.2 Hz, 2H), 7.70 – 7.66 (m, 4H), 7.65 (d, J = 3.8 Hz, 2H), 7.58 (d, J = 4.3 Hz, 2H), 7.55 (dd, J = 5.1, 1.1 Hz, 2H), 7.42 – 7.36 (m, 4H), 7.13 (dd, J = 5.1, 3.6 Hz, 2H). ^{13}C NMR not recorded due to insufficient solubility. ESI-ToF-MS: $[C_{51}H_{31}N_3S_4]^{H+}$ calc: 814.1474 amu, found: 814.1465 amu, error: 1.1 ppm.

2,6-Bis(4-(4-(2,3-dihydrothieno[3,4-b][1,4]dioxin-5-yl)phenyl)quinolin-8-yl)pyridine (L11): 2,6-Bis(4-(4-bromophenyl)quinolin-8-yl)pyridine (200 mg, 0.31 mmol), 2-(2,3-dihydrothieno[3,4-b][1,4]dioxin-5-yl)-4,4,5,5-tetramethyl-1,3,2-dioxaborolane (250 mg, 0.93 mmol), $Pd(PPh_3)_4$ (36 mg, 0.03 mmol) and Na_2CO_3 (198 mg, 1.85 mmol) were dissolved in dry DMF and purged with nitrogen for 10 min. The reaction mixture was heated to 120 °C for 48 hours. Afterwards the reaction mixture was quenched with water and extracted three times with dichloromethane, dried over Na_2SO_4, filtered and the solvent was evaporated under reduced pressure. The crude mixture was purified by flash column chromatography (two runs) using a mixture of dichloromethane/ethyl acetate 95:5 to receive the desired ligand (100 mg, 42%). ^{1}H NMR (600 MHz, CD_2Cl_2): δ 8.99 (d, J = 4.3 Hz, 2H), 8.21 (dd, J = 7.1, 1.3 Hz, 2H), 8.13 – 8.06 (m, 4H), 7.96 (t, J = 7.7 Hz, 1H), 7.93 – 7.89 (m, 4H), 7.65 (dd, J = 8.4, 7.2 Hz, 2H), 7.61 – 7.55 (m, 4H), 7.44 (d, J = 4.3 Hz, 2H), 6.38 (s, 2H), 4.43 – 4.33 (m, 4H), 4.34 – 4.24 (m, 4H). ^{13}C NMR (101 MHz, CD_2Cl_2): δ 157.6, 150.2,

149.0, 147.1, 143.2, 139.6, 136.9, 135.1, 134.1, 131.7, 130.6, 127.6, 127.2, 126.9, 126.4, 126.0, 121.9, 117.1, 98.7, 65.6, 65.2 ESI-ToF-MS: $[C_{47}H_{31}N_3O_4S_2]^{H+}$ measured: 766.1793, calculated: 766.1829, error: 4.7 ppm.

2.4. Optimized syntheses of the [Ru(N^N^N)(*N*^*N*^*N*)] complexes

General coordination procedure for the synthesis of [Ru(**L**)(**L'**)]$(PF_6)_2$: The functionalized Ru(**L**)$(MeCN)_3(PF_6)_2$ precursor (**L** = **L1**, **L2**, **L4**, or **L7**), and the free ligand **L'** (**L'** = **L1**, **L4**, **L5**, **L7**–**L11**) were placed in a microwave tube and dissolved in DMF (ratio precursor-to-ligand 1:1, see Table S2 for molarity).

Table S2. Molarity of the respective coordination reactions (typical scale 0.1-1 g).

Entry	complex	Molarity mmol
1	[Ru(dqp)(L5)]	78
2	[Ru(L7)(L7)]	34
3	[Ru(dqp)(L4)]	24
4	[Ru(dqp)(L3)]	73
5	[Ru(dqp)(L10)]	20
6	[Ru(L4)(L10)]	15
7	[Ru(dqp)(L11)]	16
8	[Ru(L7)(L9)]	46
9	[Ru(dqp)(L8)]	25
10	[Ru(L2)(L4)] (NH012)	61

The microwave tube was sealed, purged with nitrogen for 10 min and the mixture was heated to the given temperatures for the given times (Table 1). Afterwards the reaction mixture was cooled to room temperature, and the crude product was precipitated by addition of an aqueous solution NH_4PF_6. The mixture was extracted with dichloromethane, the organic layer was removed, washed with water, dried over Na_2SO_4, filtered and the solvent was removed under reduced pressure. The crude product was further purified:

Method A: By column chromatography on silica eluting with a mixture of acetonitrile, water and saturated KNO_{3aq} (40/4/1), followed by counter-ion exchange with NH_4PF_6. Minute impurities were removed by vapor diffusion of diethyl ether into an acetonitrile solution of the complex.

Method B: By column chromatography on silica eluting with dichloromethane and methanol (5%) as eluent, followed by vapor diffusion of diethyl ether into an acetonitrile solution of the complex.

[Ru(dqp)(**L1**)]$(PF_6)_2$: From ^{1}H NMR screening, analytical data matched reported data in ref. [9]. No further purification.

[Ru(dqp)(**L3**)]$(PF_6)_2$: Purification *via* Method A, analytical data matching the reported values in ref. 8.

[Ru(dqp)(**L4**)]$(PF_6)_2$: Purification *via* Method B, analytical data matching the reported values in ref. 8.

[Ru(dqp)(**L5**)]$(PF_6)_2$: Purification *via* Method A, analytical data matching the reported values in ref. 3.

[Ru(dqp)(**L8**)]$(PF_6)_2$: Purification *via* Method A. ^{1}H NMR (600 MHz, CD_3CN): δ 8.20 (t, J = 8.0 Hz, 1H), 8.17 (dd, J = 5.1, 1.3 Hz, 2H), 8.11 – 8.06 (m, 6H), 7.95 (d, J = 8.0 Hz, 2H), 7.92 – 7.89 (m, 2H), 7.89 – 7.86 (m, 4H), 7.80 – 7.77 (m, 2H), 7.75 (dd, J = 8.6, 1.0 Hz, 2H), 7.68 (dd, J = 8.2, 0.8 Hz, 2H), 7.44 (dt, J = 12.7, 5.7 Hz, 8H), 7.17 (d, J = 8.7 Hz, 4H), 7.10 (dd, J = 8.1, 5.1 Hz, 2H), 7.00 (d, J = 5.4 Hz, 2H), 3.94 – 3.89 (m, 6H). ^{13}C NMR (126 MHz, CD_3CN): δ 160.8, 158.5, 157.6, 157.3, 156.7, 149.5, 148.5, 147.0, 146.7, 138.0, 137.6, 135.2, 133.5, 132.8, 132.4, 132.2, 132.0, 131.7, 131.5, 131.3, 130.7, 129.4, 129.3, 128.5, 128.2, 128.1, 126.7, 126.7, 125.3, 125.1, 124.3, 122.2, 114.4, 55.3, 55.3. ESI-ToF-MS: $[C_{66}H_{45}BrN_6O_2Ru]^{2+}$ measured: 567.0914, calculated: 567.0910, error: 0.4 ppm.

[Ru(dqp)(**L10**)]$(PF_6)_2$: Purification *via* Method A. analytical data matching the reported values in ref. 10.

[Ru(dqp)(**L11**)]$(PF_6)_2$: Purification *via* Method A. ^{1}H NMR (500 MHz, CD_3CN): δ 8.24 – 8.17 (m, 2H), 8.15 – 8.11 (m, 4H), 8.08 (dd, J = 8.2, 1.3 Hz, 2H), 7.97 – 7.89 (m, 10H), 7.75 (ddd, J = 8.4, 7.9, 1.1 Hz, 4H), 7.69 (dd, J = 8.2, 1.0 Hz, 2H), 7.50 (dd, J = 16.8, 8.2 Hz, 6H), 7.43 (dd, J = 8.4, 7.5 Hz, 2H), 7.09 (ddd, 2H), 7.04 (d, J = 5.4 Hz, 2H), 6.51 (s, 2H), 4.41 – 4.36 (m, 4H), 4.32 – 4.27 (m, 4H). ^{13}C NMR (126 MHz, CD_3CN): δ 159.4, 158.7, 157.9, 157.8, 150.1, 148.0, 147.7, 143.7, 140.6, 139.2, 139.1, 138.7, 135.4, 134.9, 134.0, 133.8, 133.2, 133.1, 131.8, 131.2, 129.4, 129.2, 129.1, 127.8, 127.7, 126.8, 125.9, 123.1, 123.1, 116.4, 99.8, 66.0, 65.4, 64.1. ESI-ToF-MS: $[C_{70}H_{46}N_6O_4RuS_2]^{2+}$ measured: 600.1049, calculated: 600.1027, error: 2.2 ppm.

[Ru(dqp)(**L13**)]$(PF_6)_2$: From ^{1}H NMR screening, analytical data matched reported data in ref. 9. No further purification.

[Ru(**L2**)(**L4**)]$(PF_6)_2$: ^{1}H NMR (500 MHz, CD_3CN): δ 9.50 (s, br, 1H), 8.14 – 8.11 (m, 4H), 8.08 – 8.03 (m, 4H), 8.06 (s, 2H), 7.85 (d, J = 8.3 Hz, 4H), 7.77 – 7.66 (m, 8H), 7.48 – 7.41 (m, 4H), 7.37 (s, 2H), 7.10 – 7.03 (m, 4H). ESI-ToF-MS: $[C_{52}H_{33}BrN_6ORu]^{2+}$ measured: 469.0477, calculated: 469.0466, error: -1.3 ppm.

[Ru(**L4**)(**L10**)]$(PF_6)_2$: Purification *via* Method B. ^{1}H NMR (600 MHz, CD_3CN): δ 8.21 (dd, J = 12.9, 6.2 Hz, 2H), 8.20 (s, 1H), 8.18 (s, 2H), 8.14 (d, J = 5.1 Hz, 2H), 8.10 (t, J = 6.7 Hz, 4H), 7.95 – 7.92 (m, 4H), 7.90 (d, J = 7.5 Hz, 4H), 7.81 – 7.74 (m, 6H), 7.71 (d, J = 8.3 Hz, 2H), 7.57 (d, J = 7.6 Hz, 4H), 7.55 (d, J = 3.1 Hz, 2H), 7.52 (t, J = 7.7 Hz, 2H), 7.45 (t, J = 7.9 Hz, 2H), 7.41 (d, J = 5.1 Hz, 2H), 7.35 (dd, J = 12.5, 3.3 Hz, 4H), 7.11 (ddd, J = 12.0, 7.0, 4.9 Hz, 4H), 7.08 (d, J = 5.3 Hz, 2H). ^{13}C NMR (101 MHz, CD_3CN): δ 207.4, 159.5, 158.8, 158.1, 157.8, 149.8, 149.3, 148.0, 147.9, 142.4, 139.3, 138.8, 138.6, 137.6, 136.2, 136.2, 135.9, 134.4, 134.1, 133.5, 133.2, 133.2, 131.9, 131.6, 130.4, 129.3, 129.2, 127.9, 127.8, 127.7, 126.7, 126.6, 126.4, 126.2, 125.9, 125.4, 125.3, 123.3, 123.1, 30.9. ESI-ToF-MS: $[C_{80}H_{49}BrN_6RuS_4]^{2+}$ measured: 701.0563, calculated: 701.0559, error: 0.4 ppm.

[Ru(**L7**)(**L9**)]$(PF_6)_2$: Purification *via* Method B: ^{1}H NMR (500 MHz, CD_3CN): δ 8.20 (dd, J = 5.4, 1.6 Hz, 4H), 8.12 (s, 2H), 8.03 (dd, J = 7.3, 1.0 Hz, 2H), 7.92 (dd, 2H), 7.87 (dd, 2H), 7.78 (dd,

2H), 7.71 (ddd, J = 8.5, 2.7, 1.0 Hz, 4H), 7.45 – 7.36 (m, 22H), 7.04 (dd, J = 8.0, 5.4 Hz, 4H), 2.47 (s, 12H). OH not observed; ^{13}C NMR (126 MHz, CD_3CN): δ 165.4, 157.7, 157.6, 157.5, 157.3, 149.6, 149.5, 147.9, 147.3, 147.2, 139.8, 139.8, 135.3, 133.2, 133.2, 133.2, 132.6, 132.5, 132.4, 132.3, 129.7, 129.7, 129.6, 129.4, 129.4, 128.6, 128.5, 126.6, 125.5, 125.2, 125.2, 124.3, 122.4, 122.4, 116.2, 20.3. ESI-ToF-MS: $[C_{80}H_{57}BrN_6ORu]^{2+}$ measured: 649.1433, calculated: 649.1405, error: 2.2 ppm.

2.5. NMR and MS spectra

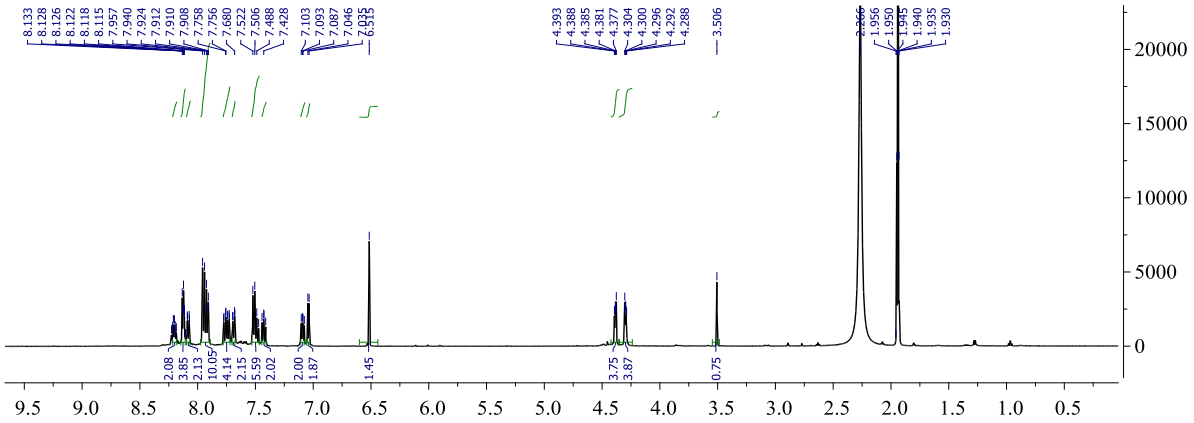

Figure S17. ^{1}H NMR spectrum of [Ru(dqp)(L11)] (CD_3CN, 500 MHz).

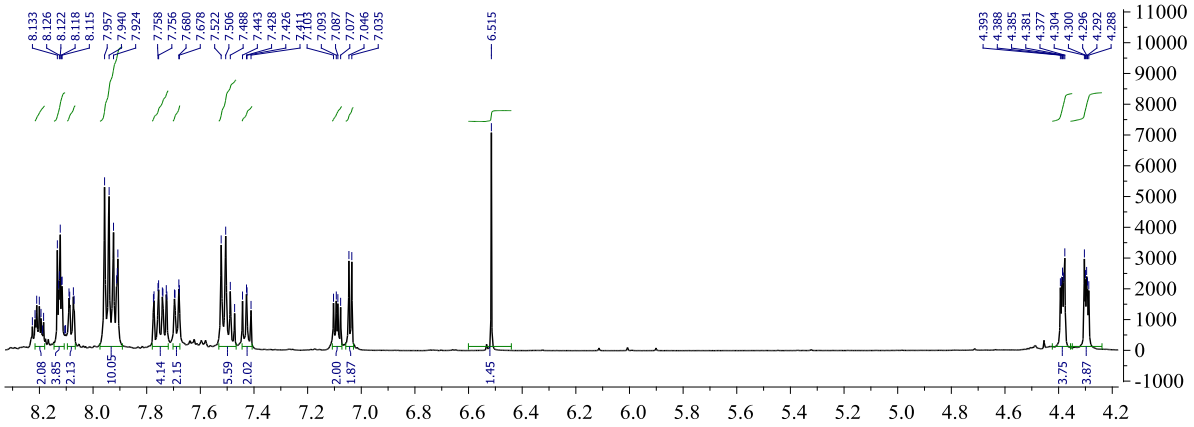

Figure S18.^{1}H NMR spectrum of [Ru(dqp)(L11)] aromatic peak area (CD_3CN, 500 MHz)

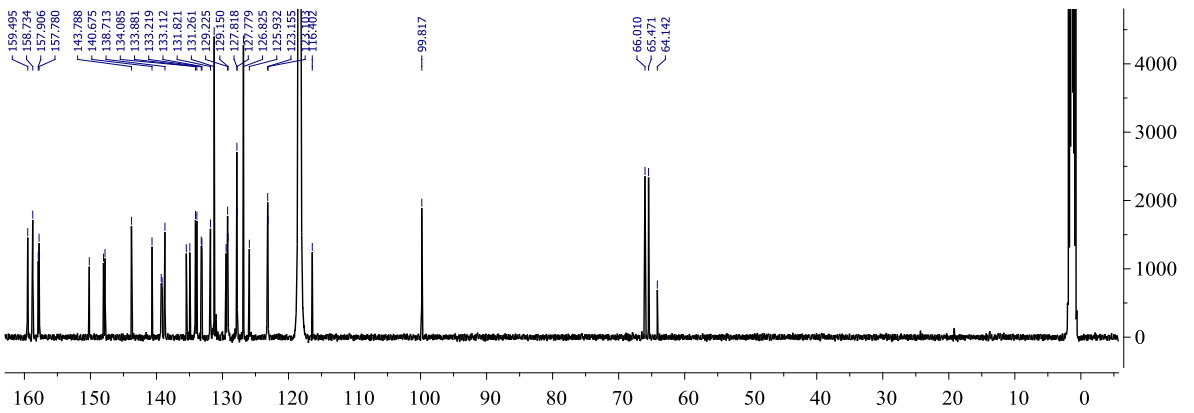

Figure S19. ^{13}C NMR spectrum of [Ru(dqp)(L11)] (CD_3CN, 125 MHz).

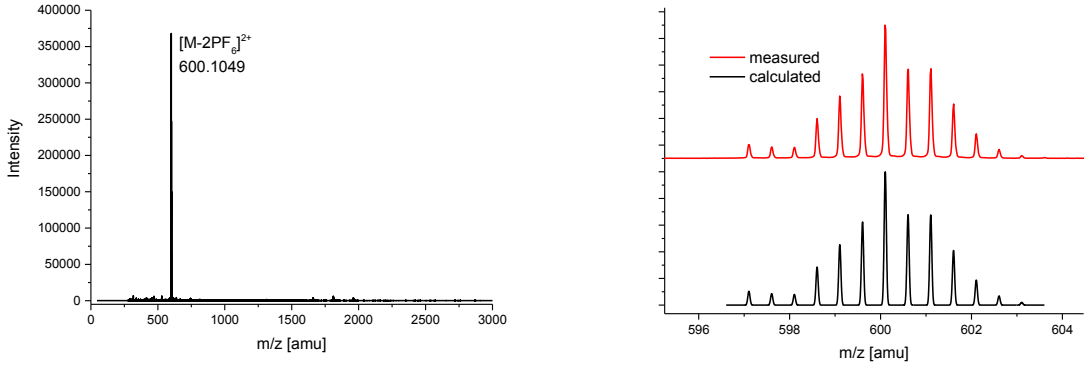

Figure S20. (Left) ESI-ToF-MS data of [Ru(dqp)(L11)] and (right) comparison of measured and calculated isotope pattern.

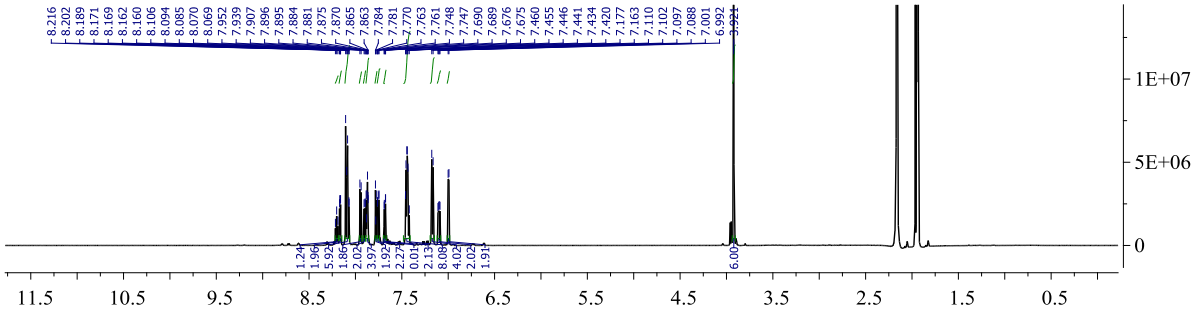

Figure S21. ^{1}H NMR spectrum of [Ru(dqp)(L8)] (CD_3CN, 600 MHz).

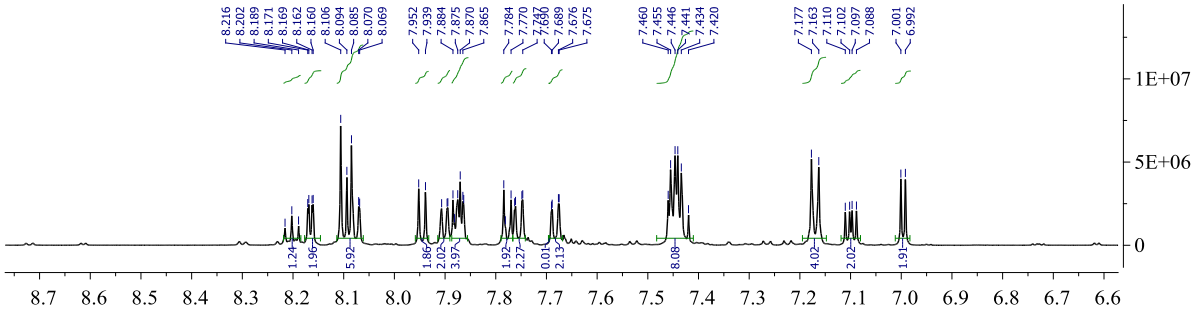

Figure S22. ^{1}H NMR spectrum of [Ru(dqp)(L8)] aromatic peak area (CD_3CN, 600 MHz).

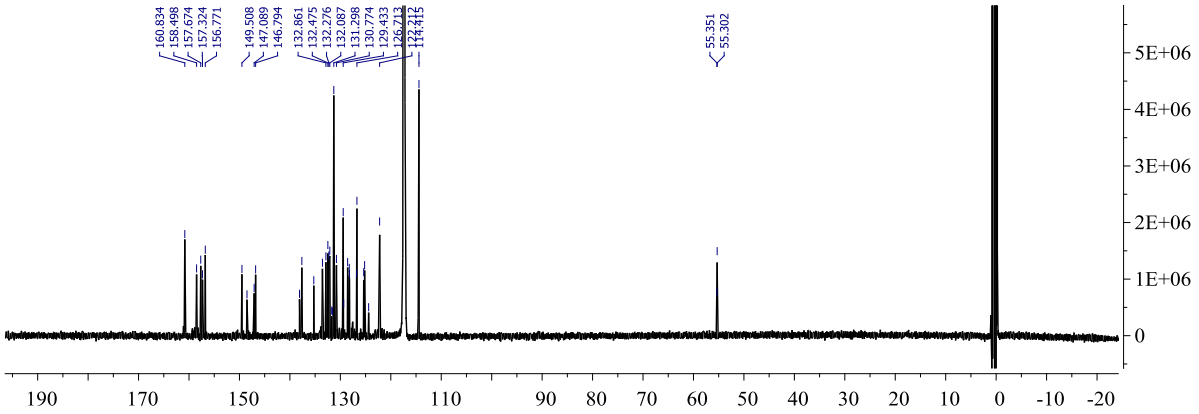

Figure S23. ^{13}C NMR spectrum of [Ru(dqp)(L8)] (CD_3CN, 126 MHz).

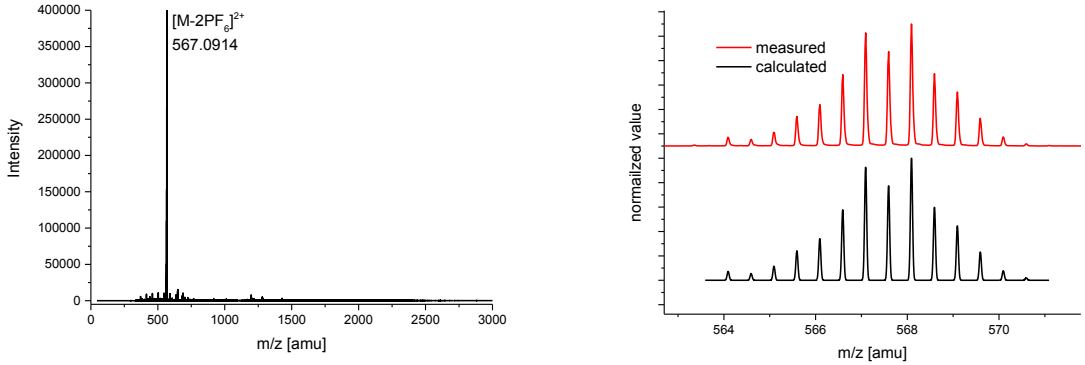

Figure S24. (Left) ESI-ToF-MS data of [Ru(dqp)(L8)] and (right) comparison of measured and calculated isotope pattern.

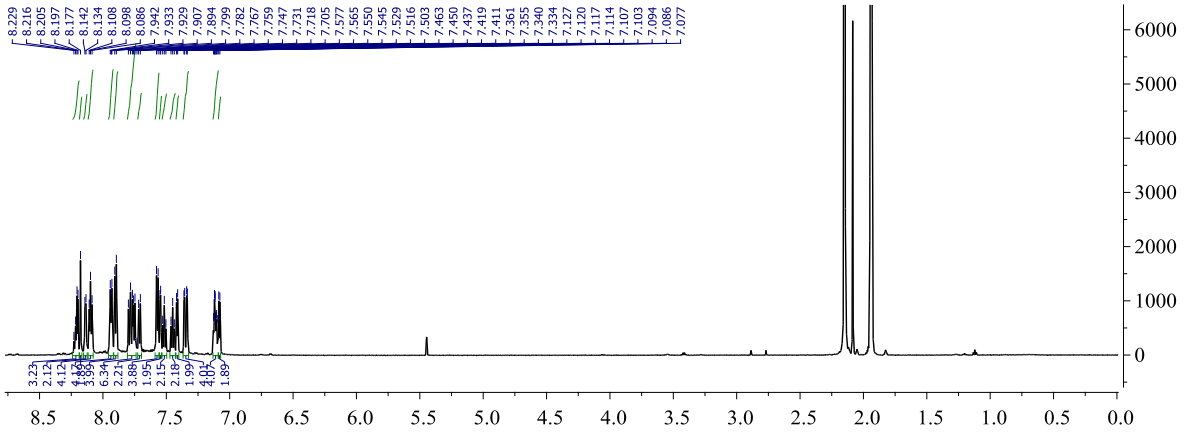

Figure S25. ^{1}H NMR spectrum of [Ru(L4)(L10)] (CD_3CN, 600 MHz).

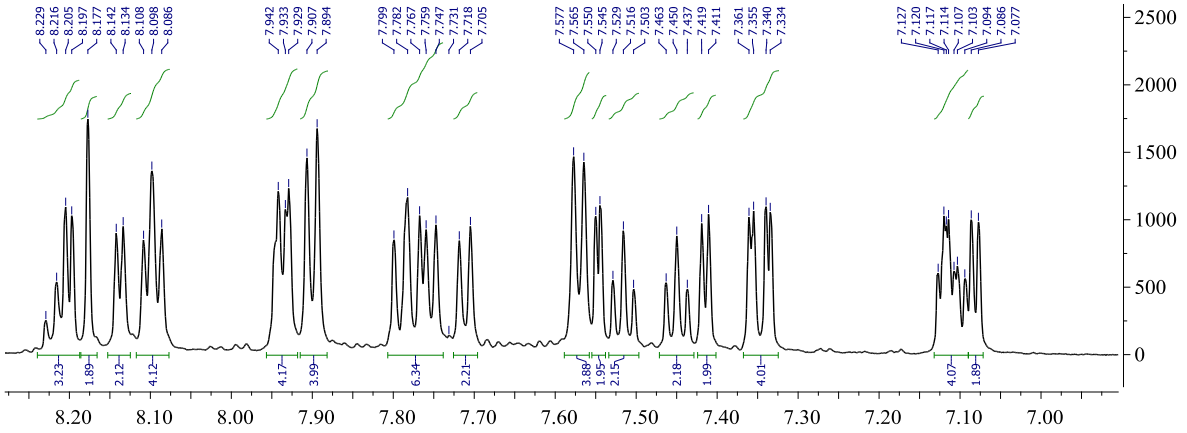

Figure S26. ^{1}H NMR spectrum of [Ru(L4)(L10)] (CD_3CN, 600 MHz).

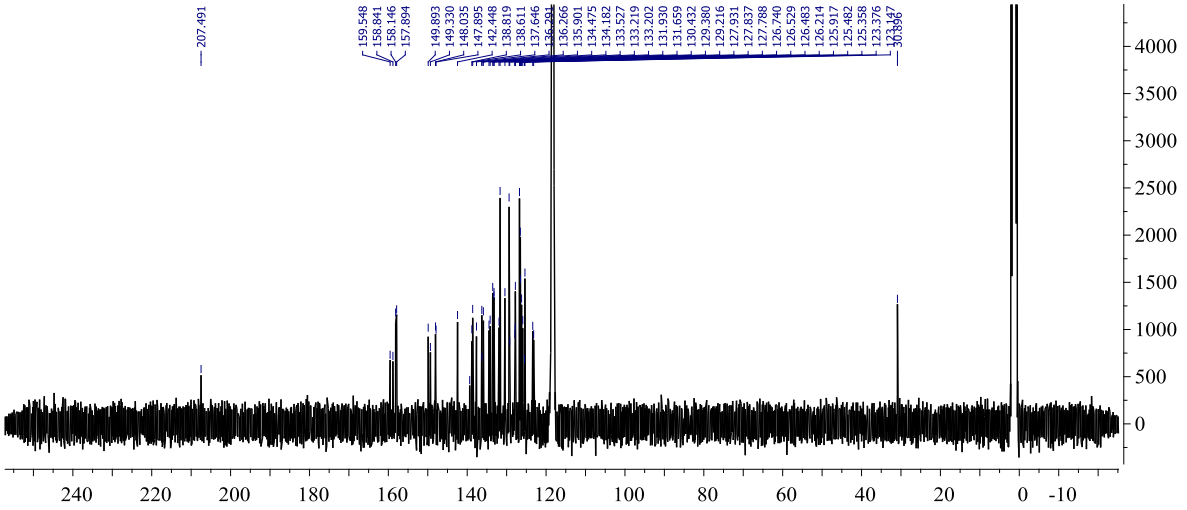

Figure S27. ^{13}C NMR spectrum of [Ru(L4)(L10)] (CD_3CN, 101 MHz).

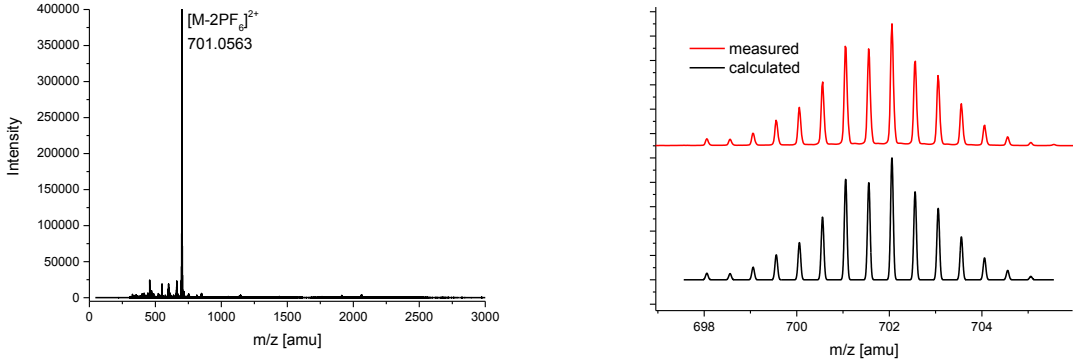

Figure S28. (Left) ESI-ToF-MS data of [Ru(L4)(L10)] and (right) comparison of measured and calculated isotope pattern.

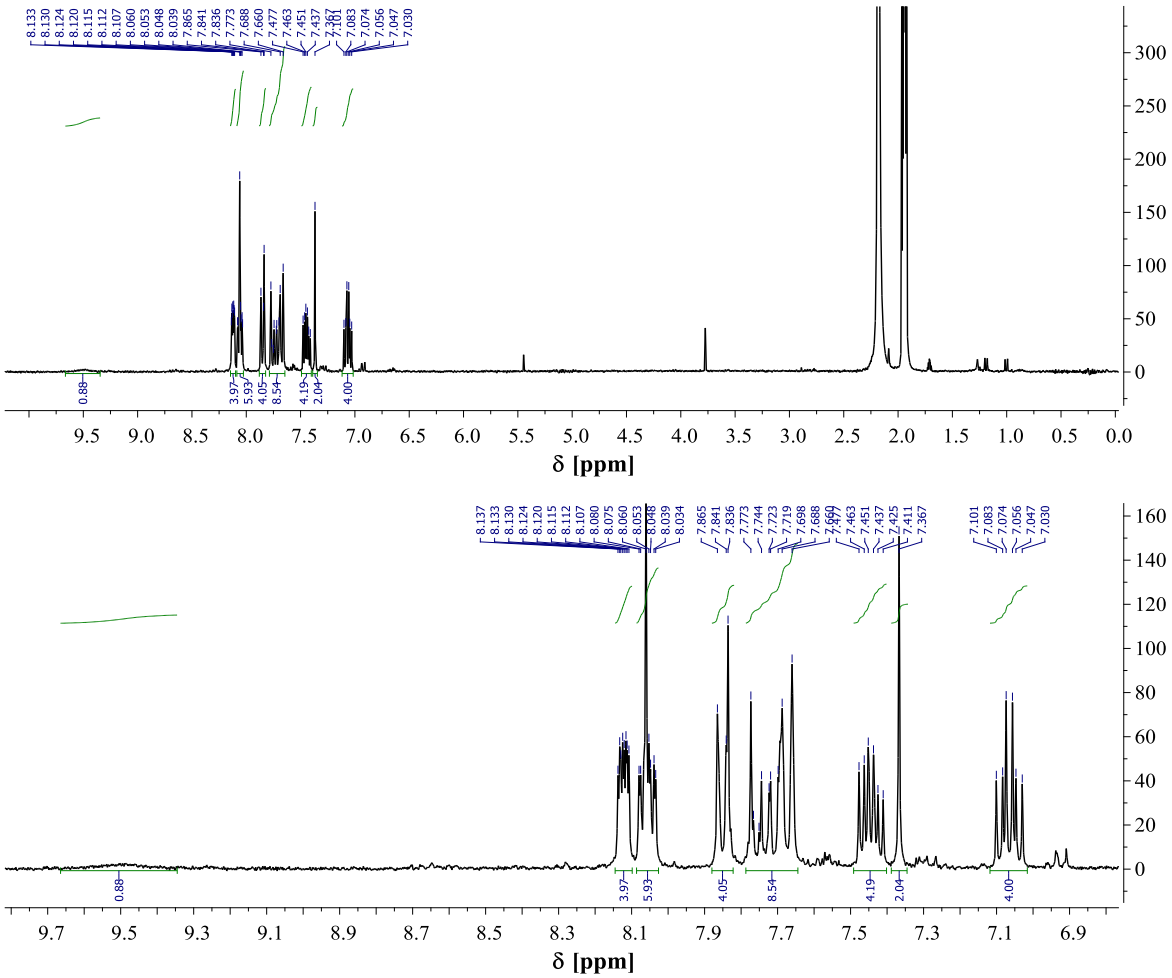

Figure S29. ^{1}H NMR spectrum of [Ru(L2)(L4)] (CD_3CN, 300 MHz) with enlarged aromatic region.

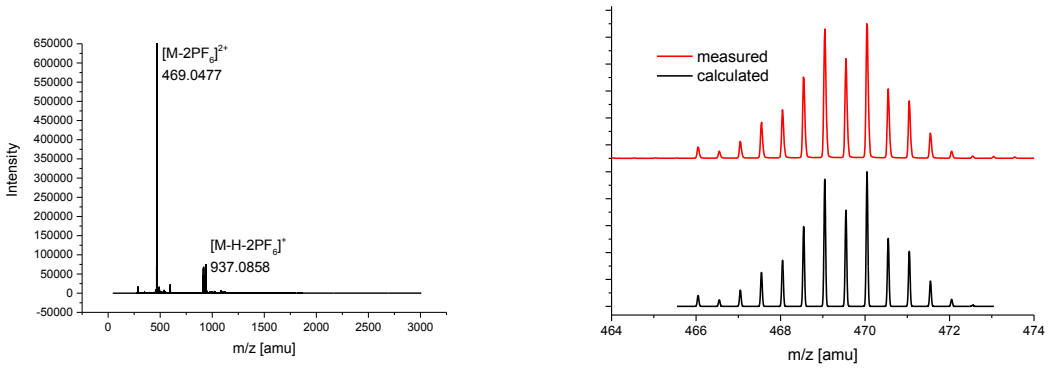

Figure S30. (Left) ESI-ToF-MS data [Ru(L2)(L4)]and (right) comparison of measured and calculated isotope pattern.

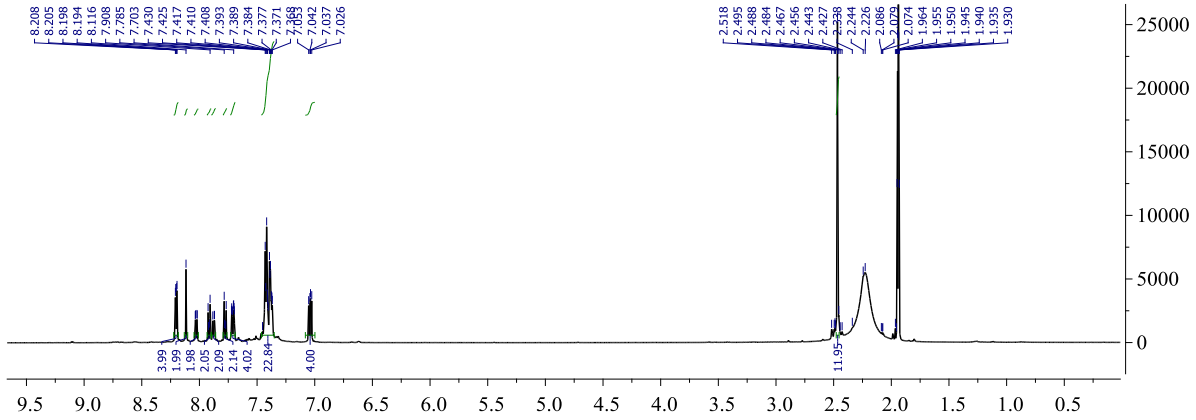

Figure S31. ^{1}H NMR spectrum of [Ru(L7)(L9)] (CD_3CN, 500 MHz).

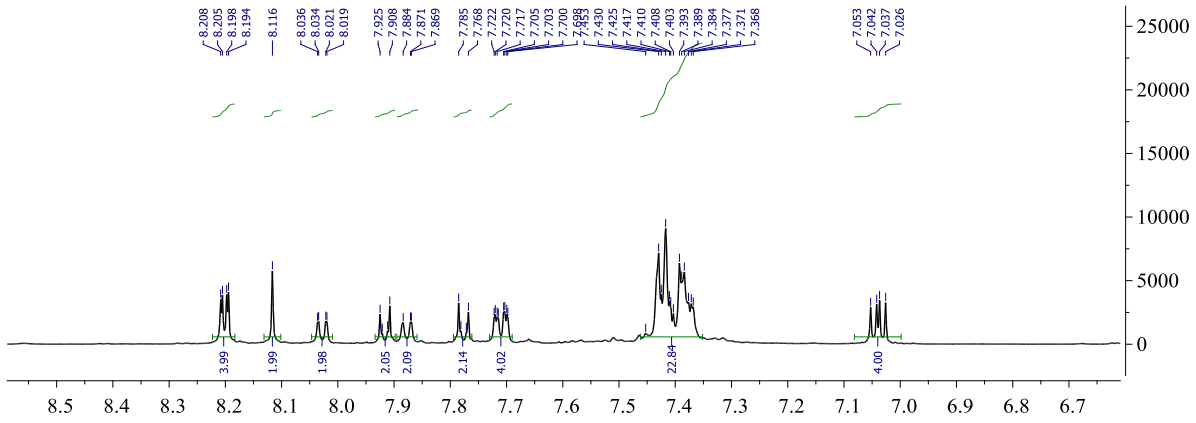

Figure S32. ^{1}H NMR spectra of [Ru(L7)(L9)] (CD_3CN, 500 MHz, aromatic region).

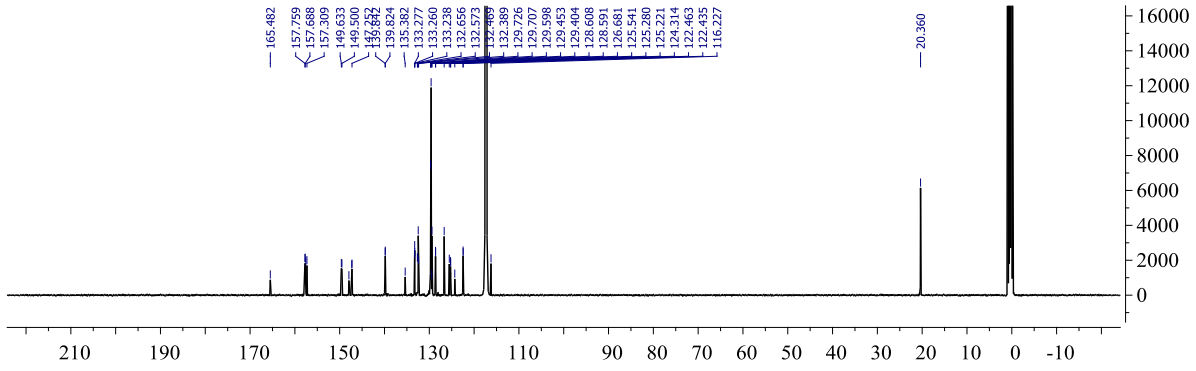

Figure S33. ^{13}C NMR spectra of [Ru(L7)(L9)] (CD_3CN, 125 MHz).

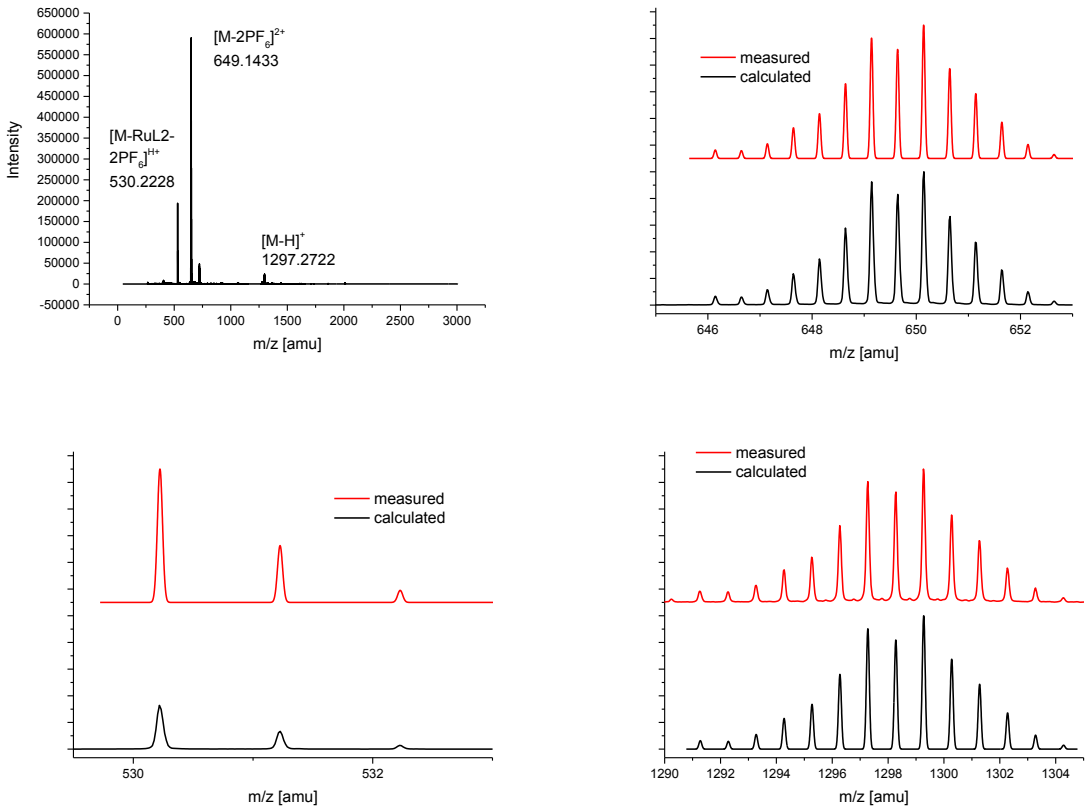

Figure S34. (Top, left) ESI-ToF-MS data of [Ru(L7)(L9)]and (top, right) comparison of measured and calculated isotope pattern; (bottom left) comparison of calculated and measured ligand isotop pattern, ligand peak arrive during ESI-Tof-MS measurement, washing step to remove ligand, shows no improvement→ instabile complex during measurements. (Bottom right) comparison of calculated and measured isotope pattern of deprotonated complex→ deprotonation of the hydroxyl group.

3. Computational results

3.1. Methodology

The theoretical calculations based on density functional theory (DFT)were performed as reported previously.[4] All calculations were performed with the Gaussian09 program package (Version A.02).[11] The functional ωB97xD[12] was selected to account for dispersion effects (except for the initial MeCN-removal using B3LYP[13, 14] due to convergence issues) have been selected, using the 6-31G* basis set for all atoms except Ru, which was described by an effective core potential and the associated orbitals (mwb28). For all calculation, the solvent environment was modelled for acetonitrile using the implemented polarization continuum model (PCM).[15, 16] The corresponding geometries of the singlet ground states were optimized from reasonable initial estimates, while the potential energy scans were performed by redundant coordinated of the stated bonds or dihedral angles. In cases of difficult SCF convergence, additional quadratic (qc) or extra quadratic (xqc) functions were used. In cases of erroneous internal coordinates, the geometry optimizations were performed in Cartesian coordinates (else internal coordinates). The true nature of all minima structures was confirmed by vibrational analysis showing no imaginary frequencies. The graphical visualizations of the three-dimensional representations were generated by GaussView5.0.8.[17]

3.2. PES of complex A towards intermediate E

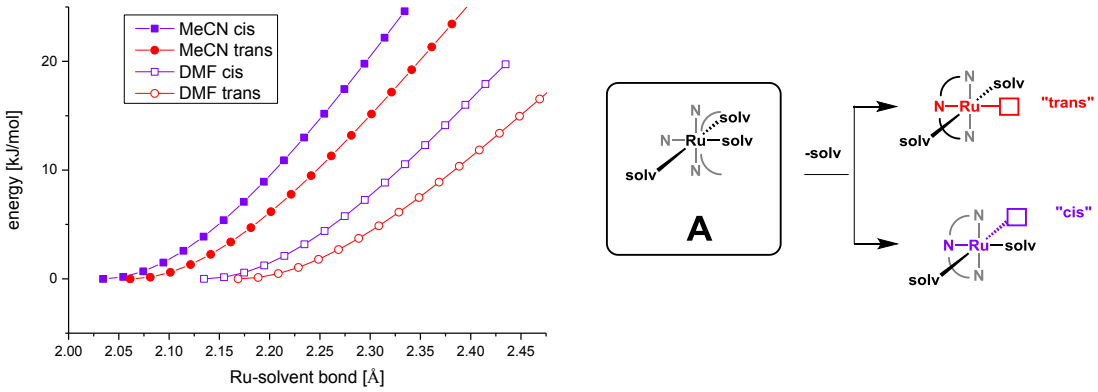

Figure S35. Potential energy scan (PES) of the solvent de-coordination from $[Ru(dqp)(solv)_3]^{2+}$ (complex E) for MeCN (filled symbols) or DMF (hollow symbols) in the *cis*-position (rectangles) and *trans*-position (circles) based on B3LYP functional (selected due to convergence problems applying the wB97xD functional). Note the general endothermic dissociation (increasing Ru-N/O distance), and more strongly bound *cis*- *vs.* *trans*-ligands, and the more labile DMF *vs.* MeCN ligand.

3.3. PES of intermediate F towards intermediate E

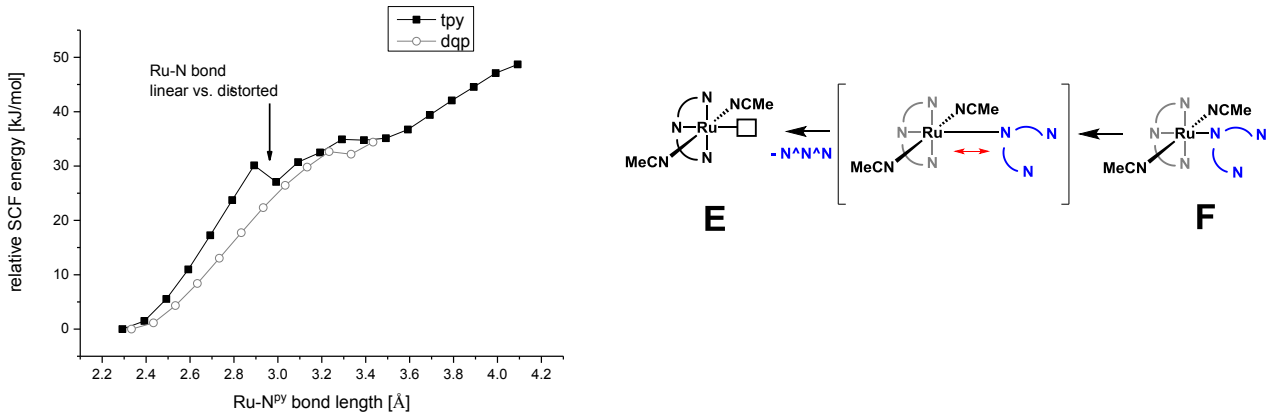

Figure S36. Potential energy scan (PES) to mimic first Ru-N^{py} bond formation (E → F) and transition state estimate via the inverse process starting from F by corresponding bond elongation (red arrow). Note the similar PES profiles for tpy and dqp suggesting similar energetic pathways for coordination. Note the plateauing around 3.3 Å due to bond breakage and further energy increase tentatively assigned to loss of π-interactions (the contribution of the basis set superposition error (BSSE) not determined).

3.4. Intermediates F

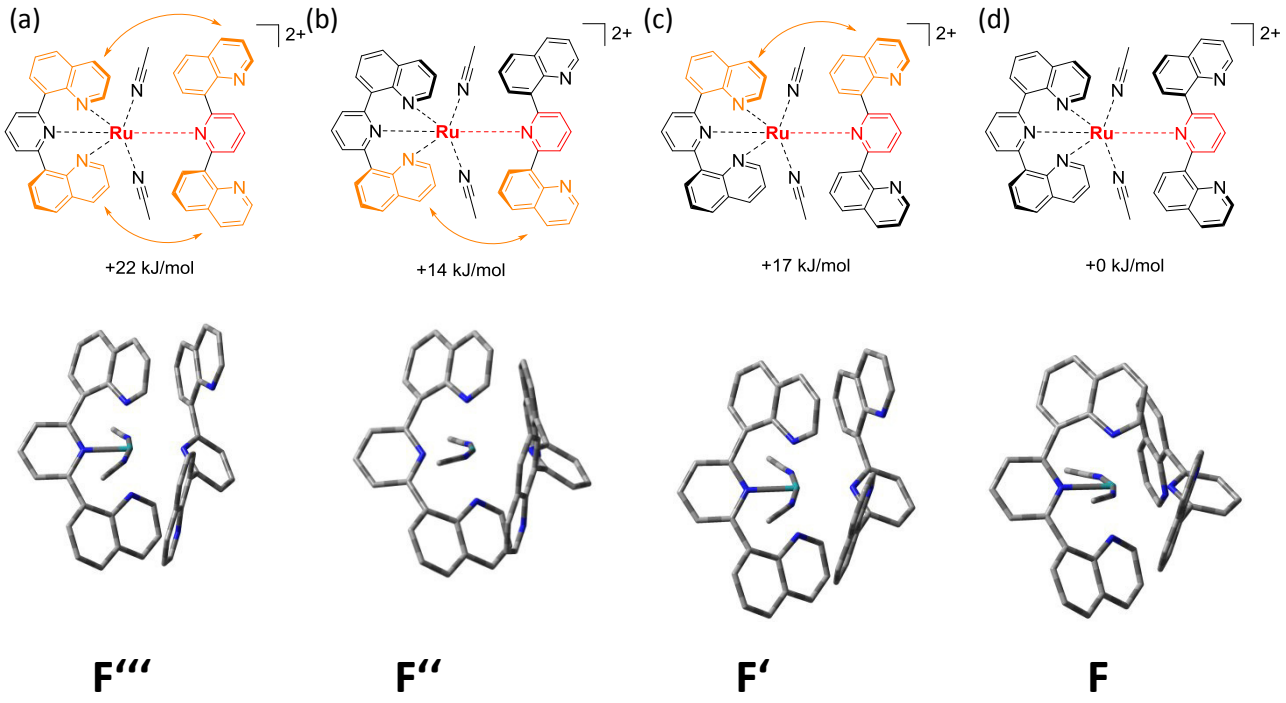

Figure S37. Chemical representation (top) and corresponding three dimensional structures from DFT calculations (bottom) illustrating the internal strain in complex F, which is formed after the first Ru-N^{py} bond formation step (shown in red). Note the steric repulsion and different degree of π-stacking of the quinoline units (orange arrows) leading to higher-energetic conformations: (a) Twofold repulsion (+22 kJ/mol), (b) and (c) with single repulsion (+14 and +17 kJ/mol), and (d) lowest-energy conformation (+0 kJ/mol). Note the correlation of the relative energies with out-of-plane deformation of the Ru-N^{py} bond and the pyridine ring (shown in red) in the order a > b > c > d.

3.5. Intermediates G

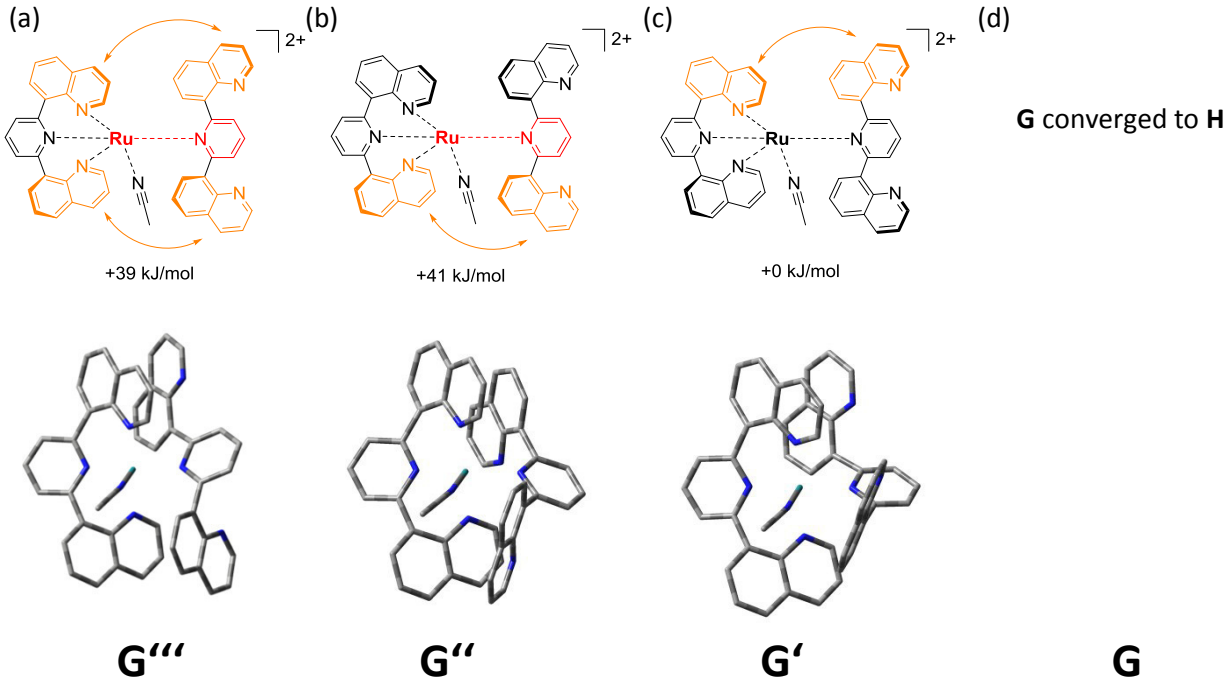

Figure S38. Chemical representation (left) and corresponding three dimensional structures from DFT calculations (right) of the G series that is formed upon abstraction of the second MeCN ligand from the corresponding F series (Figure S37). (a-c) The stacking and eclipse of hydrogens hinders the rotation of the quinoline along the interannular C^{py}–C^{qu} bond (see Figure S39). (d) The starting guess of the lowest-energy conformer G directly converged to H, suggesting a low activation barrier. Note the significant stabilization in case of G (in fact converging directly to H) and G' *vs.* G'' and G''' (+39 and +41 kJ/mol).

3.6. PES internal rotation intermediate G''' to intermediate H

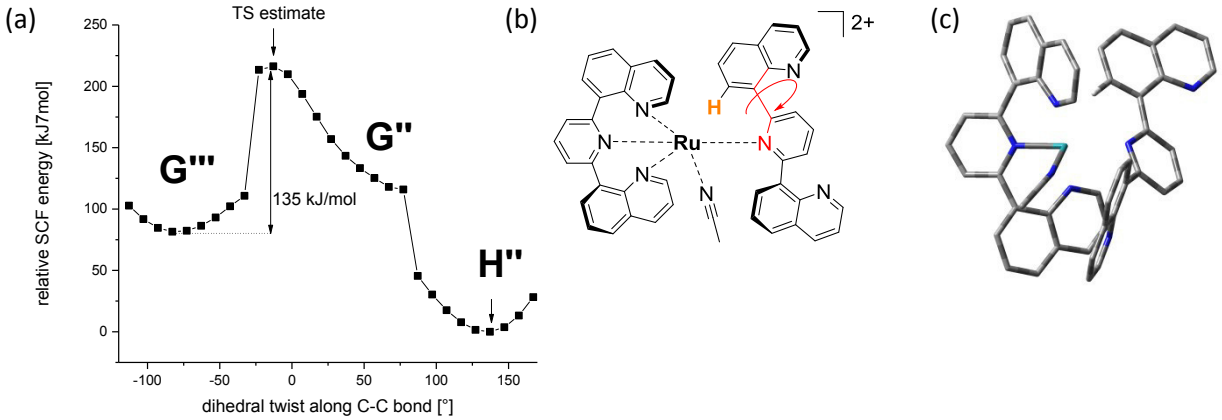

Figure S39. (a) Potential energy scan (PES, SCF energies relative to H'') of the internal rotation along the interannular C^{py}–C^{qu} bond, (b) using the C50-C61-C59-C58 dihedral (shown in red) in ±10 ° intervals starting from an intermediate geometry similar to G'' (at +50 °). From the PES, the transition state (TS) was estimated to approximately 135 kJ/mol *vs.* G at, (c) attributed to steric repulsion of the shown hydrogen atom. Note the release of the accumulated dihedral strain around -30 ° and 60 °.

3.7. Intermediate H

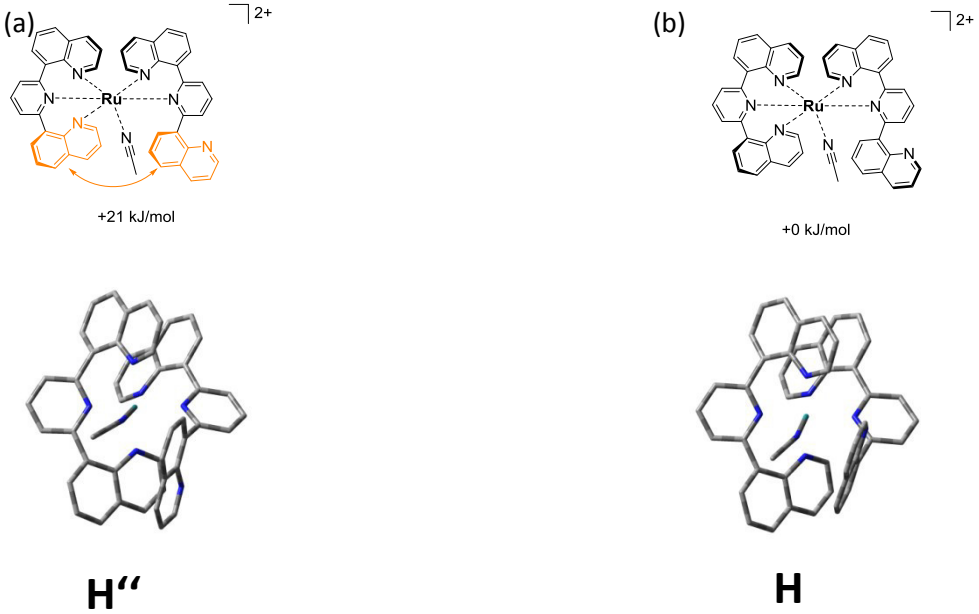

Figure S40. Chemical representation (top) and corresponding three dimensional structures from DFT calculations (bottom) of the H series that is formed after the Ru-N^{qu} bond formation from the corresponding G series. The steric repulsion originating from quinoline units (orange arrows) causes a higher -energy conformation for H'' *vs.* H (+21 kJ/mol).

3.8. Intermediate I

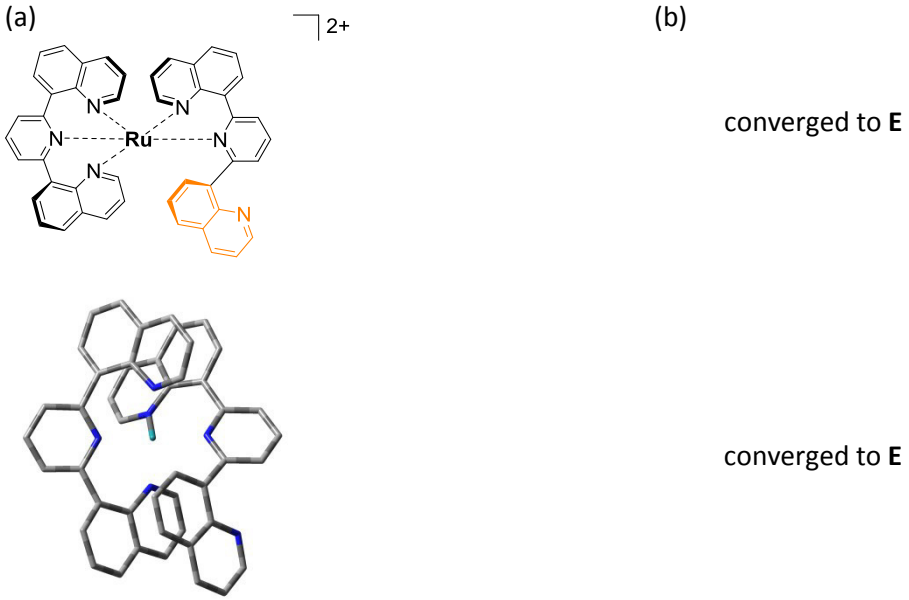

Figure S41. Chemical representation (top) and corresponding three dimensional structures from DFT calculations (bottom) of I that is formed upon release of the last MeCN ligand from H (Figure S40a). (a) The stacking and internal strain blocks the rotation of the quinoline along the interannular C^{py}–C^{qu} bond for I''. (b) The starting guess of the lowest-energy conformer I directly converged to E, suggesting a low activation barrier.

3.9. PES internal rotation I'' to final complex J

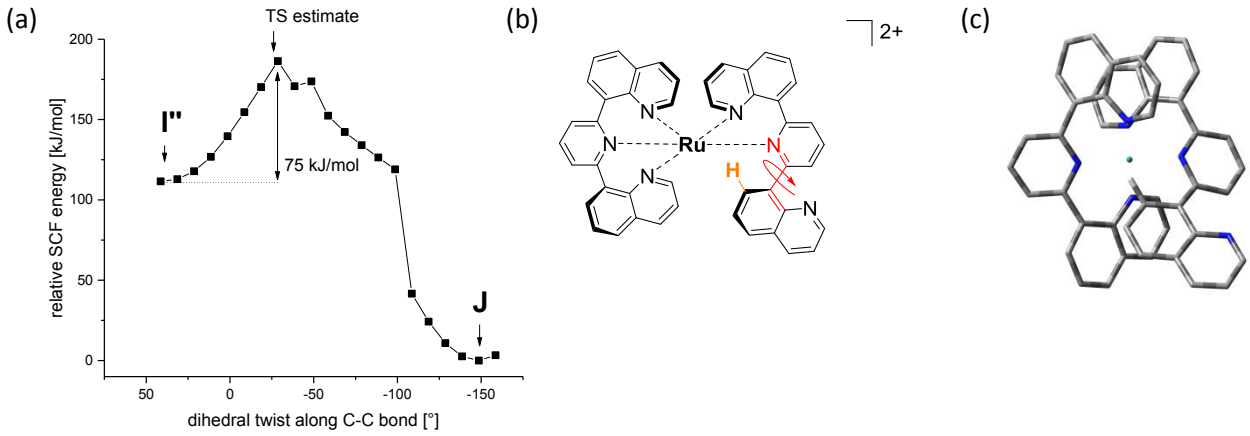

Figure S42. (a) Potential energy scan (PES, SCF energies relative to J) of the internal rotation along the interannular C^{py}–C^{qu} bond, (b) using the C3-C2-C7-C8 dihedral angle of I'' in -10 ° intervals. Note the transition state (TS) estimate of approximately +75 kJ/mol *vs.* I'', attributed to steric repulsion of the shown hydrogen atom (c, orange). Note the release of accumulated dihedral strain around -100 °.

3.10. Structure of the tpy-series

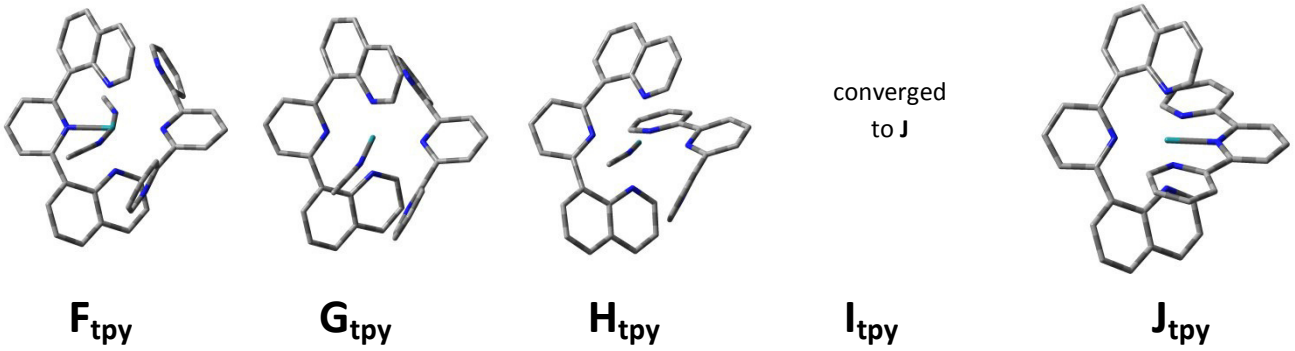

Figure S43. Three dimensional structures from DFT calculations of the tpy-based intermediates.

3.11. PES internal rotation of tpy-based J towards I”

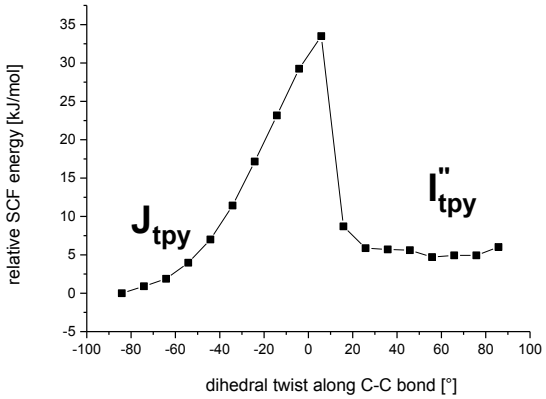

Figure S44. (a) Potential energy scan (PES, SCF energies relative to J) of the internal rotation along the interannular C^{py}–C^{qu} bond, (b) using the C1-C2-C8-C12 dihedral angle of I_{tpy} in -10 ° intervals. Note the transition state (TS) estimate of approximately +35 kJ/mol *vs.* I_{tpy}, and the release of accumulated dihedral strain around 0 °.

4. References

1. H. E. Gottlieb, V. Kotlyar and A. Nudelman, *J. Org. Chem.*, 1997, **62**, 7512-7515.
2. M. Jäger, L. Eriksson, J. Bergquist and O. Johansson, *J. Org. Chem.*, 2007, **72**, 10227-10230.
3. C. Friebe, H. Görls, M. Jäger and U. S. Schubert, *Eur. J. Inorg. Chem.*, 2013, **2013**, 4191-4202.
4. T. Schlotthauer, B. Suchland, H. Görls, G. A. Parada, L. Hammarström, U. S. Schubert and M. Jäger, *Inorg. Chem.*, 2016, **55**, 5405-5416.
5. T. Schlotthauer, R. Schroot, S. Glover, L. Hammarstrom, M. Jaeger and U. S. Schubert, *Phys. Chem. Chem. Phys.*, 2017, **19**, 28572-28578.
6. J. H. Wang and G. S. Hanan, *Synlett*, 2005, DOI: 10.1055/s-2005-868481, 1251-1254.
7. M.-P. Santoni, A. K. Pal, G. S. Hanan, A. Proust and B. Hasenknopf, *Inorg. Chem. Commun.*, 2011, **14**, 399-402.
8. M. Jaeger, R. J. Kumar, H. Goerls, J. Bergquist and O. Johansson, *Inorg. Chem.*, 2009, **48**, 3228-3238.
9. M. Abrahamsson, M. Jäger, R. J. Kumar, T. Österman, P. Persson, H.-C. Becker, O. Johansson and L. Hammarström, *J. Am. Chem. Soc.*, 2008, **130**, 15533-15542.
10. T. Schlotthauer, C. Friebe, A. M. Schwenke, M. Jäger and U. S. Schubert, *J. Mater. Chem. C*, 2017, **5**, 2636-2648.

11. M. J. Frisch, G. W. Trucks, H. B. Schlegel, G. Scuseria, M. A. E.; Robb, J. R. Cheeseman, G. Scalmani, V. Barone, B. Mennucci, G. A. Petersson, H. Nakatsuji, M. Caricato, X. Li, H. P. Hratchian, A. F. Izmaylov, J. Bloino, G. Zheng, J. L. Sonnenberg, M. Hada, M. Ehara, K. Toyota, R. Fukuda, J. Hasegawa, M. Ishida, T. Nakajima, Y. Honda, O. Kitao, H. Nakai, T. Vreven, J. Montgomery, J. A., J. Peralta, F. E.; Ogliaro, M. Bearpark, J. J. Heyd, E. Brothers, K. N. Kudin, V. N. Staroverov, R. Kobayashi, J. Normand, K. Raghavachari, A. Rendell, J. C. Burant, S. S. Iyengar, J. Tomasi, M. Cossi, N. Rega, N. J. Millam, M. Klene, J. E. Knox, J. B. Cross, V. Bakken, C. Adamo, J. Jaramillo, R. Gomperts, R. E. Stratmann, O. Yazyev, A. J. Austin, R. Cammi, C. Pomelli, J. W. Ochterski, R. L. Martin, K. Morokuma, V. G. Zakrzewski, G. A. Voth, P. Salvador, J. J. Dannenberg, S. Dapprich, A. D. Daniels, Ö. Farkas, J. B. Foresman, J. V. Ortiz, J. Cioslowski and D. J. Fox, *Journal*, 2010.
12. J.-D. Chai and M. Head-Gordon, *Phys. Chem. Chem. Phys.*, 2008, **10**, 6615-6620.
13. A. D. Becke, *J. Chem. Phys.*, 1993, **98**, 5648-5652.
14. C. T. Lee, W. T. Yang and R. G. Parr, *Physical Review B*, 1988, **37**, 785-789.
15. E. Cances, B. Mennucci and J. Tomasi, *J. Chem. Phys.*, 1997, **107**, 3032-3041.
16. J. Tomasi, B. Mennucci and R. Cammi, *Chem. Rev.*, 2005, **105**, 2999-3093.
17. R. D. D. II, T. A. Keith and J. M. Millan, *Journal*, 2008.

Publication P3

"Chemistry-on-the-complex": Functional Ru^{II} polypyridyl-type sensitizer as divergent building blocks

T. Mede, M. Jäger, U. S. Schubert, submitted.

"Chemistry-on-the-complex": Functional Ru^{II} polypyridyl-type sensitizer as divergent building blocks

Tina Mede,[†] Michael Jäger,[†,§] and Ulrich S. Schubert*[†,§]*

† Laboratory of Organic and Macromolecular Chemistry (IOMC), Friedrich Schiller University Jena, Humboldtstraße 10, 07743 Jena, Germany

§ Center for Energy and Environmental Chemistry Jena (CEEC Jena), Friedrich Schiller University Jena, Philosophenweg 7a, 07743 Jena, Germany

Abstract

Ruthenium polypyridyl type complexes are potent photoactive compounds, and have – found among others – a broad range of important application fields in biomedical diagnosis and phototherapy, energy conversion schemes such as dye-sensitized solar cells (DSSCs) as well as in molecular assemblies for tailored photo-initiated processes. In this regard, the linkage of Ru^{II} polypyridyl-type complexes is highly desirable to augment the inherent photophysical properties by a specific functional moieties, *e.g.*, with a targeting function to achieve cell selectivity, a dye or redox-active subunits for energy- and electron-transfer. However, the classical approach of performing ligand syntheses first and formation of the Ru complexes in the last steps imposes synthetic limitations with regard to tolerates functional groups or moieties as well as requires lengthy convergent routes. Alternatively, the diversification of Ru complexes after coordination (termed "chemistry-on-the-complex") provides an elegant complementary approach. In addition to the Click chemistry concept, the rapidly developing synthesis and purification methodologies permit the preparation Ru conjugates *via* amidation, alkylation and cross-coupling reactions. In this regard, recent developments in chromatography shifted the limits of purification, *e.g.*, by new commercialized surface-modified silica gels and automated instrumentation. This review provides detailed insights to apply the "chemistry-on-the-complex" concept, which is believed to stimulate the modular preparation of unpreceded molecular assemblies as well as functional materials based on Ru-based building blocks, including combinatorial approaches.

1. Background and general aspects

The rise of Ru^{II} polypyridyl-type complexes dates back to the first reported synthesis of $[Ru(bpy)_3]^{2+}$ (bpy is 2,2'-bipyridine) in 1936,[1] and the subsequent discovery of luminescence

in 1959,[2] and the assignment to charge-transfer emission[3] from a triplet state in 1968.[4] Since then, the combination of these remarkable photophysical properties,[5] nowadays assigned to the triplet metal-to-ligand-charge-transfer (^{3}MLCT) excited state, have attracted the Chemist's interest in this compound class, which is reflected by the continuously high publication numbers and, equally important, has matured to a wide range of application fields (Figure 1). In fact, the importance of Ru^{II} polypyridyl-type complexes towards application originates from the conversion of photon energy into electricity or redox-chemical energy (or *vice versa*), as well as the modulation of optical properties due to molecular interactions (luminescent sensors). Because an exhaustive overview is far beyond the scope of this review, the interested reader is referred to selected recent reviews and key references covering the role of Ru complexes in the following applications: (a) Light-into-electrical energy, *e.g.*, in dye-sensitized solar cells,[6-28] or in electro-/chemi-luminescence,[29] (b) light-into-redox energy, *e.g.*, by photoredox catalysis,[30-33] photochemical or photodynamic usage in biomedicine, (c) sensor and imaging applications, *e.g.*, NIR responsive and emissive materials,[34] oxygen detection[35] or anion sensing,[36] the labeling of carbon materials (nanotubes etc.),[37-45] or biologically relevant targets such as DNA,[46-57] cells,[58-71] or sugars.[72-75]

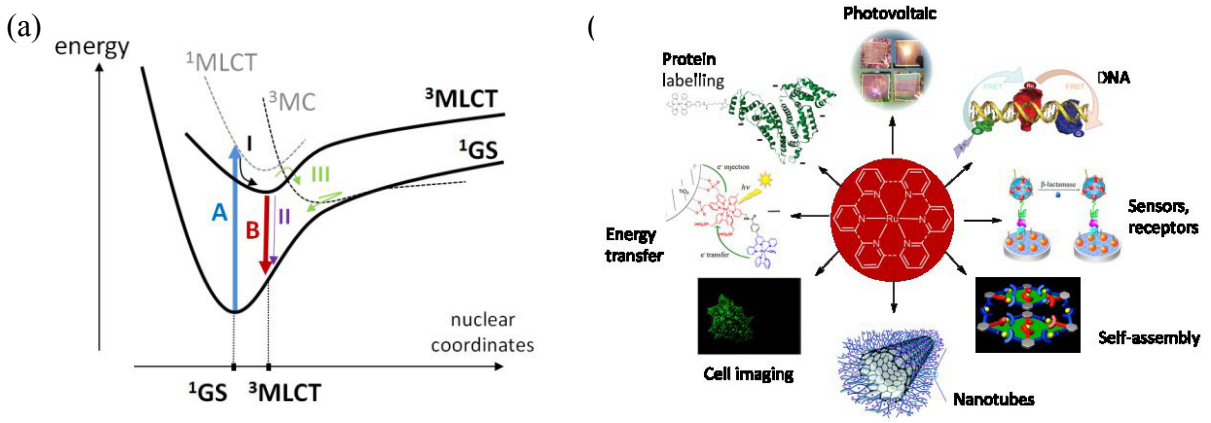

Figure 1. (a) Simplified presentative energy scheme and occurring photophysical events for RuII polypyridyl-type complexes adapted from ref. 76. Light absorption (A, vertical blue arrow) leads to population of the ^{1}MLCT state(s), which undergo rapid intersystem crossing and relaxation to the ^{3}MLCT excited state. Decay to the ground state (GS) proceeds via emission (vertical red arrow) or non-radiative pathways include direct coupling with GS (process II) or thermally-active population of ^{3}MC states (process III). (b) Representative application fields, depending on the precise excited state characteristics (i.e., lifetime, energy, or emission quantum yield). See text and references 5, 77, 78 for more details.

The versatility of Ru^{II} polypyridyl-type complexes is further evident from synergistic combinations of the previous individual aspects, *e.g.*, to form integrated chemiluminescent sensors triggered by anions or specific analyte molecules in life sciences.[79, 80] A particular

distinction for Ru complexes originates from their exceptional synthetic versatility, *e.g.*, the construction of molecular assemblies inspired by natural photosynthesis to study and mimic photo-induced electron[81-83] and energy transfer steps,[84-88] or to design sophisticated molecular machines such as switches or motors.[89-91] The seminal work dating back to the 1970s was devoted to elucidate the fundamental photophysical events and to explore the inherent photochemical properties. The ground and excited state properties have been thoroughly reviewed elsewhere (*e.g.*, see ref. 5, 77, 78). Figure 1a depicts the sequence of key photophysical events, *i.e.*, initial photon absorption, rapid intersystem crossing and relaxation to the ^{3}MLCT state(s) is observed. The intrinsic deactivation can occur via radiative processes (emission), or non-radiative decay to the ground state via direct coupling, as often observed for cyclometalated complexes deduced from their energy gap law dependence, or via thermally-activated processed mediated by ^{3}MC states which is largely affected by the ligand field. Consequently, the ^{3}MLCT state is characterized by its lifetime, energy content (emission energy) and emission quantum yield. In addition, energy- or electron transfer can occur via suitable donor and acceptor moieties, which are exploited in most of the applications of Ru^{II} polypyridyl-type complexes. Among others, the following properties have received particular great attention for optimization: (1) The enhancement of visible light absorption for a better coverage of the solar spectrum, (2) the improvement of excited state properties (energy, life time, and quantum yield), (3) the adjustment of the redox potentials, and (4) the enhancement of chemical and photostability.

Consequently, the family of reported Ru^{II} polypyridyl-type complexes has evolved tremendously to meet the specific application requirements, and is increasingly supported by ligand design that is corroborated by the increasingly reliable predictions from quantum chemical methods.[76, 92-103] The ligand modifications can be classified into variations of the scaffold (Figure 2), *i.e.*, replacing the pyridine subunits of 2,2'-bipyridine (bpy) or 2,2':6',2''-terpyridine (tpy) by five-membered *N*-heterocycles or bridgehead/annulated ring systems, as well as carbanionic donors or carbenes (Figure 2c). Consequently, a large number of conceivable bidentate (N^N) and tridentate (N^N^N) ligands can be constructed from these subunits, and further utilized to form the corresponding *tris*-bidentate complexes $[Ru(N^N)_3]^{2+}$ or *bis*-tridentate complexes $[Ru(N^N^N)_2]^{2+}$ (Figure 2b). For many applications, a certain combination of photophysical and geometrical features is desired. For example, the Λ/Δ-isomerism of $[Ru(N^N)_3]^{2+}$-type complexes may be utilized for diastereomeric interactions, or may be avoided in donor-photosensitizer-acceptor assemblies due to the possible *cis*/*trans* isomers, which can be elegantly circumvented by exploiting the

axial symmetry of $[Ru(N^N^N)_2]^{2+}$-type complexes (Figure 2b, depicted by orange and blue color), or more recently by the 2,6-di(quinolin-8-yl)pyridine (dqp) ligand family. Furthermore, the excited state properties may differ markedly, ranging from long-lived emission of $[Ru(bpy)_3]^{2+}$ and $[Ru(dqp)_2]^{2+}$ exceeding a few hundreds of nanoseconds to short-lived and, thus, practically non-emissive $[Ru(tpy)_2]^{2+}$ with less than a nanosecond. To a certain degree, the photophysical and electrochemical properties can be further adjusted by installing peripheral functional groups at the ligand scaffold. In summary, the coordination chemistry of Ru^{II} polypyridyl-type complexes has been investigated in detail, which led to established synthetic protocols of the complexation routes.

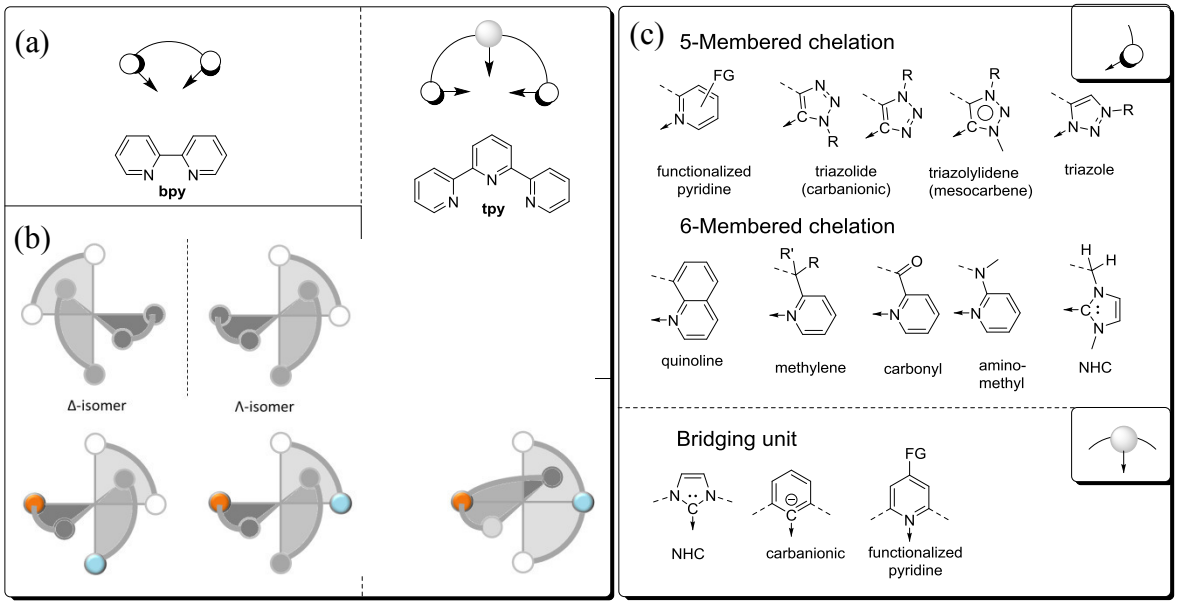

Figure 2. (a) Overview of archetypical pyridyl-based ligands bpy, tpy and dqp. (b) Coordination geometry in *tris*-bidentate (featuring Λ/Δ-isomerism) and *bis*-bidentate Ru^{II} complexes, as well as cisoid and transoid arrangement of functional motifs (orange and blue). (c) Overview of subunits used to assembly ligands for 5-membered and 6-membered chelation modes. Typical subunits are: Five-membered heterocycles, bridgeheads or ring-annelated heterocycles, as well as cyclometalates and carbenes.

The majority of Ru^{II} polypyridyl-type complexes are prepared in two stages, *i.e.*, initial ligand synthesis and the subsequent coordination steps. In this regard, the required organic intermediates and ligands can be readily synthesized as well as purified, *e.g.*, by crystallization or chromatographic methods. The coordination step is usually performed under optimized conditions for the specific complex class. For example, typical bpy- and tpy-based complexes can be obtained around 80 °C, while the dqp-based congeners or cyclometalated complexes require significantly elevated temperatures (120–140 °C). This synthesis strategy is attractive to prepare new Ru dyes from novel ligand platforms (Figure 2a), since the

purification of the Ru complexes is often the most challenging step. However, there are also undesired consequences following this route. Firstly, functional groups or moieties may not tolerate the reaction conditions (*e.g.*, nitro-groups or biologically-active targeting subunits), or the ligand may facilitate unwanted coordination modes, which leads to low yields and cumbersome purification efforts (*vide infra*). Secondly, the substitution pattern is typically introduced in the early stage of the ligand synthesis and, thus, any (systematic) modification at this position implies the repetition of all intermediate steps, including the final coordination. Although such constraints may not be as limiting for the development of novel ligand platforms for Ru complexes, they hamper the utility of functional Ru complexes for combinatorial approaches or molecular assemblies, which often pursue a convergent synthesis strategy with several synthetic steps. Nevertheless, the development of advanced molecular architectures receives increasing attention, *e.g.*, by adding a specific targeting groups for therapeutic or diagnostic applications, as well as the construction of molecular donor-acceptor materials for energy conversion applications. In this regard, performing reactions *after* the coordination step, denoted as "chemistry-on-the-complex" in the following, represents a promising complementary strategy to circumvent many the challenges left by the conventional routes and to utilize Ru complexes as functional building blocks for subsequent diversification steps. Nevertheless, only less than 3% of the reports on Ru^{II} polypyridyl-type complexes follow this strategy (Figure 3), which is mainly limited by the challenging purification. In this regard, the recent progress in column chromatography offers a versatile tool to expand the scope of this underdeveloped area.

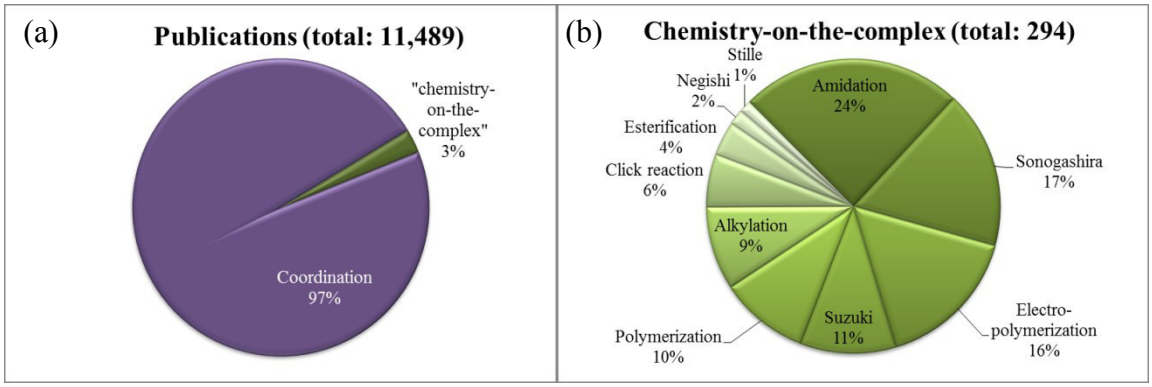

Figure 3. (a) Metrics of ruthenium complexes categorized into preparation via coordination chemistry or "chemistry-on-the-complex" based from extensive database survey.[104] (b) Distributions of the applied reaction types for "chemistry-on-the-complex".

2. Scope and terminology

This review focuses on reactions of Ru^{II} polypyridyl type complexes, referred to "chemistry-on-the-complex". Notably, such transformations have been occasionally reported throughout the years, *e.g.*, referring to "building blocks"[105, 106] or "post-coordination functionalization".[107] In view of the recent progress of modern synthetic and, moreover, purification protocols, the "chemistry-on-the-complex" concept became generally applicable to prepare novel functional materials, *e.g.*, utilizing targeting moieties for biomedical application or redox-active and catalytically active moieties for tailored energy conversion applications.

This review is organized into four main sections: First, the essentials of typical complexation routes for the ligand syntheses (section 3.1) and the corresponding coordination protocols (section 3.2) are presented, which presents the starting point for the "chemistry-on-the-complex" strategy of functionalized Ru complexes. Next, the principle reactions to install or to interconvert functional groups are introduced (section 4.1), which further refers to the "conjugation" with functional molecular fragments through C–C, C–O, C–N, C–S bond formation (section 5). Representative showcases of multimetallic Ru-containing macrocycles and star-like assemblies will be highlighted (section 5.1), followed by a section dedicated to amidation as one of the most powerful linkage methodologies (section 5.2). Subsequently, related esterification (section 5.2.2) and alkylation reactions employing N-, O-, and S-nucleophiles (section 5.3), followed by Pd-mediated cross-coupling methodologies (section 5.5), modern cycloaddition reactions (section 5.6) and various polymerization techniques (section 5.7). The second part details analytical and preparative aspects of various general purification techniques (section 6). Owing to the importance of chromatographic methods for purification, the related art and modern developments will be discussed in a separate chapter (section 7).

However, in many instances a direct comparison between several synthetic or purification methods is difficult, as the applied conditions often descend from the individual empirical experience that matured within the respective research groups. Consequently, a mere evaluation of a given method in terms of isolated yields, number of reports, number of repeated chromatographic runs, or chronicling the publications may be lead to an incomplete picture. Hence this review is intended to present representative key studies as well as to provide comprehensive tables, in order to serve for orientation for a specific reaction type or purification protocols. Particular discussion is devoted to the seminal work on polynuclear dendrons and star-like complexes (*e.g.*, Balzani, Sauvage, Newkome, Constable, Tor, Ward

and others), Ru-polymer architectures (*e.g.*, Meyer and others), Ru-metal assemblies towards artificial photosynthesis (*e.g.*, Åkermark and others), as well as methodological improvements on solid-phase amide linkages (*e.g.*, Heinze and others) and the systematic developments of chromatographic purification protocols (*e.g.*, Keene, Fletcher, and others). Additional selected showcases will be detailed to provide also detailed recent insights. In essence, the success to introduce novel synthetic methodologies to field of Ru chemistry is closely tied to the capabilities of powerful purification techniques, *i.e.*, both aspects are essential to prosper beyond the challenges set by the coordination step and to effectively extent the "chemistry-on-the-complex" approach for the aforementioned broad application fields.

3. Complexation chemistry

The classical synthesis of ruthenium complexes is based on the initial ligand synthesis and subsequent coordination as the final step. In the last decades, a broad range of heterocyclic precursors became commercial available to assemble the ligand framework, leading to the rapid development and screening of novel combinations within the past years. Equally important, the availability of ligands and prototypical Ru^{II} complexes as well as the established synthetic routes greatly facilitated their usage by groups focusing on applications,[108, 109] *e.g.*, for solar cells, imaging and sensing, as well as biomedical applications.

3.1. Ligand syntheses

The syntheses of pristine pyridyl-type ligands (bpy and tpy) originally embarked from dehydrogenating coupling reactions of pyridine, but the conditions are usually incompatible to most functional groups. A remarkable progress in the ligand synthesis was made applying ring-forming reactions, *i.e.*, Kröhnke-type reactions to construct the central pyridine ring in tridentate ligands (*e.g.*, tpy or dqp), or Skraup-type reactions to form the heterocyclic subunit from anilines (*e.g.*, phen or dqp). The most recent approach utilizes modern C-C bond forming reactions of the aromatic subunits, *i.e.*, relying on the Negishi, Stille and, particularly, Suzuki coupling protocols. Notably, the C-C couplings tolerate most of the organic functional groups, while the ring-forming reactions tolerate the versatile aryl halides groups – leading to a wide range of functionalized ligand sets.

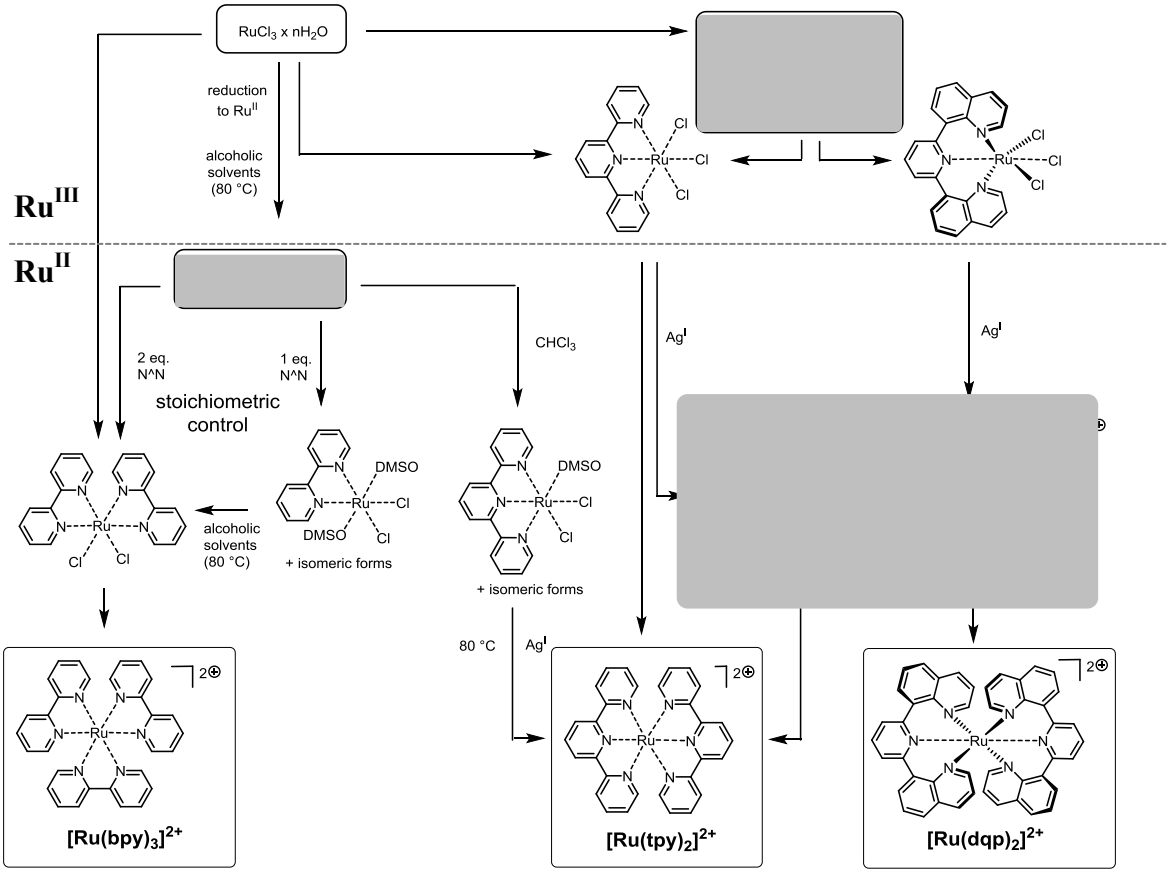

Scheme 1. Overview of the main synthetic routes towards *tris*-bidentate and *bis*-tridentate Ru^{II} polypyridyl-type complexes illustrated for the archetypical complexes $[Ru(bpy)_3]^{2+}$ (left), $[Ru(tpy)_2]^{2+}$ (middle) and $[Ru(dqp)_2]^{2+}$ (right). Synthesis embarking from the representative Ru sources (black boxes) proceeding through Ru^{III} (top) to Ru^{II} (bottom part) coordination chemistry. (a) Ru^{III} precursor suggested for π-extended N^N^N ligands. (b) Ru^{II} precursor for selective ligand exchange for bpy and tpy. (c) Bench-stable Ru^{II} intermediates for N^N^N circumventing ill-defined $[Ru^{III}(N^N^N)Cl_3]$. See text for detailed explanation.

3.2. Coordination chemistry

The preparation of Ru^{II} polypyridyl-type complexes is outlined in Scheme 1 for the prototypical complexes of *tris*-bidentate $[Ru(N^N)_3]^{2+}$ or *bis*-tridentate $[Ru(N^N^N)_2]^{2+}$. The different routes generally embark from $Ru^{III}Cl_3$ hydrate as the primary metal source, which may be converted to alternative Ru^{II} source or Ru^{III} sources (black boxes). Depending on the exact reaction conditions, the direct formation of the homoleptic Ru^{II} polypyridyl-type complexes can be achieved, however, in most cases heteroleptic Ru^{II} complexes are desired, which are usually prepared through the corresponding $[Ru^{II}(N^N)_2Cl_2]$ or $[Ru^{III}(N^N^N)Cl_3]$ intermediates. The stepwise coordination by the final chelating ligand becomes possible upon removal by the chlorides, *e.g.*, by Ag^{I}-assisted halide abstraction. In all cases, the use of Ru^{III} salts requires the concomitant reduction to Ru^{II} by the solvent (*e.g.*, alcohols) or by sacrificial

reductants (*e.g.*, *N*-alkyl morpholines). In essence, this synthetic strategy is well established for bpy and tpy ligands, but may lead to challenges when directly transferred to alternative ligand sets. Firstly, the Ru^{III} can act as an oxidant, which may open pathways for subsequent undesired ligand degradation pathways, particularly of redox-sensitive functionalities. In this context, the oxidation power of Ru^{III} is "transiently" enhanced upon Ag^{I}-promoted removal of the charge-compensating anionic chloride, so that the extent of concurring side reactions depends on the sequence of the individual coordination events and the reduction step. In addition, Ru^{III} was also found to coordinate preferentially to alcoholate oxygens, which even enforced the de-coordination from a pyridine nitrogen as revealed by the electrochemical hysteresis of an Ru complex featuring an ambidentate ligand set.[110] This observation suggests further, that the Ru^{III} state may potentially lead to false coordination with oxygen-containing functional groups, in particular if chelating modes are sterically possible. As a consequence, the bridging of (multiple) Ru centers by one chelating ligand cannot be ruled out. It appears that the acute bite angle of bpy and tpy inherently restricts the extent of wrong coordination; nevertheless, alternative binding modes were reported even for the archetypical tpy ligand framework. The work by Thummel *et al.* detailed the *pentaaza*-coordination in $[Ru(N^N^N)_2Cl]^+$ complexes from the $[Ru(N^N^N)Cl_3]$ intermediates by ^1H NMR and x-ray crystallography.[111] These two selected examples demonstrate the richness of alternative binding modes assigned to the Ru^{III} chemistry, which is further indirectly corroborated by the modest overall yields (around 50%) of the desired Ru^{II} polypyridyl-type complexes.

Hence, improved coordination routes have been developed starting from various Ru^{II} sources, *e.g.*, $[Ru^{II}(DMSO)_4Cl_2]$,[112, 113] $[Ru^{II}(arene)Cl_2]_2$ complexes (arene = cymene, benzene, mesitylene, *etc.*),[114] or the chloride-free $[Ru(MeCN)_6]^{2+}$ complex.[115] Noteworthy, the stepwise coordination of the chelating ligands (N^N or N^N^N) can be achieved exploiting the different labilities of the Ru–L bond (L = DMSO, Cl). Alessio detailed the synthetic utility of $[Ru(DMSO)_4Cl_2]$. Although various intermediate isomers with different reactivity were identified, *i.e.*, linkage of DMSO *via* the S or the O donors, respectively, as well as *cis*-/*trans*-coordination isomers of the two chloride ligands, the $[Ru^{II}(DMSO)_4Cl_2]$ precursor has been successfully utilized for a range of bidentate and tridentate ligands. In general, DMSO can be more readily replaced than chloride, which permits the introduction of two N^N ligands to form the intermediate $[Ru(N^N)_2Cl_2]$ complex. In addition, stoichiometry control of the ligand-to-precursor ratio (1:1) can yield the mono-bidentate $[Ru(N^N)(DMSO)_2Cl_2]$ intermediate. More importantly, the replacement of the remaining chlorides by the third N^N ligand required higher reaction temperatures (usually in refluxing ethylene glycol).[112]

Similarly, the Ziessel group demonstrated the versatility of $[Ru(DMSO)_4Cl_2]$ for the mild stepwise complexation for tridentate ligands based on tpy. In this case, the first coordination step is performed in chloroform to yield the $[Ru(tpy)(DMSO)Cl_2]$ intermediate, which is subjected to the coordination of a second tpy ligand upon Ag^I-promoted halide abstraction in refluxing methanol. In a similar fashion, $[Ru^{II}(arene)Cl_2]_2$ complexes (arene = cymene, benzene, mesitylene, *etc.*) were used for the stepwise coordination. As a consequence, higher yields and more reproducible synthetic protocols towards homo- and heteroleptic Ru^{II} complexes were reported, including the *mono*- and *bis*-bidentate Ru^{II} intermediates as well as the *mono*-tridentate congener. An exception is given by the dqp ligand family, which was found to require a Ru^{III} source to facilitate the selective tridentate coordination of the first dqp ligand.[116, 117] The preparation of $[Ru(dqp)(MeCN)_3]^{2+}$-based complexes was recently improved employing the defined $[Ru^{III}(PhS^iPr)_2(MeOH)Cl_3]$ precursor, applying optimized conditions from related π-extended tpy ligands.[118] Nonetheless, the Ru^{II} precursors are applicable also for a multitude of cyclometalating ligands (N^C, N^C^N, or N^N^C). For these ligands, the deprotonation of the C–H bond is necessary and often requires higher temperatures. Note that strong bases (*e.g.* BuLi) were found incompatible for tpy,[119] which suggests an even more pronounced bae-sensitivity of the corresponding complexes (*vide infra*). This challenge is elegantly circumvented by exploiting Ag^I-stabilized carbanionic ligands using Ag_2O in case of a sufficient CH-acidity, which is particularly suited for electron-deficient heterocycles (*e.g.*, 1,2,3-triazoles).[120-122]

In summary, the versatility of a synthesis route is often evaluated in terms of overall yield. However, side reactions occur inevitably to form Ru^{II} byproducts, which demand a versatile purification protocol to remove such impurities. An illustrative early example is provided by the opposing luminescence data reported for $[Ru(tptpy)_2]^{2+}$ (tbtpy is 4,4',4''-triphenyl-2,2':6',2'') by the groups of Crosby[123] and Sauvage.[124] In course of their study, Sauvage and coworkers stated the necessity to perform careful column chromatography to remove luminescent impurities.[124] Notably, the separation of dicationic Ru^{II} complexes can become elaborate or even become unsuccessful in case of intractable mixtures, which renders the applied synthetic route impractical in the final stage (section 6). In this context, the "chemistry-on-the-complex" offers an alternative strategy, as common building blocks can be prepared under optimized conditions and subsequently diversified for their desired task.

4. “Chemistry-on-the-complex”

The chemical transformation of Ruthenium complexes after coordination has been used since their rise in the 1970s. However, various alternative synonyms occur in literature, *e.g.*, post-coordination, or such reactions were not termed explicitly. In order to warrant a comprehensive overview, the chemical databases were screened by structural transformation classified by C–C, C–O, C–N, or C–S formation/breakage, complemented by a keyword search for the related name reactions, *e.g.*, “Sonogashira”, “Suzuki” or “Amidation” to name a few. All publication from this initial survey that met the “chemistry-on-the-complex” criteria were included and categorized in the following sections: First, an overview of the conversion of functional groups is provided, which usually aims at tailoring the photophysical and redox-chemical properties of the Ru sensitizer. In the subsequent section, the conjugation of Ru complexes with other functional molecular fragments will detailed, which is highly attractive for specific recognition processes (targeting functions in life science applications) or to control light-induced electron- or energy transfer processes in discrete donor-acceptor assemblies. For this task, the amidation reaction and the Sonogashira cross-coupling reaction were found most popular for biologic compounds. Nucleophilic substitution reactions (*e.g.*, Williamson etherification) as well as various cross-coupling methodologies (*e.g.*, Suzuki, Stille and Negishi reaction) are also reported. Finally, the polymerization of Ru-containing monomers is discussed, which represent an active field in material science for highly responsive sensor applications or for energy conversion.

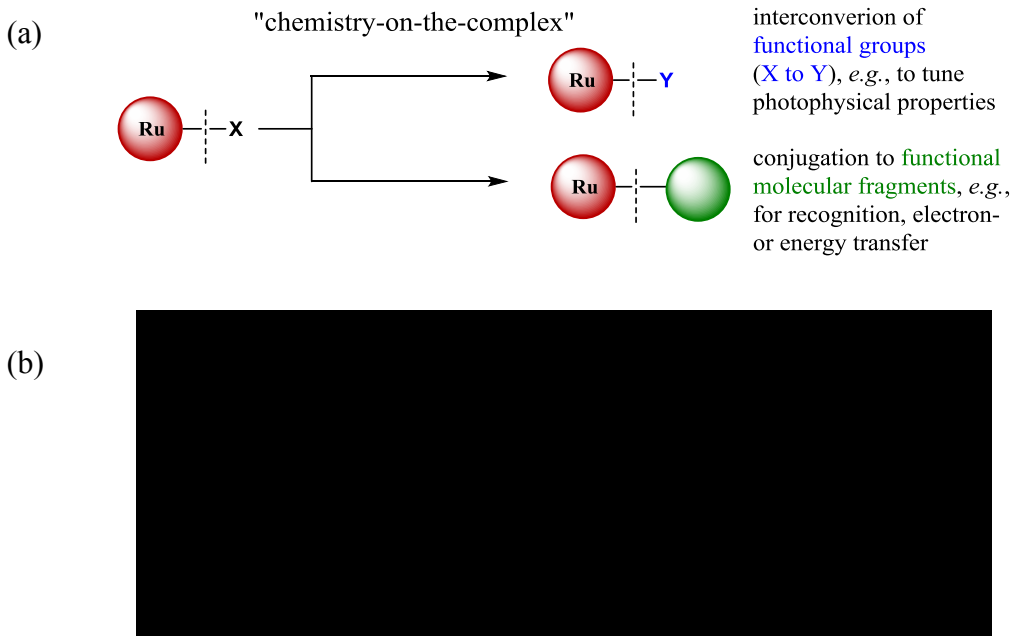

Figure 4. Schematic representation of the "chemistry-on-the-complex" methodology for (a) the conversion of functional groups and (b) the linkage with other molecular (functional) moieties (b).

4.1. Conversion of functional groups

Functionalized Ru complexes are conventionally prepared from their corresponding ligands, *i.e.*, the functional group is already introduced during ligand synthesis. Most of the typical functional groups can withstand the coordination conditions, while other may suffer from chemical instability. In the context of the more challenging purification of Ru^{II} complexes *vs.* their organic predecessors it is important to realize that even a small extent of side reactions imposes substantial tedious purification efforts (*vide infra*). For example, esters may by hydrolyzed or undergo transesterification reactions with alcoholic solvent used during the coordination steps, nitro groups may become reduced, or iodides and boronic acid derivatives may be cleaved to name only a few. Note that most functional groups pattern may also be directly accessible through coordination. However, the conversion of functional groups *after coordination* can provide a complementary strategy, in particular for modular synthesis strategies and in case of difficulties associated to undesired coordination modes during complexation. The general reactivity of Ru complexes can be grouped into redox-reactions of the metal center ($Ru^{III/II}$) as well transformations of functional groups. Firstly, higher oxidation states are stabilized by anionic ligands, *e.g.*, chloride ions are more strongly bound to Ru^{III} centers than, *e.g.*, neutral solvent molecules. In addition, the reactivity of functional groups that are bound directly to the ligand scaffold is affected by the electron withdrawal due to the cationic Ru center. Since the ligands often consist of electron-deficient heterocyclic

subunits, nucleophilic attack in case of a proper leaving group (Cl) or reduction (NO_2) can occur. Notably, cyclometalated Ru^{II} complexes can be subjected to selective CH-activation reactions of the electron-rich (carb-)anionic subunits. Finally, functional groups that are not directly bound to the ligand framework undergo their typical transformations. Scheme 2 illustrates the most important reactions of functional groups bound directly to the ligand framework, as highlighted by selected examples.

The CH-activation is selectively possible for cyclometalated complexes, whereby the carbanionic ring is halogenated or nitrated in the presence of a suitable oxidant (Scheme 2a). The nitration was achieved by $AgNO_3$/PhOCl [125] or $CuNO_3$,[126-128] while the halogenation was obtained using $CuCl_2$ or $CuBr_2$ to form the respective functionalized complexes.[129] Notably, an excess of the copper(II) halide is used to prevent undesired dimerization, which suggests the intermediate radical character that is stabilized by Ru^{III}.[129] Alternatively, the bromination can be readily achieved with *N*-bromosuccinimide (NBS),[130-135] while iodation occurs with I_2 and $PhI(OAc)_2$.[130]

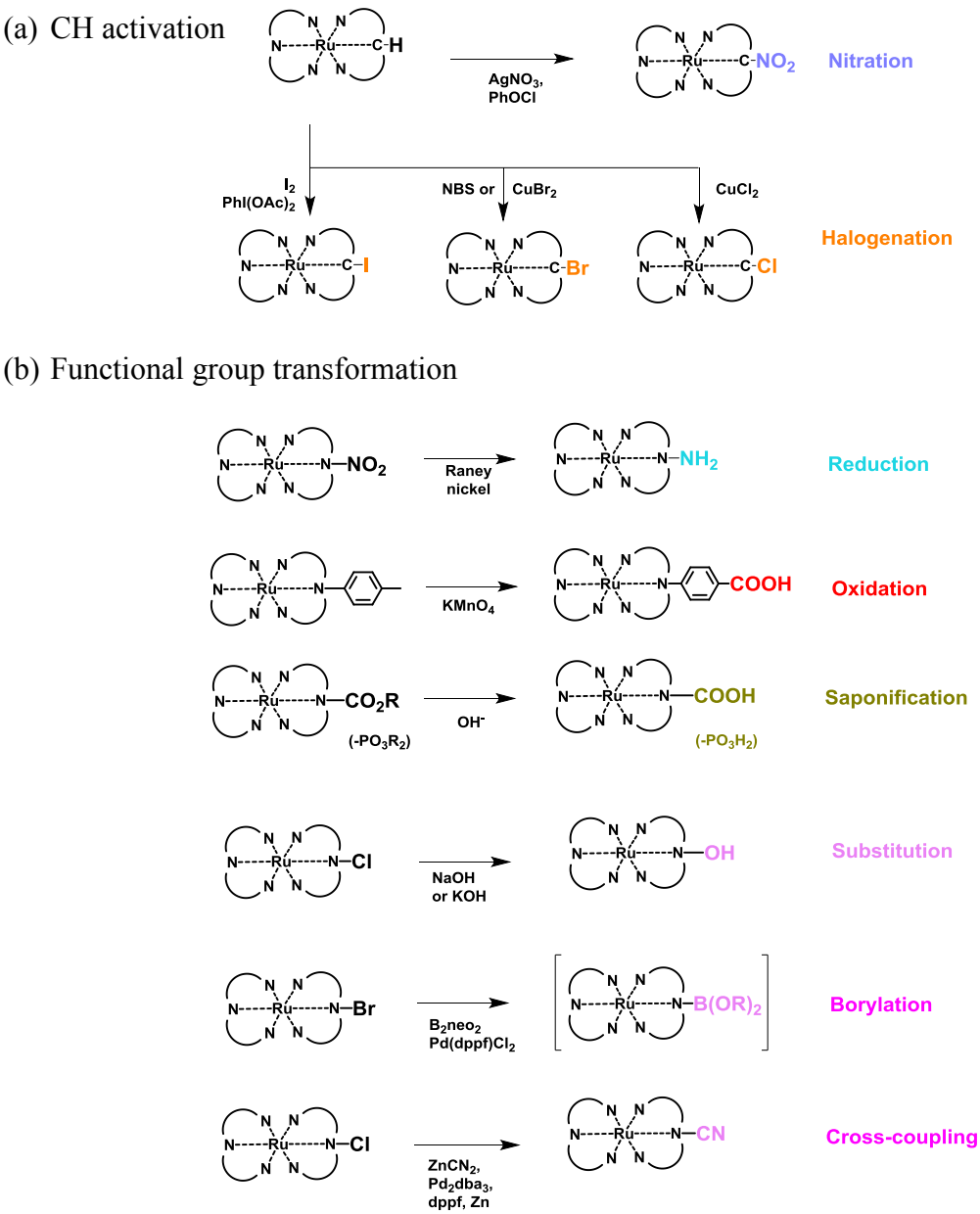

Scheme 2. Schematic representation of representative transformations of functional groups: (a) Selective CH activation of cyclometalated complexes and (b) representative functional group transformations. See also section 5 for details and further miscellaneous examples.

Scheme 2b depicts examples for representative functional group conversions, which are typical for $[Ru^{II}(N^N)_3]$-type and $[Ru^{II}(N^N^N)_2]$-type complexes. Further details and specific examples are provided in section 5, as these reactions are often applied to connect functional molecular fragments.

The conversion of nitro groups into the corresponding amino functionality can be cleanly achieved using Raney Nickel. Although the amino group is often introduced via the corresponding ligand, the transformation of the functionalized complex circumvents potential false coordination modes during complex formation. The amino group serves as a valuable

precursor for subsequent amidation reactions, which will be discussed in more detail in section 5.2. The selective oxidation of alkyl groups is rare, but reported for the benzyl positions by potassium permanganate.[136] Following this procedure, phenyl-spaced carboxylic acid groups can be introduced on the corresponding Ru^{II} complex. Given the importance of carboxylic acid groups for the immobilization of Ru^{II} complexes onto n- or p-type semiconductors (TiO_2, NiO *etc.*) for photovoltaic and photocatalytic applications, the saponification of the ester derivatives is the preferred universal route. Note that the direct coordination of the amphiphilic ligands bearing the free acid groups is challenging due to the low solubility caused by the intermolecular hydrogen bonding between the acidic carboxyl protons and the basic pyridine nitrogen atoms. Likewise, the high polarity and the possibility of acid-base equilibria enhance the solubility of the corresponding Ru^{II} complexes in protic solvents including water considerably, while the solubility in organic solvents is usually decreased. Hence, purification is often based on excessive washing as chromatographic purification is hampered by the strong adsorption onto the SiO_2 surface. Nonetheless, the hydrolysis of esters can be promoted under basic conditions by water/NEt_3 mixtures,[137, 138] LiOH,[15] NaOH[15, 16] or NBu_4OH,[19, 139-141] as well as aqueous sulfuric acid.[11, 98] Notably, the related phosphonate ester derivatives can be hydrolyzed in aqueous HCl,[142] or by trimethylsilylbromide[143] or trimethyliodide,[144] respectively.

The electron-deficient nature of the pyridine rings, which is even more enhanced by the coordinated Ru^{II} center, renders the *para*-position of chloride-decorated Ru^{II} complexes susceptible to nucleophilic replacement. For example, refluxing in aqueous NaOH[145] or KOH[146] in a water/THF mixture yields the corresponding hydroxyl substituent.

The utilization of halogen substituents has received great attention in Pd-mediated cross-coupling reactions. The borylation of bromine-decorated Ru^{II} complexes and subsequent Suzuki-Miyaura cross-coupling has been demonstrated by the Williams group using a neopentyl-based diboron reagent (B_2neo_2) and $Pd(dppf)Cl_2$.[119] Analogously, the cyano group can be introduced in a catalytic reaction employing $Pd_2(dba)_3$, dppf, $ZnCN_2$ and zinc dust.[147, 148] Numerous catalytic systems were reported for alternative C−C bond forming reactions, ranging from various combinations of Pd pre-catalysts and ligands based on phosphines[149] or *N*-heterocyclic carbenes,[150-152] to nanoparticles[153] or metal-organic frameworks (MOFs).[154] In general, after the stage of initial oxidative addition to the active catalyst,[150, 153-158] a variety of coupling partners can be used in the corresponding Suzuki-Miyaura coupling,[149, 159-161] Sonogashira reaction,[162, 163] Heck coupling [161] or Stille reactions.[164]

In summary, the aforementioned methods demonstrate various synthetic transformations of functional groups directly bound the ligand framework, which has a profound impact on the photophysical and redox-chemical properties.

5. Conjugation strategies

The previous chapter introduced the inherent reactivity and conversion of functional groups attached to the ligand scaffold. In this section, the most important methods are detailed for the coupling a Ruthenium complex with a functional molecular fragment. Noteworthy, these transformations often occur at peripheral functional groups that are decoupled from the Ru complex by various organic spacer units, so that the intrinsic reactivity resembles those of the "organic" counterparts. This strategy is termed "conjugation" in the following, owing to the success and the importance in the field of life science application, *i.e.*, to connect specific targeting or therapeutic function to the complex.

5.1. Complexation of metal-containing fragments

Dendrimers, star-shaped and macrocyclic multinuclear systems are highly attractive model compounds to study fundamental energy and electron transfer steps, including directional cascades and multi-photon processes.[165] The utility of these architectures to elucidate fundamental photophysical processes originates from their inherent symmetry to simplify data analysis, as well as synthetic advantage to link multiple units in a single step by the same type of reaction (Figure 5).

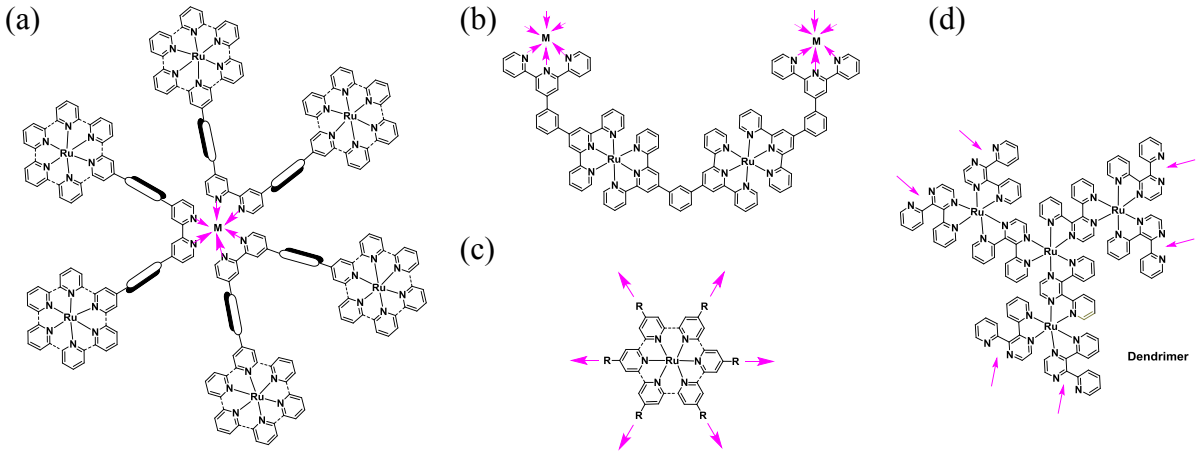

Figure 5. Schematic representation of the synthesis of stars and macrocycles: a) Synthesis of the arms-first and coordination to the core; b) macrocyclization from metal-containing fragments; c) decoration of the arms onto the ruthenium core, d) stepwise pathway for the synthesis of dendrimers (see also Figure 6). The final reaction steps are indicated by arrows (magenta).

Multimetallic macrocycles can be formed from one precursor unit, while the star-shaped congeners are composed of a core and a corona and, thus, imply two different metal-containing subunits (*e.g.*, Ru^{II}, Os^{II} or Fe^{II}). Historically, the undesired coordination modes in the fully assembled ligand framework were blocked, *e.g.*, by methylation of the pyridines. Then, a sequential coordination-deprotection-coordination strategy was pursued for the iterative synthesis of the dendrimer generations (Figure 6).[165]

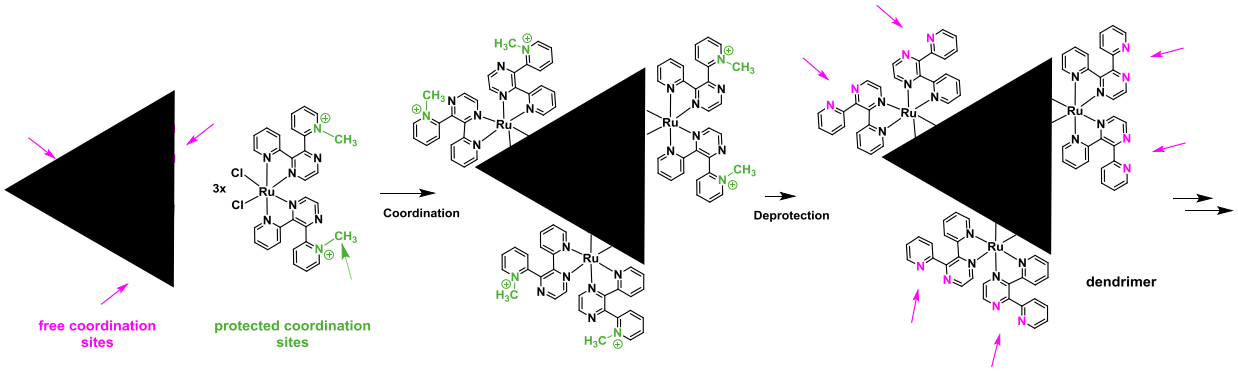

Figure 6. Assembly of polynuclear dendrons using blocked coordination sites (green). Higher-order and heterometallic dendrons accessible *via* the iterative coordination/deprotection steps. Adopted from Balzani *et al.*.[165]

Although efficient directional energy transfer was achieved in these strongly-coupled polynuclear complexes, the excited state lifetimes and quantum yields were often unfavorably altered in comparison to the $[Ru(bpy)_3]^{2+}$ reference complex. Hence, strategies to reduce the electronic communication were pursued subsequently.[165, 166] In this regard, Ru complexes were functionalized *via* attachment of the free ligands and subsequent complexation. The convergent synthesis strategy starts with the preparation of the corona followed by formation of the core in the last step (Figure 5a). Heteropentamer and heteroheptamer star complexes were synthesized by the Constable groups *via* the first strategy.[167, 168] Several Williamson ether syntheses were performed to create a spacer between the peripheral ruthenium units to the free bpy moiety, which was used to form the iron or cobalt core. Also the synthesis of a related tetranuclear architecture is reported, which contains Ru or Os in the core.[169] In this case, functionalized $[Ru(bpy)_3]^{2+}$ complexes were connected via *aza*-coupling to free bpy units that were finally complexed by osmium. Note that a variety of further dendritic and star-like structures are reported which share the complexation as the final step and, thus, will not be further discussed.

In this context, a six-membered macrocycle containing ruthenium and iron ions was synthesized in a stepwise fashion (Figure 5b).[170] The first step is the coordination of a *bis*-

terpyridine to the $[Ru(tpy)Cl_3]$ complex to obtain a binuclear compound which can be further functionalized *via* the Sonogashira reaction. In the following step, the new terpyridine units bearing an acetylene function were introduced. Two of these half rings can form the macrocycle from a $FeCl_2$ source. Another hexameric macrocycle containing iron and ruthenium centers was reported by the Newkome group.[171] In this example, a $[Ru(tpy)_2]^{2+}$ unit was equipped via the Sonogashira reaction with two tpy units, which were subsequently complexed by Fe^{II} ions to form an iron-based hexameric macrocycle with six peripheral $[Ru(tpy)_2]^{2+}$ units.

The alternative divergent strategy embarks from a highly-functionalized metal complex core (Figure 5c) to attach multiple peripheral moieties. Note that in contrast to the convergent approach, incomplete functionalization and/or side reactions are challenging to separate. In most of the cases of multimetallic assemblies, a free ligand is added followed by complexation. Lee *et al*. reported the decoration of a $[Ru(bpy)_3]^{2+}$-type core with bpy units via esterification (section 5.2).[172] The key synthetic steps involve the core formation from di(hydroxymethyl)bipyridine and a Ruthenium-cymene precursor, which was subsequently linked to six bipyridine mono-carboxylic acid units employing peptide coupling reagents (*vide infra*). The final coordination steps employed the Ag^I-activated *bis*-bidentate $[Ru(N^N)_2(acetone)_2]^{2+}$ precursor bearing peripheral ligands N^N based on bpy or phen derivatives. Notably, various monometallic star-shaped complexes were reported following the divergent approach, which will be briefly mentioned for completion albeit no final coordination step occurs. The Gerald Meyer group reported the Sonogashira coupling of a hexabromo-decorated $[Ru(bpy)_3]^{2+}$ complex to attach the methyl ester of *iso*phthalic acid for the immobilization onto TiO_2.[173-175] The successful adsorption onto TiO_2 was assigned to the 12 present anchor units, although these units bind weaker to the semiconductor than carboxylates and, moreover, display different charge transfer and electron injection kinetics due to the different electronic communication between the sensitizer and the semiconductor.[173-175] The introduction of similar anchor units is also possible *via* the copper-mediated azide-alkyne cycloaddition reactions, *e.g.*, to attach carboxyl[176] or phosphonate groups.[177] Also the usage of such highly-functionalized complexes as initiators for the controlled radical polymerization techniques is reported (section 5.7), *e.g.*, using the reversible-addition-fragmentation chain transfer (RAFT) polymerization[178, 179] as well as the atom transfer radical polymerization (ATRP).[180, 181] The latter examples feature the divergent character of multiple reactions of a central Ru unit, which descended from multimetallic architectures assembled *via* coordination and advanced the "chemistry-on-the-complex"

methodology to various other fields based on selective linkage reactions, which will be discussed in detail in the following.

5.2. Acylation reactions

5.2.1. Amidation

The amidation reaction represents a highly developed and versatile tool to link two molecular fragments, originating from the ground-breaking work in peptide chemistry. Due to mild reaction conditions and selective activation by the coupling reagents, the established protocols are generally applicable to Ru^{II} complexes, *e.g.*, for the decoration with amino acids, peptides, proteins or DNA. Because the amide bond is directional (–CONH– *vs.* –NHCO–), two complementary linkage patterns are conceivable (Figure 7a). For example, carboxyl-functionalized $[Ru(bpy)_3]^{2+}$ and amino-decorated $[Ru(bpy)_2(phen)]^{2+}$ represent the most frequently employed Ru complexes, whereas various coupling reagents are used in combination with *N*-based bases (TEA, DIPEA or pyridine) (Figure 7b). Notably, the mild conditions can be transferred beyond medicinal and biochemistry, *e.g.*, to attach polymer chains, carbon nanotubes, catalytic sites, or redox active centers additional chromophores.

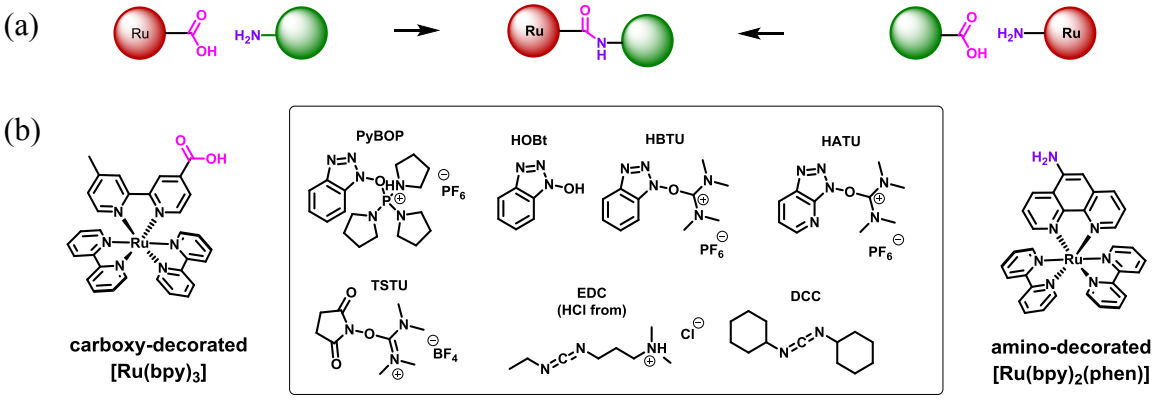

Figure 7. (a) Schematic representation of complementary amidation reactions to couple Ru complexes (red sphere) with functional moieties (green sphere). (b) Typical functionalized complexes, *i.e.*, carboxyl-decorated $[Ru(bpy)_3]^{2+}$ (left) and amino-decorated $[(Ru(bpy)_2(phen)]^{2+}$ (right), including peptide coupling reagents (middle). See text for details, and Table 1 for abbreviations of coupling reagents.

The following section is organized according to the type of functional moiety that is linked via amidation to a Ru^{II} complex. Table 1 summarizes the reported examples to detail the reaction conditions, information regarding the tolerated functional groups and moieties, and the yields (if stated). For completion, related coupling reactions (*e.g.*, thiocarbamate-linkages) are mentioned in the text.

Table 1: Reaction conditions and yields of the amidation on the ruthenium ligand scaffold.[a]

	Ref.	Tolerated substitution pattern of Ru complex	Coupling partner	Reaction conditions	Temp. [°C]	Time [h]	Yield [%]
1	[182]	None	*tert*-Butoxycarbonyl-S,S-1,2-diaminocyclohexane	$SOCl_2$, NEt_3, MeCN	Reflux	15, 2	92
2	[183]	None	Imidazolamine	$SOCl_2$, CH_2Cl_2, MeCN, NEt_3	Reflux rt	4, 1	71
3	[184]	None	Ampicillin	EDC, NHS H_2O	rt	6	-
4	[185]	Dipyridophenazine	*tert*-butyl *N*-[2-(*N*-9-fluorenylmethoxy-carbonyl)amino ethyl]glycinate	HBTU, NEt_3 MeCN; DIPEA	rt	Over night	82
5	[52]	Dipyridophenazine	Oligopetides	HATU, DIPEA, lutidine,	rt	10	-
6	[186]	None	p17 Peptide epitope	Iodoacetic anhydride, MeCN	4	8 h	-
7	[187]	Benzyl amine	Carbon nanotubes	DMF NEt_3	rt	5 Days	
8	[188]	Acetyl-aminoethyl glycine	bpy	HOBt HBTU, DIPEA, CH_2Cl_2	rt	2 Days	49, 83
9	[51]	Dipyrido phenazine	Peptides	PyBOP, DIPEA DMF	rt	Over night	-
10	[53]	Phenyl	Oligonucleotides	DMF, TBTU, Hünigs base,	rt	Over night	
11	[189]	Methyl	Tripeptide GHK	DCC HOBt DMF			30
12	[68]	Phenyl	Arg-Gly-Asp-peptide	DMF PBS	rt	4-6	57
13	[190]	Methyl	PA and Albumin	DMSO, $NaHCO_3$	rt	Over night	-
14	[191]	None	Peptides	NEt_3, DCC CH_2Cl_2/MeCN	rt	2 Days	33-59
15	[192]	Carboxylic acid	Oligonucleotides	PyBOP DIPEA NMP	rt	24	30-55
16	[63]	None	Peptides	PyBOP/HOBt, DIPEA	rt	Over night	97
17	[64]	Dipyridophenazine	Peptides	HBTU/HOBt/ DIEA, NMP DMF	rt	4	4.8
18	[66]	None	Squalene-*N*-hydroxysuccinimide	CH_2Cl_2, NEt_3	20	4	75
19	[193]	None	Succinimidyl ester	MeCN/ Net_3	40	2	74
20	[194]	(Carboxylic acids by stoichiometric control)	Aminomethyl styrene	DMTMM, DMF	rt	2 Days	65
21	[195]	Carboxylic acid	C_5F_5-actived polymer	THF, DMF, NEt_3	45	90	45%
21a	[196]	"Amino-alkyl Ru"	Poly(acrylic acid)	EDC, HOBT, DMF	rt	48	Up to 95%
22	[197]	Methyl, Diethyl-formamide	Poly(amino-styrene)	BOP, HOBt, NMM DMAP DMF	rt	2	-
23	[198]	Methyl, Vinyl	Aminoethylstyrene	BOP, DMAP, NMM, HOBt, DMF	rt	12	60
24	[199]	Phenothiazine	bpy-CO_2Et	CH_2Cl_2	rt	12	64
25	[200, 201]	None	bpy	$SOCl_2$, DMF DIPEA	100	Over night	97
26	[50]	Dipyrido	Bridging histidine	PyBOP, DIPEA	rt	Over	1-30

		phenazine				night	
27	[202]	Ester, acid, amine	bpy	CH_2Cl_2/MeCN (NEt_3, HATU)	40 (rt→50)	12 (18 →2)	90-93 (82)
28	[203]	Methyl	Ferrocenyl carboxamide	NEt_3, MeCN	41	1.5	76
29	[204]	Methyl	$[Co^{III}$(heptanoic-acido)(bis(acetyl-acetone)ethylene-diimine)$(NH_3)_2]Cl$	DMSO, TSTU, imidazole	37	Over night	
30	[205]	Ester	Ru^{II} complex	MeCN, P_1tBu	rt	4	79
31	[206, 207]	None	bpy	$SOCl_2$ THF, NEt_3 MeCN	Reflux, rt	3-4 Over night	20
32	[208]	Methyl	Diethylenetriamine pentaacetic dianhydride	MeCN, NEt_3	rt	24	100
33	[144]	Phosphonic ester	Tyrosine, alanine Carotinoide,	PyBOP, DIPEA CH_2Cl_2/MeCN	rt	12	75
34	[209]	TentaGel S Wang	Naphthalene, coumarines, anthracene, fluorene, methyl, trifluoro-methyl	CH_2Cl_2/pyridine, PyBOP	rt	12	33-80%
35	[210]	None	TEOS	NEt_3, EDC; NHS DMF, H_2O, EtOH	rt	12+ 24	-
36	[196]	Alkoxy	Block-copolymer	EDC HOBT DMF	rt	48	-
37	[211]	Ester, acid, amine	bpy	CH_2Cl_2/MeCN (NEt_3, HATU)	40 (rt→50)	12 (18 →2)	70
38	[212]	Methyl	BSA	Sodiumborate buffer, DMF	rt	2	-
39	[213]	None	Proline	BOP, HOBt, NMM,DMAP DMF	rt	47	
40	[214]	Methyl	4-Azidobutylamine	DIPEA, DMF	rt	3	80
41	[215]	Methyl	Phenothiazine and methylviologen on a lysine	PyBOP, DMF	rt	Over night	78
42	[75]	None	Adamantyl	DMF, DMTMM	rt	8	60
43	[216]	Methyl	Lys, LysLys	Phosphate buffer DMF	rt	Over night	45, 75
44	[217]	Methyl	Oligoproline	NMM, CH_2Cl_2, DCC, DMAP	rt	16	82
45	[218]	Sodium benzenesulfonate	Propagylamine aminopropan	TBTU DIPEA DMF	rt	8	94

a) EDC (ethylcarbodiimide hydrochloride), HOBT (1-hydroxybenzotriazole), PBS (phosphate buffered saline pH 7.4), DIPEA (diisopropylatethylamine), PyBOP (benzotriazol-1-yloxytris(pyrrolidino)phosphanium hexafluorophosphate), HBTU (*O*-benzotriazole-*N,N,N',N'*-tetramethyl-uronium-hexafluoro-phosphate), NMP (N-methylpyrrolidone), HATU (2-(7-aza-1H-benzotriazole-1-yl)-1,1,3,3-tetramethyluronium hexa-fluorophosphate), DCC (dicyclohexylcarbodiimide), BOP (benzotriazolyl)oxy)tris-(dimethyl-amino)phosphonium hexafluorophosphate, NMM (*N*-methylmorpholine), DMAP (4-(dimethylamino)pyridine), TSTU **(***O*-(*N*-succinimidyl)-*N,N,N',N'*-tetramethyluronium tetrafluoroborate**),** P_1tBu (phosphazene base *tert*-

butylimino-tris(dimethylamino)phosphorane), DMTMM (4-(4,6-dimethoxy-1,3,5-triazin-2-yl)-4-methylmorpholinium chloride), TRIS (**t**ris(hydroxymethyl) aminomethane).

Ru-bioconjugates. In the past decade, the amidation reaction has been widely applied to prepare metal-conjugates with biologically relevant moieties, as the Ru^{II} polypyridyl complex is stable under physiological conditions and, thus, prevents concomitant poising or undesired degradation. The ruthenium dyes were used to covalently label peptides and proteins (entries 3–6[52, 184-186] and 12–15)[68, 75, 189-192, 218-221] or DNA strands (entries 9–11), including non-covalent DNA intercalation.[51, 53, 55, 56, 189] In addition, energy and electron transfer processes are investigated to study the internal structure and the associated changes upon target binding, *e.g.*, for peptide sequences[67] or DNA strands (entry 9).[51] In addition, biological process can be visualized by Ru-conjugates, *e.g.*, the circulation within the blood system (entry 13),[190] or incorporation pathways of peptides into cells (entries 16–18).[63, 64, 66] Throughout these reports, similar amidation protocols were applied to prepare the conjugates, hence, representative examples providing details will be discussed. Gui *et al.* synthesized an aptasensor for the ultrasensitive detection of thrombin via an *in situ* generating self-enhanced luminophore by lactamase catalysis for signal amplification.[184] The synthesis was performed using 1-ethyl-3-(3-dimethylaminopropyl)carbodiimide (EDC) and *N*-hydroxy succinimide (NHS) and the product solution was used without further purification. Oh *et al.* reported a peptide-based optical biosensor, which consists of a $[Ru(bpy)_2(phen)]^{2+}$ complex and an electron-accepting methyl viologen moiety that are bridged by a polypeptide spacer. The synthesis starts form the amidation of the amino-decorated Ru complex with iodoacetic anhydride, followed by nucleophilic substitution of the iodine by the thiol-groups present in the peptide. In the absence of a target antibody, photo-induced electron transfer occurs that quenches the Ru emission, whereupon binding of a target to the peptide leads to a more extended conformation, which translates to an increased energy transfer distance and, ultimately, to an enhanced Ru emission. The authors emphasized the recognition capability of the peptide, in order to form a robust optical sensor for HIV-antibodies.[186] Sadhu *et al.* reported the coupling of an isothiocyanate-decorated $[Ru(bpy)_2(phen)]^{2+}$ complex to the amino-terminus of a lysine-PEG-ligand conjugate, whereby ligand denotes a biologically relevant targeting function (biotin, glucose, *etc.*).[67] An oligomeric receptor protein was used to bind simultaneously the Ru-decorated conjugate as well as a rhodamine dye with the same targeting function, which leads to a photo-reductive release of the rhodamine dye upon excitation of the Ru unit. Note that the preparation of the isothiocyanate-decorated Ru

complex likely follows the related *in situ* activation *via* thiophosgene from the corresponding amino-decorated Ru congener,[222] although no reference was provided by Sadhu *et al.*.[67]

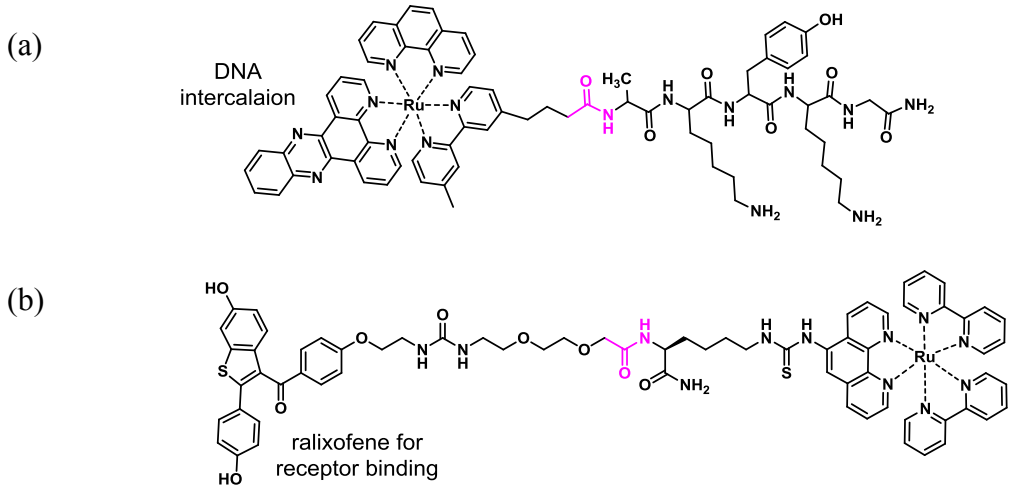

Figure 8. Schematic representation of selected examples of Ru-bioconjugates: (a) Containing peptide sequences for DNA crosslinking,[51] and (b) amide linkage to attach a ralixofene-ligand for receptor binding.[67]

Anion recognition and self-assembly. The Beer group (Table 1, entry 1 and 2)[182, 183] utilized amidation reactions to construct chiral receptors for anion recognition.[167, 168] In their first report, the twofold decoration of *bis*-carboxy bpy with the free amino group of chiral *tert*-butoxycarbonyl-R,R-1,2-diaminocyclohexane resulted in the corresponding ligand N^N, but complexation to form the $[Ru(bpy)_2(N^N)]^{2+}$ complexes lead only to intractable mixture, Alternatively, the related "chemistry-on-the-complex" approach gave the desired complex in 64% yield, which were separated into the corresponding Δ/Λ enantiomers by chiral ion exchange chromatography (section 7.1.5). However, the enantioselective recognition of chiral carboxylates via the *bis*-amide pincer moiety was not successful. Based on this amide linkage, the group reported later the related $[Ru(bpy)_2(N^N)]^{2+}$ complexes bearing an alkyl-spaced imidazole, which was subsequently quaternized with MeI. The obtained complexes were studied in mixed organic-aqueous solutions *via* luminescence spectroscopy to detect chloride, bromide, and the biologically relevant anions dihydrogen phosphate and ATP. The Williams group utilized the amide linkage to attach free bpy units to the $[Ru(bpy)_2(N^N)]^{2+}$ core, which serves for the subsequent cation complexation of Cu^{2+} and Zn^{2+} (entry 8).[188] The amidation reactions were performed using 1-hydroxybenzotriazole (HOBt), *O*-(benzotriazole-1-yl)-*N,N,N′,N′*-tetramethyluronium hexafluorophosphate (HBTU) and diisopropylethylamine (DIPEA) in dichloromethane with good isolated yields (49 and 83%, respectively). As a result

cation's multivalency, self-assembled structures can form assigned to the observed Ru emission quenching.

Ru-polymer architectures. The amidation reaction has been also applied to incorporate Ru^{II} polypyridyl-type complex into polymers. The conceptional approach shares similarities to the synthesis of star-shaped complexes and Ru-containing macrocycles (section 5.1), and can be extend to polymers with various linkages (section 5.7). One strategy relies on Ru-containing monomers and the subsequent polymerization. For example, Chen *et al.* (Table 1, entry 19) reported the amidation of a NHS-activated carboxyl-decorated $[Ru(bpy)_3]^{2+}$ complex to introduce a ring-strained polymerizable group in good yield (74%).[193] The ring opening metathesis polymerization (ROMP) was achieved using a Grubbs-Type ruthenium alkylidene initiator to reach high conversions (90%). A second example published by Lu reports the monomer synthesis *via* amidation of a *bis*-carboxyl-decorated $[Ru(bpy)_3]^{2+}$ complex by one or two equivalents of aminomethyl styrene, depending on the stoichiometry (entry 20).[194] The subsequent free radical copolymerization with aminomethyl styrene was initiated by *azo-bis*(isobutyronitrile) (AIBN) generated electroactive chemiluminescent sensors. However, the practical versatility of the polymerization technique to prepare defined homo- and copolymers greatly depends on the absence of deleterious termination reactions with the growing chains with the Ru complexes, which may explain the inferior role of this approach.

The complementary strategy to prepare Ru-polymer architectures relies on the multiple amidation of a polymer chain by Ru units in a polymer-analogous fashion. This approach benefits from optimized polymerization techniques for a given monomer to control the degree of polymerization, dispersity and functional group fidelity. Borg *et al.* reported the direct amidation of a pentafluorophenyl-activated polyacrylic acid (PAA) block using the peripheral amino-group of a $[Ru(tpy)_2]^{2+}$-based complex (entry 21).[195] The Tew group detailed the EDC and HOBT mediated amidation to introduce $[Ru(tpy)_2]^{2+}$-based complexes into the polyacrylic acid block, reaching high yields of functionalization of up to 95% according to ^1H NMR and FT-IR analysis (entry 21a).[196] The Meyer group reported various examples of the side-chain amidation of an aminoalkyl-functionalized polystyrene with a carboxyl-decorated $[Ru(bpy)_3]^{2+}$ complex (entry 22)[197, 223] as well as the complementary NHS-functionalized polystyrene,[224] including a vinyl-equipped Ru complex designed for subsequent crosslinking through electropolymerization to yield photoredox-active metallopolymeric films on the surface of an electrode (entry 23).[198]

Ru-metal assemblies. The amidation reaction has been utilized by many groups to connect Ru^{II} polypyridyl-type complexes with various functional metal complexes (Table 1, entries 24-32), designed for phototherapeutic or photocatalytic purposes, or to study fundamental energy and electron transfer processes.[50, 199-208, 211, 216, 225-227] The Barton group extended their work on Ru-peptide conjugates to attach an electron-accepting pentammine ruthenium(III) complex via a peptide linker to the DNA-intercalating $[Ru(bpy)_2(dppz)]^{2+}$ chromophore unit (entry 26). After light-induced charge transfer, the intercalated Ru^{III} led to oxidative DNA damage.[50] The Sakai group reported the direct amide linkage of an amino-decorated $[Ru(bpy)(phen)]^{2+}$ with a diester-functionalized bpy, which was subsequently complexed by Pt for light-induced hydrogen production from water. The Meyer group coupled a $[Ru(bpy)_3]^{2+}$-based chromophore to a $[Ru(tpy)(bpy)(H_2O)]^{2+}$ fragment for catalytic water oxidation, including the immobilization onto TiO_2 for a photo-electrochemical cell.[200, 201]

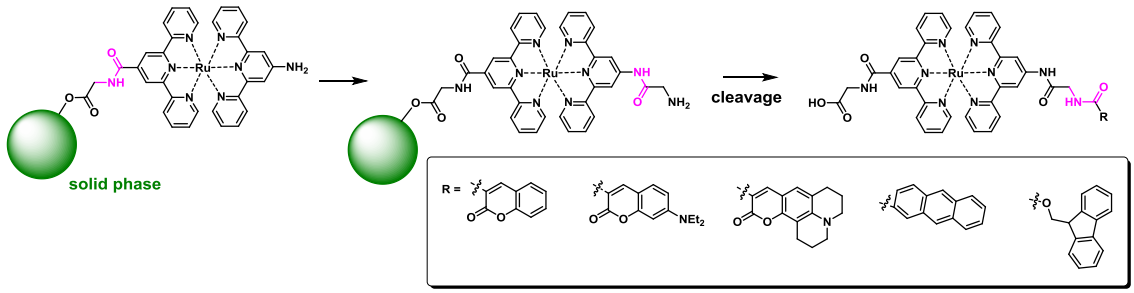

Figure 9. Schematic representation of selected examples for the solid-phase supported synthesis of amide-linked Ru-dye assemblies by Heinze and coworkers.[209]

The Heinze group advanced the application of solid-phase synthesis of metallo-amino acids,[228, 229] *i.e.*, to utilize carboxyl-decorated $[Ru(bpy)_3]^{2+}$ and amino-decorated $[Ru(bpy)_2(phen)]^{2+}$ (entry 37),[211] as well as carboxyl- and/or amino-equipped $[Ru(tpy)_2]2^{+}$-complexes (entry 30).[202, 205] The amide linkage was used to attach bpy units for subsequent coordination to $Re(CO_3)Cl$ or $PtCl_2$ fragments, as well as ferrocene units or a second $[Ru(tpy)_2]^{2+}$ unit to study fundamental energy and electron transfer processes. In the latter case, the synthesis of dinuclear metallo-amino acid complexes required the selective protection of the functional group to be inert during coupling, in order to prevent polymerization.[205]

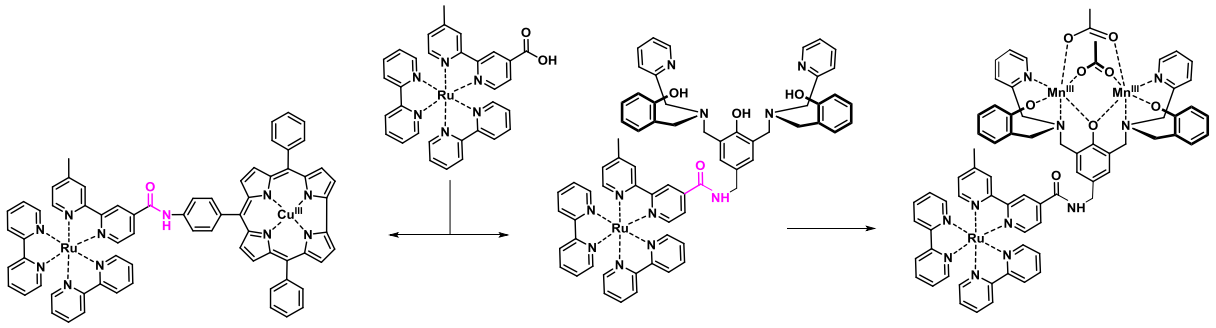

Figure 10. Schematic representation of selected examples for [Ru-Cu^{III}] an [Ru-$Mn_2^{III,III}$] dyads via amidation of a carboxy-decorated $[Ru(bpy)_3]^{2+}$ complex with a Cu^{III}-corrole (left),[230] and polydentate ligand scaffold, capable of subsequent metalation with $Mn_2^{III,III}$.[231] See Figure 10 for further examples of amidation.

Since the 2000, the groups around Åkermark, Sun, Hammarström and Styring formed a "Swedish consortium" to combine their research interest to mimic proton-coupled electron transfer and photosynthetic water splitting. The prepared architectures were composed of a $[Ru(bpy)_3]^{2+}$-based sensitizer coupled to various polydentate ligand scaffolds that are designated to complex Mn ions, which can undergo accumulative electron transfer steps upon multiple Ru excitation events. The sophisticated structure required a robust linkage strategy on the complex, in order to avoid undesired coordination in a hypothetical preassembled ligand platform.[231] The linkage to a Cu^{III}-corrole moiety was accomplished by a similar $SOCl_2$-promoted activation of the carboxy-decorated $[Ru(bpy)_3]^{2+}$ fragment to the corresponding acid chloride, followed by reaction with the cuprated aminophenyl-equipped corrole in the presence NEt_3 in 63% yield.[230] The amide linkage further served to assemble trinuclear arrays containing a central lanthanide complex (Nd, Er, Yb; see Figure 7) with two peripheral $[Ru(bpy)_3]^{2+}$ chromophores, which sensitize the NIR emission of the lanthanides by energy transfer from the Ru centers (entry 32).[208] The amidation was further applied to connect organic chromophores, *e.g.*, carotenoids (entry 33)[144] or coumarin dyes for energy transfer (entry 34),[144, 209] as well as redox-active phenothiazine or methyl viologen units.[215]

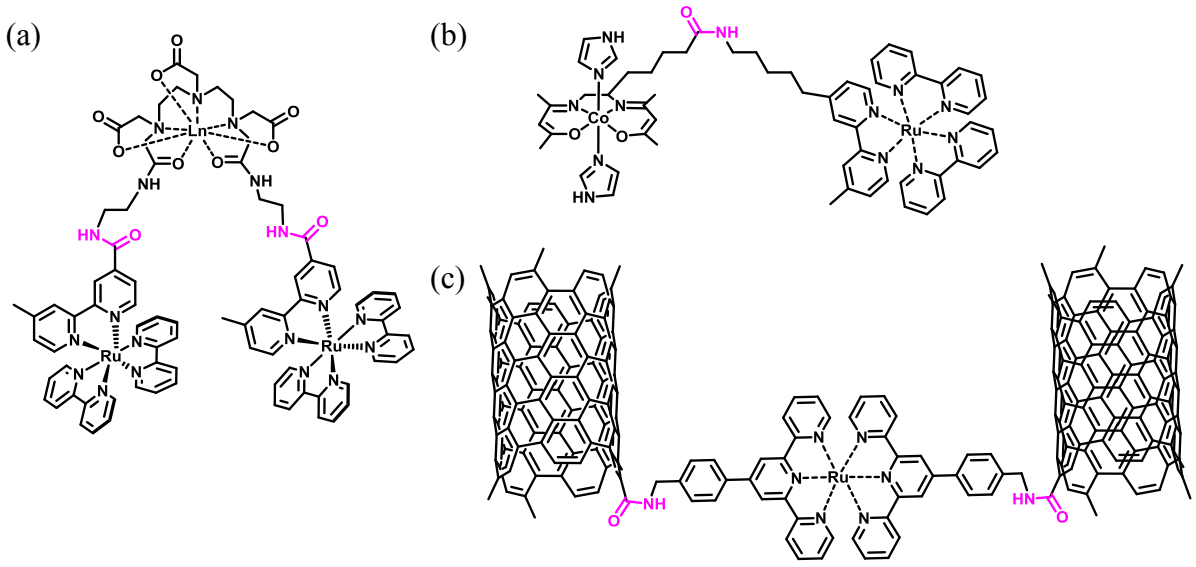

Figure 11. Schematic representation of selected examples for Ru-complexes connected via amidation to (a) lanthanide-based luminophores, (b) catalytic sites or (c) carbon nanotubes.

Additional examples are report on the wide application of the amidation to achieve biochemical activity, electroluminescence and self-assembly.[232-238]

Miscellaneous immobilization. The amidation of Ru complexes was also reported to introduce reactive moieties for surface immobilization, which will be exemplified for silica, gold-coated silicon and partially oxidized carbon nanotubes. First, the EDC-mediated coupling of aminopropyltriethoxysilane (APS) with the three peripheral carboxyl-groups of a $[Ru(phen)_3]^{2+}$-type Ru complex (Table 1, entry 35), that can be covalently incorporated into silica nanoparticles upon copolymerization with APS and tetraethoxysilane in a water-oil microemulsion.[210] The inverse strategy of covalent modifying a silica particle by a Ru complex has also been reported. In that case, the silica surface was first functionalized with polyamines and subsequently subjected to the HBTU/DIPEA-promoted amide coupling of a *bis*-carboxyl-decorated bipyridine Ru complex.[222] Alternatively, the authors investigated the *in-situ* activation of an amino-decorated phenanthroline Ru complex with thiophosgene, which yielded the corresponding thiocarbamate linkage to the polyamine surface. Secondly, the surface immobilization of gold-coated silicon chips was reported, using the ring opening of a dithiolane moiety equipped with a NHS-ester.[239] The $[Ru(bpy)_3]^{2+}$-type complex was attached via a peripheral amino-group promoted by EDC/NEt_3. Thirdly, the modification of partially oxidized carbon nanotubes has been reported (see Figure 7 and Table 1, entry 7),[240] whereby the surface carboxyl groups were converted into their acid chloride and subsequently reacted in DMF with a *bis*-aminobenzyl-decorated $[Ru(tpy)_2]^{2+}$ complex in the presence of NEt_3. The former two examples demonstrated the utility of the "chemistry-on-the-complex"

via amidation to introduce reactive silanols ethers or cyclic disulfide, which are prone to hydrolysis or cleavage under the typical reaction conditions of the alternative coordination of the corresponding ligands.

5.2.2. Esterfication

The esterification reaction is closely related to the amidation reaction, whereby the amino group is formally replaced by a hydroxyl group in the corresponding substrates. The same coupling reagents known from the amidation reactions (Figure 7b) were applied for the esterification reaction, *e.g.*, HBTU, HATU or DCC.[52] However, in many cases the ester

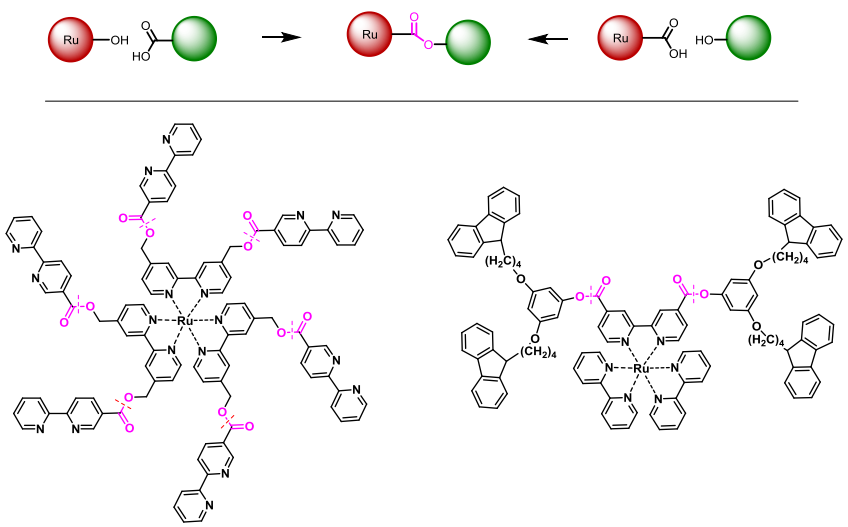

Figure 12. Schematic representation of selected examples for conjugation via esterification.

linkage serves only to cap the carboxyl-decorated Ruthenium complexes by simple alcohols rather than to append a functional moiety, which is preferentially achieved *via* amidation. In comparison to the amide linkage, the ester group is generally more prone to hydrolysis, which manifests the preferred usage as a protecting group. Notably, esterification leads to an increased solubility with respect to the free acid groups of the complexes.

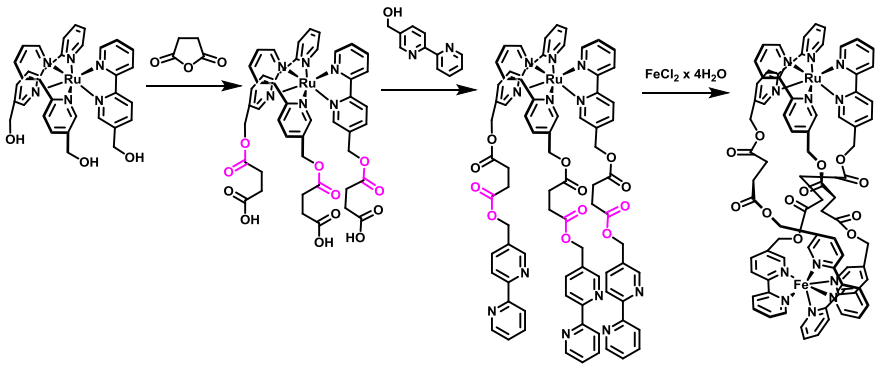

Figure 13. Schematic representation of a twofold esterification starting from hydroxymethyl-decorated $[Ru(bpy)_3]^{2+}$ by Fletcher and coworker to prepare a triple-stranded [Ru-Fe] helix.[241]

The most prominent use of esterification employs hydroxymethyl-decorated Ru complexes. For example, the ring-opening polymerization of caprolactone has been reported to be initiated by a hydroxymethyl-decorated $[Ru(dqp)_2]^{2+}$ complex, leading to the chain-end functionalized polymer.[242] An elegant example of esterification is based on succinimide anhydride to assembly dinuclear complexes.[241] First, a threefold hydroxymethyl-decorated $[Ru(bpy)_3]^{2+}$ complex is esterified with succinic anhydride, which releases carboxyl groups that are afterwards employed in esterification using HBTU in 71% yield. The three introduced bpy ligands are pre-destined for the coordination of Fe^{II} to self-assemble into a heterometallic triple-stranded helicate. Likewise, a series of trimeric, pentameric and heptameric Ru metallo-dendrimers were reported starting from the corresponding two-, tetra-, or sixfold hydroxymethyl-decorated $[Ru(bpy)_3]^{2+}$ core, which were esterified *via* of DCC and DMAP with bipyridine carboxylic acid (Figure 12b, left).[172] Afterwards, different peripheral ruthenium intermediates were coordinated bearing bpy or phen-based ligands.

Alternatively, the opposite ester linkage (Figure 12a right) was reported employing a phenol-decorated $[Ru(tpy)_2]^{2+}$ complexes, that were coupled with dithiolane-equipped aliphatic acids using by DCC/DMAP activation with a yield of up to 78%.[62] The sulfur groups were subsequently used for immobilization onto Au surfaces, in order to screen the catalytic oxidation of triphenylphosphine or antibacterial activity.

Notably, the ester linkage can also be formed by alkylation of the carboxylate. The Ma group utilized the alkylation of *bis*-carboxyl-decorated $[Ru(bpy)_3]^{2+}$ with bromo alkanes that bear one or two carbazole units, respectively, in reasonable yields (41%, Figure 12 right).[243] The Ru-oligocarbazole complexes were deposited by electrochemical coupling of the peripheral carbazole units for use in organic light emitting diodes. Note that only weak bases ($NaHCO_3$) are required for deprotonation of the carboxyl group. Another application is the

immobilization of carboxyl-decorated $[Ru(bpy)_3]^{2+}$ onto Sephadex for the photo-induced production of singlet oxygen.[244, 245] The essential linkage was achieved after reacting epichlorohydrin with the Sephadex resin, which subsequently permits the ring-opening with the carboxyl groups of the Ru complex.

5.3. Miscellaneous reactions

Miscellaneous acylation reactions were utilized for the formation of new peripheral ligand platforms on Ru complexes. For example, two twofold Mannich-type reaction was reported for both *ortho*-positions in a tyrosine-modified $[Ru(bpy)_3]^{2+}$ complex, *i.e.*, using formaldehyde and dipicolylamine under reductive conditions (Figure 14a). [246, 247] The generated chelating motif was subsequently used to assemble [Ru-Mn_2] heterometallic dyads as depicted previously in Figure 10. Karlsson *et al.* reported the conversion of $[Ru(bpy)_3]^{2+}$-based complexes bearing a peripheral dicarboxyphenol moiety, whereby the acid groups were first activated towards amidation and subsequently reacted with *ortho*-diaminophenol.[248] As a result, the formal amide intermediate undergoes cyclization to yield the corresponding benzimidazole units (Figure 14a b). After complexation to Mn^{II} ions, the capability towards catalytic water oxidation was investigated, in line with the long-standing research interest of the authors as discussed for the [Ru-Mn] assemblies featuring alternative linkage patterns and ligand scaffolds. A related condensation reaction was reported by the Aukauloo group using diamino-decorated tpy with a diketo-functionalized Ru complex (Figure 14c) to form the bridging imidazole unit.[249] Descending from seminal work in the 1990s,[250] the Rau group reported the related pyrazine ring formation starting from functionalized Ru complexes bearing the diketo-[251] or the diamino-synthon (Figure 14d and e).[252] These selected examples demonstrate that broad scope of acylation reactions and related heterocyclic ring forming reactions, which are not limited to solely conjugate molecular fragments, but can be utilized to augment the Ru sensitizer units with coordination site for other metals aiming at molecular photocatalysis.

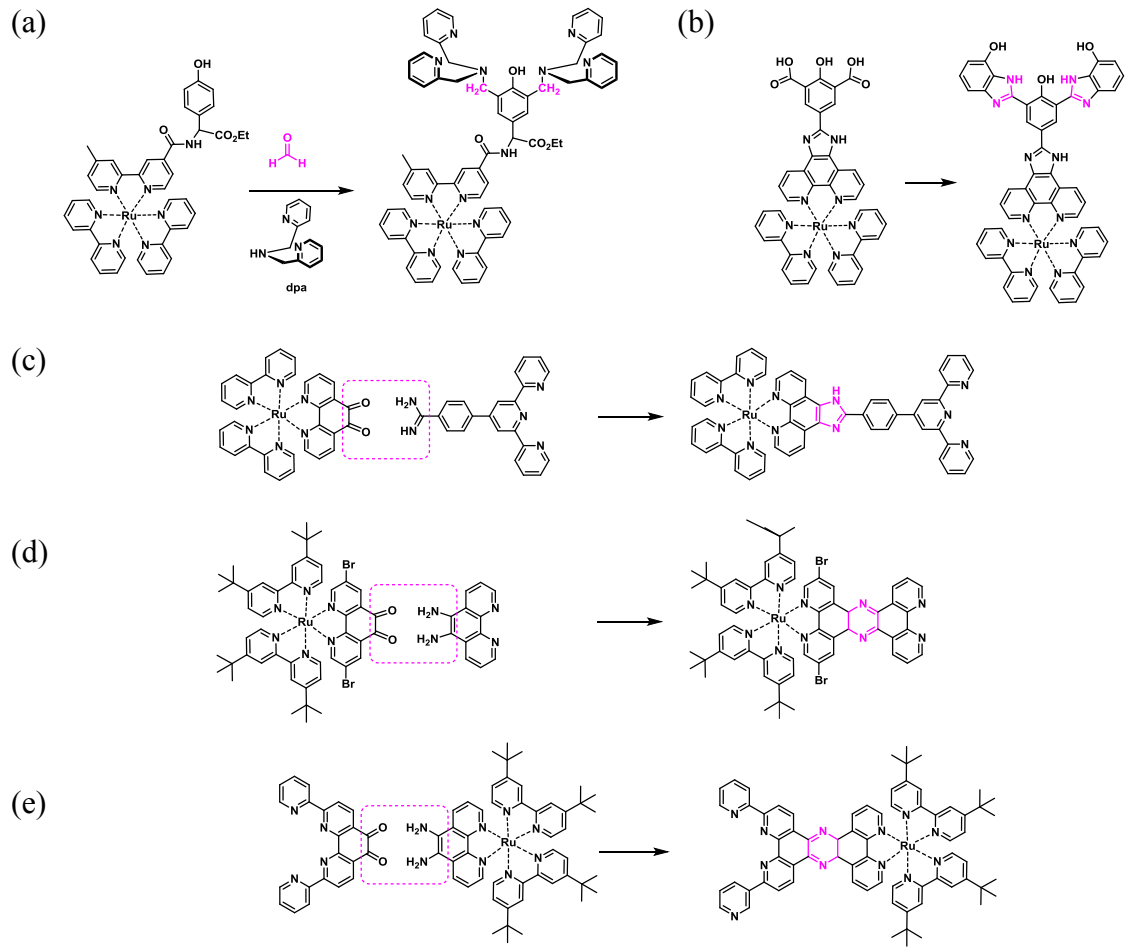

Figure 14. Schematic representation of (a) a Mannich-type reaction on a phenol-functionalized $[Ru(bpy)_3]^{2+}$ core,[246, 247] (b) the benzimidazole-formation on a $[Ru(bpy)_3]^{2+}$-based complex,[248] (c) imidazole-formation,[249] and (d) pyrazine-formation using Ru complexes bearing the (d) diketo-moieties[251] or (e) the diamino-moieties.[252]

5.4. Alkylation reactions

In the previous chapter, the formation of amide and ester linkages was detailed that preferentially proceeds *via* acylation of amino or hydroxyl groups by activated esters. Notably, ester linkages were also occasionally generated from the carboxylate via *O*-alkylation of the deprotonated form. More importantly, alkylation reactions can be utilized for conjugation to suitable *O*-, *N*-, and *S*-nucleophiles, descending preferentially from phenols, tertiary amines or pyridines, or thiols, respectively. Popular alkylating reagent comprise alkyl or benzyl halides (Cl, Br) or halide-decorated Ru^{II} polypyridyl-type complexes, which benefit from their activation towards nucleophilic aromatic substitution by the strong electron-deficiency, in analogy to pentafluorophenyl (Ph_{F5}) groups. In general, weak-to-moderate bases are applied, *e.g.*, K_2CO_3, Na_2CO_3, Cs_2CO_3, sodium or trimethylamine. Figure 15 shows the principle combinations to from the corresponding C–O, C–N, or C–S linkages formed

from the complementary substitution pattern (left *vs.* right side). Representative examples will be provided in the following paragraphs, while Table 2 summarizes reported examples for *O*-alkylation (entries 1–17), *N*-alkylation (entries 18–22), *S*-alkylation (entries 23–30), as well as miscellaneous *C*- and *P*-nucleophiles (entries 31 and 32).

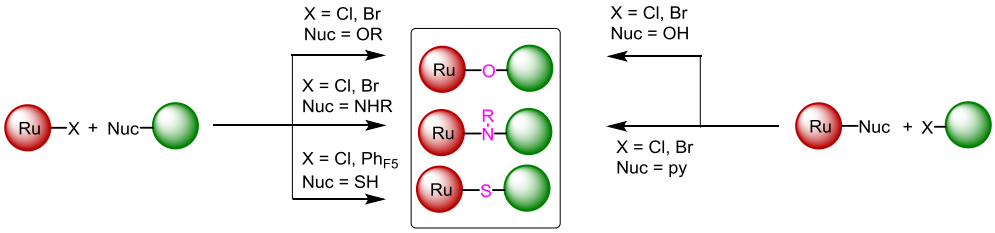

Figure 15. Schematic representation of nucleophilic substitution reaction.

Table 2. Reaction conditions and yields of alkylation reactions on the ruthenium ligand scaffold.[a]

	Nuc[c]	Ref.	Tolerated functional moieties Ru^{II} complex	Tolerated functional moieties Coupling partner	Solvent/ base	Temp. [°C]	Time [h]	Yield [%]
1	O	[166]	None	bpy	MeCN, K_2CO_3	Reflux	20	70
2	O	[168]	None	None	MeCN, DMSO K_2CO_3, NaI	80	24	40
3	O	[253]	None	None	MeCN, K_2CO_3	175	2 (μW)	20
4	O	[254]	None	Ru^{II}	MeCN, K_2CO_3	Reflux	4	34
5	O	[255]	Ether	Alkyl halide,	MeCN K_2CO_3	85	5	81
6	O	[54]	None	Alkene	MeCN, K_2CO_3,			
7	O	[74]	None	Alkyne	DMF, Cs_2CO_3	80	Over night	42-89
8	O	[256]	None	Tertiary amine, pyridine	MeOH, DMSO, MeONa	80	4	46
9	O	[257]	None	Zn porphyrine	DMF, K_2CO_3	rt	48	68
10	O	[258]	None	NDI	DMF, K_2CO_3 KI	60	72	55-75
11	O	[259]	None	NDI	DMF, K_2CO_3	60	96	40
12	O	[260]	None	TARA	DMF, K_2CO_3	60	4 Days	
13	O	[261]	TIPS-alkyne, TARA	TARA, NDI	DMF, K_2CO_3, KI	60	89	48
14	O	[262]	TIPS-alkyne, carbazole	NDI	DMF, K_2CO_3, KI	60	77	75
15	O	[263]	None	OMe, TEG, PEG	DMF, K_2CO_3, KI	60	96	70
16	O	[264]	None	Alkyne, alkene, ether	MeCN, Cs_2CO_3	Reflux	12	66
17	O	[265]	None	None	MeOH, NaCN	55	1	78
18	N	[256]	None	Tertiary amine, pyridine	MeCN, NEt_3	Reflux	3	53
19	N	[258]	None	NDI	$CHCl_3$, MeCN, KPF_6 KI	50-70	96	40-92
20	N	[266]	Vinyl	Amide, pyridine, Secondary amine	MeCN, NaI DIPEA	reflux	17	34
21	N	[267]	None	Carboxylic acid	MeOH	80 (HP)	15	67
22	N	[267]	None	Alkyl halide	MeOH	80 (HP)	17	71
23	S	[255]	Ether	Thioester	MeCN	60	15	75
24	S	[265]	None	None	THF, NaSH	115 (GB)	9	87
25	S	[265]	None	Tolyl	Hexane, THF,	115 (GB)	11	88

					BuLi[b]			
26	S	[268]	$-C_6F_4-$	Internal alkyne, thioester	DMF	rt	30 min	80-88
27	S	[268]	$-C_6F_4-$	thioester	DMF, NEt_3	-20	8	82
28	S	[69]	None	Dinitrophenyl	MeCN, NaH[b]	rt	3	32
29	S	[269, 270]	None	Thioether	DMF	rt	3	80
30	S	[269]	None	BOS-cysteine	DMF/H_2O Na_2CO_3	55	3	82
31	C	[269]	None	Fluorene	DMF, NaH[b]	65	3	60
32	P	[267]	None	Phosphonic acid	MeOH	150 (HP)	15	91

a) NDI is naphthalene diimide, TARA is triarylamine. TEG is triethylene glycol. PEG is polyethylene glycol. HP denotes high pressure (800-1250 psi, see ref. [267]). GB denotes glass bomb (see ref. [265]). b) Base used for the deprotonation of coupling partner prior to the reaction with the Ru^{II} complex. C) Type of reactive nucleophile: O denotes phenols or alcohols, S denotes sulfide or thiols, N denotes amines or pyridines, C denotes cyanide or fluorenyl anions. P denotes phosphite.

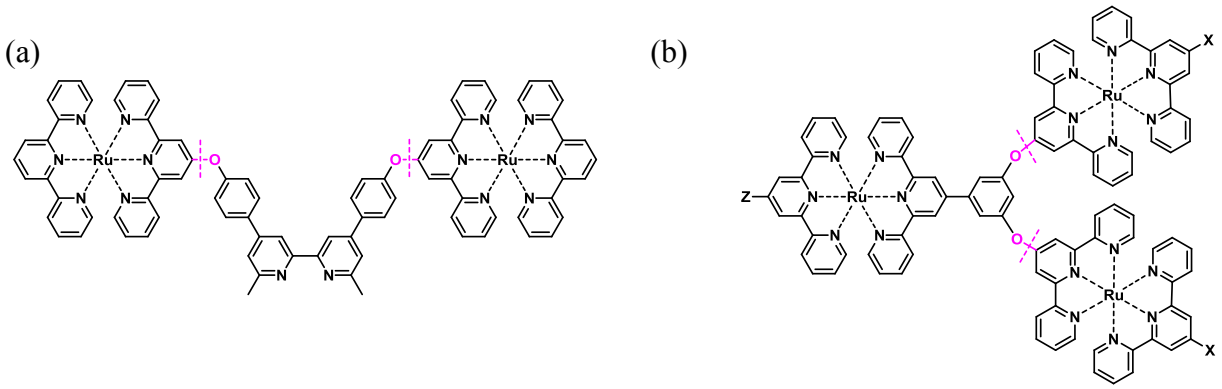

Figure 16. Schematic representation of selected examples for polynuclear complexes via *O*-alkylation chemistry from the Constable group: (a) Coupling of a *bis*-phenol-decorated bpy ligand,[168] and (b) coupling of a 1,3-dihydroxy-decorated metal complex.[254]

5.4.1. *O*-Alkylation

O-alkylation of phenolic hydroxyl group represents the most frequently method to date in order to link Ru complexes to additional functional moieties. Although the list is not intended to be exhaustive, comprehensive examples for the amidation reaction will be discussed, aiming at *e.g.* electron and energy-transfer processes, surface immobilization, or to introduce new functional groups.

Multinuclear polypyridyl-type complexes. Among the first, the Juris group reported in 2000 the alkylation of bromine-decorated $[Ru(bpy)_3]^{2+}$ complexes with hydroxyl-equipped bpy promoted by K_2CO_3 in anhydrous MeCN.[166] Afterwards, the coordination was performed to generate the peripheral $[M(bpy)_3]^{2+}$ complexes (M = Ru, Os) (Table 2, entry 1). In contrast to earlier more strongly coupled polynuclear assemblies,[165] the photophysical properties of the

subunits were mainly preserved, which initiated great interest in the following years. The Constable group systematically investigated the synthesis of polynuclear metal complexes *via* *O*-alkylation chemistry (entry 2–4).[145, 168, 253, 254] The linkage was achieved using Cl-decorated $[Ru(tpy)_2]^{2+}$ and aromatic alcohols (phenol, 1,3-dihydroxybenzene) as the *O*-nucleophiles, which enabled the attachment of bpy,[168] tpy or even pre-assembled $[Ru(tpy)_2]^{2+}$ fragments (Figure 16).[253, 254] Interestingly, the linkage *via* of hydroxyl-decorated bpy or tpy with $[Ru(tpy)_2]^{2+}$ complexes bearing peripheral benzyl bromide groups was reported problematic and led to undesired acetylation, likely originating from MeCN as the solvent.[145]

Donor-acceptor assemblies. The alkylation strategy was further applied to assemble molecular dyads, triads *etc.* to study photoinduced energy and electron transfer processes. Although the majority of such sophisticated architectures contain conjugated aromatic linkage patterns and are often assembled prior to coordination, the use of alkylation is reported. For example, free or Zn-containing porphyrins were coupled to *bis*-phenol-decorated $[Ru(tpy)_2]^{2+}$ to form the symmetric trinuclear system with a yield of 73% (Table 2, entry 9).[257] Notably, isolation of the *mono*-functionalized intermediate enabled the synthesis of the asymmetric [H_2-porphyrin]-[Ru]-[Zn-porphyrin] triads by a second Williamson ether synthesis step.

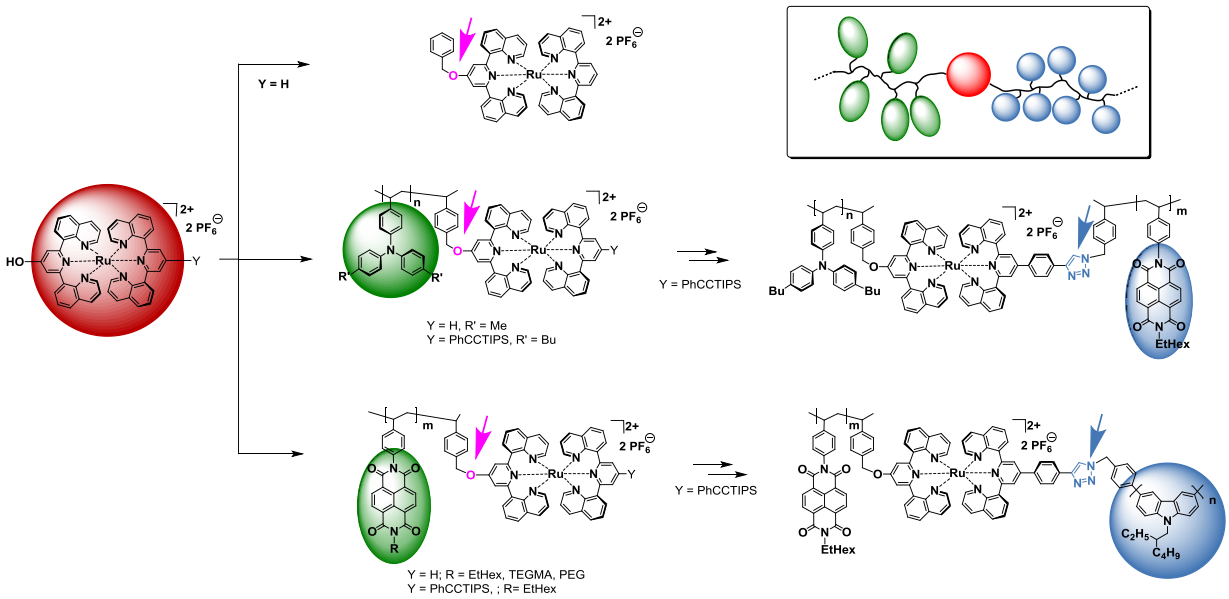

Figure 17. Schematic representation of selected examples for the modular construction of polymer based dyads and triads (box) from common $[Ru(dqp)_2]^{2+}$-based building blocks and various chain-end functionalized redox-active polymers, including reference complexes.[260-263]

In a series of recent reports, the selective chain-end modification for the modular assembly of polymer-based dyads and triads *via* *O*-alkylation was detailed (Figure 17).[258, 259, 261-263] The

"chemistry-on-the-complex" approach embarked from hydroxy-decorated $[Ru(dqp_2)]^{2+}$ complex, which was functionalized by a variety of benzylchloride-decorated of poly(triarylamine) or poly(naphthalene diimide) using K_2CO_3/KI in DMF (entries 10–15). Notably the tolerated TIPS-protected alkyne group was liberated afterwards to allow the copper-mediated azide-alkyne cycloaddition reaction (section 5.6 for more details), *i.e.*, to attach the complimentary redox-active chain. These architectures featured an efficient directional photo-induced charge separation of the modularly electronically-decoupled building blocks. The complementary linkage was reported for a bromomethyl-decorated $[Ru(bpy)_3]^{2+}$ sensitizer with a hydroxyl-pyridine motif in 70% yield (entries 1 and 8). In this way, a multidentate pyridine scaffold was introduced and subsequently metalated with Mn^{II} to mimic elementary photoinduced charge accumulation.[166, 256]

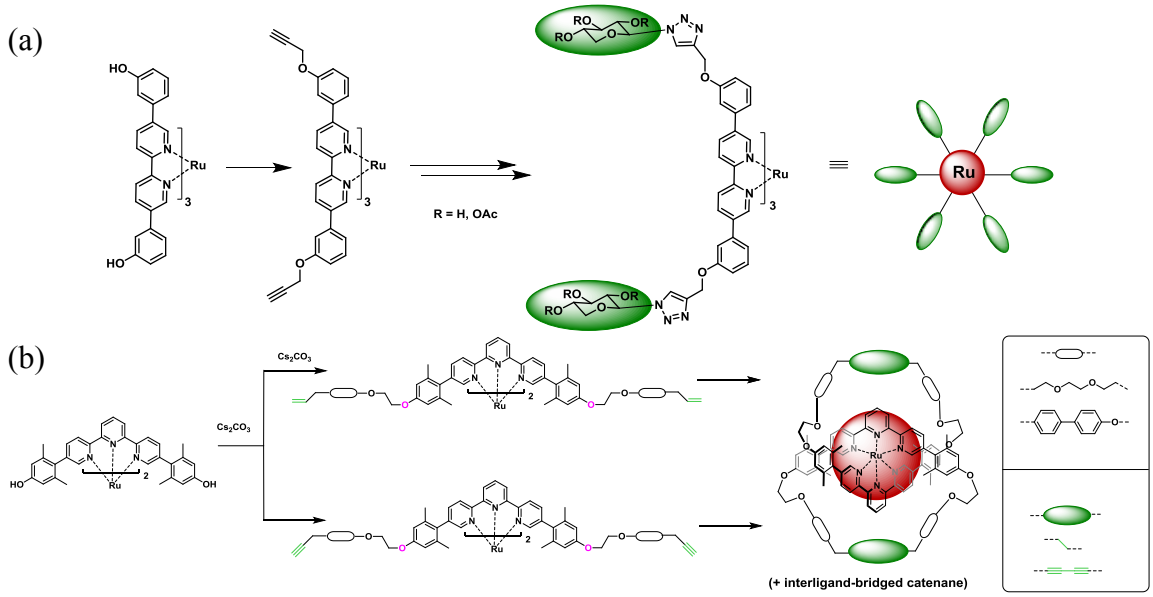

Figure 18. Schematic representation of selected examples for the synthesis of a sixfold sugar-functionalized $[Ru(bpy)_3]^{2+}$ complex,[74] and (b) $[Ru(tpy)_2]^{2+}$-based catenanes[264] *via* Williamson ether synthesis to introduce the reactive functional group.

Reactive peripheral groups. The Constable group extended their methodology established for polynuclear complexes to introduce reactive peripheral groups. Propargyl bromide was reacted with phenol-decorated $[Ru(bpy)_3]^{2+}$ complexes (Table 2, entry 7) to introduce two or six terminal alkyne groups in 89% and 42% yield, respectively. More importantly, these units provides access to the subsequent copper-mediated azide-alkyne cycloaddition reactions (section 5.6 for more details), as demonstrated for azide-containing sugars (Figure 18a). Among other, the Siegel group employed a similar strategy to introduce reactive peripheral groups for catenane formation,[264, 271] *e.g.*, reacting various phenol-decorated Ru^{II} polypyridyl-

type complexes with α,ω-substituted linkers that carry the required bromo group on one side and an alkene or alkyne moieties on the other side (Figure 18b, entry 16).[264] Subsequently, Grubbs-type olefin metathesis or Glaser-type alkyne-coupling were used to form the inter- and intra-bridged catenanes. Note that all four catenanes descend from the same Ru complex, illustrating its use as a building block in a modular fashion *via* "chemistry-on-the-complex". Another recent example to introduce an alkyl-spaced terminal alkene was published, despite no further usage was reported (Table 2, entry 6).[54] These three examples demonstrate the potential of the alkylation strategy to augment Ru complexes with various reaction functional groups, designated for subsequent chemical reactions or surface immobilization.

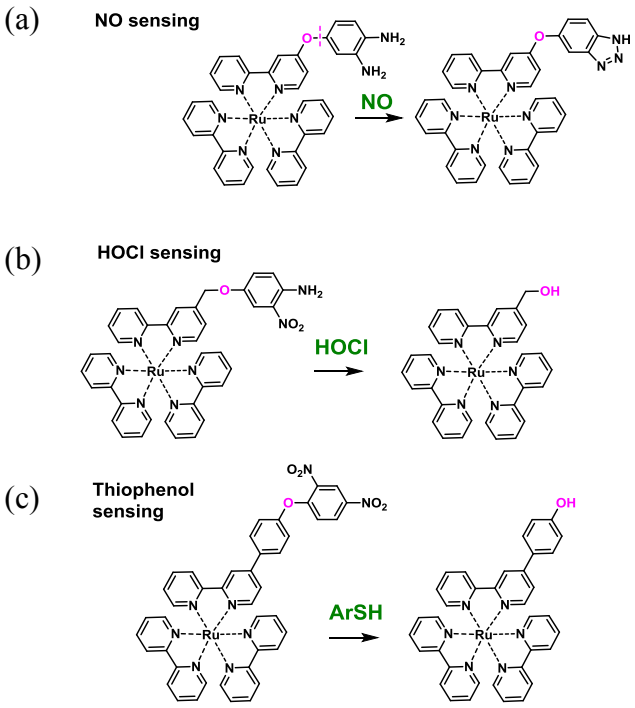

Figure 19. Schematic representation for selected examples of the Williamson ether synthesis to construct complexes bearing nitrophenols for the detection of nitric oxide (a), hypochlorite (b), and thiophenols (c) in living cells.[70, 71]

The Yuan group introduces different functionalized nitrophenols for the detection of HOCl, nitric oxide or thiophenol in living cells (Figure 19).[70, 71] These three types of sensing were verified by the change in fluorescence of the different species, which are induced by the addition of NO (Figure 19a) or cleavage reactions that are triggered by the analyte molecules (Figure 19b and c).

5.4.2. *N*-Alkylation

The nucleophilic substitution reaction can also be used for C–N bond formation. For this purpose, alkyl amines as well as aromatic amines are required. In the early stage to prepare heterometallic [Ru-Mn] complexes to explore multi-electron storage in an artificial photosystem, the benzylbromide group was utilized to connect a dipicolylamine (Figure 20).[256] In this case, the coupling of two Ru complexes was achieved *via* the secondary amino group, notably the peripheral dangling pyridines were tolerated (entry 18). Likewise, and amino-decorated [Ru] complexes was alkylated by benzylbromide derivative, which was later transformed into a Molybdenum-based oxotransferase model compound.[272]

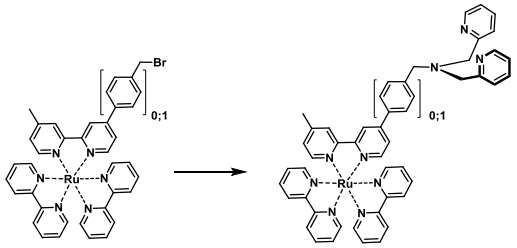

Figure 20. Schematic representation of a selected example for C–N linkage using nucleophilic substitution with secondary amines.[256]

Upon more forcing reaction conditions, the reaction of a benzylic halide with a pyridine can be utilized as an effective strategy to link Ru complexes with a functional molecular fragment, which introduces an additional positive charge by the pyridinium linkage (Figure 21). This linkage motif was used for the chain end functionalization of a poly(naphthalene diimide) acceptor (entry 19)[258] as well as for the incorporation of dipicolylamine to complex manganese.[256] The Zhong group functionalized a *bis*-vinyl-decorated $[Ru(tpy)_2]^{2+}$ complex with dipicolylamine (entry 20).[266] The obtained ruthenium complexes were copolymerized to form redox active films. In this regard, the dipicolylamine functionality was utilized for the detection of Cu^{2+} ions. A similar strategy was used to introduce anchor units on a hexameric ruthenium complex (Figure 21a and Table 2, entry 22).[267] Therefore the carboxylic acid groups can be bond directly to the pyridine units while the phosphonate groups were bond in

two steps. In the first step dibromopropane was substituted to the pyridine unit which can be functionalized in the second step with triethylphosphite. All reactions were realized in a high pressure reactor without a base. The Ward group reported the related alkylation of pyrazols, in order to introduce free binding sites to construct mixed-metal self-assemblies.[106, 107]

Note that the pyridinium linkage strategy is widely used to generate a viologen unit, *i.e.*, to react various alkylhalide-functionalized Ru complexes with mono-alkylated 4,4'-bipyridine (methyl viologen, Figure 21b). Notably, the reaction conditions are comparable to those for pyridinium linkages, and have been applied to Br-terminated polymers obtained from ATRP.[224, 273] In this architecture, the "linkage" reaction forms an electron acceptor for photo-induced electron transfer processes, which was shown to utilize the light harvesting of the polymetallic Ru polymer for the final charge separation with the methyl viologen. A similar reaction type was used to connect a single Ru complex to the chain end of a poly(naphthalene diimide) (Figure 21c),[258] which resulted in highly efficient charge separation aiming towards charge percolation along the backbone (see also Figure 19).

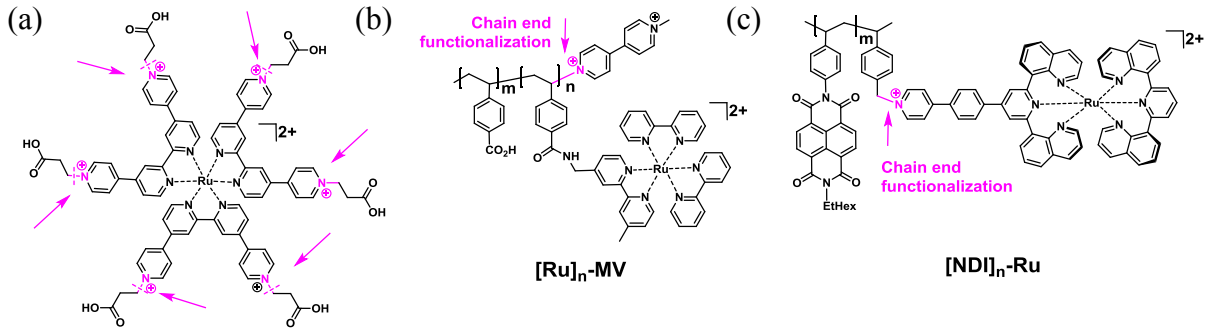

Figure 21. Schematic representation of selected examples for C–N linkage using pyridinium formation, e.g., (a) for hexa-functionalization, (b) for methyl viologen introduction to light-harvesting Ru polymer,[224] and (c) for chain-end modification of redox-active polymer with a single Ru sensitizer aiming at charge percolation pathways. [258]

5.4.3. *S*-Alkylation

The substitution reactions of halogen compounds by sulfur nucleophiles can be used for the introduction of thiol groups or the formation of the thioethers (Figure 22 and Table 2, entries 24 and 25). [265] In contrast to the O-congeners, the sodium salts can be directly applied. Wild *et al.* coupled $[Ru(tpy)_2]^{2+}$-based complexes bearing two pentafluorophenyl units (see Figure 22 and Table 2, entries 26 and 27) to form metallopolymers.[268] In addition, the para-positioned fluorine can by readily converted by a thiol that bears a conjugated spacer unit and

a terminal free tpy unit. Afterwards, the coordination polymerization with Fe^{II} ions was used to prepare heterometallic coordination polymers. The Yuan group used sulfides for the nucleophilic substitution, in order to couple a nitrophenyl compound which serves as an detector for hypochlorite in living cells as described previously.[69] Early examples for C–S couplings are presented by the Tor group, who reported the nucleophilic substitution of the reactive *meta*-position in Br-decorated $[Ru(bpy)_3]^{2+}$-type complex with thiolate nucleophiles, including a *tert*-butyloxycarbonyl (BOC)-protected terminal amino functionality.[269, 270] Remarkably, this reaction can be extended to pre-formed *C*-nucleophiles (fluorenyl anions, entry 31). Notably, the formation of C–P bond was achieved using triethyl phosphite (entry 32).[267]

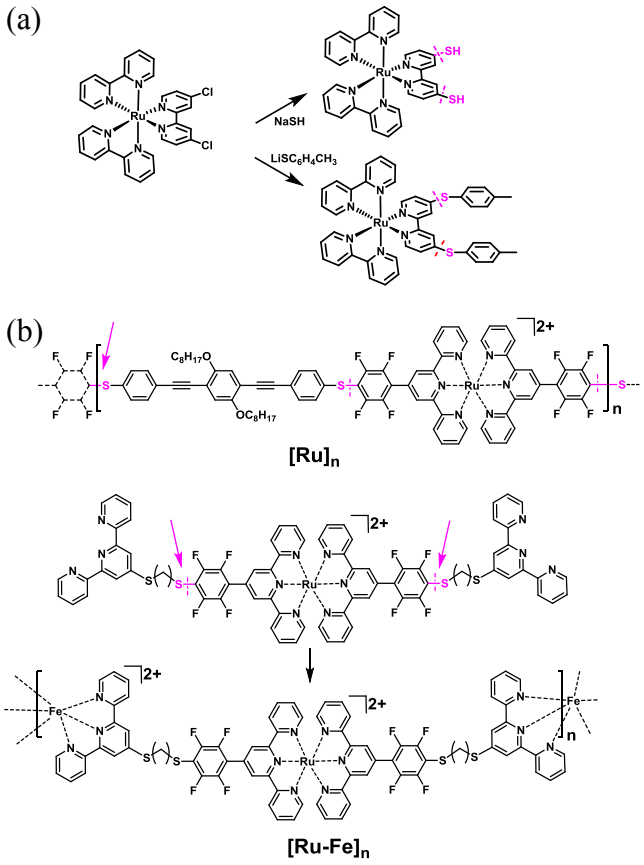

Figure 22. Schematic representation for C–S linkage: (a) *via* Cl-decorated $[Ru(bpy)_3]^{2+}$ and (b) *via* pentafluorobenzene-thiol chemistry towards (hetero-)multinuclear polymers $[Ru]_n$ and $[Ru–Fe]_n$.[268]

5.5. Metal-catalyzed cross-coupling reactions

Palladium-catalyzed cross-coupling reactions represent a powerful tool in synthetic chemistry with a broad range of substrates as well as application fields. The conventional catalytic cycle involves an active Pd^0 catalyst, which is prone to deleterious deactivation by residual oxygen. Notably, Ru^{II} polypyridyl-based complexes generally do not act as oxidant and, thus, enable

the application cross-coupling reactions. In this regard, Ru complexes bearing the desired halide group directly on the ligand scaffold can be used both for nucleophilic substitution reactions as well as for cross-coupling reactions, whereas the majority of the utilized halide-functionalized Ru complexes involve an organic spacing unit (*e.g.*, phenyl). Note that these Ar–X groups are readily introduced during the Kröhnke- or Skraup-type ligand synthesis. The importance of cross-coupling reactions further stems from the electronic communication across the conjugated linkage, so that many of the subsequent examples explore the fundamental effect of the bridge on the photophysical properties. Another beneficial geometrical feature originates from the axial symmetry, which restricts the possible conformations and, thus, facilitates the analysis of the photophysical data as well as the construction of sophisticated supramolecular architectures.

5.5.1. Sonogashira coupling

The Sonogashira cross-coupling represents the most frequently applied methodology to connect Ru complexes with various metal-containing fragments (Table 3 entry 1–14) [113, 134, 274-289] or other functional organic moieties (Table 3 entry 15–28).[35, 130, 171, 174, 175, 290-313] Notably, both complementary substrate combinations are reported, *i.e.*, the Sonogashira coupling of alkyne- or halide-functionalized Ru complexes, respectively, in good to excellent yields using typical catalyst systems composed of CuI and Pd-phosphine complexes, *e.g.*, $Pd(PPh_3)_4$, $Pd(PPh_3)_2Cl_2$, $Pd(dppf)Cl_2$, $Pd_2(dba)_3$ (PPh_3 is triphenylphosphine, dppf is 1,1'-bis(diphenylphosphino)ferrocene). The solvents and bases to scavenge the formed HX have to be selected according to the solubility of the complexes, and range from DMF, THF, and MeCN to benzene with bases like piperidine, diisopropylamine, triethylamine and Hünigs base. Also, microwave-assisted protocols were reported that led to decreased reaction time. Table 3 provides a comprehensive overview of the reported Ru complexes, as well as the used reagent, the conditions of the synthesis and the yields.

The Ziessel group showed the versatility of the Sonogashira coupling for the "chemistry-on-the-complex" methodology. For example, the Sonogashira reaction was applied to attach a pyrene unit after complexation, while the classical formation via ligand functionalization and subsequent coordination failed. The broad scope of the reaction was demonstrated for $[Ru(bpy)_3]^{2+}$, $[Ru(phen)_3]^{2+}$ and $[Ru(tpy)_2]^{2+}$ complexes containing multiple bromo functionalities in the *meta*-positions of the external pyridine units. The typical reaction conditions involve $Pd(PPh_3)_4$ as pre-catalyst, isopropylamine as base and a MeCN/benzene

solvent mixture at 60 °C, leading to moderate-to-high yields of up to 95% (Figure 23 and Table 3, entry 21).[295, 296, 306, 307]

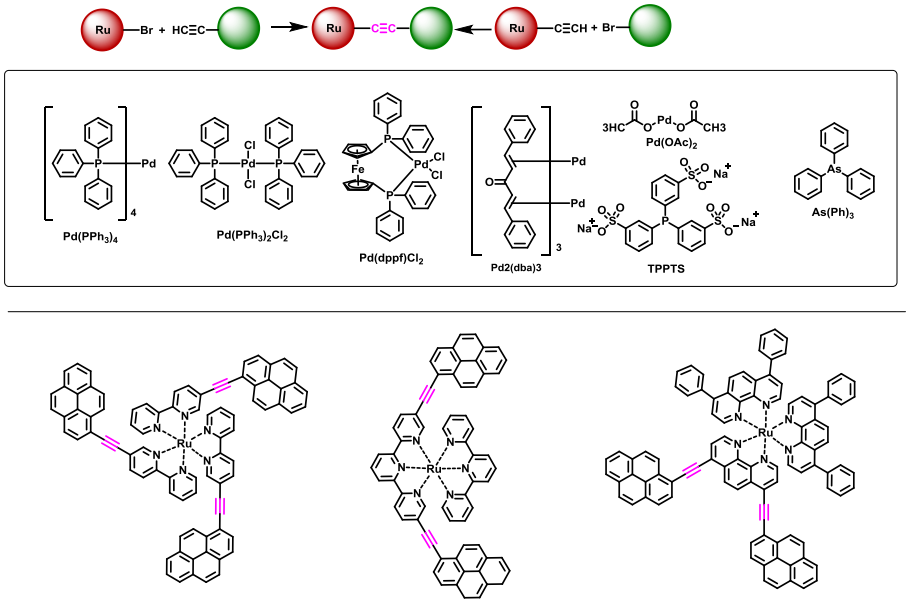

Figure 23. Schematic representation of pyrene functionalized ruthenium-phenanthroline complexes *via* Sonogashira cross-coupling.

Table 3. Reaction conditions and yields of the Sonogashira reactions on Ruthenium complexes.[a]

	Ref.	Tolerated functional moieties		Catalyst	Solvent/ base	Temp. [°C]	Time [h]	Yield [%]
		Ru^{II} complex	Coupling partner					
1	134	None	Polyoxa-metalates	$Pd(PPh_3)_2Cl_2$ CuI	DMF, NEt_3	70	1 (µW)	86
2	274	None	Zn porphyrin	$Pd(PPh_3)_4$ CuI	iPr_2NH, MeCN THF	70	24	23-79
3	275	None	Iridium complexes	$Pd(PPh_3)_2Cl_2$ CuI	DMF, NEt_3	80	24	70
4	277	None	Norbornadiene, dithienylethene	$Pd(PPh_3)_4$, CuI	DMF iPr_2NH	rt	10	40,30
5	278	Cyclo-metalation	Anthracene, thiophene	$Pd(PPh_3)_4$ CuI	DMF NaOH	80	16	34-60
6	281	Tolyl	tpy	$Pd(PPh_3)_4$ CuI	DMF iPr_2NH	rt	72	50
7	113	None	bpy	$Pd(PPh_3)_4$ CuI	MeCN iPr_2NH	rt	6 Days	32
8	282	None	phen	$Pd(PPh_3)_4$ CuI	THF iPr_2NH			51
9	283	None	Anthracene	$Pd(PPh_3)_4$, CuI	DMF, NEt_3		48	17-27
10	284	None	Thiophene, Ru^{II}	$Pd(PPh_3)_4$ CuI	DMF iPr_2NH	rt		80
11	285	Ester	Phenyl, Ester, Ether, carboxylic acid	$Pd(PPh_3)_2Cl_2$ CuI	MeCN iPr_2NH	reflux	3	32-91
12	286	None	Zn porphyrine	$Pd_2(dba)_3$, $AsPh_3$	THF MeCN iPr_2NH	reflux	2	70-90
13	287	None	Dipyrimidine	$Pd(PPh_3)_4$	MeCN	rt	6 Days	32

				CuI	iPr_2NH			
14	[288]	None	Di-*oxa*-dibenzo[a,c]-cycloheptene	$Pd(PPh_3)_4$ CuI	THF MeCN iPr_2NH	reflux	2 Days	46
15	[174, 175]	Ester, ether	Phenyl	$Pd(PPh_3)_4$ CuI	THF benzene iPr_2NH	80	4 Days	30
16	[171]	Ether	tpy	$Pd(PPh_3)_2Cl_2$ CuI	THF MeCN iPr_2NH	80	3 Days	61
17	[130]	None	TMS-alkyne	$Pd(PPh_3)_4$ CuI	DMF, NEt_3	80	18	80
18	[291]	None	Methyl viologen, benzoylpyridine	$Pd(PPh_3)_2Cl_2$ CuI	DMF, NEt_3	rt	21-24	78-83
19	[293]	phen	Nucleosides and nucleotide	$Pd(dppf)Cl_2$ CuI	DMF, NEt_3	rt	3	72-84%
20	[294]	None	Internal alkyne	$Pd(PPh_3)_4$ CuI	DMF iPr_2NH	rt	10	50-93
21	[295, 296, 306, 307]	None	Pyrene	$Pd(PPh_3)_4$ CuI	MeCN benzene iPr_2NH	60	16	86
22	[297]	None	Pyridine	$Pd(PPh_3)_4$, CuI	DMF,DM E NEt_3	80	12	78
23	[298, 299]	None	Deoxyadenosine	$Pd(OAc)_2$, TPPTS, CuI	H_2O, MeCN iPr_2NH	75		16-59
24	[300, 302]	None	Triarylborane	$Pd(PPh_3)_2Cl_2$ CuI	THF MeCN NEt_3	50	2.5	28-50
25	[308]	None	Phenyl, phen	$Pd(dppf)Cl_2$, CuI	DMF, NEt_3	rt		65-95
26	[310]	Thiophene	TIPS-alkyne	$Pd(PPh_3)_2Cl_2$ CuI	DMF NEt_3	120	1.5 (μW)	69
27	[311]	Methyl	NDI	$Pd(dppf)Cl_2$ CuI	DMF NEt_3	45	15	33
28	[312]	None	PMMA	$Pd(PPh_3)_4$, CuI	THF/NEt_3	40	3 Days	31
29	[309]	None	Tetrathia-fulvalene	$Pd(PPh_3)_4$ CuI	MeCN benzene iPr_2NH	60	16	70
30	[314]	None	Phenyl	$Pd(PPh_3)_2Cl_2$, CuI	THF iPr_2NH	rt-reflux	18 3	68
31	[311]	None	NDI	$Pd(PPh_3)_2Cl_2$ CuI	DMF NEt_3	75	15	33-55
32	[308]	None	Phenyl, phen	$Pd(dppf)Cl_2$, CuI	DMF, NEt_3	rt		65-95

a) NDI is naphthalene diimide; PMMA is poly(methylmethacrylate). dppf is 1,1′-bis(diphenylphosphino)ferrocene; TIPS is triisopropylsilyl. TPPTS is triphenylphosphine-3,3′,3″-trisulfonic acid trisodium salt.

The Sonogashira cross-coupling represent a versatile methodology to connect Ru^{II} polypyridyl-type complexes with redox-active moieties, *e.g.*, to form dyads, triads and beyond. The synthetic pathways varied from a stepwise protocol to parallelized variants depending on the symmetry of the desired architectures and, thus, the employed Ru^{II} complexes. For example, a triad composed of the subunits $[Ru(tpy)_2]^{2+}$, zinc porphyrin and

$[Os(tpy)_2]^{2+}$ was synthesized by the stepwise conjugation of the Ru^{II} fragment with the zinc porphyrin (79%) to form the corresponding dyad, which was subsequently linked by an analogous coupling to the $[Os(tpy)_2]^{2+}$-fragment in 23% yield (Table 3, entry 2).[274] Likewise, a related triad was assembled stepwise from two different zinc porphyrins, which were conjugated with the $[Ru(tpy)_2]^{2+}$ unit in the final step.[280] A $[Ru(tpy)_2]^{2+}$-based core was decorated with up to four zinc porphyrin units as reported by Ishizuka *et al.* (entry 12).[286] The coupling of the zinc porphyrins occurred in one synthetic step on a multi-functionalized ruthenium complex with a remarkably yield of up to 90%. Combined techniques between coupling and coordination are also published and described by the Schmittel group (Table 3, entry 3)[275] as well as the group around Mayer (entry 6).[281] Recently, additional Ru conjugates with Zn porphyrins with non-linear optical properties[315] as well as dual phosphorescent Ru-bodipy architectures were reported aiming at triplet triplet upconversion for photodynamic therapy applications.[316]

Matt *et al.* synthesized a polyoxometalate (POM), which was decorated with two ruthenium complexes coupled *via* the Sonogashira reaction (Table 3, entry 1).[134] While no electron transfer was observed in case of the binary mixture of the complex and the polyoxametalates, the covalent linkage between both units led to electron transfer. Various tungsten POMs were synthesized bearding peripheral iodo-aryl moieties, which were coupled in good yields (76–86%) to a cyclometalated Ru complexes bearing the acetylene functionalities on the carbanionic fragment.

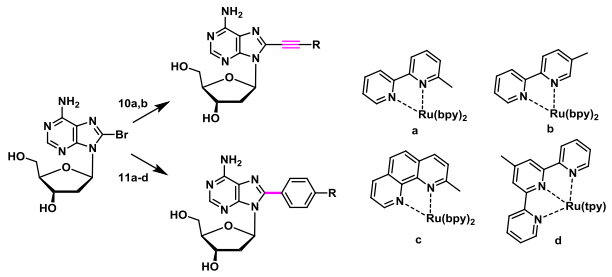

Figure 24. Schematic representation of the synthesis of ruthenium polypyridyl complexes with deoxyadenosine nucleosides via Sonogashira and Suzuki cross-coupling.[298, 299]

A direct comparison of the scope of the Sonogashira cross-coupling reaction and the related Suzuki coupling were investigated by Vrabel *et al.* (Table 3, entry 23)[298, 299] and Yang *et al.* (Table 3, entry 22).[297] Vrabel *et al.* coupled deoxyadenosine nucleosides via both reaction techniques to a series of the free ligands as well as the corresponding Ru complexes based on bpy, phen and tpy (Figure 24). Notably, the Suzuki reactions achieved for all studied examples better results than the Sonogashira couplings. The same observation was found by

Yang *et al.*, albeit less pronounced. Whereas *bis*-3,5-dibromophenyl-decorated $[Ru(tpy)_2]^{2+}$ complexes gave the *tetra*-substituted Suzuki product using pyridine boronic ester in remarkable high yield (85%), the corresponding Sonogashira coupling using acetylenic pyridine gave a slightly lower yield of 78 % (Figure 25). Although the reported yields were comparable, the Sonogashira reaction seems to lead in all cases to somewhat lower yield than the related Suzuki reaction.

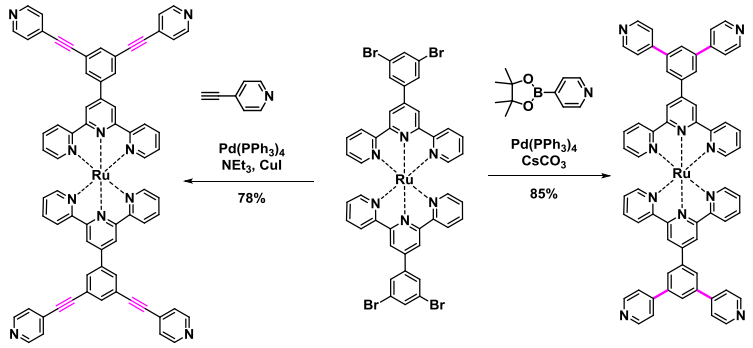

Figure 25. Schematic representation of the synthesis of a $[Ru(tpy)_2]^{2+}$ -based complex with four peripheral pyridine units *via* Sonogashira cross-coupling (left) and Suzuki cross-coupling (right).[297]

5.5.2. Suzuki coupling

The Suzuki coupling represents also a versatile and wide-spread method to connect two aromatic subunits. In contrast to the Sonoghira version, two aryl units are linked directly, *i.e.*, without an intervening alkyne. The range of reported Ru-containing substrates for Suzuki croos-coupling, *i.e.*, the corresponding halides and boronic acid derivatives, is comparable to the Sonogashira cross-coupling reaction – but not used as extensively. Table 4 lists the reported examples for the couplings of Ru^{II} polypyridyl-type complexes with metal-containing substrates (entry 1–4),[110, 119, 135, 297, 317-321] or with organic substrates (entry 5–16),[131-133, 298, 299, 322-334] including the assembly of photoactive dyads and triads. In close resemblance of related Pd-mediated cross-couplings, the catalytic systems are composed of commercially available pre-catalysts, *e.g.*, $Pd(PPh_3)_4$, $Pd(PPh_3)_2Cl_2$, $Pd(dppf)Cl_2$, $Pd(dba)_2$ with assisting phosphine ligands, e.g., Buchwald's SPHOS, bidentate dppf or the water-soluble PPh_3-derived ligand triphenylphosphine-3,3′,3″-trisulfonic acid trisodium salt (TTPPT). Brunner *et al.* reported the use of a dendronized Pd-G2 SPHOS catalyst system, which promotes the coupling of functionalized benzene boronic esters bearing phosphonic acid or carboxylic acid groups with a yield of up to 84% (entry 15).[335] Polar solvent mixtures and bases are typically employed for the Suzuki cross-coupling, *i.e.*, ranging from DMSO, DME/EtOH, $MeCN/H_2O$, DMF, THF/H_2O and Na_2CO_3, K_2CO_3, K_3PO_4, Cs_2CO_3, respectively.

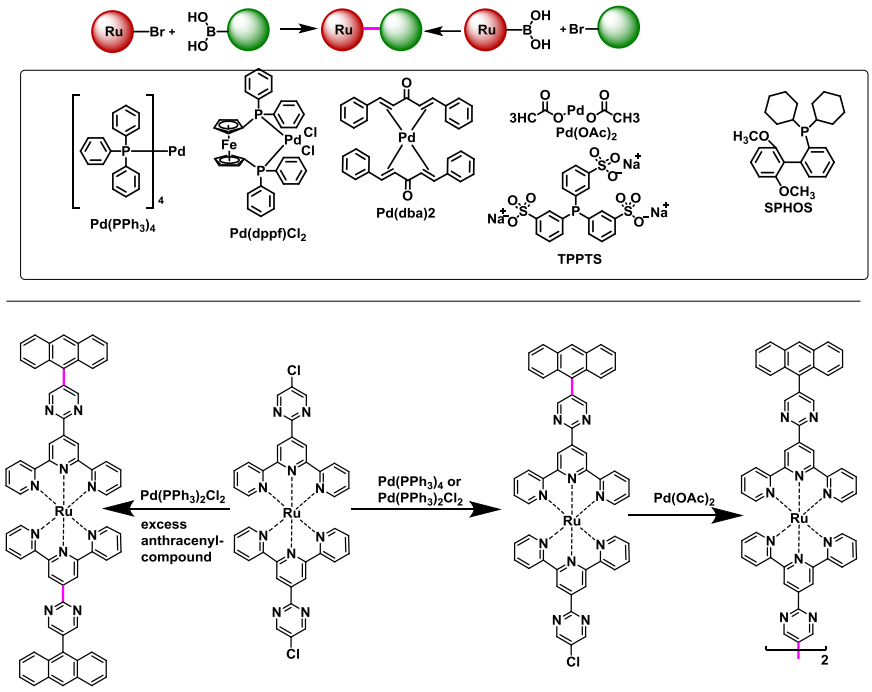

Figure 26. Schematic representation of the functionalization of $[Ru(tpy)_2]^{2+}$-based complexes with anthracene: (Left) Twofold decoration and (right) onefold decoration with subsequent reductive dimerization.[324]

The groups around Hanan, Juris and Campagna investigated the Suzuki coupling reaction of functionalized $[Ru(tpy)_2]^{2+}$ complexes bearing one or two peripheral chloropyrimidine units attached to the axial 4'-position(s) (Figure 26 and Table 4, entry 9 and 10).[324] The coupling with anthracene boronic acid was improved by using an excess of the reagents, leading to the *mono*- and *bis*-functionalized products. The $Pd(PPh_3)_4$ catalyst achieved the highest yield for the *mono*-functionalized product, which was dimerized via the remaining Cl group using $Pd(OAc)_2$ as catalyst to afford the dinuclear Ru complex (Figure 26, right). On the other hand, the usage of $Pd(PPh_3)_2Cl_2$ and an excess of boronic acid furnished the full conversion to the doubly anthracenyl-equipped complex.

Table 4. Reaction conditions and yields of Suzuki reaction on the ruthenium ligand scaffold.

	Ref	Tolerated functional moieties Ru^{II} complex	Coupling partner	Catalytic system	Solvent/ base	Temp. [°C]	Time [h]	Yield [%]
1	[297]	None	Pyridine	$Pd(PPh_3)_4$	DMF Cs_2CO_3	80	12	85
2	[119]	Tolyl	Ru^{II}, Tolyl nitrophenyl, dimethylamino, anthracene	$Pd(dppf)Cl_2$, $Pd(PPh_3)_4$ and dppf	DMSO, KOAc DME, EtOH, aq. Na_2CO_3	80	22	6-62
3	[319]	None	Ir^{III}	$Pd(PPh_3)_4$	DMSO Na_2CO_3	80	96	66
4	[320]	Phenyl	Ru^{II}, Os^{II}, indenofluorene	$Pd(PPh_3)_4$	DMF K_2CO_3	120	24	74
5	[131]	4-Vinylpyridyl	Benzoic acid	$Pd(dppf)Cl_2$	DMF K_3PO_4	85	24	
6	[133]	NDI	Benzoic acid	$Pd(PPh_3)_4$	DMF K_2CO_3	85	24	75
7	[298]	None	Deoxyadenosine	$Pd(OAc)_2$ TPPTS	H_2O, MeCN Cs_2CO_3	80		95
8	[322]	Methoxy	tpy	$Pd(PPh_3)_4$	DMF Na_2CO_3	90	48	41
9	[323]	Pyrimidine-chloride	Anthracene	$Pd(PPh_3)_2Cl_2$	DMF	110	12	83
10	[324]	Pyrimidine-chloride	Anthracene	$Pd(PPh_3)_4$	DMF K_2CO_3	110	16	49-85
11	[326, 327]	Ester, Ether, Thioether	TARA	$Pd(PPh_3)_4$	DMF K_2CO_3,	70	14	85
12	[332]	None	Thiophene	$Pd(dba)_2$ SPHOS	MeCN/H_2O K_2CO_3	100	16	55-92
13	[333]	Ether	tpy	$Pd(PPh_3)_4$	DMF/H_2O K_2CO_3	80	18	50
14	[334]	None	TMS-Aryl	$Pd(PPh_3)_4$	DMF K_2CO_3	95	15	91
15	[335]	None	Phenyl, phosphonic acid, carboxylic acid	Pd-G2, SPHOS	MeCN, H_2O, K_3PO_4	70	5	84
16	[336]	MeOPh	Benzoic acid	$Pd(PPh_3)_4$	THF, K_2CO_3	reflux	12	61

a) NDI is naphthalene diimide; TARA is triaryalmaine; Pd-G2 is dendronized Pd (see ref. [335]); SPHOS is 2-dicyclohexylphosphino-2′,6′-dimethoxybiphenyl; TPPTS is triphenylphosphine-3,3′,3″-trisulfonic acid trisodium salt; dba is dibenzylideneacetone; dppf is 1,1′-bis(diphenylphosphino)ferrocene. TMS is trimethylsilyl.

The groups around Williams and Hanan extended the Suzuki coupling to various aryls, *e.g.*, tolyl, anthracenyl, nitrophenyl or dimethylarylamine units,[119, 328] using $Pd(PPh_3)_4$ and sodium carbonate in DME/EtOH around 60% yield. Notably, the trimethylsilyl (TMS) group was reported (Table 4, entry 14),[334] which was converted by ICl to the corresponding iodo-aryl derivative to serve in a subsequent Suzuki coupling step. Additional functional groups include phenyl or triarylamino moieties bearing carboxylic acid groups for surface immobilization,[131-133, 329] as well as electropolymerizable thiophenes or bithiophenes units using $Pd(dba)_2$/ SPHOS (Table 4, entry 12).[332, 337] The Berlinguette group reported the synthetic route towards

a cyclometalated $[Ru(tpy)(N^N^C)]^{2+}$ complex for photovoltaic applications, whereby the metallating ligand contained a thiophene group as well as a triarylamine unit, while the anchoring tpy ligand bear the carboxyester groups (Table 4, entry 11).[326, 327] Since the coordination of the carboxy-decorated ligand failed, the complementary "chemistry-on-the-complex" strategy was followed to obtain the desired complex after introduction of the triarylamine unit to the thiophene with a remarkable yield of 85%.

The coupling of two or more complexes containing ruthenium, osmium or iridium centers can also be realized. There numerous examples of directly coupled dinuclear complexes *via* an oligophenyl spacer (Table 4, entries 2 and 3).[110, 119, 318, 319, 330] A systematic series by DeCola, Indelli and Scandola addressed the dependence of the photophysical processes by various conjugated bridges composed of phenyl and fluorenyl units,[320] including alkyl substituents to promote solubility as well as a dihedral twist of the aromatic bridge units.[321] The Abruña group reported various dinuclear Ru and Os complexes towards molecular electronic applications, which bear a dithienylcyclopentene-bridge that can be isomerized to control the degree of electronic communication.[317] Strongly-coupled dinuclear [Ru–Os] complexes featuring a linkage *via* the lee frequently used *meta*-position pattern were also synthesized following the Suzuki coupling methodology.[333] Various dinuclear [Ru–Pd] complexes were synthesized via Suzuki coupling to study their photochemical reactivity, *e.g.*, towards styrenes.[331] The Newkome group reported multinuclear complexes to explore fundamental self-assembly in supramolecular architectures (section 5.1),[322] including related work by others on 2D and 3D supramolecular architectures[338, 339]

5.5.3. Stille coupling

The Stille cross-coupling represent a particularly attractive methodology to connect aryl groups. Due to the absence of an auxilliary base, the associated side reactions are diminished in comparison to the Suzuki protocol (*e.g.*, de-borylation). However, these merits are paralleled by the inherent toxicity of the stannyl compounds, which may account for the lower usage of this versatile subclass of C–C bond formation reaction. There are just a few reports for bpy- and typ-based Ru complexes with boron-dipyrromethene (bodipy) or zinc porphyrins using $Pd(dqpf)Cl_2$ as catalyst in combination with CuI and trimethylamine.[340] Note that the related Suzuki coupling would require an aqueous base, which is undesirable in view of the known base-sensitivity of the bodipy unit. Another example is reported by Steen *et al.*, who reported the coupling of a thiophenebromide-functionalized $[Ru(bpy)_3]^{2+}$ complex with a bpy-thienyl stannane applying the standard catalyst $Pd(PPh_3)_4$.[341] Trouillet *et al.* reported the

copolymerization of dibromo-equipped $[Ru(bpy)_3]^{2+}$ and a quarterthiophene *bis*-stannane bearing alkyl chains.[342] Notably, the analogous incorporation of the free bpy ligand and subsequent coordination in the second step failed, demonstrating the versatility and necessity of the "chemistry-on-the-complex" to obtain the desired copolymer (Figure 27). An isolated yield of up to 51% was reported, which required the preparation of the active catalyst $Pd(PPh_3)_2$ from $Pd(PPh_3)_2Cl_2$ with an organo-lithium species before the polymerization.

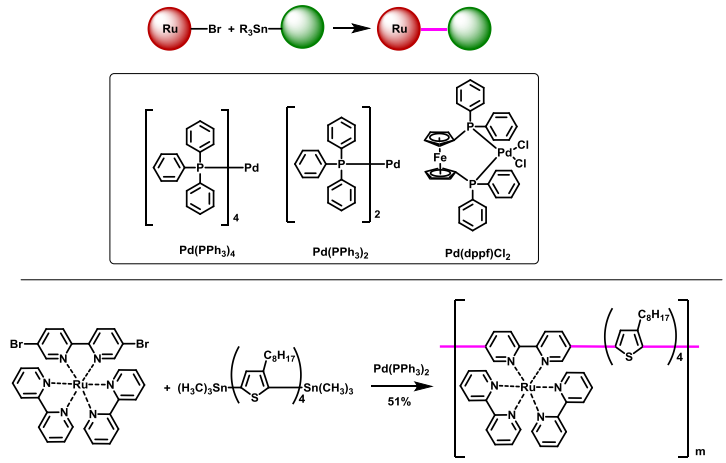

Figure 27. Schematic representation of the Stille cross-coupling forming a conjugated $[Ru(bpy)_3]^{2+}$-based metallopolymer with intervening thiophene units.

5.5.4. Negishi coupling and Yamamoto-type homocoupling

In comparison to the Sonogashira and Suzuki cross-coupling reactions, the Negishi coupling using organo-zinc reagents is rarely utilized. The Hanan group reported the Pd^0-mediated coupling of 2-pyridyl zinc bromide with a 2-bromopyridyl-decorated $[Ru(bpy)_3]^{2+}$ to construct a new bpy unit for subsequent coordination using $Pd(PPh_3)_4$ as catalyst to reach 97% yield.[343] Despite the excellent yield, the preparation and purification of organo-zinc compounds is more challenging than the related boron or tin reagents, which may explain the inferior role in synthetic chemistry. The direct coupling of halide-decorated Ru complexes was achieved in high yields (80–87%) using metallic zinc and Ni catalysts, *e.g.*, $NiCl_2(H_2O)_6$,[344] $Ni(PPh_3)_2Cl_2$,[345] or $Ni(PPh_3)_2Br_2$[346, 347] in the presence of PPh_3 as co-ligand (Figure 28). Note that these examples represent a borderline case, depending whether or not a an organo-zinc compound is formed *in situ*. If not, the homocoupling occurs via Yamamoto-type reductive dimerization, and the zinc is used to regenerate the active Ni^0 species.

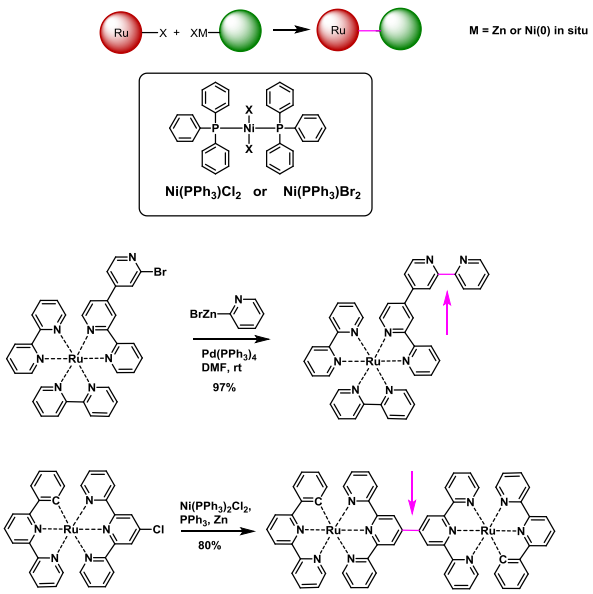

Figure 28. Schematic representation of the synthesis of dinuclear cyclometalated ruthenium complexes promoted by Zn-based reagents (Negishi reaction) or Zn-promoted reductive dimerization (Yamamoto coupling).

Bhuiyan *et al.* synthesized a Ruthenium phenanthroline dimer by coupling two with chloride functionalized complexes. The catalytic conditions are $NiCl_2$, PPh_3 with elemental zinc to obtain the dimer with a yield of 55%.[348] Furthermore, the Yamamoto coupling is frequently applied to prepare polymers using *bis*-functionalized Ru complexes, which is beyond the scope of this review and only a brief introduction is included in section 5.7. Interstingly, these conditions were found unsuitable for the homocoupling of a chloropyrimidyl-based Ru complex, which was alternatively dimerized using [$Pd(OAc)_2$]/phosphine-mediated catalysis in 49% yield.[324] Notably, no auxiallary reductant was added, which would be formally required under the reported conditions.

5.6. Azide-alkyne cycloaddition

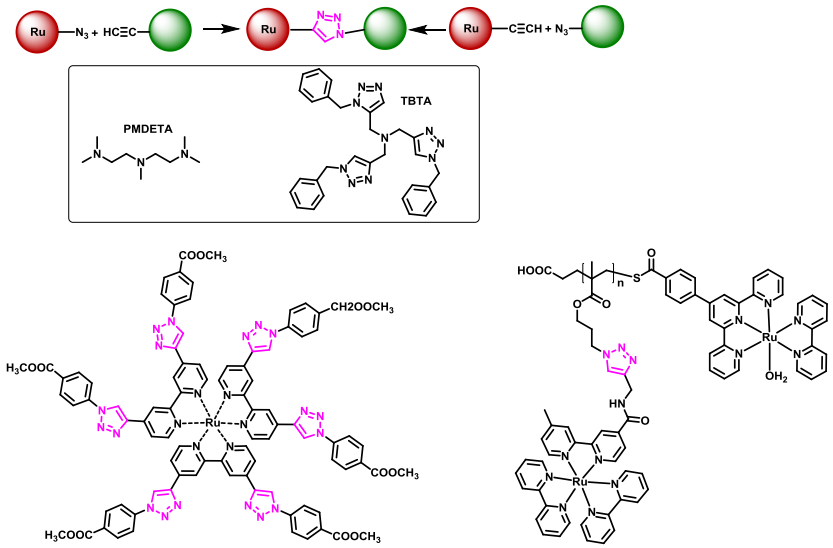

Figure 29. Schematic representation of selected examples for the "Click" reaction including the auxiliary reagents (PMDETA and TBTA).

The copper-mediated azide-alkyne cycloaddition (CuAAC) reaction has been extensively utilized during the last years to couple different functionalities onto ruthenium complexes under mild conditions. For example, the introduction of anchor units (*e.g.,* carboxylic acids or phosphonic acids), as previously discussed *via* alkylation or amidation reactions, can also be readily achieved *via* CuAAC.[176, 177] More importantly, the mild reaction conditions render this methodology particularly attractive in case of sensitive functional moieties, *e.g.*, bioconjugates. The Rau group recently reviewed in detail the "Click chemistry" for the synthesis of multiple luminescent ruthenium complexes.[349, 350] According to their classification, three main types can be distinguished, *i.e.*, the "click to chelate", "click then chelate" or "chelate then click" methodologies for various applications fields, *e.g.*, in DSSC devices, artificial photosynthetic catalysts, therapeutically applications and as functionalization for bio-molecules (*e.g.*, hormones, DNA[236]). The third technique termed "chelate than click" complements this review and will only be briefly discussed. The standard reaction conditions utilized $Cu^{II}SO_4 \times nH_2O$ as the pre-catalyst that is reductively activated by sodium ascorbate (NaAsc) to generate the active Cu^{I} species. A representative overview of selected examples is provide in Table 5, illustrating the wide range of functionalities ranging from aryl groups (entry 1),[351] to redox-active moieties (entry 2),[352] Ni cyclam catalysts for the reduction of CO_2 into CO or production of H_2 (entry 3),[353] amino acid derivatives (entry 4),[354] photo-active tryptophan residues for radical generation (entry 5)[355] or immobilization onto graphene sheets for photoactive materials (entry 6).[356] The use of ascorbic acid instead of

sodium ascorbate was used for the coupling with sugars (entry 7)[74] or protein labeling. The sodium sulfonate groups on the ruthenium scaffold led to an increased solubility of the molecule (entry 8).[218] Gerken *et al.* employed $Cu(TBTA)SO_4$ (TBTA is *tris*(benzyltriazolylmethyl)amine) and sodium ascorbate for the CuAAC reaction with *tert*-butylphenyl azide(entry 9).[357]

Table 5. Reaction conditions and yields of CuAAC click reaction on the ruthenium ligand scaffolds.[a]

	Ref	Tolerated functional moieties		Catalyst	Solvent	Temp. [°C]	Time [h]	Yield [%]
		Ru^{II} complex	Coupling partner					
1	[351]	None	Phenyl	$CuSO_4$, NaAsc	CH_2Cl_2	rt	4 Days	55
2	[352]	None	NDI	$CuSO_4$, NaAsc	CH_2Cl_2/ H_2O	rt	20	58-81
3	[353]	None	Cyclam-BOC	$CuSO_4$, NaAsc	CH_2Cl_2/ H_2O	rt	Over night	81
4	[354]	Phosphonic acid	Oligoproline	$CuSO_4$, NaAsc	EtOH/H_2 O	rt	12	
5	[355]	None	Amidoindol-propionate	$CuSO_4$, NaAsc	CH_2Cl_2/ H_2O	rt	20	90
6	[356]	None	Graphene sheet	$CuSO_4$, NaAsc	DMF/ H_2O	50	36	
7	[74]	None	Sugar	$CuSO_4$ ascorbic acid	DMF	rt	3 Days	93
8	[218]	Sulfonate salt	Protein	$CuSO_4$ ascorbic acid DIPEA	DMSO H_2O	rt	Over night	
7	[74]	None	Sugar	$CuSO_4$ ascorbic acid	DMF	rt	3 Days	93
9	[357]	None	*tert*-Butylphenyl	$CuSO_4$, NaAsc, TBTA	DMSO H_2O	100	20 min	20
10	[258]	None	NDI	CuBr, PMDETA	DMF	rt	16	71
11	[358]	None	polystyrene	CuBr, PMDETA	DMF	rt	24	
12	[273]	Amide	PMMA	CuBr, PMDETA	DMF	rt	Over night	78
13	[214]	Methyl	Proteins	$[Cu(MeCN)_4]$ $[PF_6]$	DMSO	μW[b]	45 sec	

a) NaAsc is sodium ascorbate. PMMA is poly(methylmethacrylate). BOC is *tert*-butyloxycarbonyl. TBTA is *tris*(benzyltriazolylmethyl)amine. PMDETA is *N,N,N′,N″,N″*-pentamethyldiethylenetriamine. b) 100% microwave power (see ref. [214]).

The CuAAC reaction can be performed in various aqueous organic solvents to ascertain the sufficient solubility of the sodium ascorbate or the ascorbic acid. A versatile non-aqueous catalytic system is based on CuBr in combination with *N,N,N′,N″,N″*-pentamethyldiethylenetriamine (PMDETA) as the stabilizing ligand (Figure 29). In this case, a Cu^I source is used and, thus, no reduction by ascorbate under aqueous conditions is necessary. The CuAAC is widely applied for the incorporation of the ruthenium complexes to polymers in the side chain of polystyrene (Table 5 entry 11)[358] and polypropylacrylate (see

Figure 29 and Table 5, entry 12)[273] as well as for the chain-end functionalization of redox-active polymers (entry 10).[258, 261-263] Lee *et al.* reported the use of a halide-free $[Cu(MeCN)_4]^+$ catalyst for the microwave-assisted CuAAc reaction with proteins (entry 13).[214] More examples and detailed discussion can be found in Rau's recent perspective on the scope of CuAAC for multifunctional luminescent ruthenium complexes,[349] which will not be further detailed here.

5.7. Polymerization

The synthesis of metal-containing polymers or metallopolymers is highly promising to utilize the photoactive Ru complexes as a functional component for device fabrication. Hence, the incorporation of Ru complexes has attracted significant interest, leading to a plethora of approaches in resemblance of the classification by Rau for CuAAc (section 5.6),[349] *i.e.*, the "grafting from", "grafting onto", "chelation then polymerize" and *vice versa*. However, the obtained materials often represent stoichiometrically controlled composition due to inevitable side reactions or incomplete conversion – particularly for the grafting strategies. Hence, the following paragraphs briefly present selected examples to highlight the conceptional approaches behind (Figure 30), and the interested reader is referred to the more specialized literature.[359] In this context, the groups around Meyer, Schanze, Reynolds and Papanikolas explored in detail Ru-containing polymer for light harvesting and surface immobilizations.

The different methods can be categorized according to the position of the complex in the polymer, *i.e.*, within the polymer backbone, in the side chain or at the chain terminus. The usage of ruthenium containing monomers in the side chain often involves spacer units to account for the steric demand. The complexes bearing a polymerizable group on the ligand scaffold, which are commonly polymerized *via* radical polymerization techniques, ring-opening polymerization or electropolymerization.

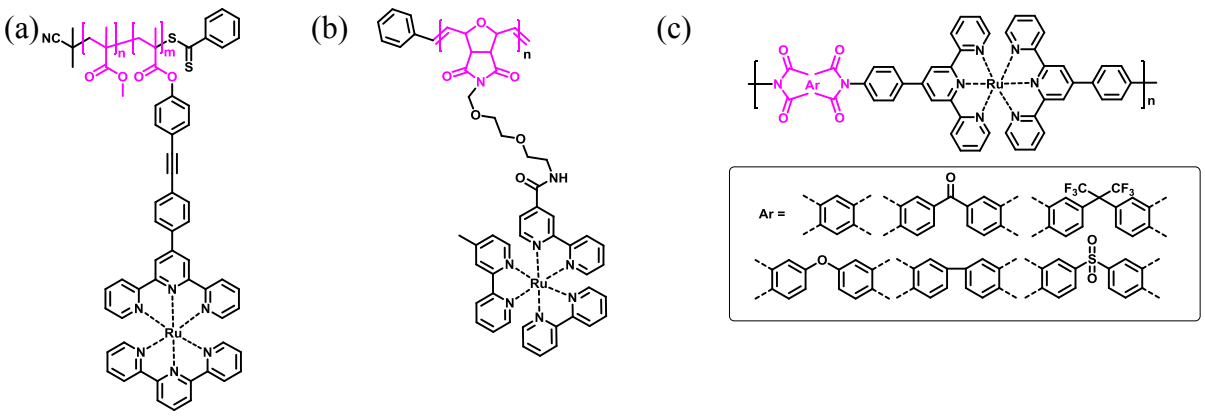

Figure 30. Schematic representation of selected examples for Ru-containing polymers. (a) RAFT copolymerization of methacrylates, (b) ROMP of norbornene-based monomers, and (c) polycondensation *via* diimide formation.

5.7.1. Radical polymerization

Numerous examples for the free radical polymerization using azobis(isobutyronitrile) (AIBN) as initiator are report, dominantly for methacrylate-based monomers (see Figure 30),[312, 360] vinyls[194, 361, 362] or styrene.[363] Furthermore a water soluble azo initiators (,2'-Azobis(2-methylpropionamidine)dihydrochloride, "V50") can be employed for the copolymerization with *N*-isopropylacrylamide (NIPAM) to form microgels.[364] For the methacrylate as well as the styrene functionalized complexes, controlled polymerization techniques are promising alternatives toward the control of dispersity and molar mass. For example, the RAFT polymerization is reported to yield polymers with low dispersity according the controlled living character of this technique.[365-367] Also, ATRP is a polymerization technique to introduce the complexes. The combination of CuBr/PMDETA (see also section 5.6) was used for the preparation of ruthenium-containing (co)polymers based on vinyl monomers[368] or styrene monomers.[224] In addition to these selected examples, alternative initiator systems were reported for ATRP and RAFT polymerizations. The latter one is used for the polymerization of (dimethylamino)ethyl methacrylate(PDMAEMA) . The ATRP technique was applied for a Ru-based metallostar that bears six initiator groups for the polymerization of MMA,[180] including a Ni-mediated version for pristine methacrylates[369] or carbazole-equipped MMA using a Ru with a single initiating site.[370, 371]

5.7.2. Ring-opening polymerization

The incorporation of $[Ru(bpy)_3]^{2+}$ units was accomplished by the corresponding succinimide-[193] or norbornene[372, 373] derivatives via ring opening metathesis polymerization (ROMP), using the Grubbs-catalyst (Figure 30). A variety of linkage patterns were reported that are mainly based on aromatic diimide moieties. Another example of for a chain-end decorated polymer is reported by Schulze *et al.*, who utilized a hydroxymethyl-decorated Ru(dqp)2]$^{2+}$ to initiate the ring opening polymerization of caprolactone to yield biodegradable polymers.[242]

5.7.3. Polycondensation

The incorporation of the ruthenium complexes in the backbone can be achieved by polycondensation reactions, *e.g.*, via diimide formation. The reaction often involves the condensation of a *bis*-amino-functionalized monomer with a *bis*-anhydride-decorated

monomer. This reaction was investigated by Ng *et al.* with a series of aryl spacer units (see Figure 30).[374] Another polycondensation was investigated by Rasmussen *et al.* which polymerized a *bis*-amino-decorated $[Ru(bpy)_3]^{2+}$ complex with glyoxal to form a conjugated backbone.[375] Wild *et al.* utilized the nucleophilic substitution of a thiols with pentafluorobenzene units to prepare metallopolymers.[268] The Heck cross-coupling reaction are used to build up a block copolymer of a ruthenium bipyridine complex in the backbone with a NLO chromophore using $Pd(OAc)_2$ and $P(OPhMe)_3$ as catalyst.[376, 377] Alternatively, a multitude of examples are reported for the preparation of metallopolymers *via* complexation, in analogy to the formation of metallostars or dendrimers (section 5.1). Due to enormous number of published examples to prepare metallopolymers from metal-containing precursors, an adequate discussion is beyond the scope of this review.

5.7.4. Electropolymerization

Another applicable polymerization technique is the electropolymerization, whereby radicals are formed during an electrochemical redox process. The radicals can recombine irreversibly to form linear or branched architectures, depending on the number of electropolymerizable units per monomer. In contrast to related radical polymerization techniques, the course of the polymerization can be controlled by the potential-time program and monitored by the corresponding current-time response. In this view, the sweep cycles in cyclic voltammetry can be utilized to initiate and stop the electropolymerization process reversibly. In case of deposition of the formed polymer, this technique offers attractive opportunities to control the film morphologies, thicknesses *etc.* Typical electropolymerizable groups comprise vinyls,[266, 378-388] arylamines,[389-392] thiophenes in all variations,[128, 332, 393-400] selenophene[401] or pyrrols (see Figure 31).[402-404] In order to form linear metallopolmyer, at least two reactive positions are necessary, while additional sites allow the formation of cross-linked networks. For example, triarylamine- and *N*-linked pyrrole Ru complexes can by electropolymerized with only one functional group of this kind, while thiophenes or vinyl groups require a minimum of two times to generate electropolymerization. In summary, the electropolymerization is a powerful technique to prepare conjugated multicolored electrochromic films, as demonstrated by extensive work by the Zhong group.

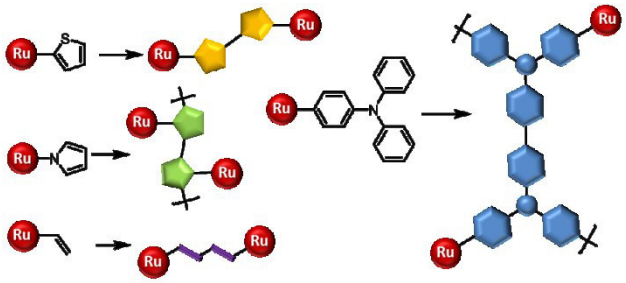

Figure 31. Schematic representation of typical electropolymerization units (thiopenes in yellow, pyrrols in green, triarylamines in blue, vinyls in purple).

6. Purification methods

This part reviews the various aspects of purifying Ru complexes in the context of the "chemistry-on-the-complex". Due to the charged nature of the educts, the byproducts and the desired target compounds, the reliable separation is challenging and often requires combinations of extraction, crystallization and chromatography protocols. The metrics of reported literature highlights the importance of chromatography, accounting for 90% of the publications (Figure 32). Nevertheless, it appears that the independent working group established own "in-house" protocols based on their own experience and available instrumentation, but restricts the interested readers to draw a strict connection to their own purification scenario. In other works, relating the molecular structure or functionality to a specific purification protocol is difficult and results often in a trial-and-error approach. Hence, this section aims to present a comprehensive list of classified purification protocols, and may help to navigate the reader to related examples.

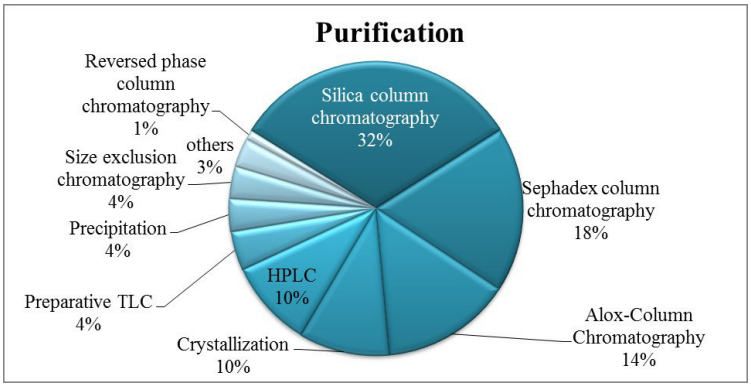

Figure 32. Metrics of applied purification methods for the "chemistry-on-the-complex" methodology.[104]

6.1. General aspects

The separation of ruthenium complexes often represents a severe practical challenge to isolate the pure target compounds after synthesis. The purification of Ru complexes can be successful using solely extraction[52, 70, 139, 185, 187, 205, 267, 297, 352, 355, 405, 406] or precipitation protocols,[54, 65, 134, 195, 196, 198, 268, 342, 352, 358] – but generally additional purification steps are mandatory. Nevertheless, these initial steps are elementary and are conventionally performed to remove organic byproducts or inorganic salts prior to the final purification *via* crystallization or chromatography. In the case of crystallization, the knowledge or development of optimal conditions for the specific target complex is crucial. The challenges arise from the optimization of the solvent mixtures and conditions, ranging from losses due to impure fractions upon fractionated collection or the small quantities that are to be separated. In this view, chromatographic protocols are highly desirable and appear promising, yet there are marked difference between the separation of charge-neutral organic molecules and charged Ru complexes. As a consequence of their ionic nature, such complexes often require more polar eluting conditions than required for neutral organic compounds. Namely, the retention among complexes bearing different organic moieties is only little affected by the associated "subtle" polarity differences. In essence, the interaction with the typical polar stationary phase (silica, alumina *etc.*) increases with smaller size and higher charge of the complexes, as illustrated by the electrostatic potential (ESP) plots of representative complexes (Figure 33). For example, the mono-cationic cyclometalated complex **A** elutes with admixed methanol on silica, while the dicationic congener **B** featuring an identical shape and size requires salt additives for elution. The steric shielding by peripheral substituents generally diminishes the extent of retention to a borderline case, which has been investigated in great detail by Fletcher and Keene for ion pairing (section 7.1.5).

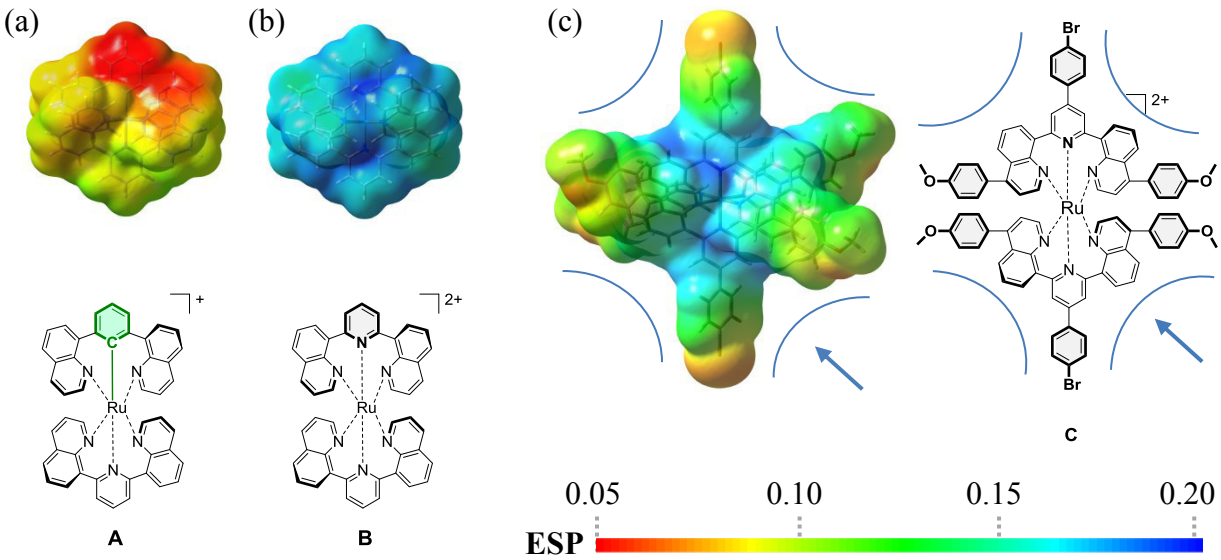

Figure 33. Electrostatic potential (ESP) plots mapped on electron density of representative Ru^{II} complexes featuring (a) cyclometalating ligands, (b) neutral polypyridyl-type ligands scaffold including (c) multiarylated ligand frameworks; counterions were omitted for clarity. Data reproduced from literature (A[407] and B/C[117]) and re-plotted to illustrate the ESP differences (isovalues of electron density set to 0.0004, color mapping adjusted from less positive (red, +0.05) to more positive (blue, +0.20) values. Note the identical shape and size of complexes A and B, but the less positive ESP of mono-cationic A (orange, <0.10) *vs.* dicationic B (blue, >0.15). Note for complex C the remaining void regions to access the complex core (indicated by arrow), but the sizable steric screening by the peripheral aryl substituents displaying intermediate ESP values (0.10 to 0.20) due to electrostatic polarization by the Ru^{II} core.

In summary, the majority of reported chromatographic purifications employ silica gel and salt-containing eluents, which works best to separate Ru complexes with large differences in size and charge. This simple argument explains the dominance of the coordination as the final synthetic step, as the Ru solvent byproduct or Ru salts can be removed rather easily. Notably, the scope of chromatography broadened significantly within the last years owing to novel commercialized stationary phases at competitive costs (surface-modified gels, size exclusion media), which permits salt-free conditions and enhanced resolution. These features are highly desirable, in particular in combination with automated purifications systems avoiding also the need of the additional counterion exchange step after ordinary column chromatography. The following section summarizes typical conditions for extraction methods (section 6.2), crystallization (section 6.3) and chromatographic methods based on adsorption (section 7) or the size-exclusion phenomena (section 7.2), including automated instrumentation techniques (section 7.3). In this regard, the recent progress in semi-preparative automated chromatography offers resource-efficient, time-saving and broadly applicable protocols.

6.2. Extraction by dialysis

One of the most facile purification steps relies on extraction. In most cases, a sufficiently large polarity difference is necessary for effective purification *via* extraction, which is often limited to the removal of neutral specimen (organic reagents, free ligands, *etc.*) from the more polar Ru complexes. Alternatively, selective solvents may be utilized – if known – for Soxhlet extractions or washing of crude products. In addition, the functionalization of the Ru complex by a polymer enables the extractive purification *via* the size exclusion effect of a dialysis membrane. In this case, smaller specimen than the molecular-weight-cut-off (MWCO) can pass the membrane between the interior to the exterior solvent reservoir. The extraction solvent is usually refreshed several times to reach quantitative extraction, which renders this method time-consuming. Nevertheless, this method can be very efficient and various molecular-weight-cut-off (MWCO) membranes are commercialized, often termed according to their pore size. Meyer and coworkers reported the grafting of azide-functionalized poly(propylacrylate) with an alkyne-decorated $[Ru(bpy)_3]^{2+}$ complex applying the CuAAc reaction, whereby excess of the unreacted complex was removed with a nominal MWCO value of 3.5 kDa.[273] Likewise, the successful separation after CuAAC-promoted grafting of alkyne-decorated $[Ru(bpy)_2(phen)]^{2+}$ to poly(4-vinylbenzylazide) is reported by Schanze and coworkers after anion metathesis to chloride (MWCO of 12–14 kDa).[358] A stimuli-responsive microgel was synthesized *via* copolymerization of a vinyl-decorated $[Ru(bpy)_3]^{2+}$ complex and *N*-isopropylacrylamide (NIPAM), utilizing a dialysis (MWCO of 10 kDa) with water as solvent (daily three times for 7 days at room temperature).[364] Ghosh *et al.* separated residual a $[Ru(bpy)_3]^{2+}$-based dye after NHS-ester coupling to a functionalized albumin (500–1000 Da MWCO, Millipore tubing).[190] The Tew group used dialysis with water to remove *N*-ethylmorpholinium chloride after ring-opening metathesis (co-)polymerization (ROMP) of a norbornene-equipped $[Ru(tpy)_2]^{2+}$ complex (MWCO of 8 kDa).[373] Notably, the authors monitored the process by conductivity measurements of the water (until 0.1 µS) and further confirmed the removal by ^{1}H NMR and FTIR analysis. Bell *et al.* reported the removal of non-covalently attached dicarboxylated $[Ru(bpy)_3]^{2+}$ complexes and colloidal anatase fractions (approximately 2 nm) by extensive dialysis (MWCO of 6–8 kDa) from the larger dye-loaded TiO_2 particles.[408] These selected examples illustrate the versatility of dialysis for purification of Ru complexes after grafting, copolymerization and immobilization onto nanoparticles, ranging from synthetic polymers based on styrenes and acrylates as well as norbornenes to polypeptides and even inorganic semiconductor particles.

6.3. Crystallization

The purification of ruthenium complexes is often achieved by crystallization. The most frequently used method is vapor diffusion of a volatile non-solvent into a stock solution under ambient conditions, while the liquid-liquid layering techniques of the non-solvent and solution is less frequently utilized. The crystallization process is initiated by the diffusion of the non-solvent, which induces nucleation due to the decreased solubility of the complexes. Next, crystal growth and Ostwald ripening occur. Depending on the ratio of nucleation *vs.* crystal growth, amorphous precipitates or x-ray suitable crystals can be obtained. In order to accelerate the crystal growth, the concentration of the complexes should be as high as possible. In practice, the vapor diffusion is often continued and may lead to the concomitant nucleation of byproducts. Nevertheless, the crystalizing product depletes from solution and eventually reaches a concentration regime, where nucleation of the byproducts is inevitable. Notably, if the solubility of the Ru byproducts is comparable, the order of crystallization is dominated by concentration – which is frequently encountered in reality. Hence, the fractionation of several batches and the recrystallization of impure crops may become necessary.

The most frequently employed solvent mixtures comprise acetonitrile as solvent and diethyl ether as non-solvent.[128, 131, 132, 290, 363] This particular combination has proven useful for various functionalized ruthenium complexes, *e.g.*, for complexes with CN functionalization.[147, 148] Acetonitrile as solvent may be replaced in special cases by acetone[54] or by dichloromethane,[147] particularly in the presence of large solubilizing organic moieties, *e.g.*, a tethered naphthalene diimide unit.[133] Alternative non-solvents with sufficiently high vapor pressure include alkanes, *i.e.*, pentane, hexanes or heptane. Given the miscibility of the non-solvent and actual solvent, alkanes are often used for THF[376, 377] or dichloromethane solutions, *e.g.*, in the case of triads containing zinc-porphyrins,[257] pyrene units,[296, 303, 306] or aromatic amino groups.[132]

The crystallization from aqueous organic solvents was reported for acetone, acetonitrile or THF. Fletcher *et al.* described the recrystallization from acetone/water and acetone/water/NH_4PF_6 mixtures, whereby the latter was employed for carboxylic acid or pendant bipyridine moieties.[241] The combination of acetone/water was further reported for various [Ru]–[Ru] and [Ru]–[Os] dyads,[166] as well as Ru complexes bearing benzothiazoles for DNA binding.[409] A mixture of acetonitrile/H_2O (1:1) was successfully used by Constable

et al. for a series of complexes bearing bridging units as well as ruthenium triads.[145] Aqueous THF was employed by Ji *et al.* for triarylamine-decorated Ru complexes.[132]

Miscellaneous solvent combinations comprise various organic-organic solvent mixtures: Acetone/ethanol for binuclear ruthenium complexes,[110, 205] acetone/ethylacetate for multicore ruthenium compounds (trimers, pentamers or heptamers)[172] or complexes bearing acid functionalities,[194] propionitrile/THF for the pyrene substituted complexes,[303] and acetonitrile/toluene for ruthenium dyads.[344] Single-solvent crystallization are reported for binuclear ruthenium compounds bearing anchoring phosphoric acid groups from MeOH,[200] ruthenium-ferrocene triads from EtOH,[225] or CuAAC-products from MeCN.[351]

In summary, crystallization from aqueous solvents or miscellaneous organic solvent mixtures require a temperature gradient (refluxing, chilling), or the evaporation of the solvent. In the latter case, the reduced volume of the solution upon evaporation may lead on the surface to undesired precipitation in addition the nucleation. Since the exact experimental conditions of crystallization are rarely reported and hard to reproduce from lab to lab, the vapor diffusion method represents a widespread and robust alternative, as the solubility upon slow admixing of the non-solvent can be controlled. Hence, fractionation can be performed easily, yet this method is often time-consuming. Thermally-induced crystallization permits larger scale but the knowledge of optimal experimental conditions becomes important, which renders this method suitable in case of established synthesis routes, *e.g.*, to prepare building blocks for the "chemistry-on-the-complex" approach (*vide supra*).

7. Chromatography

Liquid chromatographic represent the most powerful and by far most widely applied technique for the purification of Ru^{II} polypyridyl-type complexes. Two major retention modes are available, based on adsorption (section 7.1) and the size exclusion principle (section 7.2), which will be discussed by selected literature examples that provide additional insights. In analogy to the synthetic routes, a comprehensive overview will be provided by the tabulated protocols and variants in the corresponding subsections.

7.1. Adsorption chromatography

The final purification is often achieved by chromatographic methods, whereby adsorption chromatography plays the major role. Figure 34a depicts the elementary features for retention. The species diffuse from the mobile phase towards the stationary phase, where adsorption occurs and, thus, the species is retained before diffusing back into the mobile phase. The most

important stationary phases are silica (SiO_2) or alumina (Al_2O_3) including surface modification. Figure 34b depicts representative surface functionality of silica, *i.e.*, vicinal and

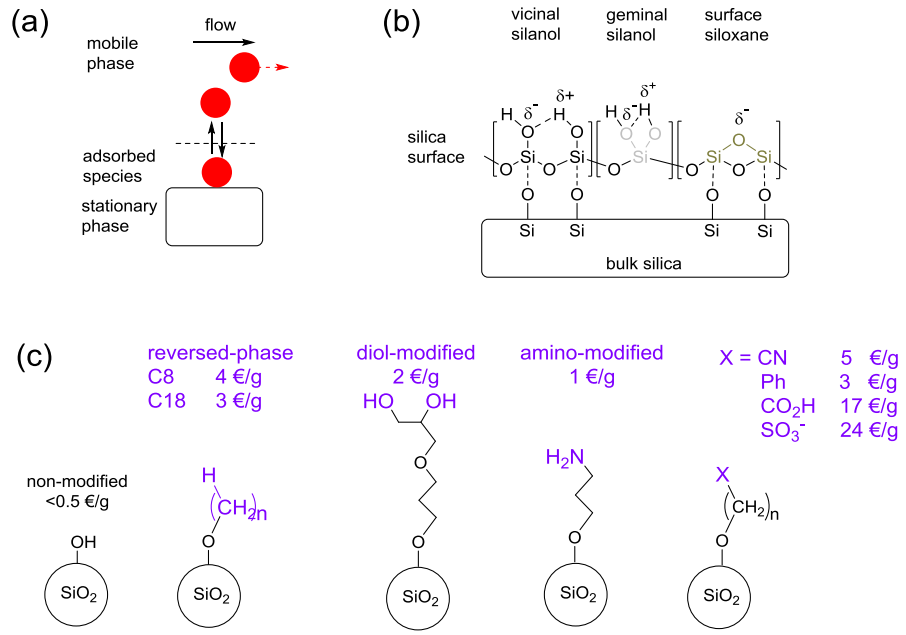

Figure 34. Overview of the (a) working principle of adsorption chromatography, (b) silica surface and (c) modified commercially available silica (price projected to 100 g).

geminal silanols and siloxanes. The Si–OH bond is substantially more acidic the organic C–OH counterpart, so that the chromatographic retention depends on hydrogen bonding interactions with the substance, *i.e.*, with lone pairs or aromatic π-systems. Their practical importance stems from the commercial availability and chemical inertness towards typical organic solvents, including aqueous and salt-containing eluents. Non-functionalized silica and alumina are often designated for single usage, while the significantly higher costs due to surface-modifications advises their re-usage (Figure 33c), *e.g.*, in automated instrumentation (section 7.3). Trivial surface-modifications of silica (section 7.1.1) or alumina (section 7.1.2) involve the deactivation by water (Brockman activity), as well was the admixing of acid/base (pH value) or salts (ionic strength) to the eluent. Since Ru complexes are usually charged, the addition of a supporting salt is most often necessary. Alternatively, the chemical transformation of the surface silanols is employed and leads to a variety of custom-modified silica gels. The most prominent examples are reversed-phase gels based on C8 and C18 alkyl chains (section 7.1.4). However, the hydrophobic layer shields the polar silica surface at the cost of diminished interactions with the charged Ru complexes, in particular if no peripheral organic moieties are present. An intermediate scenario between polar silanols and non-polar alkyl chains is given by short alkyl spacers decorated with various functional groups. Among the many, diol- and amino-modifications play a particular promising role due to their

competitive price ranging between silica and reversed-phase gels (section 7.1.3). Notably, analogous surface modifications are extended also to polymer-based resins, *i.e.*, polystyrene (PS) and poly(methylmethacrylate) (PMMA) reversed-phase media as well as carbohydrate-based stationary phases to feature diol- or amino-decorated surfaces. A more detailed overview is provided in section 7.2. dealing with size-exclusion media, which is predominantly composed of polymer-based resins. In the following section, the different stationary phases will be described in detail and evaluated for the chromatographic purification task, in order to serve as a guiding and selection tool for the specific Ru complexes to be purified.

7.1.1. Silica gel

Silica gel represents the most popular stationary phase that is applied for column chromatographic purification. The compatible eluents range from common organic solvents to aqueous mixtures, including acidic, basic or salt additives to modulate the retention via the surface's silanol groups. In the case of ruthenium polypyridyl complexes, a salt additive is often mandatory to prevent the adsorption of the charged complexes, in particular for dicationic complexes. For this task, a suitable organic solvent for the Ru complex is selected and the ionic strength is adjusted by the aqueous salt mixture. The most frequently used eluent mixtures contain acetonitrile and aqueous potassium nitrate, due to their miscibility over a broad range to maintain a high solubility of the Ru complexes. Alternative salts are applied occasionally, *e.g.*, sodium nitrate ($NaNO_3$) and potassium hexafluorophosphate (KPF_6). Notably, the use of the PF_6^- salts offers the possibility to omit the anion exchange after the chromatographic purification. Applying these typical eluent conditions enables the facile separation of differently charged specimens; however, the purification of functionalized Ru complexes with the same charges can become tedious, in particular if the polarity differences are only marginal in the ligand periphery. In this case, alternative (co-)solvents were successfully applied, *e.g.*, various mixtures of dichloromethane or acetonitrile with alcoholic solvents as water surrogates to modify the hydrogen bonding of the surface. In general, the larger the organic fragments become the less polar eluents are necessary (Figure 35), because the organic moiety sterically shields the Ru core as well as it promotes the solubility in typical organic (co)solvents (e.g., CH_2Cl_2). An overview of published solvent mixture with and without salt as well as their composition is displayed in the Table 6, including the classification of the peripheral functional moieties.

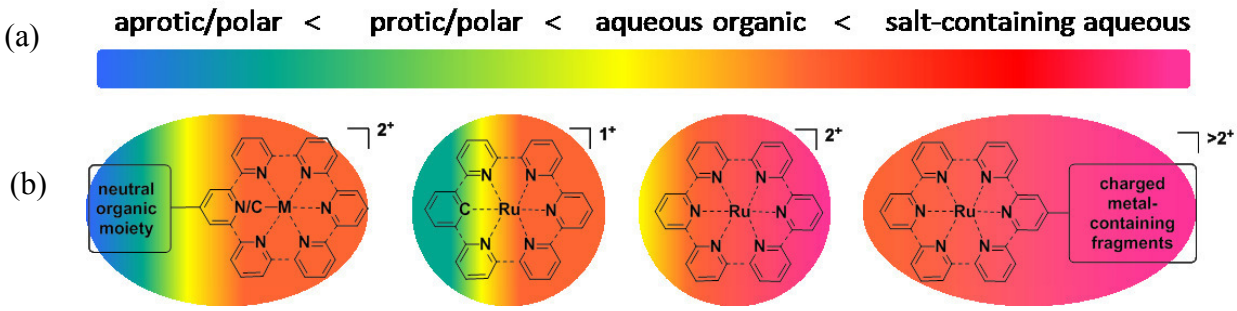

Figure 35. (a) Classification of four categories of eluents with increasing elution power and color scheme. (b) Selected types of functionalized Ru complexes with typical eluent conditions (color scheme).

Table 6. Overview of reported conditions for column chromatography using silica gel as stationary phase.

Mobile phase	Eluent ratio	Functional moiety	Ref.
CH_2Cl_2/MeOH	90/10	Peptide	68
		TARA, Ester	132
		TARA	146, 326, 327
		TARA	260
	99/1-90/10	tpy	333
	98/2-80/20	tpy, [Os]	333
	100/0-98/2	Acetylenebutoxy	134
	85/15	Bithienyl, bpy	341
CH_2Cl_2/MeCN	100/0-90/10	Indenothiophene, phenylthiophenes, bithienyl, fluorenyl,	410
	100/0-80/20	NDI	311
	98/2	Alkynethioacetate	294
	1/1	Styrene	194
$MeCN/H_2O/KNO_3$	80/18/2	Boronic acid	318, 319
	86/13.7/0.3	[Ru], $[Ir]^I$	318, 319
	88/11.8/0.2	[Ir]–[Ir]–[Ru] triad	318, 319
	98.8/10/0.2	Boronic acids, aryls, [Ru]	119
	90/15/1	Alkynebiphenyl diiodobiphenyl, [Ru], [Os]	290 289
	85/14/1	[Ru]–[Os]–[Ru] triad	288
	28/1/2	Sec-amine, [Mn]	256
	7/1/1	Trimethylpyridylaminw	256
		Pyridine,	297
	10/1/1	Acetylpyridine	297
	14/1/1	Methylpyridinium	297
	7/0.5/1	Dibromophenyl, carboxylic and phosponic acid	145, 335
	7/1/0.5-7/2/2	Thiophenebromide,	145, 335
	9/0.9/0.1	Thiophene-alkyne	310
		[Ru]–[Ru]–[Ru] triad	281
		[Ru]–[Zn]–[Ru] or [Zn]–[Ru]–[Zn] triads	279
		$[Ru]–[Zn]_{1-4}$ dyads	286
	40/4/1	Thiophene	332
		[Ru]–[Ru] dyads	330

		Terminal alkyne	258
	5/2/0.1	Alkynephenyl	308
	200/5/1	Vinyl, amide, sec.-amine, pyridine	266
	85/15/0-85/15/0.2	Pyrene	307
	70/29/1	Maleimidcaproic acid	219
	20/3/1	Maleimidcaproic acid [Ru]–[Ru] dyad, alcohol, bpy	220 110
	8/1/1-8/0/2	Sugars	411
	100/5/0.5	Ethylbromide	255
	80/17/3	[Ru]–[Zn]–[Os] triad	274
	10/1/0.1	Nucleoside	298, 299
	89/10.8/0.4	[Ir]–[Ru]–[Ir] triad	135
	80/12/4 90/5/1 50/10/2	Carotenoide, tyrosine	144
	100/7/1	Nitroaniline	68
		Dinitrophenylsulfide	69
	100/9/1	Dinitrophenylether	71
	100/10/5	[Ru]–[dyad], dithienylethene	317
$MeCN/H_2O/MeOH/KNO_3$	4/1/1/0.1	TMS-Ph	334
		[Ru]–[Ru] dyad	321
		[Ru]–bridge-[Ru] dyad	320
	5/4/1	Aminoethylglycin	188
	100/1/1-100/18/2	TMS-alkyne	301
$Acetone/H_2O/KNO_3$	9/1/0.2-0.4	NDI	311
	9/1/0.5	tpy	333
$CH_2Cl_2/MeCN/KNO_3$	100/0/0-78/20/2	NDI	311
$MeCN/KNO_3$	8/1	[Ru]–[Ru] dyad	345
	10/1	Thienyl, TIPS-alkyne	310
	9/1, 7/1	Thiophenealkyne	310
	7/1	Benzoic acid	329
		Aryls	328
		Anthracene	323
		[Ru]–[Ru] dyad	346, 347
		Cyano	148
	7/1, 10/1, 15/1	Pyrimidyl-anthracene	324
	20/1	[Ru]–[Ru] dyad	285
$CH_2Cl_2/EtOH$	98/2-90/10	Squalene	66
	200/1	Vinyl-tolyl	266
	100/0-92/8	DNA	55, 56
	100/0-60/40	DNA	55, 56
$MeCN/H_2O/KPF_6$	93/6/1	Nucleoside	293
	96/4/0.04, 95/5/0.5	Catenanes, ethers	264
$Acetone/water/NaNO_3$	100/0/0-70/30/2	Thiophene, furan	412
$MeCN/H_2O$	85/15	Multimetallic	174, 175
$CHCl_3/MeOH$	8/2-7.5/2.5	Sugar dendrimer	413
	7/1	[Ru]- [Ru] dyad, ester, amide	226
KPF_6 sat. $acetone/CH_2Cl_2$	70/30	[Zn] phthalocyanine	340

$CHCl_3$/MeCN	80/20	[Zn]–[Ru]–[Zn] triad	[257]
EtOH/H_2O/KNO_3		Pyridophenazine-phenyl	[325]
TBAOH in MeOH/H_2O	50/50	Carboxylic acid	[137]
Toluene/MeCN	40/60	[Ru]–[Ru] dyad, anthracene	[283]
MeCN/H_2O/$NaNO_3$	100/9/1	Terminal alkynes, cyano, dialkylamine	[35]

7.1.2. Alumina

Alumina as stationary phase is also well-known and frequently used for column chromatography of metal complexes. Table 7 lists the various eluents for the specific purification tasks. In comparison to silica gels, alumina is more cost-intensive, but its use enables additional features to optimize the separation. For example, the surface activity can be reduced by pre-treatment of alumina with water prior to packing (Brockman grade), or by selecting specific surface pH values (categorized as acidic, neutral or basic alumina). As a consequence, the alumina surface can be tuned to permit salt-free eluents. This is a practical advantage, because no anion exchange after purification is required. Hence, the most commonly applied combinations comprise salt-free eluents, *e.g.*, mixture of acetonitrile, dichloromethane and methanol.

Table 7. Overview of conditions for column chromatography using alumina asstationary phase.

pH Value	Mobile phase	Eluent ratio	Functional moiety	ref
neutral	CH_2Cl_2/MeOH	95/5, 97/3, 90/10	Methylbromide	[256]
		-	[Ru]–thiophene–[Os] polymer	[284]
		100/0-90/10	*N*-Methyl-ethynylbenzoylpyridine	[291]
		90/10	Adamantyl	[75]
	MeCN	100	Bromide	[414]
	MeCN/toluene	5/1	Undecanol	[365]
		2/1	Oligoproline	[415]
		3/1	Methylsulfonylphenylimidazol	[416]
	MeCN/H_2O/KNO_3	200/20/1	Cyclam, cyclam-Ni	[353]
		90/9/1	Ethylbenzoylpyridine	[291]
	Acetone	100	Propanol, methacrylate	[360]
	MeCN/MeOH/HCl →MeCN/CH_2Cl_2	9/1/0.5 1/2	bpy	[331]
	MeCN/KNO_3	7/1	Cyano	[147]
	CH_2Cl_2/MeCN	70/30	Acetyl, dimethoxybenzene	[147]
	CH_2Cl_2/MeCN/ MeOH	50/50/0-0/100/0-0/90/10	Benzoquinone	[191]
	MeCN/toluene/ EtOH	100/5/1, 100/100/1	Azide, Triazolebenzene	[356]
Acidic	CH_2Cl_2/EtOH	95/5	Butoxyacetylene	[313]
	Toluene/MeCN	60/40	[Ru]–[Ru] dyad, internal alkyne	[417]
Basic	MeCN/H_2O/KPF_6	97/2.5/0.5	Nucleosides	[293]

	CH_2Cl_2/MeOH	100/1	Bromo	[132]
		15/1	tpy	[322]
	MeCN/H_2O/KNO_3	10/1/1	Acetylenic tpy	[171]
No info	MeCN/toluene	4/1	Succinimidylester	[193]
		80/20, 60/40	Internal alkyne, pyrene	[303]
		50/50	Bromo	[113]
	CH_2Cl_2/MeOH	100/0-94/6	[Ru]–[Os] dyad	[418]
		100/0-99/1	Pyrenes	[295, 296, 307]
			Tetrathiafulvalene	[309]
		98/2,99.5/0.5	Thiophene-bpy	[305]
		92/8	Phenol	[419]
		50/1	Thiadiazoles	[420]
		97/3-90/10	Phosphine oxide, internal and terminal alkyne, [Ru]–[Ru] dyad	[113]
	MeCN/H_2O	100/0-75/25	[Ru]–[Ru] dyd, bipyrimidine	[113, 282]
	CH_2Cl_2/hexane	50/50-80/20	Thiophene-bpy	[305]
	CH_2Cl_2/MeCN	3/1	Bromo	[314]
		1/9	[Ru]–[Ru] dyad, bipyrimidine	[287]
	MeCN/Et_2O	1/1	Carbazoles	[243]
activated	Hexane/$CHCl_3$	1/1	TARA, trifluoromethyl	[141]

7.1.3. Surface-functionalized gels carrying diol and amino groups

The previous sections account for the majority of established purification protocols for Ru complexes to date. However, advanced chromatographic protocols are sought after to transfer and utilize the recent advances in (organic) synthetic methodologies. *i.e.*, to prepare and to purify more diversified Ru complexes. One powerful strategy follows the specific manipulation of the stationary phase to tailor the interaction with the compounds of interest. Among others, diol- and amino-decorated silica gels emerged as particularly promising candidates, attributed to their reduced surface polarity in comparison to pristine silica or alumina as well as their commercial availability at compatible costs. In the context of Ru complexes, salt-free eluents can be applied to omit counterion exchange and, thus, these gels are attractive as reusable packing materials, *e.g.*, in automated instrumentation (section 7.3). Besides their promising potential, the use of surface-functionalized gels for purification of Ru complexes is rare.

Schroot *et al.* used both column materials for the purification of functionalized ruthenium complexes and ruthenium-polymer conjugates, which were synthesized *via* "chemistry-on-the-complex" methodology.[258] Importantly, these modified gels furthermore enabled the replacement of an aqueous salt-containing acetonitrile eluent by CH_2Cl_2/MeOH mixtures, which are compatible with the large organic polymer residue. The successful purification was assigned to minimized aggregation and insolubility during the chromatographic run. Also, a

range of asymmetric cyclometalated complexes were purified with amino-functionalized silica.[407] Notably, the oxidation-sensitive complexes led to decomposition not only using ordinary silica with aqueous salt-containing eluents, but also during the necessary anion metathesis step. In summary, conventional flash column chromatography instruments can be equipped with diol- or amino-functionalized silica gels to provide a fast and reliable alternative (section 7.3).

7.1.4. Reversed phase silica gel

Reversed-phase silica represent one of the most popular stationary phase in automated HPLC, but the application in flash column chromatography is only occasionally found. The reversed phase can be subdivided by the number of carbon atoms of the alkyl chains. The McCusker group reported the usage of C18-decorated silica gel in combination with an alumina column for the purification of a series of cyano-decorated $[Ru(bpy)_3]^{2+}$-type complexes, which were prone to substantial side reactions during synthesis and purification.[147] However, an aqueous salt-containing eluent ($MeCN/KNO_3$, 7/1 ratio) was utilized, yet the exact role of the C18-phase was not discussed in further detail. Sadhu *et al.* described the use of pre-packed cartridges with a C18-phase for flash columns chromatography, applying a typical gradient program of H_2O/MeCN containing 0.01% triflic acid to purify $[Ru(bpy)_3]^{2+}$-lysine-protein conjugates.[67] A similar protocol was reported by Uzagare *et al.* for the separation of water-soluble sulfonated $[Ru(phen)_3]^{2+}$ complexes, relying on a eluent mixture of $MeCN/H_2O$/TFA.[218] In summary, only scattered reports for the usage of reversed phase in flash column chromatography can be found, and the main application is reported for HPLC (section 7.3)

7.1.5. Ion exchange chromatography: Sephadex

The ion exchange principle represents a widely applied technique, which relies on the displacement of ions in a pre-conditioned column by the charged target compounds (and *vice versa* for elution). Hence, the desired large specific surface is often provided by porous support materials, *e.g.*, modified dextranes. In addition to the capability of ion exchange, the size exclusion effect may be operable (see 7.2). The most popular cation-exchange materials are carboxymethyl- (CM-) or sulfopropyl- (SP-) decorated Sephadex C-25, whereby "C-25" denotes the degree of porosity. Hence, the carbohydrate backbone carries carboxylic acid moieties or sulfonate groups and, thus, this stationary phase is well suited for the separation of cationic specimen. In the context of bpy- or phen-type Ru complexes, Λ/Δ isomers or *fac*/*mer*

isomers of $[(Ru(N\hat{}N)_3]^{2+}$-type complexes can be separated. It is also useful for the purification of more simple complexes like Ru^{II} complexes bearing acid or ester groups,[197] or butyl-linked pyrene moieties,[421] additional free bpy units for iron coordination[241] or pendant amino-butane group.[239] In this case, the non-ionic impurities were eluted with water, while the retained complex was obtained by changing to an aqueous NaCl (0.25–0.40 M) eluent. A similar example was provided by Geisser *et al.* for the purification of a ferrocene-decorated $[Ru(bpy)_3]^{2+}$-complex featuring a dipeptide linkage, using Sephadex CM-50 and a phosphate buffered NaCl solution.[203]

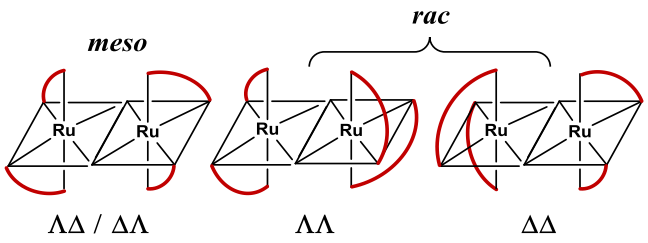

Figure 36. Schematic representation of Λ/Δ-coordination isomers, leading to the *meso* form (left) and two racemic forms (right).[422]

Λ/Δ Isomerism. The versatility of the separation properties of Sephadex for ion exchange and chiral resolution was established by the group of Keene, and continued by Fletcher. A comprehensive series of publications detail the role of different isomers, solvents, anions, temperature as well as substitution patterns. In one of the first studies, the separation of bimetallic complexes based on two $[Ru(bpy)_2]^{2+}$-fragments bridged *via* bipyrimidine was reported.[423] These complexes can exhibit three isomeric forms, *i.e.*, the *meso*-form and two *rac*-diasteromeres (Figure 36). The separation is reported challenging, yet it was achieved with Sephadex that was functionalized with strongly acidic sulfonate groups in combination with enantioselective solvents. The complex mixture was absorbed onto the anionic stationary phase and selectively eluted due to the competitive equilibria with an admixed electrolyte (typically Na^+-based). The initial separation was achieved with NaCl solution to separate impurities before the usage of the eluent for isomer separation. The best separation results were achieved with the chiral eluents containing sodium(+)toluene tartrate or sodium(-)benzoyl tartrate, but also achiral additives gave good results (sodium toluene sulfonate), showing an optimal concentration of 0.25 M. A subsequent study focused on the influence of the anion, *i.e.*, replacing ubiquitous the chloride by aliphatic acids (C2–C8 chains) as well as aromatic sulfonates and a range of benzoic acid derivatives.[424] The authors declared the distance movement and the separation ability as the two important parameters for

effective purification. While sodium chloride solutions featured a small movement and very poor separation, the usage of acetate as anion resulted in adsorption (no movement). The longer the chain length of the aliphatic part of the carboxylate became, the faster was the movement of the complex and the higher the separation of the diastereomers was found. Notably, branched alkyl chains did not increase the performance. The series of screened aromatic anions revealed the importance of the position of substituents. While *para*-substituted carboxylates led to an enhanced movement and separation, the *ortho*-substitution decreased the movement and, thus, no separation occurred. Notably, the underlying effect of ion pairing of the Ru complexes was further corroborated by ^{1}H NMR spectroscopy. Related examples of separation were reported for diastereomeric dinuclear ruthenium complexes with various bridging ligands, e.g., dipyridyl-oxadiazole[420] or dipyridyl-thiazolo-thiazole[425], as well as trinuclear complexes based on the *aza*-derivatives of bridging triphenylenes (ppz, HAT).[422, 426] In these cases, a Sephadex C-25 was employed using aqueous eluents containing NaCl, NaOTs (OTs is toluene sulfonate) or chiral dibenzoyl- or ditolouene-functionalized tartrates, whereby the latter additives undergo diastereomeric interactions and led to an enhanced enantiomeric resolution. Uppadine *et al.* investigated the influence of chiral substituents on the separation capability of Sephadex C-25 for ruthenium complexes bearing methylbenzylamine or bulky *tert*-butoxycarbonyldiaminocyclohexane moieties.[182] The separation was achieved *via* chiral anions like sodium dibenzoyl tartrate or the achiral sodium dibenzoyl-4-tosylate.

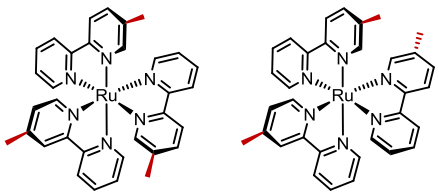

Figure 37. Schematic representation of facial (fac) and meridional (mer) $[Ru(bpyMe)_3]^{2+}$ complexes due to mutual arrangement of the three methyl substituents (shown in red).

***Fac*/*mer* isomerism**. Fletcher continued to study the challenging separation of coordination isomers of $[Ru(N^N^*)_3]^{2+}$, where N^N* denotes an asymmetric bpy ligand. In this case, facial and meridional isomers of the tris-bidentate complexes can form in a statistical ratio of 3:1 (Figure 37).[427] Sodium toluene sulfonate and sodium hexanoate were initially employed that descended from the group's previous protocols, however, effective column length of severable meters were required to achieve the full separation (hexanoate ca. 3–5 m, sulfonates up to 8 m). This length was achieved by recycling the product-containing band, *i.e.*, a

peristaltic pump was used which redirected the eluting band onto the column. In all cases, the facial isomers eluted prior to the meridional congeners, which was assigned to the hydrophobicity and mode of ion interaction. The facial arrangement led to a more closed solvent shell, while the meridional isomers formed a hydrophobic pocket that suggests more interaction with the stationary phase. However, if the complexes carried ester groups instead of alkyl chains, no separation was observed, which was tentatively assigned to the modified polarity. The methodology of chiral resolution was later transferred to the purification of Ru complexes bearing benzothiazolepyridine moieties for subsequent DNA binding.[409]

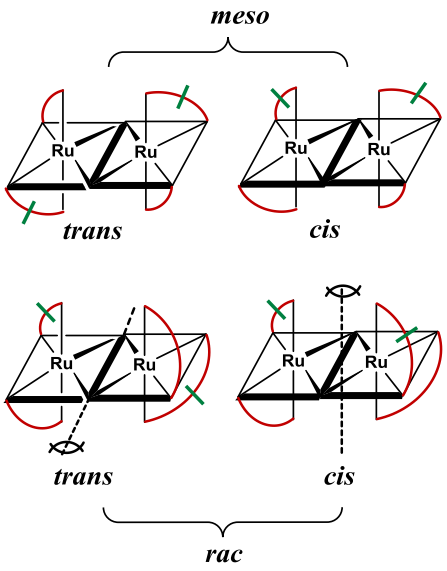

Figure 38. Schematic representation of dinuclear ruthenium complexes forming isomers.

The combination of Λ/Δ isomers and *fac*/*mer* isomers was assessed by the Keene group to separate the resulting *cis*- and *trans*-forms (Figure 38).[428] However, the authors observed incomplete separation applying their standard protocols in a single run, and instead required the recycling mode of the band was required. A higher separation was achieved for the *meso*/*rac* diastereomers using chiral anion sodium (-)*O*,*O*-di-toluene tartrate, while the *cis*- and *trans*-isomers were separated utilizing sodium toluene sulfonate. These observations parallel the later observation by Fletcher for the separation of *fac*/*mer* isomers of mononuclear Ru complexes. [427]

In summary, the ion exchange principle was studied in depth for Sephadex materials. Ion pairing was identified as a promising strategy to modulate the interaction of the complexes with the stationary phase, which enabled the separation of Λ/Δ isomers as well as of related diastereomeric bi- and trinuclear complexes. Furthermore, with the help of recycling the eluting band *via* a peristaltic pump boosted the separation efficiency, and enabled the

separation of *fac*/*mer* isomers featuring only marginal differences in terms of ion pairing interactions (void regions). However, apart from these instructive seminal reports, this advanced purification is rarely applied in the present literature.

7.2. Size exclusion material

The size exclusion principle originates from porous stationary phases, in which the compounds can diffuse. As a consequence, molecules within the pores are retained and lead to separation according to the hydrodynamic volume, which is roughly related to the molar mass. A variety of commercial size exclusion materials are available, which are listed in Table 7 with their nominal exclusion limits. These values permit a simple orientation for selection a suitable resin, but may be affected by the swelling of the material. For example, polystyrene-based resins tend to collapse under protic/aqueous conditions, while poly(methacrylate)- or carbohydrate-based resins are more suited for aqueous eluents. Another criterion, in particular if these costly materials are to be reused, is the long-term stability. In addition to undesired trapping of substance, the surface modifications or the carbohydrates backbone may undergo degradation processes, which may affect the performance over longer periods of time. Nevertheless, an enormous range of exclusion limits are commercially available, *i.e.*, ranging from 400 up to 50,000,000 Da.

Table 8. Overview of size-exclusion values.

Size-exclusion material (brand name)	Chemical nature of stationary phase	Variations	Exclusion size (Da)
Bio-Beads	Polystyrene	SX1	600-14,000
		SX3	> 2,000
		SX 8	> 1,000
		SX 12	> 400
Toyopearl	Poly(methacrylate)	HW 40	> 3,000
		HW-50	> 18,000
		HW-55	> 150,000
		HW-65	> 1,000,000
		HW-75	> 50,000,000
Sephadex	Dextran	LH 20	4,000-5,000
		G 10	700
		15	1,500
		25	1,000-5,000
		50	1,000-30,000
		75	3,000-70,000
		100	>100,000

7.2.1. Dextrane-based materials (Sephadex™/Superdex™)

Sephadex is frequently used for size exclusion chromatography applications. There are two major commercialized forms, *i.e.*, hydroxypropylate (LH-20) and non-functionalized (G-25) Sephadex. These Sephadex resins are often used for salt removal (desalination) as well as the separation of organic compounds, applying optimal solvent mixtures. Related materials are Superdex, Sepharose and Sephacryl, which differ in the carbohydrate backbone or the kind and degree of crosslinking. The following table provides an overview of typical conditions reported for several complex types.[429-431]

Table 9. Overview of conditions for column chromatography using Sephadex as stationary phase.

	Sephadex	Eluent	Functional moiety	ref
1	LH 20	-	Carboxylic acid, Alkyl	410
2	LH 20	MeCN/MeOH/H_2O 10/10/1	Phenothiazine	199
3	LH 20	H_2O	Phosphonate	200
4	LH 20	MeOH/H_2O 1/1	[Ru]–[Ru] dyad, amide	201
5	LH 20	0.1 M HNO_3	Pyrazole, benzimidazole	432
6	LH 20	Acetone/MeOH 1/1	Ester, bpy, [Fe]	241
7	LH 20	Acetone/H_2O→ Acetone/MeOH 1/1	Alkyl, ester	427
8	LH 20	MeOH	Carboxylic acid, internal alkene, thiocyanate ligands	18
9	LH 20	MeOH→MeOH/MeCN gradient	[Ru(tpy)(bpy)Cl]	213
10	LH 20	MeOH	Trifluoromethyl, bithiophenylvinyl	20
11	LH 20		Carboxylic acid, Cyano, bpy,	433
12	LH 20	H_2O	Phosphonic acid, ethynylamide	354
13	LH 20	H_2O	Phosphonic acid	143
14	LH 20	MeOH	BOC-leucine, [Ru]–leucine–[Ru] dyad	227
15	LH 20	MeCN/MeOH 1/1	Amino	206
16	LH 20	MeCN/MeOH 1/1	Carboxylic acid derivatives, pyridines, [Pt]	207
17	LH 20	H_2O	Peptide	434
18	LH 20	EtOH/MeCN 1/1	Triarylborane	302
19	LH 20	EtOH/MeCN 1/1	Triarylborane	300
20	LH 20	MeOH	Polystyrene-[Ru]	197
21	LH 20	EtOH/H_2O	chiral [Ru]	182
22	LH 20	MeCN→MeCN/MeOH 9/1	Imidazole	183
23	LH 20	H_2O	Phosphonate esters, cyano-, chloro-, and thiocyanato ligands	142
24	LH 20	MeCN/MeOH 1/1	Ferrocene	435
25	G 25	H_2O	PEG-300	218
26	G 25	Sodium borate solution	Benzo(*N*,*O*,*S*)azoles	212
27	Superdex 200	Ammonium acetate buffer (HPLC)	Proteins	436
28	Superdex 75	Phosphate buffer, NaCl-solution	Proteins	437
29	Sepharose	Acetone	[Ru] polymer	438

7.2.2. Polystyrene (Bio-Beads™)

Size exclusion chromatography is mostly used for the purification of polymers. The Bio-Beads material consists of cross-linked polystyrene with different pore sizes. The largest pore size belongs to SX1, which has the highest nominal exclusion range (600–14,000 Da). The other versions are SX3 (up to 2,000 Da), SX8 (up to 1,000 Da) and SX12 (up to 400 Da). The nonpolar material is best used with nonpolar organic solvents (toluene, CH_2Cl_2, $CHCl_3$, THF), while polar solvents (MeCN, DMF) and particular protic solvents (MeOH, H_2O) lead to a collapse of the pores. In view of Ru complexes, polar conditions are often required to promote a sufficient solubility of the complexes. One of the first examples for the purification *via* SX1 resins was reported by Chen *et al.*, who performed a ROMP of a norbornene-decorated $[Ru(bpy)_3]^{2+}$-complex and purified the obtained block copolymer applying an eluent mixture of toluene and acetonitrile (4/1).[193] Around the same time, the Schubert group began to explored the versatility of the Bio-Beads resin for the purification of metallopolymers, *e.g.*, from free radical polymerization of MMA-decorated $[Ru(bpy)_3]^{2+}$-complexes.[360] Later, the versatility of Bio-Beads was demonstrated also for dichloromethane or DMF as eluents to purify Ru-containing polymers as well as the possibility to recover the [Ru]-monomers from the product mixtures after applying various polymerization techniques. For example, the reversible-addition-fragmentation-transfer (RAFT) copolymerization of olefinic $[Ru(bpy)_3]^{2+}$- and $[Ru(tpy)_2]^{3+}$-type complexes[312, 365, 366] was investigated, as well as the Rhodium-catalyzed polymerization of alkyne-decorated $[Ru(tpy)_2]^{2+}$ complexes.[439] Breul *et al.* compared three different approaches for the incorporation of multiple $[Ru(tpy)_2]^{2+}$ units into the side chain of PMMA-backbone: (a) The copolymerization of monomeric MMA-decorated Ru complexes, (b) the complex formation from a suitable $[Ru(typ)Cl_3]$ intermediate with a tpy-functionalized PMMA, and (c) the grafting of an alkyne-containing $[Ru(tpy)_2]^{2+}$ *via* Sonogashira cross-coupling ("chemistry-on-the-complex").[312] The SX1 resins were used with DMF for the polymerization and the coordination reactions, while the grafting approach was purified on SX3 with dichloromethane as solvent, which was assigned to an improved separation of smaller molecules. In the case of a $[Ru(tpy)_2]^{2+}$-type block copolymer, which was formed by linking a telechelic $[Ru(tpy)Cl_3]$-modified PEG-chain with a telechelic tpy-decorated polystyrene was reported unsuitable, because the size exclusion limit was already reached by the individual coupling partners.[440] Instead, automated fractionation via SEC in THF was carried out using a PSS Gram preparative 100 A˚ column that is applicable to higher molar masses (see also section 7.2.3). In summary, Bio-Beads are well suited to remove small

monomeric Ru-complexes from their corresponding (co)polymers using various eluents, mainly CH_2Cl_2 and DMF.

7.2.3. Poly(methylmethacrylate) (Toyopearl™)

The Toyopearl resin family is based on cross-linked methacrylates and is usually applied for size exclusion or ion exchange chromatography of proteins and large organic compounds of biological origin, as well as for the purification of synthetic polymers. The material can be used under more polar conditions than Bio-Beads without pore collapse. In fact, even water can be applied as eluent. Although Nagai reported in 1992 already the use of ion exchange SE- Toyopearl and size exclusion HW Toyopearl for the separation of Ru^{II} complexes,[441] not more reports were found until recently. In line with their continuing interest to prepare and isolate defined Ru-based polymer architectures, Schubert and Jäger reported a series of publications that demonstrate the general versatility of Toyopearl resins.[261-263, 442, 443] In fact, the high mechanical stability in comparison to Bio-Beads allows larger pores for Toyopearl, which permits higher exclusion limits up to 50,000,000 Da (see Table 8 for comparison). Various block copolymers with a single $[Ru(dqp)_2]^{2+}$ core were successfully purified, including poly(triarylamine)s, poly(naphthalene diimide)s or poly(carbazole)s bearing hydrophobic and hydrophilic substituents, ranging from aliphatic groups (C4, C8 or C20 chains) to oligo- and poly(ethylene glycol) groups. Although the exact choice of the optimal resin depended on the size of the macromolecular architecture, the established protocols clearly confirm their general versatility. In summary, Toyopearl resins can possess high exclusion limits to complement the Bio-Beads resins for the purification of Ru-polymer-based architectures, in particular entering higher molar mass regions. Moreover, this methodology was implemented into an ordinary flash chromatography setup to save working time and efforts, as will be detailed in the following section. Hence, this methodology is believed to evolve to an invaluable tool for the reproducible purification and, thus, preparation of hitherto unpreceded architectures.

7.3. HPLC and automation in chromatography

The use of automation in chromatography is widespread, in particular for analytical high pressure liquid chromatography (HPLC). Notably, this technique is also suited for the semi-preparative scale, but requires substantial investments for the instruments and the required columns. In this regard, reversed phase silica gel plays an important role as stationary phase for HPLC, which is widely applied for (large) organic compounds with biological importance.

As a result of the identical surface chemistries as described in the preceding sections (sections 7 and 7.2), the same eluent mixtures are used. Nevertheless, the use of HPLC for the purification of Ru complexes is less frequently reported than other purification methods.

The reversed phase material can be subdivided by the length of the alkyl chain, which is bound to the silica support. The most commonly material is C18 reversed phase silica, but also C8 and C4 are encountered in the literature. More advance reversed phase modifications including functional groups, *e.g.*, cyano (CN) or amino (NH_2) groups. The usage of chiral stationary phases (CSPs) based on saccharides like cellulose or cyclodextrans enbales the separation of enantiomers. An early selected example by the DeCola group reported the purification of lysine-decorated $[Ru(bpy)_3]^{2+}$ complexes after peptide couplings chemistry.[216] Johansson and coworkers reported the challenging purification of three different isomeric forms (meridional, *cis*- and *trans*-facial) of $[Ru(dqp)_2]^{2+}$ using HPLC,[116] as well as the enantiomeric resolution of $[Ru(dqp)_2]^{2+}$ using chiral tris(tetrachloro-1,2-benzenediolato)phosphate (TRISPHAT) anions.[444]

The C18 stationary material is used for the separation of labeled oligoprolines,[354, 415] peptides,[51, 63, 64, 186, 190, 192, 221] ruthenium peptoids,[214] proteins,[212, 218] as well as desoxynucleotides,[189] with a mixture of acetonitrile and water as mobile phase including admixed triflic acid (0.1%). Kumar *et al.* synthesized a $[Ru(dqp)_2]^{2+}$-based triad, which was obtained after final oxidation of the quinone acceptor on the assembled triad scaffold. This example illustrates the necessity of "chemistry-on-the complex", because the benzoquinone did not tolerate the coordination reaction conditions. The series of Ru complexes were purified by preparative HPLC using C18 stationary phase and a mixture of water and methanol with Na_2HPO_4 or TFA as additives. In the case of related $[Ru(bpy)_3]^{2+}$-decorated oligoprolines, the Meyer group used shorter reverse phase materials (C4 and C8) were used with acetonitrile/water mixtures as mobile phase.[217] The scope of HPLC is not limited to Ru^{II} polypyridyl-type complexes, in fact, various reports exist that employ HPLC to study more labile congeners. A seminal example by Kroener *et al.* dates back to 1988, which detailed the effect of ion pairing on the retention time of various thioether ruthenium complexes, applying C8 reversed phase with a mixture of methanol and sodium heptanesulfonate.[445] Thomalla *et al.* reported the analytical characterization using HPLC on C8-functionalized silica to discern the degradation of related $[Ru(N^N)_2(SCN)_2]$ complexes used for solar cells.[446] Due to the carboxylate groups on the bidentate ligand (N^N), sulfuric acid as additive was used to control the protonation level.

An alternative HPLC application relies on the ion exchange principle. Such columns lead to a specific retention of the anions and cations, respectively, based on the interactions between the ionic compounds and the stationary phase. Hence, the main parameters to modulate the retention are the type of stationary charged groups, the charge/size of a molecule and the ionic strength or pH value of the eluent. Among others, the precise impact of these parameters was explored in detail for dextran-based stationary phases (section 7.1.5). In view of Ru^{II} compounds, these cationic complexes will interact with the stationary phase equipped with anionic moieties (*e.g.*, carboxylic acids or sulfonates). Typical resins are based on polystyrene or dextran and are widely applied for the purification of proteins or other biologically relevant compounds. For such compounds, the admixing of acid or bases can further affect the protonation state of the molecules (amino groups, acid groups, *etc.*) and, thus, are useful parameters to modulate and enhance the separation efficiency.

An early example is reported by the Meyer group in the 1990s, which employed cation exchange column chromatography for the purification of their photoactive amino acid assemblies that carried $[Ru(bpy)_3]^{2+}$ sensitizer units and organic electron donors (phenothiazine) and acceptor (methyl viologen) in the side chain. The eluent is composed of acetonitrile containing 0.6 mM phosphate buffer.[215]

Shu *et al.* explored the enantiomeric separation of racemates of 21 polypyridyl ruthenium complexes based on the phen and bpy ligand system, using chiral cyclofructan stationary phases.[447] The investigation concerned the impact of the applied eluents, additives, enantiomers, stationary column materials, counter ion, as well as the substitution position of the ligands. The authors tested three different stationary phases based on substituted cyclofructan resins, which revealed that only the aromatic substituted sugars led to enantiomeric separation, indicating that π-π interaction of the aromatic rings are crucial. The applied eluent was composed of MeOH/MeCN (70:30) containing 1% of a trimethylamine/acetic acid buffer (50/50). The alternatively tested acids (trifluoroacetic acid, formic acid) and bases (trimethylamine, ethanolamine, tributylamine) resulted in less separation for the majority of the tested complexes. The observation that the 50/50 buffer outperformed acids or bases suggested that the ionic strength is more important for the efficient separation than controlling the pH value. Hence, various ammonium salts (NH_4NO_3, $HNMe_3NO_3$, $NH_4(CO_2CF_3)$ and $NHMe_3(OAc)$ were screened, which identified trimethylammonium nitrate as the best salt. However, the low solubility in the solvents restricted the practical value and, thus, the separation was performed alternatively by acid/base variation preferentially. A higher percentage of acetonitrile led furthermore to a

decreased retention, while no major impact of the anion (PF_6^- *vs.* Cl^-) was observed. The influence of the substitution position of the ligand system was also investigated (*ortho* vs. *para* position), which revealed that electron-withdrawing *ortho*-substitution led to a higher selectivity assigned to the higher π acidity. These results were consistent with previous reports by Sun *et al.*, who investigated the separation on cyclodextran.[448, 449] In that study, eight mono- and two dinuclear complexes were tested, while best results were obtained with a naphthylethyl-carbamate functionalized β-cyclodextran, while nonaromatic moieties revealed no separation. Also the influence of salt, solvent mixture and anion reached the same results. The dinuclear ruthenium complexes consisted of peripheral phen ligands and a tetrapyridophenazine (TPPHZ) or tetra*aza*tetrapyridopentacene (TATPP) bridge. Hence, these ligand sets permit three isomeric complexes, *i.e.*, the *meso* form and the enantiomers (for details see section 7.1.5). While the TPPHZ-bridged complexes were readily separated applying the described method, the TATPP-bridged complex led only to partial separation. In a related study, further modifications of the stationary phase were tested using various chirobiotics (Teicoplanin, Teicoplanin aglycone, Vancomycin, Ristocetin A), which identified Teicoplanin as the superior decoration for the stationary phase under comparable purification conditions.[448] Browne *et al.* used Teicoplanin-functionalized silica as the stationary phase for the HPLC purification of a dinuclear ruthenium complex bearing peripheral bpy ligands and a bispyridine-1,2,4-triazole bridge.[450] In that report, two chromatographic runs were required for a complete purification. In the first run, the homo-chiral stereoisomers were separated from the mixed hetero-chiral complexes using an solvent mixture of acetonitrile/methanol/aqueous NH_4AcO (60/20/20), while the hetero-chiral isomers were separated in the second run using ethanol instead of methanol. Another study detailing the purification of related ruthenium complexes was published by Nagai.[441] Three $[Ru(bpy)_3]^{2+}$-based complexes bearing alanine, phenylalanine and tyrosine moieties were investigated in terms of their separation by HPLC using a C8-decorated silica gel, normal silica gel and tartaric acid functionalized silica. As a result of the systematic optimization, a ternary solvent mixture of $MeOH/H_2O/CH_2Cl_2$ in ratio of 6/2/2 containing LiCl as supportive salt was identified.

In summary, HPLC is utilized since two decades to analyzed and separated Ru^{II} polypyridyl-type complexes. The stationary phase is often C8-reversed phase silica gel, probably due to the broad applicability to other compounds, while specific (chiral) surface modifications became available in the last years, *e.g.*, based on dextrans. In this regard, the details of ion

pairing, recycling modes *etc.* were found to be in excellent agreement to the ordinary column chromatography setup as detailed in section 7.1.5.[423]

8. Conclusion

Ruthenium polypyridyl complexes are widely utilized for sensing and recognition, biomedical applications or in energy conversion. In the past, versatile synthetic routes were developed to prepare the corresponding complexes, often via coordination of the fully assembled ligand as the final step. Given the evolving synthetic methodology to couple sophisticated functional moieties, *e.g.*, redox-sensitive, temperature-sensitive or alternative chelating motifs, the application of the classic routes may become prohibitively challenging. Alternatively, the transformation of functionalized Ru complexes receives growing interest, as it enables divergent synthetic routes (modular building blocks, combinatorial approaches), as well as circumvents the intrinsic challenges from chemical instabilities during coordination can be circumvented (*e.g.*, biologically-active targeting functions), but also functional molecular assemblies and machines can be constructed. The most prominent examples for conjugation of Ru^{II} polypyridyl-type complexes with functional moieties involve amidation reactions descending from peptide-coupling, various types of alkylation reactions, metal-catalyzed cross coupling reactions mainly based on the Sonogashira and Suzuki-type reaction, as well as azide-alkyne cycloaddition reactions. However, the versatility and success of the "chemistry-on-the-complex" approach inevitable depends on general and robust purification protocols, which involve the separation of ionic Ru complexes. In this regard, the recent significant developments of chromatographic protocols hold to key to this prerequisite, *i.e.*, replacing or complementing ordinary silica and alumni gels by new commercially available stationary phases for adsorption and size exclusion chromatography, or automated instrumentation by HPLC or recycling modes. However, the applied purification protocols in literature often originate from the respective group's expertise. Hence, a comprehensive survey of available protocols along with tolerated functional moieties is provided, including exact eluting conditions (solvent, additives, pH value, ion pairing, *etc.*). In summary, the recent progress of synthetic and purification protocols demonstrate the potential of the "chemistry-on-the-complex" approach, which is believed to shift the frontiers of functional Ru^{II} polypyridyl-type complexes, and likely also other metal complexes. Consequently, new opportunities are provided by "chemistry-on-the-complex" approach to extent the usage of Ru complexes towards modern application fields beyond the chemist's expertise of coordination chemistry.

Acknowledgement

We thank the Thüringer Ministerium für Wirtschaft, Wissenschaft und Digitale Gesellschaft (TMWWDG) and the innovation center CEEC Jena, RIS 3 for financial support.

Conflict of interests

There are no conflicts of interest to declare.

References

1. F. H. Burstall, *J. Chem. Soc. (resumed)*, 1936, 173-175.
2. J. P. Paris and W. W. Brandt, *J. Am. Chem. Soc.*, 1959, **81**, 5001-5002.
3. D. M. Klassen and G. A. Crosby, *J. Chem. Phys.*, 1968, **48**, 1853-1858.
4. J. N. Demas and G. A. Crosby, *J. Mol. Spectrosc.*, 1968, **26**, 72-77.
5. D. W. Thompson, A. Ito and T. J. Meyer, *Pure Appl. Chem.*, 2013, **85**, 1257-1305.
6. A. S. Polo, M. K. Itokazu and N. Y. Murakami Iha, *Coord. Chem. Rev.*, 2004, **248**, 1343-1361.
7. G. C. Vougioukalakis, A. I. Philippopoulos, T. Stergiopoulos and P. Falaras, *Coord. Chem. Rev.*, 2011, **255**, 2602-2621.
8. P. G. Bomben, K. C. D. Robson, B. D. Koivisto and C. P. Berlinguette, *Coord. Chem. Rev.*, 2012, **256**, 1438-1450.
9. J.-F. Yin, M. Velayudham, D. Bhattacharya, H.-C. Lin and K.-L. Lu, *Coord. Chem. Rev.*, 2012, **256**, 3008-3035.
10. K. C. D. Robson, P. G. Bomben and C. P. Berlinguette, *Dalton Trans.*, 2012, **41**, 7814-7829.
11. A. Breivogel, S. Wooh, J. Dietrich, T. Y. Kim, Y. S. Kang, K. Char and K. Heinze, *Eur. J. Inorg. Chem.*, 2014, 2720-2734.
12. K. Chen, Y.-H. Hong, Y. Chi, W.-H. Liu, B.-S. Chen and P.-T. Chou, *J. Mater. Chem.*, 2009, **19**, 5329-5335.
13. C.-C. Chou, P.-H. Chen, F.-C. Hu, Y. Chi, S.-T. Ho, J.-J. Kai, S.-H. Liu and P.-T. Chou, *J. Mater. Chem. A*, 2014, **2**, 5418-5426.
14. C.-C. Chou, F.-C. Hu, K.-L. Wu, T. Duan, Y. Chi, S.-H. Liu, G.-H. Lee and P.-T. Chou, *Inorg. Chem.*, 2014, **53**, 8593-8599.
15. C.-C. Chou, F.-C. Hu, H.-H. Yeh, H.-P. Wu, Y. Chi, J. N. Clifford, E. Palomares, S.-H. Liu, P.-T. Chou and G.-H. Lee, *Angew. Chem. Int. Ed.*, 2014, **53**, 178-183.
16. C.-C. Chou, K.-L. Wu, Y. Chi, W.-P. Hu, S. J. Yu, G.-H. Lee, C.-L. Lin and P.-T. Chou, *Angew. Chem. Int. Ed.*, 2011, **50**, 2054-2058.
17. C. Coluccini, N. Manfredi, M. M. Salamone, R. Ruffo, M. G. Lobello, F. De Angelis and A. Abbotto, *J. Org. Chem.*, 2012, **77**, 7945-7956.
18. L. Giribabu, V. K. Singh, M. Srinivasu, C. V. Kumar, V. G. Reddy, Y. Soujnya and P. Y. Reddy, *J. Chem. Sci.*, 2011, **123**, 371-378.
19. A. Grabulosa, M. Beley, P. C. Gros, S. Cazzanti, S. Caramori and C. A. Bignozzi, *Inorg. Chem.*, 2009, **48**, 8030-8036.
20. M. Hussain, A. Islam, I. Bedja, R. K. Gupta, L. Han and A. El-Shafei, *Phys. Chem. Chem. Phys.*, 2014, **16**, 14874-14881.
21. H. Kisserwan and T. H. Ghaddar, *Dalton Trans.*, 2011, **40**, 3877-3884.
22. H. Kisserwan, A. Kamar, T. Shoker and T. H. Ghaddar, *Dalton Trans.*, 2012, **41**, 10643-10651.
23. C.-Y. Li, C. Su, H.-H. Wang, P. Kumaresan, C.-H. Hsu, I. T. Lee, W.-C. Chang, Y. S. Tingare, T.-Y. Li, C.-F. Lin and W.-R. Li, *Dyes Pigm.*, 2014, **100**, 57-65.
24. G. Li, K. Hu, C. Yi, K. L. Knappenberger, G. J. Meyer, S. I. Gorelsky and M. Shatruk, *J. Phys. Chem. C*, 2013, **117**, 17399-17411.

25. M. K. Nazeeruddin, P. Pechy, T. Renouard, S. M. Zakeeruddin, R. Humphry-Baker, P. Comte, P. Liska, L. Cevey, E. Costa, V. Shklover, L. Spiccia, G. B. Deacon, C. A. Bignozzi and M. Graetzel, *J. Am. Chem. Soc.*, 2001, **123**, 1613-1624.
26. T. Rawling, C. Austin, F. Buchholz, S. B. Colbran and A. M. McDonagh, *Inorg. Chem.*, 2009, **48**, 3215-3227.
27. T. Rawling, F. Buchholz and A. M. McDonagh, *Aust. J. Chem.*, 2008, **61**, 405-408.
28. T. Swetha, S. Niveditha, K. Bhanuprakash, A. Islam, L. Han, I. M. Bedja, R. Fallahpour and S. P. Singh, *Inorg. Chem. Commun.*, 2015, **51**, 61-65.
29. L. Hu and G. Xu, *Chem. Soc. Rev.*, 2010, **39**, 3275-3304.
30. K. Zeitler, *Angew. Chem. Int. Ed.*, 2009, **48**, 9785-9789.
31. J. M. R. Narayanam and C. R. J. Stephenson, *Chem. Soc. Rev.*, 2011, **40**, 102-113.
32. C. K. Prier, D. A. Rankic and D. W. C. MacMillan, *Chem. Rev.*, 2013, **113**, 5322-5363.
33. J. W. Tucker and C. R. J. Stephenson, *J. Org. Chem.*, 2012, **77**, 1617-1622.
34. H. Xiang, J. Cheng, X. Ma, X. Zhou and J. J. Chruma, *Chem. Soc. Rev.*, 2013, **42**, 6128-6185.
35. W. Wu, S. Ji, W. Wu, H. Guo, X. Wang, J. Zhao and Z. Wang, *Sens. Actuators, B*, 2010, **149**, 395-406.
36. P. D. Beer and P. A. Gale, *Angew. Chem. Int. Ed.*, 2001, **40**, 486-516.
37. Z. Guo and S. Dong, *Anal. Chem.*, 2004, **76**, 2683-2688.
38. F. Frehill, J. G. Vos, S. Benrezzak, A. A. Koos, Z. Konya, M. G. Ruether, W. J. Blau, A. Fonseca, J. B. Nagy, L. P. Biro, A. I. Minett and M. in het Panhuis, *J. Am. Chem. Soc.*, 2002, **124**, 13694-13695.
39. M. Majumder, X. Zhan, R. Andrews and B. J. Hinds, *Langmuir*, 2007, **23**, 8624-8631.
40. M. Abrahamsson, H.-C. Becker, L. Hammarström, C. Bonnefous, C. Chamchoumis and R. P. Thummel, *Inorg. Chem.*, 2007, **46**, 10354-10364.
41. B. Jousselme, G. Bidan, M. Billon, C. Goyer, Y. Kervella, S. Guillerez, E. A. Hamad, C. Goze-Bac, J.-Y. Mevellec and S. Lefrant, *J. Electroanal. Chem.*, 2008, **621**, 277-285.
42. L. Kavan, I. Exnar, J. Cech and M. Graetzel, *Chem. Mater.*, 2007, **19**, 4716-4721.
43. H. T. Shi, L. L. Du, K. C. Lo, W. J. Xiong, W. K. Chan and D. L. Phillips, *J. Phys. Chem. C*, 2017, **121**, 8145-8152.
44. J. Zhao, J. Ma, X. Nan and B. Tang, *Org. Electron.*, 2016, **30**, 52-59.
45. P. Zhang, H. Huang, J. Huang, H. Chen, J. Wang, K. Qiu, D. Zhao, L. Ji and H. Chao, *ACS Appl. Mater. Interfaces*, 2015, **7**, 23278-23290.
46. J. H. Kenten, S. Gudibande, J. Link, J. J. Willey, B. Curfman, E. O. Major and R. J. Massey, *Clin. Chem.*, 1992, **38**, 873-879.
47. D. Saadallah, M. Bellakhal, S. Amor, J.-F. Lefebvre, M. Chavarot-Kerlidou, I. Baussanne, C. Moucheron, M. Demeunynck and D. Monchaud, *Chem. Eur. J.*, 2017, **23**, 4967-4972.
48. O. S. Wolfbeis, M. Bohmer, A. Durkop, J. Enderlein, M. Gruber, I. Klimant, C. Krause, J. Kurner, G. Liebsch, Z. Lin, B. Oswald and M. Wu, *Springer Ser. Fluoresc.*, 2002, **2**, 3-42.
49. J. Zhang, H. Qi, Y. Li, J. Yang, Q. Gao and C. Zhang, *Anal. Chem.*, 2008, **80**, 2888-2894.
50. K. E. Augustyn, E. D. A. Stemp and J. K. Barton, *Inorg. Chem.*, 2007, **46**, 9337-9350.
51. K. D. Copeland, A. M. K. Lueras, E. D. A. Stemp and J. K. Barton, *Biochemistry*, 2002, **41**, 12785-12797.
52. T. Joshi, V. Pierroz, S. Ferrari and G. Gasser, *ChemMedChem*, 2014, **9**, 1419-1427.
53. A. Kienzler, R. Flehr, R. A. Kramer, S. Gehne, M. U. Kumke and W. Bannwarth, *Bioconjugate Chem.*, 2011, **22**, 1852-1863.
54. A. Mamo, A. Aureliano and A. Recca, *Molecules*, 2010, **15**, 1324-1339.
55. D. Ossipov, S. Gohil and J. Chattopadhyaya, *J. Am. Chem. Soc.*, 2002, **124**, 13416-13433.
56. D. Ossipov, P. I. Pradeepkumar, M. Holmer and J. Chattopadhyaya, *J. Am. Chem. Soc.*, 2001, **123**, 3551-3562.
57. Y. Xiong and L.-N. Ji, *Coord. Chem. Rev.*, 1999, **185–186**, 711-733.
58. E. Baggaley, J. A. Weinstein and J. A. G. Williams, *Coord. Chem. Rev.*, 2012, **256**, 1762-1785.
59. M. R. Gill, J. Garcia-Lara, S. J. Foster, C. Smythe, G. Battaglia and J. A. Thomas, *Nat. Chem.*, 2009, **1**, 662-667.

60. F. R. Svensson, M. Abrahamsson, N. Stromberg, A. G. Ewing and P. Lincoln, *J. Phys. Chem. Lett.*, 2011, **2**, 397-401.
61. J. Wen, H. Yan, P. Y. Xia, Y. Q. Xu, H. J. Li and S. G. Sun, *Sci. China Chem.*, 2017, **60**, 799-805.
62. E. K. Beloglazkina, A. G. Majouga, E. A. Manzheliy, A. A. Moiseeva, Y. V. Lin'kova and N. V. Zyk, *Polyhedron*, 2015, **85**, 800-808.
63. L. Blackmore, R. Moriarty, C. Dolan, K. Adamson, R. J. Forster, M. Devocelle and T. E. Keyes, *Chem. Commun.*, 2013, **49**, 2658-2660.
64. L. Cosgrave, M. Devocelle, R. J. Forster and T. E. Keyes, *Chem. Commun.*, 2010, **46**, 103-105.
65. C. Ding, S. Wei and H. Liu, *Chem. Eur. J.*, 2012, **18**, 7263-7268.
66. F. Dosio, B. Stella, A. Ferrero, C. Garino, D. Zonari, S. Arpicco, L. Cattel, S. Giordano and R. Gobetto, *Int. J. Pharm. (Amsterdam, Neth.)*, 2013, **440**, 221-228.
67. K. K. Sadhu, T. Eierhoff, W. Romer and N. Winssinger, *J. Am. Chem. Soc.*, 2012, **134**, 20013-20016.
68. K. Adamson, C. Dolan, N. Moran, R. J. Forster and T. E. Keyes, *Bioconjugate Chem.*, 2014, **25**, 928-944.
69. R. Zhang, Z. Ye, B. Song, Z. Dai, X. An and J. Yuan, *Inorg. Chem.*, 2013, **52**, 10325-10331.
70. R. Zhang, Z. Ye, G. Wang, W. Zhang and J. Yuan, *Chem. Eur. J.*, 2010, **16**, 6884-6891.
71. R. Zhang, Z. Ye, Y. Yin, G. Wang, D. Jin, J. Yuan and J. A. Piper, *Bioconjugate Chem.*, 2012, **23**, 725-733.
72. M. Gottschaldt, U. S. Schubert, S. Rau, S. Yano, J. G. Vos, T. Kroll, J. Clement and I. Hilger, *ChemBioChem*, 2010, **11**, 649-652.
73. E. C. Constable and S. Mundwiler, *Polyhedron*, 1999, **18**, 2433-2444.
74. E. C. Constable, C. E. Housecroft, M. Neuburger and P. Roesel, *Chem. Commun.*, 2010, **46**, 1628-1630.
75. Y. Pellegrin, R. J. Forster and T. E. Keyes, *Inorg. Chim. Acta*, 2008, **361**, 2683-2691.
76. M. Jäger, L. Freitag and L. González, *Coord. Chem. Rev.*, 2015, **304**, 146-165.
77. A. Juris, V. Balzani, F. Barigelletti, S. Campagna, P. Belser and A. von Zelewsky, *Coord. Chem. Rev.*, 1988, **84**, 85-277.
78. S. Campagna, F. Puntoriero, F. Nastasi, G. Bergamini and V. Balzani, in *Photochemistry and Photophysics of Coordination Compounds I*, eds. V. Balzani and S. Campagna, Springer-Verlag Berlin, Berlin, 2007, vol. 280, pp. 117-214.
79. S. Li, C. Liu, B. Han, J. Luo and G. Yin, *Microchim. Acta*, 2017, **184**, 1669-1675.
80. M. Mazloum-Ardakani, M. A. Sheikh-Mohseni and M. Salavati-Niasari, *Electroanalysis*, 2016, **28**, 1370-1376.
81. T. J. Meyer and M. H. V. Huynh, *Inorg. Chem.*, 2003, **42**, 8140-8160.
82. P. P. Laine, S. Campagna and F. Loiseau, *Coord. Chem. Rev.*, 2008, **252**, 2552-2571.
83. M. Falkenstroem, O. Johansson and L. Hammarstroem, *Inorg. Chim. Acta*, 2007, **360**, 741-750.
84. M. H. V. Huynh, D. M. Dattelbaum and T. J. Meyer, *Coord. Chem. Rev.*, 2005, **249**, 457-483.
85. C. N. Fleming, K. A. Maxwell, J. M. DeSimone, T. J. Meyer and J. M. Papanikolas, *J. Am. Chem. Soc.*, 2001, **123**, 10336-10347.
86. J. F. Endicott, M. J. Uddin and H. B. Schlegel, *Res. Chem. Intermed.*, 2002, **28**, 761-777.
87. M. D. Ward and F. Barigelletti, *Coord. Chem. Rev.*, 2001, **216-217**, 127-154.
88. M. D. Ward, *Int. J. Photoenergy*, 1999, **1**, 121-133.
89. A. Carella, C. Coudret, G. Guirado, G. Rapenne, G. Vives and J.-P. Launay, *Dalton Trans.*, 2007, 177-186.
90. H. Ohtsu and K. Tanaka, *Angew. Chem. Int. Ed.*, 2012, **51**, 9792-9795.
91. T. Kojima, T. Sakamoto and Y. Matsuda, *Inorg. Chem.*, 2004, **43**, 2243-2245.
92. M. Presselt, B. Dietzek, M. Schmitt, S. Rau, A. Winter, M. Jäger, U. S. Schubert and J. Popp, *J. Phys. Chem. A*, 2010, **114**, 13163-13174.
93. S. Fantacci and F. De Angelis, *Coord. Chem. Rev.*, 2011, **255**, 2704-2726.
94. C. Daniel, in *Density-Functional Methods for Excited States. Topics in Current Chemistry*, eds. N. Ferre, M. Filatov and M. HuixRotllant, 2016, vol. 368, pp. 377-413.

95. T. B. Demissie, K. Ruud and J. H. Hansen, *Organometallics*, 2015, **34**, 4218-4228.
96. O. S. Odongo, M. J. Heeg, Y.-J. Chen, P. Xie and J. F. Endicott, *Inorg. Chem.*, 2008, **47**, 7493-7511.
97. T. Österman, M. Abrahamsson, H. C. Becker, L. Hammarström and P. Persson, *J. Phys. Chem. A*, 2012, **116**, 1041-1050.
98. A. Breivogel, M. Meister, C. Förster, F. Laquai and K. Heinze, *Chem. Eur. J.*, 2013, **19**, 13745-13760.
99. O. P. J. Vieuxmaire, R. E. Piau, F. Alary, J.-L. Heully, P. Sutra, A. Igau and M. Boggio-Pasqua, *J. Phys. Chem. A*, 2013, **117**, 12821-12830.
100. R. L. Lord, M. M. Allard, R. A. Thomas, O. S. Odongo, H. B. Schlegel, Y.-J. Chen and J. F. Endicott, *Inorg. Chem.*, 2013, **52**, 1185-1198.
101. T. Guillon, M. Boggio-Pasqua, F. Alary, J.-L. Heully, E. Lebon, P. Sutra and A. Igau, *Inorg. Chem.*, 2010, **49**, 8862-8872.
102. T. Österman and P. Persson, *Chem. Phys.*, 2012, **407**, 76-82.
103. A. B. P. Lever, *Coord. Chem. Rev.*, 2010, **254**, 1397-1405.
104. SciFinder, 27.02.2018
105. Y. Tor, *Synlett*, 2002, 1043-1054.
106. A. J. Metherell and M. D. Ward, *RSC Advances*, 2016, **6**, 10750-10762.
107. Q. H. Wei, S. P. Argent, H. Adams and M. D. Ward, *New J. Chem.*, 2008, **32**, 73-82.
108. U. S. Schubert, A. Winter and G. R. Newkome, *Terpyridine-based Materials*, Wiley-VCH-Verlag, Weinheim, 2011.
109. U. S. Schubert, H. Hofmeier and G. R. Newkome, *Modern Terpyridine Chemistry*, Wiley-VCH-Verlag, Weinheim, 2006.
110. O. Johansson and R. Lomoth, *Inorg. Chem.*, 2008, **47**, 5531-5533.
111. Y. Jahng, R. P. Thummel and S. G. Bott, *Inorg. Chem.*, 1997, **36**, 3133-3138.
112. E. Alessio, *Chem. Rev.*, 2004, **104**, 4203-4242.
113. R. Ziessel, V. Grosshenny, M. Hissler and C. Stroh, *Inorg. Chem.*, 2004, **43**, 4262-4271.
114. K. Wada, T. Mizutani and S. Kitagawa, *J. Org. Chem.*, 2003, **68**, 5123-5131.
115. M. A. Abbas, C. D. McMillen and J. L. Brumaghim, *Inorg. Chim. Acta*, 2017, **468**, 308-315.
116. M. Jäger, R. J. Kumar, H. Görls, J. Bergquist and O. Johansson, *Inorg. Chem.*, 2009, **48**, 3228-3238.
117. T. Schlotthauer, B. Suchland, H. Görls, G. A. Parada, L. Hammarström, U. S. Schubert and M. Jäger, *Inorg. Chem.*, 2016, **55**, 5405-5416.
118. M.-P. Santoni, A. K. Pal, G. S. Hanan, A. Proust and B. Hasenknopf, *Inorg. Chem. Commun.*, 2011, **14**, 399-402.
119. C. J. Aspley and J. A. Gareth Williams, *New J. Chem.*, 2001, **25**, 1136-1147.
120. J. P. Byrne, J. A. Kitchen, O. Kotova, V. Leigh, A. P. Bell, J. J. Boland, M. Albrecht and T. Gunnlaugsson, *Dalton Trans.*, 2014, **43**, 196-209.
121. V. Leigh, W. Ghattas, R. Lalrempuia, H. Muller-Bunz, M. T. Pryce and M. Albrecht, *Inorg. Chem.*, 2013, **52**, 5395-5402.
122. B. Schulze and U. S. Schubert, *Chem. Soc. Rev.*, 2014, **43**, 2522-2571.
123. M. L. Stone and G. A. Crosby, *Chem. Phys. Lett.*, 1981, **79**, 169-173.
124. M. Beley, J. P. Collin, J. P. Sauvage, H. Sugihara, F. Heisel and A. Miehe, *J. Chem. Soc., Dalton Trans.*, 1991, 3157-3159.
125. L. Fetzer, B. Boff, M. Ali, M. Xiangjun, J.-P. Collin, C. Sirlin, C. Gaiddon and M. Pfeffer, *Dalton Trans.*, 2011, **40**, 8869-8878.
126. A. M. Clark, C. E. F. Rickard, W. R. Roper and L. J. Wright, *Organometallics*, 1999, **18**, 2813-2820.
127. S. Despax, F. Jia, M. Pfeffer and P. Hebraud, *Phys. Chem. Chem. Phys.*, 2014, **16**, 10491-10502.
128. C. Friebe, B. Schulze, H. Görls, M. Jäger and U. S. Schubert, *Chem. Eur. J.*, 2014, **20**, 2357-2366.

129. S. H. Wadman, R. W. A. Havenith, M. Lutz, A. L. Spek, G. P. M. van Klink and G. van Koten, *J. Am. Chem. Soc.*, 2010, **132**, 1914-1924.
130. C. Coudret and S. Fraysse, *Chem. Commun.*, 1998, 663-664.
131. Z. Ji, M. He, Z. Huang, U. Ozkan and Y. Wu, *J. Am. Chem. Soc.*, 2013, **135**, 11696-11699.
132. Z. Ye, B. Song, Y. Yin, R. Zhang and J. Yuan, *Dalton Trans.*, 2013, **42**, 14380-14383.
133. Z. Ji and Y. Wu, *J. Phys. Chem. C*, 2013, **117**, 18315-18324.
134. B. Matt, C. Coudret, C. Viala, D. Jouvenot, F. Loiseau, G. Izzet and A. Proust, *Inorg. Chem.*, 2011, **50**, 7761-7768.
135. V. L. Whittle and J. A. G. Williams, *Dalton Trans.*, 2009, 3929-3940.
136. P. G. Potvin, P. U. Luyen and J. Bräckow, *J. Am. Chem. Soc.*, 2003, **125**, 4894-4906.
137. J.-Y. Shao, N. Fu, W.-W. Yang, C.-Y. Zhang, Y.-W. Zhong, Y. Lin and J. Yao, *RSC Adv.*, 2015, **5**, 90001-90009.
138. S. Soman, Y. Xie and T. W. Hamann, *Polyhedron*, 2014, **82**, 139-147.
139. A. Grabulosa, M. Beley and P. C. Gros, *Eur. J. Inorg. Chem.*, 2008, 1747-1751.
140. C. Kreitner, A. K. C. Mengel, T. K. Lee, W. Cho, K. Char, Y. S. Kang and K. Heinze, *Chem. Eur. J.*, 2016, **22**, 8915-8928.
141. T. Kono, N. Masaki, M. Nishikawa, R. Tamura, H. Matsuzaki, M. Kimura and S. Mori, *ACS Appl. Mater. Interfaces*, 2016, **8**, 16677-16683.
142. H. Zabri, I. Gillaizeau, C. A. Bignozzi, S. Caramori, M.-F. Charlot, J. Cano-Boquera and F. Odobel, *Inorg. Chem.*, 2003, **42**, 6655-6666.
143. M. R. Norris, J. J. Concepcion, C. R. K. Glasson, Z. Fang, A. M. Lapides, D. L. Ashford, J. L. Templeton and T. J. Meyer, *Inorg. Chem.*, 2013, **52**, 12492-12501.
144. H. Wolpher, S. Sinha, J. Pan, A. Johansson, M. J. Lundqvist, P. Persson, R. Lomoth, J. Bergquist, L. Sun, V. Sundstroem, B. Akermark and T. Polivka, *Inorg. Chem.*, 2007, **46**, 638-651.
145. E. C. Constable, P. Harverson, C. E. Housecroft, E. Nordlander and J. Olsson, *Polyhedron*, 2006, **25**, 437-458.
146. C. J. Wood, K. C. D. Robson, P. I. P. Elliott, C. P. Berlinguette and E. A. Gibson, *RSC Adv.*, 2014, **4**, 5782-5791.
147. C. E. McCusker and J. K. McCusker, *Inorg. Chem.*, 2011, **50**, 1656-1669.
148. J. Wang, Y.-Q. Fang, G. S. Hanan, F. Loiseau and S. Campagna, *Inorg. Chem.*, 2005, **44**, 5-7.
149. T. E. Barder, S. D. Walker, J. R. Martinelli and S. L. Buchwald, *J. Am. Chem. Soc.*, 2005, **127**, 4685-4696.
150. T. Hatakeyama, S. Hashimoto, K. Ishizuka and M. Nakamura, *J. Am. Chem. Soc.*, 2009, **131**, 11949-11963.
151. E. A. B. Kantchev, C. J. O'Brien and M. G. Organ, *Angew. Chem. Int. Ed.*, 2007, **46**, 2768-2813.
152. C. Valente, S. Calimsiz, K. H. Hoi, D. Mallik, M. Sayah and M. G. Organ, *Angew. Chem. Int. Ed.*, 2012, **51**, 3314-3332.
153. D. Astruc, *Inorg. Chem.*, 2007, **46**, 1884-1894.
154. A. Dhakshinamoorthy, A. M. Asiri and H. Garcia, *Chem. Soc. Rev.*, 2015, **44**, 1922-1947.
155. S. H. Cho, J. Y. Kim, J. Kwak and S. Chang, *Chem. Soc. Rev.*, 2011, **40**, 5068-5083.
156. A. C. Frisch and M. Beller, *Angew. Chem. Int. Ed.*, 2005, **44**, 674-688.
157. H. B. Li, C. Seechurn and T. J. Colacot, *ACS Catalysis*, 2012, **2**, 1147-1164.
158. C. Seechurn, M. O. Kitching, T. J. Colacot and V. Snieckus, *Angew. Chem. Int. Ed.*, 2012, **51**, 5062-5085.
159. S. Kotha, K. Lahiri and D. Kashinath, *Tetrahedron*, 2002, **58**, 9633-9695.
160. A. F. Littke, C. Y. Dai and G. C. Fu, *J. Am. Chem. Soc.*, 2000, **122**, 4020-4028.
161. N. T. S. Phan, M. Van Der Sluys and C. W. Jones, *Adv. Synth. Catal.*, 2006, **348**, 609-679.
162. R. Chinchilla and C. Najera, *Chem. Rev.*, 2007, **107**, 874-922.
163. R. Chinchilla and C. Najera, *Chem. Soc. Rev.*, 2011, **40**, 5084-5121.
164. P. Espinet and A. M. Echavarren, *Angew. Chem. Int. Ed.*, 2004, **43**, 4704-4734.
165. V. Balzani, A. Juris, M. Venturi, S. Campagna and S. Serroni, *Chem. Rev.*, 1996, **96**, 759-834.
166. A. Borje, O. Kothe and A. Juris, *New J. Chem.*, 2001, **25**, 191-193.

167. E. C. Constable and P. Harverson, *Polyhedron*, 1999, **18**, 1891-1901.
168. E. C. Constable, C. E. Housecroft, M. Neuburger, I. Poleschak and M. Zehnder, *Polyhedron*, 2003, **22**, 93-108.
169. J. Otsuki, A. Imai, K. Sato, D.-M. Li, M. Hosoda, M. Owa, T. Akasaka, I. Yoshikawa, K. Araki, T. Suenobu and S. Fukuzumi, *Chem. Eur. J.*, 2008, **14**, 2709-2718.
170. I. Eryazici and G. R. Newkome, *New J. Chem.*, 2009, **33**, 345-357.
171. S. Li, C. N. Moorefield, C. D. Shreiner, P.-S. Wang, R. Sarkar and G. R. Newkome, *New J. Chem.*, 2011, **35**, 2130-2135.
172. D. N. Lee, B. K. Soh, S. H. Kim, Y. M. Jun, S. H. Yoon, W.-Y. Lee and B. H. Kim, *J. Organomet. Chem.*, 2008, **693**, 655-666.
173. Y. Zhang, E. Galoppini, P. G. Johansson and G. J. Meyer, *Pure Appl. Chem.*, 2011, **83**, 861-868.
174. P. G. Johansson, Y. Zhang, M. Abrahamsson, G. J. Meyer and E. Galoppini, *Chem. Commun.*, 2011, **47**, 6410-6412.
175. P. G. Johansson, Y. Zhang, G. J. Meyer and E. Galoppini, *Inorg. Chem.*, 2013, **52**, 7947-7957.
176. K. P. Chitre, E. Guillén, A. S. Yoon and E. Galoppini, *Eur. J. Inorg. Chem.*, 2012, 5461-5464.
177. M. Braumueller, M. Schulz, M. Staniszewska, D. Sorsche, M. Wunderlin, J. Popp, J. Guthmuller, B. Dietzek and S. Rau, *Dalton Trans.*, 2016, **45**, 9216-9228.
178. G. Zhou, J. He and I. I. Harruna, *J. Polym. Sci., Part A: Polym. Chem.*, 2007, **45**, 4225-4239.
179. G. Zhou, J. He and I. I. Harruna, *J. Polym. Sci., Part A: Polym. Chem.*, 2007, **45**, 4204-4210.
180. L. Viau, M. Even, O. Maury, D. M. Haddleton and H. Le Bozec, *C. R. Chim.*, 2005, **8**, 1298-1307.
181. X. Wu, J. E. Collins, J. E. McAlvin, R. W. Cutts and C. L. Fraser, *Macromolecules*, 2001, **34**, 2812-2821.
182. L. H. Uppadine, F. R. Keene and P. D. Beer, *J. Chem. Soc., Dalton Trans.*, 2001, 2188-2198.
183. M. S. Vickers, K. S. Martindale and P. D. Beer, *J. Mater. Chem.*, 2005, **15**, 2784-2790.
184. G.-F. Gui, Y. Zhuo, Y.-Q. Chai, Y. Xiang and R. Yuan, *Anal. Chem.*, 2014, **86**, 5873-5880.
185. T. Joshi, G. J. Barbante, P. S. Francis, C. F. Hogan, A. M. Bond, G. Gasser and L. Spiccia, *Inorg. Chem.*, 2012, **51**, 3302-3315.
186. K. J. Oh, K. J. Cash, V. Hugenberg and K. W. Plaxco, *Bioconjugate Chem.*, 2007, **18**, 607-609.
187. M. Somik, R. Balavinayagam, G. Lauren, H. Steven, A. B. Gary, F. Phil, S. Shramik and G. Shubhra, *Nanotechnology*, 2012, **23**, 485405.
188. C. P. Myers, B. P. Gilmartin and M. E. Williams, *Inorg. Chem.*, 2008, **47**, 6738-6747.
189. A. Myari, N. Hadjiliadis and A. Garoufis, *Eur. J. Inorg. Chem.*, 2004, 1427-1439.
190. A. Ghosh, C. J. Buettner, A. A. Manos, A. J. Wallace, M. F. Tweedle and J. E. Goldberger, *Biomacromolecules*, 2014, **15**, 4488-4494.
191. K. S. Schanze and K. Sauer, *J. Am. Chem. Soc.*, 1988, **110**, 1180-1186.
192. K. Ypsilantis, S. Karkabounas, E. Georgiou, I. Zelovitis and A. Garoufis, *Inorg. Chim. Acta*, 2014, **421**, 152-159.
193. B. Chen and H. F. Sleiman, *Macromolecules*, 2004, **37**, 5866-5872.
194. Y. Lu, *Photochem. Photobiol. Sci.*, 2010, **9**, 392-397.
195. L. z. Borg, A. L. Domanski, A. Breivogel, M. Burger, R. Berger, K. Heinze and R. Zentel, *J. Mater. Chem. C*, 2013, **1**, 1223-1230.
196. K. A. Aamer, W. H. de Jeu and G. N. Tew, *Macromolecules*, 2008, **41**, 2022-2029.
197. G. D. Smith, K. A. Maxwell, J. M. DeSimone, T. J. Meyer and R. A. Palmer, *Inorg. Chem.*, 2000, **39**, 893-898.
198. T. Kajita, R. M. Leasure, M. Devenney, D. Friesen and T. J. Meyer, *Inorg. Chem.*, 1998, **37**, 4782-4794.
199. G. Ajayakumar, M. Kobayashi, S. Masaoka and K. Sakai, *Dalton Trans.*, 2011, **40**, 3955-3966.
200. D. L. Ashford, W. Song, J. J. Concepcion, C. R. K. Glasson, M. K. Brennaman, M. R. Norris, Z. Fang, J. L. Templeton and T. J. Meyer, *J. Am. Chem. Soc.*, 2012, **134**, 19189-19198.
201. D. L. Ashford, D. J. Stewart, C. R. Glasson, R. A. Binstead, D. P. Harrison, M. R. Norris, J. J. Concepcion, Z. Fang, J. L. Templeton and T. J. Meyer, *Inorg. Chem.*, 2012, **51**, 6428-6430.
202. J. Dietrich, U. Thorenz, C. Foerster and K. Heinze, *Inorg. Chem.*, 2013, **52**, 1248-1264.
203. B. Geisser and R. Alsfasser, *Inorg. Chim. Acta*, 2003, **344**, 102-108.

204. R. J. Holbrook, D. J. Weinberg, M. D. Peterson, E. A. Weiss and T. J. Meade, *J. Am. Chem. Soc.*, 2015, **137**, 3379-3385.
205. C. Kreitner, M. Grabolle, U. Resch-Genger and K. Heinze, *Inorg. Chem.*, 2014, **53**, 12947-12961.
206. H. Ozawa, M. Haga and K. Sakai, *J. Am. Chem. Soc.*, 2006, **128**, 4926-4927.
207. H. Ozawa, Y. Yokoyama, M.-a. Haga and K. Sakai, *Dalton Trans.*, 2007, 1197-1206.
208. S. J. A. Pope, B. J. Coe, S. Faulkner and R. H. Laye, *Dalton Trans.*, 2005, 1482-1490.
209. K. Heinze and K. Hempel, *Chem. Eur. J.*, 2009, **15**, 1346-1358.
210. C. H. Song, Z. Q. Ye, G. L. Wang, D. Y. Jin, J. L. Yuan, Y. F. Guan and J. Piper, *Talanta*, 2009, **79**, 103-108.
211. J. Dietrich, A. Wuensche von Leupoldt, M. Grabolle, U. Resch-Genger and K. Heinze, *Eur. J. Inorg. Chem.*, 2013, 3009-3019.
212. R. Gobetto, G. Caputo, C. Garino, S. Ghiani, C. Nervi, L. Salassa, E. Rosenberg, J. B. A. Ross, G. Viscardi, G. Martra, I. Miletto and M. Milanesio, *Eur. J. Inorg. Chem.*, 2006, 2839-2849.
213. C. M. Hartshorn, K. A. Maxwell, P. S. White, J. M. DeSimone and T. J. Meyer, *Inorg. Chem.*, 2001, **40**, 601-606.
214. J. Lee, D. G. Udugamasooriya, H.-S. Lim and T. Kodadek, *Nat. Chem. Biol.*, 2010, **6**, 258-260.
215. S. L. Mecklenburg, B. M. Peek, J. R. Schoonover, D. G. McCafferty, C. G. Wall, B. W. Erickson and T. J. Meyer, *J. Am. Chem. Soc.*, 1993, **115**, 5479-5495.
216. M. Staffilani, E. Hoess, U. Giesen, E. Schneider, F. Hartl, H.-P. Josel and L. De Cola, *Inorg. Chem.*, 2003, **42**, 7789-7798.
217. D. R. Striplin, S. Y. Reece, D. G. McCafferty, C. G. Wall, D. A. Friesen, B. W. Erickson and T. J. Meyer, *J. Am. Chem. Soc.*, 2004, **126**, 5282-5291.
218. M. C. Uzagare, I. Claussnitzer, M. Gerrits and W. Bannwarth, *Org. Biomol. Chem.*, 2012, **10**, 2223-2226.
219. D. Hvasanov, A. F. Mason, D. C. Goldstein, M. Bhadbhade and P. Thordarson, *Org. Biomol. Chem.*, 2013, **11**, 4602-4612.
220. D. Hvasanov, E. V. Nam, J. R. Peterson, D. Pornsaksit, J. Wiedenmann, C. P. Marquis and P. Thordarson, *J. Org. Chem.*, 2014, **79**, 9594-9602.
221. C. A. Puckett and J. K. Barton, *Bioorg. Med. Chem.*, 2010, **18**, 3564-3569.
222. G. Abbott, R. Brooks, E. Rosenberg, M. Terwilliger, J. B. A. Ross and O. O. L. Ichire, *Organometallics*, 2014, **33**, 2467-2478.
223. D. A. Friesen, T. Kajita, E. Danielson and T. J. Meyer, *Inorg. Chem.*, 1998, **37**, 2756-2762.
224. Z. Fang, A. Ito, S. Keinan, Z. Chen, Z. Watson, J. Rochette, Y. Kanai, D. Taylor, K. S. Schanze and T. J. Meyer, *Inorg. Chem.*, 2013, **52**, 8511-8520.
225. K. Heinze, K. Hempel and M. Beckmann, *Eur. J. Inorg. Chem.*, 2006, 2040-2050.
226. C. Kreitner and K. Heinze, *Dalton Trans.*, 2016, **45**, 5640-5658.
227. T. Okamura, T. Iwamura, S. Seno, H. Yamamoto and N. Ueyama, *J. Am. Chem. Soc.*, 2004, **126**, 15972-15973.
228. K. Heinze, M. Beckmann and K. Hempel, *Chem. Eur. J.*, 2008, **14**, 9468-9480.
229. K. Heinze, K. Hempel, S. Tschierlei, M. Schmitt, J. Popp and S. Rau, *Eur. J. Inorg. Chem.*, 2009, 3119-3126.
230. Y. Gao, J. Liu, W. Jiang, M. Xia, W. Zhang, M. Li, B. Akermark and L. Sun, *J. Porphyrins Phthalocyanines*, 2007, **11**, 463-469.
231. A. Johansson, M. Abrahamsson, A. Magnuson, P. Huang, J. Martensson, S. Styring, L. Hammarstrom, L. C. Sun and B. Akermark, *Inorg. Chem.*, 2003, **42**, 7502-7511.
232. D. Chang, E. Lindberg and N. Winssinger, *J. Am. Chem. Soc.*, 2017, **139**, 1444-1447.
233. E. Du, X. Hu, S. Roy, P. Wang, K. Deasy, T. Mochizuki and Y. Zhang, *Chem. Commun.*, 2017, **53**, 6033-6036.
234. M. Miyaji, K. Kitamoto, H. Ozawa and K. Sakai, *Eur. J. Inorg. Chem.*, 2017, **2017**, 1237-1244.
235. Y. Qi, J. Tang, P. He and F. Yang, *Inorg. Chem. Commun.*, 2016, **70**, 22-26.
236. V. Sartor, J. Irvoas, G. Bordeau and N. Chouini-Lalanne, *Eur. J. Inorg. Chem.*, 2017, **2017**, 2661-2670.

237. A. Schmidt, M. Hollering, J. Han, A. Casini and F. E. Kuehn, *Dalton Trans.*, 2016, **45**, 12297-12300.
238. H. Wang, Y. Yuan, Y. Zhuo, Y. Chai and R. Yuan, *Anal. Chem.*, 2016, **88**, 2258-2265.
239. S. Zanarini, E. Rampazzo, D. Bich, R. Canteri, L. Della Ciana, M. Marcaccio, E. Marzocchi, M. Montalti, C. Panciatichi, C. Pederzolli, F. Paolucci, L. Prodi and L. Vanzetti, *J. Phys. Chem. C*, 2008, **112**, 2949-2957.
240. H. Li, J. Wu, Y. Jeilani, C. Ingram and I. Harruna, *J. Nanopart. Res.*, 2012, **14**, 1-14.
241. N. C. Fletcher, R. T. Brown and A. P. Doherty, *Inorg. Chem.*, 2006, **45**, 6132-6134.
242. M. Schulze, M. Jäger and U. S. Schubert, *Macromol. Rapid Commun.*, 2012, **33**, 579-584.
243. Y. Zhu, C. Gu, S. Tang, T. Fei, X. Gu, H. Wang, Z. Wang, F. Wang, D. Lu and Y. Ma, *J. Mater. Chem.*, 2009, **19**, 3941-3949.
244. J. L. Bourdelande, J. Font, G. Marquès and M. Valiente, *J. Photochem. Photobiol. A: Chem.*, 1996, **95**, 235-238.
245. J. L. Bourdelande, J. Font, G. Marques, A. A. Abdel-Shafi, F. Wilkinson and D. R. Worrall, *J. Photochem. Photobiol. A: Chem.*, 2001, **138**, 65-68.
246. L. Sun, M. Burkitt, M. Tamm, M. K. Raymond, M. Abrahamsson, D. LeGourriérec, Y. Frapart, A. Magnuson, P. H. Kenéz, P. Brandt, A. Tran, L. Hammarström, S. Styring and B. Åkermark, *J. Am. Chem. Soc.*, 1999, **121**, 6834-6842.
247. L. Sun, M. K. Raymond, A. Magnuson, D. LeGourriérec, M. Tamm, M. Abrahamsson, P. Huang Kenéz, J. Mårtensson, G. Stenhagen, L. Hammarström, S. Styring and B. Åkermark, *J. Inorg. Biochem.*, 2000, **78**, 15-22.
248. E. A. Karlsson, B.-L. Lee, R.-Z. Liao, T. Akermark, M. D. Karkas, V. S. Becerril, P. E. M. Siegbahn, X. Zou, M. Abrahamsson and B. Akermark, *ChemPlusChem*, 2014, **79**, 936-950.
249. C. Herrero, A. Quaranta, R.-A. Fallahpour, W. Leibl and A. Aukauloo, *J. Phys. Chem. C*, 2013, **117**, 9605-9612.
250. J. Bolger, A. Gourdon, E. Ishow and J.-P. Launay, *J. Chem. Soc., Chem. Commun.*, 1995, 1799-1800.
251. M. Karnahl, S. Tschierlei, C. Kuhnt, B. Dietzek, M. Schmitt, J. Popp, M. Schwalbe, S. Krieck, H. Gorls, F. W. Heinemann and S. Rau, *Dalton Trans.*, 2010, **39**, 2359-2370.
252. F. L. Huber, D. Nauroozi, A. K. Mengele and S. Rau, *Eur. J. Inorg. Chem.*, 2017, 4020-4027.
253. B. Bozic-Weber, E. C. Constable, E. Figgemeier, C. E. Housecroft and W. Kylberg, *Energy Environ. Sci.*, 2009, **2**, 299-305.
254. E. C. Constable, R. W. Handel, C. E. Housecroft, A. F. Morales, B. Ventura, L. Flamigni and F. Barigelletti, *Chem. Eur. J.*, 2005, **11**, 4024-4034.
255. S. Liatard, J. Chauvin, F. Balestro, D. Jouvenot, F. Loiseau and A. Deronzier, *Langmuir*, 2012, **28**, 10916-10924.
256. K. E. Berg, A. Tran, M. K. Raymond, M. Abrahamsson, J. Wolny, S. Redon, M. Andersson, L. C. Sun, S. Styring, L. Hammarstrom, H. Toftlund and B. Akermark, *Eur. J. Inorg. Chem.*, 2001, 1019-1029.
257. P. K. Poddutoori, P. Poddutoori and B. G. Maiya, *J. Porphyrins Phthalocyanines*, 2006, **10**, 1049-1060.
258. R. Schroot, T. Schlotthauer, U. S. Schubert and M. Jaeger, *Macromolecules*, 2016, **49**, 2112-2123.
259. J. Kuebel, R. Schroot, M. Waechtler, U. S. Schubert, B. Dietzek and M. Jaeger, *J. Phys. Chem. C*, 2015, **119**, 4742-4751.
260. R. Schroot, C. Friebe, E. Altuntas, S. Crotty, M. Jaeger and U. S. Schubert, *Macromolecules*, 2013, **46**, 2039-2048.
261. T. Schlotthauer, R. Schroot, S. Glover, L. Hammarstrom, M. Jaeger and U. S. Schubert, *Phys. Chem. Chem. Phys.*, 2017, **19**, 28572-28578.
262. R. Schroot, T. Schlotthauer, B. Dietzek, M. Jager and U. S. Schubert, *Chem. Eur. J.*, 2017, **23**, 16484-16490.
263. R. Schroot, T. Schlotthauer, M. Jager and U. S. Schubert, *Macromol. Chem. Phys.*, 2017, **218**, 1600534.

264. J. C. Loren, P. Gantzel, A. Linden and J. S. Siegel, *Org. Biomol. Chem.*, 2005, **3**, 3105-3116.
265. L. E. Hansen, E. R. Glowacki, D. L. Arnold, G. J. Bernt, B. Chi, R. J. Fites, R. A. Freeburg, R. F. N. Rothschild, M. C. Krieg, W. A. Howard and J. M. Tanski, *Inorg. Chim. Acta*, 2003, **348**, 91-96.
266. Z.-L. Gong, B.-B. Cui, W.-W. Yang, J. Yao and Y.-W. Zhong, *Electrochim. Acta*, 2014, **130**, 748-753.
267. N. Baumann, P. S. Gamage, T. N. Samarakoon, J. Hodgson, J. Janek and S. H. Bossmann, *J. Phys. Chem. C*, 2010, **114**, 22763-22772.
268. A. Wild, A. Winter, M. D. Hager, H. Görls and U. S. Schubert, *Macromol. Rapid Commun.*, 2012, **33**, 517-521.
269. D. J. Hurley and Y. Tor, *Tetrahedron Lett.*, 2001, **42**, 7217-7220.
270. D. Tzalis and Y. Tor, *Angew. Chem. Int. Ed.*, 1997, **36**, 2666-2668.
271. J. C. Loren, M. Yoshizawa, R. F. Haldimann, A. Linden and J. S. Siegel, *Angew. Chem. Int. Ed.*, 2003, **42**, 5702-5705.
272. A. B. Ducrot, B. A. Coulson, R. N. Perutz and A.-K. Duhme-Klair, *Inorg. Chem.*, 2016, **55**, 12583-12594.
273. Z. Fang, A. Ito, H. Luo, D. L. Ashford, J. J. Concepcion, L. Alibabaei and T. J. Meyer, *Dalton Trans.*, 2015, **44**, 8640-8648.
274. H. T. Uyeda, Y. Zhao, K. Wostyn, I. Asselberghs, K. Clays, A. Persoons and M. J. Therien, *J. Am. Chem. Soc.*, 2002, **124**, 13806-13813.
275. M. Schmittel, Q. Shu and M. E. Cinar, *Dalton Trans.*, 2012, **41**, 6064-6068.
276. S. Fraysse, C. Coudret and J.-P. Launay, *J. Am. Chem. Soc.*, 2003, **125**, 5880-5888.
277. S. Fraysse, C. Coudret and J.-P. Launay, *Eur. J. Inorg. Chem.*, 2000, 1581-1590.
278. S. Fraysse, C. Coudret and J.-P. Launay, *Tetrahedron Lett.*, 1998, **39**, 7873-7876.
279. T. V. Duncan, K. Song, S.-T. Hung, I. Miloradovic, A. Nayak, A. Persoons, T. Verbiest, M. J. Therien and K. Clays, *Angew. Chem. Int. Ed.*, 2008, **47**, 2978-2981.
280. T. V. Duncan, T. Ishizuka and M. J. Therien, *J. Am. Chem. Soc.*, 2007, **129**, 9691-9703.
281. F. Dumur, C. R. Mayer, E. Dumas, J. Marrot and F. Secheresse, *Tetrahedron Lett.*, 2007, **48**, 4143-4146.
282. R. Ziessel and C. Stroh, *Tetrahedron Lett.*, 2004, **45**, 4051-4055.
283. N. Vila, Y.-W. Zhong, J. C. Henderson and H. D. Abruna, *Inorg. Chem.*, 2010, **49**, 796-804.
284. S. Goeb, A. De Nicola and R. Ziessel, *J. Org. Chem.*, 2005, **70**, 6802-6808.
285. G. J. Jin, G. Chen, J. L. Xia, J. Yin, G.-A. Yu and S. H. Liu, *Transition Met. Chem.*, 2011, **36**, 611-615.
286. T. Ishizuka, L. E. Sinks, K. Song, S.-T. Hung, A. Nayak, K. Clays and M. J. Therien, *J. Am. Chem. Soc.*, 2011, **133**, 2884-2896.
287. A. Harriman, A. Mayeux, C. Stroh and R. Ziessel, *Dalton Trans.*, 2005, 2925-2932.
288. A. C. Benniston, A. Harriman, P. Li and C. A. Sams, *J. Am. Chem. Soc.*, 2005, **127**, 2553-2564.
289. A. C. Benniston, A. Harriman, P. Li, P. V. Patel and C. A. Sams, *J. Org. Chem.*, 2006, **71**, 3481-3493.
290. A. C. Benniston, A. Harriman, P. Li, P. V. Patel, J. P. Rostron and C. A. Sams, *J. Phys. Chem. A*, 2006, **110**, 9880-9886.
291. N. Leventis, A.-M. M. Rawashdeh, I. A. Elder, J. Yang, A. Dass and C. Sotiriou-Leventis, *Chem. Mater.*, 2004, **16**, 1493-1506.
292. J.-P. Launay, C. Coudret and C. Hortholary, *J. Phys. Chem. B*, 2007, **111**, 6788-6797.
293. D. J. Hurley and Y. Tor, *J. Am. Chem. Soc.*, 2002, **124**, 3749-3762.
294. C. Hortholary and C. Coudret, *J. Org. Chem.*, 2003, **68**, 2167-2174.
295. C. Goze, D. V. Kozlov, D. S. Tyson, R. Ziessel and F. N. Castellano, *New J. Chem.*, 2003, **27**, 1679-1683.
296. C. Goze, D. V. Kozlov, F. N. Castellano, J. Suffert and R. Ziessel, *Tetrahedron Lett.*, 2003, **44**, 8713-8716.
297. J. Yang, J. K. Clegg, Q. Jiang, X. Lui, H. Yan, W. Zhong and J. E. Beves, *Dalton Trans.*, 2013, **42**, 15625-15636.

298. M. Vrabel, R. Pohl, I. Votruba, M. Sajadi, S. A. Kovalenko, N. P. Ernsting and M. Hocek, *Org. Biomol. Chem.*, 2008, **6**, 2852-2860.
299. M. Vrabel, R. Pohl, B. Klepetarova, I. Votruba and M. Hocek, *Org. Biomol. Chem.*, 2007, **5**, 2849-2857.
300. E. Sakuda, C. Matsumoto, Y. Ando, A. Ito, K. Mochida, A. Nakagawa and N. Kitamura, *Inorg. Chem.*, 2015, **54**, 3245-3252.
301. S. Ramachandra, K. C. Schuermann, F. Edafe, P. Belser, C. A. Nijhuis, W. F. Reus, G. M. Whitesides and L. De Cola, *Inorg. Chem.*, 2011, **50**, 1581-1591.
302. E. Sakuda, Y. Ando, A. Ito and N. Kitamura, *Inorg. Chem.*, 2011, **50**, 1603-1613.
303. D. V. Kozlov, D. S. Tyson, C. Goze, R. Ziessel and F. N. Castellano, *Inorg. Chem.*, 2004, **43**, 6083-6092.
304. S. Ji, W. Wu, W. Wu, P. Song, K. Han, Z. Wang, S. Liu, H. Guo and J. Zhao, *J. Mater. Chem.*, 2010, **20**, 1953-1963.
305. A. Harriman, G. Izzet, S. Goeb, A. De Nicola and R. Ziessel, *Inorg. Chem.*, 2006, **45**, 9729-9741.
306. C. Goze, C. Sabatini, A. Barbieri, F. Barigelletti and R. Ziessel, *Inorg. Chem.*, 2007, **46**, 7341-7350.
307. C. Goze, C. Sabatini, A. Barbieri, F. Barigelletti and R. Ziessel, *Eur. J. Inorg. Chem.*, 2008, 1293-1299.
308. E. C. Glazer, D. Magde and Y. Tor, *J. Am. Chem. Soc.*, 2007, **129**, 8544-8551.
309. C. Goze, S.-X. Liu, C. Leiggener, L. Sanguinet, E. Levillain, A. Hauser and S. Decurtins, *Tetrahedron*, 2008, **64**, 1345-1350.
310. E. C. Constable, E. Figgemeier, C. E. Housecroft, S. L. Kokatam, E. A. Medlycott, M. Neuburger, S. Schaffner and J. A. Zampese, *Dalton Trans.*, 2008, 6752-6762.
311. F. Chaignon, F. Buchet, E. Blart, M. Falkenstroem, L. Hammarstroem and F. Odobel, *New J. Chem.*, 2009, **33**, 408-416.
312. A. M. Breul, J. Schaefer, C. Friebe, F. Schluetter, R. M. Paulus, G. Festag, M. D. Hager, A. Winter, B. Dietzek, J. Popp and U. S. Schubert, *Macromol. Chem. Phys.*, 2012, **213**, 808-819.
313. A. Baker, J. Jaud, J.-P. Launay and J. Bonvoisin, *Inorg. Chim. Acta*, 2005, **358**, 3513-3518.
314. P. Farras, H. Waller and A. C. Benniston, *Chem. Eur. J.*, 2016, **22**, 1133-1140.
315. A. Nayak, J. Park, K. De Mey, X. Hu, T. V. Duncan, D. N. Beratan, K. Clays and M. J. Therien, *ACS Cent. Sci.*, 2016, **2**, 954-966.
316. J. Wang, Y. Lu, N. McGoldrick, C. Zhang, W. Yang, J. Zhao and S. M. Draper, *J. Mater. Chem. C*, 2016, **4**, 6131-6139.
317. Y.-W. Zhong, N. Vila, J. C. Henderson, S. Flores-Torres and H. D. Abruna, *Inorg. Chem.*, 2007, **46**, 10470-10472.
318. K. J. Arm and J. A. G. Williams, *Dalton Trans.*, 2006, 2172-2174.
319. K. J. Arm and J. A. Williams, *Chem. Commun.*, 2005, 230-232.
320. S. Welter, N. Salluce, A. Benetti, N. Rot, P. Belser, P. Sonar, A. C. Grimsdale, K. Muellen, M. Lutz, A. L. Spek and L. De Cola, *Inorg. Chem.*, 2005, **44**, 4706-4718.
321. M. T. Indelli, C. Chiorboli, L. Flamigni, L. De Cola and F. Scandola, *Inorg. Chem.*, 2007, **46**, 5630-5641.
322. X. Lu, X. Li, K. Guo, T.-Z. Xie, C. N. Moorefield, C. Wesdemiotis and G. R. Newkome, *J. Am. Chem. Soc.*, 2014, **136**, 18149-18155.
323. R. Passalacqua, F. Loiseau, S. Campagna, Y.-Q. Fang and G. S. Hanan, *Angew. Chem. Int. Ed.*, 2003, **42**, 1608-1611.
324. J. Wang, Y.-Q. Fang, L. Bourget-Merle, M. I. J. Polson, G. S. Hanan, A. Juris, F. Loiseau and S. Campagna, *Chem. Eur. J.*, 2006, **12**, 8539-8548.
325. B. Schaefer, H. Goerls, M. Presselt, M. Schmitt, J. Popp, W. Henry, J. G. Vos and S. Rau, *Dalton Trans.*, 2006, 2225-2231.
326. K. C. D. Robson, B. D. Koivisto and C. P. Berlinguette, *Inorg. Chem.*, 2012, **51**, 1501-1507.
327. S. S. R. Muise, H. A. Severin, B. D. Koivisto, K. C. D. Robson, E. Schott and C. P. Berlinguette, *Organometallics*, 2011, **30**, 6628-6635.
328. E. A. Medlycott, G. S. Hanan, F. Loiseau and S. Campagna, *Chem. Eur. J.*, 2007, **13**, 2837-2846.

329. Z. Ji, G. Natu, Z. Huang, O. Kokhan, X. Zhang and Y. Wu, *J. Phys. Chem. C*, 2012, **116**, 16854-16863.
330. M. Jaeger, R. J. Kumar, H. Goerls, J. Bergquist and O. Johansson, *Inorg. Chem.*, 2009, **48**, 3228-3238.
331. A. Inagaki, H. Nakagawa, M. Akita, K. Inoue, M. Sakai and M. Fujii, *Dalton Trans.*, 2008, 6709-6723.
332. C. Friebe, H. Goerls, M. Jaeger and U. S. Schubert, *Eur. J. Inorg. Chem.*, 2013, 4191-4202.
333. E. Coronado, P. Gavina, S. Tatay, R. Groarke and J. G. Vos, *Inorg. Chem.*, 2010, **49**, 6897-6903.
334. O. Bossart, L. De Cola, S. Welter and G. Calzaferri, *Chem. Eur. J.*, 2004, **10**, 5771-5775.
335. F. Brunner, N. Marinakis, C. Wobill, M. Willgert, C. D. Ertl, T. Kosmalski, M. Neuburger, B. Bozic-Weber, T. Glatzel, E. C. Constable and C. E. Housecroft, *J. Mater. Chem. C*, 2016, **4**, 9823-9833.
336. A. Bessette, M. Cibian, J. G. Ferreira, B. N. DiMarco, F. Belanger, D. Desilets, G. J. Meyer and G. S. Hanan, *Dalton Trans.*, 2016, **45**, 10563-10576.
337. T. Schlotthauer, C. Friebe, A. M. Schwenke, M. Jäger and U. S. Schubert, *J. Mater. Chem. C*, 2017, **5**, 2636-2648.
338. D. Liu, Z. Jiang, M. Wang, X. Yang, H. Liu, M. Chen, C. N. Moorefield, G. R. Newkome, X. Li and P. Wang, *Chem. Commun.*, 2016, **52**, 9773-9776.
339. C. Shen, A. D. W. Kennedy, W. A. Donald, A. M. Torres, W. S. Price and J. E. Beves, *Inorg. Chim. Acta*, 2017, **458**, 122-128.
340. F. Odobel and H. Zabri, *Inorg. Chem.*, 2005, **44**, 5600-5611.
341. R. O. Steen, L. J. Nurkkala, S. J. Angus-Dunne, C. X. Schmitt, E. C. Constable, M. J. Riley, P. V. Bernhardt and S. J. Dunne, *Eur. J. Inorg. Chem.*, 2008, 1784-1794.
342. L. Trouillet, A. De Nicola and S. Guillerez, *Chem. Mater.*, 2000, **12**, 1611-1621.
343. Y.-Q. Fang, M. I. J. Polson and G. S. Hanan, *Inorg. Chem.*, 2003, **42**, 5-7.
344. F. Loiseau, R. Passalacqua, S. Campagna, M. I. J. Polson, Y.-Q. Fang and G. S. Hanan, *Photochem. Photobiol. Sci.*, 2002, **1**, 982-990.
345. E. C. Constable, A. M. W. Cargill Thompson and S. Greulich, *J. Chem. Soc., Chem. Commun.*, 1993, 1444-1446.
346. M. Polson, C. Chiorboli, S. Fracasso and F. Scandola, *Photochem. Photobiol. Sci.*, 2007, **6**, 438-443.
347. M. I. J. Polson, F. Loiseau, S. Campagna and G. S. Hanan, *Chem. Commun.*, 2006, 1301-1303.
348. A. A. Bhuiyan and X. Du, *J. Arkansas Acad. Sci.*, 2013, **67**, 28-33.
349. N. Zabarska, A. Stumper and S. Rau, *Dalton Trans.*, 2016, **45**, 2338-2351.
350. A. Stumper, M. Lämmle, A. K. Mengele, D. Sorsche and S. Rau, *Eur. J. Inorg. Chem.*, 2018, DOI: 10.1002/ejic.201701126.
351. A. Kroll, K. Monczak, D. Sorsche and S. Rau, *Eur. J. Inorg. Chem.*, 2014, **2014**, 3462-3466.
352. A. Baron, C. Herrero, A. Quaranta, M.-F. Charlot, W. Leibl, B. Vauzeilles and A. Aukauloo, *Inorg. Chem.*, 2012, **51**, 5985-5987.
353. C. Herrero, A. Quaranta, S. El Ghachtouli, B. Vauzeilles, W. Leibl and A. Aukauloo, *Phys. Chem. Chem. Phys.*, 2014, **16**, 12067-12072.
354. D. Ma, S. E. Bettis, K. Hanson, M. Minakova, L. Alibabaei, W. Fondrie, D. M. Ryan, G. A. Papoian, T. J. Meyer, M. L. Waters and J. M. Papanikolas, *J. Am. Chem. Soc.*, 2013, **135**, 5250-5253.
355. S. Sheth, A. Baron, C. Herrero, B. Vauzeilles, A. Aukauloo and W. Leibl, *Photochem. Photobiol. Sci.*, 2013, **12**, 1074-1078.
356. H.-X. Wang, K.-G. Zhou, Y.-L. Xie, J. Zeng, N.-N. Chai, J. Li and H.-L. Zhang, *Chem. Commun.*, 2011, **47**, 5747-5749.
357. J. B. Gerken, M. L. Rigsby, R. E. Ruther, R. J. Pérez-Rodríguez, I. A. Guzei, R. J. Hamers and S. S. Stahl, *Inorg. Chem.*, 2013, **52**, 2796-2798.
358. Y. Sun, Z. Chen, E. Puodziukynaite, D. M. Jenkins, J. R. Reynolds and K. S. Schanze, *Macromolecules*, 2012, **45**, 2632-2642.
359. J. H. Alstrum-Acevedo, M. K. Brennaman and T. J. Meyer, *Inorg. Chem.*, 2005, **44**, 6802-6827.

360. E. Holder, M. A. R. Meier, V. Marin and U. S. Schubert, *J. Polym. Sci., Part A: Polym. Chem.*, 2003, **41**, 3954-3964.
361. H. Shimakoshi, M. Nishi, A. Tanaka, K. Chikama and Y. Hisaeda, *Chem. Commun.*, 2011, **47**, 6548-6550.
362. P. Giannopoulos, A. K. Andreopoulou, C. Anastasopoulos, D. Raptis, G. Sfyri, J. K. Kallitsis and P. Lianos, *RSC Adv.*, 2016, **6**, 8256-8266.
363. M. Heller and U. S. Schubert, *Macromol. Rapid Commun.*, 2002, **23**, 411-415.
364. F. Pinaud, R. Millereux, P. Vialar-Trarieux, S. Pinet, I. Gosse, N. Sojic, V. Ravaine and B. Catargi, *J. Phys. Chem. B*, 2015, **119**, 12954-12961.
365. B. Happ, C. Friebe, A. Winter, M. D. Hager and U. S. Schubert, *Eur. Polym. J.*, 2009, **45**, 3433-3441.
366. B. Happ, J. Kubel, M. G. Pfeffer, A. Winter, M. D. Hager, B. Dietzek, S. Rau and U. S. Schubert, *Macromol. Rapid Commun.*, 2015, **36**, 671-677.
367. T. Ueki, M. Shibayama and R. Yoshida, *Chem. Commun.*, 2013, **49**, 6947-6949.
368. E. K. Pefkianakis, N. P. Tzanetos and J. K. Kallitsis, *Chem. Mater.*, 2008, **20**, 6254-6262.
369. R. M. Johnson, P. S. Corbin, C. Ng and C. L. Fraser, *Macromolecules*, 2000, **33**, 7404-7412.
370. A. A. Farah and W. J. Pietro, *Inorg. Chim. Acta*, 2004, **357**, 3813-3824.
371. A. A. Farah and W. J. Pietro, *J. Polym. Sci., Part A: Polym. Chem.*, 2005, **43**, 6057-6072.
372. M. L. Disabb-Miller, Y. Zha, A. J. DeCarlo, M. Pawar, G. N. Tew and M. A. Hickner, *Macromolecules*, 2013, **46**, 9279-9287.
373. Y. Zha, M. L. Disabb-Miller, Z. D. Johnson, M. A. Hickner and G. N. Tew, *J. Am. Chem. Soc.*, 2012, **134**, 4493-4496.
374. W. Y. Ng, X. Gong and W. K. Chan, *Chem. Mater.*, 1999, **11**, 1165-1170.
375. S. C. Rasmussen, D. W. Thompson, V. Singh and J. D. Petersen, *Inorg. Chem.*, 1996, **35**, 3449-3450.
376. Z. Peng, A. R. Gharavi and L. Yu, *J. Am. Chem. Soc.*, 1997, **119**, 4622-4632.
377. Q. Wang, L. Wang and L. Yu, *J. Am. Chem. Soc.*, 1998, **120**, 12860-12868.
378. B.-B. Cui, H.-J. Nie, C.-J. Yao, J.-Y. Shao, S.-H. Wu and Y.-W. Zhong, *Dalton Trans.*, 2013, **42**, 14125-14133.
379. B.-B. Cui, C.-J. Yao, J. Yao and Y.-W. Zhong, *Chem. Sci.*, 2014, **5**, 932-941.
380. Z. Fang, S. Keinan, L. Alibabaei, H. Luo, A. Ito and T. J. Meyer, *Angew. Chem. Int. Ed.*, 2014, **53**, 4872-4876.
381. R. M. Leasure, T. Kajita and T. J. Meyer, *Inorg. Chem.*, 1996, **35**, 5962-5963.
382. J. A. Moss, R. Argazzi, C. A. Bignozzi and T. J. Meyer, *Inorg. Chem.*, 1997, **36**, 762-763.
383. J. A. Moss, J. C. Yang, J. M. Stipkala, X. Wen, C. A. Bignozzi, G. J. Meyer and T. J. Meyer, *Inorg. Chem.*, 2004, **43**, 1784-1792.
384. H.-J. Nie, J. Yao and Y.-W. Zhong, *J. Org. Chem.*, 2011, **76**, 4771-4775.
385. J.-Y. Shao, C.-J. Yao, B.-B. Cui, Z.-L. Gong and Y.-W. Zhong, *Chin. Chem. Lett.*, 2016, **27**, 1105-1114.
386. J. Yang, M. Sykora and T. J. Meyer, *Inorg. Chem.*, 2005, **44**, 3396-3404.
387. C.-J. Yao, Y.-W. Zhong, H.-J. Nie, H. D. Abruna and J. Yao, *J. Am. Chem. Soc.*, 2011, **133**, 20720-20723.
388. J. H. Tang, Y. Q. He, J. Y. Shao, Z. L. Gong and Y. W. Zhong, *Sci. Rep.*, 2016, **6**, 35253.
389. M. Masuda, N. Nakamura and H. Ohno, *J. Electrochem. Soc.*, 2013, **160**, G3135-G3138.
390. C.-J. Yao, Y.-W. Zhong and J. Yao, *Inorg. Chem.*, 2013, **52**, 10000-10008.
391. H. B. Yildiz, B. B. Carbas, S. Sonmezoglu, M. Karaman and L. Toppare, *Int. J. Hydrogen Energy*, 2016, **41**, 14615-14629.
392. C. Fan, C. Ye, X. Wang, Z. Chen, Y. Zhou, Z. Liang and X. Tao, *Macromolecules*, 2015, **48**, 6465-6473.
393. K. Araki, H. Endo, G. Masuda and T. Ogawa, *Chem. Eur. J.*, 2004, **10**, 3331-3340.
394. V. Aranyos, A. Hagfeldt, H. Grennberg and E. Figgemeier, *Polyhedron*, 2004, **23**, 589-598.
395. C. Friebe, M. Jaeger and U. S. Schubert, *RSC Adv.*, 2013, **3**, 11686-11690.

396. F. Haddache, A. Le Goff, N. Spinelli, P. Gairola, K. Gorgy, C. Gondran, E. Defrancq and S. Cosnier, *Electrochim. Acta*, 2016, **219**, 82-87.
397. W. Huang, L. Wang, H. Tanaka and T. Ogawa, *Eur. J. Inorg. Chem.*, 2009, 1321-1330.
398. S. Sherry Zhu, R. P. Kingsborough and T. M. Swager, *J. Mater. Chem.*, 1999, **9**, 2123-2131.
399. Q. Shu, C. Adam, N. Sojic and M. Schmittel, *Analyst*, 2013, **138**, 4500-4504.
400. X. J. Zhu and B. J. Holliday, *Macromol. Rapid Commun.*, 2010, **31**, 904-909.
401. A. Et Taouil, J. Husson and L. Guyard, *J. Electroanal. Chem.*, 2014, **728**, 81-85.
402. A. Deronzier, J.-C. Moutet and D. Zsoldos, *J. Phys. Chem.*, 1994, **98**, 3086-3089.
403. A. R. Guadalupe, X. Chen, B. P. Sullivan and T. J. Meyer, *Inorg. Chem.*, 1993, **32**, 5502-5512.
404. M. Ito, T. Tsukatani and H. Fujihara, *J. Mater. Chem.*, 2005, **15**, 960-964.
405. C. A. Kent, B. P. Mehl, L. Ma, J. M. Papanikolas, T. J. Meyer and W. Lin, *J. Am. Chem. Soc.*, 2010, **132**, 12767-12769.
406. M. Myahkostupov and F. N. Castellano, *Inorg. Chem.*, 2011, **50**, 9714-9727.
407. T. Schlotthauer, G. A. Parada, H. Görls, S. Ott, M. Jäger and U. S. Schubert, *Inorg. Chem.*, 2017, **56**, 7720-7730.
408. T. D. M. Bell, C. Pagba, M. Myahkostupov, J. Hofkens and P. Piotrowiak, *J. Phys. Chem. B*, 2006, **110**, 25314-25321.
409. C. B. Spillane, J. L. Morgan, N. C. Fletcher, J. G. Collins and F. R. Keene, *Dalton Trans.*, 2006, 3122-3133.
410. S. Aghazada, P. Gao, A. Yella, G. Marotta, T. Moehl, J. Teuscher, J. E. Moser, F. De Angelis, M. Gratzel and M. K. Nazeeruddin, *Inorg. Chem.*, 2016, **55**, 6653-6659.
411. R. Kikkeri, D. Grunstein and P. H. Seeberger, *J. Am. Chem. Soc.*, 2010, **132**, 10230-10232.
412. J. Husson, M. Beley and G. Kirsch, *Tetrahedron Lett.*, 2003, **44**, 1767-1770.
413. R. Kikkeri, I. Garcia-Rubio and P. H. Seeberger, *Chem. Commun.*, 2009, 235-237.
414. L. Cassidy, S. Horn, L. Cleary, Y. Halpin, W. R. Browne and J. G. Vos, *Dalton Trans.*, 2009, 3923-3928.
415. W. S. Aldridge, III, B. J. Hornstein, S. Serron, D. M. Dattelbaum, J. R. Schoonover and T. J. Meyer, *J. Org. Chem.*, 2006, **71**, 5186-5190.
416. G.-B. Jiang, W. Li, J. Wang, B.-J. Han, G.-J. Lin, Y.-Y. Xie, H.-L. Huang and Y.-J. Liu, *Transition Met. Chem.*, 2014, **39**, 849-858.
417. E. Sondaz, J. Jaud, J.-P. Launay and J. Bonvoisin, *Eur. J. Inorg. Chem.*, 2002, 1924-1927.
418. S. Diring, R. Ziessel, F. Barigelletti, A. Barbieri and B. Ventura, *Chem. Eur. J.*, 2010, **16**, 9226-9236.
419. J. Ma, J. Wu, W. Liu, P. Wang and Z. Fan, *Spectrochim. Acta, Part A*, 2012, **94**, 340-345.
420. C. Richardson, P. J. Steel, D. M. D'Alessandro, P. C. Junk and F. R. Keene, *J. Chem. Soc., Dalton Trans.*, 2002, 2775-2785.
421. M.-Y. Wei, S.-D. Wen, X.-Q. Yang and L.-H. Guo, *Biosens. Bioelectron.*, 2009, **24**, 2909-2914.
422. D. M. D'Alessandro and F. Richard Keene, *Dalton Trans.*, 2006, 1060-1072.
423. N. C. Fletcher, P. C. Junk, D. A. Reitsma and F. R. Keene, *J. Chem. Soc., Dalton Trans.*, 1998, 133-138.
424. N. C. Fletcher and F. R. Keene, *J. Chem. Soc., Dalton Trans.*, 1999, 683-690.
425. J. A. Zampese, F. R. Keene and P. J. Steel, *Dalton Trans.*, 2004, 4124-4129.
426. T. J. Rutherford, O. Van Gijte, A. Kirsch-De Mesmaeker and F. R. Keene, *Inorg. Chem.*, 1997, **36**, 4465-4474.
427. N. C. Fletcher, M. Nieuwenhuyzen and S. Rainey, *J. Chem. Soc., Dalton Trans.*, 2001, 2641-2648.
428. B. T. Patterson and F. R. Keene, *Inorg. Chem.*, 1998, **37**, 645-650.
429. J. A. Smith and F. R. Keene, *Chem. Commun.*, 2006, 2583-2585.
430. T. Sasaki, M. Naka, F. Nakamura and T. Tanaka, *J. Biol. Chem.*, 1992, **267**, 21518-21523.
431. G. Orellana, M. C. Moreno-Bondi, E. Segovia and M. D. Marazuela, *Anal. Chem.*, 1992, **64**, 2210-2215.
432. J. J. Concepcion, J. W. Jurss, M. R. Norris, Z. Chen, J. L. Templeton and T. J. Meyer, *Inorg. Chem.*, 2010, **49**, 1277-1279.

433. C. A. Kent, D. Liu, T. J. Meyer and W. Lin, *J. Am. Chem. Soc.*, 2012, **134**, 3991-3994.
434. D. M. Ryan, M. K. Coggins, J. J. Concepcion, D. L. Ashford, Z. Fang, L. Alibabaei, D. Ma, T. J. Meyer and M. L. Waters, *Inorg. Chem.*, 2014, **53**, 8120-8128.
435. M. Diaz-Serrano, A. Rosado, D. Santana, E. Z. Vega and A. R. Guadalupe, *J. Phys.: Conf. Ser.*, 2013, **421**, 1-5.
436. R. Liu, Y. Lv, X. Hou, L. Yang and Z. Mester, *Anal. Chem.*, 2012, **84**, 2769-2775.
437. H. C. Fry, A. Lehmann, L. E. Sinks, I. Asselberghs, A. Tronin, V. Krishnan, J. K. Blasie, K. Clays, W. F. DeGrado, J. G. Saven and M. J. Therien, *J. Am. Chem. Soc.*, 2013, **135**, 13914-13926.
438. S. L. Bommarito, S. P. Lowerybretz and H. D. Abruna, *Inorg. Chem.*, 1992, **31**, 495-502.
439. A. M. Breul, J. Kübel, B. Häupler, C. Friebe, M. D. Hager, A. Winter, B. Dietzek and U. S. Schubert, *Macromol. Rapid Commun.*, 2014, **35**, 747-751.
440. C. Ott, D. Wouters, H. M. L. Thijs and U. S. Schubert, *J. Inorg. Organomet. Polym. Mater.*, 2007, **17**, 241-249.
441. T. Nagai, *J. Chromatogr.*, 1992, **606**, 33-42.
442. R. Schroot, U. S. Schubert and M. Jäger, *Macromolecules*, 2016, **49**, 8801-8811.
443. R. Schroot, U. S. Schubert and M. Jäger, *Macromolecules*, 2017, **50**, 1319-1330.
444. S. Sharma, F. Lombeck, L. Eriksson and O. Johansson, *Chem. Eur. J.*, 2010, **16**, 7078-7081.
445. R. Kroener, M. J. Heeg and E. Deutsch, *Inorg. Chem.*, 1988, **27**, 558-566.
446. M. Thomalla and H. Tributsch, *C. R. Chim.*, 2006, **9**, 659-666.
447. Y. Shu, Z. S. Breitbach, M. K. Dissanayake, S. Perera, J. M. Aslan, N. Alatrash, F. M. MacDonnell and D. W. Armstrong, *Chirality*, 2015, **27**, 64-70.
448. P. Sun, A. Krishnan, A. Yadav, F. M. MacDonnell and D. W. Armstrong, *J. Mol. Struct.*, 2008, **890**, 75-80.
449. P. Sun, A. Krishnan, A. Yadav, S. Singh, F. M. MacDonnell and D. W. Armstrong, *Inorg. Chem.*, 2007, **46**, 10312-10320.
450. W. R. Browne, C. M. O'Connor, C. Villani and J. G. Vos, *Inorg. Chem.*, 2001, **40**, 5461-5464.

For Table of Contents use only

"Chemistry-on-the-complex": Functional Ru^{II} polypyridyl-type sensitizer as divergent building blocks

Tina Mede, Michael Jäger, Ulrich S. Schubert

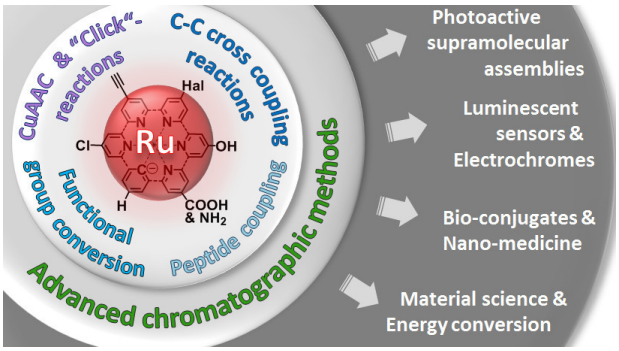

Publication P4

Mild electropolymerization and monitoring of continuous film formation for photoredox-active Ru metallopolymers

T. Schlotthauer, C. Friebe, A. M. Schwenke; M. Jäger; U. S. Schubert *J. Mat. Chem. C* **2017**, *5*, 2636-2648.

The paper as well as the supporting information (free of charge) is available online under: doi.org/10.1039/c6tc05548f

Journal of Materials Chemistry C

PAPER

View Article Online
View Journal | View Issue

Cite this: J. Mater. Chem. C, 2017, 5, 2636

Mild electropolymerization and monitoring of continuous film formation for photoredox-active Ru metallopolymers†

T. Schlotthauer,‡[a] C. Friebe,‡[ab] A. M. Schwenke,[ac] M. Jäger*[abc] and U. S. Schubert*[abc]

Received 22nd December 2016,
Accepted 11th February 2017

DOI: 10.1039/c6tc05548f

rsc.li/materials-c

The electropolymerization of a ruthenium(II) 2,6-di(quinolin-8-yl)pyridine complex with two pendant bithienyl-groups is investigated in detail. The associated redox potentials enable mild anodic electropolymerization without the need for boron trifluoride diethyl etherate (BFEE), which promotes undesired side reactions. Continuous film growth in the presence of acid or alternative electrolytes is achieved even for large cycle numbers (500), as detailed by the evolution of the peak current densities and the cathodic charge upon re-reduction of the film. The latter analysis permits a complementary analysis, particularly in the case of distorted CVs caused by charge transport limitations within the film. Notably, electropolymerization can also be performed potentiostatically at low anodic (over-)potentials even at prolonged reaction times, which leads to films with enhanced electrochemical properties. A high film porosity of spherical-like agglomeration networks is confirmed by SEM investigations, whereby higher control is found under slower and/or milder electropolymerization conditions. The films show the preserved electrochemical and optical properties of the Ru sensitizer, *i.e.*, a defined and stable redox process, strong UV-vis absorption up to 600 nm, emission in the NIR range, and effective electrochemical switching promoted by the quaterthiophene bridge.

Polythiophene-based thin-film structures, including poly(alkylthiophene)s, poly(3,4-ethylenedioxythiophene)s, *etc.*, represent popular materials for applications in (photo)electronics, *e.g.*, light harvesting, electroluminescent and electrochromic devices, and OFET or sensor materials. They feature high electrical conductivities (up to 100 S cm^{-1}), broad UV-vis absorption, and electrochromism.[1,2] Polythiophenes are often prepared *via* cross-coupling reactions or chemical oxidation of thiophene monomers,[3] and are subsequently solution-processed through deposition techniques. Alternatively, polythiophenes are easily accessible *via* electropolymerization techniques with concomitant deposition,[4–6] which allows the direct coating of an electrode surface in a single step. As a consequence of the oxidation state during the deposition process, the internal structure and resulting morphology differ markedly from that of charge-neutral, solution-processed polythiophenes. Hence, electropolymerized films are usually highly porous and display less internal orientation of the chains, causing a larger film–solution interface at the expense of a lower intrinsic electrical conductivity. The latter may also be caused by detrimental side reactions of the film due to the applied anodic potentials and additives during and after electropolymerization and, thus, mild protocols are sought after to balance such detrimental effects.

Oligo- or polythiophene segments are also utilized for advanced functional semiconducting coatings, *e.g.*, by incorporation of organic pigments and redox-active moieties to achieve light harvesting and charge storage, respectively.[7–9] In this regard, metal complexes received particular interest due to their electrochemical, photophysical, and catalytic properties,[10,11] and recently due to their capability of anion separation.[12] In addition to various metallayne-based materials,[13,14] polypyridine-based ruthenium complexes are versatile photosensitizers with distinguished redox and excited-state properties, extraordinary stability *etc.* and, thus, they are widely utilized in energy-conversion schemes,[15] photoredox catalysis,[16,17] as mechanical actuators,[18] or in sensing[19] and medical applications.[20] Immobilization *via* electropolymerization is usually achieved by coupling vinyl[21,22] or thienyl units,[6,10] which are readily installed at the ligand scaffold (Fig. 1). The electropolymerization of Ru^{II} complexes based on

[a] Laboratory of Organic and Macromolecular Chemistry (IOMC), Friedrich Schiller University Jena, Humboldtstraße 10, 07743 Jena, Germany. E-mail: michael.jager.iomc@uni-jena.de
[b] Center for Energy and Environmental Chemistry Jena (CEEC Jena), Friedrich Schiller University Jena, Philosophenweg 7a, 07743 Jena, Germany
[c] Jena Center for Soft Matter (JCSM), Friedrich Schiller University Jena, Philosophenweg 7, 07743 Jena, Germany

† Electronic supplementary information (ESI) available. See DOI: 10.1039/c6tc05548f

‡ These authors contributed equally to this work.

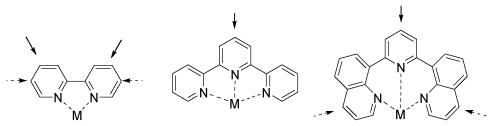

Fig. 1 Schematic representation of typical ligands for electropolymerizable Ru^{II} complexes based on 2,2′-bipyridine (bpy, left), 2,2′:6′,2″-terpyridine (tpy, middle), and 2,6-di(quinolin-8-yl)pyridine (dqp, right). Arrows indicate typical attachment positions of the electropolymerizable groups. See text for references.

bpy (bpy is 2,2′-bipyridine) and tpy (tpy is 2,2′:6′,2″-terpyridine) ligands has been reported and relies mainly on vinyl,[21,22] thiophene or 3,4-ethylenedioxythiophene (EDOT) units.[21–33] However, the combination of advantageous excited-state properties and beneficial structural features for directional linear polymer growth remains a longstanding goal.[34–36] In this regard, the recently developed $[Ru(dqp)_2]^{2+}$ congener (dqp is 2,6-di(quinolin-8-yl)pyridine) adopts an ideal octahedral coordination geometry,[37,38] which results in an extraordinary combination of photophysical properties and geometrical features: (a) enhanced metal-to-ligand charge-transfer (MLCT) excited-state lifetimes of up to several microseconds, (b) red-shifted absorption (up to 600 nm) and emission (up to 800 nm), and (c) enhanced photostability with respect to $[Ru(bpy)_3]^{2+}$.[38–40] Hence, $[Ru(dqp)_2]^{2+}$ photosensitizers became also attractive for photo-/electrochemical applications, sensing, and biomedical applications.[41–44]

We previously reported $[Ru(dqp)_2]^{2+}$ complexes bearing two monothiophene units, which required boron trifluoride diethyl etherate (BFEE) for electropolymerization.[45,46] The binding of BFEE to the thienyl sulphur leads to the activation of the thienyl moieties for electropolymerization by decreasing the aromatic character. The re-investigation of the electropolymerization performance gave a low maximal surface coverage of about 10^{-9} mol cm^{-2}, which is assigned to the limiting charge-transport kinetics during potentiodynamic cycling, and/or to detrimental side reactions at high required potentials. Co-polymerization with thiophene gave thicker films, which can be regarded as randomly incorporated $[Ru(dqp)_2]^{2+}$ complexes into polythiophene chains.[46] Nonetheless, the obtained films suffered from electrochemical instability despite the milder anodic potentials, which is attributed to irreversible reactions of the oligothiophene segments. Similar observations are reported for a series of Ru^{II} and Os^{II} complexes bearing thienyl, bithienyl, or terthienyl groups.[28] It has been noted that matching the redox potentials of the metal centres and the oligothienyl bridge facilitates charge transport.[10] However, the combination of the tpy ligand and bithienyl groups leads to an inevitable potential difference of either +220 mV (Os) or −240 mV (Ru).[28] Notably, $[Ru(dqp)_2]^{2+}$ possesses a substantially lower redox potential than $[Ru(bpy)_3]^{2+}$ or $[Ru(tpy)]^{2+}$ (by −0.18 V), which reduces the formal gap with regard to the bridge and may lead to an improved electropolymerization behavior (*vide infra*).

The progress of electropolymerization is often illustrated by the evolution of cyclic voltammograms (CVs) over a few cycles. However, the absence of further analytical data (current densities, scan-rate-dependent electrochemistry or electrochemical impedance spectroscopy, *etc.*) often precludes a direct comparison among the studies. Moreover, many depicted CVs deviate from the ideal peak shape, which challenges the interpretation of the current (densities), particularly in view of partial electrochemical instability as frequently observed in subsequent analyses. Hence, we set out to screen typical experimental conditions[21–33] and to evaluate the electrochemical data in a systematic and consistent manner – in particular in the case of distorted CV curves. In this study, we present the detailed analysis of two bifunctionalized $[Ru(dqp)_2]^{2+}$ complexes, bearing two thienyl (**I**) or two bithienyl moieties (**II**). The electropolymerizable units are covalently linked *via* a phenylene ring to maintain their intrinsic redox potentials and to enable sizable electronic communication (Scheme 1). Notably, the novel complex **II** lowers the calculated electrochemical gap with respect to the bridge to only 60 mV.

Monomer synthesis and analytical characterization

The preparation of the new complex **II** relies on a chemistry-on-the-complex approach, *i.e.*, applying Suzuki–Miyaura cross coupling using bithiophene boronic acid pinacol ester and the same precursor complex as used for **I** (Scheme 1).[45] The reaction mixture was heated to 100 °C for 16 h. However, incomplete formation of the title complex and the occurrence of single- and double-dehalogenated species according to MS analysis were noticed. The purification of the complex was carried out *via* column chromatography using amino-functionalized silica and a mixture of dichloromethane and methanol (98 : 2). The analytically pure compound was obtained by diffusion-controlled crystallization (21%) and characterized by NMR spectroscopy

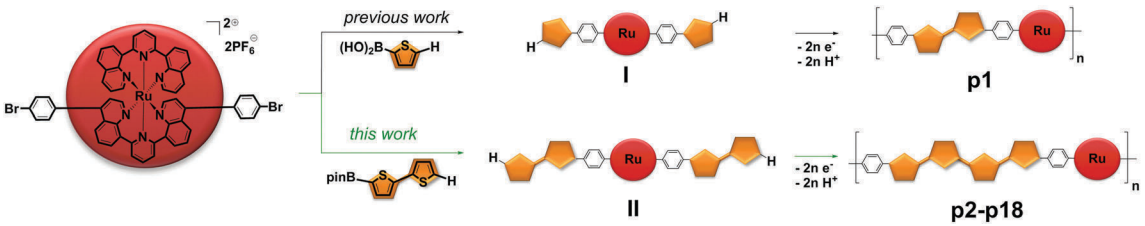

Scheme 1 Schematic representation of the synthesis of the bithiophene-functionalized complex *via* Suzuki–Miyaura cross coupling ($Pd(dba)_2$, SPHOS, K_2CO_3, CH_3CN/H_2O (2 : 1), 100 °C) and subsequent electrochemical polymerization (pin is pinacolato, SPHOS is 2-dicyclohexylphosphino-2′,6′-dimethoxybiphenyl).

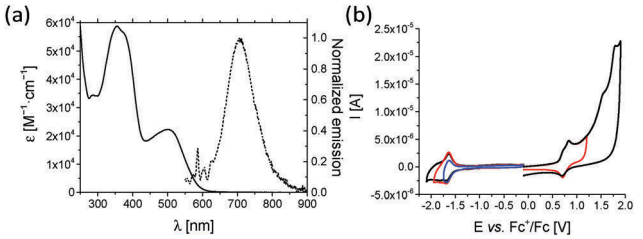

Fig. 2 (a) UV-vis absorption and emission spectra (10^{-6} M in CH_3CN) and (b) cyclic voltammograms (10^{-4} M in CH_3CN with 0.1 M Bu_4NPF_6) of **II**.

(Fig. S1–S4, ESI†) and ESI-ToF mass spectrometry (Fig. S5, ESI†). The low isolated yield is attributed mainly to the purification process, which is necessary to remove the side products containing only one bithienyl group. The UV-vis absorption spectrum of **II** resembles that of **I**, *i.e.*, it consists of two characteristic regions (Fig. 2a). Below 400 nm, the absorption is dominated by ligand-centred (LC) and bithiophene-based transitions. The long-wavelength band between 400 and 600 nm is assigned to MLCT transitions. In agreement with a previous study, the extended ligand π-conjugation leads to a bathochromically shifted MLCT band (λ_{max} = 503 nm, ε_{max} = 20 000 M^{-1} cm^{-1}) with respect to the parental $[Ru(dqp)_2]^{2+}$.[40] The room-temperature emission displays a large Stokes shift of 6400 cm^{-1}, which is typical for a ^{3}MLCT state, and is centred at 706 nm (1.76 eV). The similarly red-shifted emission of **I** and **II** supports the localization of the excited state on the functionalized quinoline units on the basis of a detailed analysis for the related complexes.[40] The electrochemical characterization of **II** by cyclic voltammetry revealed the anticipated redox reactions (Fig. 2b): a reversible process is apparent at *ca.* +0.7 V *vs.* Fc^+/Fc, which is assigned to the Ru^{III}/Ru^{II} couple. Irreversible oxidation occurs around +0.84 V, which is attributed to the bithiophene moiety. The potential value closely resembles the reported value (+0.87 V).[47] Additional irreversible anodic processes occur at higher potentials (>+1.5, +1.8 V). In the cathodic region, a reversible process is observed at −1.65 V, which is attributed to typical ligand-centred reductions.[40]

Methodology and monitoring of potentiodynamic electropolymerization

In the following section, the systematic screening of typical parameters and conditions is presented, *i.e.*, the role of BFEE, alternative solvents and supporting electrolytes, the potential mode and range, polymerization time, and the usage of additives. If not stated otherwise, electropolymerization was carried out on ITO-coated glass slides in acetonitrile containing 0.1 M Bu_4NPF_6 as the electrolyte, the potentials are reported *vs.* $AgNO_3$/Ag (−0.094 V *vs.* Fc^+/Fc), and the absolute currents are converted into current densities to assist a meaningful comparison. First, we revisited the fate of the thienyl-equipped complex **I** upon prolonged electropolymerization in the presence of BFEE on a glassy carbon electrode (Fig. 3). The obtained CVs of **p1** virtually superimpose those of our previous report, which confirms the

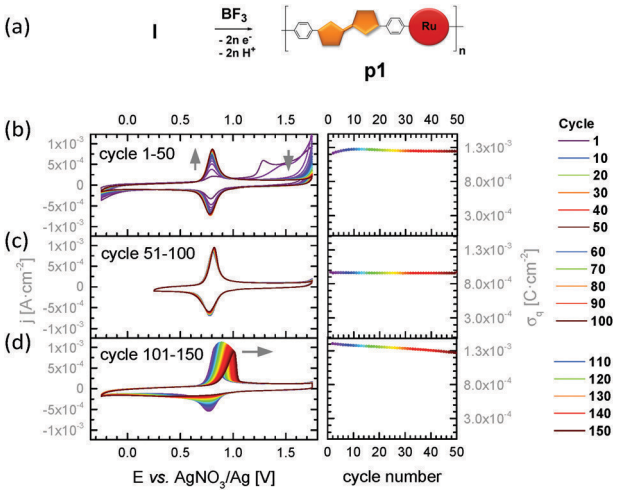

Fig. 3 Development of the CV of **p1** during potentiodynamic electropolymerization (potentials *vs.* $AgNO_3$/Ag, 200 mV s^{-1}, 0.1 M Bu_4NPF_6 in CH_3CN, 5 vol% BFEE) of thienyl-equipped complex **I**, illustrating typical regimes: (a) schematic representation of **p1**, (b) initial growth (cycles 1 to 50, applying −0.25 to +1.75 V), (c) stagnation of growth (cycles 51 to 100, applying +0.25 to +1.75 V), and (d) over-oxidation of the film (cycles 101 to 150, applying −0.25 to +1.75 V with 5 s rest time at +1.75 V). Arrows indicate evolution of peak currents during cycling. Right panel displays cathodic charges per half-cycle. Note the offset in (c) due to the shorter reduction time caused by the changed vertex potential (from −0.25 to +0.25 V), and decreasing cathodic charges in (d) assigned to over-oxidation.

reproducibility and the control of the electropolymerization process: the thienyl-related peaks (>+1.3 V) disappear during the first three cycles and the Ru-based wave evolves at an almost constant potential with narrow peak splits (10 mV). Within the first ten cycles, the peak current density rises and then begins to level off (cycle 10 to 50), as illustrated by the color coding (Fig. 3b). Within the next 50 cycles, the cathodic reversal potential was adjusted to reduce the cycling time, but only a marginal growth and a slight anodic peak shift were observed (Fig. 3c). Within the final 50 cycles, a hold time of 5 s was applied at +1.75 V to prolong the transit time in the anodic regime, which leads to a pronounced peak shift by +300 mV and a severe broadening of the cathodic wave (Fig. 3d). Despite the redox processes of the film, two further contributions are observed: re-reduction of non-consumed monomers (particularly during the first cycles), and the cell's background current. The cathodic charges (σ_q) were calculated from the CV data for each reduction half-cycle. Surprisingly, comparable cathodic charges were observed throughout the entire electropolymerization process for **p1**, even during the first few cycles (Fig. 3b, right). The transferred charges slightly increase up to the 15th cycle and remain nearly constant afterwards. They arise from the sum of film re-reduction and cathodic processes at low potentials, while the former increase and the latter diminish during the course of electropolymerization. During the next 50 cycles (51 to 100), the lower cathodic vertex potential leads to less time for reduction and, thus, the cathodic charge value initially drops (by 25%) but remains constant afterwards (Fig. 3c, right). This phenomenon indicates charge transport limitations

during cycling within the potential window (*vide infra*). Next, the prolonged oxidation (5 s hold time at +1.75 V) leads to decreasing cathodic charges, which is attributed to over-oxidation of the film. Notably, the reduction wave is severely broadened, which indicates a particularly slowed re-reduction of the film. This hypothesis is corroborated by impedance spectroscopy data taken during a separate electropolymerization run of **I**, which confirms the correlation of film growth and increasing film resistance of **p1** from the corresponding Nyquist plots (>10 cycles, Fig. S6, ESI†). In essence, the maximum of transferred charges for **p1** is reached at 15 cycles and amounts to 1.3×10^{-3} C cm^{-2} or a surface coverage of $\Gamma = 1.4 \times 10^{-8}$ mol cm^{-2}. The data are consistent with the generally accepted mechanism of electropolymerization,[5] *i.e.*, the film grows quickly during the initial cycles, while further growth is influenced by restricted charge transport and ultimately by side reactions to produce detrimental charge trap sites.

Next, we tested the electropolymerization of the bithiophene-equipped complex **II** under identical conditions, *i.e.*, using BFEE as the additive and the same potential-time program on a glassy carbon electrode. Qualitatively similar features were observed in the CVs of film **p2** but at a much faster rate, *i.e.*, the rise of the Ru^{III}/Ru^{II} wave as well as the peak broadening and increasing peak split occurred already within the first 50 cycles (Fig. S7, ESI†). In contrast to the thienyl-equipped complex **I**, the bithienyl-based congener **II** revealed continuous electropolymerization without significant levelling. Although the CV shape deviates from the ideal behavior, a threefold increase of the cathodic charges (4.3×10^{-3} C cm^{-2}) was achieved already after 50 cycles, which corresponds to a surface coverage of 4.5×10^{-8} mol cm^{-2}. The peak shape and values agree well with those of a report on related terpyridine-based complexes using BFEE as an additive.[28] In summary, the initial benchmarking tests for **I** and **II** in the presence of BFEE revealed the successful electropolymerization but also indicate side reactions and/or kinetic limitations in the later stage. Hence, a more detailed analysis of the CV data becomes highly desirable, *e.g.*, determination of the number of intermittently stored charges and/or impedance spectroscopy to estimate film conductivities (*vide infra*).

Lewis-acid-free electropolymerization

In our previous experiments, a discoloration of the electropolymerization solution in the presence of BFEE was observed over time even when the solutions were stored in the dark at −18 °C, which indicates undesired chemical side reactions. Hence, we tested the electropolymerization of **II** on ITO-coated glass slides in the absence of BFEE, which was previously found to be crucial for thienyl-decorated **I**.[45] In addition, the anodic reversal potential was lowered (+1.5 V) to minimize potential side reactions of the formed quaterthienyl bridge (Fig. 4b). Indeed, the electropolymerization proceeds smoothly to form the film **p3** without the formation of asymmetric peak shapes in the CV (Fig. 4b). The comparison of the evolving peak currents and cathodic charges shows a linear relationship for the first 50 cycles. Afterwards, a clear deviation was observed, which is tentatively assigned to the onset of significant

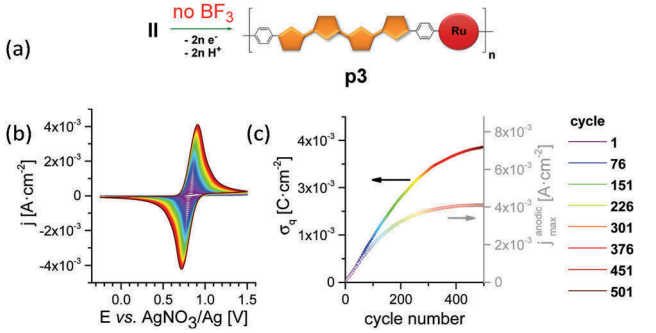

Fig. 4 BFEE-free conditions: (a) schematic representation of **p3**. (b) Development of the cyclic voltammogram of **II** (b) during potentiodynamic electropolymerization (in CH_3CN with 0.1 M Bu_4NPF_6; 200 mV s^{-1}). (c) Cathodic charge (left axis) and peak current (right axis) over the course of the polymerization.

kinetic contributions of the charge transport upon potential cycling (Fig. 4c). For example, the peak current reaches a plateau around the 400th cycle, yet the cathodic charges continue to evolve (Fig. 4c). The electropolymerization was stopped after 500 cycles. The obtained red, non-transparent film on ITO-coated glass slides reached a higher final cathodic charge (5.7×10^{-3} C cm^{-2}) and surface coverage (5.8×10^{-8} mol cm^{-2}) than the film obtained in the presence of BFEE (**p2**), or a fourfold increase compared to **p1**. In addition, no discoloration was noticed (*vide supra*). Hence, all subsequent experiments to screen the experimental parameters were carried out on ITO without BFEE.

Acid–base dependence

The course of electropolymerization should also be affected by the continuous release of protons (decreasing pH value), particularly in the later stage. The build-up of proton concentration retards the final deprotonation to re-aromatize the bridge. Hence, deprotonation should become less favorable during electropolymerization, yet the exact contribution of the released protons is less studied.[5] In order to scavenge the released protons, the addition of a Brønstedt base is an attractive possibility. However, our attempts to utilize the sterically hindered base 2,6-lutidine resulted in collapsed cyclovoltammetric signals (**p4**). No cathodic wave was observed and the anodic wave ceased during cycling, which is characteristic of film decomposition and/or ill-defined reactions. In fact, it remains challenging to select a suitable base that is non-nucleophilic with respect to reactive bithienyl/quaterthienyl cations and electrochemically stable at the applied anodic potential. An alternative strategy relies on water to "buffer" the released protons. Hence, a few drops of water were added before the start of the electropolymerization of **II** (1 mol% H_2O). The electropolymerization (**p5a**) was decelerated based on the cathodic charges, which reached only 50% of the value obtained without water. Furthermore, an additional feature beside the Ru^{III}/Ru^{II} wave is present in the CV (Fig. S8, ESI†). Notably, immersing a fresh electrode and continuing the electropolymerization from the same solution yielded a "normal" CV without the formation of the shoulder (**p5b**), although the obtained cathodic charges were still lower than those achieved without the addition of water.

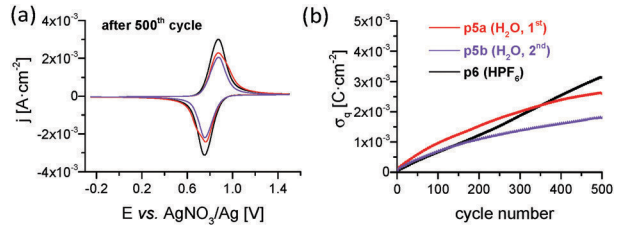

Fig. 5 Effect of pH value: (a) CVs of the 500th cycle of **p5a**, **p5b**, and **p6** during potentiodynamic electropolymerization (−0.25 to +1.5 V *vs.* $AgNO_3$/Ag, 200 mV s^{-1}, 500 cycles; 0.1 M Bu_4NPF_6 in CH_3CN) containing HPF_6 (0.3 mM black) or H_2O (1 mol%) for two consecutive runs with fresh electrodes (red: 1st and violet: 2nd). (b) Development of corresponding cathodic charges.

The addition of an excess of HPF_6 (0.3 mM) in a control experiment confirmed that the presence of protons indeed decreases the film growth rate (**p6**). Remarkably, linear growth was observed, which led ultimately to higher cathodic charges than for **p5a** after the 350th cycle (Fig. S9, ESI†). No levelling was observed for **p6** to reach a final cathodic charge of 3.1×10^{-3} C cm^{-2} (Fig. 5). In summary, we assign these observations in accordance with the literature: in the presence of water or nucleophilic impurities, side reactions may occur to diminish the film growth,[28] whereas the addition of acid retards the growth in the early stage but may also prevent the aforementioned side reactions due to protonation. At this stage, a quantitative analysis of the pH dependence is beyond the scope of this work, but applying slightly acidic conditions may be beneficial in practical terms to scavenge residual nucleophilic impurities and, thus, to sustain continuous film growth.

Reproducibility and monomer recovery

The impact and scope of changing the reaction conditions on the polymerization performance were investigated, *e.g.*, decreasing the pH value, potential side reactions of the monomers, and consumption of nucleophilic impurities (*vide supra*). In order to exclude the contributions of the forming film, fresh electrodes were re-immersed into the same solution after 500 cycles, and electropolymerization was performed under otherwise identical conditions (Fig. S10, ESI†). Fig. 6 depicts the final CVs and cathodic charges. The first run reproduced the previously established values, *i.e.*, **p7a** shows a similar cathodic charge

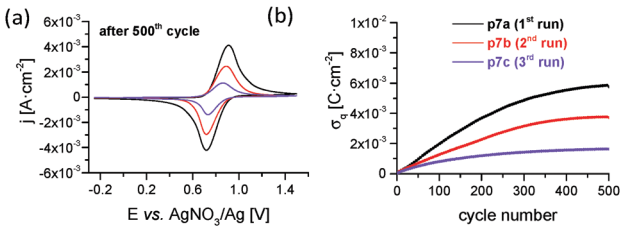

Fig. 6 (a) CVs of the 500th cycle of **p7a–c** for the consecutive potentiodynamic electropolymerization runs (−0.25 to +1.5 V *vs.* $AgNO_3$/Ag, 200 mV s^{-1}, in CH_3CN with 0.1 M Bu_4NPF_6) from the same solution with fresh electrodes (black: 1st, red: 2nd, and violet: 3rd). (b) Development of the corresponding cathodic charges.

(5.9×10^{-3} C cm^{-2}) and surface coverage (6.1×10^{-8} mol cm^{-2}), which again confirms the reliability of the electropolymerization process and analysis. In the second and third run, decreased film growth was noticed, *i.e.*, the transferred charges after 500 cycles dropped to 3.7×10^{-3} C cm^{-2} and $\Gamma = 3.9 \times 10^{-8}$ mol cm^{-2} (**p7b**) and finally to 1.6×10^{-3} C cm^{-2} and $\Gamma = 1.7 \times 10^{-8}$ mol cm^{-2} (**p7c**). The analysis of the cathodic charges during electropolymerization revealed that the film growth during the last cycles of a given run is significantly lower than that of the first cycles in the consecutive run. For example, the change in cathodic charge ($\Delta\sigma_q$) during the last five cycles of **p7a** ($\Delta\sigma_q = 2.1 \times 10^{-5}$ C cm^{-2}) is significantly lower than that in the initial stage of **p7b** (8.4×10^{-5} C cm^{-2}) or **p7c** (5.2×10^{-5} C cm^{-2}). Secondly, the consecutive runs showed a slower film growth, even during the first cycles. Note that the amount of consumed monomer during each electropolymerization run is negligible in comparison to the initial bulk concentration, while the re-immersion of a fresh electrode also homogenizes the solution. Hence, comparable monomer concentrations for each run (**p7a–c**) are anticipated. We attribute the decreasing film growth within a run to the previously assigned limiting charge-transport kinetics of the formed film, while the slower polymerization in the initial stages within the series (**p7a–c**) is assigned to changes of the reaction medium. A closer inspection of the CVs (taken at comparable cathodic charge values) further reveals that the CV peaks are broadened and possess a larger split for the later runs. A plausible hypothesis assumes side reactions of one electropolymerizable group of the monomer so that such products may accumulate during the runs. Their incorporation into the film would interrupt the linear chain growth and, thus, may hamper the charge transport and film growth rate. In order to test this hypothesis, the crude complex was isolated after the electropolymerization. One portion was re-subjected to electropolymerization, while the second portion was purified by washing with methanol, which removes soluble impurities but not any Ru complexes.[48] The ^{1}H NMR spectrum of the recovered material confirms little amounts of side products (Fig. S11, ESI†), and the ESI-ToF MS analysis identified the O_2-adduct among others (Fig. S12, ESI†). Next, the electropolymerization for the pristine complex (**p8a**), the crude recovered material (**p8b**), and the re-purified portion (**p8c**) was compared. The anodic vertex potential was reduced to +1.2 V in order to diminish the effect of side reactions (Fig. S13, ESI†).[49] In line with previous results, the observed cathodic charge of pure **p8a** is lower than before (3.9×10^{-3} C cm^{-2}) due to the shorter transition time in the anodic region. The re-purified batch performs better than the crude batch (2.7×10^{-3} C cm^{-2} *vs.* 1.6×10^{-3} C cm^{-2}). The observed diminished film growth and the shifted peak potentials among the consecutive runs using fresh electrodes suggest that the changes of the reaction medium and/or contributions from monomer side reactions affect the film growth – in addition to the previously identified limitations due to the redox kinetics of the film (*vide supra*). More importantly, the data from series **p8a–c** emphasize the possibility of recycling the monomer, despite the slightly reduced activity during electropolymerization. Notably, the side reactions may be promoted by the released protons, which can

activate the electropolymerization in a similar fashion like the Lewis acid (BFEE), or potentially by an interfering specimen, which may form by the electrolysis at the counter electrode.

Effect of solvent and conducting salt

In view of the unknown side reactions, we tested exemplarily the effect of an alternative conducting salt (Bu_4NClO_4) and an alternative solvent (CH_2Cl_2), since an enhanced charge-transfer performance was observed for PEDOT using perchlorate as the counter ion.[5] Hence, we employed Bu_4NClO_4 in CH_3CN as the electrolyte, but the solubility of **II** was significantly lower in this case. Hence, the lower applicable concentration disfavors the bimolecular coupling step and, thus, leads to slower film growth as indicated by the smaller peak current densities (Fig. S14, ESI†). Applying the original settings (500 cycles, −0.25 to +1.5 V, Fig. S14, ESI†), a final cathodic charge of 2.2×10^{-3} C cm^{-2} was obtained for **p9a**. The subsequent run (**p9b**), using a fresh electrode in the same solution, revealed the typical decrease of cathodic charges to half of the previous value, which suggests that the electrolyte has a negligible effect on the outcome of the electropolymerization. Next, dichloromethane was tested as an alternative solvent (Fig. S15, ESI†). The CV data of electropolymerization in dichloromethane (**p10**) reveal some marked differences in comparison to the data obtained in acetonitrile. The first scan revealed the Ru^{III}/Ru^{II} couple (+0.95 V) and the onset of electropolymerization at potentials >1.1 V (Fig. 7a). The constant half-wave potential and the larger peak splits assigned to the Ru^{III}/Ru^{II} couple are well explained by the known larger ohmic resistance of the electrolyte solution (dichloromethane *vs.* acetonitrile). In addition, the film growth is significantly less pronounced than in acetonitrile as judged from the associated current densities. Notably, a distinct quasi-reversible redox wave around +0.7 V is noticed during the first ten scans, which shifts to higher potentials during the course of electropolymerization and ultimately superimposes with the Ru^{III}/Ru^{II} wave in the late stage of electropolymerization, which reproduces the previously observed peak shapes in acetonitrile (Fig. 7b). The observation of the transient redox process is tentatively assigned to the slower polymerization process in dichloromethane and may be explained by several factors, *e.g.*, the role of the released protons, which influence the irreversible coupling step (*vide supra*), or different film morphologies due to the alternated deposition/solubility. However, precisely assigning and discerning these factors remain speculative and are beyond the scope of this work. More importantly, the obtained film **p10** shows a comparable final cathodic charge (4.4×10^{-3} C cm^{-2}) and surface coverage (4.6×10^{-8} mol cm^{-2}) with respect to the acetonitrile-born films.

In summary, the hitherto reported variations of all BFEE-free potentiodynamic electropolymerization runs suggest the general robustness and reproducibility but reveal subtle differences, which are assigned to the role of the pH value (**p4–p6**), among consecutive runs (**p7a–c**) and recovered materials (**p8a–c**), as well as due to changing the electrolyte (**p9** and **p10**). In most cases, the cathodic charges begin to level in the late stage, which is assigned to the kinetic contribution of charge transport through the film during the potential sweep time. In addition to the film, the redox behavior further depends on counter-ion mobility, the extent of trap sites from side reactions, *etc.* In view of the latter, we finally investigated the scope of electropolymerization at milder applied potentials.

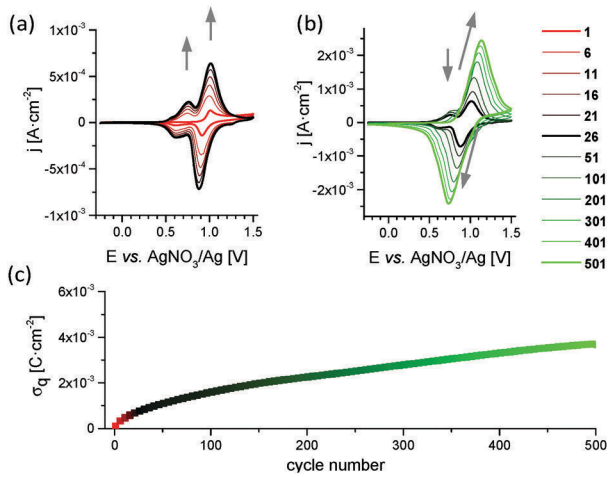

Fig. 7 CVs of **p10** during the early stage (a, red to black) and later stage (b, black to green). Arrows indicate characteristic changes with increasing cycle number. (c) Development of the corresponding cathodic charges over the course of potentiodynamic electropolymerization (−0.25 to +1.5 V *vs.* $AgNO_3/Ag$, 200 mV s^{-1}, 500 cycles; 0.1 M Bu_4NPF_6 in CH_2Cl_2).

Potentiostatic electropolymerization

The electropolymerization process was studied under potentiostatic control, *i.e.*, applying a fixed anodic potential for 60 min. Every five minutes, a CV cycle was recorded to monitor the polymerization progress. The timescale of the potentiostatic experiment was chosen to correspond closely to that of the potentiodynamic experiments. In other words, the sweep time through the oxidizing regime in the potentiodynamic mode (>0.8 V, 200 mV s^{-1}) amounts to approximately six seconds so that each "cycle" in the potentiostatic experiments resembles approximately 50 cycles of the potentiodynamic experiments. Importantly, the applied potentials (+1.1, +1.0, and +0.9 V) are significantly lower than the anodic vertex potentials of the previous potentiodynamic experiments (1.2 to 1.5 V). Hence, over-oxidation processes should be minimized, yet the driving forces for electropolymerization as well as for charge transport through the film are also diminished. However, the latter restriction is qualitatively compensated by the absence of the reduction half-cycle during electropolymerization (except for the diagnostic CV run every 5 min). Indeed, controlled electropolymerization was achieved in all three cases, even by applying the lowest potential (Fig. S16, ESI†).

The final CVs for **p11** (+1.1 V), **p12** (+1.0 V), and **p13** (+0.9 V) are depicted in Fig. 8 and resemble the typical peak shapes, except that the current at the fixed anodic potential almost returns to the baseline due to the hold time of 5 min. The two

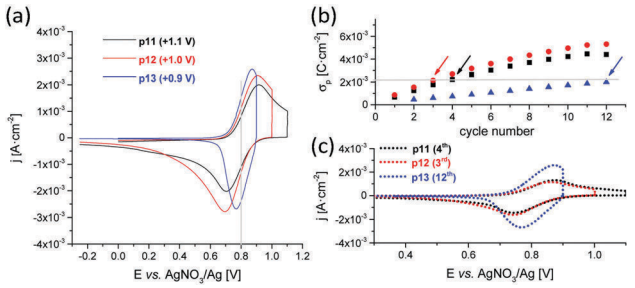

Fig. 8 (a) Cyclic voltammograms of **p11–p13** at the end of the potentiostatic electropolymerization attempts at different holding potentials (60 min, in CH_3CN with 0.1 M Bu_4NPF_6). The grey vertical line illustrates higher current densities at +0.8 V for milder holding potentials. (b) Respective cathodic charges over the course of the polymerization recorded every 5 min by a CV run. The grey horizontal line indicates comparable cathodic charges (2.1×10^{-3} C cm^{-2}) obtained for **p11** (4th cycle, black), **p12** (3rd cycle, red), and **p13** (12th cycle, blue). (c) Corresponding cyclic voltammograms with comparable cathodic charges (2.1×10^{-3} C cm^{-2}) showing different peak shapes and heights (dashed lines) assigned to kinetic contributions upon discharging of the films.

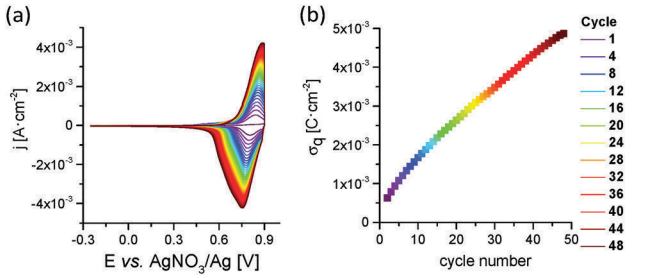

Fig. 9 Continuous potentiostatic electropolymerization of **p15** (+0.9 V *vs.* $AgNO_3$/Ag, 240 min; 0.1 M Bu_4NPF_6 in CH_3CN; CV measured after every 5 min). Development of the CV (a) and of the corresponding cathodic charges (b). Note the larger cathodic CV wave due to the hold time.

higher working potentials lead to similar peak shapes of **p11** and **p12** and, thus, correspond to similar cathodic charges, which grow with each "cycle" but begin to level after the 6th cycle. The mildest studied potential of +0.9 V (**p13**) leads to a significantly lower peak split in the CVs but also to significantly reduced film growth, as revealed by the comparison of the cathodic charges (Fig. 8b). The narrow waves in the CVs indicate a faster redox behavior in the order **p13** > **p12** > **p11**, as revealed by the current densities obtained at the given potential (0.8 V, Fig. 8a, grey vertical line). Note that the potential windows of the CVs differ and that the calculated cathodic charges may be affected accordingly (*vide infra*). Hence, the cyclic voltammograms with comparable cathodic charges should be compared, *e.g.*, the 4th (**p11**), 3rd (**p12**), and 12th cycle (**p13**), which correspond to 2.1×10^{-3} C cm^{-2} (Fig. 8c). The CVs of **p11** and **p12** display a similar distinct tailing towards less positive potentials, whereas **p13** shows a significantly smaller peak split. In other words, as the same number of charges is extracted, the process occurs more readily for the film prepared by the mildest electropolymerization potential (**p13**). This behavior seems plausible assuming fewer defects by over-oxidation or slower film growth to form better film morphologies; both are expected to sustain charge or counter ion mobility. Hence, we tested the scope of an extended potentiostatic electropolymerization time. The first experiment was performed at +1.0 V with a replenished monomer solution after 60 and 120 min (Fig. S17, ESI†). Indeed, well-defined CVs were obtained with steadily increasing cathodic charges after 60 min (**p14a**, 1.6×10^{-3} C cm^{-2}), after 120 min (**p14b**, 3.2×10^{-3} C cm^{-2}), and after 180 min (**p14c**, 4.5×10^{-3} C cm^{-2}). Slightly slower growth is observed towards the end of each run as well as among the three runs, in line with the results of the series **p7a–c** (*vide supra*). The pronounced step after refreshing the solutions can be explained by the soaking of the film with a new monomer and its additional contribution. The second experiment was conducted at +0.9 V for an extended time of 240 min without refreshing the solution (Fig. S18, ESI†). The analysis of **p15** reveals continuous electropolymerization reaching a high final cathodic charge of 5.0×10^{-3} C cm^{-2} and a surface coverage of 5.2×10^{-8} mol cm^{-2} (Fig. 9). This value is similar to those of **p11** and **p12**, but the CVs of **p15a** remain sharp even in the late stage of electropolymerization. Notably, the cathodic charges continue to evolve with only marginal levelling and the milder hold potential still sustains the electropolymerization despite the lower driving force (overpotential). Finally, the potentiostatic polymerization at +0.9 V was also conducted in dichloromethane, yielding a final cathodic charge that is comparable to its potentiodynamically prepared congener for **p16** (3.2×10^{-3} C cm^{-2}). This result corroborates the previous assignments, *i.e.*, milder conditions diminish undesired side reactions. In summary, the potentiostatic method is a mild complementing electropolymerization technique even at low anodic potentials. The complete results are compiled in Table 1, namely the electropolymerization conditions and the obtained cathodic charges as well as the corresponding surface coverages during *in situ* CV analysis (200 mV s^{-1}). Note that in the case of potentiostatic electropolymerization, the hold time at the anodic potential results in larger cathodic waves and, thus, increased cathodic charges in comparison to the values of potentiodynamically prepared films. Hence a more stringent comparison of the electrochemical properties is provided by CV analysis in the absence of the monomer (*vide infra*).

Film structure and morphology

The structure and morphology of the electropolymerized films were exemplarily analysed by optical profilometry and scanning electron microscopy (SEM, Fig. 10). First, thinner films on ITO-coated glass slides were prepared potentiodynamically in analogy to **p3**, scratched, and exemplarily analysed (Fig. 11). The film thickness was calculated from the height difference between the surface and the bottom of the scratch, which is tentatively assigned to the ITO surface due to its higher hardness (*vide infra*). In the case of the 35 electropolymerization cycles (**p17**), a uniform film with a height of 70 nm was obtained, while 100 cycles (**p18**) led to an average thickness of 230 nm, in good correlation with the threefold cycle number. However, the thicker film revealed a less uniform film surface, in qualitative agreement with film growth that departs from linear behavior after approximately 100 cycles (*vide supra*).

Table 1 Summary of electropolymerized films[a]

Entry	Film	E_{polym}[b] [V]	Cycle number	Additive/conditions	σ_q [$\times 10^{-3}$ C cm^{-2}]	Γ [$\times 10^{-8}$ mol cm^{-2}]
1	**p1**	−0.25 to 1.75		BFEE	1.3	1.4
2	**p2**	−0.25 to 1.75		BFEE	4.3	4.5
3	**p3**	−0.25 to 1.5		—	5.7	5.8
4	**p4**	−0.25 to 1.5	500	Lutidine	—[c]	—[c]
5	**p5a**	−0.25 to 1.5	500	H_2O (1 mol%)	2.6	2.7
	p5b	−0.25 to 1.5	500	H_2O (1 mol%)	1.8	1.9
6	**p6**	−0.25 to 1.5	500	HPF_6 (0.3 mM)	3.1	3.2
7	**p7a**	−0.25 to 1.5	500		5.9	6.1
	p7b				3.7	3.9
	p7c				1.6	1.7
8	**p8a**	−0.25 to 1.2	500	Pristine	3.9	4.0
	p8b			Crude	1.6	1.7
	p8c			Re-purified	2.7	2.8
9	**p9a**	−0.25 to 1.5	500	Bu_4NClO_4[d]	2.2	2.3
	p9b				1.1	1.1
10	**p10**	−0.25 to 1.5	500	CH_2Cl_2[e]	4.4	4.6
11	**p11**	1.1	60 min	—	4.2[f]	4.4[f]
12	**p12**	1.0	60 min	—	5.3[f]	5.5[f]
13	**p13**	0.9	60 min	—	2.0[f]	2.1[f]
14	**p14a**	1.0	60 min	—	1.6[f]	1.7[f]
	p14b		+60 min	[g]	3.2[f]	3.3[f]
	p14c		+60 min	[g]	4.5[f]	4.7[f]
15	**p15**	0.9	240 min	—	5.0[f]	5.2[f]
16	**p16**	0.9	60 min	CH_2Cl_2[e]	3.2[f]	3.3[f]

[a] Performed in 0.1 M Bu_4NPF_6 in CH_3CN solutions containing the complex in 1 mg mL^{-1}, if not stated otherwise. [b] Stated *vs.* $AgNO_3$/Ag. [c] Non-defined CV assigned to decomposition. [d] Bu_4NClO_4 instead of Bu_4NPF_6. [e] CH_2Cl_2 instead of CH_3CN. [f] Note that potentiostatic data are affected by different charging and potentials compared to potentiodynamically prepared films, see text. [g] Fresh monomer solution after 60 min.

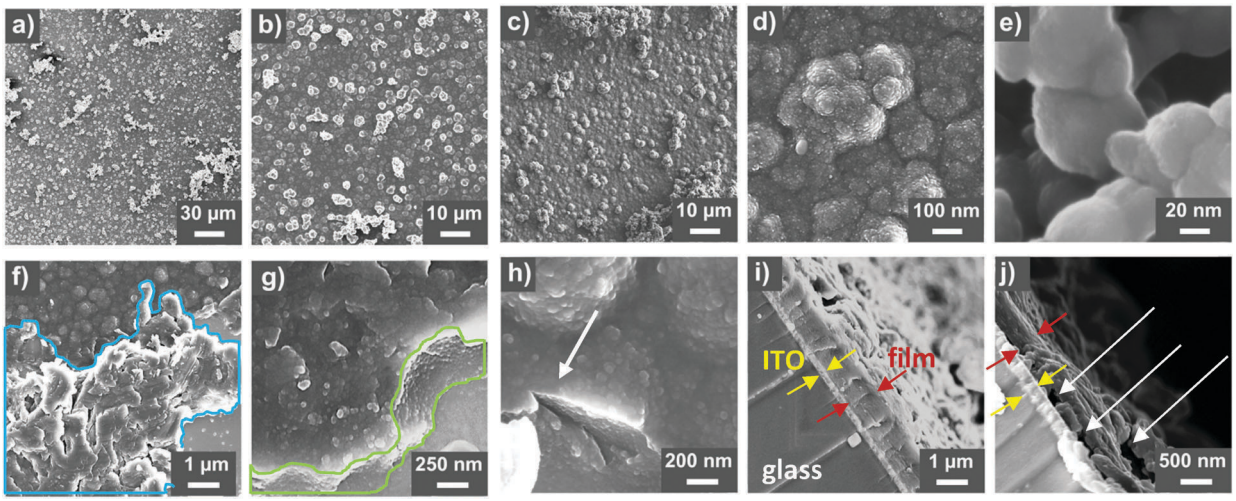

Fig. 10 Representative SEM images of electropolymerized films on ITO-coated glass slides (0.1 M Bu_4NPF_6 in CH_3CN). (a–e) Surface of intact films at different magnification values (a, b, d and e) and secondary electron detection (c) for more realistic depth perception. (f) Scratched surface showing the intact region (upper part), displaced debris from scratching (blue-framed area) and the slide surface (bottom right). (g and h) Magnification of a scratch edge (green-framed area) showing an internal spherical substructure. (i and j) Cross-section of a manually broken slide showing the glass support, ITO layer (yellow), and film (red) as marked by arrows of the intact thick film (i) and thinner partially detached film (j) as indicated by white arrows.

In order to obtain additional structural information, representative films were analysed by scanning electron microscopy (Fig. 10). The films possess a typical highly porous structure, which is resolved even to sub-micrometer scale (Fig. 10a–e). In line with the profilometry data, the surface is relatively flat as revealed by secondary electron detection (Fig. 10c). Notably, the film surface shows spherical substructures as well as islands of agglomerated particles on the sub-micrometer scale. In the case of slow film growth, significantly fewer agglomerates were found, while more rapid electropolymerization seems to favor these agglomerates. However, the relative amounts depend on the exact method of preparation (Fig. S19 to S23, ESI†): the spherical particles exhibit diameters of up to 1 µm for films that were obtained from Bu_4NPF_6-based electrolytes. The tendency to agglomerate and to form cross-linked networks was particularly observed for potentiostatically prepared films (Fig. S23, ESI†). When synthesized in a Bu_4NClO_4-containing solution, the particles are smaller ($\leq$300 nm) and only insignificant

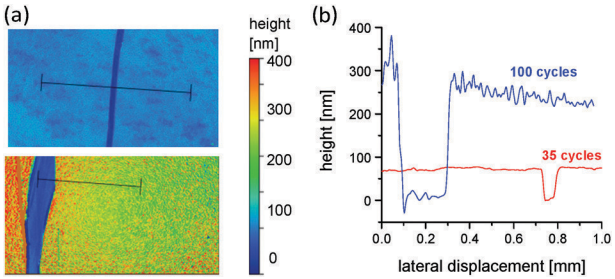

Fig. 11 (a) Optical profilometry images of electropolymerized films on ITO-coated glass slides after 35 cycles (**p17**, top) or 100 cycles (**p18**, bottom). (b) Cross-sectional profiles in the edge region of the films. Bottom of scratch assigned to the slide surface.

agglomeration is observed (Fig. S21, ESI†). The films obtained from dichloromethane (Bu_4NPF_6) show a more dense arrangement of homogenously distributed columnar objects, which are composed of similar spherical particles as formed in acetonitrile-born films (*vide supra*). The observed features conform with the proposed mechanism for electropolymerization in solution and deposition once a critical size or solubility is reached.[5,50] In general, the observed convex ("spherical-like") substructures with comparable domain sizes are in line with a minimized interface between the solution and the electropolymerized material, while network-like aggregation agrees with the proposed deposition once a critical size is achieved. In the cases of slow electropolymerization, the deposition process has more time to occur and, thus, may lead to more ordered structures with less agglomerated debris. In addition to the films' surface characterization, the interior is investigated in the region of a manually applied scratch (*cf.* optical profilometry). Fig. 10f shows a region with typical topographical features, *i.e.*, the film surface, the slide's surface, and the scratch with the displaced material. The latter appears to be much smoother than the bulk film surface, which is tentatively assigned to mechanical compression or folding of the film due to the scratching process. Hence, scratch regions where the material is torn apart were investigated (Fig. 10g–h). The interior is composed of spherical agglomerated particles with similar sizes as found for the surface, which suggests a homogeneous internal film structure. Finally, the film was investigated by mechanically breaking the slide from the backside transversally and imaging the formed cross section (Fig. 10i–j). In the case of thick films, the obtained cross section is flat and relatively uniform, and the material adheres to the ITO layer. In contrast, thin films are partially detached (Fig. 10j), which is attributed to the mechanical instability upon sample preparation in line with the observation of the displaced material found by the surface analysis (*vide supra*). More importantly, the glass substrate, the ITO layer, and the film can be readily identified in all cases and, thus, enable the estimation of average film heights – a valuable parameter to interpret the functional film properties (*vide infra*). However, since many films are inhomogeneous due to precipitated agglomerates on top of the surface, the given film thickness values represent average values and should be taken with caution in the case of high inhomogeneity. Note that previous reports also state similar challenges to obtain reliable structural film data, *e.g.*, by AFM microscopy.[28]

Optical and electrochemical properties

The electrical and optical properties of the prepared films were investigated by rinsing the film with solvent and re-immersion in fresh electrolyte solution using cyclic voltammetry and impedance spectroscopy as well as by steady-state UV-vis absorption and emission spectroscopy. The cyclic voltammograms of the films generally reproduce the final CV cycles from the corresponding electropolymerization (Fig. S24, ESI†), *i.e.*, CVs with the same peak shape, identical peak potentials, current densities, and associated cathodic charges (Fig. S24, ESI†). The only marked differences were found for the potentiostatically prepared films, which revealed lower cathodic charges than those obtained from the previous analysis, assigned to the extended time at the anodic hold potential. Hence, in view of a consistent comparison of the films, the data from the film's CV should be used and is detailed in the following. The oxidation–reduction process of the films is dominated by a stable and well-defined redox process around +0.73 V *vs.* Fc^+/Fc, which is assigned to both the Ru^{III}/Ru^{II} couple and the formed quaterthiophene unit.[51] Only for the films obtained from a water-containing electrolyte, the CV signal is less defined and shows two shoulders beside the main peak, which were also previously detected during electropolymerization. Since the electropolymerization data already indicated kinetic contributions of the formed films, the redox behavior was further examined by variation of the scan rate (Fig. S25 to S33, ESI†).

The scan-rate dependence is exemplified for the series **p7a–c**, prepared under potentiodynamic conditions. The cathodic charge values generally increase as more time is available to sweep the potential range but begin to converge around 20 mV s^{-1} (Fig. S34, ESI†). Hence, the calculated cathodic charges at low scan rates provide a consistent analysis among the potentiodynamically and potentiostatically prepared films to minimize kinetic contributions (*vide supra*). As expected, the scan-rate dependence of the cathodic charges is more pronounced in the series **p7a** > **p7b** > **p7c**, which emphasizes a larger impact for thicker films. Next, the peak current densities were interpreted and reveal a linear relation with respect to the applied scan rate only for small scan rates ($\leq$20 mV s^{-1}), while a square-root dependence was found for higher rates. Notably, the film **p9a**, obtained from a Bu_4NClO_4–electrolyte solution, maintains a linear relationship up to 500 mV s^{-1}, which indicates a faster redox process, in line with the reported enhanced charge-transfer ability for related PEDOT.[5] However, a more detailed analysis is beyond the scope of this seminal analysis since many contributing factors differ among the films and the exact interplay of these factors is unknown. More importantly, the formal half-wave potential of the main peak is unaffected by the scan rate, but the corresponding peak splits show marked differences. Fig. 12 depicts the scan-rate dependence of the selected films, highlighting the exceptional behavior of **p15** and **p16**, which were both prepared potentiostatically at a mild potential (+0.9 V). In contrast to most films, their peak splits

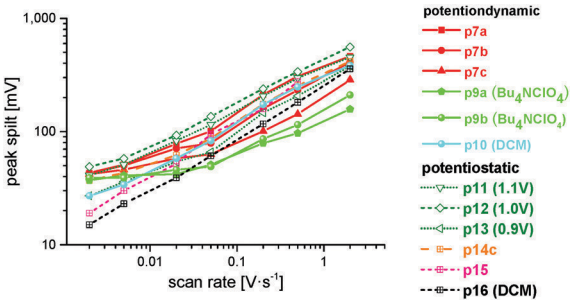

Fig. 12 General dependence of the observed peak splits with varying scan rate (2 to 2000 mV s^{-1}) of the selected films after rinsing and re-immersion in fresh monomer-free electrolyte solution (0.1 M Bu_4NPF_6 in CH_3CN; **p9a** and **p9b** measured in 0.1 M Bu_4NClO_4 in CH_3CN). Note the exceptionally low peak splits and retained linear dependence for **p15** and **p16** (see text).

sustain the linear dependence within the investigated scan rate range, and the extrapolation of each curve yields an intercept of only 2.5 mV, which comes very close to the ideal value of zero peak split in the absence of any kinetic contributions (*e.g.*, in the case of monolayers). In summary, the lowest applied scan rate (2 mV s^{-1}) resembles quasi-stationary conditions and, thus, the inherent "thermodynamic" properties of the film. As a consequence, the CVs generally become much narrower and, in some instances, minor pre-peaks were detectable. This observation parallels the features observed during slow electropolymerization in CH_2Cl_2 (*vide supra*). More importantly, this result clearly demonstrates that milder electropolymerization conditions lead to continuous polymerization and that the charges can be stored and/or extracted without high overpotentials.

In order to evaluate the electrochemical and structural data of the films, it is illustrative to relate film thicknesses with peak splits and cathodic charges obtained for low scan rates. Fig. 13 summarizes the electrochemical and structural data for the films for which reliable data were available. In the following, the electrochemical features are discussed firstly, followed by the interpretation with respect to the structural data. The potentiodynamically prepared films **p7a–c** show a larger average film thickness with increasing cathodic charges, whereas the peak

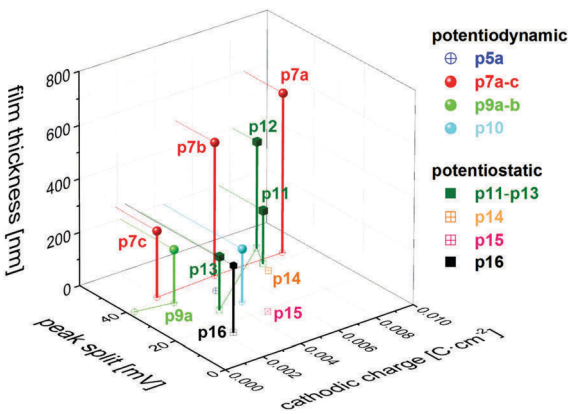

Fig. 13 3D Representation of the key properties: peak split and cathodic charge at a slow scan rate (2 mV s^{-1}) *vs.* estimated film thickness.

split remains nearly unaffected. This observation indicates that the redox behavior of these films is controlled by inherent thermodynamic factors. The perchlorate-born film **p9a** displays a combination of cathodic charge, peak split, and film thickness similar to **p7c**, while **p9b** displays an exceptional combination of negligible cathodic charge accompanied by a relatively high peak split. Notably, the CH_2Cl_2-derived film **p10** shows a cathodic charge comparable to **p7b** but a significantly lower peak split and a lower film thickness. The potentiostatically prepared films reveal a similar behavior, *i.e.*, higher cathodic charges are associated with larger peak splits. All films prepared at higher potentials, namely at +1.1 V (**p11**) or +1.0 V (**p12** and **p14**), show similar peak splits to the potentiodynamically prepared films, while all films prepared at +0.9 V show significantly smaller peak splits. The exceptional behavior of **p15** and **p16**, as judged previously from the electropolymerization data, is also reflected by the film's CV data, *i.e.*, a peak split as low as 15 mV and a sizeable cathodic charge. Unfortunately, the relation of electrochemical data and structural data is less clear, attributed to the inhomogeneity and the derived average thicknesses (*vide supra*), which precludes a more detailed interpretation at this stage and suggests more detailed future studies. Nevertheless, a qualitative trend can be established from the series **p7a–c** and **p11–p13**, *i.e.*, increased film thicknesses are associated with larger cathodic charges and peak splits.

Electrochemical impedance spectroscopy (EIS) was executed to gain further insights into the film conductivity behavior of the obtained films. All of the investigated films share similar EIS features (Fig. S35 to S41, ESI†) so that a common simple equivalent circuit that mimics the electrolyte, the film–electrolyte interface, and the film bulk properties was selected. Further details on the individual circuit elements are provided in the ESI† (Fig. S42 and Section 5.2). The films were pre-conditioned by applying a constant potential prior to EIS measurement, and the data were collected in the frequency range from 1 Hz to 1 MHz. The recorded EIS data revealed instrumental artefacts above 50 kHz due to reference electrode polarization (Fig. S35, ESI†) as well as a low signal-to-noise ratio below 5 Hz so that the analysis was confined to the intermediate frequency range. The Nyquist plots generally display a semi-circle at intermediate conditioning potentials, which is in line with the generally accepted mechanism of charge transport,[5,10,28,46] *i.e.*, the preconditioning potential controls the number of charge carriers and acceptor sites. However, the analysis of the experimental data was found to be challenging in the case of very inhomogeneous films (*vide supra*) so that we again restrict the interpretation deliberately to those films that yield reliable fits. The complete data are presented in the ESI† (Table S1).

In all cases, the derived electrolyte resistance values (53 to 74 Ω) correspond well to the values determined experimentally *via iR*-compensation. However, the parameters describing the interface differ markedly among the films without showing a clear trend. This observation parallels the large structural variations observed by SEM analysis (*vide supra*) and indicates the limits of the applied equivalent circuit to account, *e.g.*, for film inhomogeneity. In contrast, the internal film features

Table 2 Calculated film conductivities at +0.85 V *vs.* $AgNO_3$/Ag from EIS analysis

Entry	Film	R_{bulk}[a] [Ω]	A[b] [cm^2]	D[c] [nm]	σ_{film} [S cm^{-1}]
1	**p7a**	11.7	1.4	600	3.7×10^{-6}
2	**P7b**	11.6	1.2	500	3.6×10^{-6}
3	**P7c**	16	1.1	250	1.4×10^{-6}
4	**p10**	3.9	1.2	200	4.2×10^{-6}
5	**p11**	12.6	1.3	200	1.2×10^{-6}
6	**p12**	23.9	1.3	400	1.3×10^{-6}
7	**p13**	3.3	1.4	200	4.3×10^{-6}
8	**p16**	10.4	1.2	250	2.0×10^{-6}

[a] Bulk film resistance. [b] Macroscopic film area. [c] Film thickness estimated from SEM.

(namely the bulk film resistances) yielded more robust fit values and, thus, enabled the calculation of the formal film conductivities (σ_{film}), which were obtained after applying a pre-conditioning potential of +0.85 V using the film bulk resistance (EIS), the macroscopic area, and the film heights (SEM). Table 2 lists film conductivities, which are in the range of 1–5 $\times$ 10^{-6} S cm^{-1}. Notably, these values should be regarded as film-specific conductivities, and the inherent conductivity of the material should be higher, *e.g.*, the film porosity causes a lower effective area (volume) for charge transport (*vide infra*). Next, we investigated the effect of the pre-conditioning potential on the film conductivities of representative films (**p7a**, **p13**, and **p16**). The full data are provided in Table S2 to S4 (ESI†), while the calculated film conductivities are depicted in Fig. 14. The acetonitrile-born films **p7a** and **p13** resemble the expected behavior, *i.e.*, the conductivities culminate at the formal half-wave potential due to the optimal number of free charge carriers and acceptor sites.[5,10,28,46] The highest film conductivity was observed at +0.80 V with a three- to four-fold increase compared to the values obtained from film screening (Table 2). Surprisingly, film **p16** revealed an exceptional behavior with lower conductivity values spread over a broad potential range, and we are currently investigating the phenomena in more detail.

In summary, the highest calculated film conductivity is as high as 2.7 $\times$ 10^{-5} S cm^{-1}, while the bulk conductivity may be even higher and is expected to depend largely on the film structure including defects. These values are still lower compared to the related Ru complexes,[27,28] assigned to the intervening phenylene unit, which diminishes the conjugation by out-of-plane torsion.

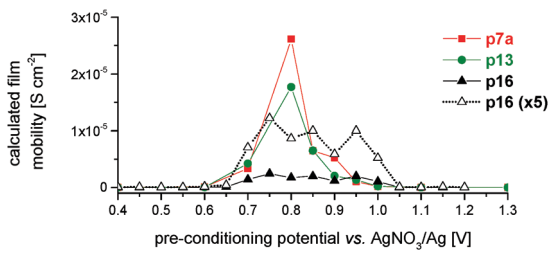

Fig. 14 Calculated film conductivities of representative films at various pre-conditioning potentials.

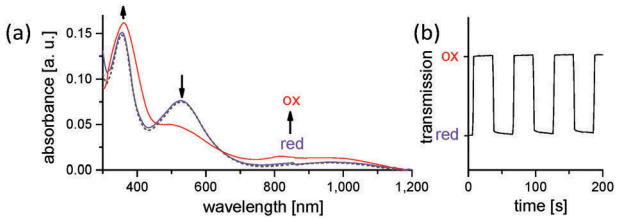

Fig. 15 (a) UV-vis–NIR changes during film oxidation and re-reduction for **p17**. (b) Response of potential switching between the reduced and oxidized states (<2 s response time).

The UV-vis absorption spectra of the obtained polymer films generally resemble that of the monomer in solution, *i.e.*, a distinct absorption band in the UV region and a broader, less intense band in the longer-wavelength region (Fig. S43, ESI†). Whereas the ligand-centred transitions in the UV region occur at identical wavelengths, the visible region (>400 nm) reveals a bathochromic shift of the MLCT transitions as well as transitions that are tentatively assigned to the quaterthiophene unit.[51] The films show weak room-temperature emission at around 780 nm, which corresponds to a bathochromic shift compared to the monomer solution by *ca.* 660 cm^{-1} (0.08 eV). Furthermore, the electrochromic characteristics of the films were studied by recording the absorption spectra during stepwise application of an oxidative potential (Fig. 15a). The film oxidation leads to minor changes in the UV region, while the typical optical changes in the visible and NIR regions are observed,[21,26] *i.e.*, a pronounced decrease of the MLCT band is observed accompanied by the simultaneous emergence of a very broad signal between 700 and 1200 nm. The latter is assigned to LMCT transitions of the formed Ru^{III} system. Subsequent re-reduction of the film regenerates the initial spectrum, while the excellent stability was confirmed upon switching between oxidizing and re-reducing potentials (Fig. 15b) with a fast switching time (<2 s), which is defined by achieving 95% of the full transmission change.[52]

Conclusions

A bis-bithienyl-equipped Ru^{II} complex (**II**) based on a 2,6-di(quinolin-8-yl)pyridine ligand framework was synthesized *via* a facile chemistry-on-the-complex approach. The electroactive subunits, *i.e.*, the Ru fragment and the bithienyl moieties, are connected by a *para*-phenylene linker to preserve their inherent photochemical and electrochemical properties. The subunits possess improved matching of their redox potentials (*ca.* 0.060 V) with respect to $[Ru(bpy)_3]^{2+}$ or $[Ru(tpy)_2]^{2+}$, which has been suggested to enhance the electropolymerization performance. Electropolymerization was investigated and analysed in depth to evaluate the scope of a mild and continuous process. The re-inspection of the related bis-thienyl congener (**I**) confirmed the necessity of BFEE as the additive and results in severe peak shifts and broadening but no substantial film growth. The severe deviation of the CVs from the ideal peak shape prompted us to evaluate the cathodic charges instead, which minimizes the

effect of kinetic contributions of the films. This analysis proved to be consistent and reliable throughout all studied films in this work. The related polymerization of the bis-bithienyl complex **II** proceeds much faster than for **I**, but the associated current densities and/or cathodic charges also level off. Notably, side reactions of the monomer by BFEE were observed so that BFEE free electropolymerization conditions were extensively screened (500 cycles). The systematic variation of the reaction conditions was likewise analysed by the cathodic charges since kinetic limitations of the film limit the reliability of interpreting the current densities, particularly in the late stage. In summary, the BFEE free electropolymerization of **II** was found to be very robust and to occur in the presence of water, acid, alternative electrolytes and/or solvents. The potentiostatic protocols sustained the electropolymerization process even in the case of mild potentials (+0.9 V) and extended time scales (4 h). The film structures of the prepared films were investigated by optical profilometry and SEM, which confirmed the formation of a highly porous bulk film layer with varying amounts of agglomerates on top. The occurrence of the agglomerates is particularly apparent in the case of fast or harsh electropolymerization protocols, which seems to control the film inhomogeneity. The ''pure'' films were also investigated in fresh, monomer-free electrolyte solution, which generally reproduced the electropolymerization data and, thus, confirmed the validity of the presented charge analysis. Well-defined redox processes were observed, including the expected scan-rate dependence of the cathodic charges and peak splits. Notably, the peak current densities and peak potentials converge at low scan rates to yield thermodynamic estimates, except for the films prepared under the mildest conditions, which showed a peak split as low as 15 mV. These results demonstrate that charges can be injected and extracted with very low associated overpotentials (driving forces). The impedance analysis of the selected films revealed film-specific conductivities up to 3×10^{-5} S cm^{-1}. Furthermore, the films proved to be redox-stable with switchable electrochromism, *i.e.*, bleachable absorption in the visible region (up to 650 nm), as well as a weak room-temperature photoluminescence at 780 nm.

In summary, electropolymerization and film stability greatly benefit from BFEE-free conditions, which lead to surface coverages up to 10^{-7} mol cm^{-2}, which are comparable to those reported in the recent literature.[21,26,53,54] The resulting morphology confirms the large internal film–solution interface within the highly porous network, which suggests the applicability of such electropolymerized films for sensors or heterogeneous photocatalytic applications. Future work will be devoted to applying the optimized conditions and to further utilizing the effect of increased conjugation,[28] *i.e.*, to precisely adjust the Ru^{III}/Ru^{II} redox potential to the polymerizable unit as well as to omit the intervening phenylene bridge.

Acknowledgements

M. J. acknowledges the Carl Zeiss Foundation and Friedrich Schiller University for financial support. The SEM facilities of the Jena Center for Soft Matter (JCSM) were established with a grant from the German Research Council (DFG) and the European Fonds for Regional Development (EFRE).

Notes and references

1 *Handbook of Thiophene-Based Materials*, ed. I. F. Perepichka and D. F. Perepichka, John Wiley & Sons, Ltd, Chichester, UK, 2009.
2 A. C. Grimsdale, K. L. Chan, R. E. Martin, P. G. Jokisz and A. B. Holmes, *Chem. Rev.*, 2009, **109**, 897–1091.
3 R. D. McCullough, *Adv. Mater.*, 1998, **10**, 93–116.
4 C. Friebe, M. D. Hager, A. Winter and U. S. Schubert, *Adv. Mater.*, 2012, **24**, 332–345.
5 J. Heinze, B. A. Frontana-Uribe and S. Ludwigs, *Chem. Rev.*, 2010, **110**, 4724–4771.
6 M. O. Wolf, *J. Inorg. Organomet. Polym. Mater.*, 2006, **16**, 189–199.
7 A. Mishra, C.-Q. Ma and P. Bäuerle, *Chem. Rev.*, 2009, **109**, 1141–1276.
8 L. Groenendaal, F. Jonas, D. Freitag, H. Pielartzik and J. R. Reynolds, *Adv. Mater.*, 2000, **12**, 481–494.
9 G. A. Sotzing, J. R. Reynolds and P. J. Steel, *Chem. Mater.*, 1996, **8**, 882–889.
10 B. J. Holliday and T. M. Swager, *Chem. Commun.*, 2005, 23–36.
11 M. O. Wolf, *Adv. Mater.*, 2001, **13**, 545–553.
12 X. Su, H. J. Kulik, T. F. Jamison and T. A. Hatton, *Adv. Funct. Mater.*, 2016, **26**, 3394–3404.
13 C.-L. Ho, Z.-Q. Yu and W.-Y. Wong, *Chem. Soc. Rev.*, 2016, **45**, 5264–5295.
14 W.-Y. Wong and C.-L. Ho, *Acc. Chem. Res.*, 2010, **43**, 1246–1256.
15 A. Hagfeldt, G. Boschloo, L. Sun, L. Kloo and H. Pettersson, *Chem. Rev.*, 2010, **110**, 6595–6663.
16 C. K. Prier, D. A. Rankic and D. W. C. MacMillan, *Chem. Rev.*, 2013, **113**, 5322–5363.
17 J. J. Concepcion, J. W. Jurss, M. K. Brennaman, P. G. Hoertz, A. O. Patrocinio, N. Y. Murakami Iha, J. L. Templeton and T. J. Meyer, *Acc. Chem. Res.*, 2009, **42**, 1954–1965.
18 S. Bonnet and J.-P. Collin, *Chem. Soc. Rev.*, 2008, **37**, 1207–1217.
19 D.-L. Ma, V. P.-Y. Ma, D. S.-H. Chan, K.-H. Leung, H.-Z. He and C.-H. Leung, *Coord. Chem. Rev.*, 2012, **256**, 3087–3113.
20 M. R. Gill and J. A. Thomas, *Chem. Soc. Rev.*, 2012, **41**, 3179–3192.
21 Y.-W. Zhong, C.-J. Yao and H.-J. Nie, *Coord. Chem. Rev.*, 2013, **257**, 1357–1372.
22 A. M. Lapides, D. L. Ashford, K. Hanson, D. A. Torelli, J. L. Templeton and T. J. Meyer, *J. Am. Chem. Soc.*, 2013, **135**, 15450–15458.
23 L. Wang, K. Fan, Q. Daniel, L. Duan, F. Li, B. Philippe, H. Rensmo, H. Chen, J. Sun and L. Sun, *Chem. Commun.*, 2015, **51**, 7883–7886.
24 C. Friebe, B. Schulze, H. Görls, M. Jäger and U. S. Schubert, *Chem. – Eur. J.*, 2014, **20**, 2357–2366.
25 B.-B. Cui, C.-J. Yao, J. Yao and Y.-W. Zhong, *Chem. Sci.*, 2014, **5**, 932–941.

26 C.-J. Yao, Y.-W. Zhong, H.-J. Nie, H. D. Abruña and J. Yao, *J. Am. Chem. Soc.*, 2011, **133**, 20720–20723.
27 X. J. Zhu and B. J. Holliday, *Macromol. Rapid Commun.*, 2010, **31**, 904–909.
28 J. Hjelm, R. W. Handel, A. Hagfeldt, E. C. Constable, C. E. Housecroft and R. J. Forster, *Inorg. Chem.*, 2005, **44**, 1073–1081.
29 J. A. Moss, J. C. Yang, J. M. Stipkala, X. Wen, C. A. Bignozzi, G. J. Meyer and T. J. Meyer, *Inorg. Chem.*, 2004, **43**, 1784–1792.
30 R. M. Leasure, T. Kajita and T. J. Meyer, *Inorg. Chem.*, 1996, **35**, 5962–5963.
31 C. P. Horwitz and Q. Zuo, *Inorg. Chem.*, 1992, **31**, 1607–1613.
32 T. F. Guarr and F. C. Anson, *J. Phys. Chem.*, 1987, **91**, 4037–4043.
33 C. D. Ellis, L. D. Margerum, R. W. Murray and T. J. Meyer, *Inorg. Chem.*, 1983, **22**, 1283–1291.
34 A. Juris, V. Balzani, F. Barigelletti, S. Campagna, P. Belser and A. von Zelewsky, *Coord. Chem. Rev.*, 1988, **84**, 85–277.
35 J.-P. Sauvage, J.-P. Collin, J.-C. Chambron, S. Guillerez, C. Coudret, V. Balzani, F. Barigelletti, L. De Cola and L. Flamigni, *Chem. Rev.*, 1994, **94**, 993–1019.
36 T. J. Meyer, *Pure Appl. Chem.*, 1986, **58**, 1193–1206.
37 L. Hammarström and O. Johansson, *Coord. Chem. Rev.*, 2010, **254**, 2546–2559.
38 M. Abrahamsson, M. Jäger, T. Österman, L. Eriksson, P. Persson, H.-C. Becker, O. Johansson and L. Hammarström, *J. Am. Chem. Soc.*, 2006, **128**, 12616–12617.
39 M. Jäger, R. J. Kumar, H. Görls, J. Bergquist and O. Johansson, *Inorg. Chem.*, 2009, **48**, 3228–3238.
40 T. Schlotthauer, B. Suchland, H. Görls, G. A. Parada, L. Hammarström, U. S. Schubert and M. Jäger, *Inorg. Chem.*, 2016, **55**, 5405–5416.
41 A. Frei, R. Rubbiani, S. Tubafard, O. Blacque, P. Anstaett, A. Felgenträger, T. Maisch, L. Spiccia and G. Gasser, *J. Med. Chem.*, 2014, **57**, 7280–7292.
42 G. A. Parada, L. A. Fredin, M.-P. Santoni, M. Jäger, R. Lomoth, L. Hammarström, O. Johansson, P. Persson and S. Ott, *Inorg. Chem.*, 2013, **52**, 5128–5137.
43 G. Ragazzon, P. Verwilst, S. A. Denisov, A. Credi, G. Jonusauskas and N. D. McClenaghan, *Chem. Commun.*, 2013, **49**, 9110–9112.
44 R. Schroot, C. Friebe, E. Altuntas, S. Crotty, M. Jäger and U. S. Schubert, *Macromolecules*, 2013, **46**, 2039–2048.
45 C. Friebe, H. Görls, M. Jäger and U. S. Schubert, *Eur. J. Inorg. Chem.*, 2013, 4191–4202.
46 C. Friebe, M. Jäger and U. S. Schubert, *RSC Adv.*, 2013, **3**, 11686–11690.
47 After reference potential conversion of AgCl/Ag to Fc^{+}/Fc by 0.425 V.
48 As indicated by the colourless filtrates.
49 Note that a lower potential also results in lower overpotential for charges to pass trap sites.
50 S. Sadki, P. Schottland, N. Brodie and G. Sabouraud, *Chem. Soc. Rev.*, 2000, **29**, 283–293.
51 J. J. Apperloo, L. B. Groenendaal, H. Verheyen, M. Jayakannan, R. A. J. Janssen, A. Dkhissi, D. Beljonne, R. Lazzaroni and J.-L. Brédas, *Chem. – Eur. J.*, 2002, **8**, 2384–2396.
52 C. L. Gaupp, D. M. Welsh, R. D. Rauh and J. R. Reynolds, *Chem. Mater.*, 2002, **14**, 3964–3970.
53 Z. Fang, S. Keinan, L. Alibabaei, H. Luo, A. Ito and T. J. Meyer, *Angew. Chem., Int. Ed.*, 2014, **53**, 4872–4876.
54 V. Aranyos, A. Hagfeldt, H. Grennberg and E. Figgemeier, *Polyhedron*, 2004, **23**, 589–598.

Publication P5

Modular assembly of poly(naphthalene diimide) and Ru(II) dyes for an efficient light-Induced charge separation in hierarchically controlled polymer architectures

R. Schroot, T. Schlotthauer, U. S. Schubert, M. Jäger, *Macromolecules* **2016***, 49,* 2112-2123.

The paper as well as the supporting information (free of charge) are available online under: doi.org/10.1021/acs.macromol.5b02717

Macromolecules

Article

pubs.acs.org/Macromolecules

Modular Assembly of Poly(naphthalene diimide) and Ru(II) Dyes for an Efficient Light-Induced Charge Separation in Hierarchically Controlled Polymer Architectures

Robert Schroot,[†,#] Tina Schlotthauer,[†,#] Ulrich S. Schubert,[*,†,‡] and Michael Jäger[*,†,‡]

[†]Laboratory of Organic and Macromolecular Chemistry (IOMC) and [‡]Center for Energy and Environmental Chemistry Jena (CEEC Jena), Friedrich Schiller University Jena, 07743 Jena, Germany

Supporting Information

ABSTRACT: Hierarchically well-defined multielectron acceptor−photosensitizer (A_n−P) assemblies were prepared by nitroxide-mediated polymerization of a styrenic naphthalene diimide and subsequent decoration of the chain terminus by a $[Ru(dqp)_2]^{2+}$ photosensitizer (dqp is 2,6-di(quinolin-8-yl)-pyridine). In view of a facile modular design, three synthetic linkage procedures were explored aiming at tailored light-initiated energy and electron transfer processes. The polymers were conveniently purified by column chromatography using amino- or diol-functionalized silica gels and were characterized in detail by NMR, MS, and UV−vis-SEC measurements. The electrochemical and absorption data confirmed the preserved individual redox and optical properties of the building blocks. The detailed steady-state emission measurements revealed an efficient quenching of the photosensitizer exceeding 86−96% with respect to reference complexes and the partial sensitization of/by polymer-based excited states. The results demonstrate the general versatility to construct photoredox-active macromolecules from tailored building blocks.

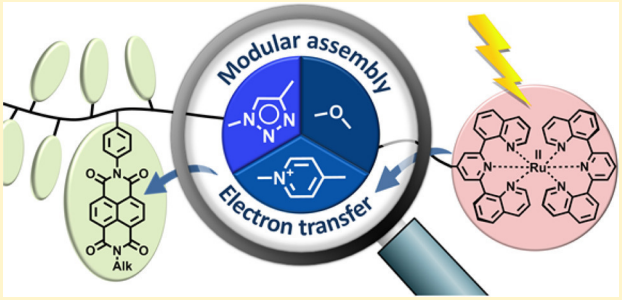

INTRODUCTION

The conversion of light energy into electrical energy and/or chemical bond energy is a key process for an environmentally friendly and sustainable power supply,[1] i.e., in photovoltaics and photosynthesis. Thereby, the latter process relies on the utilization of the generated charge carriers in coupled catalytic processes and thereby enables the storage as fuels with high energy density.[2,3] The energy conversion process is initiated by photon absorption to generate an excited state, followed by the primary charge separation, subsequent charge translocation, and ultimately the collection on an electrode (photovoltaics) or the consumption in catalytic reactions (photosynthesis). In order to obtain a high overall efficiency, all forward steps should be well tuned to minimize any undesired recombination processes.

One promising approach on a molecular level utilizes functional building blocks, i.e., electron donors (D), acceptors (A), and photosensitizer (P), which can be connected to form defined architectures with more complex functionality, i.e., photoinitiated charge separation. The strength of this (supramolecular) strategy is demonstrated by the highly efficient charge separation in molecular triad (D−P−A) systems reaching unit quantum efficacy.[4] Nevertheless, the photogenerated charges are locally trapped in such model compounds because a directional percolation pathway is essential to utilize the charge carriers in photovoltaic or photosynthetic applications. In this regard, the recent advances in polymer chemistry provide an invaluable synthetic platform to overcome the challenge of connecting multiple functional (redox-active) units. In particular, modern controlled radical polymerization techniques (e.g., NMP or RAFT polymerization processes)[5−8] enable the facile preparation of redox-active polymers (D_n and/or A_m) with a controlled degree of polymerization and dispersity ($Đ$). The utilization of functional monomers assures the formation of the fully functionalized polymer, which is often challenging to reach in a grafting approach. In addition, the facile preparation of telechelic polymers enables a postpolymerization functionalization specifically at the chain terminus, which can fulfill two important tasks with respect to efficient charge separation: First, the decoration with a terminal photosensitizer leads to *hierarchically* controlled polymer architectures, as demonstrated for D_n−P and P−A_m dyads.[9,10] Second, the simple modular assembly of the functional building blocks (D_n, P, A_m) assures a high variability to design and synthesis to explore new assembly generations.

Polymers based on naphthalene diimide (NDI) are intensively investigated as n-type semiconductors. The NDI unit exhibits reversible reduction steps, which are as well as the optical and physical properties tunable by different substituents on the molecular scaffold.[11−13] Additionally, their sizable planar π-system is capable for self-organization, e.g., a face-to-face

Received: December 16, 2015
Revised: February 15, 2016
Published: March 3, 2016

DOI: 10.1021/acs.macromol.5b02717
Macromolecules 2016, 49, 2112−2123

stacking of the units.[14−17] Main-chain conjugated NDI polymers are typically prepared by polycondensation and reach high charge charier mobilities,[18,19] whereas side-chain decorated polymers are conveniently prepared by controlled radical polymerization procedures.[10] Ruthenium polypyridyl complexes are widely used photosensitizer due to their metal-to-ligand charge transfer (MLCT) character of the excited state.[20−22] In addition to the ubiquitous $[Ru(bpy)_3]^{2+}$ complexes (bpy is 2,2′-bipyridine), e.g. in polymer-based architectures,[4,23−25] similar complexes based on 2,6-di-(quinolin-8-yl)pyridine (dqp) ligands have received increasing attention. This photosensitizer subclass displays comparably long excited states (microsecond time scale) combined with a red-shifted absorption (up to 550 nm) for an enhanced coverage of the solar spectrum.[26−28] Moreover, the parent complex $[Ru(dqp)_2]^{2+}$ was shown to exhibit an enhanced photostability in comparison to $[Ru(bpy)_3]^{2+}$.[28] Notably, very efficient photoinitiated charge separation (>95%) was achieved in D−P−A triads based on the $[Ru(dqp)_2]^{2+}$ core,[29] whereas the effective primary charge separation was recently demonstrated for a polymer-based P−A_m dyad by time-resolved spectroscopy,[10] irrespective of the highly flexible unsaturated linkage.

In this contribution, various linkage patterns are explored to prepare acceptor-photosensitizer (P−A_m) dyads based on poly(naphthalene diimides) (pNDI) and $[Ru(dqp)_2]^{2+}$-based complexes. Both functional building blocks (A_m, P) are individually synthesized and subsequently connected by nucleophilic substitution or by the application of the copper-(I)-catalyzed azide−alkyne cycloaddition (CuAAC) reaction. Chromatographic purification protocols were developed to facilitate the challenging purification of the macromolecular structures. The building blocks and dyads were characterized in detail by NMR spectroscopy, mass spectrometry, electrochemistry, and optical spectroscopy. The second part addresses the energy- and electron-transfer processes for the various linkages by steady-state absorption and emission spectroscopy. First, the quenching efficiency of the Ru-based emission was determined between the dyads and suitable reference complexes. Hence, complexes with the same substitution pattern at the ligand framework were synthesized to account for the (unknown) differences in the MLCT excited state character, i.e., emission quantum yield. Second, excitation spectra were recorded to shed light on the origin and fate of the polymer-based emission.[10] Hence, the steady-state optical characterization will provide first insights into energy- and electron-transfer pathways. In combination with the investigated synthetic procedures, the presented work and the results show the suitability of the various orthogonal linkages to ensure efficient Ru emission quenching. The facile modular assembly is believed to assist the design and synthesis of future architectures, e.g., D_n−P−A_m triads.

EXPERIMENTAL SECTION

Materials. All reagents were purchased from ABCR, Acros Organics, Alfa Aesar, Apollo Scientific, Sigma-Aldrich, or TCI Chemicals and were used without further purification unless otherwise noted. Dry pyridine and dry *N*,*N*-dimethylformamide (DMF) were commercially available. All solvents were degassed before use. THF was dried using a PureSolv-EN solvent purification system (Innovative Technology). $[Ru(dqp)(dqp\text{-}OH)][PF_6]_2$ (**3**, dqp is 2,6-di(quinolin-8-yl)pyridine, dqp-OH is 4-hydroxy-2,6-di(quinolin-8-yl)pyridine), 4-bromophenyl-2,6-di(quinolin-8-yl)pyridine (dqp-ph-Br), $[Ru(dqp)(dqp\text{-}ph\text{-}Br)][PF_6]_2$, and $[Ru(dqp)(CH_3CN)_3][PF_6]_2$ were prepared as previously described.[9,30,31] dba is dibenzylidene acetone. SPhos is 2-dicyclohexylphosphino-2′,6′-dimethoxybiphenyl. PMDETA is *N*,*N*,*N*′,*N*″,*N*″-pentamethyldiethylenetriamine.

*N-(2-Ethylhexyl)naphthalene-1,8-dicarboxyanhydride-4,5-dicarboxyimide (Adopted from Ref 32) (**1**).* Five microwave vials were each charged with 1,4,5,8-naphthalenetetracarboxylic dianhydride (0.800 g, 2.980 mmol), 2-ethylhexylamine (0.480 mL, 2.980 mmol), and dry DMF (20 mL). After the vials were capped and flushed with nitrogen for 10 min, the brown suspension was homogenized by ultrasound sonication. Subsequently, the vials were heated using microwave irradiation to 75 °C for 5 min and then to 140 °C for 15 min. The batches were combined, and the excess of solvent was removed under reduced pressure; the brown residue was resuspended in acetone (100 mL) and added dropwise to 1 M aqueous HCl (150 mL). The solid was filtered off and washed with water. The crude product was used without further purification (5.430 g, 96%, purity approximately 80% by ^{1}H NMR). ^{1}H NMR (300 MHz, $CDCl_3$): δ 8.83 (s, 4H, NaphH), 4.35−4.00 (m, 2H, CH_2), 2.12−1.86 (m, 1H, CH), 1.51−1.17 (m, 8H, 4 × CH_2), 1.06−0.69 (m, 6H, 2 × CH_3).

*N-(2-Ethylhexyl)-N′-(4-vinylphenyl)-naphthalene-1,4,5,8-dicarboxydiimide (Adopted from Ref 33) (**2**).* Crude **1** (5.430 g, 1 equiv), 4-aminostyrene (2.040 g, 1.2 equiv, 17.120 mmol), and $ZnSO_4 \cdot 1H_2O$ (1.540 g, 0.6 equiv, 8.560 mmol) were dissolved in dry pyridine (100 mL) under nitrogen. The mixture was heated to reflux for 4 h. Then the black reaction mixture, which contained white solids, was added dropwise to 1 M aqueous HCl (800 mL). After filtration the residue was dissolved in CH_2Cl_2 and washed with brine and water. The organic layer was dried over $MgSO_4$. Subsequently, the crude product was purified by two flash column chromatography runs (silica, eluent: CH_2Cl_2) to yield a yellow solid (3.300 g, 60%). ^{1}H NMR (250 MHz, $CDCl_3$): δ 8.81 (s, 4H, NaphH), 7.61 (d, J = 8.5 Hz, 2H, ArH), 7.29 (d, J = 8.5, 2H, ArH), 6.81 (dd, J = 17.5, 11.0 Hz, 1H, C**H**═CH_2), 5.84 (d, J = 17.5 Hz, 1H, CH═C**H**$_2$-trans), 5.37 (d, J = 11.0 Hz, 1H, CH═C**H**$_2$-cis), 4.32−4.02 (m, 2H, CH_2), 2.07−1.84 (m, 1H, CH), 1.49−1.21 (m, 8H, 4 × CH_2), 1.02−0.82 (m, 6H, 2 × CH_3). ^{13}C NMR (101 MHz, $CDCl_3$): δ 163.2, 163.0, 138.6, 136.0, 133.8, 131.4, 131.1, 128.6, 127.3, 127.1, 127.0, 126.9, 126.7, 115.5, 44.7, 38.0, 30.7, 28.6, 24.1, 23.0, 14.1, 10.6. Elem anal. calcd for $C_{30}H_{28}N_2O_4$: C, 74.98%; H, 5.87%; N, 5.83%; found: C, 75.10%; H, 5.75%; N, 5.69%. MS (ESI-ToF) m/z: 481.280 ($[M + H]^+$). T_d = 230 °C.

*$[Ru(dqp)(dqp\text{-}ph\text{-}C{\equiv}C{-}H)][PF_6]_2$ (**4**).* A vial was charged with $[Ru(dqp)(dqp\text{-}ph\text{-}Br)][PF_6]_2$ (0.030 g, 0.025 mmol) and $Pd(PPh_3)_4$ (0.003 g, 0.003 mmol). The vial was sealed and purged with nitrogen. Then dry DMF (3.0 mL), a fine suspension of copper(I) iodide (0.0005 g, 0.003 mmol) in DMF (0.078 mL), triethylamine (1.5 mL), and triisopropylsilylacetylene (0.006 mL) were added. Subsequently, the reaction mixture was heated to 60 °C for 16 h. Afterward, the reaction was cooled to room temperature and was precipitated in aqueous NH_4PF_6. The red precipitate was extracted from the aqueous phase with CH_2Cl_2, and the organic extracts were washed with water, dried over Na_2SO_4, and concentrated under reduced pressure. The crude product was purified by column chromatography using a mixture of acetonitrile/H_2O/$KNO_{3(aq)}$ (40/4/1) as eluent. The product fractions were combined, and the anion exchange was performed by precipitation in an aqueous NH_4PF_6 solution (0.029 g, 91%).

Deprotection. The complex (0.016 g, 0.012 mmol) was deprotected by stirring with tetrabutylammonium fluoride (0.003 g, 0.012 mmol) in a mixture of THF (2.0 mL) and MeOH (1.0 mL) overnight. The reaction mixture was quenched with water. Subsequently, the solvent was evaporated under reduced pressure, and the crude product was redissolved in a minimum amount of acetonitrile and precipitated in an aqueous NH_4PF_6 solution. The product was filtered, washed with water, and dried to yield **4** as an red solid (0.014 g, 98%). ^{1}H NMR (600 MHz, CD_3CN): δ 8.17 (t, J = 8.0 Hz, 1H), 8.12 (dd, J = 5.2, 1.4 Hz, 2H), 8.11 (s, 2H), 8.09−8.07 (m, 4H), 8.07 (s, 2H), 7.95 (m, 2H), 7.91−7.87 (m, 4H), 7.74 (dd, J = 7.4, 1.1 Hz, 2H), 7.72−7.65 (m, 6H), 7.47 (dd, J = 16.0, 8.4 Hz, 4H), 7.11−7.00 (m, 4H), 3.58 (s, 1H). ^{13}C NMR (151 MHz, CD_3CN): δ 159.5, 159.4, 158.1, 157.7, 149.4, 147.6, 147.4, 139.1, 138.6, 138.5, 137.3, 134.4, 133.9, 133.8, 132.8, 132.7, 131.6 (2×), 128.9, 128.6,

DOI: 10.1021/acs.macromol.5b02717
Macromolecules 2016, 49, 2112−2123

127.8 (2×), 127.6, 127.5, 126.2, 124.8, 123.0, 122.9, 83.4, 81.2. HR-ESI ($[C_{54}H_{34}N_6Ru]^{2+}$) *m/z*: calcd 434.0939, found: 434.0966. Error: 4.6 ppm.

*[Ru(dqp)(dqp-ph-py)][PF$_6$]$_2$ (**5**).* A microwave vial was charged with [Ru(dqp)(dqp-ph-Br)][PF$_6$]$_2$ (0.090 g, 0.098 mmol), 4-pyridylboronic acid (0.014 g, 0.114 mmol), Pd(dba)$_2$ (0.003 g, 0.006 mmol), SPhos (0.007 g, 0.018 mmol), and K_2CO_3 (0.040 g, 0.293 mmol). Then acetonitrile (3.0 mL) and water (1.5 mL) were added, and the vial was sealed. The solution was purged with nitrogen for 10 min and heated to 100 °C for 16 h. Afterward, the reaction mixture was allowed to cool to room temperature; subsequently, the mixture was added into an aqueous NH_4PF_6 solution. The fine suspension was extracted three times with CH_2Cl_2, and the combined organic layers were washed with water and brine. After drying over Na_2SO_4 the solvent was evaporated under reduced pressure, and the crude product was purified by flash column chromatography (diol-functionalized silica, eluent: CH_2Cl_2/acetonitrile 95/5). Finally, diffusion-controlled crystallization (diethyl ether into acetonitrile solution) gave the desired complex **5** (0.060 g, 67%). ^{1}H NMR (400 MHz, CD_3CN): δ 8.69 (d, J = 5.9 Hz, 2H), 8.25−8.15 (m, 3H), 8.17−8.13 (m, 2H), 8.12−8.06 (m, 8H), 8.00−7.94 (m, 2H), 7.94−7.88 (m, 4H), 7.74 (dd, J = 7.4, 1.2 Hz, 2H), 7.71 (ddd, J = 8.1, 3.3, 1.2 Hz, 6H), 7.48 (dd, J = 15.9, 8.4 Hz, 4H), 7.13−7.01 (m, 4H). ^{13}C NMR (101 MHz, CD_3CN): δ 159.5 (2×), 158.1, 157.8, 151.4, 149.7, 147.6, 147.5, 140.7, 139.2, 138.6, 138.5, 137.6, 134.5, 134.0, 132.8 (2×), 131.6, 129.2, 128.9 (2×), 127.8 (2×), 127.6, 127.5, 126.3, 123.1, 122.9, 122.4. HR-ESI ($[C_{57}H_{37}N_7Ru]^{2+}$) *m/z*: calcd: 460.6071, found: 460.6075. Error: 0.8 ppm.

Polymerization (Adopted from Ref 9) and Azide Functionalization. *Chloro-End-Functionalized Poly(naphthalene diimide) Cl-**p2**$_{17}$.* A glass tube equipped with a septum, and an external overhead flushing with nitrogen was used for the polymerization (see Supporting Information). The reaction vessel was charged with **2** (0.500 g, 1.040 mmol), *N*-(*tert*-butyl)-*O*-(1-(4-(chloromethyl)-phenyl)ethyl)-*N*-(2-methyl-1-phenylpropyl)hydroxylamine (CMSt-TIPNO) (0.019 g, 0.052 mmol), and anisole (4.0 mL), purged with nitrogen for 20 min, and placed in a preheated oil bath (120 °C). After 17 h the reaction mixture was diluted with CH_2Cl_2 and was precipitated in cold MeOH. Unreacted monomer was removed by preparative SEC (Bio-Beads S-X1, CH_2Cl_2). The polymer was obtained as a bright yellow powder after precipitation in MeOH. Yield: 0.400 g. SEC ($CHCl_3$/IPA/NEt_3 94/2/4, PS calibration): M_n = 6400 g/mol, $Đ$ = 1.11. ^{1}H NMR (300 MHz, $CDCl_3$): δ 9.04−7.98 (br), 7.78−6.66 (br), 4.73−4.42 (br), 4.36−3.60 (br), 2.92−1.71 (br), 1.51−1.05 (br), 1.05−0.45 (br). MS (MALDI-ToF, DCTB + NaTFA) *m/z*: 7,384 ($[(C_{30}H_{28}N_2O_4)_{15}C_9H_{10}Cl + Na]^+$).

*Azide-End-Functionalized Poly(naphthalene diimide) N$_3$-**p2**$_{17}$. Safety advice: sodium azide is very toxic; personal protection precautions should be taken. Heavy metal azides are explosive. Do not use metal spatula.* A glass vial was charged with Cl-**p2**$_{17}$ (0.033 g, 0.005 mmol, 1 equiv) and sodium azide (0.001 g, 0.016 mmol, 3 equiv), capped, and placed under a nitrogen atmosphere. Dry DMF (1 mL) was added, and the reaction mixture was immersed in an oil bath at 60 °C at which the polymer dissolved. After 48 h CH_2Cl_2 and water were added to the formed suspension, and the layers were separated. The aqueous layer was extracted two times with CH_2Cl_2. The combined organic layers were washed with brine and dried over Na_2SO_4. After removal of the solvent under reduced pressure, a yellow solid was obtained. Yield: 0.033 g. SEC ($CHCl_3$/IPA/NEt_3 94/2/4, PS calibration): M_n = 6300 g/mol, $Đ$ = 1.08. ^{1}H NMR (300 MHz, $CDCl_3$): δ 9.04−7.98 (br), 7.78−6.66 (br), 4.56−4.22 (br), 4.23−3.60 (br), 2.83−1.65 (br), 1.51−1.05 (br), 1.05−0.45 (br). MS (MALDI-ToF, DCTB + NaTFA) *m/z*: 7,391 ($[(C_{30}H_{28}N_2O_4)_{15}C_9H_{10}N_3 + Na]^+$). IR (KBr): $\tilde{\nu}$ [cm^{-1}] = 2100 (w, $\nu_{as}(N_3)$).

*End-Functionalization Procedures (Dyads and Reference Complexes). [Ru(dqp)(dqp-O-**p2**$_{17}$)][PF$_6$]$_2$ (**D1**).* A vial was charged with Cl-**p2**$_{17}$ (0.062 g, 0.009 mmol, 2 equiv), K_2CO_3 (0.001 g, 0.009 mmol, 2 equiv), and **3** (0.005 g, 0.009 mmol, 1 equiv), sealed, and placed under a nitrogen atmosphere. Dry DMF (1.0 mL) was added, and the resulting solution was heated to 60 °C. The reaction progress was monitored by TLC (aluminum oxide, CH_2Cl_2/MeOH 95/5) and analytical size exclusion chromatography (DMAc + 0.08% NH_4PF_6, diode array detection). After 24 h only little conversion was noticed; thus, potassium iodide (0.002 g, 0.001 mmol, 2 equiv) was added as catalyst. After an additional 24 h and TLC analysis, further base and potassium iodide were added. The reaction was continued until no further conversion was monitored by TLC (in total 72 h). The mixture was diluted with a minimum amount of THF and precipitated into aqueous NH_4PF_6 solution. The red precipitate was filtered off and washed with water. Unreacted complex **3** was recovered by column chromatography (diol-functionalized silica; eluent: CH_2Cl_2 to CH_2Cl_2/MeOH 95/5). The polymer-containing product was purified from excess polymer Cl-**p2**$_{17}$ by column chromatography (aluminum oxide; eluent: CH_2Cl_2 to CH_2Cl_2/MeOH 95/5). The dyad **D1** was obtained as a red powder after drying (0.020 g, 55%). ^{1}H NMR (600 MHz, $CDCl_3$): δ 8.89−8.00 (br, **p2**$_{17}$), 8.06 (br, Ru), 8.00 (br, Ru), 7.92 (br, Ru), 7.84 (br, Ru), 7.77 (br, Ru), 7.65 (br, Ru). 7.54 (br, Ru), 7.48 (br, Ru), 7.57−6.37 (br, **p2**$_{17}$), 5.67−5.40 (br, linker), 4.25−3.71 (br, **p2**$_{17}$), 3.07−1.70 (br, **p2**$_{17}$), 1.47−1.04 (br, **p2**$_{17}$), 0.99−0.47 (br, **p2**$_{17}$).

*[Ru(dqp)(dqp-ph-py-**p2**$_{17}$)][PF$_6$]$_3$ (**D2**).* Cl-**p2**$_{17}$ (0.013 g, 0.002 mmol, 2 equiv) and **5** (0.001 mg, 0.001 mmol, 1 equiv) were dissolved in a mixture of $CHCl_3$ and CH_3CN (0.32 and 0.07 mL), and the resulting solution was heated to 50 °C. After 48 h the conversion was very low as monitored by TLC (aluminum oxide, CH_2Cl_2/MeOH 95/5) and analytical size exclusion chromatography (DMAc + 0.08% NH_4PF_6, diode array detection). Subsequently, KPF_6 (0.37 mg, 0.002 mmol, 2 equiv) and potassium iodide (0.33 mg, 0.002 mmol, 2 equiv) were added, and the reaction mixture was heated to 70 °C until the complex was fully converted (48 h, reaction progress monitored by TLC). The solvent was removed under reduced pressure, and the excess of polymer was removed by column chromatography (aluminum oxide; eluent: CH_2Cl_2 to CH_2Cl_2/MeOH 95/5). The desired product was dissolved in a minimal amount of THF and was precipitated into aqueous NH_4PF_6 solution, filtered off, and washed with water. After drying the dyad **D2** was obtained as a red powder (isolated yield: 0.003 g, 40%). ^{1}H NMR (600 MHz, CD_2Cl_2): δ 9.06−8.14 (br, **p2**$_{17}$), 8.10 (br, Ru), 8.00 (br, Ru), 7.82 (br, Ru), 7.69 (br, Ru), 7.54 (br, Ru), 7.48 (br, Ru), 7.65−6.68 (br, **p2**$_{17}$), 6.21−5.91 (br, linker), 4.46−3.76 (br, **p2**$_{17}$), 3.18−1.70 (br, **p2**$_{17}$), 1.47−1.00 (br, **p2**$_{17}$), 0.99−0.51 (br, **p2**$_{17}$).

*[Ru(dqp)(dqp-ph-tr-**p2**$_{17}$)][PF$_6$]$_2$ (**D3**).* A microwave vial was charged with N$_3$-**p2**$_{17}$ (0.015 g, 0.003 mmol, 1 equiv) and **4** (0.009 g, 0.008 mmol, 3 equiv), sealed, and place under a nitrogen atmosphere. Then dry DMF (1.0 mL), a solution of copper(I) bromide (0.001 g, 0.005 mmol, 2 equiv) in DMF (0.1 mL), and a solution of PMDETA (0.02 mL, 0.24 M in DMF) were added. Subsequently, the reaction mixture was stirred at room temperature. The reaction progress was monitored by TLC (aluminum oxide, CH_2Cl_2/MeOH 95/5) and analytical size exclusion chromatography (DMAc + 0.08% NH_4PF_6, diode array detection). After 16 h the solution was concentrated under reduced pressure, and the crude product was redissolved in CH_2Cl_2 and water. The organic layer was separated, and the aqueous layer was extracted two times with CH_2Cl_2. The organic extracts were combined, excess of solvent was removed under reduced pressure, and the crude product was purified by column chromatography (amino-functionalized silica; eluent: CH_2Cl_2/MeOH 98/2). The dyad **D3** was obtained as red solid (0.013 g, 71%). ^{1}H NMR (600 MHz, CD_2Cl_2): δ 8.67−8.14 (br, **p2**$_{17}$), 8.23 (br, Ru), 8.02 (br, Ru), 7.94 (br, Ru), 7.90 (br, Ru), 7.86 (br, Ru), 7.74 (br, Ru), 7.62 (br, Ru), 7.46 (br, Ru), 7.14 (br, Ru), 7.08 (br, Ru), 7.04 (br, Ru), 7.51−6.90 (br, **p2**$_{17}$), 5.57−5.40 (br, linker), 4.10−3.74 (br, **p2**$_{17}$), 2.11−1.62 (br, **p2**$_{17}$), 1.62−1.39 (br, **p2**$_{17}$), 1.36−0.97 (br, **p2**$_{17}$), 0.90−0.60 (br, **p2**$_{17}$).

*[Ru(dqp)(dqp-O-bn)][PF$_6$]$_2$ (**C1**).* A microwave vial was charged with [Ru(dqp)(dqp-OH)][PF$_6$]$_2$ (0.008 g, 0.007 mmol), potassium iodide (0.005 g, 0.030 mmol), and K_2CO_3 (0.004 g, 0.030 mmol), sealed, and placed under a nitrogen atmosphere. Subsequently, dry DMF (1 mL) and a solution of benzyl chloride in DMF (0.082 mL, 0.27 M) were added via a syringe. The resulting mixture was stirred at

DOI: 10.1021/acs.macromol.5b02717
Macromolecules 2016, 49, 2112−2123

Scheme 1. Synthesis of Monomer 2 and Subsequent Polymerization and Postpolymerization Modification[a]

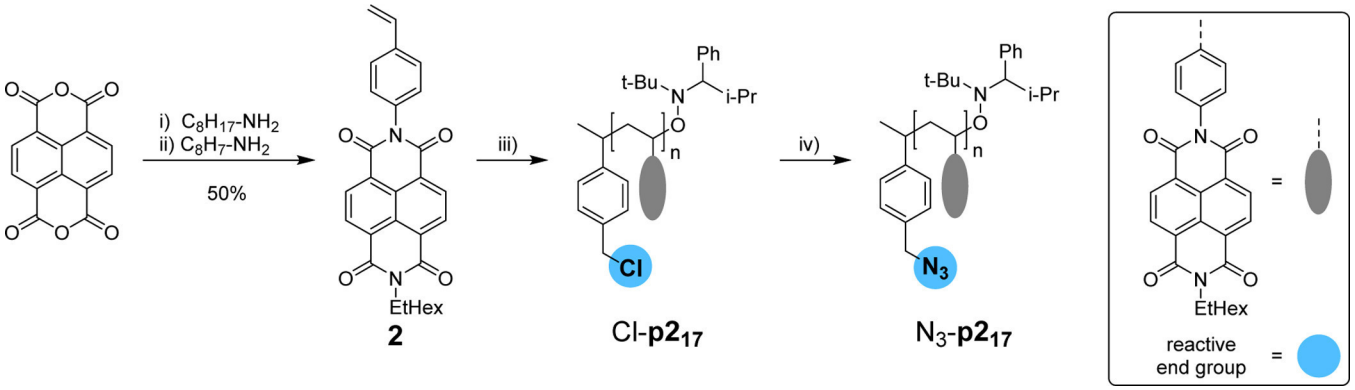

[a]Reagents and conditions: (i) DMF, microwave irradiation, N_2, 75 °C (5 min), 140 °C (15 min); (ii) 4-aminostyrene, $ZnSO_4 \cdot 1H_2O$, pyridine, reflux, 4 h; 50% over both steps; (iii) CMSt-TIPNO, anisole, N_2, 120 °C, 17 h; (iv) NaN_3, DMF, N_2, 60 °C, 48 h.

60 °C, until TLC analysis (silica, eluent: acetonitrile/H_2O/$KNO_{3\ (aq)}$ 40/4/1) showed complete conversion. After 16 h, the reaction mixture was allowed to cool to room temperature and was precipitated into an aqueous NH_4PF_6 solution. The red precipitate was filtered off, washed with water, and redissolved in acetonitrile. Then the solvent was evaporated under reduced pressure, and the crude product was purified by flash column chromatography (diol-functionalized silica; eluent: CH_2Cl_2/MeOH 95/5). Finally, diffusion-controlled crystallization with acetonitrile and diethyl ether gave the desired complex (0.007 g, 75%). ^{1}H NMR (600 MHz, CD_3CN): δ 8.15 (t, J = 8.0 Hz, 1H), 8.12 (dd, J = 5.1, 1.3 Hz, 2H), 8.10−8.04 (m, 6H), 7.87 (d, J = 8.0 Hz, 2H), 7.73 (ddd, J = 17.5, 7.4, 1.1 Hz, 4H), 7.68 (ddd, J = 8.2, 5.0, 1.0 Hz, 4H), 7.54−7.49 (m, 4H), 7.49−7.40 (m, 7H), 7.06 (ddd, J = 9.1, 8.2, 5.2 Hz, 4H), 5.40 (d, J = 11.4 Hz, 1H), 5.31 (d, J = 11.4 Hz, 1H). ^{13}C NMR (151 MHz, CD_3CN): δ 167.2, 159.6, 159.5, 158.6, 157.9, 147.7, 147.5, 138.9, 138.6, 138.4, 136.4, 134.1, 133.9, 132.9, 132.6, 131.7, 131.5, 129.9, 129.7, 129.1, 128.9, 127.8, 127.6, 123.0, 122.9, 116.0, 72.2. HR-ESI ($[C_{53}H_{36}N_6ORu]^{2+}$) m/z: calcd: 437.0992; found: 437.1020. Error: 4.9 ppm.

Note: the methylene protons of the benzyl group cause two doublets (5.40 and 5.31 ppm), which is assigned to a restricted conformational freedom and a resulting nonequivalence of the protons.

[Ru(dqp)(dqp-ph-py-bn)](PF$_6$)$_3$ ***(C2)***. A microwave vial was charged with [Ru(dqp)(dqp-ph-py)][PF_6]$_2$ (0.010 g, 0.008 mmol), potassium iodide (0.003 g, 0.017 mmol), and acetonitrile (0.5 mL), sealed, and placed under a nitrogen atmosphere. Subsequently, a solution of benzyl chloride in DMF (0.062 mL, 0.27 M) was added via a syringe, and the reaction mixture was heated to 70 °C, until TLC analysis (silica; eluent: acetonitrile/H_2O/$KNO_{3\ (aq)}$ 40/4/1) showed complete conversion. After 16 h, the reaction was allowed to cool to room temperature and was precipitated into an aqueous NH_4PF_6 solution. The aqueous solution was extracted three times with dichloromethane, and the combined organic layers were washed with water and brine. After drying over Na_2SO_4 the solvent was evaporated under reduced pressure, and the crude product was purified by flash column chromatography (amine-functionalized silica; eluent: CH_2Cl_2/MeOH 95/5). The desired complex was isolated as a dark red solid (0.011 g, 92%). ^{1}H NMR (600 MHz, CD_3CN): δ 8.80 (d, J = 7.0 Hz, 2H), 8.35 (d, J = 7.0 Hz, 2H), 8.22−8.16 (m, 4H), 8.14 (dd, J = 5.1, 1.4 Hz, 2H), 8.12 (s, 1H), 8.11−8.07 (m, 7H), 7.92 (m, 4H), 7.75 (dd, J = 7.4, 1.1 Hz, 2H), 7.74−7.68 (m, 4H), 7.55−7.43 (m, 10H), 7.12−7.03 (m, 4H), 5.74 (s, 2H). ^{13}C NMR (151 MHz, CD_3CN): δ 159.5 (2×), 158.3, 157.7, 156.6, 148.8, 147.6, 147.5, 145.5, 140.6, 139.2, 138.6 (2×), 136.2, 134.5, 134.1 (2×), 134.0, 132.8, 132.7, 131.7, 131.6, 130.8, 130.5, 130.2, 130.1, 130.0, 129.7, 129.0, 127.8 (2×), 127.6, 127.5, 126.5, 126.4, 123.1, 123.0, 64.7. HR-ESI ($[C_{64}H_{44}N_7Ru]^{3+}$) m/z: calcd: 337.4228, found: 337.4250. Error: 4.7 ppm.

[Ru(dqp)(dqp-ph-tr-bn)][PF$_6$]$_2$ ***(C3)***. A microwave vial was charged with [Ru(dqp)(dqp-ph-C≡C−H)] (0.008 g, 0.007 mmol) and copper(I) bromide (0.002 g, 0.014 mmol), sealed, and placed under a nitrogen atmosphere. Subsequently, dry DMF (1 mL), a solution of PMDETA in DMF (0.058 mL, 0.24 M), and a solution of benzyl azide in CH_2Cl_2 (0.028 mL, 0.5 M) were added via a syringe. Then the reaction mixture was heated at 60 °C, until TLC analysis (silica; eluent: acetonitrile/H_2O/$KNO_{3\ (aq)}$ 40/4/1) showed complete conversion. After 16 h, the reaction mixture was allowed to cool to room temperature and precipitated into an aqueous NH_4PF_6 solution. The red precipitate was filtered off, washed with water, and redissolved in acetonitrile. Subsequently the solvent was evaporated under reduced pressure, and the crude product was purified via flash column chromatography (amine-functionalized silica; eluent: CH_2Cl_2/MeOH 95/5). The complex was isolated as a dark red solid (0.008 g, 84%). ^{1}H NMR (600 MHz, CD_3CN): δ 8.26 (s, 1H), 8.17 (dd, J = 9.3, 6.7 Hz, 1H), 8.15 (s, 2H), 8.14 (dd, J = 5.1, 1.3 Hz, 2H), 8.08 (dd, J = 2.3, 1.3 Hz, 3H), 8.07 (s, 3H), 8.06−8.01 (m, 4H), 7.90 (dt, J = 7.9, 1.9 Hz, 4H), 7.74 (dd, J = 7.4, 1.1 Hz, 2H), 7.72−7.68 (m, 4H), 7.52−7.43 (m, 4H), 7.44−7.35 (m, 4H), 7.06 (ddd, J = 8.7, 7.5, 4.8 Hz, 4H), 5.62 (s, 2H). ^{13}C NMR (151 MHz, CD_3CN): δ 159.5, 159.4, 158.0, 157.7, 149.9, 147.6, 147.5, 147.3, 139.1, 138.5 (2×), 136.7, 136.2, 134.4, 133.9 (2×), 132.8 (2×), 131.5 (2×), 129.9, 129.4, 129.0, 128.9, 127.8, 127.7, 127.6, 127.5, 127.1, 126.0, 123.0, 122.9, 122.6, 54.5. HR-ESI ($[C_{61}H_{41}N_9Ru]^{2+}$) m/z: calcd: 500.6259, found: 500.6272. Error: 1.0 ppm.

RESULTS AND DISCUSSION

The modular assembly of the dyads relies on two stages, i.e., the individual preparation of the functional building blocks and their covalent coupling by polymer-analogous reactions.

Preparation of Building Blocks. The styrenic naphthalene diimide (NDI) **2** was prepared from 1,4,5,8-naphthalenetetracarboxylic dianhydride by an optimized two-step synthesis compared to our previous reported method (Scheme 1).[10] The procedure requires fewer synthetic steps and only one chromatographic purification step, which results in significantly improved yields (50% compared to 10%): First, the monoimide was prepared by the reaction of the dianhydride with 2-ethylhexylamine in DMF under microwave irradiation.[32] The crude product **1** contained approximately 20% bis-alkylated product but was used without further purification. Next, the styrenic group was introduced by the reaction of compound **1** with an excess of 4-aminostyrene in pyridine in the presence of zinc(II) sulfate as described for similarly functionalized NDIs.[33]

The styrenic monomer **2** was polymerized by nitroxide-mediated polymerization (NMP) using the functional initiator CMSt-TIPNO (Scheme 1) as reported previously.[10] Because of the similar solubility of monomer and polymer, the removal of

DOI: 10.1021/acs.macromol.5b02717
Macromolecules 2016, 49, 2112−2123

Scheme 2. Synthesis of Functional Ruthenium Complexes 4 and 5[a]

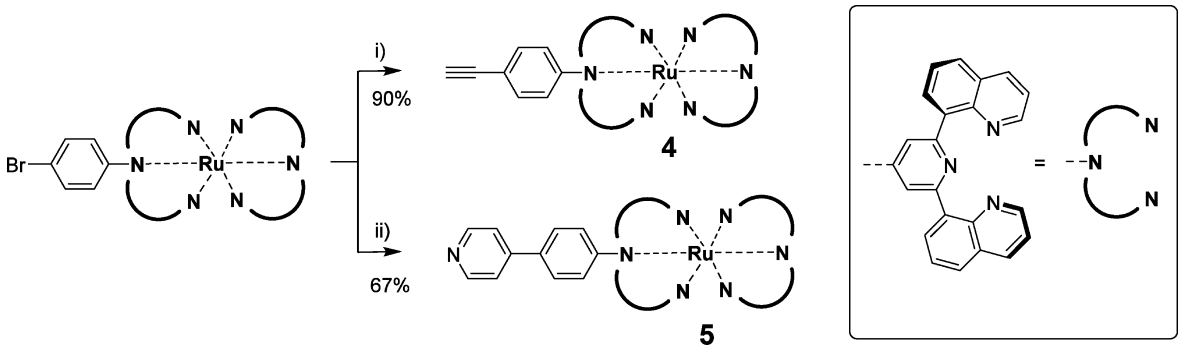

[a]Reagents and conditions: (i) TIPS−C≡C−H, $Pd(PPh_3)_4$, CuI, Et_3N, DMF, N_2, 60 °C, 16 h, Bu_4NF, THF, MeOH, RT, overnight, 90% isolated yield; (ii) 4-pyridineboronic acid, $Pd(dba)_2$, SPhos, K_2CO_3, CH_3CN, H_2O, 100 °C, 16 h, 67% isolated yield.

Scheme 3. Synthesis of Reference Complexes C1−C3 and the Respective Dyads D1−D3[a]

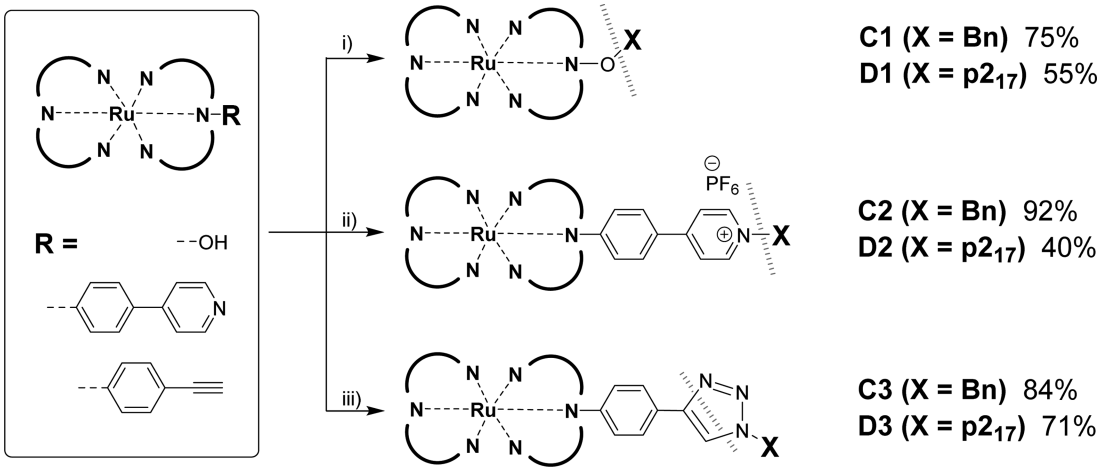

[a]Reagents and conditions: (i) K_2CO_3, KI, DMF, N_2, 60 °C, 72 h; (ii) KI, KPF_6, $CHCl_3$, CH_3CN, N_2, 70 °C, 96 h; (iii) CuBr, PMDETA, DMF, N_2, RT, 16 h. Gray dashed line illustrates the newly formed bond.

unreacted monomer was performed by preparative size-exclusion chromatography (Bio-Beads S-X1). The obtained polymer was characterized by analytical size exclusion chromatography and revealed a molar mass of 6400 g/mol (PS calibration) with a low dispersity ($Đ$ = 1.11). The ^{1}H NMR spectrum shows the typical broad NDI resonances in the aromatic region, whereby the resonance of the distinct chloromethyl group (around 4.6 ppm) enables the determination of the degree of polymerization and to monitor the progress of the functionalization reactions (*vide infra*). The chloromethyl group of Cl-**p2**$_{17}$ (the subscripted number represents the degree of polymerization according to NMR) was converted into the azide functionality. Note that **p2**$_{17}$ refers in the following to the polymer with the initiator's benzyl unit except the end group (chlorine, azide, or a ruthenium fragment; *vide infra*). The reaction was performed with sodium azide in DMF at 60 °C, resulting in a quantitative substitution of the chloride as judged from the shift of the methylene proton resonances in the ^{1}H NMR of N_3-**p2**$_{17}$ (from 4.6 to 4.4 ppm). The azide functionality was further confirmed by IR data, showing the appearance of the typical band at 2100 cm^{-1} (see Supporting Information). The analysis of pNDIs by mass spectrometry proved to be challenging applying standard conditions.[10] However, tuning the MALDI conditions enabled the identification of a characteristic series with the NDI repeating unit (480 amu). The centers of the unresolved isotope peaks can be assigned to specimen formed by nitroxide cleavage; i.e., the fragments carry the characteristic end groups (Cl or N_3) for the corresponding polymers (see Supporting Information). The comparison of the SEC data revealed negligible differences in molar mass and dispersity and, thus, indicates the absence of polymer degradation and undesired couplings during the azide functionalization (see Supporting Information).

The hydroxyl-decorated Ru complex (**3**) was synthesized according to a literature procedure,[9] whereas the functional complexes **4** and **5** were prepared by a "chemistry-on-the-complex" approach (Scheme 2). This methodology allows a simple preparation from reported [Ru(dqp)(dqp-ph-Br)]-$[PF_6]_2$. The alkyne functionality was introduced by Sonogashira cross-coupling in DMF/Et_3N with $Pd(PPh_3)_4$ as catalyst. After deprotection with tetrabutylammonium fluoride, the desired complex **4** was obtained in excellent yield (90%). The corresponding pyridine-equipped complex **5** was prepared by Suzuki cross-coupling using 4-pyridineboronic acid in 67% yield. The apparent lower yield of **5** is attributed to losses during purification and isolation of the pure product. Both new complexes were characterized by 1D and 2D NMR spectroscopy and HR-MS (see Supporting Information).

DOI: 10.1021/acs.macromol.5b02717
Macromolecules 2016, 49, 2112−2123

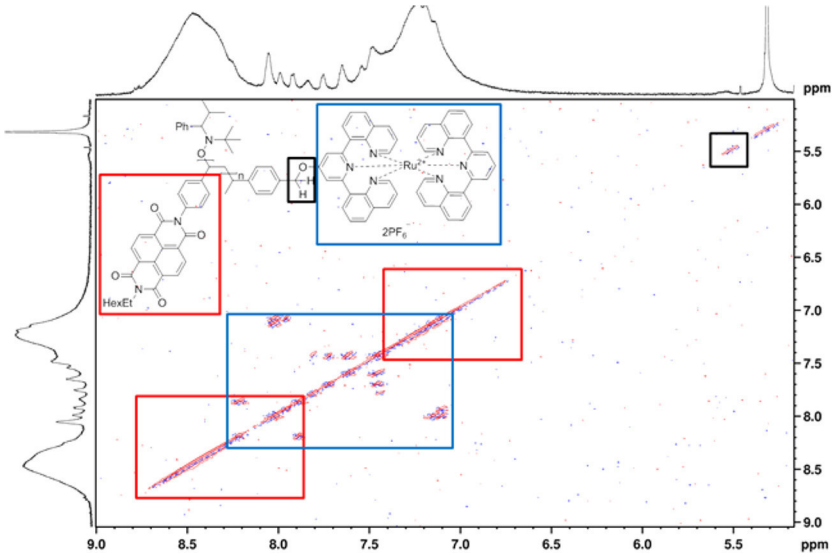

Figure 1. COSY NMR (600 MHz, CD_2Cl_2) of **D1** with typical resonances of the polymer (red), the complex's ligand scaffold (blue), and the linker (black).

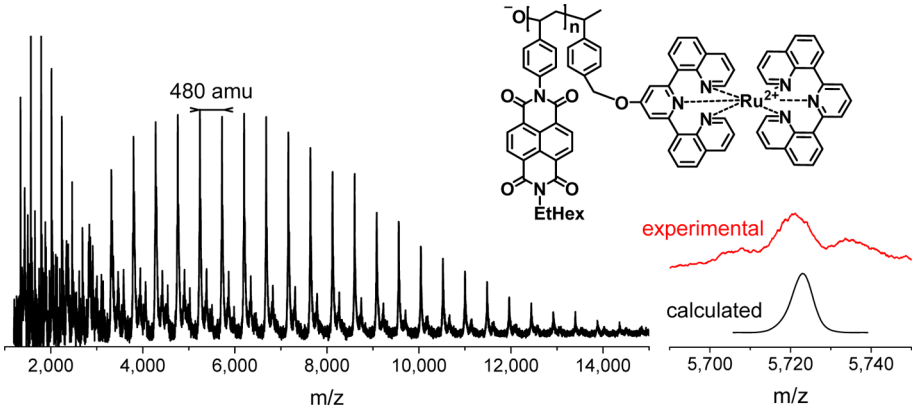

Figure 2. MALDI-ToF MS of **D1** with proposed structure of the fragments and with experimental (red) and calculated (black) isotopic pattern (matrix: dithranol + NaTFA).

Modular Assembly. Three different linkage reactions were investigated for the synthesized telechelic polymers and functionalized ruthenium complexes. A series of P−A_m dyads (Scheme 3) were prepared, i.e., Williamson ether synthesis from a hydroxyl group (top), quaternization of a pyridine unit (middle), and CuAAC reaction of a terminal alkyne (bottom). Additionally, the corresponding benzylated complexes (**C1**−**C3**) were synthesized analogously to the dyads, in order to serve as proper reference complexes for the quantitative emission quenching studies (*vide infra*). The comparable yields of the latter references complexes indicate the efficiency of the postpolymerization reactions, which will be detailed in the following paragraph.

Method Development (Nucleophilic Substitutions). The reaction of complex **3** and pNDI was reported previously;[10] however, the reaction with Cl-$\mathbf{p2}_{17}$ gave only low conversions to dyad **D1** and a more complicated purification procedure upon applying the reported conditions (Scheme 3, top). The reaction progress was monitored by thin-layer chromatography (TLC) and analytical size-exclusion chromotagraphy (SEC), which revealed no further conversion after 1 day. Hence, potassium iodide was added to enhance the reactivity in analogy to the Finkelstein reaction, which led to significantly increased conversion. Surprisingly, the reported purification protocol resulted in an incomplete separation of **D1** from complex **3**. This observation is rationalized by a decreased net polarity difference, which shifts the subtle balance between solubilization (promoted by the pNDI fragment) and retention (caused by the dicationic Ru complex fragment) unfavorably. Consequently, the shorter polymer chains of $\mathbf{p2}_{17}$ (6400 g/mol) vs. reported pNDI (9000 g/mol)[10] would lead to a dominating contribution of the Ru^{II}, in line with the aforementioned difficulties to remove complex **3**. Although the excess of nonfunctionalized polymer is readily removed by column chromatography on aluminum oxide (eluent: CH_2Cl_2/MeOH 18/1), the corresponding chromatography on silica revealed as nonsuitable. Organic solvent mixtures as used previously lead to no elution, which is attributed to the stronger interaction of the dicationic Ru^{II} fragment to silica. Using typical eluent systems for Ru^{II} complexes (a mixture of acetonitrile and aqueous potassium nitrate) resulted in severe streaking and coelution (attributed to solubility issues of the pNDI). Hence, we tested amino- and diol-functionalized silica gels, which are commercially available and benefit from a reduced surface polarity. This stationary phase can be run with all common solvents (mixtures) as eluents and, indeed, allowed

DOI: 10.1021/acs.macromol.5b02717
Macromolecules 2016, 49, 2112−2123

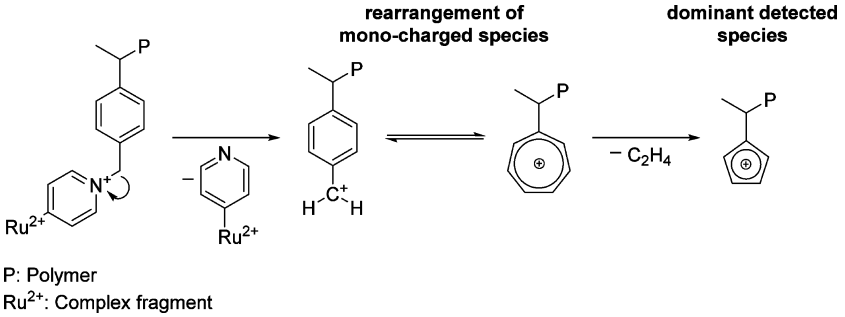

Figure 3. Proposed fragmentation of **D2** including benzyl cleavage, resulting in the formation of a singly charged polymer species and subsequent consecutive reactions.

the successful separation. Notably, no counterion exchange is necessary and thus facilitates the purification over the traditional eluent systems used on silica.[34] The ^{1}H NMR spectrum of **D1** is well resolved and agrees with the previous report;[10] i.e., it clearly confirms the characteristic shift of the bridging methylene protons in comparison to Cl-$\mathbf{p2}_{17}$ (4.57 ppm to 5.57 ppm) and the presence of the ligand scaffold of the Ru(II) fragment (Figure 1).

Further reoptimization of the mass spectrometry conditions led to the successful analysis by MALDI-ToF MS (Figure 2). The spectrum shows a peak distribution with the mass difference (Δm = 480 g/mol) of a naphthalene diimide unit. Although no isotope-resolved spectra could be obtained, the peaks can be assigned to a species generated by the fragmentation of the TIPNO group (see also Supporting Information).

An alternative nucleophilic substitution reaction was investigated for Cl-$\mathbf{p2}_{17}$ and the 4-pyridyl-decorated complex (**5**). As stated above, the reaction showed almost no conversion after 24 h at 50 °C. Therefore, potassium iodide and potassium hexafluorophosphate (as a source of non-nucleophile counterions to prevent the potential cleavage of the pyridinium) were added, and the temperature was raised to 70 °C. After 2 days, the quantitative conversion of complex **5** was achieved according to 3D SEC (see Supporting Information). The excess of polymer was removed by column chromatography on aluminum oxide to yield **D2** (40%). The apparent low yield arises from the small reaction scale and losses upon sampling.[35] The ^{1}H NMR spectrum confirmed the successful linkage on the basis of the shifts of the bridging methylene protons to 6 ppm (see Supporting Information). An intense fragmentation of **D2** was detected in the MALDI-ToF MS spectrum (see Supporting Information). The major series displays the typical spacing of the NDI repeating unit indicating the absence of the Ru fragment, as judged from the narrow peaks. This series can be rationalized by the typical elimination of the TIPNO group occurring at one polymer chain terminus (as also observed for the nonfunctionalized polymer), whereas the other chain terminus would correspond to C_7H_8. The latter fragment can be explained by the fragmentation of the pyridinium−Ru^{II} subunit (+3). Thereby, the carbon−nitrogen bond of the benzylpyridinium moiety is cleaved, and a singly charged polymer fragment is formed (Figure 3). Subsequently the rearrangement and the elimination of ethyne lead to a cyclopentadienyl cation as the dominant detected species, which is well-known for benzylic compounds.[36] Additionally, a second series appears at low molar masses in the mass spectrum. Surprisingly, this distribution indicates doubly charged specimen (Δm = 240 g/mol) and is tentatively assigned to the dyad after cleavage of the nitrogen−oxygen bond of the TIPNO (see Supporting Information).

Linkage via Triazole Formation. The dyad **D3** was prepared by copper(I)-catalyzed azide−alkyne cycloaddition of complex **4** with the azide-functionalized polymer N_3-$\mathbf{p2}_{17}$. The reaction was carried out using a standard protocol with copper(I) iodide, PMDETA, and DMF. After 16 h the reaction showed full conversion of the polymer (checked by TLC and SEC), and the dyad **D3** was isolated in good yields (71%) after column chromatography (*vide supra*). The yield compared to the observed full conversion of the polymer is attributed to losses due to samples which were taken to monitor the reaction progress. Consistent with the dyads **D1** and **D2**, the successful attachment of the complex at the polymer was proved by ^{1}H NMR spectroscopy, as the signals of the methylene protons of the linker are shifted from 4.3 to 5.6 ppm. The dyad **D3** exhibits the same fragmentation behavior in the MALDI-ToF MS as **D1**, i.e., the nitrogen−oxygen bond of the TIPNO end group is cleaved (see Supporting Information).

Table 1. Electrochemical Data from Cyclovoltammetry[a]

	E_{red} [V] (NDI^0/NDI^-)	E_{red} [V] (NDI^-/NDI^{2-})	E_{ox} [V] (Ru^{III}/Ru^{II})	E_{red} [V] (L^0/L^-)	E_{red} [V] ($L^-/^{2-}$)
D1	−1.05	−1.51	+0.54	−1.83	n.d.
D2	−1.05	−1.50	+0.51	−1.74	−1.94
D3	−1.05	−1.52	+0.51	−1.79	−1.97

[a] $E_{1/2}$ vs. $Fc^{+/0}$ in DMF containing 0.1 M $TBAPF_6$ using a scan rate of 200 mV/s.

Electrochemistry. The electrochemical properties of the dyads were analyzed by cyclic voltammetry using a standard three-electrode setup. The first cycle of each experiment was used for the analysis of the electrochemical processes. This approach ensures a clean electrode surface and prevents contaminations from side products, which may influence the measurement or alter the electrode's surface due to irreversible reactions.[37−39] A detailed analysis of the raw electrochemical data is further complicated due to the background signals; thus, a correction by subtraction of a blank measurement was executed to allow a more comprehensive analysis. The deviations from the ideal peak shape, particularly of the weak signals of the ruthenium fragment, are tentatively attributed to additional contributing parameters, e.g., different electron transfer rates, reorientation of the polymer chain upon accumulative charging, adsorption, etc. (see Figure 4 (left) and Supporting Information). More importantly, the redox couples can be assigned to the corresponding units and are summarized in Table 1 (reported vs. Fc^+/Fc^0). The cyclo-

DOI: 10.1021/acs.macromol.5b02717
Macromolecules 2016, 49, 2112−2123

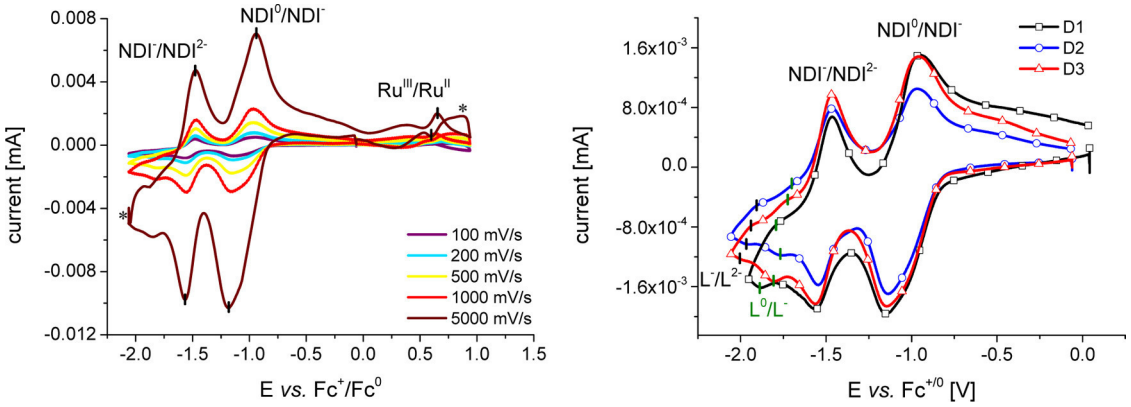

Figure 4. Left: background corrected cyclovoltammogram of **D1** showing two quasi-reversible reduction steps corresponding to the polymer (NDI^0/NDI^- and NDI^-/NDI^{2-}) and one reversible oxidation attributed to the ruthenium (Ru^{III}/Ru^{II}). Right: background corrected data of the negative potential range enabling the detection of the reduction of the ligand scaffold (L^0/L^- and L^-/L^{2-}) (0.1 M $TBAPF_6$, DMF, 500 mV/s). All shown spectra were smoothed using a 10-point moving average filter to remove a systematic noise pattern. Artifacts and displacements (marked with an asterisk) are caused by the applied analysis procedure (subtraction of the blank spectra without analyte).

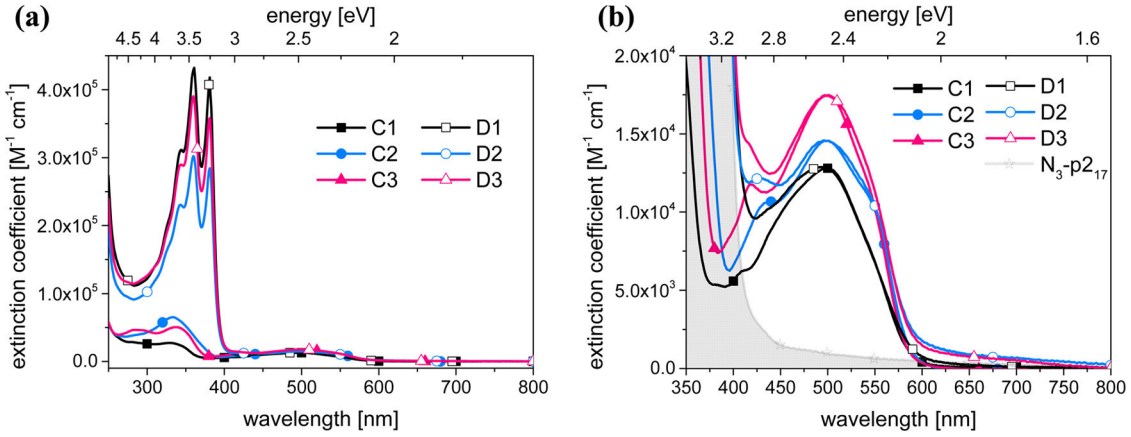

Figure 5. Absorption data of the reference complexes (**C1**−**C3**) and the corresponding dyads (**D1**−**D3**) in dichloromethane. (a) UV−vis spectral region illustrating the dominant UV absorption of the pNDI chains. (b) Inset of the MLCT region illustrating preserved optical properties of the Ru photosensitizer (gray area depicts the low-energy tail of the pNDI absorption).

voltammogram of **D3** is exemplarily shown in Figure 4 (left) with various scan rates. Two quasi-reversible reduction steps at −1.0 and −1.5 V were clearly detected corresponding to the naphthalene diimide units of the polymer. The asymmetry of the reduction peaks is assigned to kinetic effects besides the diffusion-controlled electron transfer, e.g., conformational changes within the polymer. The tailing of the anodic wave, i.e., upon reoxidation of the NDI^- units, is more pronounced for faster scan rates and indicates the kinetic effects of the accumulative charging. In fact, any deviations become less pronounced at slower scan rates (<500 mV/s). The reversible oxidation of the ruthenium center was detected as a small signal centered around 0.5 V. Interestingly, the respective potentials are similar for all prepared dyads, indicating that the nature of the linker has only a minor influence on the electrochemical properties of the metal center. Additional redox waves were observed at potentials below −1.51 V (Figure 4, right) and are assigned to the reduction of the complex fragment. The first ligand-centered reduction occurs at typical electrochemical potentials, i.e., between −1.74 and −1.83 V. Consequently, the exact potential is more strongly influenced by the substituent, i.e., the electron-donating ether bridge decreases the potential (−1.83 V), while the electron-deficient pyridinium moiety leads to less negative potentials (−1.74 V). The same trend is found for the second reduction step; however, this redox process was not determined for **D1** due to the necessary strong negative potential. In the case of **D2** an additional reduction of the pyridinium unit is expected around −1.4 to −1.5 V, which is probably overlapped by the intense NDI reduction.

Optical Spectroscopy. The steady-state optical properties of the dyads enable the analysis of photoinitiated processes, which will be related to the constituting functional building blocks, i.e., the pNDI block and the Ru^{II} photosensitizer. Thereby, the absorption spectra yield valuable information on potential interactions (e.g., H- or J-aggregation), while emission and excitation data detail both the properties as well as the origin of the excited states and enable the discussion of energy or electron transfer steps (*vide infra*). Previous studies have identified the formation of the charge-separated state and the quenching of the ^{3}MLCT emission, accompanied by additional polymer-based emissive states.[10] More importantly, the emission quantum yield serves as quantitative measure for the efficiency of light-induced processes, e.g., charge separation.

Absorption Spectroscopy. The absorption spectra of the model complexes (**C1**−**C3**) and the corresponding dyads (**D1**−**D3**) are depicted in Figure 5. The UV region is dominated by the intense absorption bands attributed to the $\pi \rightarrow \pi^*$ transitions of the NDI units (panel a). The spectral

DOI: 10.1021/acs.macromol.5b02717
Macromolecules 2016, 49, 2112−2123

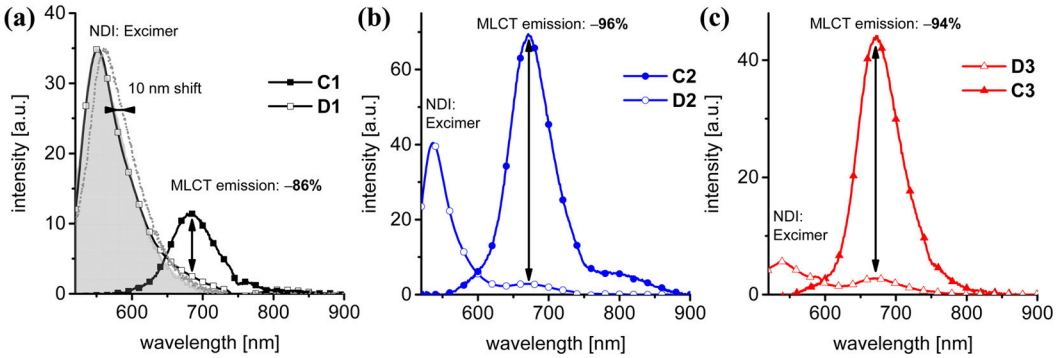

Figure 6. Emission data of the reference complexes and the corresponding dyads (aerated dichloromethane, room temperature, iso-absorbing solutions at 500 nm excitation). Arrows indicate quenching of the ^{3}MLCT emission (in %) of the dyad vs. the reference complex, respectively. Note the lower emission intensity of **C1** compared to **C2** and **C3** caused by a lower intrinsic quantum yield (not reported). (a) Ether-linked complex **C1** complemented by polymer-based emission (**D1**: gray area; dotted line: pNDI) to illustrate residual MLCT contribution. (b, c) Pyridinium- and triazole-linked congeners.

shape resembles the spectrum of individual naphthalene diimide units, e.g., absorption maxima centered at 360 and 380 nm. In line with a previous report, the absence of additional detectable features indicates negligible NDI–NDI interactions in solution, as expected upon aggregate formation in solution.[10] The visible region is governed by the Ru photosensitizer (panel b). The reference complexes (**C1**–**C3**) exhibit the typical metal-to-ligand charge transfer (MLCT) bands centered at 500 nm. The enhanced absorptivity of complexes **C2** and **C3** are attributed to the ligand's extend π-system, in agreement with a previous report.[31] More importantly, the spectral characteristics are preserved upon attachment of the polymer chain. These findings corroborate the electrochemical data and confirm the modular character of the photosensitizer–polymer assemblies, i.e., preserved optical properties of the individual building blocks (see Supporting Information).

Emission Spectroscopy. The reference complexes and respective dyads were investigated by steady-state emission spectroscopy under ambient conditions, i.e., in aerated dichloromethane at room temperature using iso-absorbing solutions at 500 nm excitation (Figure 6). The reference complexes display the typical Ru-based emission from the ^{3}MLCT state between 650 and 700 nm, which is slightly affected by the substitution pattern. In agreement with a previous report,[31] the electron-releasing alkoxy substitution (**C1**) leads to a bathochromic shift of approximately 15 nm in comparison to the π-extended phenyl-decorated complexes **C2** and **C3**. In agreement with the energy gap law, i.e., the emission decay is more efficient for lower excited state energies within a series,[22] the absolute quantum yield of **C1** is also significantly lower than for the phenyl-decorated congeners. More importantly, the emission spectra of the corresponding dyads differ markedly from the reference complexes. In all cases, the Ru emission is quenched and an additional emission centered at 550 nm is observed. A similar profile of the high-energy emission band is observed for the pristine pNDI and is therefore attributed to polymer-based emissive states (*vide infra*).[10] The efficiency of the ^{3}MLCT excited state quenching (Q_{MLCT}) is calculated from the residual Ru-based emission with respect to the corresponding reference complexes (Table 2). Noteworthy, the contribution of the overlapping polymer-based emission is accounted by subtracting a scaled pNDI spectrum, as depicted in Figure 6a. Following this procedure, the quenching efficiency was averaged between 650 and 700 nm (see Supporting Information) to yield reliable values for **C1** (86%), **C2** (96%), and **C3** (94%). Within the experimental errors, the ^{3}MLCT quenching appears to be independent of the length of the linker.

Table 2. UV–Vis Data of the Reference Complexes and Dyads[a]

	λ_{Abs} (MLCT) [nm]	λ_{Em} (MLCT) [nm]	Q_{MLCT} [%]
C1	500	684	
C2	500	670	
C3	500	670	
D1	496	684	86
D2	499	669	96
D3	500	669	94

[a] λ_{Abs} (MLCT) is the absorption maximum of the MLCT, λ_{Em} (MLCT) is the emission maximum of the MLCT, and Q_{MLCT} is the calculated quenching efficiency compared to the respective reference complex.

The origin of the polymer-based emission was investigated in more detail using diluted samples to circumvent inner filter effects in the previous data (*vide supra*). The UV–vis absorption spectra of monomer **2**, the nonfunctionalized pNDI, and the Ru-decorated polymer retain the typical absorption bands at 360 and 380 nm (Figure 7, panel a). In comparison to the monomer, both polymer compounds show decreased absorption at 380 nm as well as a slight tailing of the bathochromic shoulder. In addition, significant spectral shifts are observed at shorter wavelength, i.e., decreased absorption (<280 nm) and increased absorption (280–340 nm). These observations suggest that a certain fraction of the NDI chromophores experience a different local environment, e.g., solvent excluded volume within the polymer. In addition, the high local concentration and the spatial proximity of the NDI units may lead to partial (transient) aggregation or stacking of NDI units as commonly observed in solution.[15,40–46] This assignment is corroborated by the steady-state emission data (Figure 7b). Upon excitation at 360 nm, the monomer displays no detectable emission in line with related derivatives,[14] whereas the corresponding polymer displays a pronounced emission band around 413 nm. This observation is attributed to interacting NDI units, similar to the reported J-aggregates formed in solution.[15] Additionally, the emission band around 550 nm is detected at high polymer concentrations (×30)

DOI: 10.1021/acs.macromol.5b02717
Macromolecules 2016, 49, 2112–2123

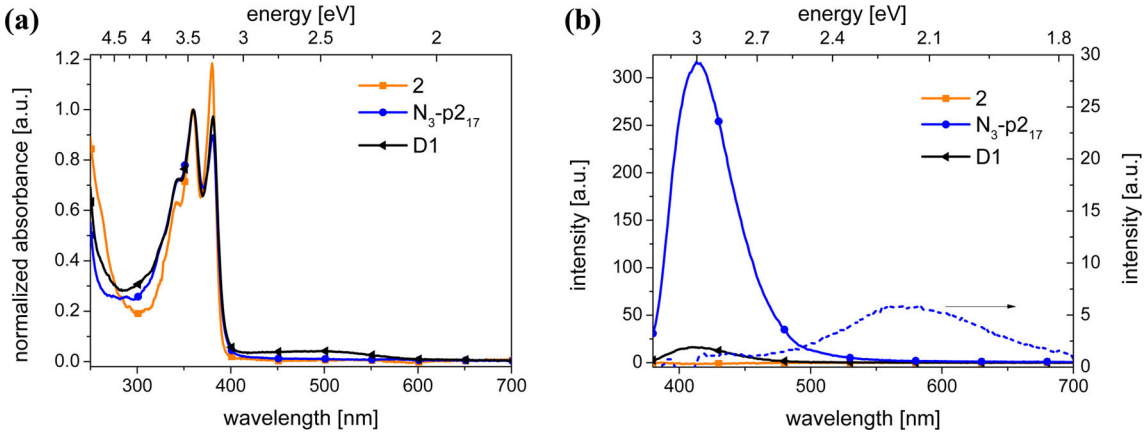

Figure 7. (a) Normalized absorption spectra (at 360 nm, optical density approximately 0.1) of **2**, N_3-**p2**$_{17}$, and **D1** in dichloromethane. (b) Emission spectra (excitation at 360 nm) showing emission bands centered at 413 nm (solid line, left axis) and 550 nm (concentrated sample of N_3-**p2**$_{17}$, optical density at 360 nm 2.5, dashed line refers to right axis as indicated by arrow, excitation at 360 nm).

(Figure 7, right inset, or see Supporting Information), which is reported for naphthalene diimide dimers (excimers) and their subsequent emission.[14,15,47−53] Apparently, upon higher concentrations more aggregated NDI specimen are formed and, thus, result in an apparent bathochromic emission shift. The corresponding excitation spectra recorded at 413 and 550 nm detection, respectively, yield spectral profiles that are significantly broadened with respect to the absorption spectrum (see Supporting Information). On the basis of all presented experimental data, the absorption of a UV photon in the nonfunctionalized polymer leads to either an excited NDI state (in a stack or aggregate, emission at 413 nm) or an excimer state (emission at 550 nm), which can undergo secondary processes to populate emissive states that are not accessible for isolated NDI units. For completion, the two-dimensional excitation−emission plots corroborate the made assignments; i.e., both polymer-based emissions show small Stokes shifts in contrast to the substantial spectral shift arising from the Ru emission (Supporting Information). In the case of the dyad (**D1**), the emission intensity at 413 nm is decreased significantly in comparison to the nonfunctionalized polymer, which is assigned to additional energy transfer processes involving the Ru fragment. However, any Ru sensitization is difficult to discern due to the subsequent charge separation on the basis of the steady-state data. Nevertheless, the quenching of the UV-emission and the occurrence of the polymer-based emission (*vide supra*) may open attractive avenues to sensitize the Ru dye. Time-resolved measurements are in due course to detail the associated rate constants for energy and electron transfer. Noteworthy, the higher emission energy of the polymer-based emission vs the MLCT emission corroborate our previous detailed analysis of electron-transfer from the energetically most favorable Ru-based excited state.[10]

CONCLUSION

The use of a commercial NMP initiator enabled the synthesis of a well-defined telechelic poly(naphthalene diimide). The chain end was subsequently functionalized with a ruthenium(II) photosensitizer employing three different reactions—two nucleophilic substitutions and the CuAAC reaction. In addition to the high conversion, the straightforward purification of the functional architectures using functionalized silica allowed the facile isolation in good yields. All compounds were fully characterized by NMR, MS, and SEC measurements, including three reference complexes to detail the spectroscopic properties of the prepared dyads.

The electrochemical potentials of the building blocks redox processes are retained in the corresponding dyads; i.e., the polymer shows two large quasi-reversible reduction waves at −1.0 and −1.5 V, respectively. Additionally the reversible oxidation of the ruthenium center was detected around +0.5 V, whereas the reduction potential of the ligand scaffold is influenced by the electron-deficient or electron-donating nature of the linker. The absorption spectra of the A_n−P dyads display intense absorption bands centered at 360 and 380 nm, which are based on the $\pi \rightarrow \pi^*$ transitions of the NDI units, and the typical MLCT band of the ruthenium photosensitizer at 500 nm. Steady-state emission spectroscopy revealed that the MLCT emission of the ruthenium dye is efficiently quenched in the dyads, attributed to charge separation between the Ru^{II} center and a NDI acceptor. A quenching efficiency of >86% was determined for the series of linkage pattern with respect to corresponding reference complexes. Furthermore, additional energy transfer processes involving the polymer and the ruthenium dye were observed, which may be exploited for future light harvesting processes.

In conclusion, the presented modular assembly of hierarchically defined A_n−P dyads was achieved by efficient coupling reactions. More importantly, the long-lived excited state of the photosensitizer is exploited to promote efficient charge separation irrespective of the flexible saturated linkage pattern. Because of the orthogonality of the presented methods, future functional photoredox-active A_n−P−D_m architectures can be envisioned and readily synthesized, including facile purification protocols.

ASSOCIATED CONTENT

Supporting Information

The Supporting Information is available free of charge on the ACS Publications website at DOI: 10.1021/acs.macromol.5b02717.

Additional instrumental details and analytical data (NMR, MS, SEC, UV−vis, and cyclic voltammetry) are provided for completion (PDF)

DOI: 10.1021/acs.macromol.5b02717
Macromolecules 2016, 49, 2112−2123

AUTHOR INFORMATION

Corresponding Authors

*E-mail ulrich.schubert@uni-jena.de (U.S.S.).
*E-mail michael.jager.iomc@uni-jena.de (M.J.).

Author Contributions

#R.S. and T.S. contributed equally to this work. All authors have given approval to the final version of the manuscript.

Funding

M.J. was financially supported by the Carl-Zeiss Foundation and the Friedrich Schiller University Jena ("Nachwuchsförderung").

Notes

The authors declare no competing financial interest.

ACKNOWLEDGMENTS

We thank Sarah Crotty for MALDI-ToF analysis, Nicole Fritz for ESI-ToF analysis, Annett Urbanek for MALDI-TOF measurements, and Dr. Peter Bellstedt for help with the NMR measurements.

ABBREVIATIONS

PMDETA, *N*,*N*,*N*′,*N*′,*N*″-pentamethyldiethylenetriamine; IPA, isopropyl alcohol.

REFERENCES

(1) Lewis, N. S.; Nocera, D. G. *Proc. Natl. Acad. Sci. U. S. A.* **2006**, *103* (43), 15729−15735.
(2) Concepcion, J. J.; House, R. L.; Papanikolas, J. M.; Meyer, T. J. *Proc. Natl. Acad. Sci. U. S. A.* **2012**, *109* (39), 15560−15564.
(3) Gust, D.; Moore, T. A.; Moore, A. L. *Acc. Chem. Res.* **2009**, *42* (12), 1890−1898.
(4) Alstrum-Acevedo, J. H.; Brennaman, M. K.; Meyer, T. J. *Inorg. Chem.* **2005**, *44* (20), 6802−6827.
(5) Nicolas, J.; Guillaneuf, Y.; Lefay, C.; Bertin, D.; Gigmes, D.; Charleux, B. *Prog. Polym. Sci.* **2013**, *38* (1), 63−235.
(6) Rizzardo, E.; Solomon, D. H. *Aust. J. Chem.* **2012**, *65* (8), 945−969.
(7) Moad, G.; Rizzardo, E.; Thang, S. H. *Aust. J. Chem.* **2005**, *58* (6), 379−410.
(8) Hadjichristidis, N.; Iatrou, H.; Pitsikalis, M.; Mays, J. *Prog. Polym. Sci.* **2006**, *31* (12), 1068−1132.
(9) Schroot, R.; Friebe, C.; Altuntas, E.; Crotty, S.; Jäger, M.; Schubert, U. S. *Macromolecules* **2013**, *46* (6), 2039−2048.
(10) Kübel, J.; Schroot, R.; Wächtler, M.; Schubert, U. S.; Dietzek, B.; Jäger, M. *J. Phys. Chem. C* **2015**, *119* (9), 4742−4751.
(11) Suraru, S.-L.; Würthner, F. *Angew. Chem., Int. Ed.* **2014**, *53* (29), 7428−7448.
(12) Huang, C.; Barlow, S.; Marder, S. R. *J. Org. Chem.* **2011**, *76* (8), 2386−2407.
(13) Zhan, X.; Facchetti, A.; Barlow, S.; Marks, T. J.; Ratner, M. A.; Wasielewski, M. R.; Marder, S. R. *Adv. Mater.* **2011**, *23* (2), 268−284.
(14) Bhosale, S. V.; Jani, C. H.; Langford, S. J. *Chem. Soc. Rev.* **2008**, *37* (2), 331−342.
(15) Kumar, M.; George, S. J. *Chem. - Eur. J.* **2011**, *17* (40), 11102−11106.
(16) Sakurai, S.-i.; Areephong, J.; Bertone, L.; Lin, N.-T.; Sakai, N.; Matile, S. *Energy Environ. Sci.* **2011**, *4* (7), 2409−2416.
(17) Yushchenko, O.; Villamaina, D.; Sakai, N.; Matile, S.; Vauthey, E. *J. Phys. Chem. C* **2015**, *119* (27), 14999−15008.
(18) Zhou, W.; Wen, Y.; Ma, L.; Liu, Y.; Zhan, X. *Macromolecules* **2012**, *45* (10), 4115−4121.
(19) Sommer, M. *J. Mater. Chem. C* **2014**, *2* (17), 3088−3098.
(20) Juris, A.; Balzani, V.; Barigelletti, F.; Campagna, S.; Belser, P.; Vonzelewsky, A. *Coord. Chem. Rev.* **1988**, *84*, 85−277.
(21) Campagna, S.; Puntoriero, F.; Nastasi, F.; Bergamini, G.; Balzani, V. Photochemistry and photophysics of coordination compounds: Ruthenium. In *Photochemistry and Photophysics of Coordination Compounds I*; Balzani, V., Campagna, S., Eds.; Springer-Verlag: Berlin, 2007; Vol. *280*, pp 117−214.
(22) Thompson, D. W.; Ito, A.; Meyer, T. J. *Pure Appl. Chem.* **2013**, *85* (7), 1257−1305.
(23) Fang, Z.; Ito, A.; Keinan, S.; Chen, Z.; Watson, Z.; Rochette, J.; Kanai, Y.; Taylor, D.; Schanze, K. S.; Meyer, T. J. *Inorg. Chem.* **2013**, *52* (15), 8511−8520.
(24) Puodziukynaite, E.; Wang, L.; Schanze, K. S.; Papanikolas, J. M.; Reynolds, J. R. *Polym. Chem.* **2014**, *5* (7), 2363−2369.
(25) Sun, Y.; Chen, Z.; Puodziukynaite, E.; Jenkins, D. M.; Reynolds, J. R.; Schanze, K. S. *Macromolecules* **2012**, *45* (6), 2632−2642.
(26) Abrahamsson, M.; Jäger, M.; Österman, T.; Eriksson, L.; Persson, P.; Becker, H.-C.; Johansson, O.; Hammarström, L. *J. Am. Chem. Soc.* **2006**, *128* (39), 12616−12617.
(27) Jäger, M.; Kumar, R. J.; Görls, H.; Bergquist, J.; Johansson, O. *Inorg. Chem.* **2009**, *48* (7), 3228−3238.
(28) Abrahamsson, M.; Jäger, M.; Kumar, R. J.; Österman, T.; Persson, P.; Becker, H.-C.; Johansson, O.; Hammarström, L. *J. Am. Chem. Soc.* **2008**, *130* (46), 15533−15542.
(29) Kumar, R. J.; Karlsson, S.; Streich, D.; Jensen, A. R.; Jäger, M.; Becker, H.-C.; Bergquist, J.; Johansson, O.; Hammarström, L. *Chem. - Eur. J.* **2010**, *16* (9), 2830−2842.
(30) Jäger, M.; Eriksson, L.; Bergquist, J.; Johansson, O. *J. Org. Chem.* **2007**, *72* (26), 10227−10230.
(31) Jäger, M.; Kumar, R. J.; Görls, H.; Bergquist, J.; Johansson, O. *Inorg. Chem.* **2009**, *48* (7), 3228−3238.
(32) Tambara, K.; Ponnuswamy, N.; Hennrich, G.; Pantos, G. D. *J. Org. Chem.* **2011**, *76* (9), 3338−3347.
(33) Baron, A.; Herrero, C.; Quaranta, A.; Charlot, M.-F.; Leibl, W.; Vauzeilles, B.; Aukauloo, A. *Chem. Commun.* **2011**, *47* (39), 11011−11013.
(34) The fair yield (55%) for **D1** is attributed to an incomplete conversion. However, the starting material can be recovered and is available for further reactions. Furthermore, under optimized conditions (addition of KI at the reaction start) yields up to 75% were reached for similar systems (unpublished results).
(35) At least five samples with an approximated volume of 20−40 μL were taken during the reaction. With respect to the reaction scale (volume: 0.4 mL; see Experimental Section) the amount of lost material due to sampling has to be considered and causes the apparent low yield although a full conversion was detected.
(36) Hesse, M.; Meier, H.; Zeeh, B. *Spectroscopic Methods in Organic Chemistry*, 2nd ed.; Georg Thieme Verlag: Stuttgart, 2007.
(37) Nicholson, R. S.; Shain, I. *Anal. Chem.* **1964**, *36* (4), 706−723.
(38) Van Benschoten, J. J.; Lewis, J. Y.; Heineman, W. R.; Roston, D. A.; Kissinger, P. T. *J. Chem. Educ.* **1983**, *60* (9), 772.
(39) Bard, A. J. F.; Larry, R. *Electrochemical Methods*, 2nd ed.; Wiley: New York, 2001.
(40) Ganesan, P.; van Lagen, B.; Marcelis, A. T. M.; Sudhölter, E. J. R.; Zuilhof, H. *Org. Lett.* **2007**, *9* (12), 2297−2300.
(41) Bell, T. D. M.; Bhosale, S. V.; Forsyth, C. M.; Hayne, D.; Ghiggino, K. P.; Hutchison, J. A.; Jani, C. H.; Langford, S. J.; Lee, M. A. P.; Woodward, C. P. *Chem. Commun.* **2010**, *46* (27), 4881−4883.
(42) Licchelli, M.; Orbelli Biroli, A.; Poggi, A. *Org. Lett.* **2006**, *8* (5), 915−918.
(43) Rajdev, P.; Molla, M. R.; Ghosh, S. *Langmuir* **2014**, *30* (8), 1969−1976.
(44) Kar, H.; Molla, M. R.; Ghosh, S. *Chem. Commun.* **2013**, *49* (39), 4220−4222.
(45) Das, A.; Ghosh, S. *Macromolecules* **2013**, *46* (10), 3939−3949.
(46) Shao, H.; Seifert, J.; Romano, N. C.; Gao, M.; Helmus, J. J.; Jaroniec, C. P.; Modarelli, D. A.; Parquette, J. R. *Angew. Chem., Int. Ed.* **2010**, *49* (42), 7688−7691.
(47) Kumar, M.; George, S. J. *Nanoscale* **2011**, *3* (5), 2130−2133.
(48) Barros, T. C.; Brochsztain, S.; Toscano, V. G.; Filho, P. B.; Politi, M. J. *J. Photochem. Photobiol., A* **1997**, *111* (1−3), 97−104.

DOI: 10.1021/acs.macromol.5b02717
Macromolecules 2016, 49, 2112−2123

(49) Kulkarni, C.; George, S. J. *Chem. - Eur. J.* **2014**, *20* (16), 4537−4541.
(50) Licchelli, M.; Linati, L.; Orbelli Biroli, A.; Perani, E.; Poggi, A.; Sacchi, D. *Chem. - Eur. J.* **2002**, *8* (22), 5161−5169.
(51) Tu, S.; Kim, S. H.; Joseph, J.; Modarelli, D. A.; Parquette, J. R. *J. Am. Chem. Soc.* **2011**, *133* (47), 19125−19130.
(52) Molla, M. R.; Gehrig, D.; Roy, L.; Kamm, V.; Paul, A.; Laquai, F.; Ghosh, S. *Chem. - Eur. J.* **2014**, *20* (3), 760−771.
(53) Lasitha, P.; Prasad, E. *RSC Adv.* **2015**, *5* (52), 41420−41427.

DOI: 10.1021/acs.macromol.5b02717
Macromolecules 2016, 49, 2112−2123

Publication P6

Hydrophilic poly(naphthalene diimide) based acceptor-photosensitizer dyads: Towards water-processible modular photoredox-active architectures

R. Schroot, T. Schlotthauer, M. Jäger, U. S. Schubert, *Macromol. Chem. Phys.* **2017**, *218*, 1600534.

The paper as well as the supporting information (free of charge) are available online under: doi.org/10.1002/macp.201600534

Macromolecular Journals

Macromolecular Chemistry and Physics

Hydrophilic Poly(naphthalene diimide)-Based Acceptor–Photosensitizer Dyads: Toward Water-Processible Modular Photoredox-Active Architectures

Robert Schroot, Tina Schlotthauer, Michael Jäger,* Ulrich S. Schubert*

Hydrophilic naphthalene diimide based acceptor polymers are prepared by the incorporation of triethylene glycol or poly(ethylene glycol) side chains in the monomers and subsequent nitroxide-mediated polymerization (NMP). The kinetic investigation of the polymerization reveals a controlled chain growth as well as a narrow molar mass distribution. Due to the utilization of a functional NMP initiator, a single Ru(II) photosensitizer unit is readily attached at the polymers chain terminus by a modular approach to construct water soluble photoredox-active acceptor–photosensitizer dyads. The analysis of the optical properties by steady-state absorption and emission spectroscopy reveals preserved optical absorption properties of the individual building blocks, and, more importantly, an efficient quenching of the Ru(II) emission assigned to intramolecular charge transfer from the complex to the acceptor polymer. The results demonstrate the versatility of side chain modifications to prepare water-processible photoredox-active architectures under preservation of the modular character known from hydrophobic systems.

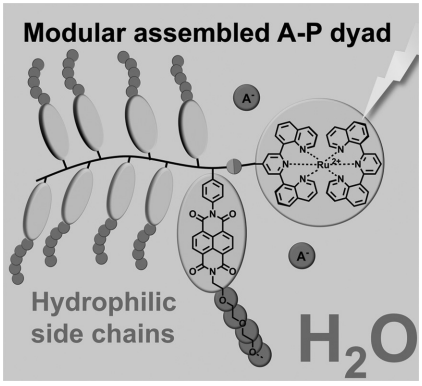

1. Introduction

The conversion of sunlight into storable energy forms, e.g., electrical or chemical bond energy, can be realized in photoredox-active architectures consisting of light harvesting and charge transport units.[1] In such devices the initial light absorption of the photosensitizer (P) leads to an excited state, followed by a primary charge separation and an additional separation and transport of the generated charges in the attached donor or acceptor moieties, i.e., p - or n-conducting building blocks. Finally, the generated charges are collected at an electrode or are consumed in a catalytic reaction.[2,5]

The presented approach toward photoredox-active architectures is based on a modular design, e.g., a ruthenium-based photosensitizer and electron acceptor or donor polymers, which can be prepared separately and finally linked together. Hence, the individual parts can be optimized and a high flexibility in the final architecture is achieved. Recently, we demonstrated the suitability of this modular approach by the preparation of a series of

R. Schroot, T. Schlotthauer, Dr. M. Jäger, Prof. U. S. Schubert
Laboratory of Organic and Macromolecular Chemistry (IOMC)
Friedrich Schiller University Jena
Humboldtstraße 10, 07743 Jena, Germany
E-mail: michael.jager.iomc@uni-jena.de;
ulrich.schubert@uni-jena.de
R. Schroot, T. Schlotthauer, Dr. M. Jäger, Prof. U. S. Schubert
Center for Energy and Environmental Chemistry Jena (CEEC Jena)
Friedrich Schiller University Jena
Philosophenweg 7a, 07743 Jena, Germany

DOI: 10.1002/macp.201600534

acceptor–photosensitizer dyads[6] and, in addition, the desired charge separation was proved by spectroscopic studies.[7]

Besides the optical and electrochemical properties, the processability and the control of the morphology play a crucial role with respect to the fabrication of working devices. Therefore, the introduction of hydrophilic phase-forming moieties in the applied polymers is a potent strategy to guarantee the solubility in environmentally friendly polar solvents, e.g., water or alcohols,[8–13] to allow the application of orthogonal solvents in the layer-by-layer processes[11] and to control the morphology by self-assembly of the macromolecules.[14–19]

In this contribution, the synthesis of oligo- and poly(ethylene glycol) (PEG) decorated naphthalene diimide (NDI)-based styrenic polymers is presented in order to increase the hydrophilicity of acceptor–photosensitizer dyads and, thereby, the solubility and processability in polar solvents in comparison with the alkyl-substituted analogs.[6] The versatility of the general scope is demonstrated by kinetic investigations of the nitroxide-mediated polymerization (NMP) polymerization and the modular construction of a hydrophilic acceptor–photosensitizer dyad (A–P dyad) using a ruthenium(II) complex. The influence of the PEG substitution on the synthetic procedure as well as the physical and optical properties is investigated with respect to the preservation of the modular character.

2. Experimental Section

All reagents were purchased from ABCR, Acros Organics, Alfa Aesar, Apollo Scientific, Sigma-Aldrich, or TCI chemicals, and were used without further purification unless otherwise noted. Dry pyridine and dry *N*-*N*-dimethylformamide (DMF) were commercially available. All solvents were degassed before use. Methoxytriethylene glycol amine (MTEG-NH_2) was prepared according to literature procedures following a Gabriel synthesis protocol[20,21] and subsequent hydrazinolysis.[21,22] Methoxypoly(ethylene glycol) amine 550 (MPEG-NH_2 550) was prepared by Staudinger reaction according to the literature.[23] [Ru(dqp)(dqpOH)][PF_6]$_2$[24] (dqp is 2,6-di(quinolin-8-yl)pyridine, dqp-OH is 4-hydroxy-2,6-di(quinolin-8-yl)pyridine) and [Ru(dqp)$_2$][PF_6]$_2$[25] were prepared as described previously.

2.1. *N*-(MTEG)-naphthalene-1,8-dicarboxyanhydride-4,5-dicarboxyimide (3)

A vial was charged with 1,4,5,8-naphthalenetetracarboxylic dianhydride (0.657 g, 2.451 mmol), methoxytriethylene glycol amine (0.400 g, 2.451 mmol), and dry DMF (17 mL). After the vial was capped and flushed with nitrogen for 20 min, the brown suspension was homogenized by ultrasound sonication for 10 min. Afterward, the vial was heated 5 min at 75 °C and 15 min at 140 °C under microwave irradiation. Subsequently, the solvent was removed under reduced pressure and CH_2Cl_2 as well as water were added and the phases were separated. The aqueous phase was extracted five times with CH_2Cl_2 (5 × 50 mL). The combined organic layers were concentrated and the crude product was used without further purification (0.870 g, 86%, purity ≈80% according to NMR, impurities by bisfunctionalized diimide). ^{1}H NMR (300 MHz, $CDCl_3$): δ 8.82 (s, 4H, NaphH), 4.55–4.41 (m, 2H, CH_2), 3.90–3.82 (m, 2H, CH_2), 3.76–3.68 (m, 2H, CH_2), 3.68–3.53 (m, 4H, CH_2), 3.53–3.43 (m, 2H, CH_2), 3.32 (s, 3H, CH_3).

2.2. *N*-(MTEG)-*N*′-(vinylphenyl)-naphthalene-1,4,5,8-dicarboxydiimide (1)

Crude *N*-(MTEG)-naphthalene-1,8-dicarboxyanhydride-4,5-dicarboxyimide (0.870 g, 1 eq.), 4-aminostyrene (0.301 g, 1.2 eq, 2.530 mmol), and $ZnSO_4 \cdot 1H_2O$ (0.227 g, 0.6 eq, 1.263 mmol) were dissolved in dry pyridine (15 mL) under nitrogen. The mixture was heated to reflux for 4 h. The crude product was precipitated in 1 M HCl (120 mL), filtered off, and washed with water. The solid was redissolved in CH_2Cl_2, washed with water as well as brine, dried over Na_2SO_4, and the solvent was removed under reduced pressure. Purification by column chromatography (silica, CH_2Cl_2) gave the product as bright yellow solid (0.585 g, 54%). ^{1}H NMR (300 MHz, $CDCl_3$): δ 8.79 (s, 4H, NaphH), 7.61 (d, J = 8.4 Hz, 2H, ArH), 7.30 (d, J = 8.4 Hz, 2H, ArH), 6.81 (dd, J = 17.6, 10.9 Hz, 1H, C**H** = CH_2), 5.84 (d, J = 17.6 Hz, 1H, CH = C**H**$_2$-trans), 5.37 (d, J = 10.9 Hz, 1H, CH = C**H**$_2$-cis), 4.48 (t, J = 5.9 Hz, 2H, CH_2), 3.87 (t, J = 5.8 Hz, 2H, CH_2), 3.67–3.55 (m, 4H, CH_2), 3.53–3.44 (m, 2H, CH_2), 3.33 (s, 3H, CH_3). ^{13}C NMR (63 MHz, $CDCl_3$): δ 163.1, 163.0, 138.7, 136.1, 134.0, 131.5, 131.2, 128.7, 127.4, 127.2, 127.0, 126.9, 115.6, 72.0, 70.8, 70.7, 70.3, 67.9, 59.0, 39.8. HR-ESI ([$C_{29}H_{26}N_2O_7$]Na^+) *m*/*z*: calc: 537.1632, found: 537.1629, Error: 0.7 ppm.

2.3. *N*-(MPEG 550)-naphthalene-1,8-dicarboxyanhydride-4,5-dicarboxyimide (4)

A vial was charged with 1,4,5,8-naphthalenetetracarboxylic dianhydride (0.488 g, 1.818 mmol), MPEG-NH_2 550 (1.000 g, 1.818 mmol), and dry DMF (20 mL). After the vial was capped and flushed with nitrogen for 20 min, the brown suspension was homogenized by ultrasound sonication for 10 min. Afterward, the vial was heated 5 min at 75 °C and 15 min at 140 °C under microwave irradiation. Subsequently, the solvent was removed under reduced pressure, CH_2Cl_2 and water were added, and the phases were separated. The aqueous phase was extracted five times with CH_2Cl_2. The combined organic layers were concentrated and the crude product was used without further purification (1.600 g, quantitative, purity ≈75% according to NMR, impurities by DMF and bisfunctionalized diimide). ^{1}H NMR (300 MHz, $CDCl_3$): δ 8.82 (s, 4H, NaphH), 4.57–4.37 (m, 2H, CH_2), 3.90–3.82 (m, 2H, CH_2), 3.79–3.41 (m, 48H, CH_2), 3.38 (s, 3H, CH_3).

2.4. *N*-(MPEG 550)-*N*′-(vinylphenyl)-naphthalene-1,4,5,8-dicarboxydiimide (2)

Crude *N*-(MPEG 550)-naphthalene-1,8-dicarboxyanhydride-4,5-dicarboxyimide (1.000 g, 1 eq.), 4-aminostyrene (0.174 g, 1.2 eq, 1.463 mmol), and $ZnSO_4 \cdot 1H_2O$ (0.131 g, 0.6 eq, 0.732 mmol) were dissolved in dry pyridine (30 mL) under nitrogen. The mixture

Table 1. Prepared polymers as well as experimental conditions and analytical data.

Entry	Polymer[a)]	Monomer	*M*/*I*	M_n [g mol^{-1}][b)]	*Đ*
1	**Cl-P1**$_8$	**1**	20	4900	1.11
2	**Cl-P1**$_{16}$	**1**	20	7900	1.13
3	**Cl-P2**$_{10}$	**2**	20	16 000	1.26
4	**Cl-P2**$_8$	**2**	20	14 000	1.14
5	**Cl-P2**$_{11}$	**2**	20	16 700	1.28

[a)]All reactions were carried out in anisole with CMSt-TIPNO as initiator, the subscripted number represents the degree of polymerization determined by ^{1}H NMR; [b)]Determined by SEC (chloroform/*iso*-propanol/triethylamine [94:2:4], PS calibration).

was heated to reflux overnight. The crude product was diluted with CH_2Cl_2, filtered, and concentrated under reduced pressure. Due to the high polarity of the compounds, the pure product (dark green to brown oil) was isolated by preparative size-exclusion chromatography (SEC) (Bio-Beads S-X3) and not by a silica column (0.690 g, 62%). ^{1}H NMR (300 MHz, $CDCl_3$): δ 8.78 (s, 4H, NaphH), 7.60 (d, J = 8.5 Hz, 2H, ArH), 7.29 (d, J = 8.5 Hz, 2H, ArH), 6.80 (dd, J = 17.5, 11.0 Hz, 1H, C**H** = CH_2), 5.84 (d, J = 17.5 Hz, 1H, CH = C**H**$_2$-trans), 5.35 (d, J = 11.0 Hz, 1H, CH = C**H**$_2$-cis), 4.54–4.36 (m, 2H, CH_2), 4.01–3.79 (m, 2H, CH_2), 3.79–3.46 (m, 42H, CH_2), 3.37 (s, 3H, CH_3). ^{13}C NMR (101 MHz, $CDCl_3$): δ 163.0, 162.8, 138.6, 136.0, 133.8, 131.4, 131.1, 128.6, 127.3, 127.0, 126.9, 126.8, 115.5, 71.9, 70.6 (2×), 70.5, 70.1, 67.8, 59.0, 39.6. MS (matrix-assisted laser desorption/ionization time-of-flight (MALDI-TOF), dithranol) *m*/*z*: 933.4 ([$C_{22}H_{11}N_2O_4(C_2H_4O)_{12}CH_3$]+Na$^+$). Note that some batches still contained NDI-(MPEG 550)$_2$ as minor impurity, as this side product is hard to separate from the monomer in larger batches (see the Results and Discussion section and Figure S14 in the Supporting Information). This byproduct was expected and proved to be inert in the polymerization (vide infra).

2.5. General Polymerization Procedure

A glass tube equipped with a septum and an external overhead flushing with nitrogen was used for the polymerizations (Figure S1, Supporting Information). The reaction vessel was charged with monomer, initiator and solvent, purged with nitrogen for 20 min and placed in a preheated oil bath (120 °C). The purification is described for each polymer. Experimental conditions and analytical data are given in Table 1.

Cl-P1$_8$ was prepared according to the general procedure using **1** (0.200 g, 0.389 mmol), *N*-(*tert*-butyl)-*O*-(1-(4-(chloromethyl) phenyl)ethyl)-*N*-(2-methyl-1-phenylpropyl)hydroxylamine (CMSt-TIPNO) (0.007 g, 0.019 mmol) and anisole (1.2 mL). After 24 h the reaction mixture was diluted with CH_2Cl_2 and unreacted monomer was removed by preparative SEC (Bio-Beads S-X1, CH_2Cl_2). The polymer was obtained as brown solid after precipitation in MeOH. Yield: 0.050 g. SEC ($CHCl_3$/*i*-PrOH /NEt_3 94/2/4, polystyrene (PS) calibration): M_n = 4900 g mol^{-1}, *Đ* = 1.11. ^{1}H NMR (300 MHz, $CDCl_3$): δ 9.14–8.09 (br), 7.90–6.73 (br), 4.87–4.09 (br), 3.90–3.70 (br), 3.70–3.60 (br), 3.60–3.45 (br), 3.45–3.35 (br), 3.35–3.11 (br). 2.96–0.13 (br).

Cl-P1$_{16}$ was prepared according to the general procedure using **1** (0.286 g, 0.556 mmol), CMSt-TIPNO (0.010 g, 0.028 mmol), and anisole (1.65 mL). Samples were taken for SEC and NMR analysis. After 48 h the reaction mixture was diluted with CH_2Cl_2 and unreacted monomer was removed by preparative SEC (Bio-Beads S-X1, CH_2Cl_2). Yield: 0.125 g. SEC ($CHCl_3$/*i*-PrOH/NEt_3 94/2/4, PS calibration): M_n = 7900 g mol^{-1}, *Đ* = 1.13.

Cl-P2$_{10}$ was prepared according to the general procedure using **2** (0.120 g, 0.130 mmol), CMSt-TIPNO (0.002 g, 0.006 mmol), and anisole (0.5 mL). After 25 h the reaction mixture was diluted with CH_2Cl_2 and unreacted monomer was removed by preparative SEC (Bio-Beads S-X1, CH_2Cl_2). The polymer was obtained as brown solid after precipitation in pentane. Yield: 0.062 g. SEC ($CHCl_3$/*i*-PrOH/NEt_3 94/2/4, PS calibration): M_n = 16 000 g mol^{-1}, *Đ* = 1.26. ^{1}H NMR (300 MHz, $CDCl_3$): δ 9.28–8.01 (br), 8.01–6.70 (br), 4.95–4.09 (br), 4.09–3.45 (br), 3.45–3.15 (br), 2.96–0.67 (br).

Cl-P2$_8$ was prepared according to the general procedure using **2** (0.420 g, 0.457 mmol), CMSt-TIPNO (0.009 g, 0.023 mmol), and anisole (1.0 mL). After 18 h the reaction mixture was diluted with CH_2Cl_2 and unreacted monomer was removed by preparative SEC (Bio-Beads S-X1, CH_2Cl_2). The polymer was obtained as brown solid after precipitation in pentane. Yield: 0.152 g. SEC ($CHCl_3$/*i*-PrOH/NEt_3 94/2/4, PS calibration): M_n = 14 000 g mol^{-1}, *Đ* = 1.14.

Cl-P2$_{11}$ was prepared according to the general procedure using **2** (containing 8% NDI-(MPEG 550)$_2$,[26] 0.700 g, 0.685 mmol), CMSt-TIPNO (0.013 g, 0.034 mmol), and anisole (2.5 mL). Samples were taken for SEC and NMR analysis. After 72 h the reaction mixture was diluted with CH_2Cl_2 and unreacted monomer was removed by preparative SEC (Bio-Beads S-X1, CH_2Cl_2). The polymer was obtained as brown solid after precipitation in pentane. Yield: 0.110 g. SEC ($CHCl_3$/*i*-PrOH/NEt_3 94/2/4, PS calibration): M_n = 16 700 g mol^{-1}, *Đ* = 1.28.

2.6. End Functionalization Procedure

Ru-P2$_{10}$**.** A vial was charged with **Cl-P2**$_{10}$ (0.020 g, 0.0015 mmol, 1 eq.), K_2CO_3 (0.001 g, 0.006 mmol, 4 eq.), KI (0.001 g, 0.006 mmol, 4 eq.), and [Ru(dqp)(dqpOH)][PF_6]$_2$ (0.003 g, 0.003 mmol, 2 eq.). Then, the vial was sealed, evacuated, and flushed with nitrogen. Dry DMF (0.5 mL) was added and the resulting solution was heated to 60 °C. The reaction progress was monitored by thin layer chromatography (TLC) (aluminum oxide, CH_2Cl_2/MeOH 95/5) and analytical size exclusion chromatography (DMAc + 0.08% NH_4PF_6, diode array detection). The reaction was continued until no further conversion was monitored (96 h). The mixture was diluted with a minimum amount of tetrahydrofuran (THF). The following precipitation into aqueous NH_4PF_6 solution was not successful. For this purpose, the solvent was removed under

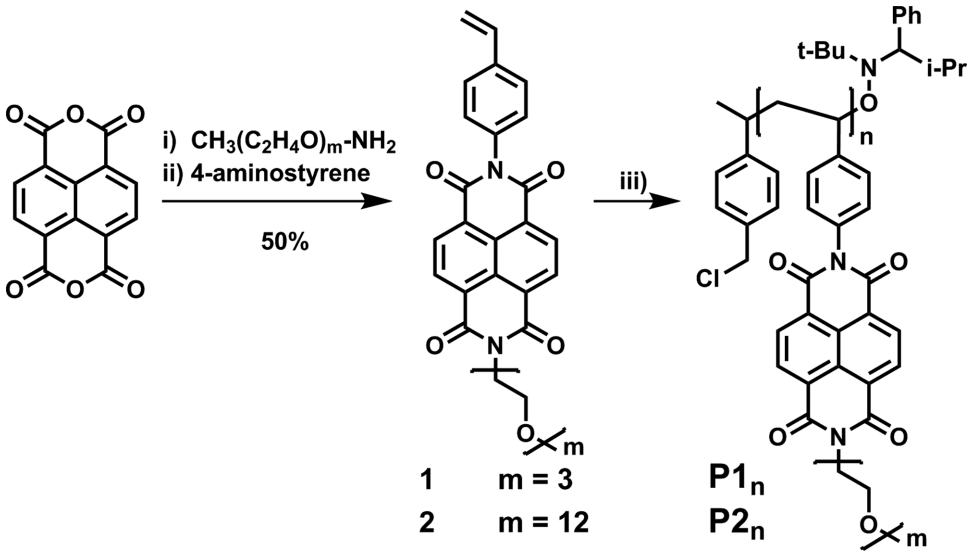

Scheme 1. Schematic representation of the synthesis of monomers 1 and 2 as well as subsequent polymerization. Conditions: i) DMF, microwave irradiation, N2, 75 °C (5 min), 140 °C (15 min); ii) 4-aminostyrene, $ZnSO_4 \cdot 1H_2O$, pyridine, reflux, 4 h; 50% over both steps. iii) CMSt-TIPNO, anisole, N2, 120 °C.

reduced pressure and the residual solid was redissolved in CH_2Cl_2 and filtered. The resulting clear solution was transferred onto a preparative size-exclusion chromatography column (Toyopearl HW-55F, CH_2Cl_2/MeOH 95/5) to give the dyad **Ru-P2**$_{10}$ as red solid (0.015 g, 70%). ^{1}H NMR (300 MHz, CD_2Cl_2): δ 9.03–8.16 (br, **P2**$_{10}$), 8.05 (br, Ru), 7.97 (br, Ru), 7.89 (br, Ru), 7.73 (br, Ru), 7.65 (br, Ru), 7.48 (br, Ru), 7.60–6.57 (br, **P2**$_{10}$), 5.58–5.41 (br, linker), 4.63–4.02 (br, **P2**$_{10}$), 3.96–3.38 (br, **P2**$_{10}$), 3.32 (s, **P2**$_{10}$), 2.96–0.70 (br, **P2**$_{10}$).

3. Results and Discussion

3.1. Monomer Synthesis and Polymerization

The monomers **1** and **2** were prepared by a two-step synthesis from 1,4,5,8-naphthalenetetracarboxylic dianhydride in analogy to previously described NDIs (Scheme 1).[6] In the first step, the respective monoimide was prepared by reaction with MTEG-NH_2 or MPEG-NH_2 550 in DMF under microwave irradiation. The obtained crude product, containing minor impurities of unfunctionalized and bis-functionalized compounds, was used without further purification. The subsequent reaction with 4-aminostyrene gave the product in good yields. Noteworthily, the isolation of **2** was precluded by ordinary column chromatography due to the high polarity of the compound. As a consequence, the monomer was purified by SEC using the Bio-Beads S-X3 resin. Thereby, in particular the separation of the desired monomer and the bis-PEGylated species NDI-(MPEG 550)$_2$ in larger scales is challenging due to overlapping peaks during elution. All collected fractions were checked with ^{1}H NMR and were combined in case of less than 10% impurity of this side product (Figure S14, Supporting Information). The side product is expected to be indifferent in the later polymerization as it contains no polymerizable group.

The polymerizations were carried out in anisole at 120 °C with the commercial functional NMP initiator CMSt-TIPNO. The unreacted monomer was subsequently removed by preparative SEC (Bio-Beads S-X1). The isolated polymers as well as the experimental conditions and analytical data are listed in Table 1. The labeling of the polymers (P) is based on the used monomers (**1** or **2**), the functional endgroup (Cl), and the degree of polymerization (DP) as subscripted number. The ^{1}H NMR spectra show the typical broad NDI resonance at 8.5 ppm and a second broad signal of the phenylene units (7.2 ppm) in the aromatic region. The signal of the chloromethyl group, which is used to determine the DP, appears at ≈4.5 ppm (see chapter NMR data in the Supporting Information). The MTEG and MPEG 550 protons were found as overlapping signals between 4.0 and 3.0 ppm. All polymers were characterized by analytical SEC and revealed narrow dispersities.

3.2. Kinetic Investigations

In order to prepare polymers with tailored molar masses the knowledge of the reaction kinetics and rate constants is required. Therefore, we performed kinetic studies for the polymerization of monomers **1** and **2**.

The nitroxide-mediated polymerization deviates from the ideal living polymerization process due to reversible and (irreversible) termination reactions. Considering all these processes—reversible dissociation (k_d)

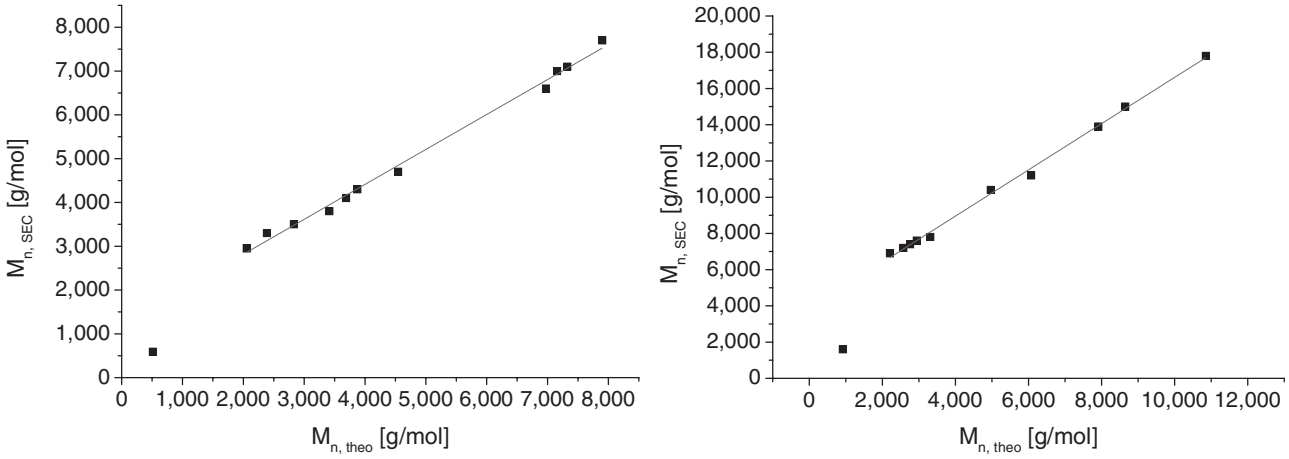

Figure 1. Plot of the molar mass determined by SEC (eluent: chloroform/*iso*-propanol/triethylamine [94:2:4], PS calibration) versus the theoretical molar mass based on the conversion (^{1}H NMR). Left: Cl-P1$_{16}$; right: Cl-P2$_{11}$.

and recombination (k_c) and irreversible termination (k_t) leading to the accumulation of persistent radicals—the evolution of the monomer concentration after an induction period is given by Equation (1)[27–29]

$$\ln\frac{[M]_o}{[M]_t}=\frac{3}{2}k_p\left(\frac{k_d[I]_o}{3k_tk_c}\right)^{1/3}t^{2/3} \quad (1)$$

Consequently, in the case of a controlled NMP mechanism the plot of $\ln[M]_0/[M]_t$ versus time to the power of two-thirds should result in a straight line. Whether the equation applies for the polymerization processes of **1** and **2** will be discussed in the following chapter.

The conversion of the polymerization reactions was determined by ^{1}H NMR based on the ratio of the vinyl groups compared to the aromatic NDI resonances and by UV–vis SEC based on the integral of the monomer and the polymer peak. Importantly, both methods gave values in the same range (Figure S26, Supporting Information). Therefore, the assumption that the monomer is exclusively converted into polymer can be made and enables the calculation of theoretical molar masses based on NMR conversion, *M*/*I* ratio, and the molar mass of the monomer.

In the case of **Cl-P1**$_{16}$, the plot of the theoretical and the SEC molar mass values reveals a linear relationship for molar masses above 2 000 g mol^{-1} (Figure 1, left). Moreover, the molar masses of the PS calibration are in the same range as the theoretical ones, suggesting a solution behavior of the polymer similar to PS, i.e., as a random coil. In contrast, a large discrepancy between the SEC molar mass and the theoretical value was observed for **Cl-P2**$_{11}$ (Figure 1, right). Apparently, the solution behavior of the polymer **Cl-P2**$_{11}$ differs strongly from a PS random coil. As the SEC data overestimate the molar mass (PS calibration) and **Cl-P2**$_{11}$ can be described as comb polymer with poly(ethylene glycol) side chains, one can tentatively assume that the polymer tends to form a rod-like structure in solution.[30]

The kinetic plots and the SEC elugrams for the preparation of **Cl-P1**$_{16}$ are shown in Figure 2 and Figure S29 (Supporting Information), respectively. As expected for a controlled polymerization the plot of the evolution of the monomer concentration versus $t^{2/3}$ (Figure 2, left) shows a linear behavior in the beginning indicating a reaction in the equilibrium period as described by Equation (1). However, a flatten of the graph is seen for reaction times over 24 h ($t^{2/3}$ = 8 h$^{2/3}$), which represents a decreasing reaction rate, i.e., termination reactions gain significance and the polymerization does not take place in an equilibrium state anymore. The slope *m* of the linear fit of the data in the equilibrium region enables the calculation of the product of all important rate constants (Equation (2)). With this value in hand (Table 2), reaction times required to reach a certain conversion can be calculated, also in comparison to other monomers (vide infra). The controlled character of the polymerization process is, additionally, revealed by the linear increase of the molar mass with the conversion and, moreover, also the dispersity decreases until 70% conversion (Figure 2, right). The slight increase in dispersity at even higher conversions is, again, an indicator for rising termination reactions.

$$\frac{k_pk_d^{1/3}}{k_t^{1/3}k_c^{1/3}}=\frac{\frac{2}{3}m\cdot 3^{1/3}}{[I]_o^{1/3}} \quad (2)$$

The experimental conditions for the polymerization leading to **Cl-P2**$_{11}$ are shown in Table 1 and Table 2. As it can be seen, most parameters, i.e., applied initiator, solvent, and *M*/*I* ratio, were identical to the preparation of **Cl-P1**$_{16}$. The only difference is a slightly higher dilution of the reaction mixture due to solubility reasons.

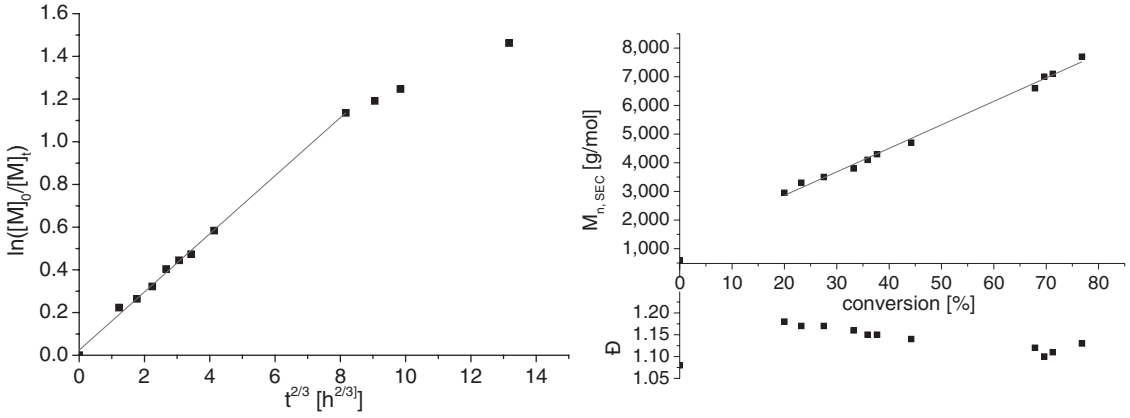

Figure 2. Kinetic data for the polymerization leading to Cl-P1$_{16}$. Left: Evolution of the monomer concentration versus $t^{2/3}$. The concentration was determined by ^{1}H NMR. Right: Data plots of the molar mass and dispersity versus conversion showing a linear increase of the molar mass. Molar masses and dispersity were determined by SEC (eluent: chloroform/*iso*-propanol/triethylamine [94:2:4], PS calibration), the conversion by ^{1}H NMR.

The reaction progress, i.e., the growth of the polymer chains, is clearly visualized by the plot of the SEC elugrams (Figure 3, left). Apparently, the reaction rate is low and only minor amounts of polymer are formed during the first hours of the reaction. Then a steady increase of the molar mass is observed and a satisfying conversion is reached after 72 h. Noteworthily, the low-molar mass tailing and the broadening of the polymer's SEC signal are indicative for increasing termination/side reactions at longer reaction times. The linear increase of the molar mass with the conversion but also the slightly increasing dispersity is additionally demonstrated by the respective plots (Figure 3, right).

The plot of the evolution of the monomer concentration versus $t^{2/3}$ enables a detailed analysis of the influence of the MPEG 550 side chains on the polymerization kinetic (Figure 4). At the first sight, deviations from the expected behavior (linear increase in the equilibrium period and flattening at the end of the reaction) are noticed. In this way, an induction period occurs at the beginning (≈15–20 min) followed by the equilibrium range. Afterward, the reaction rate decreases as indicated by the two data points below the linear fit at ≈8 and 10 $h^{2/3}$—probably due to more pronounced termination reactions—but finally an increase of the reaction rate is detected. This rise is very unusual and at the moment we can only speculate on its origin. However, in our opinion three different reasons may be plausible: (1) Solvent effects, e.g., viscosity changes, influence k_d and k_c (similar to the Trommsdorff–Norrish effect in free radical polymerization (FRP)); (2) k_d increases with the degree of polymerization as known for some monomers;[31] or (3) due to side reactions, e.g., decomposition of free nitroxide over the long reaction period, new propagating radicals are formed, which probably also explains the increasing dispersity seen by SEC. Despite these deviations from the ideal reaction kinetics, the obtained polymer features a narrow molar mass distribution and a defined molar mass.

Table 2. Initiator concentration and calculated rate constants for the investigated polymerizations leading to Cl-P1$_{16}$ and Cl-P2$_{11}$ as well as reevaluated data of p(EtHex-NDI) from previous reports.[7]

Entry	Polymer	$[I]_0$ [mmol L^{-1}]	$k_p k_d^{1/3}(k_t k_c)^{-1/3}$ [L$^{1/3}$ h$^{-2/3}$ mol$^{-1/3}$]
1	Cl-P1$_{16}$	16.85	0.51
2	Cl-P2$_{11}$	13.70	0.15
3	p(EtHex-NDI)	16.50	0.87

A comparison of the calculated reaction rate constants (Equation (2), Table 2) between **Cl-P1**$_{16}$ and **Cl-P2**$_{11}$ reveals a 3.4× smaller value for the latter one, i.e., the polymerization proceeds much slower. This finding is not surprising as the large MPEG 550 side chain presumably induces a sterical hindrance as often observed for the grafting through of comb copolymers.[32,33] Noteworthily, the reaction rate constant of **Cl-P1**$_{16}$ is already decreased by the factor 1.7 in comparison to the polymerization of the 2-ethylhexyl substituted monomer (Table 2, entry 3)[6,7] in DMF under otherwise identical conditions (Figure S27, Supporting Information).

3.3. End Functionalization with Ru(II) Dye

The end functionalization of polymer **Cl-P2**$_{10}$ with [Ru(dqp)(dqpOH)][PF$_6$]$_2$ leading to the dyad **Ru-P2**$_{10}$ was accomplished by nucleophilic substitution of the initiator's chloromethyl group in analogy to reported procedures (Scheme 2).[6] Noteworthily, in case of chain–chain couplings during the polymerization, a decoration with two Ru(II) complexes could be possible due to the availability of two reactive end groups. However, this side reaction was avoided by the relatively low polymerization conversion (60%) and, in addition, this highly charged side product

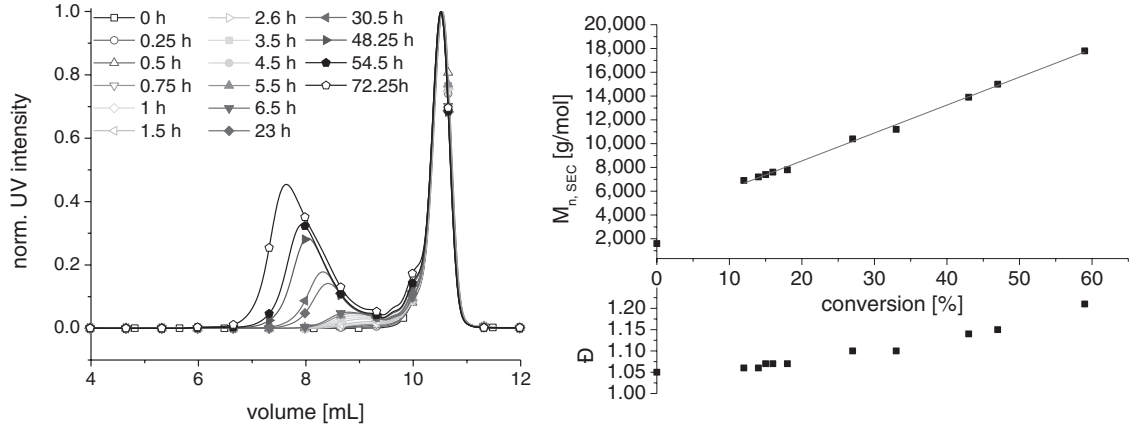

Figure 3. Left: UV–vis–SEC traces (340 nm) for the preparation of Cl-P2$_{11}$ showing the polymer growth with increasing reaction time. The traces are normalized to the monomer signal. Noteworthily, the small initial shoulder of the monomer signal is assigned to traces of NDI-(MPEG 550)$_2$. Right: Data plots of the molar mass and dispersity versus conversion. Molar masses and dispersity were determined by SEC (eluent: chloroform/*iso*-propanol/triethylamine [94:2:4], PS calibration), the conversion by ^{1}H NMR.

(+4) would be readily detected by TLC or UV–vis SEC. Due to the increased hydrophilicity of the polymer, the usual precipitation of the crude product in aqueous NH_4PF_6 solution to remove inorganic salts was not successful. Instead, these impurities were removed by filtration of a CH_2Cl_2 solution of the crude product. Subsequently, the pure polymer dyad was isolated by the established purification by preparative size-exclusion chromatography using the Toyopearl HW-55F resin.

3.4. Solubility of the Polymers and the Dyad

The hydrophilicity of the polymers **Cl-P1**$_8$ and **Cl-P2**$_{10}$ is increased compared to the alkyl substituted analogs due to the polar tri- and poly(ethylene glycol) side chain. Thereby, the hydrophilicity increases with the size of the side chain and, consequently, also the solubility in polar solvents.

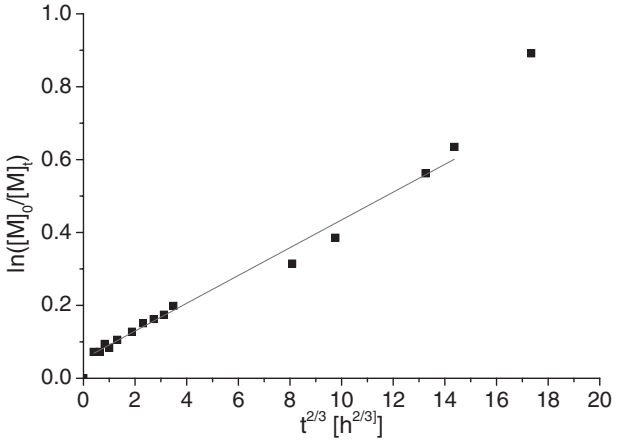

Figure 4. Evolution of the monomer concentration versus $t^{2/3}$ for the preparation of Cl-P2$_{11}$. The concentration was determined by ^{1}H NMR.

Additionally, a dependence of the solubility on the degree of polymerization of the copolymer is expected.[34,35]

In this regard the monomer **1** is soluble in halogenated solvents and also in acetone, whereas the respective polymer **Cl-P1**$_8$ is not soluble in acetone. In contrast, the MPEG 550 decorated monomer and the respective polymers are much more hydrophilic and are soluble in polar solvents, e.g., acetone, ethanol, methanol, or water. The water solubility of the polymer **Cl-P2**$_{10}$ strongly depends on the degree of polymerization, i.e., polymers with a degree of polymerization above six to eight are only limited or moderately soluble in water. The dyad **Ru-P2**$_{10}$ is highly soluble in common organic solvents, e.g., THF, CH_2Cl_2, or $CHCl_3$, and is also moderately soluble in water, enabling an assembly in a wide range of solvents with different polarity. Noteworthily, the water solubility of the compound is expected to be further increased by substitution of the hexafluorophosphate counterion with chloride. As a consequence, these materials represent an important step toward water-processible architectures and, moreover, are expected to allow a self-assembly in combination hydrophobic building blocks, e.g., electron donors. In this regard, preliminary tests showed the possibility to prepare water-based solutions of the dyad **Ru-P2**$_{10}$, which were used for drop casting of thin films (Figure S35, Supporting Information). Further investigations with respect to other film-forming techniques, e.g., spin coating or doctor blading and a detailed characterization of the films are ongoing and will be reported in due course.

3.5. Optical Spectroscopy

The optical properties of the compounds **Cl-P1**$_8$, **Cl-P2**$_{11}$, and **Ru-P2**$_{10}$ as well as the contingent influence of

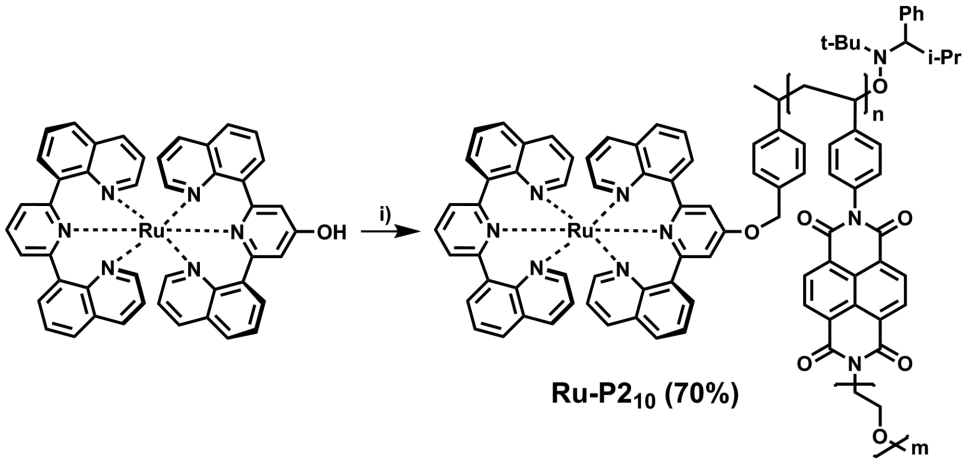

Scheme 2. Schematic representation of the synthesis of the dyad Ru-P2$_{10}$. Reagents and conditions: **Cl-P2$_{10}$**, K2CO3, KI, DMF, N2, 60 °C, 94 h.

various solvents were explored by UV–vis absorption and steady-state emission spectroscopy. The absorption spectra of the compounds in various solvents are shown in Figure 5. The NDI-based polymers feature the typical absorption bands at 360 and 380 nm. The metal-to-ligand charge transfer (MLCT) absorption band of the ruthenium dye is additionally visible around 500 nm in the spectrum of **Ru-P2$_{10}$**. An increasing polarity of the solvent results in changes of the absorption spectrum, i.e., decreased absorption at 380 nm as well as a slight bathochromic shift and increased absorptivity at shorter wavelengths (250 to 340 nm). This behavior is in particular pronounced for **Cl-P1$_8$**. These observations imply conformational changes, i.e., the chemical environment of the NDI chromophores changes induced by the solvents polarity. In solutions of small NDI molecules similar observations are associated with a stacking of individual units and the formation of J or H aggregates.[36–45] Consequently, high polar solvents may lead to a partial aggregation of NDI units in the polymer. The changes in the solution behavior seem to be most prominent for **Cl-P1$_8$** and less significant for **Cl-P2$_{11}$** and **Ru-P2$_{10}$** as the spectral changes are marginal in comparison to the literature examples.[36] In the case of **Cl-P1$_8$**, which is not soluble in pure MeOH, the broadening of the absorption band may additionally be attributed to a partial collapsing of the solvated polymer coil and the formation of aggregates.

As the stacking of NDI units is accompanied by major changes of the emission properties, a comprehensive study of the prepared compounds was conducted by steady-state emission spectroscopy. However, the expected intensive emission of stacked NDI units upon excitation at 360 nm could not be detected in any solvent (Figures S30–S32, Supporting Information). Consequently, the predominate existence of nonemissive isolated NDI units can be assumed in the investigated concentra-

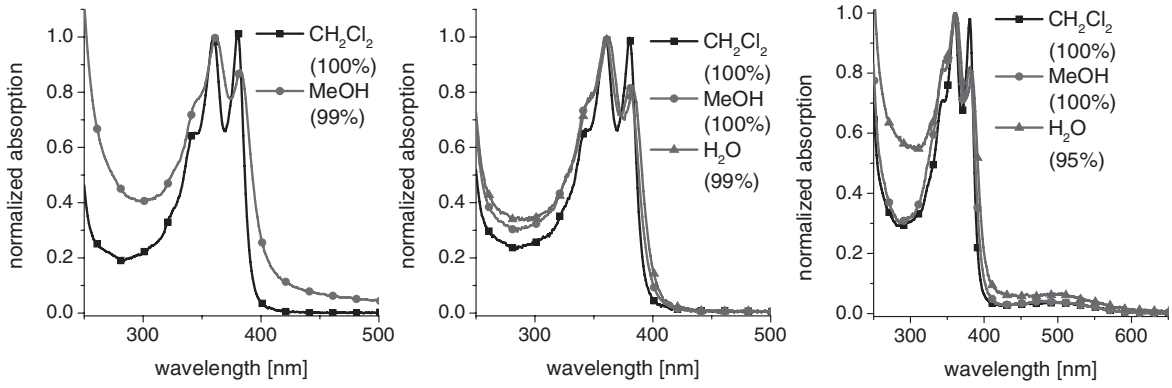

Figure 5. Left: UV–vis absorption spectra of Cl-P1$_8$ in various solvents. Middle: UV–vis absorption spectra of Cl-P2$_{11}$ in various solvents. Right: UV–vis absorption spectra of Ru-P2$_{10}$ in various solvents. Stock solutions in CH_2Cl_2 or MeOH were used. The noted percentages indicate the fraction of pure solvent, while the rest represents the volume fraction of the stock solution (aerated solutions, ≈10^{-7} M, absorbance <0.1, no inner filter effects).

tion range (10^{-7} M).[36,46] This observation is somehow surprising as previously reported alkyl-chain decorated poly(naphthalene diimide)s feature an emission at 413 nm despite the restricted conformational freedom of the polystyrene backbone (Figure S33, Supporting Information).[6] In our opinion, this observation may be a consequence of the sterical hindrance of the PEG side chain, i.e., the side chain promotes the formation of rod-like structures (vide supra) with the highest possible distance between the individual NDI units in a single polymer chain. In the case of **Cl-P1**$_8$, a very weak feature was detected between 500 and 600 nm (Figure S30, Supporting Information), which may be tentatively attributed to the very weak formation of intermolecular excimers as described in the literature.[45]

Last but not least, we were interested whether the polymer is capable of quenching the dye's MCLT emission as reported for related systems, i.e., whether the compounds are suitable for light-induced charge separation applications.[6] The respective graph illustrating the recorded emission spectra of **Ru-P2**$_{10}$ and the reference complex $[Ru(dqp)_2][PF_6]_2$ upon excitation at 500 nm is shown in Figure 6. The comparison of the spectra clearly reveals the quantitative MLCT emission quenching and corroborates an electron transfer from the energetically most favorable Ru-based excited state to the NDI polymer.[6] Please note that the complex $[Ru(dqp)_2][PF_6]_2$ shows spectral properties very similar to the complex $[Ru(dqp)(dqp\text{-}O\text{-}Bn)][PF_6]_2$,[6] which features the same substitution pattern as the dyad **Ru-P2**$_{10}$ (Figure S34, Supporting Information). The detected emission around 560 nm is attributed to NDI excimer formation due to the high concentration of the solution (more than ten times higher as for the analysis of the optical properties of the polymers).

In summary, the introduction of hydrophilic MPEG side chains does not change the desired optical properties of the dyad, i.e., the absorptivity of the individual building blocks is preserved and the emission quenching is not influenced.

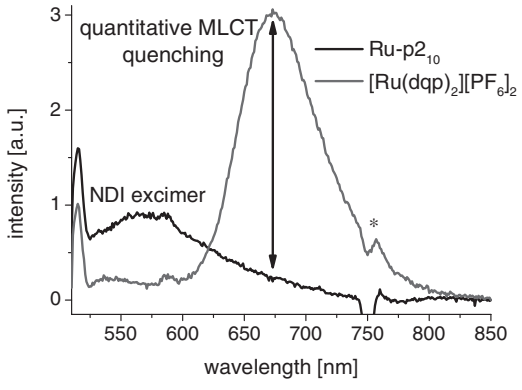

Figure 6. Emission data of the reference complex and the dyad Ru-P2$_{10}$ (aerated dichloromethane, room temperature, isoabsorbing solutions at 500 nm excitation, ≈10^{-6} M). Artefacts are marked with an asterisk.

4. Conclusions

Two styrenic naphthalene diimide based monomers with methyltriethylene or methylpoly(ethylene glycol) side chains were synthesized and subsequently polymerized using a functional commercial NMP initiator. The polymerization kinetics was analyzed for both monomers and revealed the controlled formation of well-defined telechelic polymers up to a conversion of 80 or 60%, respectively. For the MTEG substituted analog, the reaction rate decreases upon higher conversions due to the accumulation of persistent radicals. In contrast, the MPEG decorated pNDI revealed an increase of the reaction rate after longer reactions times, probably caused by secondary initiation reactions or kinetic effects.

The MPEG decorated telechelic polymer was examplarily functionalized with a Ru(II) photosensitizer on the chain terminus to construct a hydrophilic acceptor–photosensitizer dyad by nucleophilic substitution. The dyad was readily purified by preparative size-exclusion chromatography.

Due to the polar side chains, the monomers, the respective polymers, and the dyad feature an increased hydrophilicity and an improved solubility in polar solvents. Therefore, the MPEG substituted polymer and the respective dyad are well soluble in protic solvents, e.g., methanol or ethanol, and even paartially soluble in water. Thereby, the solubility in water decreases with an increasing DP.

The optical properties of the polymers and the dyad as well as a possible solvent influence were analyzed by steady-state absorption and emission spectroscopy. Whereas no strong influence of the solvent on the optical properties was found, the dyad showed an efficient emission quenching due to a proposed electron transfer from the ruthenium complex to the NDI polymer.

In conclusion, the incorporation of hydrophilic poly(ethylene glycol) side chains can be readily achieved and leads to an increase of the solubility of the polymers in polar solvents, while the desired modular character of the architecture with respect to the synthetic approach and the optical properties is preserved. The high hydrophilicity is beneficial for assembly of the materials in water-based solvents and, moreover, is expected to assist the assembly in combination with hydrophobic counterparts, e.g., in thin films or materials. The assembly of the hydrophilic dyads and the construction of amphiphilic donor–photosensitizer–acceptor triads by the utilization of bifunctional photosensitizers is under current investigation.

Supporting Information

Supporting Information is available from the Wiley Online Library or from the author.

Acknowledgements: The authors thank Annett Urbanek for MALDI-ToF measurements as well as Dr. Peter Bellstedt and the NMR platform of the IAAC/IOMC for help with the NMR measurements. Financial support by the Carl-Zeiss-Foundation, the Friedrich Schiller University Jena ("Nachwuchsförderung"), and the Thüringer Ministerium für Wirtschaft, Wissenschaft und Digitale Gesellschaft (TMWWDG), is kindly acknowledged.

Received: November 14, 2016; Revised: December 20, 2016; Published online: January 25, 2017; DOI: 10.1002/macp.201600534

Keywords: functional building blocks; light induced charge transfer; modular synthesis; nitroxide-mediated polymerization; ruthenium(II) polypyridyl complex

[1] N. S. Lewis, D. G. Nocera, *Proc. Natl. Acad. Sci. USA* **2006**, *103*, 15729.
[2] L. Hammarström, *Acc. Chem. Res.* **2015**, *48*, 840.
[3] V. Balzani, G. Bergamini, P. Ceroni, *Angew. Chem., Int. Ed.* **2015**, *54*, 11320.
[4] J. J. Concepcion, R. L. House, J. M. Papanikolas, T. J. Meyer, *Proc. Natl. Acad. Sci. USA* **2012**, *109*, 15560.
[5] J. H. Alstrum-Acevedo, M. K. Brennaman, T. J. Meyer, *Inorg. Chem.* **2005**, *44*, 6802.
[6] R. Schroot, T. Schlotthauer, U. S. Schubert, M. Jäger, *Macromolecules* **2016**, *49*, 2112.
[7] J. Kübel, R. Schroot, M. Wächtler, U. S. Schubert, B. Dietzek, M. Jäger, *J. Phys. Chem. C* **2015**, *119*, 4742.
[8] A. Facchetti, *Chem. Mater.* **2011**, *23*, 733.
[9] Z. He, H. Wu, Y. Cao, *Adv. Mater.* **2014**, *26*, 1006.
[10] J. C. Brendel, H. Burchardt, M. Thelakkat, *J. Mater. Chem.* **2012**, *22*, 24386.
[11] Z. Wu, C. Sun, S. Dong, X.-F. Jiang, S. Wu, H. Wu, H.-L. Yip, F. Huang, Y. Cao, *J. Am. Chem. Soc.* **2016**, *138*, 2004.
[12] P. Wittmeyer, S. Traser, R. Sander, K. B. Sondergeld, A. Ungefug, R. Weiss, M. Rehahn, *Macromol. Chem. Phys.* **2016**, *217*, 1473.
[13] C.-C. Hung, H.-C. Wu, Y.-C. Chiu, S.-H. Tung, W.-C. Chen, *J. Polym. Sci. Polym. Chem.* **2016**, *54*, 3224.
[14] F. Mathias, A. Fokina, K. Landfester, W. Tremel, F. Schmid, K. Char, R. Zentel, *Macromol. Rapid Commun.* **2015**, *36*, 959.
[15] M. He, F. Qiu, Z. Lin, *J. Mater. Chem.* **2011**, *21*, 17039.
[16] Y. Lee, E. D. Gomez, *Macromolecules* **2015**, *48*, 7385.
[17] E. Moulin, J.-J. Cid, N. Giuseppone, *Adv. Mater.* **2013**, *25*, 477.
[18] L. zur Borg, C. Schuell, H. Frey, R. Zentel, *Macromol. Rapid Commun.* **2013**, *34*, 1213.
[19] P. M. Reichstein, S. Gödrich, G. Papastavrou, M. Thelakkat, *Macromolecules* **2016**, *49*, 5484.
[20] S. Kohmoto, E. Mori, K. Kishikawa, *J. Am. Chem. Soc.* **2007**, *129*, 13364.
[21] C. Wendeln, S. Rinnen, C. Schulz, T. Kaufmann, H. F. Arlinghaus, B. J. Ravoo, *Chem. Eur. J.* **2012**, *18*, 5880.
[22] J. D. Revell, D. Gantenbein, P. Krattiger, H. Wennemers, *Pept. Sci.* **2006**, *84*, 105.
[23] P. A. Ledin, N. Kolishetti, G.-J. Boons, *Macromolecules* **2013**, *46*, 7759.
[24] R. Schroot, C. Friebe, E. Altuntas, S. Crotty, M. Jäger, U. S. Schubert, *Macromolecules* **2013**, *46*, 2039.
[25] M. Abrahamsson, M. Jäger, R. J. Kumar, T. Österman, P. Persson, H.-C. Becker, O. Johansson, L. Hammarström, *J. Am. Chem. Soc.* **2008**, *130*, 15533.
[26] This side product is indifferent in the later polymerization.
[27] G. Gryn'ova, C. Y. Lin, M. L. Coote, *Polym. Chem.* **2013**, *4*, 3744.
[28] J. Nicolas, Y. Guillaneuf, C. Lefay, D. Bertin, D. Gigmes, B. Charleux, *Prog. Polym. Sci.* **2013**, *38*, 63.
[29] D. Bertin, D. Gigmes, S. R. A. Marque, P. Tordo, *Chem. Soc. Rev.* **2011**, *40*, 2189.
[30] A. M. Striegel, W. W. Yau, J. J. Kirkland, D. D. Bly, in *Modern Size-Exclusion Liquid Chromatography*, John Wiley & Sons, Inc., Hoboken, NJ, USA **2009**, pp. 92–115.
[31] O. Guerret, J.-L. Couturier, F. Chauvin, H. El-Bouazzy, D. Bertin, D. Gigmes, S. Marque, H. Fischer, P. Tordo, in *Advances in Controlled/Living Radical Polymerization*, Vol. *854*, American Chemical Society, Ed: K. Matyjaszewski, Washington, DC **2003**, pp. 412–423.
[32] C. Feng, Y. Li, D. Yang, J. Hu, X. Zhang, X. Huang, *Chem. Soc. Rev.* **2011**, *40*, 1282.
[33] H.-I. Lee, J. Pietrasik, S. S. Sheiko, K. Matyjaszewski, *Prog. Polym. Sci.* **2010**, *35*, 24.
[34] B. A. Miller-Chou, J. L. Koenig, *Prog. Polym. Sci.* **2003**, *28*, 1223.
[35] S. Hocine, M.-H. Li, *Soft Matter* **2013**, *9*, 5839.
[36] M. Kumar, S. J. George, *Chem. Eur. J.* **2011**, *17*, 11102.
[37] P. Rajdev, M. R. Molla, S. Ghosh, *Langmuir* **2014**, *30*, 1969.
[38] M. R. Molla, D. Gehrig, L. Roy, V. Kamm, A. Paul, F. Laquai, S. Ghosh, *Chem. Eur. J.* **2014**, *20*, 760.
[39] S. Tu, S. H. Kim, J. Joseph, D. A. Modarelli, J. R. Parquette, *J. Am. Chem. Soc.* **2011**, *133*, 19125.
[40] H. Shao, J. Seifert, N. C. Romano, M. Gao, J. J. Helmus, C. P. Jaroniec, D. A. Modarelli, J. R. Parquette, *Angew. Chem., Int. Ed.* **2010**, *49*, 7688.
[41] T. C. Barros, S. Brochsztain, V. G. Toscano, P. B. Filho, M. J. Politi, *J. Photochem. Photobiol. A* **1997**, *111*, 97.
[42] T. D. M. Bell, S. V. Bhosale, C. M. Forsyth, D. Hayne, K. P. Ghiggino, J. A. Hutchison, C. H. Jani, S. J. Langford, M. A. P. Lee, C. P. Woodward, *Chem. Commun.* **2010**, *46*, 4881.
[43] X. Zhan, A. Facchetti, S. Barlow, T. J. Marks, M. A. Ratner, M. R. Wasielewski, S. R. Marder, *Adv. Mater.* **2011**, *23*, 268.
[44] S. Basak, N. Nandi, A. Baral, A. Banerjee, *Chem. Commun.* **2015**, *51*, 780.
[45] M. Kumar, S. J. George, *Nanoscale* **2011**, *3*, 2130.
[46] S. V. Bhosale, C. H. Jani, S. J. Langford, *Chem. Soc. Rev.* **2008**, *37*, 331.

Publication P7

A multidonor-photosensitizer-multiacceptor triad for long-lived directional charge separation

T. Schlotthauer, R. Schroot, S. Glover, L. Hammarström, M. Jäger, U. S. Schubert,
PCCP, **2017**, *19*, 28572-28578.

The paper as well as the supporting information (free of charge) is available online under: doi.org/10.1039/c7cp05593e

PCCP

PAPER

View Article Online
View Journal | View Issue

Cite this: *Phys. Chem. Chem. Phys.*, 2017, **19**, 28572

A multidonor–photosensitizer–multiacceptor triad for long-lived directional charge separation†

Tina Schlotthauer,[a] Robert Schroot,[a] Starla Glover,[b] Leif Hammarström,[b] Michael Jäger *[ac] and Ulrich S. Schubert *[ac]

Received 16th August 2017,
Accepted 10th October 2017

DOI: 10.1039/c7cp05593e

rsc.li/pccp

The modular assembly of a directional photoredox-active multidonor–photosensitizer–multiacceptor (D_n–P–A_m) architecture is presented. The triad assembly features a central Ru(II) sensitizer equipped with pendant polymer chains consisting of multiple triarylamine (pTARA) and naphthalene diimide (pNDI) units, respectively. Upon excitation, the efficient formation (>96%) of charge separation (CS) was observed featuring similar CS lifetimes (400 ns) as related molecular triads. In contrast, a significant additional longer-lived CS component (2400 ns, 30%) is observed indicating multiple contributing pathways.

The efficient conversion of light energy into a redox-chemical potential is a longstanding goal. On a molecular level, a multitude of artificial photosystems have been designed from individual photo- and redox-active building blocks.[1–7] These subunits perform the elementary steps of light absorption (by photosensitizer, P) and charge storage (by electron donor, D; electron acceptor, A) to generate a photo-induced charge separation. Within such assemblies, the individual (photo)-redox potentials dictate the thermodynamic driving forces for electron transfer, while the linkage pattern (bridge) between the units control the kinetics, which can be tuned in terms of electronic communication and the mutual distances.[8–11] Among other photosensitizers, polypyridyl-type Ru^{II} complexes display remarkable photophysical properties,[12–14] particularly $[Ru(bpy)_3]^{2+}$-based (bpy is 2,2′-bipyridine) complexes. Recently, $[Ru(dqp)_2]^{2+}$-type (dqp is 2,6-di(quinolin-8-yl)pyridine) complexes have emerged due to their advantageous combination of photophysical properties and axial symmetry, as well as enhanced photostability in comparison to $[Ru(bpy)_3]^{2+}$.[15,16] Typical electron donor units are based on electron-rich aromatics (*e.g.*, phenothiazine, triarylamines), while electron-deficient heterocycles (*e.g.*, methyl viologen, aromatic diimides) or quinones often serve as electron acceptors.[17–20] Numerous advanced molecular systems (triads, D–P–A; tetrades *etc.*) have been devised, that feature high molecular symmetry, adjusted redox potentials, and distinct spectroscopic signatures to elucidate the charge separation events. Noteworthy, extraordinary long-lived charge separation with excellent quantum yield has been achieved.[17–20] However, charge migration and storage – as desired for device application – implies formally multiple units, leading to increasingly elaborative syntheses, which impedes the practical value despite the powerful design principles. In this context, polymer chemistry offers not only appealing opportunities to connect multiple units, but also to further exploit the macromolecule's architecture (Fig. 1).[2,21] The capability to apply some of the principles in the design of macromolecular architectures is exemplified for light harvesting,[2,21] *e.g.*, using Ru^{II}-decorated oligopeptides[22–24] or polystyrene (PS),[25,26] poly(propylmethacrylate) (PPMA),[27] poly(3-hexylthiophene) (P3HT),[28] poly(fluorene)[29] or poly(fluorene-*co*-thiophene).[30] The seminal studies utilized statistical polymers *via* free radical polymerizations and/or grafting strategies, *e.g.*, to randomly embed D–P–A subunits within a P_n polymer chain (Fig. 1a). Efficient light harvesting and long-lived charge separation was demonstrated, although the generated charges are trapped locally due to the absent percolation pathway as a consequence of the random incorporation. In this regard, the reactive chain terminus offers an elegant opportunity to design directional macromolecular architectures. For example, a single viologen acceptor was appended to the P_n chain terminus, leading to approximately 30% emission quenching assigned to energy transfer and subsequent charge separation.[26] Similarly, an inverted architecture was devised with a single sensitizer coupled to a multi-acceptor chain, which displayed quantitative charge separation.[31,32] The immobilization of polymer-based dyads onto semiconductor interfaces (Fig. 1b and c), in analogy to dye sensitized solar cells,[33] was also reported. Due to the rapid interfacial electron injection and the semi-conductors band structure, long-lived charge separation up to hundreds

[a] *Laboratory of Organic and Macromolecular Chemistry (IOMC), Friedrich Schiller University Jena, Humboldtstraße 10, 07743 Jena, Germany. E-mail: michael.jager.iomc@uni-jena.de, Ulrich.schubert@uni-jena.de*
[b] *Department of Chemistry – Ångström Laboratory, Uppsala University, Box 523, SE75120 Uppsala, Sweden*
[c] *Center for Energy and Environmental Chemistry Jena (CEEC Jena), Friedrich Schiller University Jena, Philosophenweg 7a, 07743 Jena, Germany*

† Electronic supplementary information (ESI) available: Synthetic procedures as well as additional characterization data (NMR, MS, SEC, UV/vis data). See DOI: 10.1039/c7cp05593e

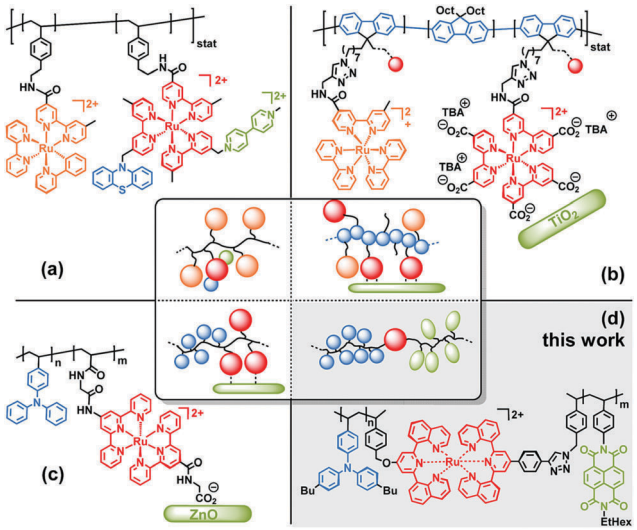

Fig. 1 Illustrative examples of macromolecular Ru-based photosystems composed of photosensitizer (in orange/red), electron donors (in blue) and electron acceptors (in green). Typical polypyridyl-type ligands based on bpy (a and b), tpy (c), and dqp (this work) framework, electron donors based on aromatic amines (a: phenothiazine; c and d: triarylamines) or polyfluorene (b), electron acceptors (a: methyl viologen, d: naphthalene diimide) or inorganic semiconductors (b: TiO_2, c: ZnO). Polymer backbones based on styrene (a and d), acrylates (c) or conjugated fluorene (b), forming statistical copolymers (a and b) or block-copolymers (c and d). See text for further details.

of microseconds was observed (Fig. 1b).[30] The progress in polymer chemistry further enabled the utilization of conjugated polymers, which were shown to act as electron donors in charge separation.[29,30] From a hierarchical perspective, the immobilized block-copolymer depicted in Fig. 1c features a multi-donor triarylamine polymer corona on a multi-acceptor ZnO particle with interjacently embedded photoactive Ru^{II} units. Notably, the detailed analysis required substantial molecular modelling to interpret the multiexponential decay data, which arises from the conformational freedom of the flexible polymer as well as defects due to incomplete grafting and/or chain-end functionalization.

In this contribution, a novel fully polymer-based architecture is explored (Fig. 1d and Scheme 1). The D_n–P–A_m triad consists of a single bifunctional photosensitizer, which can be selectively excited in the visible light region. The two functional groups were used to selectively attach precisely one multi-donor and one multi-acceptor chain. Triarylamine and naphthalene diimide units were selected as versatile donor and acceptor units, respectively, which are, *e.g.*, investigated in self-assembled naphthalene diimide (NDI) stacks for electron transport.[34,35] Hence, the resulting block-copolymer-type D_n–P–A_m architecture assures a percolation pathway for charge transport, in analogy to typical transport mechanisms in organic semiconductors.[36] The linkage pattern around the central Ru sensitizer unit adopts an axial geometry, in order to maximize the spatial separation of the charge-carrying units and, thus, is expected to minimize charge recombination. In addition, the synthesis relies on a modular chemistry-on-the-complex strategy including optimized purification protocols.

Modular syntheses and analytical characterization

The synthesis from donor dyads (D_n–P)[37] and acceptor dyads (P–A_m)[31,32] was extended to prepare a novel covalently linked multidonor–photosensitizer–multiacceptor (D_n–P–A_m) triad. Hence, the essential aspects in the design and preparation will be briefly recalled. In order to assist the readability throughout this manuscript, the functional building blocks and the corresponding properties are color-coded, *i.e.*, the photosensitizer in red, the electron donors in blue and electron acceptors in green, respectively. The donor and acceptor units were selected due to their transparency in the visible region, suitable redox potentials with respect to light-induced electron transfer, and

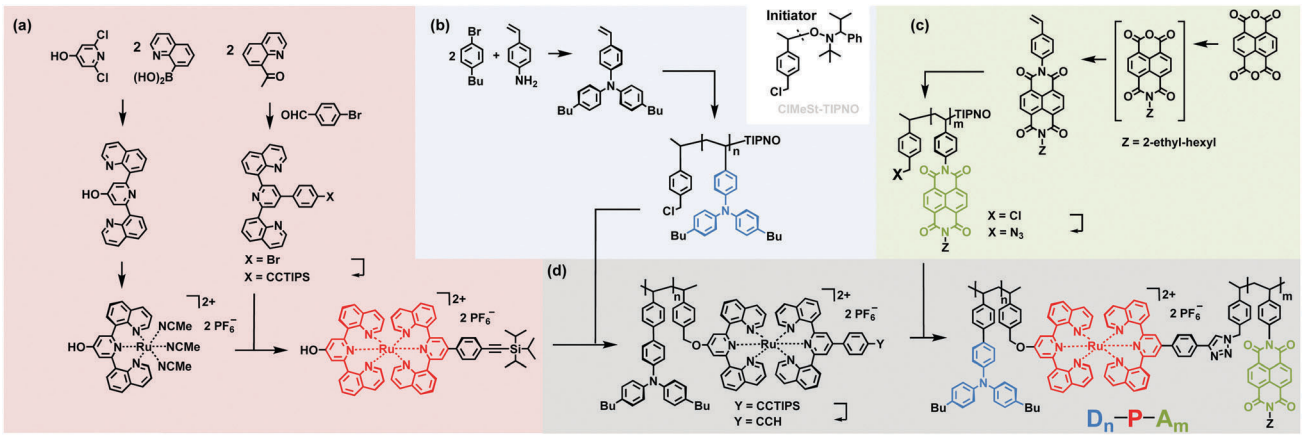

Scheme 1 Modular assembly strategy from building blocks. Syntheses of building blocks (colored boxes, a–c): (a) the bis-functionalized ruthenium photosensitizer, (b) the benzyl-chloride decorated poly(triarylamine) and (c) the azide-decorated poly(naphthalene diimide). Modular assembly (grey box, d) *via* Williamson ether synthesis and CuAAC reagents. Note the divergent character with at most five linear steps from commercially available starting reagents. For reagents and conditions see ESI.†

distinguishable spectroscopic signatures in the reduced/oxidized form. Following a divergent synthesis approach with at most five linear steps (Scheme 1), the chosen chemistry-on-the-complex approach and the developed purification protocols permits the quantitative functionalization by independently prepared polymers. The bis-functionalized Ru^{II} complex is readily prepared *via* stepwise coordination of the two ligands (Scheme 1a),[38] which bear the desired hydroxyl or tri-isopropylsilyl (TIPS)-protected alkyne groups. The telechelic donor and acceptor polymers were prepared *via* nitroxide-mediated polymerization (NMP) from the styrenic triarylamine (Scheme 1b) or styrenic naphthalene diimide (Scheme 1c),[32,37] which originate from vinyl aniline *via* the Hartwig–Buchwald coupling or stepwise condensation of naphthalene tetracarboxylic dianhydride.[31,37] Noteworthy, the desired polymer end group is already introduced *via* the commercially available NMP initiator. In addition, the terminal benzyl chloride unit is readily converted to the corresponding azide group after polymerization. Further experimental details and analytical characterization are provided in the ESI† (Fig. S2–S21). In summary, the divergently prepared building blocks are equipped with orthogonal functional groups to assist the modular assembly of the triad, the redox-active polymers poly(triarylamine) (pTARA) and poly(naphthalene diimide) (pNDI). Next, the D_n–P–A_m triad was prepared by Williamson ether synthesis to connect the pTARA-chain, followed by copper(I) catalyzed azide–alkyne cycloaddition (CuAAC) to attach the pNDI-chain (Scheme 1d). It should be noted, that the former polymer-analogous reactions required potassium iodide to facilitate efficient etherification *via* benzyl halide.[32] The covalent linkage of the donor dyad was confirmed by ^{1}H NMR spectroscopy *via* the characteristic benzylic protons at the linkage position (Fig. S10, ESI†). Size-exclusion chromatography (SEC) monitored by UV/vis further corroborates the covalent linkage, as shown by the characteristic polymer and Ru^{II} signatures at the same elution time (Fig. S20, ESI†).[32] Next, the silyl group was quantitatively cleaved by TBAF to release the free alkyne group, which served for the final CuAAC reaction with the azide-decorated pNDI-chain. The course of the reaction was easily monitored by UV/vis SEC and continued until no further conversion was observed. Notably, prolonged heating at elevated temperatures (80 °C) was necessary to obtain D_n–P–A_m applying our previously optimized protocol,[32] which stresses the necessity and utility of this highly efficient coupling strategy for such polymer-analogous reactions.[39,40] The purification was readily achieved by the preparative SEC using Toyopearl beads. Fig. 2a highlights the excellent separation, *i.e.*, the desired triad elutes first as judged by the characteristic absorption of pTARA (300 nm, grey shaded area) and pNDI (360 nm, black line). The ^{1}H NMR spectrum of D_n–P–A_m features the three building blocks (Fig. 2b, bottom), *i.e.*, the typical broad resonances of the aromatic protons of the NDI units (8.3 to 9.0 ppm and 7.0 to 7.5 ppm) and of the TARA units (6.3 to 7.0 ppm), as well as the minor signals arising from the single ruthenium unit (7.5 to 8.3 ppm). All attempts to obtain reliable mass spectrometry data failed, which is attributed to the challenges to record mass spectra of block copolymers, particularly in case of the cationic charge of the Ru^{II} fragment.

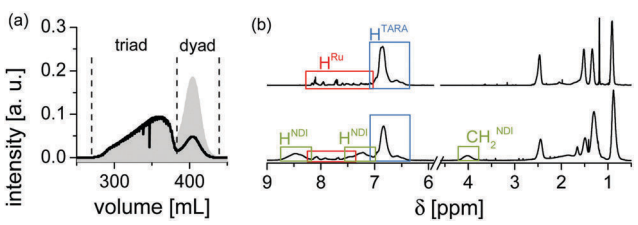

Fig. 2 (a) SEC elugram of the final separation using with UV monitoring typical for pNDI (360 nm, black curve) and for pTARA (300 nm, grey shaded area). (b) ^{1}H NMR spectra (600 MHz, CD_2Cl_2) of the dyad (top) and triad (bottom) with assigned characteristic protons. See Scheme 1 for corresponding molecular representations of the dyad and the triad.

Optical and electrochemical properties

In the following paragraph, the essential photophysical and electrochemical properties of the triad and related reference systems (Fig. 4) will be presented. The absorption spectrum of the triad resembles those of the individual components (Fig. 3), *i.e.*, identical maxima as pTARA (310 nm, blue-shaded), pNDI (360 and 386 nm, green-shaded), and the central $[Ru(dqp)_2]^{2+}$ unit (500 nm) as detailed previously,[31] indicating that no major perturbations in electronic character are introduced by linking of the triad. Hence the subsystems P, D_n–P and P–A_m (Fig. 4a–c) are ideal reference systems for thermodynamic and kinetic analysis. The steady state emission spectrum of P displays the typical ^{3}MLCT-based emission around 700 nm,[38] whereas both reference dyads D_n–P and P–A_m feature a second component (<650 nm) that has been previously assigned to polymer-based emission.[31,32] The donor dyad D_n–P shows a slightly lowered ^{3}MLCT emission intensity than P, which is reasonable in view of the unfavorable energetics for reductive quenching by the pTARA.[31] In contrast, the triad displays almost quantitative Ru emission quenching (96%), as detailed for the P–A_m dyad,[31] which indicates similar electron transfer to the pNDI fragment for D_n–P–A_m (*vide infra*). In line with steady state emission data, the electrochemical data are consistent with the postulated quenching pathways for the triad. The driving forces for

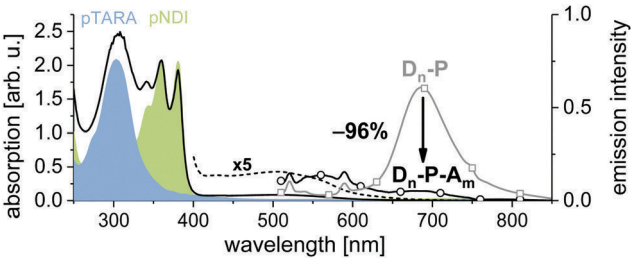

Fig. 3 Absorption spectra of the polymeric building blocks pTARA (blue-shaded area) and pNDI (green-shaded area) and the triad (black curve). Note the amplified signal (×5, dashed line) to illustrate the weak absorption band of the single Ru photosensitizer unit (400–600 nm). Steady-state emission spectra of the precursor dyad (grey line, rectangles) and the triad (black line, circles). Note polymer-based emission (<650 nm) and the ^{3}MLCT emission (around 700 nm), the latter revealing strong quenching (−96%) between dyad (D_n–P) and triad after subtracting residual polymer-based emission.

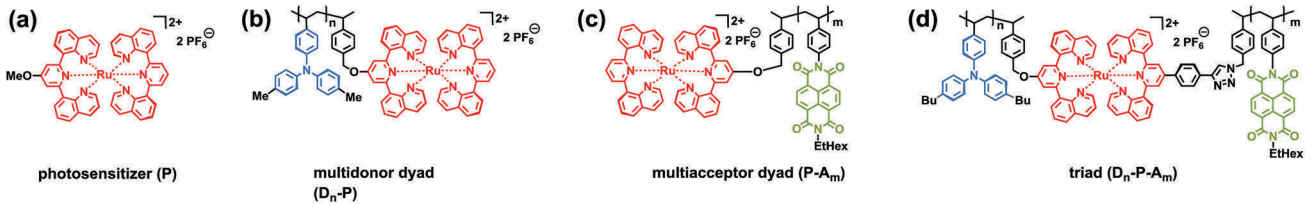

Fig. 4 Molecular representation of the triad including reference subsystems investigated by time-resolved spectroscopy: (a) photosensitizer core (P), (b) multidonor–photosensitizer dyad (D_n–P), (c) photosensitizer–multiacceptor dyad (P–A_m), and (d) multidonor–photosensitizer–multiacceptor triad (D_n–P–A_m). See ref. 31 and 37 for syntheses and steady state properties.

electron transfer can be estimated from the formal excited state potential of the photosensitizer with respect to the redox potential of the polymers. The calculated driving forces suggest primary oxidative quenching (ΔG = −0.25 eV) with secondary electron transfer to regenerate the photosensitizer (−0.25 eV), whereas the reductive quenching pathway is unfavorable (+0.20 eV) as detailed previously.[31] Next, the spectroelectrochemical features of the redox-active subunits will be briefly recalled (Fig. S23, ESI†),[31,41] which are essential for the interpretation of the transient absorption data. The oxidized donor ($pTARA^+$) exhibits a strong absorption around 690 nm, and the reduced acceptor ($pNDI^-$) displays characteristic maxima at 475 and 610 nm. The oxidized photosensitizer (Ru^{III}) features a decrease of the ^{1}MLCT band (around 500 nm) and broad absorptions above 700 nm.

The time-resolved emission and transient absorption measurements (Fig. 5) were performed to investigate the light–induced events of the triad in detail, including the reference systems shown in Fig. 4. The observed emission lifetime of P (760 ns in DCM) is considerably shorter than that reported in MeCN (3000 ns),[38] in line with the solvent effects leading to an analogously decreased lifetime of $[Ru(bpy)_3]^{2+}$ (bpy is 2,2′-bipyridine).[42] The D_n–P dyad reveals a slightly shorter emission lifetime (660 ns) (Fig. S24, ESI†), in agreement with the steady state emission data. An additional short-lived component on the time-scale of the excitation pulse (*ca.* 10 ns) is observed in the dyad, which is absent in the case of the pristine photosensitizer unit. This distinct feature is assigned to polymer-based emission (*vide infra*), which stretched out to the ^{3}MLCT region as confirmed by the steady state emission data. A similarly short-lived emission (<10 ns) is detected for the P–A_m dyad (Fig. S24d, ESI†), but without any detectable long-lived ^{3}MLCT emission. These findings parallel our previous time-correlated single photon counting (TCSPC) data that showed efficient ^{3}MLCT emission quenching within 10 ns (90%).[31] In order to clarify the contribution by polymer-based emission (<650 nm) for the D_n–P–A_m triad, time-correlated single photon counting (TCSPC) measurements were performed using suitable filters for the polymer-based region (band pass, 450–650 nm) and the ^{3}MLCT region (long pass, >715 nm, Fig. S26, ESI†). Although the polymer-based emission is reasonably well described by a mono-exponential decay (τ = 3 ns, Fig. S27, ESI†), adding a second decay component improved the fit (Table S1, ESI†). Likewise, the fit of the ^{3}MLCT region requires a second more long-lived component (49 ns, 22%). This finding parallels the observed multiexponential emission decay in a Ru-NDI dyad with flexible linkage, assigned to several conformers with different mutual distances and orientations and, thus, electron transfer rates.[43] A similar scenario is conceivable for the unsaturated polymer backbone, which gives rise to an even more complicate ensemble of geometries.[44] A Stern–Vollmer analysis using the donor D_n–P subunit and unbound NDI-based acceptors revealed the diffusional quenching pathway (Fig. S28, ESI†) and, thus, further corroborates the successful linkage of the covalent D_n–P–A_m triad.

Transient absorption (TA) spectra were recorded between 400 and 730 nm (Fig. 5 and Fig. S29–S32, ESI†) to identify and follow the (intermediate) states by virtue of their spectroelectrochemical signatures. Upon excitation, the reference complex (P) shows the typical ^{1}MLCT bleach and ^{3}MLCT absorptions at longer wavelengths, which are partially overlapped by stimulated emission (Fig. S29, ESI†). The spectral decay is characterized by several isosbestic points and follows mono-exponential kinetics (730 ns), which is in satisfying agreement with the emission lifetime. The TA data of the D_n–P dyad shows a generally similar

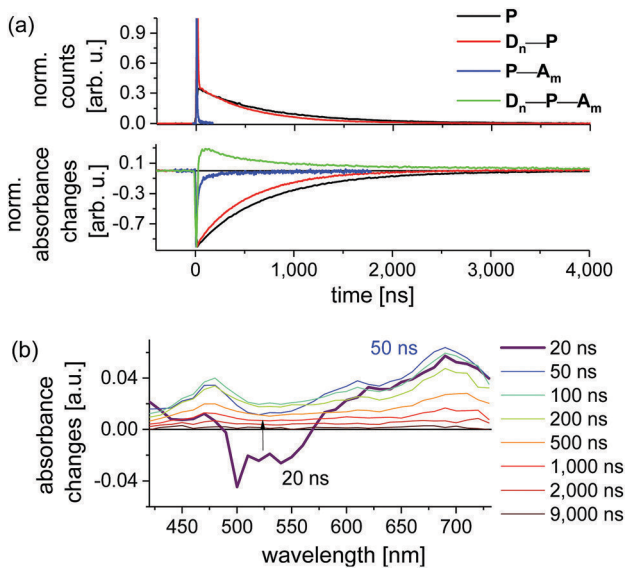

Fig. 5 (a) Time-resolved emission (top) and transient absorption traces (bottom) in de-aerated DCM upon excitation at 532 nm (except for D_n–P–A_m at 500 nm). Emission recorded at 700 nm (except P–A_m at 690 nm), all transient absorption traces taken at 500 nm. Note the biexponential decay in the case of D_n–P–A_m with time constants of 430 and 2400 ns (see Fig. S32, ESI†). (b) TA data showing the rapid formation of a charge-separated state and slow subsequent recombination. Note the fast ^{1}MLCT recovery, as well as the positive TA signatures of $pNDI^-$ (475 and 610 nm) and $pTARA^+$ (690 nm) in accordance with the spectroelectrochemical data (Fig. S23, ESI†).

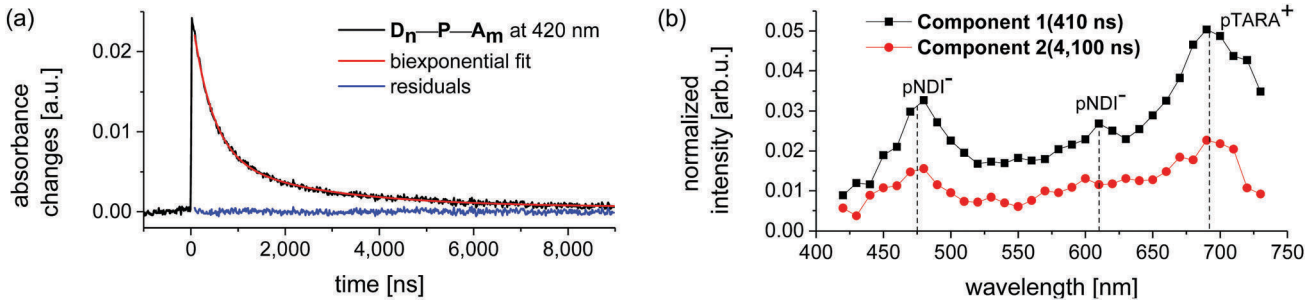

Fig. 6 Transient absorption data of D_n–P–A_m: (a) spectral recovery at 420 nm with biexponential fit. (b) Spectral signatures derived from global analysis (>100 ns) applying biexponential kinetics. Dashed lines visualize typical absorptions of the reduced pNDI (475 and 610 nm) and oxidized pTARA (690 nm). Note the similar spectral signatures of component 1 (black curve) and 2 (red curve) indicative for the fully charge separated state D_n^+–P–A_m^-.

behavior (Fig. S30, ESI†), except for an unusually strong negative TA contribution at short time scales (<20 ns) and higher wavelengths (>550 nm, Fig. S30b, ESI†). In comparison to P, the isosbestic point at 435 nm is preserved, while the ones at 575 or 655 nm are absent. The TA recovery of D_n–P was followed at 470 nm and is best described by a mono-exponential decay (530 ns), although including a second component enhances the fit at early times (Fig. S30, ESI†). Hence, a biexponential global fit of the TA data was performed to verify this hypothesis. The spectral profile of the long-lived component (520 ns) matches perfectly that of pristine P, including the identical isosbestic points, while the spectrum of the short-lived component (6 ns) resembles that of the polymer-based emission. A similar short-lived polymer-based TA feature was also found for P–A_m (Fig. S31, ESI†). In contrast, the long-lived ^{3}MLCT-based TA signal is absent, in line with our previous study that revealed fast initial charge separation (<1.6 ns).[31] In fact, a weak NDI^- signature was observed on the time scale of the excitation pulse (Fig. S31b, ESI†). As judged from absent build-up of the corresponding TA signatures, the charge recombination seems faster than charge separation, so that the TA recovery is completed within 100 ns (Fig. 5a).[31] In marked contrast, the D_n–P–A_m triad shows the immediate formation of the fully charge separated (CS) state, as identified by the concomitant ^{1}MLCT recovery and the evolving positive TA signatures of $pNDI^-$ and $pTARA^+$ (Fig. 5b). More importantly, the TA signal decays orders of magnitude slower than in the reference dyad, following multiexponential kinetics (Fig. S32, ESI†). The associated lifetimes of a biexponential fit are 430 ns (71%) and 2400 ns (29%). Performing the global fit of the 2D TA data revealed identical spectral profiles of the two components, which are characteristic for the fully charge separated state (Fig. 6). Notably, the charge separation persists even longer than observed for $[Ru(dqp)_2]^{2+}$-based related molecular triads (140–200 ns).[45] A further assignment, *e.g.*, as reported for an extremely long-lived molecular tetrades with distinct spectroscopic signatures,[17] is precluded due to the invariant spectral signatures of the repeating units. In addition, the ensemble of conformations is also unknown (*vide supra*) but can be estimated from extensive molecular modelling in analogy to the polymer-based light harvesting and electron transfer studies as reported by Papanikolas *et al.*[7,46] In general, the back-folding of the flexible polymer chain leads to shorter formal electron transfer distances than the one set by the sensitizer and the first repeat unit along the attached chain. Hence, multiple electron transfer pathways can exist explaining the observed multiexponential emission decay. Notably, the emission decay within a few nanoseconds confirms efficient charge separation, while the timescale of recombination is two orders of magnitude longer. The multi-exponential character of the emission and recombination indicates multiple pathways, which are practically indistinguishable due to the identical signatures of the repeating units, yet long-lived charge separation is observed within the polymer assembly. Although such spectroscopic properties seem unfavorable in terms of a full spectroscopic analysis, the simple modular preparation and the resemblance of organic semiconductors may open promising routes to tune subsequent charge transport.[36]

Conclusions

An efficient divergent modular synthesis was established to prepare a multidonor–photosensitizer–multiacceptor triad (D_n–P–A_m), *i.e.*, only five linear synthetic steps from commercially available materials and facile purification. The functional building blocks were selected according to their photophysical and electrochemical properties (P, D_n, and A_m), and were connected in a modular fashion. After selective excitation of the photosensitizer in the visible light region, quantitative charge separation was observed. Detailed steady state and time-resolved spectroscopy of the triad and the related subsystems confirmed long-lived charge separation, despite the unsaturated flexible linkage pattern among the units that is usually avoided in model systems. Multiexponential decay was observed, in line with the conformational freedom and ensemble of electron transfer pathways. Nevertheless, the advantages and the future perspective to utilize such triad assembly originate from the synthetic advance in polymer chemistry,[47] *e.g.*, to assure an internal redox-cascade by block-copolymer,[41] to incorporate phase-forming substituents[48] to achieve self-organization for energy conversion,[35] to embed conjugated organic semiconductors,[49] and/or to provide local redox gradients to power molecular machines.

Conflicts of interest

There are no conflicts to declare.

Acknowledgements

Financial support by the Carl-Zeiss-Foundation, the Friedrich Schiller University Jena ("Nachwuchsförderung") and the Thüringer Ministerium für Wirtschaft, Wissenschaft und Digitale Gesellschaft (TMWWDG), and the Swedish Research Council (grant no. 2012-3926) is kindly acknowledged. The authors thank Annett Urbanek for MALDI-ToF measurements as well as Dr Peter Bellstedt and the NMR platform of the IAAC/IOMC for help with the NMR measurements.

References

1 V. Balzani, G. Bergamini and P. Ceroni, *Angew. Chem., Int. Ed.*, 2015, **54**, 11320–11337.
2 J. H. Alstrum-Acevedo, M. K. Brennaman and T. J. Meyer, *Inorg. Chem.*, 2005, **44**, 6802–6827.
3 J. J. Concepcion, R. L. House, J. M. Papanikolas and T. J. Meyer, *Proc. Natl. Acad. Sci. U. S. A.*, 2012, **109**, 15560–15564.
4 L. Hammarström, *Acc. Chem. Res.*, 2015, **48**, 840–850.
5 V. Balzani, A. Credi and M. Venturi, *ChemSuSchem*, 2008, **1**, 26–58.
6 V. Balzani, L. Moggi, M. F. Manfrin, F. Bolletta and M. Gleria, *Science*, 1975, **189**, 852–856.
7 Z. A. Morseth, T. V. Pho, A. T. Gilligan, R. J. Dillon, K. S. Schanze, J. R. Reynolds and J. M. Papanikolas, *J. Phys. Chem. B*, 2016, **120**, 7937–7948.
8 N. S. Hush, *Coord. Chem. Rev.*, 1985, **64**, 135–157.
9 B. Albinsson and J. Martensson, *J. Photochem. Photobiol., C*, 2008, **9**, 138–155.
10 O. S. Wenger, *Coord. Chem. Rev.*, 2009, **253**, 1439–1457.
11 M. Natali, S. Campagna and F. Scandola, *Chem. Soc. Rev.*, 2014, **43**, 4005–4018.
12 S. Campagna, F. Puntoriero, F. Nastasi, G. Bergamini and V. Balzani, in *Photochemistry and Photophysics of Coordination Compounds I*, ed. V. Balzani and S. Campagna, Springer-Verlag Berlin, Berlin, 2007, vol. 280, pp. 117–214.
13 A. Juris, V. Balzani, F. Barigelletti, S. Campagna, P. Belser and A. von Zelewsky, *Coord. Chem. Rev.*, 1988, **84**, 85–277.
14 D. W. Thompson, A. Ito and T. J. Meyer, *Pure Appl. Chem.*, 2013, **85**, 1257–1305.
15 L. Hammarström and O. Johansson, *Coord. Chem. Rev.*, 2010, **254**, 2546–2559.
16 M. Abrahamsson, M. Jäger, R. J. Kumar, T. Österman, P. Persson, H.-C. Becker, O. Johansson and L. Hammarström, *J. Am. Chem. Soc.*, 2008, **130**, 15533–15542.
17 H. Imahori, D. M. Guldi, K. Tamaki, Y. Yoshida, C. P. Luo, Y. Sakata and S. Fukuzumi, *J. Am. Chem. Soc.*, 2001, **123**, 6617–6628.
18 J. Hankache and O. S. Wenger, *Chem. Commun.*, 2011, **47**, 10145–10147.
19 M. H. V. Huynh, D. M. Dattelbaum and T. J. Meyer, *Coord. Chem. Rev.*, 2005, **249**, 457–483.
20 J. Hankache, M. Niemi, H. Lemmetyinen and O. S. Wenger, *Inorg. Chem.*, 2012, **51**, 6333–6344.
21 Z. A. Morseth, L. Wang, E. Puodziukynaite, G. Leem, A. T. Gilligan, T. J. Meyer, K. S. Schanze, J. R. Reynolds and J. M. Papanikolas, *Acc. Chem. Res.*, 2015, **48**, 818–827.
22 D. M. Ryan, M. K. Coggins, J. J. Concepcion, D. L. Ashford, Z. Fang, L. Alibabaei, D. Ma, T. J. Meyer and M. L. Waters, *Inorg. Chem.*, 2014, **53**, 8120–8128.
23 S. E. Bettis, D. M. Ryan, M. K. Gish, L. Alibabaei, T. J. Meyer, M. L. Waters and J. M. Papanikolas, *J. Phys. Chem. C*, 2014, **118**, 6029–6037.
24 D. Ma, S. E. Bettis, K. Hanson, M. Minakova, L. Alibabaei, W. Fondrie, D. M. Ryan, G. A. Papoian, T. J. Meyer, M. L. Waters and J. M. Papanikolas, *J. Am. Chem. Soc.*, 2013, **135**, 5250–5253.
25 G. Leem, S. Keinan, J. Jiang, Z. Chen, T. Pho, Z. A. Morseth, Z. Hu, E. Puodziukynaite, Z. Fang, J. M. Papanikolas, J. R. Reynolds and K. S. Schanze, *Polym. Chem.*, 2015, **6**, 8184–8193.
26 Z. Fang, A. Ito, S. Keinan, Z. Chen, Z. Watson, J. Rochette, Y. Kanai, D. Taylor, K. S. Schanze and T. J. Meyer, *Inorg. Chem.*, 2013, **52**, 8511–8520.
27 Z. Fang, A. Ito, H. Luo, D. L. Ashford, J. J. Concepcion, L. Alibabaei and T. J. Meyer, *Dalton Trans.*, 2015, **44**, 8640–8648.
28 L. Wang, E. Puodziukynaite, E. M. Grumstrup, A. C. Brown, S. Keinan, K. S. Schanze, J. R. Reynolds and J. M. Papanikolas, *J. Phys. Chem. Lett.*, 2013, **4**, 2269–2273.
29 G. Leem, Z. A. Morseth, E. Puodziukynaite, J. Jiang, Z. Fang, A. T. Gilligan, J. R. Reynolds, J. M. Papanikolas and K. S. Schanze, *J. Phys. Chem. C*, 2014, **118**, 28535–28541.
30 E. Puodziukynaite, L. Wang, K. S. Schanze, J. M. Papanikolas and J. R. Reynolds, *Polym. Chem.*, 2014, **5**, 2363–2369.
31 J. Kübel, R. Schroot, M. Wächtler, U. S. Schubert, B. Dietzek and M. Jäger, *J. Phys. Chem. C*, 2015, **119**, 4742–4751.
32 R. Schroot, T. Schlotthauer, U. S. Schubert and M. Jäger, *Macromolecules*, 2016, **49**, 2112–2123.
33 B. E. Hardin, H. J. Snaith and M. D. McGehee, *Nat. Photonics*, 2012, **6**, 162–169.
34 A. L. Sisson, N. Sakai, N. Banerji, A. Furstenberg, E. Vauthey and S. Matile, *Angew. Chem., Int. Ed.*, 2008, **47**, 3727–3729.
35 O. Yushchenko, D. Villamaina, N. Sakai, S. Matile and E. Vauthey, *J. Phys. Chem. C*, 2015, **119**, 14999–15008.
36 H. Baessler and A. Koehler, *Topics in Current Chemsitry*, Springer Verlag, Berlin Heidelberg, 2012, vol. 312, pp. 1–66.
37 R. Schroot, C. Friebe, E. Altuntas, S. Crotty, M. Jäger and U. S. Schubert, *Macromolecules*, 2013, **46**, 2039–2048.
38 M. Jäger, R. J. Kumar, H. Görls, J. Bergquist and O. Johansson, *Inorg. Chem.*, 2009, **48**, 3228–3238.
39 U. Mansfeld, C. Pietsch, R. Hoogenboom, C. R. Becer and U. S. Schubert, *Polym. Chem.*, 2010, **1**, 1560–1598.
40 C.-H. Wong and S. C. Zimmerman, *Chem. Commun.*, 2013, **49**, 1679–1695.
41 R. Schroot, U. S. Schubert and M. Jäger, *Macromolecules*, 2015, **48**, 1963–1971.
42 J. V. Caspar and T. J. Meyer, *J. Am. Chem. Soc.*, 1983, **105**, 5583–5590.
43 D. W. Dixon, N. B. Thornton, V. Steullet and T. Netzel, *Inorg. Chem.*, 1999, **38**, 5526–5534.

44 Adding a third component further improved the fit (see Table S1 (ESI†) for comparison).
45 R. J. Kumar, S. Karlsson, D. Streich, A. R. Jensen, M. Jäger, H.-C. Becker, J. Bergquist, O. Johansson and L. Hammarström, *Chem. – Eur. J.*, 2010, **16**, 2830–2842.
46 C. N. Fleming, K. A. Maxwell, J. M. DeSimone, T. J. Meyer and J. M. Papanikolas, *J. Am. Chem. Soc.*, 2001, **123**, 10336–10347.
47 R. Schroot, M. Jäger and U. S. Schubert, *Chem. Soc. Rev.*, 2017, **46**, 2754–2798.
48 R. Schroot, T. Schlotthauer, M. Jäger and U. S. Schubert, *Macromol. Chem. Phys.*, 2017, **218**, DOI: 10.1002/macp.201600534.
49 R. Schroot, T. Schlotthauer, B. Dietzek, M. Jäger and U. S. Schubert, *Chem. – Eur. J.*, 2017, DOI: 10.1002/chem.201704180.

Publication P8

Block copolymer-type architecture with a central Ru^{II} sensitizer core: Conjugated poly(carbazole) for enhanced charge separation

R. Schroot, T. Schlotthauer, B. Dietzek, M. Jäger, U. S. Schubert, *Chem. Soc. Rev.* **2017**, *46*, 2754-2798.

The paper as well as the supporting information (free of charge) are available online under: doi.org/10.1002/chem.201704180

ChemPubSoc Europe

DOI: 10.1002/chem.201704180

CHEMISTRY
A European Journal
Full Paper

Donor–Acceptor Systems |*Hot Paper*|

Extending Long-lived Charge Separation Between Donor and Acceptor Blocks in Novel Copolymer Architectures Featuring a Sensitizer Core

Robert Schroot,[a, b] Tina Schlotthauer,[a, b] Benjamin Dietzek,[b, c] Michael Jäger,*[a, b] and Ulrich S. Schubert*[a, b]

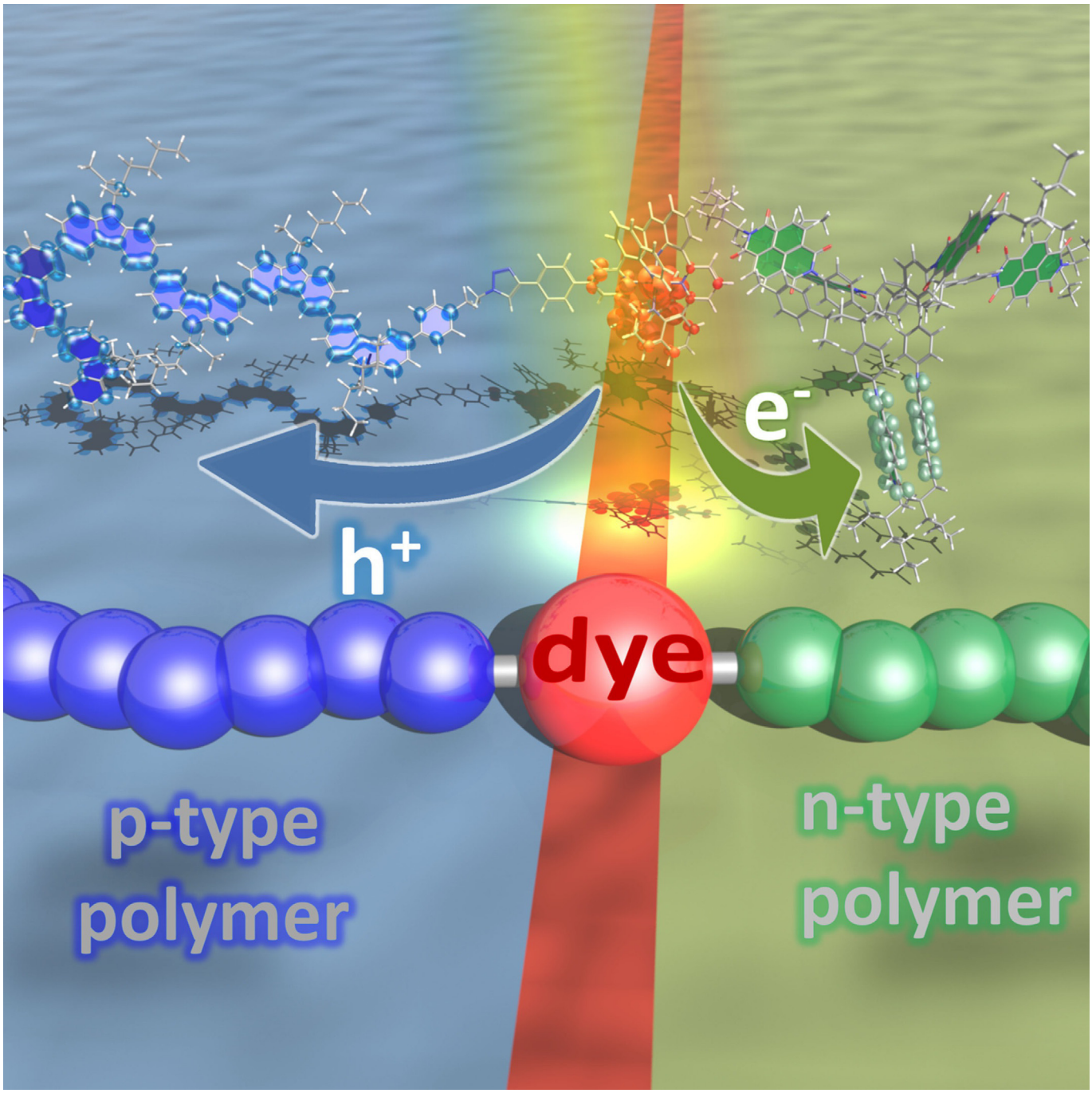

Abstract: A bifunctional Ru^{II} photosensitizer unit was decorated with one n- and one p-type polymer chain to form precisely controlled hierarchical copolymer-type architectures for light-induced charge separation. The applied modular chemistry-on-the-complex strategy benefits from separately prepared building blocks and their orthogonal linkage in the two final assembly steps. Upon visible light absorption, electron transfer is initiated between the conjugated poly(3,6-carbazole) chain and the styrenic poly(naphthalene diimide) segments. Steady-state and time-resolved spectroscopy show complete charge separation within a few nanoseconds (>95% efficiency) persisting several tens of microseconds. The recombination is significantly reduced in comparison to low-molecular model systems or to non-conjugated congeners, reflecting the higher charge mobility in conjugated polymers. In summary, the modularity of the presented approach is expected to serve as a versatile platform to tailor the interface between the charge transport domains in a systematic fashion.

Introduction

The efficient interconversion of photoenergy into electrical or chemical bond energy can be achieved, among other ways, by molecular photosystems composed of functional building blocks.[1–6] The versatility of this approach relies on precisely tailored units for light absorption and charge separation, as demonstrated in molecular triads reaching impressive quantum efficiencies (up to 95%).[2] After photon absorption by the photosensitizer (**P**), electron transfer steps occur to the attached donor (**D**) and/or acceptor (**A**) sites and the individual rates are controlled by the nature of the linkage (bridge).[7–11] Very long charge-separated (CS) lifetimes exceeding the microsecond timescale can be achieved,[12] for example, to harness the generated electrochemical potential in photovoltaic or by coupled catalytic processes. In this regard, Ru^{II} polypyridyl-type complexes often serve as versatile photosensitizer owing to their remarkable excited state properties.[13] In molecular **D–P–A** systems, the charges reside ultimately on the single donor and acceptor sites and often inevitably recombine, before they can be harnessed. Hence, the incorporation of multiple donor/acceptor sites is attractive, but the convergent syntheses are often (prohibitively) elaborate in the case of low-molecular model systems.

Alternatively, polymer chemistry offers an elegant route to tailored photo- and electrochemically active macromolecules,[14] which a priori provide charge percolation pathways, can perform charge accumulation as well as a phase segregation of the donor/acceptor domains—in close resemblance of modern organic photovoltaics.[15–21] The versatility to design and construct macromolecular photosystems is evident from the reports on Ru-decorated oligopeptides,[15,16] poly(styrene)s,[18] poly(acrylates)s,[19] poly(thiophene)s,[22] poly(fluorene)[21] or poly(fluorene-*co*-thiophene).[20] Notably, most of the early examples comprised statistical assemblies and/or grafted macromolecules, mainly due to the available polymerization techniques (and their limitations) at that time. As a consequence, most of the aforementioned macromolecules are devoid of charge percolation pathways, despite their simple preparation. In order to diminish unfruitful recombination of the photo-generated charges, the (macro)molecular assembly must sustain charge transport, for example, to reach external electrodes or catalytically active sites. The recent advances in polymer science enables an a priori design and the facile preparation of well-defined functional macromolecules from photo- and redox-active building blocks. In other words, functionalized polymers can be tailored and prepared (e.g., multi-donor ($\mathbf{D_n}$) and multi-acceptor ($\mathbf{A_m}$) polymers) with the desired optoelectronic properties.[14] More importantly, such building blocks can be interconnected afterwards through the chain end's functional group in a modular fashion, leading to advanced architectures. In addition, such divergent syntheses further minimize substantially the synthetic efforts, which permits the systematic exploration of $\mathbf{D_n}$–**P**–$\mathbf{A_m}$ architectures. Recently, we reported the facile synthesis of telechelic poly(triarylamine) and poly(naphthalene diimide) by nitroxide-mediated polymerization (NMP), and their facile modular assembly was reported for various dyads ($\mathbf{D_n}$–**P** or **P**–$\mathbf{A_m}$).[23–27] Notably, the efficient charge separation upon excitation was demonstrated,[25,28] revealing a remarkably long-lived component (2,400 ns) that is tentatively assigned to charge migration within the polymer.

In this contribution, the poly(triarylamine) block of the previous $\mathbf{D_n}$–**P**–$\mathbf{A_m}$ architecture was replaced by a conjugated telechelic poly(3,6-*N*-alkylcarbazole), since conjugated polymers are known to feature higher charge charrier mobilities[29–35] and, thus, may prolong the CS life time.

[a] *R. Schroot, T. Schlotthauer, Dr. M. Jäger, Prof. Dr. U. S. Schubert*
Laboratory of Organic and Macromolecular Chemistry (IOMC)
Friedrich Schiller University Jena
Humboldtstraße 10, 07743 Jena (Germany)
E-mail: michael.jager.iomc@uni-jena.de
ulrich.schubert@uni-jena.de

[b] *R. Schroot, T. Schlotthauer, Prof. Dr. B. Dietzek, Dr. M. Jäger, Prof. Dr. U. S. Schubert*
Center for Energy and Environmental Chemistry Jena (CEEC Jena)
Friedrich Schiller University Jena
Philosophenweg 7a, 07743 Jena (Germany)

[c] *Prof. Dr. B. Dietzek*
Institute for Physical Chemistry and Abbe Center of Photonics (ACP)
Friedrich Schiller University Jena
Helmholtzweg 4, 07743 Jena (Germany)
and
Leibniz Institute for Photonic Technology (IPHT)
Albert-Einstein-Straße 9, 07743 Jena (Germany)

Supporting information and the ORCID identification number(s) for the author(s) of this article can be found under https://doi.org/10.1002/chem.201704180.

Results and Discussion

Synthesis and characterization

The desired triad can be readily prepared due to the chosen modular character of the-chemistry-on-the-complex approach as outlined in Scheme 1. The individual syntheses of the poly(3,6-carbazole) (**pCarb**),[36] the poly(naphthalene diimide) (**pNDI**),[24] and the bis-functionalized Ru^{II} precursor complex[24,28] have been reported. The novel donor dyad $\mathbf{D_n}$–**P** was prepared from telechelic poly(3,6,-carbazole) via the copper(I) catalyzed azide–alkyne cycloaddition (CuAAC). The applied reagents, that is, $Cu^{I}Br$ as catalyst, PMDETA as base and DMF as solvent are known to be efficient for the linkage of related azide-decorated polymers with complexes.[24] However, longer reaction times and elevated temperatures were required as shown by analytical size-exclusion chromatography (SEC) and TLC analysis. The purification was conveniently accomplished by preparative SEC using a commercial resin (Toyopearl HW-55F). The successful linkage was confirmed by UV/Vis SEC analysis and MALDI-TOF mass spectrometry (Figure S8). The synthesis of the corresponding reference complex (**P**) was reported previously,[24] whereas the synthesis of the triad embarked from the bis-functionalized Ru^{II} precursor (X = OH).[28] First, the precursor dyad $\mathbf{P–A_m}$ was prepared analogously to our established protocols.[24] The nucleophilic substitution of the hydroxyl group with benzyl-halide decorated poly(naphthalene diimide) afforded $\mathbf{P–A_m}$ in very good yields (75%). Next, the terminal alkyne group was quantitatively deprotected with (nBu$_4$)NF without the need of chromatographic purification. The final coupling step by CuAAC as described above gave the desired $\mathbf{D_n–P–A_m}$ triad. Notably, an excess of the donor polymer was used to account for residual macrocycles,[36] which cannot undergo coupling and are readily separated by preparative SEC. In contrast, the removal of unreacted acceptor dyad to obtain pure $\mathbf{D_n–P–A_m}$ was more challenging due to the marginal increase in molar mass of the triad versus the dyad. This hypothesis is corroborated by the ^{1}H NMR spectra of **pCarb**, $\mathbf{P–A_m}$ and $\mathbf{D_n–P–A_m}$ (Figure 1), which reveal the characteristic but weak resonances of the poly(carbazole) in the final $\mathbf{D_n–P–A_m}$ triad. Although no MS data could be obtained to confirm the covalent linkage, the comprehensive 3D SEC analysis strongly suggests the covalent linkage. As expected, the elution profiles feature mono-modal distributions with decreased elution times due to the increased size (hydrodynamic volume) of the compounds, and the associated UV/Vis spectra correspond to the building blocks (see Supporting Information Section 5 for explanation and Figures S11–S15).

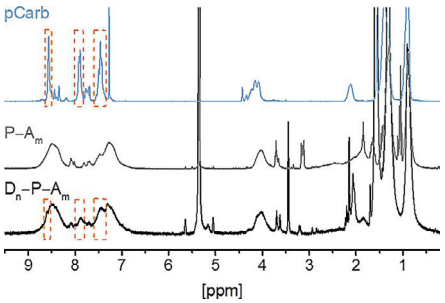

Figure 1. Proton NMR spectra of **pCarb**, $\mathbf{P–A_m}$ and $\mathbf{D_n–P–A_m}$ (300 MHz, $CDCl_3$ or CD_2Cl_2). The appearance of broad resonances of pCarb at approximately 7.4, 7.9 and 8.6 ppm (orange doted boxes) indicates the successful preparation of the triad $\mathbf{D_n–P–A_m}$. Note residual solvent signals in the aliphatic region of the triad.

Steady-state spectroscopy

The photophysical properties of the triad and the respective subsystems were investigated by steady-state and time-resolved spectroscopy. The light-induced electron transfer within the acceptor dyad $\mathbf{P–A_m}$ has been established previously,[24,25] hence we deliberately limit the discussion to the reference photosensitizer (**P**), the novel donor dyad ($\mathbf{D_n–P}$) and the final $\mathbf{D_n–P–A_m}$ triad. Figure 2 depicts the absorption spectra of the new compounds, which display the additive spectral features

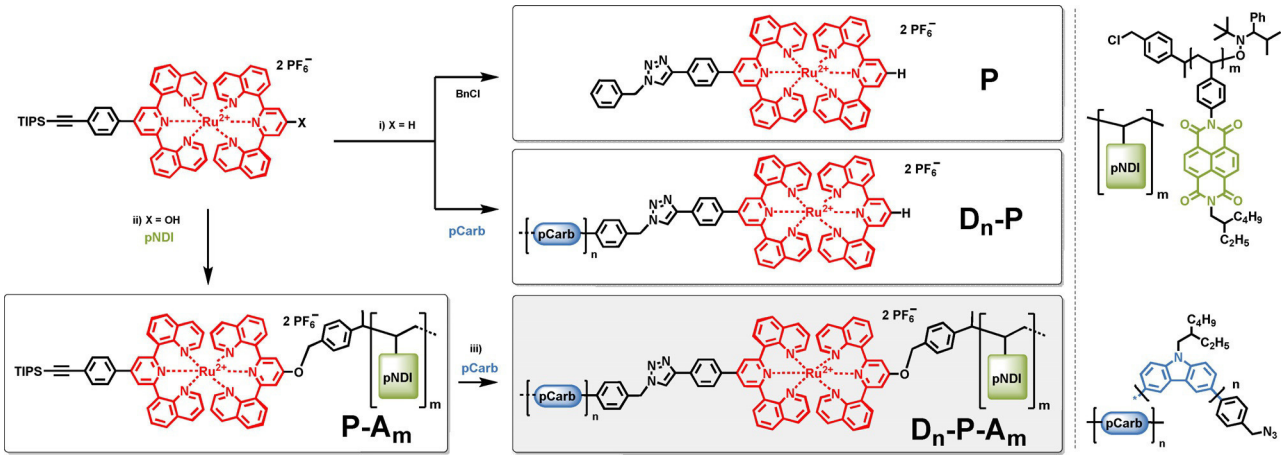

Scheme 1. Modular assembly of the photosystem $\mathbf{D_n–P–A_m}$ (grey shaded) including the reference subsystems **P**, $\mathbf{D_n–P}$, and $\mathbf{P–A_m}$ (black boxes) starting from building blocks: Bis-functionalized Ru-precursor (red) and telechelic polymers **pCarb** (blue) and **pNDI** (green). See right side for chemical structures. Reagents and conditions: i) CuBr, PMDETA, DMF, N_2, 80 °C, 101 h; ii) K_2CO_3, KI, DMF, N_2, 60 °C, 77 h; iii) (a) (nBu$_4$)NF·H_2O, THF, (b) CuBr, PMDETA, DMF, N_2, 80 °C, 96 h.

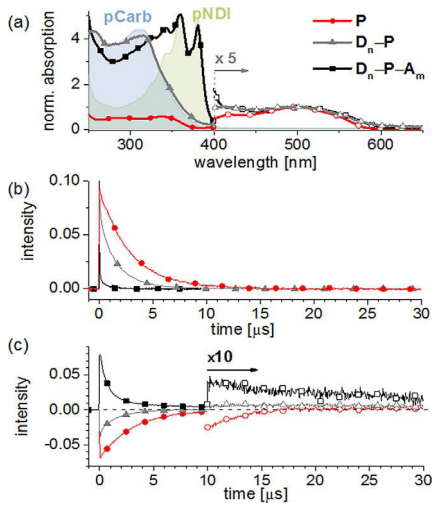

Figure 2. (a) Normalized absorption spectra of $\mathbf{D_n}$–**P** (grey), $\mathbf{D_n}$–**P**–$\mathbf{A_m}$ (black) and **P** (red) in CH_2Cl_2 (solid symbols). The colored-shaded area depicts the absorption spectra of the individual polymers **pCarb** and **pNDI**. Note the scaling (×5) of the ^{1}MLCT region (>400 nm) to assist visibility of Ru-based absorption (hollow symbols). (b) Time-resolved emission in purged CH_2Cl_2 (λ_{exc} = 500 nm, λ_{det} = 750 nm except for **P** with 700 nm). Note the significantly faster quenching of $\mathbf{D_n}$–**P**–$\mathbf{A_m}$ vs. **P** or $\mathbf{D_n}$–**P** (λ_{em} = 700 nm). The red-shifted emission detection was chosen to minimize polymer-based contribution (see text). (c) Transient absorption traces of **P**′, $\mathbf{D_n}$–**P** (470 nm) and $\mathbf{D_n}$–**P**–$\mathbf{A_m}$ (475 nm) indicating the formation of a long-lived charge separated state in the triad. Note, that scaling (×10) after 10 µs to assist visibility (hollow symbols).

of the individual building blocks (Figure S19). The polymers dominate the absorption in the UV region, that is, poly(carbazole) (312 nm) and poly(naphthalene diimide) (360 and 380 nm), whereas the Ru^{II} complex exclusively absorbs above 400 nm and stretching up to 600 nm. Note that these spectral features ensure the selective excitation of the photosensitizer by visible light, which benefits the analysis of the light-induced events with respect to less hierarchically and functionally defined polymer architectures (vide supra).[2] The steady state emission spectra are composed of Ru-based ^{3}MLCT emission (around 690 nm) and polymer-assigned emission below 650 nm (Figure S21), in agreement with reported data of poly(3,6-carbazoles)[37] and poly(naphthalene diimide).[24,25] Upon comparison of the ^{3}MLCT emission of **P** versus $\mathbf{D_n}$–**P**, a noticeable quenching (−25%) was observed (Figure S21), which is assigned to reductive quenching. The poly(3,6-carbazole) exhibits a formal redox potential of 0.22 V vs. $Fc^{+/0}$ (Figure S16), which gives a driving force estimate of +0.24 eV for reductive quenching (see Supporting Information Section 6 for details). Note, that this value represents a conservative upper bound estimate, as the (attractive) coulombic work term and the favorable entropic factors due to multiple donor sites are neglected. Hence, in view of the long excited state lifetimes, the minor reductive quenching pathway cannot be ruled out and the transient absorption data further supports this hypothesis (vide infra). Note, that ^{3}MLCT quenching by energy transfer is unlikely due the unfavorable energetics, as the emission of the poly(carbazole) occurs at higher energies (<650 nm).[37] More importantly, the triad $\mathbf{D_n}$–**P**–$\mathbf{A_m}$ shows an almost quantitative ^{3}MLCT emission quenching by 96% (Figure S22), in excellent agreement with the oxidative quenching that has been previously identified for the **P**–$\mathbf{A_m}$ subsystem.[25] In order to facilitate the unambiguous identification of the charge-separated states in the following section, the spectral signatures of the reduced poly(naphthalene diimide) ($\mathbf{pNDI^-}$) and the oxidized poly(carbazole) ($\mathbf{pCarb^+}$) were determined (see Supporting Information Section 7 for details).

Time-resolved measurements

Next, time-resolved emission and transient absorption (TA) measurements were performed to detail the light-induced charge separation. Representative ^{3}MLCT emission traces of the triad and the references are displayed in Figure 2b. The photosensitizer **P** exhibits a mono-exponential decay with a lifetime of 2.9 µs, while the donor dyad $\mathbf{D_n}$–**P** gives 1.7 µs. The formal decrease in lifetime (−41%) is in qualitative agreement with the decreased steady state emission intensity (−25%).[38] More importantly, the triad $\mathbf{D_n}$–**P**–$\mathbf{A_m}$ features an emission decay on a much shorter time scale (<10 ns, Figure S25), which suggests an almost quantitative oxidative quenching (>99%) based on the lifetimes data. In order to confirm these hypotheses, transient absorption (TA) spectra were recorded in the visible region (10 nm intervals) to identify the intermediately formed states (Figure 3). In the case of **P**, the TA traces decay with a lifetime similar to that obtained from emission measurements (Figure 2c), and the spectral domain shows several isosbestic points (Figure S26). Similarly, the TA signals of $\mathbf{D_n}$–**P** decay with

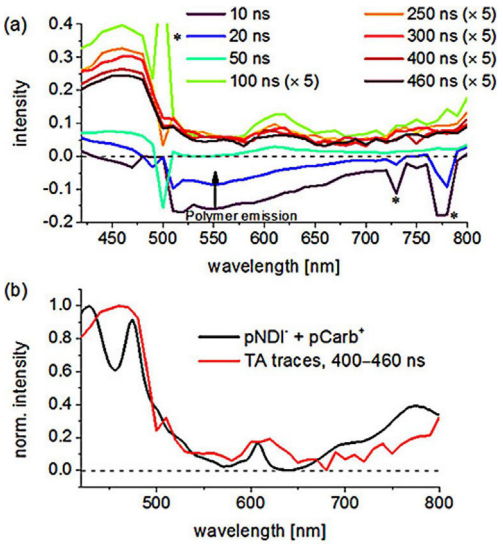

Figure 3. (a) Transient absorption data of $\mathbf{D_n}$–**P**–$\mathbf{A_m}$ from 10 to 460 ns showing the formation of absorption features characteristic for the reduced $\mathbf{pNDI^-}$ (470 and 605 nm) and the oxidized $\mathbf{pCarb^+}$ (430 and above 600 nm) (purged solution, CH_2Cl_2, excitation at 500 nm). Note, that all spectra from 100 to 460 ns were scaled by the factor five to enhance the visibility of the spectral changes. (b) The combined absorption spectra of the reduced $\mathbf{pNDI^-}$ and the oxidized $\mathbf{pCarb^+}$ (see Supporting Information Section 7) resemble the TA traces from 400 to 460 ns and indicate the formation of a charge separated state. Spectral artefacts from pulse and Raman scatter are marked with an asterisk. Spectral intervals are 10 nm.

comparable lifetimes as determined from emission measurements, but the spectral domain revealed an additional component below 700 nm at short timescales (< 30 ns). The origin is traced to polymer-based emission from the corresponding emission profiles (Figure S26a), in excellent agreement with the previously assigned polymer-based emission.[25] At longer time scales, the global fit gives a spectral signature that differs from the photosensitizer due to contributions by reductive quenching. In marked contrast, the triad $\mathbf{D_n–P–A_m}$ shows short-lived Ru emission but long-lived TA signals. The TA decay at 475 nm is best described by a biexponential kinetics with associated lifetimes of 0.7 μs (83%) and 7.2 μs (17%). The faster component is comparable to those of a related molecular triad (< 200 ns) and, thus, is assigned to the corresponding initial charge-separated state. The slower recombination is reasonable in view of the unsaturated flexible linkage to the polymer. More importantly, the long-lived component exhibits the prolonged charge separation by a factor of 3 with respect to the poly(triarylamine)-based (**pTARA**) congener (2.4 μs).[28] In both cases the light-induced charge separation proceeds primarily via oxidative quenching to transfer an electron first to the acceptor chain and subsequently to regenerate the active photosensitizers by secondary electron transfer from the donor chain. Although the linkage pattern is reversed among both triads, which may affect the kinetics of initial oxidative quenching,[39] the recombination of the fully charge separated state depends on the overall distance of the oxidized donor and reduced acceptor units, which would be the same again for both triads. Based on this hypothesis, the observed difference in recombination is interpreted in terms of the different nature of the donor chains. In the case of the **pTARA**-based triad, the redox active units are electronically decoupled through the saturated backbone and the charge migration follows a hoping mechanism. Instead, the **pCarb**-based triad consists of carbazole subunits with sizable electronic coupling. As a consequence, the hole may delocalize more readily,[40] which would facilitate a more efficient spatial charge separation and consequently also the observed diminished recombination rates.

Global analysis

Global fits of the corresponding TA data were performed to discern possible spectral differences and to summarize the transient absorption data (Figure 4). Note, that only the long-lived parts (> 100 ns) were used to exclude contributions from polymer-based emission (< 30 ns, Figure S26). As a consequence, the obtained lifetimes vary slightly but generally reproduce the previous values from selected wavelengths. The photosensitizer **P** features four isosbestic points due to the ^{1}MLCT bleach, positive ^{3}MLCT absorptions and ^{3}MLCT emission. Upon decoration with the donor chain, the $\mathbf{D_n–P}$ dyad features systematic changes of the isosbestic points. The bathochromic shifts around 450 and 700 nm, and the hypsochromic shift at 750 nm are attributed to the interactions between the donor chain and excited photosensitizer. Polymer-based emission should by ceased (vide supra) and, thus, reductive quenching may occur to generate $\mathbf{pCarb^+}$ and $\mathbf{P^-}$. The oxidized polymer

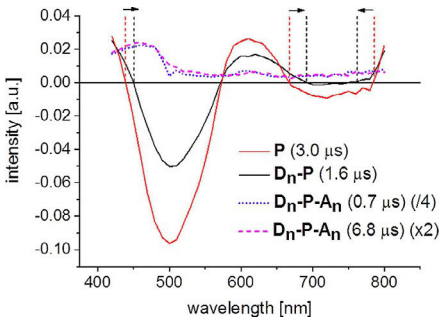

Figure 4. Comparison of TA profiles obtained from the global fit of the TA data with associated lifetimes: P (red, 3.0 μs), $\mathbf{D_n–P}$ (black, 1.6 μs) and $\mathbf{D_n–P–A_m}$ with first (blue, 0.7 μs) and second component (magenta, 6.8 μs). Note the same spectral feature of the two components $\mathbf{D_n–P–A_m}$. Note the indicative shifts of isosbestic points for $\mathbf{D_n–P}$ vs. P marked by dashed lines and arrows.

features positive TA contributions in the NIR region according to the redox titration data (Figure S18), while the reduced Ru complex formally re-populated the ^{1}MLCT bleach. Both features are qualitatively present in the spectral profile. In conjunction with the shorter emission lifetime versus **P**, reductive quenching for $\mathbf{D_n–P}$ on the microsecond time scale cannot be excluded. Finally, the $\mathbf{D_n–P–A}$ shows markedly different spectral components from the previous cases, due to very efficient electron transfer steps to form the fully charge separated state. Both components display identical spectra, which corroborates the previous assignment of long-lived charge separation. However, a further analysis at this stage is precluded, as the repeat units are spectroscopically invariant. In order to confirm charge percolation, we currently pursue the attachment of a distal reporter unit with distinct optical signature. Nevertheless, charge transport within organic semiconductors is well known,[40] and the prolonged CS lifetime between site-isolated poly(triarylamine) versus conjugated poly(carbazole) qualitatively agrees with the anticipated higher charge mobility.

Conclusion

Telechelic redox-active and conjugated polymers were utilized as building blocks to demonstrate the facile assembly to $\mathbf{D_n–P–A_m}$ architectures,[14] which can be regarded as block copolymers with a single interjacent photosensitizer unit. The modularity of the approach was ensured by the orthogonal linkage and the facile purification protocols, which enabled the successful design based on inherent optical and redox-chemical properties of the building blocks. Despite the small scale of prepared material necessary to conduct this study, the modularity and the divergent synthesis permits the scaling for each building block (polymer) independently, and to apply the optimal conditions for the coupling step–which is a strategic advantage over grafting approaches or statistical copolymers leading inevitably to defect sites. Hence, novel functional macromolecules were designed and prepared, which feature optical transparency of the polymers in the visible light region and, thus, the selective excitation of the photosensitizer occurs to assure quantitative light-induced electron transfer. Efficient

charge separation was observed, as unambiguously identified by transient absorption spectroscopy. The charge separated state features a long-lived component with a remarkably long life time component (7 μs), which is assigned to the possibility of charge transfer to other sites. The comparison of a non-conjugated poly(triarylamine) versus conjugated poly(3,6-carbazole) donor chains revealed a lifetime enhancement by a factor of three, which indicates the utility of conjugated polymers to achieve long-lived light-induced charge separation.

In summary, this novel approach towards polymer-based photosystems relies on the divergent preparation of the building blocks, and their versatile post-polymerization linkage through a modern chemistry-on-the-complex approach. As a consequence, libraries of $\mathbf{D_n–P–A_m}$ structures can be readily designed and prepared to independently optimize charge separation and charge transport. Further opportunities include the construction of redox cascades on a molecular level for directional charge transfer,[26] as well as phase separation using hydrophilic/hydrophobic substitution patterns.[23] Hence, the presented method is expected to serve as a versatile platform also for related fields to tailor (photo-)electroactive organo-based materials, for example, OFETs, OLEDs, or to transduce the optical stimulus into a long-lived redox-chemical and or redox-mechanical response.

Experimental Section

Instrumental details, further experimental details, as well as analytical, electrochemical and spectroscopic data can be found in the Supporting Information.

[Ru(dqp)(dqp-ph-trz-pCarb)][PF_6]$_2$ (D_n–P). A vial was charged with **pCarb** (9.00 mg, 2.14 μmol, 1 equiv.) as well as [Ru(dqp)(dqp-ph-C≡C-TIPS)][PF_6]$_2$ (4.29 mg, 4.29 μmol, 2 equiv.), sealed, evacuated and flushed with nitrogen. Then dry DMF (1.00 mL), CuBr (0.62 mg, 4.29 μmol, 2 equiv.) as solution in DMF (0.17 mL) and PMDETA as solution in DMF (0.02 mL, 0.24 M, 2 equiv.) were added. The mixture was stirred for 24 h at RT before the temperature was increased to 60 °C as no conversion was detected by UV/Vis-SEC. After additional 24 h the temperature was increased to 80 °C and stirring was continued for 53 h until no further conversion was detected. The reaction mixture was precipitated in an aqueous solution of NH_4PF_6. Then CH_2Cl_2 was added and the aqueous phase was extracted. The combined organic extracts were dried over Na_2SO_4, filtered and concentrated under reduced pressure. The crude product was purified by preparative SEC using the Toyopearl HW-50F resin (2 mg (pure product) + 3 mg (product + minor impurities of the starting complex)). ^{1}H NMR (400 MHz, CD_2Cl_2): δ = 8.75–8.30 (br, pCarb), 8.30–7.95 (br, Ru), 7.95–7.80 (br, pCarb), 7.80–7.62 (br, Ru), 7.62–7.31 (br, pCarb + Ru), 7.31–6.87 (br, pCarb + Ru), 4.34–3.88 (br, pCarb), 2.37–1.93 (br, pCarb), 1.52–1.0 (br, pCarb) 0.97–0.88 (br, pCarb).

[Ru(dqp-*O*-pNDI)(dqp-ph-C≡C-TIPS)][PF_6]$_2$ (P–A_m). A vial was charged with **pNDI** (0.070 g, 0.008 mmol, 1 equiv.), K_2CO_3 (0.001 g, 0.032 mmol, 4 equiv.), KI (0.003 g, 0.016 mmol, 2 equiv.) and [Ru(dqp-ph-C≡CH)(dqpOH)][PF_6]$_2$ (0.018 g, 0.014 mmol, 1.7 equiv.), sealed and placed under a nitrogen atmosphere. Dry DMF (1.0 mL) was added and the resulting solution was heated to 60 °C. The reaction progress was monitored by TLC (aluminum oxide, CH_2Cl_2/MeOH 95:5) and analytical size exclusion chromatography (DMAc + 0.08% NH_4PF_6, diode array detection). The reaction was continued until no further conversion was monitored by TLC (77 h). The mixture was diluted with a minimum amount of THF and precipitated into aqueous NH_4PF_6 solution. The red precipitate was re-dissolved in CH_2Cl_2 and water. The layers were separated and the aqueous phase was further extracted with CH_2Cl_2 (3×). The combined organic batches were washed with brine, dried over Na_2SO_4 and concentrated under reduced pressure. Preparative size-exclusion chromatography (Toyopearl HW-55F, CH_2Cl_2/MeOH 95:5) gave the dyad **D2** as red solid (0.060 g, 75%). ^{1}H NMR (300 MHz, CD_2Cl_2): δ 9.11–8.17 (br, pNDI), 8.11 (br, Ru), 8.08 (br, Ru), 7.91 (br, Ru), 7.71 (br, Ru), 7.63–6.47 (br, pNDI), 5.61–5.48 (br, linker), 4.38–3.73 (br, pNDI), 3.17–1.56 (br, pNDI), 1.56–1.03(br, pNDI), 1.19 (s, TIPS), 1.03–0.34 (br, pNDI).

Deprotection. A vial was charged with **D2** (0.058 g, 0.058 mmol) and THF (3 mL) and the resulting solution was cooled to 0 °C. Then tetra-*n*-butylammonium fluoride (0.002 g, 0.007 mmol, 1.2 equiv.) was added as solution in THF (0.150 mL) and the reaction mixture was stirred for 30 minutes. Subsequently the reaction was quenched with water and the mixture was precipitated in an aqueous NH_4PF_6 solution. The aqueous phase was extracted with CH_2Cl_2. The combined organic extracts were concentrated under reduced pressure. The red solid was used without further purification (0.058 g, 100%). ^{1}H NMR (300 MHz, CD_2Cl_2): δ 9.04–8.15 (br, pNDI), 8.06 (br, Ru), 8.02 (br, Ru), 7.82 (br, Ru), 7.71 (br, Ru), 7.48 (br, Ru), 7.63–6.58 (br, pNDI), 5.59–5.46 (br, linker), 4.42–3.77 (br, pNDI), 3.04–1.55 (br, pNDI), 1.55–1.12 (br, pNDI), 1.00–0.59 (br, pNDI).

[Ru(dqp-*O*-pNDI)(dqp-ph-trz-pCarb)][PF_6]$_2$ (D_n–P–A_m). A vial was charged with **P–A_m** (0.015 g, 0.0015 mmol, 1 equiv.) and **pCarb** (0.019 g, 0.0045 mmol, 3 equiv.), sealed and place under a nitrogen atmosphere. Then dry DMF (1.5 mL), a solution of copper(I) bromide (0.0004 g, 0.003 mmol, 2 equiv.) in DMF (0.160 mL) and a solution of PMDETA (0.013 mL, 2 equiv., 0.24 M in DMF) were added. The reaction mixture was heated to 80 °C for 96 h. After cooling to room temperature, the solution was precipitated in an aqueous NH_4PF_6 solution and the aqueous layer was extracted with CH_2Cl_2 (4×). The combined organic phases were dried over Na_2SO_4 and concentrated under reduced pressure. Purification by preparative size-exclusion chromatography (Toyopearl HW-55F) gave the product as red solid (0.004 g, 19% + 0.010 g, 48% (with minor impurities of the dyad after first purification run) ^{1}H NMR (300 MHz, CD_2Cl_2): δ = 8.88–8.15 (br, pCarb + pNDI), 8.06 (br, Ru), 7.85 (br, Ru + pCarb), 7.66 (br, Ru), 7.43 (br, Ru), 7.61–6.60 (br, pCarb + pNDI), 5.17–5.07 (br, linker), 4.48–3.71 (br, pCarb + pNDI), 3.08–1.71 (br, pNDI), 1.42–1.01 (br, pCarb + pNDI), 1.01–0.54 (br, pCarb + pNDI).

Acknowledgements

Financial support by the Friedrich Schiller University Jena ("Nachwuchsförderung") and the Thüringer Ministerium für Wirtschaft, Wissenschaft und Digitale Gesellschaft (TMWWDG) is kindly acknowledged. The authors thank Annett Urbanek for MALDI-ToF measurements as well as Dr. Peter Bellstedt and the NMR platform of the IAAC/IOMC for help with the NMR measurements.

Conflict of interest

The authors declare no conflict of interest.

Keywords: complex chemistry · donor–acceptor systems · electron transfer · ruthenium · time-resolved spectroscopy

[1] V. Balzani, L. Moggi, M. F. Manfrin, F. Bolletta, M. Gleria, *Science* **1975**, *189*, 852 – 856.
[2] J. H. Alstrum-Acevedo, M. K. Brennaman, T. J. Meyer, *Inorg. Chem.* **2005**, *44*, 6802 – 6827.
[3] V. Balzani, A. Credi, M. Venturi, *ChemSuSchem* **2008**, *1*, 26 – 58.
[4] J. J. Concepcion, R. L. House, J. M. Papanikolas, T. J. Meyer, *Proc. Natl. Acad. Sci. USA* **2012**, *109*, 15560 – 15564.
[5] V. Balzani, G. Bergamini, P. Ceroni, *Angew. Chem. Int. Ed.* **2015**, *54*, 11320 – 11337; *Angew. Chem.* **2015**, *127*, 11474 – 11492.
[6] L. Hammarström, *Acc. Chem. Res.* **2015**, *48*, 840 – 850.
[7] N. S. Hush, *Coord. Chem. Rev.* **1985**, *64*, 135 – 157.
[8] B. Albinsson, J. Martensson, *J. Photochem. Photobiol., C* **2008**, 9, 138 – 155.
[9] M. Gilbert, B. Albinsson, *Chem. Soc. Rev.* **2015**, *44*, 845 – 862.
[10] M. Natali, S. Campagna, F. Scandola, *Chem. Soc. Rev.* **2014**, *43*, 4005 – 4018.
[11] O. S. Wenger, *Coord. Chem. Rev.* **2009**, *253*, 1439 – 1457.
[12] H. Imahori, D. M. Guldi, K. Tamaki, Y. Yoshida, C. P. Luo, Y. Sakata, S. Fukuzumi, *J. Am. Chem. Soc.* **2001**, *123*, 6617 – 6628.
[13] D. W. Thompson, A. Ito, T. J. Meyer, *Pure Appl. Chem.* **2013**, *85*, 1257 – 1305.
[14] R. Schroot, M. Jager, U. S. Schubert, *Chem. Soc. Rev.* **2017**, DOI: 10.1039/C1036CS00811A.
[15] S. E. Bettis, D. M. Ryan, M. K. Gish, L. Alibabaei, T. J. Meyer, M. L. Waters, J. M. Papanikolas, *J. Phys. Chem. C* **2014**, *118*, 6029 – 6037.
[16] D. Ma, S. E. Bettis, K. Hanson, M. Minakova, L. Alibabaei, W. Fondrie, D. M. Ryan, G. A. Papoian, T. J. Meyer, M. L. Waters, J. M. Papanikolas, *J. Am. Chem. Soc.* **2013**, *135*, 5250 – 5253.
[17] Z. A. Morseth, L. Wang, E. Puodziukynaite, G. Leem, A. T. Gilligan, T. J. Meyer, K. S. Schanze, J. R. Reynolds, J. M. Papanikolas, *Acc. Chem. Res.* **2015**, *48*, 818 – 827.
[18] G. Leem, S. Keinan, J. Jiang, Z. Chen, T. Pho, Z. A. Morseth, Z. Hu, E. Puodziukynaite, Z. Fang, J. M. Papanikolas, J. R. Reynolds, K. S. Schanze, *Polym. Chem.* **2015**, *6*, 8184 – 8193.
[19] Z. Fang, A. Ito, H. Luo, D. L. Ashford, J. J. Concepcion, L. Alibabaei, T. J. Meyer, *Dalton Trans.* **2015**, *44*, 8640 – 8648.
[20] E. Puodziukynaite, L. Wang, K. S. Schanze, J. M. Papanikolas, J. R. Reynolds, *Polym. Chem.* **2014**, *5*, 2363 – 2369.
[21] G. Leem, Z. A. Morseth, E. Puodziukynaite, J. Jiang, Z. Fang, A. T. Gilligan, J. R. Reynolds, J. M. Papanikolas, K. S. Schanze, *J. Phys. Chem. C* **2014**, *118*, 28535 – 28541.
[22] L. Wang, E. Puodziukynaite, E. M. Grumstrup, A. C. Brown, S. Keinan, K. S. Schanze, J. R. Reynolds, J. M. Papanikolas, *J. Phys. Chem. Lett.* **2013**, *4*, 2269 – 2273.
[23] R. Schroot, T. Schlotthauer, M. Jäger, U. S. Schubert, *Macromol. Chem. Phys.* **2017**, 1600534-n/a.
[24] R. Schroot, T. Schlotthauer, U. S. Schubert, M. Jäger, *Macromolecules* **2016**, *49*, 2112 – 2123.
[25] J. Kübel, R. Schroot, M. Wächtler, U. S. Schubert, B. Dietzek, M. Jäger, *J. Phys. Chem. C* **2015**, *119*, 4742 – 4751.
[26] R. Schroot, U. S. Schubert, M. Jäger, *Macromolecules* **2015**, *48*, 1963 – 1971.
[27] R. Schroot, C. Friebe, E. Altuntas, S. Crotty, M. Jäger, U. S. Schubert, *Macromolecules* **2013**, *46*, 2039 – 2048.
[28] T. Schlotthauer, R. Schroot, S. Glover, L. Hammarström, M. Jäger, U. S. Schubert, *PCCP*, DOI: 10.1039/C7CP05593E.
[29] E. M. Barea, G. Garcia-Belmonte, M. Sommer, S. Hüttner, H. J. Bolink, M. Thelakkat, *Thin Solid Films* **2010**, *518*, 3351 – 3354.
[30] J. Veres, S. D. Ogier, S. W. Leeming, D. C. Cupertino, S. Mohialdin Khaffaf, *Adv. Funct. Mater.* **2003**, *13*, 199 – 204.
[31] A. J. Heeger, *Chem. Soc. Rev.* **2010**, *39*, 2354 – 2371.
[32] C. Liao, F. Yan, *Polym. Rev.* **2013**, *53*, 352 – 406.
[33] J.-F. Morin, M. Leclerc, D. Adès, A. Siove, *Macromol. Rapid Commun.* **2005**, *26*, 761 – 778.
[34] Y. He, W. Hong, Y. Li, *J. Mater. Chem. C* **2014**, *2*, 8651 – 8661.
[35] X. Guo, M. Baumgarten, K. Muellen, *Prog. Polym. Sci.* **2013**, *38*, 1832 – 1908.
[36] R. Schroot, U. S. Schubert, M. Jäger, *Macromolecules* **2017**, *50*, 1319 – 1330.
[37] Y. C. Chen, G. S. Huang, C. C. Hsiao, S. A. Chen, *J. Am. Chem. Soc.* **2006**, *128*, 8549 – 8558.
[38] Note the unknown quantum yields of the photosensitzer and the donor dyad, which influence the observed steady state emission intensity in addition to the quenching pathways.
[39] Y. Luo, K. Barthelmes, M. Wächtler, A. Winter, U. S. Schubert, B. Dietzek, *Chem. Eur. J.* **2017**, *23*, 4917 – 4922.
[40] H. Baessler, A. Koehler in *Unimolecular and Supramolecular Electronics I: Chemistry and Physics Meet at Metal-Molecule Interfaces* Springer-Verlag Berlin Heidelberg, **2012**, 312, 1 – 65.

Manuscript received: September 6, 2017
Accepted manuscript online: September 8, 2017
Version of record online: November 2, 2017